

*Analysis and Design of Integrated Circuit–Antenna Modules.*

Edited by K.C. Gupta, Peter S. Hall

Copyright © 2000 John Wiley & Sons, Inc.

ISBNs: 0-471-19044-6 (Hardback); 0-471-21667-4 (Electronic)

# **Analysis and Design of Integrated Circuit– Antenna Modules**

---

# Analysis and Design of Integrated Circuit– Antenna Modules

---

Edited by

**K. C. GUPTA**

*University of Colorado*

**PETER S. HALL**

*University of Birmingham*



A WILEY-INTERSCIENCE PUBLICATION

**JOHN WILEY & SONS, INC.**

NEW YORK/CHICHESTER/WEINHEIM/BRISBANE/SINGAPORE/TORONTO

Designations used by companies to distinguish their products are often claimed as trademarks. In all instances where John Wiley & Sons, Inc., is aware of a claim, the product names appear in initial capital or ALL CAPITAL LETTERS. Readers, however, should contact the appropriate companies for more complete information regarding trademarks and registration.

Copyright © 2000 by John Wiley & Sons, Inc. All rights reserved.

No part of this publication may be reproduced, stored in a retrieval system or transmitted in any form or by any means, electronic or mechanical, including uploading, downloading, printing, decompiling, recording or otherwise, except as permitted under Sections 107 or 108 of the 1976 United States Copyright Act, without the prior written permission of the Publisher. Requests to the Publisher for permission should be addressed to the Permissions Department, John Wiley & Sons, Inc., 605 Third Avenue, New York, NY 10158-0012, (212) 850-6011, fax (212) 850-6008, E-Mail: PERMREQ @ WILEY.COM.

This publication is designed to provide accurate and authoritative information in regard to the subject matter covered. It is sold with the understanding that the publisher is not engaged in rendering professional services. If professional advice or other expert assistance is required, the services of a competent professional person should be sought.

**ISBN 0-471-21667-4**

This title is also available in print as ISBN 0-471-19044-6.

For more information about Wiley products, visit our web site at [www.Wiley.com](http://www.Wiley.com).

---

# Contributors

---

**Eric W. Bryerton**, Department of Electrical and Computer Engineering, University of Colorado at Boulder, Campus Box 425, Boulder, CO 80309-0425

**Jacques Citerne**, LCST, INSA Rennes, CNRS UPRES A6075, 20 Avenue des Buttes de Coesmes, 3043 Rennes, France

**Martin J. Cryan**, Dipartimento di Ingegneria Electronica e dell'Informazione, Università degli Studi di Perugia, Perugia, Italy

**M'hamed Drissi**, LCST, INSA Rennes, CNRS UPRES A6075, 20 Avenue des Buttes de Coesmes, 3043 Rennes, France

**Vincent F. Fusco**, Department of Electrical and Electronic Engineering, Queens University of Belfast, Ashby Building, Stranmillis Road, Belfast BT7 1NN, UK

**Hooshang Ghafouri-Shiraz**, School of Electronic and Electrical Engineering, The University of Birmingham, Edgbaston, Birmingham B15 2TT, UK

**Raphael Gillard**, LCST, INSA Rennes, CNRS UPRES A6075, 20 Avenue des Buttes de Coesmes, 3043 Rennes, France

**K. C. Gupta**, Department of Electrical and Computer Engineering, University of Colorado at Boulder, Campus Box 425, Boulder, CO 80309-0425

**Peter S. Hall**, School of Electronic and Electrical Engineering, The University of Birmingham, Edgbaston, Birmingham B15 2TT, UK

**Tatsuo Itoh**, Center for High Frequency Electronics, Department of Electronics, Department of Electrical Engineering, 405 Hilgard Avenue, University of California, Los Angeles, CA 90095

**Rajan P. Parrikar**, Space Systems/LORAL, 3825 Fabian Way, Palo Alto, CA 94303

**Zoya Popović**, Department of Electrical and Computer Engineering, University of Colorado at Boulder, Boulder, CO 80309-0425

**Yongxi Qian**, Center for High Frequency Electronics, Department of Electronics, Department of Electrical Engineering, 405 Hilgard Avenue, University of California, Los Angeles, CA 90095

**Wayne A. Shiroma**, Department of Electrical Engineering, 2540 Dole Street, University of Hawaii, Honolulu, HI 96822

**Lawrence R. Whicker**, LRW Associates, P.O. Box 2530, Matthews, NC 28106

**Robert A. York**, Department of Electrical Engineering, University of California, Santa Barbara, CA 93106

---

# Contents

---

<b>1</b>	<b>Introduction</b>	<b>1</b>
	Peter S. Hall and K. C. Gupta	
1.1	Development of Circuit–Antenna Modules	1
1.2	Terminology Used in Circuit–Antenna Modules	3
1.3	Applications of Circuit–Antenna Modules	4
1.4	Glossary of Circuit–Antenna Module Types	6
1.5	Levels of Integration	6
1.6	The Design Process	14
1.7	Analytical Outcomes and Circuit–Antenna Module Performance Parameters	16
1.8	Overview of the Book	17
	References	20
<b>2</b>	<b>Review of the CAD Process</b>	<b>23</b>
	K. C. Gupta and Peter S. Hall	
2.1	The Design Process	23
2.2	CAD for Microwave Circuits	29
2.3	CAD for Printed Microwave Antennas	47
2.4	CAD Considerations for Integrated Circuit–Antenna Modules	61
2.5	Summary	67
	References	67
<b>3</b>	<b>Circuit Simulator Based Methods</b>	<b>72</b>
	Peter S. Hall, Vincent F. Fusco, and Martin J. Cryan	
3.1	Introduction to Equivalent Circuit Simulation	72
3.2	Linear Simulation Using Equivalent Circuit Models	83
3.3	Nonlinear Simulation Using Equivalent Circuit Models	97
3.4	Conclusions	116
	References	117

<b>4</b>	<b>Multiport Network Method</b>	<b>121</b>
	K. C. Gupta and Rajan P. Parrikar	
4.1	Introduction: Network Modeling of Antennas	121
4.2	Multiport Network Model (MNM) for Microstrip Patches	122
4.3	MNM for Two-Layer Microstrip Antennas	147
4.4	MNM for Integrated Circuit–Antenna Modules	161
4.5	Summary and Remarks	167
	References	168
<b>5</b>	<b>Full Wave Analysis in the Frequency Domain</b>	<b>172</b>
	Raphael Gillard, M’hamed Drissi, and Jacques Citerne	
5.1	Introduction	172
5.2	Lumped Elements in the Method of Moments	174
5.3	Analysis of Active Linear Circuits and Antennas	189
5.4	Extension of the Approach to Nonlinear Devices	211
5.5	Conclusion	217
	References	219
<b>6</b>	<b>Full Wave Electromagnetic Analysis in the Time Domain</b>	<b>222</b>
	Yongxi Qian and Tatsuo Itoh	
6.1	Introduction	222
6.2	FDTD Fundamentals and Implementation Issues	224
6.3	FDTD Analysis of Passive Circuits and Antennas	241
6.4	Extended FDTD for Active Circuits and Integrated Antennas	249
	References	256
<b>7</b>	<b>Phase-Locking Dynamics in Integrated Antenna Arrays</b>	<b>259</b>
	Robert A. York	
7.1	Introduction	259
7.2	Systems of Coupled Oscillators	260
7.3	Scanning by Edge Detuning	272
7.4	Externally Locked Arrays	280
7.5	Phase Noise in Oscillator Arrays	283
7.6	PLL Techniques	291
7.7	Perspective	295
	Appendix: Kurokawa’s Substitution	296
	References	298

<b>8</b>	<b>Analysis and Design of Oscillator Grids and Arrays</b>	<b>301</b>
	Wayne A. Shiroma, Eric W. Bryerton, and Zoya Popović	
8.1	Introduction	301
8.2	Full-Wave Modeling of Planar Grids	304
8.3	Grid Oscillator Analysis	308
8.4	Synthesis of the Optimum Grid Equivalent Circuit	314
8.5	Benchmarking Grid Oscillator Performance	317
8.6	Optimizing Grid Performance	320
8.7	Oscillator Design Using Power Amplifier Techniques	323
8.8	Conclusion	328
	References	330
<b>9</b>	<b>Analysis and Design Considerations for Monolithic Microwave Circuit Transmit–Receive (T–R) Modules</b>	<b>333</b>
	Lawrence R. Whicker	
9.1	Introduction	333
9.2	Present Developments on Active T–R Modules	341
9.3	T–R Module Design Considerations	342
9.4	Present Trends and Future Directions	350
	References	357
<b>10</b>	<b>Integrated Transmit–Receive Circuit–Antenna Modules for Radio on Fiber Systems</b>	<b>358</b>
	Hooshang Ghafouri-Shiraz	
10.1	System Requirements for Radio on Fiber	359
10.2	Optical Generation of Millimeter-Wave Signals	360
10.3	Optical Detection of Millimeter-Wave Signals	369
10.4	New Configurations for Radios on Fiber Systems	372
10.5	Design of Diplexer–Antenna Unit	375
10.6	PhotoHBT–Patch Antenna Integration	386
10.7	RF Transmit–Receive Module for the Radio on Fiber System	394
10.8	Summary and Concluding Remarks	404
	References	407
<b>11</b>	<b>Conclusions</b>	<b>410</b>
	Peter S. Hall and K. C. Gupta	
11.1	Introduction	410
11.2	Overview of Analytical Methods	411
11.3	The Future	415
	References	416
	<b>Index</b>	<b>419</b>



---

# Preface

---

The latest breakthrough in the continuing miniaturization of electronic systems is made possible by the integration of circuit functions and radiating elements into single modules. In a typical system implementation, electronic circuits and antenna subsystems are often provided by different equipment vendors. Traditionally, electronic circuits and antenna systems have been designed by different groups of designers using different types of design tools, working independently on either side of a well-defined interface, very often with very little interaction. This approach leads to separately packaged circuit and antenna subsystems, connected by appropriate cables or waveguides.

Integration of circuits and antennas into single modules has been made possible by the common technological features of radio frequency (RF) and microwave circuits and printed microstrip antennas. The basic microstrip technology used for the design of microstrip lines and other planar transmission structures (used extensively in hybrid and monolithic microwave integrated circuits) has been the cornerstone for the development of microstrip antennas. Using the commonality in technology to combine circuit and antenna functions in single modules represents a significant step in further miniaturization of RF and microwave modules for a variety of applications including active phased arrays and wireless communication systems. So-called quasi-optic systems that are used by grid arrays to generate high powers at millimeter wavelengths are another important example. In several of these areas, the use of circuit–antenna modules is sufficiently well developed that designers are now requiring computer based tools for analysis, synthesis, and simulation. The need for a book bringing these aspects together is thus apparent and we hope that this volume is a timely contribution.

Traditionally, microwave circuit designers and antenna designers have used different types of design tools. However, the design of integrated circuit–antenna modules calls for concurrent design of both the circuit and antenna functions. Such design requires a new set of design tools applicable to both domains or a hybrid combination of tools so far used separately for circuit and antenna designs.

Analysis of circuit–antenna modules requires an appreciation of the various analytical methods and their application, but also some understanding of the

technology types and their application. In addressing these two needs, it is necessary first to set the scene and to lay some foundation, then to give a detailed account of analytic methods, and finally to review some operational and technology types that have very specific and somewhat different analytical needs. This is the framework we have adopted in putting this book together. After the introductory chapter, the CAD process is reviewed. Four types of analysis methods are then described in detail. Although not exhaustive, these chapters are representative of the various methods currently being studied. Two chapters are then devoted to an analysis of very specific configurations, namely, injection locked oscillator arrays and grid based structures. The following two chapters indicate some important applications. They are devoted to monolithic based modules and modules incorporating optical control. The book is then drawn together in a concluding chapter.

Chapter 1 serves to set the context of the analysis of circuit–antenna modules. The development of such modules is described together with some explanation of the terminology currently used. A glossary of types is presented. This chapter aims to show the range of configurations currently being studied and to highlight the design challenges. The likely design parameters are then given, together with a review of the design process for which analysis tools have to be developed. Finally, an overview of the book chapters is given.

In order to develop designs for integrated circuit–antenna modules, an appreciation of the computer-aided design process is necessary. Chapter 2 starts with a discussion of the design process in general. Conventional design, computer-aided design, and knowledge based design approaches are outlined. Separate CAD procedures for microwave circuits and printed microstrip antennas, as practiced conventionally, are described. Then the discussion converges on CAD considerations for integrated circuit–antenna modules implemented at various levels of integration (nonintegrated, partially integrated, and fully integrated).

Simulations based on equivalent circuit analysis methods can provide fast results with sufficient accuracy for first-pass designs. Chapter 3 gives an introduction to equivalent circuit modeling of circuits and antennas. Both linear and nonlinear simulations are described with examples including oscillating patch antennas, amplified patches, frequency doubling transponders, and oscillator locking.

The multiport network method offers enhanced accuracy compared with simple equivalent circuit methods and can be integrated with active device models. Chapter 4 introduces the concept of the multiport network model as developed for single-layer and two-layer microstrip patch antennas. Applications of the multiport network method to integrated circuit–antenna modules are discussed.

The field integral equation solved by the method of moments is now a well-established tool for antenna and passive circuit analysis. The inclusion of lumped elements has been described some time ago. In Chapter 5, the description is extended to nonlinear structures such as diodes and transistors, with results showing good agreement with measurements. The transmission line matrix (TLM) and the finite difference time domain (FDTD) method are two numerical techniques that overcome the need for the large matrix inversion necessary for the method of

moments. Of the two, the FDTD method is extremely simple to implement and very flexible. Chapter 6 outlines the method and its extension to active integrated antennas.

Injection locked integrated antenna arrays possess dynamic characteristics that are attractive for many applications, such as simple beam scanning and reduced phase noise. Their behavior cannot be easily analyzed using the above methods, so simplified equivalent circuit methods have to be used. In Chapter 7, the dynamic behavior is comprehensively described using such methods.

Grid structures now offer the possibility of providing most of the functionality of transmitter and receiver components in a distributed array form with interconnections by quasi-optical beams. The advantages are very efficient power combining, graceful degradation, increased dynamic range, and reduced noise figures. In Chapter 8, analysis using full wave methods combined with equivalent circuit device models is described. By way of example, oscillator synthesis and grid optimization are successfully performed.

One of the major challenges for circuit-antenna modules is the phased array element fabricated entirely in monolithic technology, in which the transceiver and antenna are both contained on the same chip. This poses what is perhaps the ultimate test of an analysis or simulation tool. To set the scene for further research and development in this area, the requirements for phased array modules are reviewed in Chapter 9. The coverage ranges from conventional phased arrays with separate transceiver and antenna to more recent integrated configurations.

Circuit-antenna modules can form a low cost component in the wireless local access into fiber optic based networks, to provide high capacity services to domestic or office users. Chapter 10 reviews this important application area and gives examples of the analysis challenges inherent in their design. One such challenge is the accurate design of filters for separation of the local oscillator from the signal, in the presence of the antenna. In this work the equivalent circuit based methods, described in Chapter 3, are used and the strengths and weaknesses of this approach are noted.

A short chapter in which some conclusions are drawn completes the book. The current status of computer-aided design tools is summarized from the earlier chapters. Some thoughts on the likely future challenges that analysis will face are then given. The chapter concludes with comments on what now remains to be done to present designers with a full and flexible array of software to facilitate fast and accurate design.

Recognition of the need for preparing a book on this topic emerged out of the two workshops on this subject organized by the two editors of this book and presented at the 1995 IEEE International Microwave Symposium in Orlando and the 1995 IEEE International Symposium on Antennas and Propagation held at Newport Beach. Both of these workshops were very well received and discussion brought out the need for making a book on the analysis and design of integrated circuit-antenna modules available to a wider audience. The present book is the result of those suggestions.

This book results from the joint efforts of the sixteen contributors in eleven different institutions in the United States and Europe. A book on an emerging topic like integrated circuit–antenna modules would not have been possible without such collaboration. We are grateful to colleagues and the administrations in these institutions for the support needed for such a project. Specifically, at the University of Colorado, we thank Ms. Ann Geesaman who very efficiently handled the administrative chores involved.

*University of Colorado at Boulder*  
*University of Birmingham, UK*

K. C. GUPTA  
PETER S. HALL

# **Analysis and Design of Integrated Circuit– Antenna Modules**

---

## WILEY SERIES IN MICROWAVE AND OPTICAL ENGINEERING

---

**KAI CHANG**, Editor  
*Texas A&M University*

- FIBER-OPTIC COMMUNICATION SYSTEMS, Second Edition • *Govind P. Agrawal*
- COHERENT OPTICAL COMMUNICATIONS SYSTEMS • *Silvello Betti, Giancarlo De Marchis and Eugenio Iannone*
- HIGH-FREQUENCY ELECTROMAGNETIC TECHNIQUES: RECENT ADVANCES AND APPLICATIONS • *Asoke K. Bhattacharyya*
- COMPUTATIONAL METHODS FOR ELECTROMAGNETICS AND MICROWAVES • *Richard C. Booton, Jr.*
- MICROWAVE RING CIRCUITS AND ANTENNAS • *Kai Chang*
- MICROWAVE SOLID-STATE CIRCUITS AND APPLICATIONS • *Kai Chang*
- DIODE LASERS AND PHOTONIC INTEGRATED CIRCUITS • *Larry Coldren and Scott Corzine*
- MULTICONDUCTOR TRANSMISSION-LINE STRUCTURES: MODAL ANALYSIS TECHNIQUES • *J. A. Brandão Faria*
- PHASED ARRAY-BASED SYSTEMS AND APPLICATIONS • *Nick Fourikis*
- FUNDAMENTALS OF MICROWAVE TRANSMISSION LINES • *Jon C. Freeman*
- OPTICAL SEMICONDUCTOR DEVICES • *Mitsuo Fukuda*
- MICROSTRIP CIRCUITS • *Fred Gardiol*
- HIGH-SPEED VLSI INTERCONNECTIONS: MODELING, ANALYSIS, AND SIMULATION • *A. K. Goel*
- FUNDAMENTALS OF WAVELETS: THEORY, ALGORITHMS, AND APPLICATIONS • *Jaideva C. Goswami and Andrew K. Chan*
- ANALYSIS AND DESIGN OF INTEGRATED CIRCUIT ANTENNA MODULES • *K. C. Gupta and Peter S. Hall*
- PHASED ARRAY ANTENNAS • *R. C. Hansen*
- HIGH-FREQUENCY ANALOG INTEGRATED CIRCUIT DESIGN • *Ravender Goyal (ed.)*
- MICROWAVE APPROACH TO HIGHLY IRREGULAR FIBER OPTICS • *Huang Hung-Chia*
- NONLINEAR OPTICAL COMMUNICATION NETWORKS • *Eugenio Iannone, Francesco Matera, Antonio Mecozzi, and Marina Settembre*
- FINITE ELEMENT SOFTWARE FOR MICROWAVE ENGINEERING • *Tatsuo Itoh, Giuseppe Pelosi and Peter P. Silvester (eds.)*
- SUPERCONDUCTOR TECHNOLOGY: APPLICATIONS TO MICROWAVE, ELECTRO-OPTICS, ELECTRICAL MACHINES, AND PROPULSION SYSTEMS • *A. R. Jha*
- OPTICAL COMPUTING: AN INTRODUCTION • *M. A. Karim and A. S. S. Awwal*
- INTRODUCTION TO ELECTROMAGNETIC AND MICROWAVE ENGINEERING • *Paul R. Karmel, Gabriel D. Colef, and Raymond L. Camisa*
- MILLIMETER WAVE OPTICAL DIELECTRIC INTEGRATED GUIDES AND CIRCUITS • *Shiban K. Koul*
- MICROWAVE DEVICES, CIRCUITS AND THEIR INTERACTION • *Charles A. Lee and G. Conrad Dalman*
- ADVANCES IN MICROSTRIP AND PRINTED ANTENNAS • *Kai-Fong Lee and Wei Chen (eds.)*
- OPTICAL FILTER DESIGN AND ANALYSIS: A SIGNAL PROCESSING APPROACH • *Christi K. Madsen and Jian H. Zhao*

OPTOELECTRONIC PACKAGING • A. R. Mickelson, N. R. Basavanthally, and Y. C. Lee (eds.)  
OPTICAL CHARACTER RECOGNITION • Shunji Mori, Hirobumi Nishida, and Hiromitsu Yamada  
ANTENNAS FOR RADAR AND COMMUNICATIONS: A POLARIMETRIC APPROACH • Harold Mott  
INTEGRATED ACTIVE ANTENNAS AND SPATIAL POWER COMBINING • Julio A. Navarro and Kai Chang  
FREQUENCY CONTROL OF SEMICONDUCTOR LASERS • Motoichi Ohtsu (ed.)  
SOLAR CELLS AND THEIR APPLICATIONS • Larry D. Partain (ed.)  
ANALYSIS OF MULTICONDUCTOR TRANSMISSION LINES • Clayton R. Paul  
INTRODUCTION TO ELECTROMAGNETIC COMPATIBILITY • Clayton R. Paul  
ELECTROMAGNETIC OPTIMIZATION BY GENETIC ALGORITHMS • Yahya Rahmat-Samii and Eric Michielssen (eds.)  
INTRODUCTION TO HIGH-SPEED ELECTRONICS AND OPTOELECTRONICS • Leonard M. Riazat  
NEW FRONTIERS IN MEDICAL DEVICE TECHNOLOGY • Arye Rosen and Harel Rosen (eds.)  
ELECTROMAGNETIC PROPAGATION IN MULTI-MODE RANDOM MEDIA • Harrison E. Rowe  
ELECTROMAGNETIC PROPAGATION IN ONE-DIMENSIONAL RANDOM MEDIA • Harrison E. Rowe  
NONLINEAR OPTICS • E. G. Sauter  
INP-BASED MATERIALS AND DEVICES: PHYSICS AND TECHNOLOGY • Osamu Wada and Hideki Hasegawa (eds.)  
DESIGN OF NONPLANAR MICROSTRIP ANTENNAS AND TRANSMISSION LINES • Kin-Lu Wong  
FREQUENCY SELECTIVE SURFACE AND GRID ARRAY • T. K. Wu (ed.)  
ACTIVE AND QUASI-OPTICAL ARRAYS FOR SOLID-STATE POWER COMBINING • Robert A. York and Zoya B. Popović (eds.)  
OPTICAL SIGNAL PROCESSING, COMPUTING AND NEURAL NETWORKS • Francis T. S. Yu and Suganda Jutamulia  
SiGe, GaAs, AND INP HETEROJUNCTION BIPOLAR TRANSISTORS • Jiann Yuan  
ELECTRODYNAMICS OF SOLIDS AND MICROWAVE SUPERCONDUCTIVITY • Shu-Ang Zhou

## CHAPTER ONE

---

# Introduction

---

### **PETER S. HALL**

School of Electronic and Electrical Engineering  
The University of Birmingham, Edgbaston  
Birmingham, UK

### **K. C. GUPTA**

Department of Electrical and Computer Engineering  
University of Colorado  
Boulder, CO

## **1.1 DEVELOPMENT OF CIRCUIT–ANTENNA MODULES**

The term “circuit–antenna module” describes that class of devices in which a microwave or radio frequency circuit is integrated with a radiator. In conventional wireless or radar systems the antenna and circuit have been considered as separate subsystems. This has led to developments of partial systems by two communities, each of which was expert in the design of its own technology but which in general knew little about the complexities of the other’s area. The two communities, like the technology, interacted across a well-defined interface in which parameters such as impedance, frequency, and power were sufficient to allow the system to be constructed.

This situation is satisfactory in many cases and will no doubt continue to be sufficient for many future systems. There have been isolated instances in the past



where this interface has been broken down, such as the development of the active monopole [1,2] in the mid-1960s, but until recently integration of antennas and circuits has led to too many difficulties to justify its widespread investigation and use. Indeed, even with the enormous increase in activity in printed and microstrip antennas, the contradictory requirements for antennas and circuit substrates, identified in the early 1980s and amplified in subsequent work [3–5], seemed to reinforce this perception. At the core of this contradiction is, on the one hand the need for thick, low dielectric constant substrates to enhance microstrip antenna efficiency by loose wave trapping, and on the other hand, the need for thin, high dielectric constant substrates for good circuit action.

There have been several major developments in the last decade or so which have led to the current increase in the importance of circuit–antenna integration. The first and perhaps most important is the need for the generation of substantial power in and beyond the millimeter-wave band. It is clear that single devices will not generate the required power, due to the problem of extracting heat from ever decreasing active device feature size. Circuit combining quickly becomes inefficient due to high losses in suitable transmission media. These difficulties have led to much activity in quasi-optical power combining and active integrated antennas, and two recent books and a review paper emphasize the importance of this topic [6–8].

However, there are other applications where integrated circuit–antenna modules will be important. In large phased arrays there are advantages if the transmit–receive function is distributed across the array. Large losses in the distribution network are avoided and the concept of graceful degradation is introduced. Although such active arrays, in general, do not utilize circuit–antenna integration, the proximity of the transmit–receive module to the antenna places them in a category close to integrated modules, and in future such arrays may benefit from the new technology. Personal communications and vehicle telematics are also vibrant areas where future requirements may be fulfilled with integrated circuit–antenna modules.

One of the visions of this technology is the single-chip transceiver, in which the antenna, transmitter, and receiver are made on a single piece of semiconductor substrate. In principle, baseband signals and dc bias are the only connections necessary to the chip. A further extension of the concept would be to perform appropriate digital signal processing on the same chip. Issues arise as to the best type of semiconductor for this hybrid arrangement, and progress is rapid in determining optimum characteristics or in combining, for instance, silicon and gallium arsenide materials into a single chip. There have been examples of single-chip transceivers having some degree of integration (e.g., see [9,10]). There is a wide range of applications for such modules, from array elements to low cost miniature communicators or sensors.

There is obviously an immense need for analysis and simulation tools to aid the designer in the development of new circuit–antenna modules. In the last two decades computer based tools for circuit design and antenna design have progressed significantly, such that, in setting up a development laboratory, software costs are equivalent to or may exceed the cost of test equipment. A designer now has much

more assurance that a first prototype will have performance close to what is required. It is not true to say, however, that designs will work the first time. What is true is that the number of iterations to reach a satisfactory design have been reduced.

In the last decade many new circuit–antenna modules have been developed and we are now at a stage where some canonical forms are emerging. For example, patch or slot oscillators and amplified printed antennas have been studied for some time and useful configurations established. Inevitably, analytic and simulation tools lag behind these developments, but there are now emerging a range of methods that will serve the various needs of designers. This book aims to bring the methods together within the context of both the technology and the way that computer methods are applied to its development and exploitation.

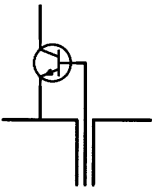
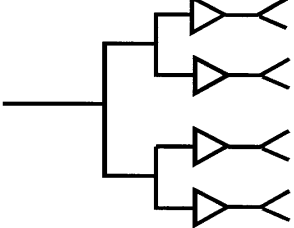
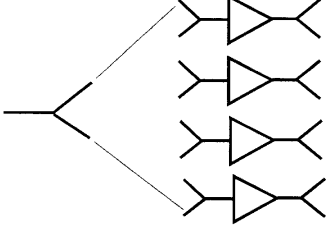
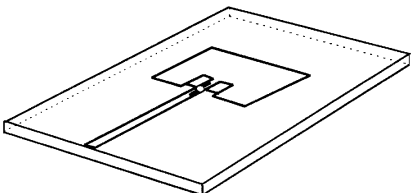
This first chapter aims to give an introduction, together with some background, to integrated circuit–antenna module technology. Some of the terminology is first explained before typical applications are summarized. A glossary of types then serves as an overview of the existing techniques. A discussion follows on the levels of integration found in practical devices and the design process; these give some insight into the types of analysis needed by researchers and designers. Finally, an overview of the following chapters in the book is given.

## 1.2 TERMINOLOGY USED IN CIRCUIT–ANTENNA MODULES

In reviewing the development of this technology some important terminology will be used. It is appropriate here to specify this terminology and to clarify its use as much as possible. Table 1.1 illustrates the four terms in current use. In this book the term circuit–antenna module is taken to be an active integrated antenna or the element in a quasi-optic array. The term may also cover active array elements where there is some degree of interaction between the antenna and circuit. It may also strictly apply to active wire antennas, although in this book there are no examples of wire antennas. The analysis methods may nevertheless be applicable to those types also.

It is clear that the first two types are distinct. However, the division between quasi-optic arrays and active integrated antennas is less well defined. Lin and Itoh [8] suggest that active integrated antennas together with grid methods are two forms of quasi-optic techniques. Both can be used in power combining. In grids the elements are very closely spaced. In active integrated antenna arrays conventional array spacing is used. This classification is useful and in some places in this book active integrated antennas are referred to as quasi-optic. However, when an active integrated antenna element is used on its own, such as in an identification transponder, then the term quasi-optic, which, it is assumed, refers to the manipulation of quasi-Gaussian beams as in optical systems, is less clear. It is inappropriate, however, to labor such classifications and Table 1.1 merely indicates the close association of these two types.

**TABLE 1.1 Terminology of Antenna–Circuit Models<sup>a</sup>**

Terminology	Example
Active antenna [1,2] Transistor in wire antenna	
Active array [11,12] Transmit–receive modules close to radiating elements of array	
Quasi-optic array [13] Space fed distributed amplifying or receiving array Grid oscillator array Element spacing much less than in conventional array	
Active integrated antennas [8] Intimate integration of circuit and antenna Usually printed circuit or MMIC technology Use as single element or array Can form quasi-optical array	

<sup>a</sup>References serve as examples of these types; see Table 1.3 for full glossary.

**1.3 APPLICATIONS OF CIRCUIT–ANTENNA MODULES**

The potential for application of such technology is large. Although the penetration of the original active antennas into mass market applications was relatively small, it is expected the quasi-optic and active integrated antennas will have many applications

where the potential for low cost manufacture will be attractive. Table 1.2 gives some of the possible applications. Some comments are made below.

- *Active Antennas* The insertion of active devices into antennas makes them nonreciprocal. Hence many early active antennas were receive only, where improvements in noise figure, bandwidth, and size reduction can be obtained. However, the poor noise performance and stability of early transistors impeded progress and application was limited.
- *Active Arrays* These are now a large and important subset of phased array activities and have applications in both military and civilian systems. In general, the high degree of integration seen in active integrated antennas is not yet used. Consequently, little reference to them is made in this book. However, in future these two types may merge to produce high performance,

**TABLE 1.2 Applications of Circuit-Antenna Modules Technology**

Type	Applications <sup>a</sup>
Active antennas	Broadcast receive antenna [14] Vehicle radio antenna [1,2] Vehicle TV antenna [15]
Active array	Ground, ship, or airborne radar [11] Satellite radar [12] Satellite communications antennas [12]
Quasi-optic arrays	Millimeter and submillimeter wave Power generation [16] Beam scanning [17,18,19] Signal processing [20,21,22] Terrestrial communications Fiber network local access [23] Space communications [6,7] Automotive applications [9] Transport tolling and highway surveillance [24] Military radars, surveillance, and missile homing [19] Imaging [25]
Active integrated antennas	
Single elements	Tagging Cars and trains [24] Products in manufacturing plants Items on construction sites Personnel monitoring and wireless smart cards [26,27] Indoor communications [28] Cellular handsets [29]
Arrays	As quasi-optic arrays

<sup>a</sup>References are publications where the applications have been cited by authors.

high integration phased arrays and then integrated analysis tools will be important for their design.

- *Quasi-optic Arrays* Although quasi-optic grid systems were first developed for power combining and generation at millimeter wavelengths, a wide range of functions can be performed such as amplification, frequency multiplication, phase shifting, isolation, modulation, and switching. This means that it is possible to perform most, if not all, typical transceiver functions and to construct complete systems using quasi-optic technology. There are many application areas, as indicated in Table 1.2.
- *Active Integrated Antennas* Single integrated antenna elements offer small size and high capability with the potential for low cost. This opens up a range of applications such as tagging and personal communications and sensors. When used in arrays these elements can perform functions similar to quasi-optic grid components. However, the two types have distinct performance and manufacturing characteristics and it remains to be seen which will be used in specific applications.

#### 1.4 GLOSSARY OF CIRCUIT–ANTENNA MODULE TYPES

The glossary of types of circuit–antenna modules given in Table 1.3 illustrates the wide range of configurations. The glossary is by no means exhaustive and provides a representative selection of the various types. It appears that integration has been applied to most types of transmission media and antenna types that are appropriate to printed circuit and monolithic production. In addition, early types used wire radiators. This means that various electromagnetic analyses will be used where these are appropriate to the given structure and that these must be integrated with linear or nonlinear device analysis. This leads to the various analytic approaches given in this book and a brief introduction to these approaches is given at the end of this chapter, in the overview of the book contents.

#### 1.5 LEVELS OF INTEGRATION

It is clear from Table 1.3 that differing levels of integration can be specified and these are identified in Table 1.4. In conventional types in which no integration is attempted, it is usual to specify equal impedances, often  $50\ \Omega$ , on either side of an interface plane. The circuit and antennas can then be designed and analyzed separately, usually by the two groups of specialists mentioned at the beginning of this chapter. The circuit–antenna subsystem performance can then be found using a conventional signal or link budget formulation at the signal frequency. If the system is multifrequency, such as in frequency division multiplex communications, then out-of-band performance or linearity must be specified. However, in general the

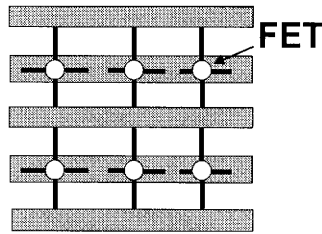
**TABLE 1.3 Glossary of Types of Circuit–Antenna Modules**

<i>Active Antennas</i>	
<p>Amplifying antenna [1,14]</p>	
<p>Electrically short or wideband antennas [30]</p>	
<p>Reduced mutual coupling array element [31]</p>	
<i>Active Arrays</i>	
<p>Fully active [11]</p>	
<p>Semiactive [12]</p>	

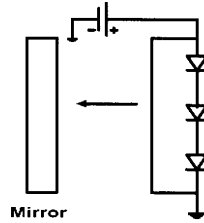
TABLE 1.3 (Continued)

*Quasi-optic Arrays*

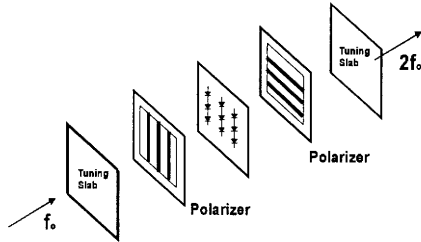
Grid oscillator [16]



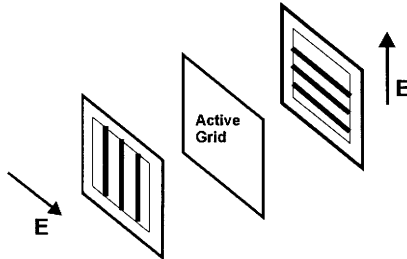
Grid phase shifter [20]



Grid frequency doubler [32]



Grid amplifier [13]

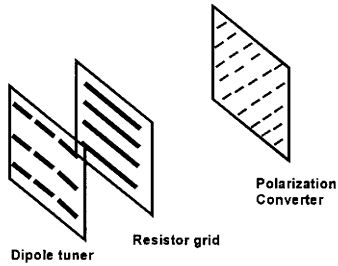


antenna and circuit can be specified separately and thus nonconcurrent analysis is needed.

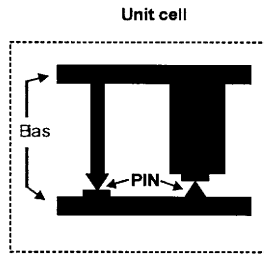
If the circuit is used to match the antenna, then the arrangement can be considered to be partially integrated, in that overall performance can only be determined by analysis that includes both elements. The example shown in Table 1.4 is that of the amplifier used to increase the bandwidth of the circuit–antenna combination beyond

TABLE 1.3 (Continued)

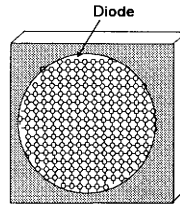
Grid isolator/  
directional coupler  
[21]



Grid modulator [22]

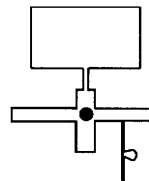


Grid switching arrays  
[25,33]



*Active Integrated Antennas—Single Elements*

Oscillating antennas  
[34,35]



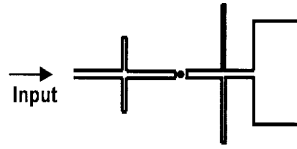
that indicated by the antenna alone; a circuit based method can be used to determine the overall performance. In the example, a through-the-substrate pin connection is used that can be characterized as a transmission line, and the ground plane prevents the patch radiation and microstrip circuit-fringing fields from interacting.

In many cases discussed in this book, the antenna and circuit are so intimately integrated that the analysis needs to take into account the interaction through both

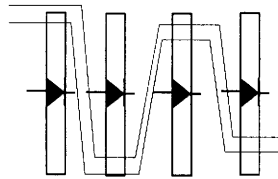


TABLE 1.3 (Continued)

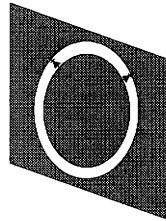
Amplifying antennas  
[36,37]



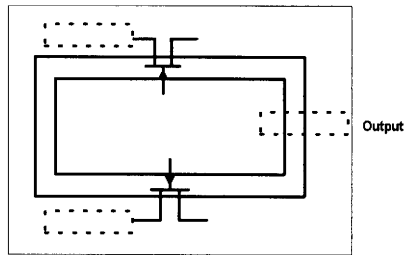
Frequency conversion  
antennas [38]



Mixing antennas [39]



Self-oscillating mixer  
antennas [40]



Frequency agile  
antennas [41]

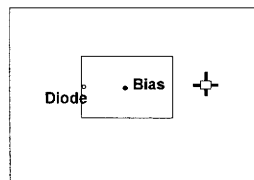
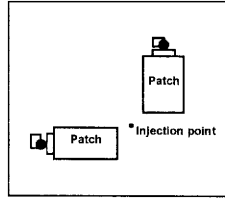
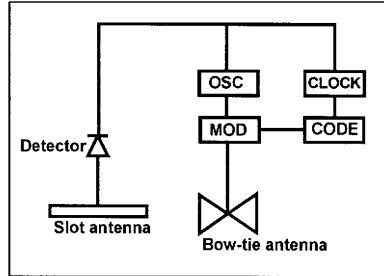


TABLE 1.3 (Continued)

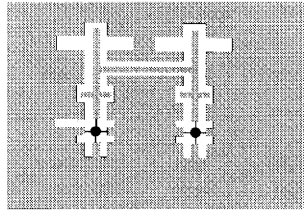
Polarization agile antennas [42]



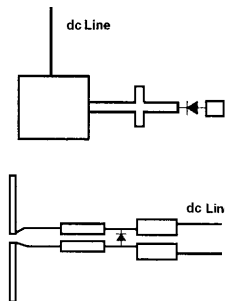
Transponders [26]



Optically controlled antennas [43]



Rectennas [44]

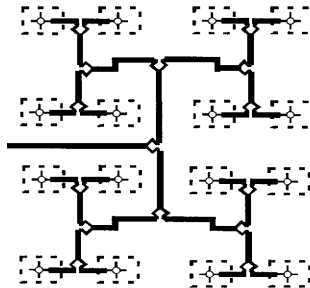


the circuit connections and the fields. For example, in the patch oscillator, the radiation fields in the patch will clearly interact with the transistor circuit lines and indeed with the dc bias circuitry. In the grid technology the very small element spacing means that concurrent analysis is mandatory for successful analysis and design.

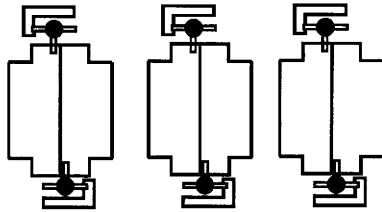
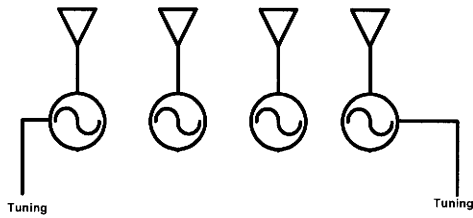
TABLE 1.3 (Continued)

Active Integrated Antennas—Arrays

Power combining arrays [45]



Beam scanning arrays [17,18]



Beam switching arrays [19]

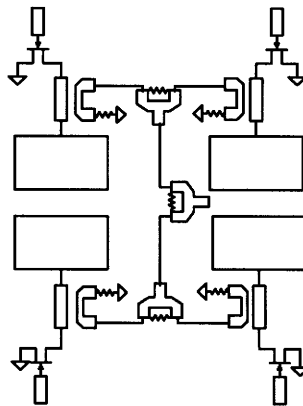
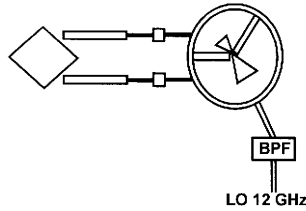
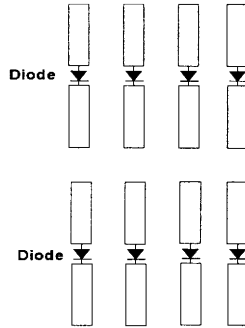


TABLE 1.3 (Continued)

Frequency conversion arrays	See “Frequency conversion antennas” above
Optically controlled oscillating arrays	See “Optically controlled antennas” above
Retrodirective arrays [46]	

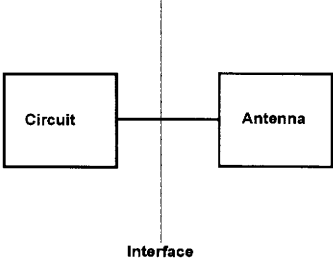
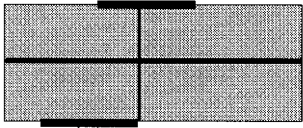
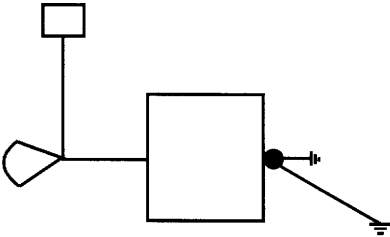


Active radomes and lenses [47–49]



The classifications in Table 1.4 relate to the physical configuration. However, they also suggest another classification, namely, the way in which analysis is approached. It is possible to get approximate results for some intimately integrated systems using circuit based methods only and these allow very rapid analysis and design. For example, the operating frequency of the patch oscillator shown can be estimated using a first-order transmission line model of the patch and a conventional transistor equivalent circuit, solved by simple circuit analysis methods, such as nodal or loop analysis. Output power across a range of frequencies can then approximately be obtained by harmonic balance analysis of the same circuit. As such methods are now embodied in commercial circuit design software, this level of design is extremely accessible; it can also be relatively rapid and thus allow optimization. On the other hand, it is difficult to apply such methods to quasi-optical grid devices and methods such as moments and Floquet modes must be used, in addition to the circuit analysis of the device models. In general, such methods will require substantial computation times.

**TABLE 1.4 Classification of Levels of Circuit–Antenna Integration**

Classification	Example
<p>Nonintegrated (conventional)                      Impedance equal, and hence matched, on either side of interface                      Each part analyzed separately</p>	
<p>Partial integration                      Antenna and circuit interaction through transmission line                      Performance analyzed by circuit based methods</p>	<p>Patch and integrated antenna for bandwidth expansion [50]</p> 
<p>Full integration                      Antenna and circuit interaction through transmission line and field coupling                      Performance analyzed by concurrent electromagnetic and device analysis</p>	<p>Patch oscillator [8]</p> 

**1.6 THE DESIGN PROCESS**

Consideration of the engineering design process applied to circuit–antenna modules provides insight into the needs of designers for various levels of analyses. Figure 1.1 gives a flowchart for design. The process can be divided into two distinct activities. The first is an approximate design exercise, which very often has to take place in a relatively short period of time and may relate to the activity between receipt of a call for proposal and the completion of that proposal. A specification is issued. The design group must decide whether it can meet all or most of those specifications. In many cases the new module will be similar to those already designed; perhaps the operating frequency or power level may be changed. The group will use its collective experience to find an appropriate configuration. Some initial analysis may then be performed to give assurance that the final module is suitable. A fast “breadboard”

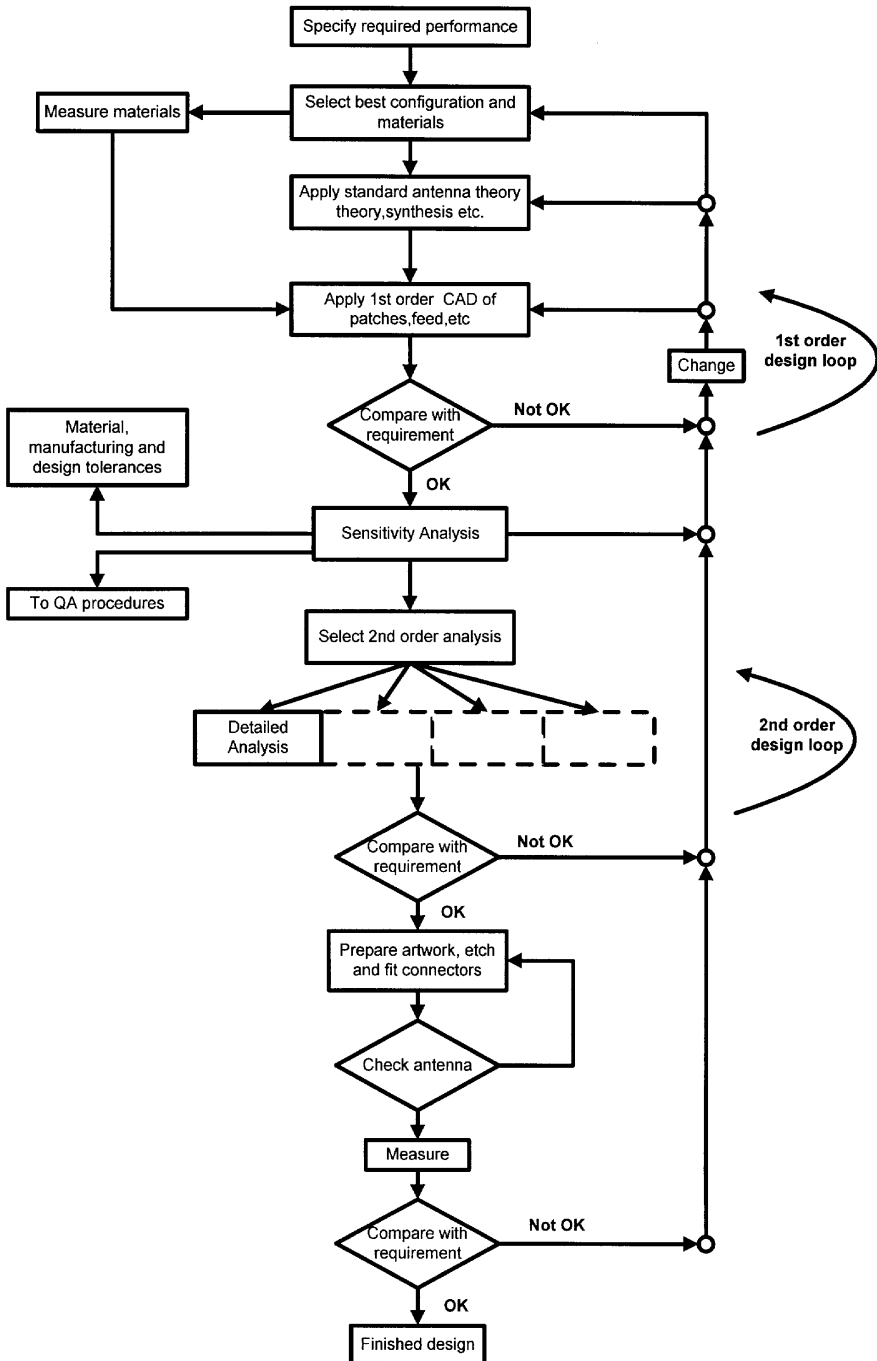


FIGURE 1.1 The design process.

model may be built and a few design and build iterations may be performed. Alternatively, a decision may be made on a single breadboard design.

The second design activity must incorporate a number of additional features. A full design will need to consider manufacturing effects. For example, material and device tolerances will have to be established and sensitivity analysis performed on the design. Here fast analysis with moderate accuracy is useful. However, for a final design all effects must be included and higher order methods must be used. More detail of the design process is given in Chapter 2, but this initial view stresses the importance of both fast analytic tools with moderate accuracy and more accurate analysis that may take longer to perform.

### 1.7 ANALYTICAL OUTCOMES AND CIRCUIT–ANTENNA MODULE PERFORMANCE PARAMETERS

Analysis of antennas aims to yield antenna parameters such as input impedance, radiation patterns, and gain. Circuit analysis will calculate oscillation frequency, amplifier gain, mixer conversion gain, and nonlinear parameters such as spectral content and linearity. In analysis of circuit–antenna modules both sets of parameters will be required in general. Table 1.5 lists these parameters. Integration of antenna and circuit functions will usually result in nonreciprocal action and Table 1.5 lists parameters for either transmit or receive. It is clear that many more parameters need to be specified than in nonintegrated systems.

As no antenna terminal is available it is impossible to specify antenna gain, transmitter power, or receiver gain. Therefore new parameters have been established [50–52]. For transmitters, effective isotropic radiated power is specified: it is the product of the power available from the oscillator and the power gain of the antenna and is usually specified in the peak direction. Similarly, for mixer receive antennas,

**TABLE 1.5 Performance Parameters for Circuit–Antenna Modules**

Transmit	Receive
Frequency	Center frequency
Effective isotropic radiated power	Bandwidth
Phase noise	Noise figure
Amplitude noise	Isotropic receive gain
Stability	Isotropic conversion loss
Spectral content	Linearity
Radiation pattern	Radiation pattern
Beamwidth	Beamwidth
Polarization	Polarization

isotropic conversion loss is the product of the mixer conversion loss and the antenna power gain, again specified in the peak direction.

For antennas with integrated amplifiers, power gain must now include the amplifier gain. For receive amplifier antennas, the noise figure includes the added noise from the amplifier and the external noise received by the antenna. However, in many practical cases external noise will be much smaller than the amplifier noise and the parameter will have values similar to those obtained for an equivalent isolated amplifier.

## 1.8 OVERVIEW OF THE BOOK

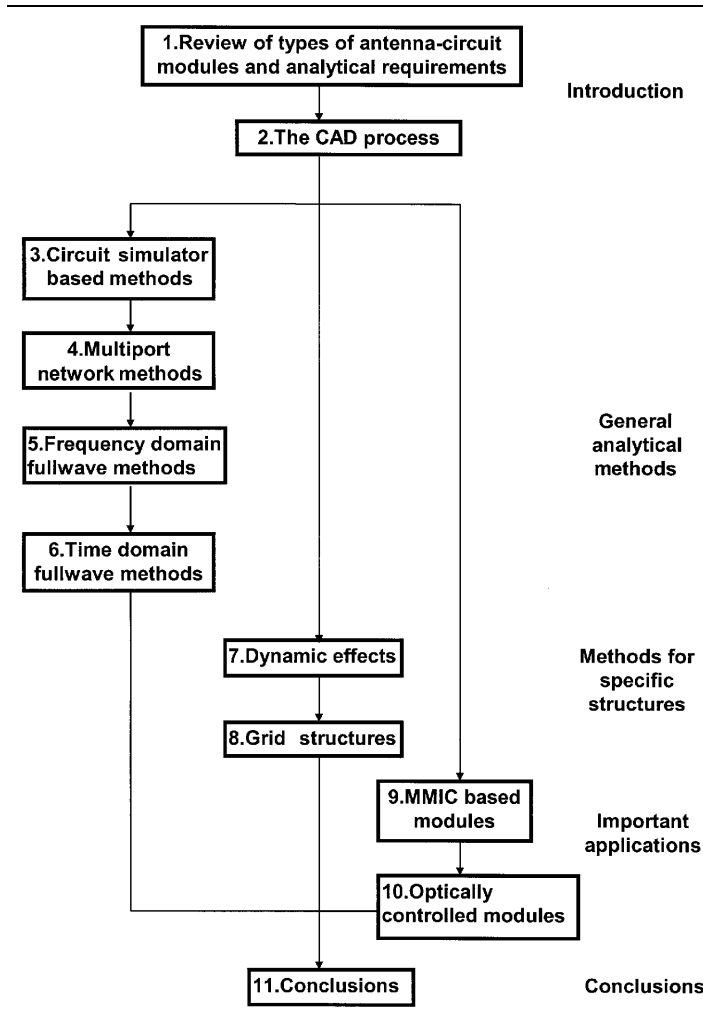
Analysis of circuit–antenna modules involves both an appreciation of the various analytical methods and their applications, and also some understanding of the technology types and their applications. In addressing these two needs, it is necessary first to set the scene and to lay some foundations, then to give detailed accounts of analytic methods, and finally to review some operational and technology types that have very specific and somewhat different analytical needs. Table 1.6 shows how these themes are addressed in this book. After the introductory chapter, the CAD process is reviewed. Four types of analysis methods are then described in detail. Although not exhaustive, these chapters are representative of the various methods currently being studied. Two chapters are then devoted to the analysis of very specific configurations, namely, injection locked oscillator arrays and grid based structures. The following two chapters indicate some important applications. They are devoted to monolithic based modules and modules incorporating optical control. The book is then drawn together in a concluding chapter. The following notes give some introduction to each of the chapters.

*Chapter 1—Introduction* This introductory chapter serves to set the context of the analysis of circuit–antenna modules. The development of such modules is described together with some explanation of the terminology currently used. A glossary of types is presented that aims to show the range of configurations currently being studied and to highlight the design challenges. The likely design parameters are then given, together with a review of the design process in which analysis tools have to serve. Finally, an overview of the book chapters is given.

*Chapter 2—Review of the CAD Process* In order to develop designs for integrated circuit–antenna modules, an appreciation of the computer-aided design process is necessary. This chapter starts with a discussion of the design process in general. Conventional design, computer-aided design, and knowledge based design approaches are outlined. CAD procedures for microwave circuits and printed microstrip antennas, as practiced separately, are described. Then the discussion converges on CAD considerations for integrated circuit–antenna modules implemented at various levels of integration (nonintegrated, partially integrated, and fully integrated).



TABLE 1.6 Flow Chart of Book Contents



*Chapter 3—Circuit Simulator Based Methods* Simulations based on equivalent circuit analysis methods can provide fast results with accuracies useful for first-pass design. This chapter gives an introduction to equivalent circuit modeling of circuits and antennas. Both linear and nonlinear simulations are described with examples including oscillating patch antennas, amplified patches, frequency doubling transponders, and oscillator locking.

*Chapter 4—Multiport Network Method* The multiport network method offers enhanced accuracy compared to simple equivalent circuit methods and can be integrated with active device models. This chapter introduces the concept of the multiport network model as developed for single-layer and two-layer microstrip patch antennas. Applications of the multiport network method to

integrated circuit–antenna modules are discussed.

*Chapter 5—Full Wave Analysis in the Frequency Domain* The field integral equation solved by the method of moments is now a well-established tool for antenna and passive circuit analysis. The inclusion of lumped elements has been described some time ago. In this chapter, the description is extended to nonlinear structures such as diodes and transistors, with results showing good agreement with measurements.

*Chapter 6—Full Wave Electromagnetic Analysis in the Time Domain* The transmission line matrix (TLM) and the finite-difference time domain (FDTD) method are two numerical techniques that overcome the need for the large matrix inversion necessary for the method of moments. Of these two, the FDTD method is extremely simple to implement and very flexible. This chapter outlines the method and its extension to active integrated antennas.

*Chapter 7—Phase-Locking Dynamics in Integrated Antenna Arrays* Injection locked integrated antenna arrays possess dynamic characteristics that are attractive for many applications, such as simple beam scanning and reduced phase noise. Their behavior cannot easily be analyzed using the above methods, so that simplified equivalent circuit methods have to be used. In this chapter the dynamic behavior is described comprehensively using such methods.

*Chapter 8—Analysis and Design of Oscillator Grids and Arrays* Grid structures now offer the possibility of providing most of the functionality of transmitter and receiver components in a distributed array form with interconnections by quasi-optical beams. The advantages are very efficient power combining, graceful degradation, increased dynamic range, and reduced noise figures. In this chapter analyses using full wave methods combined with equivalent circuit device models are described. By way of example, oscillator synthesis and grid optimization are successfully performed.

*Chapter 9—Analysis and Design Considerations for Monolithic Microwave Circuit Transmit–Receive Modules* One of the major challenges for circuit–antenna modules is the phased array element fabricated entirely in monolithic technology, in which the transceiver and antenna are both contained on the same chip. This then poses what is perhaps the ultimate test of an analysis or simulation tool. To set the scene for further research and development in this area, the requirements for phased array modules are reviewed in this chapter. The coverage is from conventional phased arrays with separate transceiver and antenna to more recent integrated configurations.

*Chapter 10—Integrated Transmit–Receive Circuit–Antenna Modules for Radio on Fiber Systems* Circuit–antenna modules can form a low cost component in wireless local access into fiber optic based networks, to provide high capacity services to domestic or office users. This chapter reviews this important application area and gives examples of the analysis challenges inherent in their design. One such challenge is the accurate design of filters for separation of the local oscillator from the signal, in the presence of the antenna. In this work the equivalent circuit based methods, described in

Chapter 3, are used and the strengths and weaknesses of this approach are noted.

*Chapter 11—Conclusions* The book is completed by a short chapter in which some conclusions are drawn. The current status of computer-aided design tools is summarized from the earlier chapters. Some thoughts on the likely future challenges that analysis will face are then given. The chapter is then closed by comments on what now remains to be done to present designers with a full and flexible array of software to facilitate fast and accurate design.

## REFERENCES

1. Copeland, J. R., Robertson, W. J., and Verstraete, R. G., "Antennafier arrays," *IEEE Trans. Antennas Propag.*, vol. AP-12, Mar. 1964, pp. 277–283.
2. Meinke, H. H., "Active antennas," *Nachrichtentech. Z.*, vol. 19, Dec. 1966, pp. 697–705.
3. James, J. R., Henderson, A., and Hall, P. S., "Microstrip antenna performance is determined by substrate constraints," *Microwave Syst. News*, vol. 12, no. 8, 1982, pp. 73–84.
4. Pozar, D. M., "Considerations for millimetric wave printed antennas," *IEEE Trans. Antennas Propag.*, vol. AP-3, no. 1, Sept. 1983, pp. 740–747.
5. James, J. R., and Hall, P. S. (eds.), *Handbook of Microstrip Antennas*, IEE, Peter Peregrinus, London, 1991.
6. Navarro, L. A., and Chang, K., *Integrated Active Antennas and Spatial Power Combining*, Wiley, New York, 1996.
7. York, R. A., and Popovic, Z. B. *Active and Quasi-Optical Arrays for Solid State Power Combining*, Wiley, New York, 1997.
8. Lin, J., and Itoh, T., "Active integrated antennas," *IEEE Trans. Antennas Propag.*, vol. 42, no. 12, Dec. 1994, pp. 2186–2194.
9. Singer, M., Strohm, K. M., Luy, L.-R., and Biebl, E. M., "Active SIMMWC-antenna for automotive applications," IEEE MTT-S International Symposium, Denver, June 1997, pp. 1265–1268.
10. Roy, L., "30 GHz GaAs Monolithic Low Noise Amplifier-Antennas," IEEE MTT-S International Symposium, Denver, June 1977, pp. 967–970.
11. Mailloux, R. L., *Phased Array Antenna Handbook*, Artech House, Boston, 1994, pp. 40f.
12. Roederer, A. G., "Semi-active satellite antennas," *Journ. Int. Nice Antennes*, vol. 12–14, Nov. 1992, pp. 569–577.
13. Weikle, R. M., Kim, H. M., Hacker, J. B., DeLisio, M. R., Popovic, Z. B., and Rutledge, D. B. "Transistor oscillators and amplifier grids," *Proc. IEEE*, vol. 80, Nov. 1992, pp. 1800–1809.
14. Wheeler, H. A., "Small antennas," *IEEE Trans. Antennas Propag.*, vol. AP-23, July 1975, pp. 462–469.
15. Taguchi, M., Fujimoto, T., and Tanaka, K., "CPW fed active dipole antenna for television receivers," *Electron. Lett.*, vol. 30, no. 22, 27 Oct. 1994, pp. 1815–1816.
16. Popovic, Z. B., Weikle, R. M., Kim, H. M., and Rutledge, D. B., "A 100-MESFET planar grid oscillator," *IEEE Trans. Microwave Theory Tech.*, vol. MTT-39, Feb. 1991, pp. 193–200.

17. York, R. A., "Novel beam scanning techniques for low cost commercial applications," SPIE International Conference on Millimetre Waves and Applications, San Diego, July 1995.
18. Hall, P. S., and Haskins, P. M., "Microstrip active patch array with beam scanning," *Electron. Lett.*, vol. 128, 22 Oct. 1992, pp. 2056–2058.
19. Chew, S. T., and Itoh, T., "A  $2 \times 2$  beam-switched active antenna array," IEEE MTT-S International Microwave Symposium, Orlando, 16 May 1995, pp. 925–928.
20. Lam, W. W., Jou, C. R., Chen, H. Z., Stolt, K. S., Luhmann, N. C., and Rutledge, D. B., "Millimetre-wave diode grid phased shifters," *IEEE Trans. Microwave Theory Tech.*, vol. MTT-36, May 1988, pp. 902–907.
21. Hollung, S., Markovic, M., Shiroma, W., and Popovic, Z. B., "A quasi-optical isolator," *IEEE Microwave Guided Wave Lett.*, vol. 6, no. 5, May 1996, pp. 205–207.
22. Markovic, M., Hollung, S., and Popovic, Z. B., "Quasi-optical phase modulators," *IEEE MTT-S Int. Symp. Dig.*, San Francisco, June 1996, pp. 1247–1250.
23. Kykkotis, C., Ghafouri-Shiraz, H., and Hall, P. S., "New configurations for integrated optical-fibre-fed radio systems," *Microwave Opt. Technol. Lett.*, vol. 17, no. 6, 20 Apr. 1998, pp. 339–345.
24. Adachi, R., Maeda, K., Fukagawa, T., and Hasegawa, M., "Microwave card system with a high interference immunity utilising a spread spectrum method," Asia-Pacific Microwave Conference, 1994, pp. 463–466.
25. Goldsmith, P. F., Huguenin, G. R., Kapitzky, J., and Moore, E. L., "Focal plane imaging systems for millimetre wavelengths," *IEEE Trans. Microwave Theory Tech.*, vol. MTT-41, Oct. 1993, pp. 1664–1675.
26. Probartz, C. W., and Itoh, T., "A microwave non-contact identification transponder using subharmonic interrogation," *IEEE Trans. Microwave Theory Tech.*, vol. MTT-43, July 1995, pp. 1673–1679.
27. Hawkes, R., Davies, I., and Price, W. (eds.), *Integrated Circuit Cards, Tags and Tokens*, BPS Professional Books, Oxford, 1990.
28. Zheng, M., Andrews, L. W., Hall, P. S., Gardner, P., Chen, Q., and Fusco, V. F., "Active integrated antenna oscillator stability and phase noise reduction," International Conference on Microwave and Millimeter Wave Technology, ICMMT-98, Aug. 1998, Beijing.
29. McGirr, A., and Camwell, P., "Tuneable elevated microstrip antenna for cellular hand-helds," Symposium on Antenna Technology and Applied Electromagnetics, Winnipeg, Aug. 1990, pp. 278–283.
30. Maclean, T. S. M., and Ramsdale, P. A., "Short active aerials for transmission," *Int. J. Electron.*, vol. 36, Feb. 1974, pp. 261–269.
31. Daniel, L. P., and Terret, C., "Mutual coupling between antennas—optimisation of transistor parameters in active antenna design," *IEEE Trans. Antennas Propag.*, vol. AP-23, July 1975, pp. 513–516.
32. Lam, W. W., Jon, C. R., Chen, H., Stolt, K. S., Luhmann, N. C., and Rutledge, D. B., "Millimetre-wave diode grid frequency doubler," *IEEE Trans. Microwave Theory Tech.*, vol. MTT-36, Nov. 1988, pp. 1507–1514.
33. Stephen, K. D., Spooner, P. H., and Goldsmith, P. F., "Quasi-optical millimetre wave hybrid and monolithic PIN diode switches," *IEEE Trans. Microwave Theory Tech.*, vol. MTT-41, Oct. 1993, pp. 1791–1798.

34. Nogi, S., Lin, J., and Itoh, T., "Mode analysis and stabilisation of a spatial power combining array with strongly coupled oscillators," *IEEE Trans. Microwave Theory Tech.*, vol. MTT-41, Oct. 1993, pp. 1827–1837.
35. Kawasaki, S., and Itoh, T., "Quasi-optical planar arrays with FETs and slots," *IEEE Trans. Microwave Theory Tech.*, vol. MTT-41, Oct. 1993, pp. 1838–1844.
36. Robert, B., Razban, T., and Papiernik, A., "Compact amplifier integration in square patch," *Electron. Lett.*, vol. 19, Sept. 1992, pp. 1808–1810.
37. Hall, P. S., "Analysis of radiation from active microstrip antennas," *IEE Proc. Microwave Antennas Propag.*, vol. 141, no. 5, Oct. 1994, pp. 359–366.
38. Nam, S., Uwano, T., and Itoh, T., "Microstrip-fed planar frequency-multiplying space combiner," *IEEE Trans. Microwave Theory Tech.*, vol. WY-35, Dec. 1987, pp. 1271–1276.
39. Stephan, K. D., Camileri, N., and Itoh, T., "A quasi-optical polarisation duplexed balanced mixer for millimetre wave applications," *IEEE Trans. Microwave Theory Tech.*, vol. MTT-32, Jan. 1984, pp. 97–102.
40. Hwang, V. D., and Itoh, T., "Quasi-optical HEMT and MESFET self oscillating mixers," *IEEE Trans. Microwave Theory Tech.*, vol. MTT-36, Dec. 1988, pp. 1701–1705.
41. Haskins, P. M., Hall, P. S., and Dahele, J. S., "Active patch antenna with diode tuning," *Electron. Lett.*, vol. 27, no. 20, 26 Sept. 1991, pp. 1846–1847.
42. Haskins, P. M., and Dahele, J. S., "Compact active polarisation-agile antennas using square patch," *Electron. Lett.*, vol. 3, no. 1, Aug. 1995, pp. 1305–1306.
43. Kawasaki, S., and Itoh, T., "Optical tuning range comparison of uniplanar active integrated antenna using MESFET, GaAs HEMT and pseudomorphic HEMT," Proceedings Fourth International Symposium Space Terahertz Technology, Mar. 1993, pp. 149–156.
44. Yoo, T., McSpadden, J., and Chang, K., "35 GHz rectenna implemented with a patch and microstrip dipole antenna," *IEEE MTT-S Int. Symp. Dig.*, 1992, pp. 345–348.
45. Birkeland, J., and Itoh, T., "A 16-element quasi-optical FET oscillator power combining array with external injection locking," *IEEE Trans. Microwave Theory Tech.*, vol. MTT-40, Mar. 1992, pp. 475–481.
46. Probanz, C. W., and Itoh, T., "Conformal retrodirective array for radar applications using a heterodyne phased scattering element," IEEE MTT-S International Microwave Symposium, Orlando, 16 May 1995, pp. 905–908.
47. Park, R. H., "Radant lens: alternative to expensive phased arrays," *Microwave J.*, Sept. 1981, pp. 101–105.
48. Rao, J. B. L., and Patel, D. P., "Voltage controlled ferroelectric lens phased arrays," IEEE Antenna and Propagation Society International Symposium, Baltimore, 1996, pp. 1624–1627.
49. Shuley, N. V., "Diode loaded frequency selective surfaces," *Journ. Int. Nice Antennes*, Nov. 1992, pp. 313–315.
50. An, H., Nauwelaers, B., and Van de Capelle, A., "Broadband active microstrip array element," *Electron. Lett.*, vol. 27, no. 25, 1991, pp. 2378–2379.
51. Stephen K. D., and Itoh, T., "A planar quasi-optical subharmonically pumped mixer characterised by isotropic conversion loss," *IEEE Trans. Microwave Theory Tech.*, vol. MTT-32, Jan. 1994, pp. 97–102.
52. An, H., Nauwelaers, B., and Van de Capelle, A., "Noise figure measurements of receiving active microstrip antennas," *Electron. Lett.*, vol. 29, no. 18, 1993, pp. 1594–1596.

## CHAPTER TWO

---

# Review of the CAD Process

---

### **K. C. GUPTA**

Department of Electrical and Computer Engineering  
University of Colorado  
Boulder, CO

### **PETER S. HALL**

School of Electronic and Electrical Engineering  
The University of Birmingham  
Edgbaston, Birmingham, UK

A review of the engineering design process and its application to design of radio frequency (RF) and microwave circuits and to the design of printed antennas is a prerequisite for development of design methods for integrated circuit–antenna modules. Most of the current design practices involve an extensive use of computers and this discipline is popularly known as *computer-aided design* (CAD). This chapter is a review of design processes as applicable to integrated circuit–antenna modules.

## **2.1 THE DESIGN PROCESS**

### **2.1.1 Anatomy of the Design Process**

The sequence of various steps in a typical design process [1] is shown in Fig. 2.1. One starts with problem identification. This phase is concerned with determining the

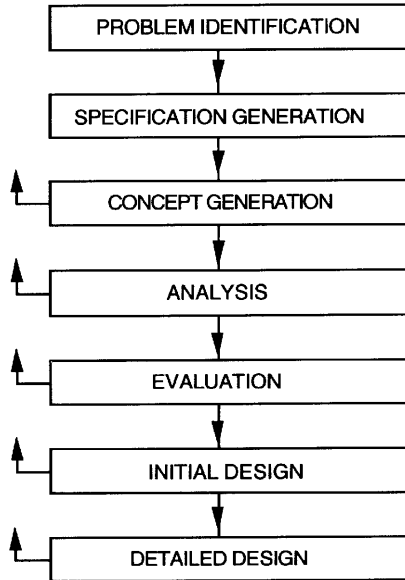


FIGURE 2.1 Sequence of steps in a typical design process.

need for a product. A product is identified, resources allocated, and end-users are targeted. The next step is drawing up the product design specification (PDS), which describes the requirements and performance specifications of the product. This is followed by a *concept generation* stage where preliminary design decisions are made. Several alternatives will normally be considered. Decisions taken at this stage determine the general configuration of the product and, thus, have enormous implications for the remainder of the design process. At each of these design stages, there is usually a need for feedback to earlier stages and reworking of the previous steps. The analysis and evaluation of the conceptual design lead to concept refinement, for example, by placing values on numerical attributes. The performance of the conceptual design is tested for its response to external inputs and its consistency with the design specifications. These steps lead to an *initial* design.

The step from initial design to the final detailed design involves modeling, computer-aided analysis, and optimization. CAD tools currently available to us for RF and microwave design primarily address this step only.

A review of the sequence of steps in Fig. 2.1 points out that the analysis of the design, an integrated circuit–antenna module in our case, is needed at two different stages of the design process. Once the concept embodying the configuration for the module is arrived at, there is a need for analysis to evaluate the potential performance of the tentative design. At this stage, approximate design methods (such as the one based on the transmission line model for a microstrip patch) provide a computationally efficient approach. The second place in the design process where an analysis is needed is in the last step, which converts the initial design into an optimized detailed design. Accuracy of the analysis process here gets translated

directly into a match between the design performance and the design specifications. At this stage we need an accurate computer-aided analysis.

The design process outlined above can be considered to consist of two segments. Initial steps starting from the product identification to the initial design may be termed as *design-in-the-large* [2]. The second segment that leads from an initial design to the detailed design has been called *design-in-the-small*. It is for this second segment that the most current microwave CAD tools have been developed.

It is in the *design-in-the-large* segment that important and expensive design decisions are made. Here, the previous experience of the designers plays a significant role and a *knowledge based system* is the most likely candidate technology that could help designers. Understanding this part of the design process is a prerequisite for developing successful design tool for integrated circuit–antenna modules. An extensive discussion on the knowledge based design and related topics is available in a three-volume treatise on artificial intelligence in engineering design [3].

There are three design philosophies applicable to the design of integrated circuit–antenna modules and other design domains. These are (1) conventional design procedure, (2) CAD approach, and (3) knowledge-aided design (KAD) approach.

### 2.1.2 Conventional Design Procedures

The conventional design process is the methodology that designers used before the CAD methods and software were developed. A flow diagram depicting the conventional design procedure is shown in Fig. 2.2. One starts with the desired design specifications and arrives at an initial configuration for the integrated circuit–antenna module. Available design data and previous experience are helpful in selecting this initial configuration. Analysis and synthesis procedures are used for deciding values of various parameters of the module. A laboratory model is constructed for the initial design and measurements are carried out for evaluating its characteristics. Performance achieved is compared with the desired specifications; if the given specifications are not met, the module is modified. Adjustment, tuning, and trimming mechanisms incorporated in the module are used for carrying out these modifications. Measurements are carried out again and the results are compared with the desired specifications. The sequence of modifications, measurements, and comparison is carried out iteratively until the desired specifications are achieved. At times the specifications are compromised in view of the practically feasible performance of the module. The final integrated circuit–antenna configuration thus obtained is sent for prototype fabrication. This procedure had been used for the design of microwave circuits and antennas for quite some time. However, it has become increasingly difficult to use this iterative experimental method successfully because of the following considerations:

1. Increased complexity of modern systems demands more precise and accurate design of circuit–antenna subsystems. Consequently, the effect of tolerances in the design has become increasingly important.



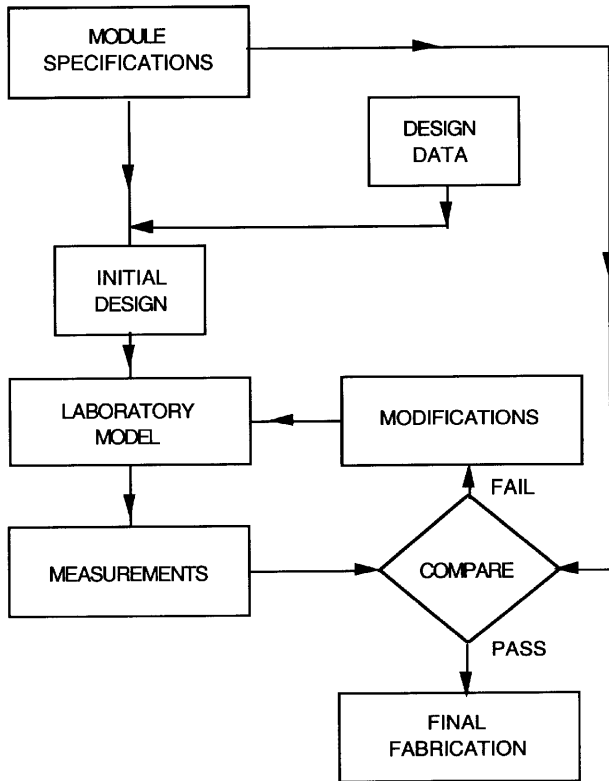


**FIGURE 2.2** The conventional design procedure that was used for microwave design before CAD methods were developed.

2. A larger variety of active and passive components are now available for achieving a given circuit-antenna module function. The choice of the appropriate circuit or antenna structure becomes difficult if the iterative experimental approach is used.
3. It is very difficult to incorporate any modifications in the module fabricated by integrated circuit technology.

The method developed for dealing with this situation is known as *computer-aided design* (CAD). Computer-aided design, in its strict interpretation, may be taken to mean any design process where the computer is used as a tool. However, usually the word CAD implies that without the computer as a tool, that particular design process would have been impossible or much more difficult, more expensive, more time consuming, and less reliable and more than likely would have resulted in an inferior product.

### 2.1.3 CAD Approach

A typical flow diagram for CAD procedure is shown in Fig. 2.3. As before, one starts with a given set of specifications. Synthesis methods and available design data (at times prestored in computer memory) help to arrive at the initial design. The performance of this initial module is evaluated by a computer-aided analysis. Numerical models for various components (passive and active) used in the module are needed for the analysis. These are called from the library of subroutines developed for this purpose. Circuit–antenna module characteristics obtained as results of the analysis are compared with the given specifications. If the results fail to satisfy the desired specifications, the designable parameters of the circuit are altered in a systematic manner. This constitutes the key step in the optimization. Several optimization strategies include sensitivity analysis of the module for calculating changes in the designable parameters. The sequence of circuit analysis, comparison with the desired performance, and parameter modification is performed iteratively until the specifications are met or the optimum performance of the module (within the given constraints) is achieved. The module is now fabricated and the experimental measurements are carried out. Some modifications may still be required if the modeling and/or analysis are not accurate enough. However, these modifications are hopefully very small. The aim of the CAD method is to minimize the experimental iterations as far as practicable.

The process of CAD, as outlined above, consists of three important segments, namely, (1) modeling, (2) analysis, and (3) optimization. Modeling involves characterization of various active and passive components to the extent of providing a numerical model that can be handled by the computer. In the case of microwave circuit–antenna modules, one comes across a variety of active and passive elements. Semiconductor devices used include bipolar transistors and MESFETs, point contact and Schottky barrier detectors, varactor and PIN diodes, and also transferred electron and avalanche devices. Passive elements used in microwave modules include sections of various transmission structures, lumped components, dielectric resonators, nonreciprocal components and planar (two-dimensional) elements, and a variety of radiating element configurations. Transmission structures could be coaxial line, waveguide, stripline, microstrip line, coplanar line, slot line, or a combination of these. Not only do these transmission structures need to be characterized fully for impedance, phase velocity, and so on, but it also becomes necessary to model the parasitic reactances caused by geometrical discontinuities in these transmission lines.

Modeling of components in microwave circuits had been the main difficulty in successful implementation of CAD techniques at microwave frequency. However, the electromagnetic (EM) simulation techniques developed over the last decade have helped to construct adequate models and bring microwave hybrid and monolithic circuit CAD software to a level of maturity. Modeling still remains the major bottleneck for CAD of certain classes of microwave circuits such as coplanar waveguide CPW circuits, multilayered circuits, and integrated circuit–antenna modules. Current research in efficient use of EM simulation techniques [4] and in

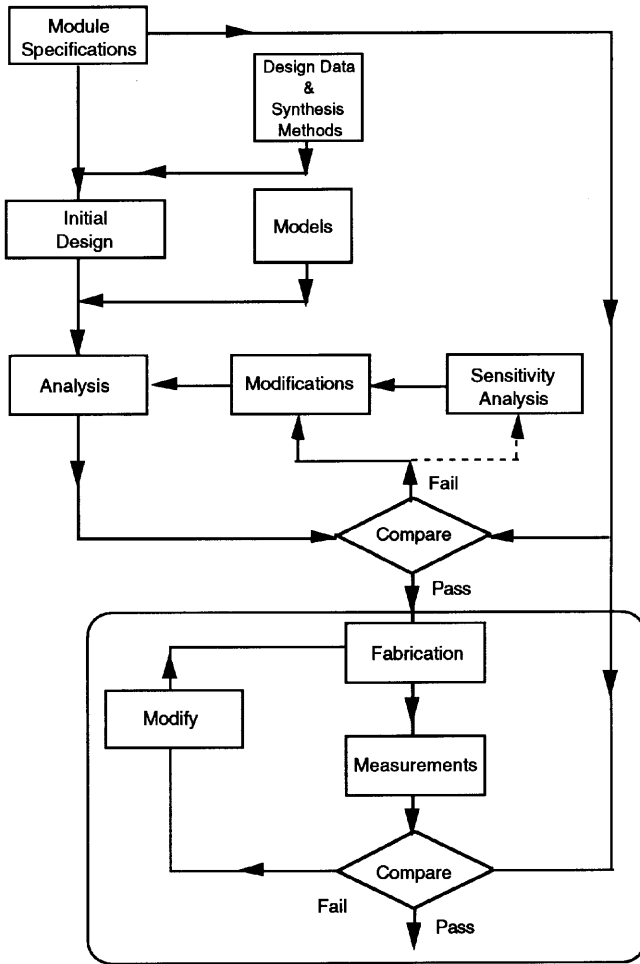


**FIGURE 2.3** Computer-aided design methodology suitable for integrated circuit-antenna modules.

use of artificial neural network models [5,6] will lead to further improvement in CAD tools for microwave circuits and antennas.

**2.1.4 Knowledge-Aided Design (KAD) Approach**

Development of knowledge aids may be based on developing a task structure [7,8] for the design process. A generic task-oriented methodology involves (1) a description of the tasks, (2) proposed methods for it, (3) decomposition of the task into subtasks, (4) methods available for various subtasks, (5) knowledge required for implementing various methods, and (6) any control strategies for these methods.

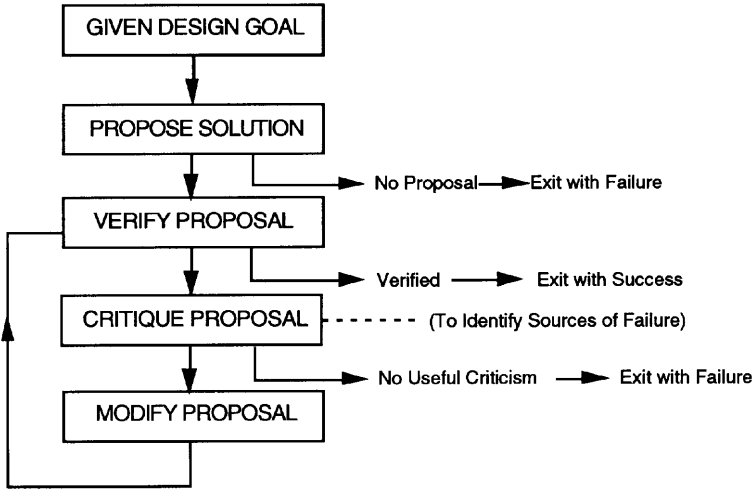


**FIGURE 2.4** Propose–Critique–Modify (PCM) approach for arriving at an initial design.

A method for accomplishing a generic design task is known as the propose–critique–modify (PCM) approach, shown in Fig. 2.4. This approach consists of the following:

1. Proposal of partial or complete design solutions.
2. Verification of proposed solutions.
3. Critiquing the proposal by identifying causes of failure, if any.
4. Modification of proposals to satisfy design goals.

The use of knowledge based approaches to the initial stages of microwave circuit and antenna design is an area that needs to be explored. We currently heavily depend on the accumulated experience of senior designers for executing these design steps. Recognizing the significant contribution of these steps to the final design, efforts in developing technology aids for this purpose would be worthwhile.

Knowledge based systems developed for initial design of integrated circuit–antenna modules would also be very helpful for instruction or training of design engineers. For example, a system that can present all the relevant options for, say, designs of oscillator–antennas at millimeter-wave frequencies could educate the designer about the relative merits of various configurations as well as lead to a design for meeting a particular set of specifications.

## 2.2 CAD FOR MICROWAVE CIRCUITS

As discussed in Section 2.1.3 on CAD Approach, three important segments of CAD are (1) modeling, (2) analysis, and (3) optimization. This section is an overview of

these three aspects as applicable to microwave CAD. Details of microwave circuit CAD methodology are available in several books [9–11]. This section deals with microwave circuit CAD techniques based on network analysis. This approach is used extensively for practical design of microwave hybrid and integrated circuits. Field simulation and analysis techniques based on frequency domain and time domain electromagnetic simulation methods are also applicable to component and circuit analyses. Electromagnetic solvers on big computers are also now fast enough to carry out optimization. These aspects are discussed later in Chapter 5, Full-Wave Analysis in the Frequency Domain, and Chapter 6, Full-Wave Electromagnetic Analysis in the Time Domain.

### 2.2.1 Modeling of Circuit Components

An accurate and reliable characterization of microwave circuit components is one of the basic prerequisites of successful CAD. The degree of accuracy to which the performance of microwave integrated circuits can be predicted depends on the accuracy of characterization and modeling of components. Kinds of elements and passive devices that need to be characterized depend on the transmission medium used for circuit design. Most research efforts aimed at characterization for CAD purposes have been reported for microstrip lines [12,13]. Some results are available for slot lines and fin lines also [12,14,15]. However, for coplanar lines and suspended substrate transmission structures, modeling techniques are still in a state of infancy.

In addition to the transmission media, implementation of CAD requires characterization of various junctions and discontinuities in transmission structures. Effects of these junctions and discontinuities become more and more significant as one moves from the microwave frequency range to millimeter waves. At higher frequencies, radiation associated with discontinuities needs to be considered. Variations of effects of two typical discontinuities with frequency are illustrated in Fig. 2.5 (from [16]). Figure 2.5a shows the input VSWR introduced by right-angled bends in 25- $\Omega$  and 75- $\Omega$  microstrip lines (on a 0.079-cm thick substrate with  $\epsilon_r = 2.5$ ). We note that the input VSWR caused by the 90° bend increases monotonically with frequency and is larger for low impedance (wider) lines, the specific values being 3.45 for a 25- $\Omega$  line at 10 GHz as compared to 1.30 for a 75- $\Omega$  line at the same frequency. Figure 2.5b shows the effect of discontinuity reactance on the behavior of a step (change-in-width) discontinuity. The reflection coefficient increases from its nominal value. At 12 GHz, this increase is about 1% for a 40- $\Omega$  to 60- $\Omega$  step, and about 3% for a 30- $\Omega$  to 70- $\Omega$  impedance change. These results are based on quasistatic characterization of these discontinuities [9] and are included to show that the discontinuity reactances should not be ignored for design at X-band or higher frequencies.

Quasistatic results for microstrip discontinuity characterization have been available since the late 1970s [9,12,17] and have been used in some of the commercially available CAD packages. A more accurate analysis of bends, T-junctions, and crossings (based on field matching using equivalent parallel-plate waveguide

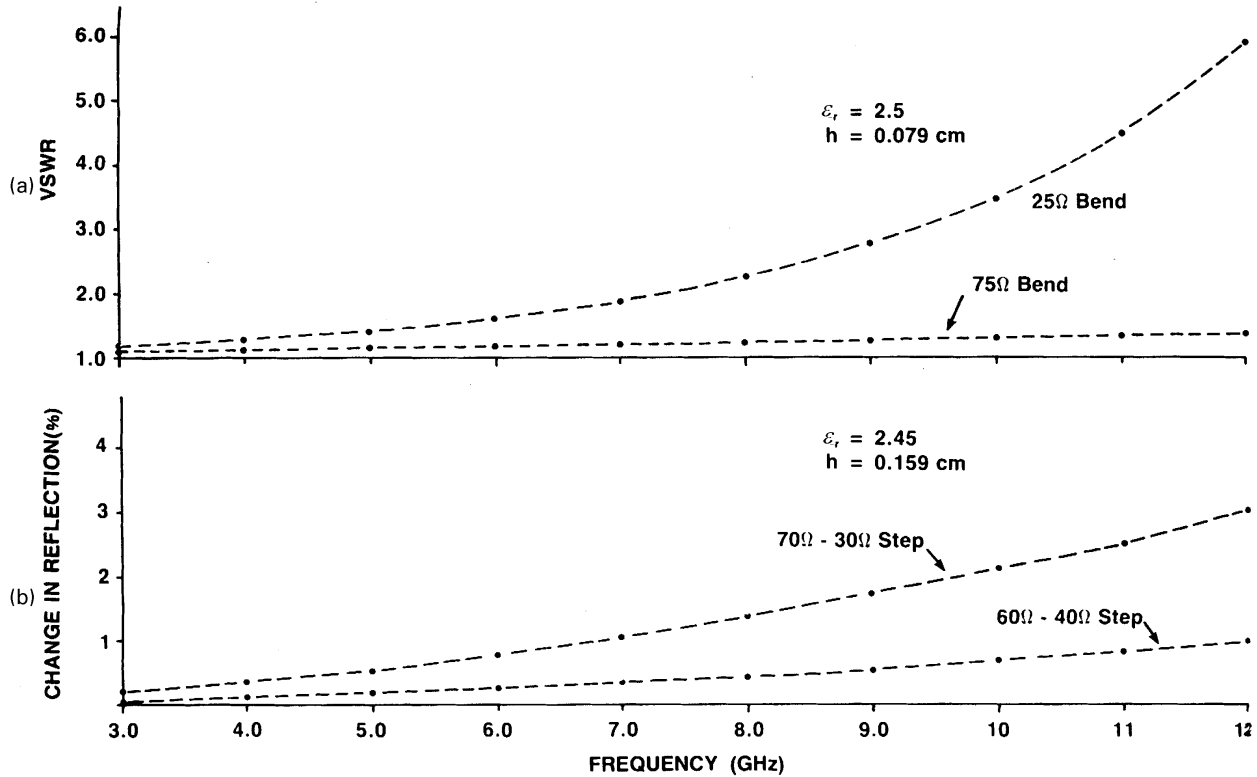


**FIGURE 2.5** (a) Frequency variations of VSWR introduced by right-angled bends in 25-Ω and 75-Ω microstrip lines. (b) Frequency variations of the percentage changes in reflection coefficients introduced by two step discontinuities in microwave circuits. (From [16], copyright © 1988 by John Wiley & Sons; reprinted with permission.)

models of discontinuity configurations) became available later [18]. Vigorous hybrid-mode frequency-dependent characterizations of microstrip open ends and gaps were reported around 1981–1982 [19–21]. These results are based on Galerkin's method in the spectral transform domain. This technique has been extended to other types of discontinuities also [22,23]. The most powerful tool for modeling of transmission line discontinuities in planar microwave circuits is electromagnetic simulation based on moment-method solution of integral equations for current distribution in microstrip or CPW circuits [24–27]. Models based on this approach are used extensively in commercially available microwave CAD software.

Even when accurate numerical results are available, efficient transfer of these results for CAD is not straightforward. Lumped element models with closed-form expressions for values of various parameters [9] have been the most commonly used approach. Many of these closed-form expressions suffer from limited validity with respect to various parameters (impedance, frequency, geometry, etc.) and limit the accuracy of CAD. The substantial progress in the state-of-the-art in microwave CAD that has taken place during the last decade is by improvements of transmission line component models in these softwares.

Recent applications of artificial neural network (ANN) computing to modeling of microwave components [5,6,28,29] is an attractive alternative for CAD-oriented models. In this approach, electromagnetic simulation is used to obtain  $S$ -parameters for all the components to be modeled over the ranges of designable parameters for which these models are expected to be used. An ANN model for each one of the components is developed by training an ANN configuration using the data obtained from EM simulations. A simultaneous training-*cum*-testing approach developed at the University of Colorado [30] is well-suited for this purpose. Such ANN models have been shown to retain the accuracy obtainable from EM simulators and at the same time exhibit the efficiency (in terms of computer time required) that is obtained from lumped network models normally implemented in commercially available microwave network simulators (like the HP MDS).

In addition to the modeling of transmission lines and their discontinuities, implementation of the CAD procedure requires accurate models for various active devices like GaAs MESFETs, varactors, and PIN diodes. Equivalent circuit models for small signal and large signal behaviors of active devices are included in Sections 3.1.4 and 3.1.5 of the next chapter. The ANN modeling approach is also well-suited for modeling of active devices (including thermal effects) [31].

### 2.2.2 Computer-Aided Analysis Techniques

As discussed in Section 2.1 and shown in Figs. 2.2 and 2.3, computer-aided analysis constitutes the key step in the CAD procedure. Since the analysis forms a part of the optimization loop, the analysis subprogram is executed again and again (typically 100 times or more) for a specific circuit design. For this reason, an efficient analysis algorithm constitutes the backbone of any CAD package.

Any general microwave circuit can be viewed as an arbitrarily connected ensemble of multiport components as illustrated in Fig. 2.6. The circuit shown

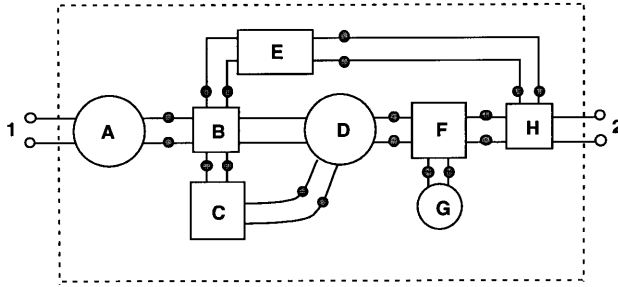


FIGURE 2.6 A general microwave circuit viewed as an ensemble of multiport components.

here consists of eight components (A, B, C, D, E, F, G, H), of which G is a one-port component; A, E, and C are two-port components; D, F, and H are three-port components; and B is a four-port component. Different ports of these components are connected together. There are two external ports (1 and 2). The analysis problem in this case may be stated as follows: characterization of components A through H being known (say, in terms of individual S-matrices), find the S-matrix of the overall combination with reference to the two external ports 1 and 2. The outcome of this analysis will be a  $2 \times 2$  S-matrix. The process of evaluating the circuit performance from the known characterizations of its constituents is termed *circuit analysis*. It requires two inputs: components' characterizations and the topology of interconnections. The analysis process is depicted symbolically in Fig. 2.7.

The two approaches used for frequency domain analysis of linear microwave circuits are *nodal admittance matrix analysis* and *scattering matrix analysis*.

**2.2.2.1 Nodal Admittance Matrix Method** In this method, the voltages  $V_N$  at all the nodes of the circuit to be analyzed are assumed as unknowns. A set of equations is constructed based on the fact that the sum of the currents flowing into any node in the circuit is zero. In microwave circuits the nodal equations are usually set up in the definite form; that is, the voltage of each node is taken with respect to a designated node of the circuit, which is called the *reference node*. The equations are

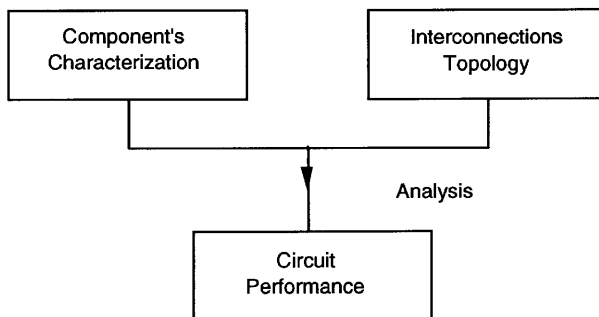


FIGURE 2.7 Block diagram representation of the circuit analysis process.



easily set up in the form of a matrix expression [10]:

$$\mathbf{Y}\mathbf{V}_N = \mathbf{I}_{N_0} \tag{2.1}$$

where  $\mathbf{Y}$  = a square nodal admittance matrix (a degree of this matrix equals the number of nodes in the analyzed circuit);

$\mathbf{V}_N$  = a vector of node voltages taken with respect to a point outside the circuit;

$\mathbf{I}_{N_0}$  = a vector of terminal currents of the independent current sources connected between the nodes and the reference node of the circuit.

The structure of the nodal Y-matrix can be illustrated by considering a circuit example shown in Fig. 2.8. The circuit equations are derived from the application of Kirchhoff's current law at each node of the circuit.

**Node 1:**

$$Y_1 V_{N1} + Y_2(V_{N1} - V_{N2}) + Y_5(V_{N1} - V_{N3}) = I_{N1} \tag{2.2}$$

**Node 2:**

$$Y_3 V_{N2} + Y_2(V_{N2} - V_{N1}) + Y_4(V_{N2} - V_{N3}) + y_{11} V_{N2} + y_{12} V_{N3} = 0 \tag{2.3}$$

**Node 3:**

$$Y_6 V_{N3} + Y_4(V_{N3} - V_{N2}) + Y_5(V_{N3} - V_{N1}) + y_{21} V_{N2} + y_{22} V_{N3} = 0 \tag{2.4}$$

These equations may be written in matrix form as

$$\begin{matrix} \text{Node} & 1 & 2 & 3 \\ \begin{matrix} 1 \\ 2 \\ 3 \end{matrix} & \begin{bmatrix} Y_1 + Y_2 + Y_5 & -Y_2 & -Y_5 \\ -Y_2 & Y_2 + Y_3 + Y_4 + y_{11} & -Y_4 + y_{12} \\ -Y_5 & -Y_4 + y_{21} & Y_4 + Y_5 + Y_6 + y_{22} \end{bmatrix} & \begin{bmatrix} V_{N1} \\ V_{N2} \\ V_{N3} \end{bmatrix} \\ & = \begin{bmatrix} I_{N1} \\ 0 \\ 0 \end{bmatrix} & \end{matrix} \tag{2.5}$$

Equation 2.5 is an example of Eq. 2.1 formulated for the circuit shown in Fig. 2.8. In a general case, the nodal admittance matrix of a circuit may be derived using the rules developed for various circuit components [10], such as an admittance  $Y$ , independent current and voltage sources, controlled current and voltage sources, and multiterminal elements including sections of transmission lines, coupled line sections, MESFETs, and bipolar transistors. It can be shown that a multiterminal device (element) does not have to be replaced by its equivalent circuit composed of two-terminal elements.

When a multiterminal device is described by its definite admittance matrix  $\mathbf{y}_d$ , the elements of  $\mathbf{y}_d$  may be entered into the matrix  $\mathbf{Y}$  of the whole circuit only if the reference node of the device agrees with the reference node of the whole circuit.

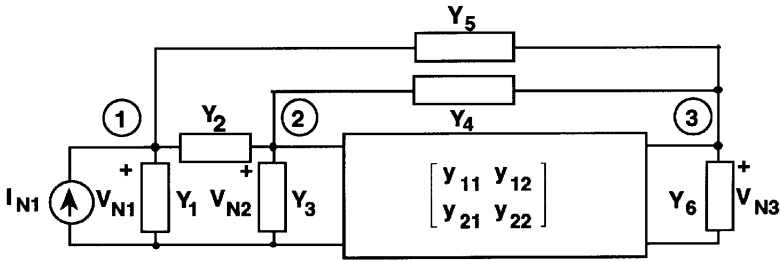


FIGURE 2.8 A network example for illustrating the nodal admittance matrix method.

Figure 2.9 presents a three-terminal device as a two-port network, with terminal 3 taken as the reference node. The definite admittance matrix of the device is given by the following equation:

$$\begin{bmatrix} I_1 \\ I_2 \end{bmatrix} = \begin{bmatrix} y_{11} & y_{12} \\ y_{21} & y_{22} \end{bmatrix} \begin{bmatrix} V_1 \\ V_2 \end{bmatrix} \tag{2.6}$$

If the reference node of the three-terminal device agrees with the reference node of the whole circuit, and if node 1 of the terminal device is connected to node  $i$  of the circuit and node 2 to node  $j$ , the terms of the definite admittance matrix  $y_d$  of the device are added to the nodal admittance matrix  $\mathbf{Y}$  of the whole circuit:

$$\begin{matrix} & (i) & & (j) & \\ \begin{matrix} (i) \\ (j) \end{matrix} & \begin{bmatrix} \vdots & \vdots \\ \cdots & y_{11} & \cdots & y_{12} & \cdots \\ \vdots & \vdots \\ \cdots & y_{21} & \cdots & y_{22} & \cdots \\ \vdots & \vdots \end{bmatrix} & & & \end{matrix} \tag{2.7}$$

The conversion of a multiterminal element admittance matrix from indefinite form (with the reference node being an undefined node external to the circuit) into definite

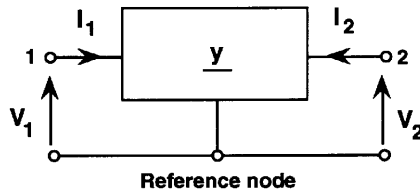


FIGURE 2.9 Three-terminal device as a two-port network with one terminal taken as its reference node.

form, and vice versa, can be performed easily because the indefinite admittance matrix of an  $n$  terminal circuit satisfies the following relations:

$$\sum_{i=1}^n y_{ij} = 0, \quad \text{for } j = 1, 2, \dots, n \quad (2.8a)$$

$$\sum_{j=1}^n y_{ij} = 0, \quad \text{for } i = 1, 2, \dots, n \quad (2.8b)$$

The nodal admittance matrix  $\mathbf{Y}$  and the right-hand vector  $\mathbf{I}_N$  of Eq. 2.1 are constructed in accordance with the rules developed for various components [10]. The resulting matrix  $\mathbf{Y}$  and the vector  $\mathbf{I}_N$  are computed at the frequency of interest. The entries  $Y_{ij}$  of the nodal admittance matrix may become very small or very large as the circuit function (response) is computed for different values of frequency. The most important are values of the main diagonal entries  $Y_{ii}$  of the nodal admittance matrix. For example, if an inductor and a capacitor are connected to node  $i$ , at a series resonant frequency of these elements, the entry  $Y_{ii}$  becomes undefined. Also, the nodal admittance matrix of a circuit with dependent sources may become singular and the set of circuit equations cannot be solved. In microwave circuits, we assume very often a lossy circuit. The determinant of the nodal admittance matrix of such a circuit is a polynomial in the frequency variable  $\omega$ . The matrix  $\mathbf{Y}$  becomes singular at the zeros of the polynomial, and the system of circuit equations has no solution.

Computer-aided analysis of microwave circuits in the frequency domain based on the nodal admittance matrix requires multiple computation of the solution of a system of linear equations with complex coefficients. An important problem is the numerical instability of a solution process performed by computer, which may occur if the so-called condition number of the coefficient matrix of the linear equation system is too large.

The nodal admittance matrix in general is a sparse matrix, which means that many entries of the matrix are equal to zero, particularly for large circuits. In conventional numerical procedures used to solve a system of linear equations, the arithmetic operations are performed on all nonzero and zero-valued entries of the coefficient matrix. The whole solution procedure involves  $n^3/3 + n^2 - n/3$  complex number multiplications and divisions ( $n$  is the order of the coefficient matrix). To save computation time and minimize storage requirements, the sparsity of the coefficient matrix must be taken into account in the solution procedure.

**2.2.2.2 Computation of Circuit Functions** The solution of the nodal matrix expression (Eq. 2.1) provides us with the numerical values of all node voltages of a circuit. In most practical cases, as, for example, filter or amplifier design, there is one source of excitation in the circuit and we are interested in one or two voltages in the circuit.

For the sake of clarity in the considerations to follow, we assume that an independent source of one ampere has been connected between node 1 and the

reference node and that the output node is node  $n$ . The node voltage equations are now

$$\mathbf{YV} = \mathbf{I}_N = \begin{bmatrix} 1 \\ 0 \\ \vdots \\ 0 \end{bmatrix} \quad (2.9)$$

Let  $\mathbf{e}_i$  be a vector of zero entries except the  $i$ th, which is one. The postmultiplication of a matrix by  $\mathbf{e}_i$  results in extracting the  $i$ th column from the matrix. If matrix  $\mathbf{Z}$  is the inverse of  $\mathbf{Y}$ , then  $\mathbf{YZ} = \mathbf{I}$ , where  $\mathbf{I}$  is an identity matrix of order  $n$ . By postmultiplication of  $\mathbf{YZ}$  by  $\mathbf{e}_1$ , we have

$$\mathbf{YZe}_1 = \begin{bmatrix} 1 \\ 0 \\ \vdots \\ 0 \end{bmatrix} \quad (2.10)$$

From Eqs. 2.9 and 2.10, we can conclude

$$\mathbf{V} = \mathbf{Ze}_1 \quad (2.11)$$

We define a transfer function  $H(j\omega)$  as the ratio of the output voltage  $V_k$  to the input current  $I_1$  of the independent current source connected between node 1 and the reference node:

$$H(j\omega) = \frac{V_k}{I_1} = |H(j\omega)|e^{j\phi(\omega)} \quad (2.12)$$

The magnitude of  $H(j\omega)$  is called the *gain of the circuit* and  $\phi(\omega)$  is the phase. The term  $|H(j\omega)|$  is directly related to the available power gain:

$$G_T = \frac{P_L}{P_{SA}} = 4\text{Re}\{Y_S\}\text{Re}\{Y_L\}|H(j\omega)| \quad (2.13)$$

In Eq. 2.13,  $P_L$  is the active power dissipated in the load admittance  $Y_L$  connected between the output node and the reference node, and  $P_{SA}$  is the available power of the current source with the internal admittance  $Y_S$ .

In filter design problems, the quantity *insertion loss* is more commonly used:

$$\text{IL} = -20 \log(|Y_S + Y_L| \cdot |H(j\omega)|) \quad (2.14)$$

Other circuit functions are also important. We have the input impedance

$$Y_{\text{in}} = \frac{I_1}{V_1} - Y_S \quad (2.15)$$

or, equivalently, the reflection coefficient

$$\Gamma_{in} = \frac{Y_{in} - Y_S}{Y_{in} + Y_S} = 1 - 2 \frac{V_1}{I_1} Y_S \tag{2.16}$$

These network functions can be computed, once the node voltages  $V_1$  and  $V_k$  are determined.

**2.2.2.3 Scattering Matrix Analysis** Scattering matrix analysis is applicable to any general microwave circuit configuration when all the circuit components are modeled in terms of their scattering parameters. In this method of analysis [9], the circuit diagram is configured such that there are no unconnected ports. That is, sources (along with their source impedances) are connected to the input ports, and all output ports are terminated in respective loads. For circuit analysis, it is adequate to consider matched sources and matched loads. Consider the example of an impedance matching circuit and its equivalent representation shown in Fig. 2.10a,b. For implementing this method, this circuit may be depicted as shown in Fig. 2.11a. Independent sources (Fig. 2.11b) in such a representation may be described by the relation

$$b_g = s_g a_g + c_g \tag{2.17}$$

where  $c_g$  is the wave impressed by the generator. For sources that are matched (or isolated)  $s_g = 0$  and  $b_g = c_g$ . All other components in the circuit are described by

$$\mathbf{b}_i = S_i \mathbf{a}_i \tag{2.18}$$

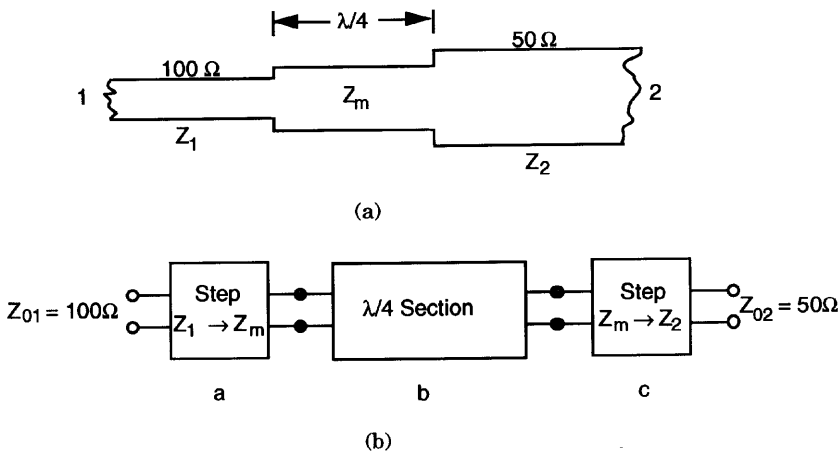


**FIGURE 2.10** (a) A quarter-wave matching network. (b) Interconnected multiport representation of the circuit in part (a).

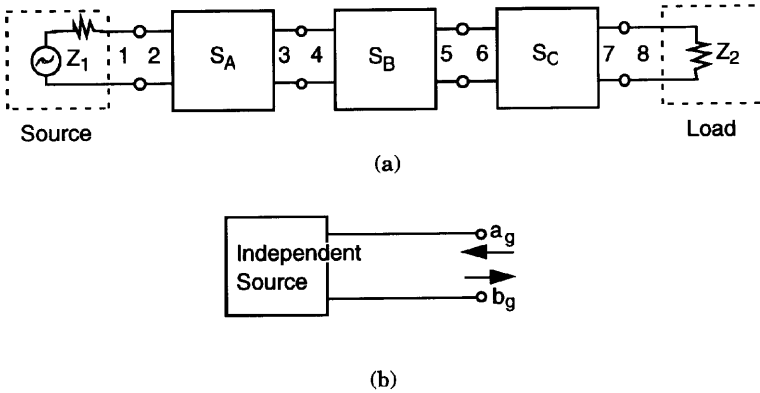


**FIGURE 2.11** (a) Network of Fig. 2.10a rewritten for implementing the generalized scattering-matrix analysis procedure. (b) Independent source introduced for scattering matrix analysis.

where  $\mathbf{a}_i$  and  $\mathbf{b}_i$  are incoming and outgoing wave variables, respectively, for the  $i$ th component with  $n_i$  ports and  $S_i$  is the scattering matrix.

The governing relation for all components (say the total number is  $m$ ) in the circuit can be put together as

$$\mathbf{b} = S\mathbf{a} + \mathbf{c} \tag{2.19}$$

where

$$\mathbf{b} = \begin{bmatrix} \mathbf{b}_1 \\ \mathbf{b}_2 \\ \vdots \\ \mathbf{b}_m \end{bmatrix}, \quad \mathbf{a} = \begin{bmatrix} \mathbf{a}_1 \\ \mathbf{a}_2 \\ \vdots \\ \mathbf{a}_m \end{bmatrix}, \quad \text{and} \quad \mathbf{c} = \begin{bmatrix} \mathbf{c}_1 \\ \mathbf{c}_2 \\ \vdots \\ \mathbf{c}_m \end{bmatrix} \tag{2.20}$$

Here,  $\mathbf{b}_i$ ,  $\mathbf{a}_i$ ,  $\dots$ , are themselves vectors with the number of elements equal to the number of ports of that particular component. The size of vector  $\mathbf{b}$ ,  $\mathbf{a}$ , or  $\mathbf{c}$  is equal to the total number of ports of all the components in the modified network representation. For the network shown in Fig. 2.11a, this number is 8: counting one port for the source; two ports each for the three components A, B, and C; and one port for the load. The vector  $\mathbf{c}$  will have nonzero values only for the output ports of independent sources in the network. For the network of Fig. 2.11a,

$$\mathbf{c} = [c_1, 0, 0, 0, 0, 0, 0, 0]^T \tag{2.21}$$

The output port of the source has been numbered 1, and the superscript T indicates transpose of a vector or matrix.

The matrix  $\mathbf{S}$  is a block diagonal matrix whose submatrices along the diagonal are the scattering matrices of various components. In the general case, the matrix  $\mathbf{S}$  may be written as

$$\mathbf{S} = \begin{bmatrix} (S_1) & 0 & - & - & 0 \\ 0 & (S_2) & - & - & 0 \\ - & - & (-) & - & - \\ - & - & - & (-) & - \\ 0 & 0 & - & - & (S_m) \end{bmatrix} \quad (2.22)$$

where 0's represent null matrices. For the network of Fig. 2.11a, the S-matrix will look like

$$\mathbf{S} = \begin{bmatrix} [S_{11}^S] & 0 & 0 & 0 & 0 \\ 0 & \begin{bmatrix} S_{22}^A & S_{23}^A \\ S_{32}^A & S_{33}^A \end{bmatrix} & 0 & 0 & 0 \\ 0 & 0 & \begin{bmatrix} S_{44}^B & S_{45}^B \\ S_{54}^B & S_{55}^B \end{bmatrix} & 0 & 0 \\ 0 & 0 & 0 & \begin{bmatrix} S_{66}^C & S_{67}^C \\ S_{76}^C & S_{77}^C \end{bmatrix} & 0 \\ 0 & 0 & 0 & 0 & [S_{88}^L] \end{bmatrix} \quad (2.23)$$

where  $S_{11}^S$  and  $S_{88}^L$  are one-port S-parameter characterizations for the source and the load, respectively. When both the source and the load are matched,  $S_{11}^S = S_{88}^L = 0$ . The other three  $(2 \times 2)$  S-matrices characterize components A, B, and C, respectively.

Equation 2.19 contains the characterizations of individual components but does not take into account the constraints imposed by interconnections. For a pair of connected ports, the outgoing wave variable at one port must equal the incoming wave variable at the other (assuming that wave variables at two ports are normalized with respect to the same impedance level). For example, if the port  $j$  of one component is connected to port  $k$  of the other component, as shown in Fig. 2.12, the incoming and outgoing wave variables are related as

$$a_j = b_k \quad \text{and} \quad a_k = b_j \quad (2.24)$$

or

$$\begin{bmatrix} b_j \\ b_k \end{bmatrix} = \begin{bmatrix} 0 & 1 \\ 1 & 0 \end{bmatrix} \begin{bmatrix} a_j \\ a_k \end{bmatrix} = [\Gamma]_{jk} \begin{bmatrix} a_j \\ a_k \end{bmatrix} \quad (2.25)$$

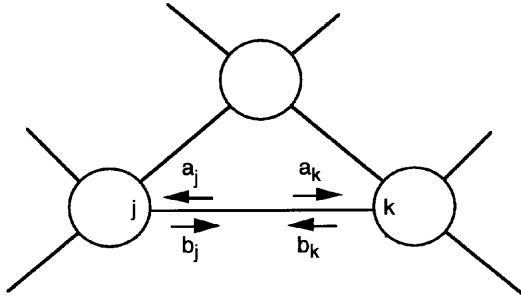


FIGURE 2.12 Interconnection of ports  $j$  and  $k$ .

We can extend  $[\Gamma]_{jk}$  to write an interconnection matrix describing all the connections in the circuit. We express

$$\mathbf{b} = \mathbf{\Gamma}a \tag{2.26}$$

where  $\mathbf{\Gamma}$  is a square matrix of the same size as that of  $\mathbf{S}$ . The size of the  $\mathbf{\Gamma}$ -matrix is given by the sum total of the ports in all the components in the circuit. The size is  $8 \times 8$  in the example of Fig. 2.11a. For the example of Fig. 2.11a, the  $\mathbf{\Gamma}$ -matrix may be written as

$$\begin{bmatrix} b_1 \\ b_2 \\ b_3 \\ b_4 \\ b_5 \\ b_6 \\ b_7 \\ b_8 \end{bmatrix} = \begin{bmatrix} 0 & 1 & 0 & 0 & 0 & 0 & 0 & 0 \\ 1 & 0 & 0 & 0 & 0 & 0 & 0 & 0 \\ 0 & 0 & 0 & 1 & 0 & 0 & 0 & 0 \\ 0 & 0 & 1 & 0 & 0 & 0 & 0 & 0 \\ 0 & 0 & 0 & 0 & 0 & 1 & 0 & 0 \\ 0 & 0 & 0 & 0 & 1 & 0 & 0 & 0 \\ 0 & 0 & 0 & 0 & 0 & 0 & 0 & 1 \\ 0 & 0 & 0 & 0 & 0 & 0 & 1 & 0 \end{bmatrix} \begin{bmatrix} a_1 \\ a_2 \\ a_3 \\ a_4 \\ a_5 \\ a_6 \\ a_7 \\ a_8 \end{bmatrix} \tag{2.27}$$

Note that the matrix is symmetrical and there is only a single 1 in any row or any column. The latter signifies that any port is connected only to one other port. This excludes the possibility of three ports being connected at one single point. If such a junction exists in a circuit, it must be considered a three-port component, as shown in Fig. 2.13. The ports  $a'$ ,  $b'$ , and  $c'$  of this new component depicting the junction  $j$  are connected to the parts  $a$ ,  $b$ , and  $c$ , respectively, in a one-to-one manner and the nature of the  $\mathbf{\Gamma}$ -matrix is similar to the one as indicated in Eq. 2.27.

Equations 2.19 and 2.26 describe the circuit completely and may be combined into a single equation as

$$\mathbf{\Gamma}a = \mathbf{S}a + \mathbf{c} \tag{2.28}$$

or  $(\mathbf{\Gamma} - \mathbf{S})\mathbf{a} = \mathbf{c}$ .



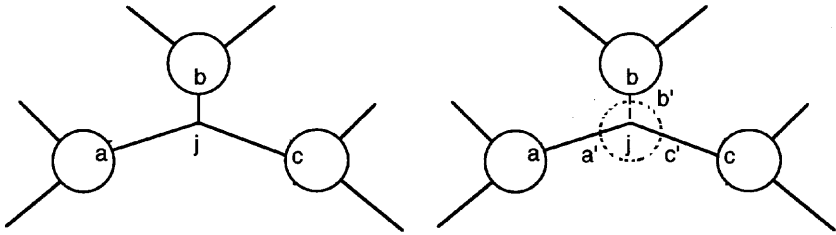


FIGURE 2.13 A three-way connection at  $j$  treated as a three-port component.

Setting  $(\Gamma - S) = \mathbf{W}$ , we have

$$\mathbf{a} = \mathbf{W}^{-1} \mathbf{c} = \mathbf{M} \mathbf{c} \tag{2.29}$$

$\mathbf{W}$  is called the connection-scattering matrix. For our example of Fig. 2.11a,  $\mathbf{W}$  may be written as

$$\begin{matrix}
 & \begin{matrix} 1 & 2 & 3 & 4 & 5 & 6 & 7 & 8 \end{matrix} \\
 \begin{matrix} 1 \\ 2 \\ 3 \\ 4 \\ 5 \\ 6 \\ 7 \\ 8 \end{matrix} & \left[ \begin{array}{cccccccc}
 -S_{11}^S & 1 & 0 & 0 & 0 & 0 & 0 & 0 \\
 1 & -S_{11}^A & -S_{12}^A & 0 & 0 & 0 & 0 & 0 \\
 0 & -S_{21}^A & -S_{22}^A & 1 & 0 & 0 & 0 & 0 \\
 0 & 0 & 1 & -S_{11}^B & -S_{12}^B & 0 & 0 & 0 \\
 0 & 0 & 0 & -S_{21}^B & -S_{22}^B & 1 & 0 & 0 \\
 0 & 0 & 0 & 0 & 1 & -S_{11}^C & -S_{12}^C & 0 \\
 0 & 0 & 0 & 0 & 0 & -S_{21}^C & -S_{22}^C & 1 \\
 0 & 0 & 0 & 0 & 0 & 0 & 1 & -S_{11}^L
 \end{array} \right]
 \end{matrix} \tag{2.30}$$

We note that the main diagonal elements in  $\mathbf{W}$  are the negative of the reflection coefficients at the various component ports. The other (nondiagonal) elements of  $\mathbf{W}$  are the negative of the transmission coefficients between different ports of the individual components. All other elements are zero except for those corresponding to the two ports connected together (the  $\Gamma$ -matrix elements) which are 1's. The zero/nonzero pattern in the  $\mathbf{W}$ -matrix depends only on the topology of the circuit and does not change with component characterizations or frequency of operation. The tridiagonal pattern of Eq. 2.30 is a characteristic of a chain of two-port components cascaded together.

The circuit analysis involves solution of the matrix equation (2.29) to find components of the vector  $\mathbf{a}$ . Variable  $a$ 's corresponding to loads at various external ports are found by choosing the vector  $\mathbf{c}$  to consist of a unity at one of the external

ports and zeros elsewhere. This leads to the evaluation of a column of the S-matrix of the circuit. Say, for  $c_j = 1$  and all other  $c_{i,i \neq j} = 0$ , we find values of vector  $\mathbf{a}$ . Then

$$S_{lj} = \frac{b_l}{a_j} = a_{l'} \quad \left( a_i = \begin{cases} 1, & \text{for } i = j \\ 0, & \text{otherwise} \end{cases} \right) \quad (2.31)$$

where  $l'$  is the load port corresponding to the  $l$ th port of the circuit and  $j$  is the other circuit port (for which the impressed wave variable is unity). Equation 2.31 yields the  $j$ th column of the scattering matrix. Considering the example of Fig. 2.11a, if we make  $c_1 = 1$ , other  $c$ 's being zero, then the first column of the matrix for the circuit in Fig. 2.10 (i.e., cascade of three components A, B, and C) is given by

$$S_{11} = a_1 = M_{11}, \quad S_{21} = a_8 = M_{81} \quad (2.32)$$

Here subscripts of  $S$  refer to circuit ports of Fig. 2.10 and subscripts of  $a$  correspond to component ports of Fig. 2.11a. For obtaining the second column of the S-matrix, we take  $c_8 = 1$  and other  $c$ 's to be zero and find  $a_1$  and  $a_8$  again to yield

$$S_{21} = a_1 = M_{81}, \quad S_{22} = a_8 = M_{88} \quad (2.33)$$

It may be noted that Eq. 2.29 yields much more information (namely, wave variables at all the internal connected ports also) than what is needed for calculation of the S-matrix of the circuit. Knowledge of the wave variables at internal ports is needed for carrying out a sensitivity analysis of the circuit using the adjoint network method. For this reason, the present method is suitable for CAD purposes.

**2.2.2.4 Analysis of Nonlinear Circuits** The computer-aided circuit analysis techniques discussed above are applicable to linear circuits only. For design of nonlinear circuits, such as oscillators, frequency multipliers, and mixers, it becomes necessary to modify the analysis technique. A general analysis procedure for nonlinear microwave circuits is discussed in this section.

*Linear and Nonlinear Subnetworks* In many nonlinear microwave circuits, the nonlinearity is restricted to a single device (e.g., a MESFET or Schottky diode) operating in the nonlinear region. Since the rest of the circuit is linear, it is desirable to separate the circuit into linear and nonlinear subnetworks that may be treated separately. Nonlinear and linear subnetworks are shown schematically in Fig. 2.14. It may be noted that the linear part of the device model and the package equivalent circuit are also included in the linear subnetwork.

The nonlinear subnetwork consists of nonlinear circuit elements in the device model (nonlinear controlled current sources, diodes, voltage-dependent capacitors, current-dependent resistors, etc.). These nonlinear components (and hence the resulting nonlinear subnetwork) are usually best simulated in terms of time

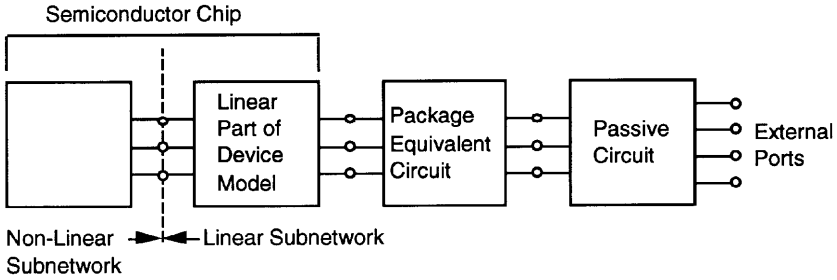


FIGURE 2.14 Separation of a nonlinear microwave circuit in linear and nonlinear subnetworks.

domain voltage and current vectors  $\mathbf{v}(t)$  and  $\mathbf{i}(t)$ . A general time domain representation of the nonlinear subnetwork could be of the form [32,33]

$$\mathbf{i}(t) = \mathbf{f} \left\{ \mathbf{i}(t), \frac{d\mathbf{i}}{dt}, \mathbf{v}(t), \frac{d\mathbf{v}}{dt} \right\} \tag{2.34}$$

where vector  $\mathbf{f}$  is a nonlinear function of various currents, voltages, and their time derivatives. Higher order derivatives may also appear. For the present discussion, it is assumed that the vector function  $\mathbf{f}$  is known (hopefully analytically) from the nonlinear modeling of the device.

The linear subnetwork, on the other hand, can easily be analyzed by a frequency domain circuit analysis program and characterized in terms of an admittance matrix as

$$\mathbf{I}(\omega) = \mathbf{Y}(\omega)\mathbf{V}(\omega) + \mathbf{J}(\omega) \tag{2.35}$$

where  $\mathbf{V}$  and  $\mathbf{I}$  are the vectors of voltage and current phasors at the subnetwork ports,  $\mathbf{Y}$  represents its admittance matrix, and  $\mathbf{J}$  is a vector of Norton equivalent current sources.

Analysis of the overall nonlinear circuit (linear subnetwork plus nonlinear subnetwork) involves continuity of currents given by Eqs. 2.34 and 2.35 at the interface between linear and nonlinear subnetworks.

*Harmonic Balance Method* In principle, the solution to the nonlinear circuit problem can always be found by integrating the differential equations that describe the system. However, in most microwave nonlinear circuits we are interested in the steady-state response with periodic excitations and periodic responses with a limited number of significant harmonics. In such a situation, the *harmonic balance technique* is much more efficient.

In the harmonic balance technique [34], the nonlinear network is decomposed into a minimum possible number of linear and nonlinear subnetworks. The

frequency domain analysis of the linear subnetwork is carried out at a frequency  $\omega_0$  and its harmonics. The characterization in Eq. 2.35 is thus generalized as:

$$I_k(k\omega_0) = Y(k\omega_0)V_k(k\omega_0) + J_k(k\omega_0) \quad (2.36)$$

where  $k = 1, \dots, N$ , with  $N$  being the number of significant harmonics considered. The nonlinear subnetwork is analyzed in the time domain and the response obtained is in the form of Eq. 2.34. A Fourier expansion of the currents yields

$$\mathbf{i}(t) = \left( \text{Re} \sum_{k=0}^N \mathbf{F}_k(k\omega_0) \exp(jk\omega_0 t) \right) \quad (2.37)$$

where coefficients  $\mathbf{F}_k$  are obtained by a fast Fourier transform (FFT) algorithm. The piecewise harmonic balance technique involves a comparison of Eqs. 2.36 and 2.37 to yield a system of equations as

$$\mathbf{F}_k(k\omega_0) - \mathbf{Y}(k\omega_0)\mathbf{V}_k(k\omega_0) - \mathbf{J}_k(k\omega_0) = \mathbf{0}, \quad k = 0, 1, \dots, N \quad (2.38)$$

The solution of this system of equations yields the response of the circuit in terms of voltage harmonics  $V_k$ . Numerically, the solution of Eq. 2.38 is obtained by minimizing the harmonic balance error

$$\Delta\varepsilon_b(\mathbf{V}) = \left\{ \sum_{k=0}^N |\mathbf{F}_k(k\omega_0) - \mathbf{Y}(k\omega_0)\mathbf{V}(k\omega_0) - \mathbf{J}_k(k\omega_0)|^2 \right\}^{1/2} \quad (2.39)$$

Optimization techniques used for circuit optimization are used for solving Eq. 2.38 and thus obtaining steady-state periodic solution of nonlinear circuits.

In most of the circuit-antenna module applications, only the steady-state response is needed and the harmonic balance method discussed above is appropriate for this purpose. However, when transient response is also desired (as for evaluating certain modulation aspects of grid oscillators), it becomes necessary to use time domain techniques. The FDTD method discussed in Chapter 6 is suitable for that purpose.

### 2.2.3 Circuit Optimization

Optimization is an important step in the CAD process and, as depicted in Fig. 2.15, converts an initial (and quite often unacceptable) design into an optimized final design meeting the given specifications. Optimization procedures involve iterative modifications of the initial design, followed by circuit analysis and comparison with the specified performance.

There are two different ways of carrying out the modification of designable parameters in an optimization process. These are known as *gradient methods* and *direct search methods* of optimization. Gradient methods use information about the derivatives of the performance functions (with respect to designable parameters) for

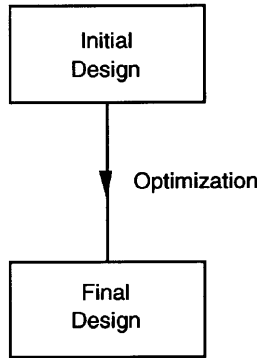


FIGURE 2.15 Role of the optimization process.

arriving at the modified set of parameters. This information is obtained from the sensitivity analysis. On the other hand, the direct search methods do not use gradient information, and parameter modifications are carried out by searching for the optimum in a systematic manner. A flowchart for the optimization process is shown in Fig. 2.16.

The optimization methods useful for integrated circuit–antenna modules are identical to those used in other disciplines and are well documented in the literature [9–11].

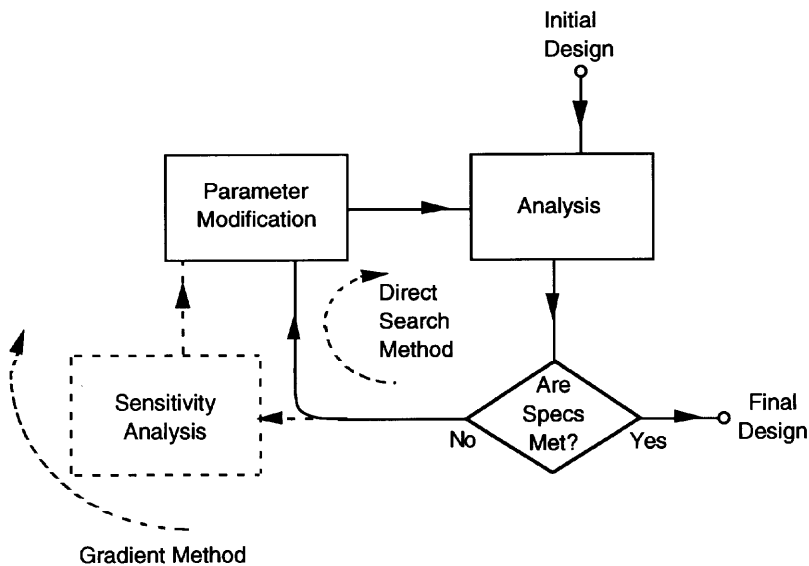


FIGURE 2.16 Flowcharts for direct search and gradient methods of optimization.

## 2.3 CAD FOR PRINTED MICROWAVE ANTENNAS

CAD techniques for microwave antennas are not as well developed as those for microwave circuits. One of the factors responsible for this situation is the variety of different configurations used for radiators at microwave frequencies. Design techniques used for, say, reflector antennas, are different from those needed for wire antennas (dipoles, Yagi arrays, etc.), which are quite different from those for slotted waveguide array or printed microstrip antennas, for that matter. The class of antennas most appropriate for integration with circuits are printed microstrip patches and slot radiators. CAD considerations for this group of antennas are discussed in this section.

### 2.3.1 Modeling of Printed Patches and Slots

General CAD methodology depicted in Fig. 2.3 is appropriate for microstrip patches and slot radiators also. Design of microstrip patches has been studied more widely (e.g., see [35]) than that of slot radiators. Two kinds of modeling approaches are used for microstrip patches: equivalent network models and numerical models based on EM simulation methods.

**2.3.1.1 Network Models for Microstrip Patches** The similarity of microstrip patch radiators to microstrip resonators has led to the development of three kinds of network models for microstrip patches: (1) transmission line model [35, Chap. 10], (2) cavity model [36], and (3) multiport network model [35, Chap. 9].

*Transmission Line Model* The transmission line model is the simplest of the network models for microstrip patch antennas. In this model, a rectangular microstrip antenna patch is viewed as a resonant section of a microstrip transmission line. A detailed description of the transmission line model is available in literature [35,37–39]. The basic concept is shown in Fig. 2.17, which illustrates the transmission line models for (a) an unloaded rectangular patch, (b) a rectangular patch with a feedline along the radiating edge, and (c) a rectangular patch with a feedline along the non-radiating edge.  $Z_{0p}$  is the characteristic impedance of a microstrip line of width  $W_p$ , and  $\epsilon_{\text{rep}}$  is the corresponding effective dielectric constant.  $B_e$  and  $G_e$  are capacitive and conductive components of the edge admittance  $Y_e$ . The susceptance  $B_e$  accounts for the fringing field associated with the radiating edge of the width  $W_p$ , and  $G_e$  is the conductance contributed by the radiation field associated with each edge. Power carried away by the surface wave(s) excited along the slab may also be represented by a lumped loss and added to  $G_e$ . In Fig. 2.17b,c,  $Z_{0f}$  and  $\epsilon_{\text{ref}}$  are the characteristic impedance and the effective dielectric constant for the feeding microstrip line of width  $W_f$ . In both of these cases, the parasitic reactances associated with the junction between the line and the patch have not been taken into account.

Transmission line models may also be developed for two-port rectangular microstrip patches [40,41]. These configurations are used in the design of series-fed linear (or planar) arrays. Models for two types of two-port rectangular microstrip

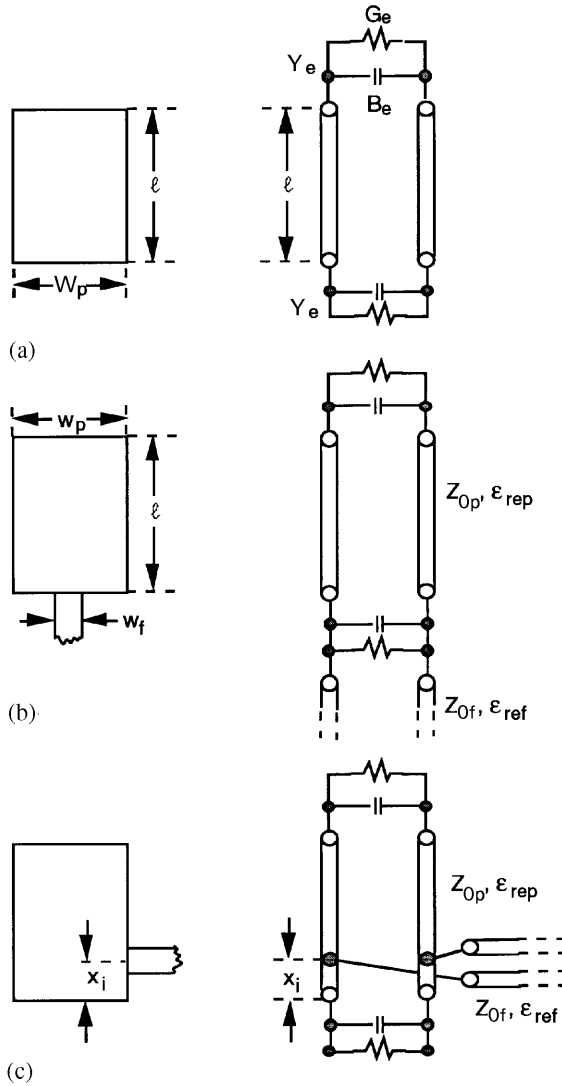


**FIGURE 2.17** Transmission line models for three rectangular microstrip patch configurations: (a) unloaded patch, (b) feedline along the radiating edge, and (c) feedline along the nonradiating edge.

patches are shown in Fig. 2.18. Figure 2.18a illustrates the equivalent transmission line network when the two ports are located along the radiating edges, and Fig. 2.18b shows the transmission line model [41] when the two ports are along the nonradiating edges. It has been shown [40,41] that, when the two ports are located along the nonradiating edges, transmission from port 1 to port 2 can be controlled by

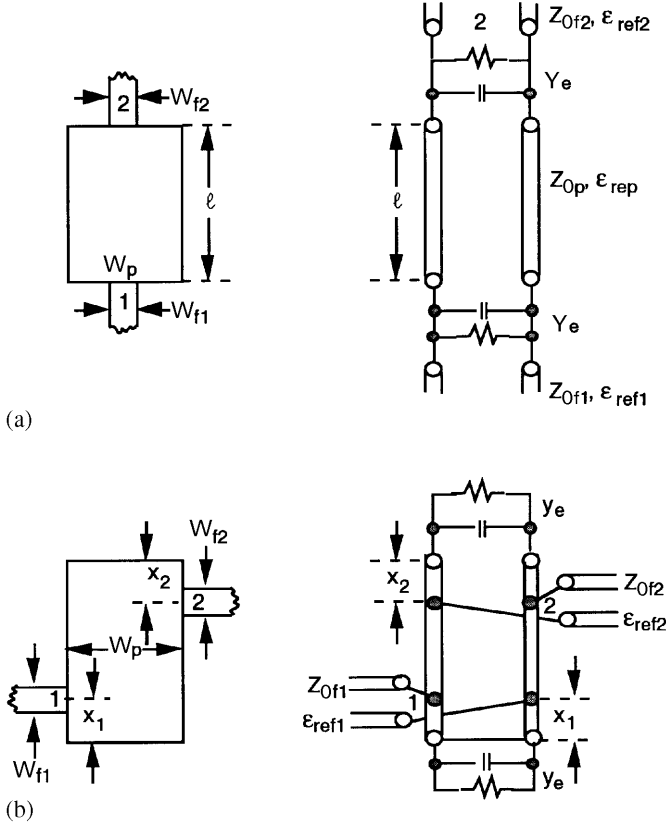


**FIGURE 2.18** Transmission-line modes for two-port rectangular microstrip patch antennas: (a) feedlines along radiating edges and (b) feedlines along nonradiating edges.

suitable choices of distances  $x_1$  and  $x_2$ . Again, the two models shown in Figs. 2.18a,b do not incorporate the parasitic reactances associated with the feedline–patch junctions.

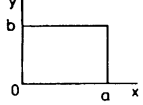
There are several limitations inherent to the concept of the transmission line model for microstrip antennas. The basic assumptions include: (1) fields are uniform at the width  $W_p$  of the patch; and (2) there are no currents transverse to the length  $l$  of the patch. Detailed analysis of the rectangular patches has shown [42] that, even at a frequency close to resonance, field distribution along the radiating edge is not always uniform. Also, the transverse currents are caused by the feeding mechanism and are invariably present. Moreover, the circularly polarized rectangular microstrip antennas (whose operation depends on the excitation of two orthogonal modes) cannot be represented by the transmission line model discussed above. Clearly, a more accurate method for modeling of microstrip antennas is needed.

*Cavity Model* A planar two-dimensional cavity model for microstrip patch antennas [43,44] offers considerable improvement over the one-dimensional trans-



**TABLE 2.1** Variation of Modal Fields ( $\Psi_{mn}$ ) and Resonant Wavenumbers ( $k_{mn}$ ) for Various Patch Geometries Analyzed by the Cavity Method

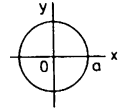
Rectangle



$$\Psi_{mn} = \cos \frac{m\pi}{a} x \cos \frac{n\pi}{b} y$$

$$k_{mn} = \sqrt{\left(\frac{m\pi}{a}\right)^2 + \left(\frac{n\pi}{b}\right)^2}$$

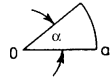
Circle (disk)



$$\Psi_{mn} = J_n(k_{mn}\rho)e^{jn\phi}$$

$$J'_n(k_{mn}a) = 0$$

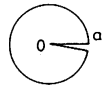
Circular segment



$$\Psi_{mv} = J_v(k_{mv}\rho) \cos v\phi$$

$$v = n\pi/\alpha, J'_v(k_{mv}a) = 0$$

Disk with slot

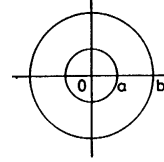


$$\Psi_{mn} = J_{n/2}(k_{mn}\rho) \cos(n\phi/2)$$

$$J'_{n/2}(k_{mn}a) = 0$$

$$\alpha \approx 2\pi, v = n/2$$

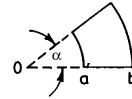
Circular ring



$$\Psi_{mn} = [N'_n(k_{mn}a)J_n(k_{mn}\rho) - J'_n(k_{mn}a)N_n(k_{mn}\rho)]e^{jn\phi}$$

$$\frac{J'_n(k_{mn}a)}{N'_n(k_{mn}a)} = \frac{J'_n(k_{mn}b)}{N'_n(k_{mn}b)}$$

Circular ring segment

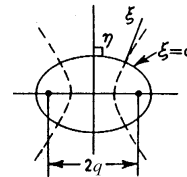


$$\Psi_{mn} = [N'_v(k_{mv}a)J_v(k_{mv}\rho) - J'_v(k_{mv}a)N_v(k_{mv}\rho)] \cos v\phi$$

$$v = n\pi/\alpha$$

$$\frac{J'_v(k_{mv}a)}{N'_v(k_{mv}a)} = \frac{J'_v(k_{mv}b)}{N'_v(k_{mv}b)}$$

Ellipse



Even modes:

$$\Psi_{mn} = \text{Re}_m(\xi, \chi e_n) S e_m(\eta, \chi e_n)$$

$$\text{Re}_m(a, \chi e_n) = 0, \chi e_n = kq$$

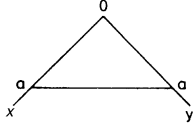
$$\text{major axis} = 2q \cosh a$$

$$\text{minor axis} = 2q \sinh a$$

Odd modes:

Replacing  $e$  by  $o$  in the above

Right isosceles



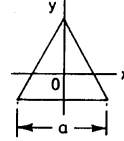
$$(a) \Psi_m = \cos \frac{m\pi}{a}x - \cos \frac{m\pi}{a}y$$

$$k_m = \sqrt{2} \frac{m\pi}{a}$$

$$(b) \Psi_m = \cos \frac{m\pi}{a}x \cos \frac{m\pi}{a}y$$

$$k_m = \sqrt{2} \frac{m\pi}{a}$$

Equilateral triangle



$$\begin{aligned} \Psi_{mn} &= \cos \frac{2\pi l}{3b} \left( \frac{u}{2} + b \right) \\ &\times \cos \left( \frac{\pi(m+n)(v-w)}{9b} \right) \\ &+ \cos \left[ \frac{2\pi m}{3b} \left( \frac{u}{2} + b \right) \right] \\ &\times \cos \left( \frac{\pi(n-l)(v-w)}{9b} \right) \\ &+ \cos \left[ \frac{2\pi n}{3b} \left( \frac{u}{2} + b \right) \right] \\ &\times \cos \frac{\pi(l-m)(v-w)}{9b} \end{aligned}$$

$$l = -(m+n), \quad u = \frac{\sqrt{3}}{2}x + \frac{1}{2}y,$$

$$v-w = -\frac{\sqrt{3}}{2}x + \frac{3}{2}y,$$

$$b = a/2\sqrt{3},$$

$$k_{mn}^2 = \left( \frac{4\pi}{3a} \right)^2 (m^2 + n^2 + mn)$$

Source: From [43], copyright © 1979 by IEEE; reproduced with permission.

mission line model discussed in the previous section. In this method of modeling, the microstrip patch is considered as a two-dimensional resonator surrounded by a perfect magnetic wall around the periphery. The fields underneath the patch are expanded in terms of the resonant modes of the two-dimensional resonator. This approach is applicable to a variety of patch geometries. These geometries, the corresponding modal variations denoted by  $\Psi_{mn}$ , and the resonant wavenumbers  $k_{mn}$  are shown in Table 2.1 [43].  $E$  and  $H$  fields are related to  $\Psi_{mn}$  by

$$\mathbf{E}_{mn} = \Psi_{mn} \hat{\mathbf{z}} \quad (2.40)$$

$$\mathbf{H}_{mn} = \hat{\mathbf{z}} \times \nabla_t \Psi_{mn} / j\omega\mu \quad (2.41)$$

where  $\hat{\mathbf{z}}$  is a unit vector normal to the plane of the patch. Resonant wavenumbers  $k_{mn}$  are solutions of

$$(\nabla_t^2 + k_{mn}^2)\Psi_{mn} = 0 \quad (2.42)$$

with

$$\frac{\partial \Psi_{mn}}{\partial p} = 0 \quad (2.43)$$

on the magnetic wall (periphery of the patch).  $\nabla_t$  is the transverse part of the del operator and  $p$  is perpendicular to the magnetic wall.

The fringing fields at the edges are accounted for by extending the patch boundary outward and considering the effective dimensions to be somewhat larger than the physical dimensions of the patch. The radiation is accounted for by considering the effective loss tangent of the dielectric to be larger than the actual value. If the radiated power is estimated to be  $P_r$ , the effective loss tangent  $\delta_e$  may be written as

$$\delta_e = \frac{P_r + P_d}{P_d} \delta_d \quad (2.44)$$

where  $P_d$  is the power dissipated in the dielectric substrate and  $\delta_d$  is the loss tangent for the dielectric medium. The effective loss tangent given by Eq. 2.44 can be modified further to incorporate the conductor loss  $P_c$ . The modified loss tangent  $\delta_e$  is given by

$$\delta_e = \frac{P_r + P_d + P_c}{P_d} \delta_d \quad (2.45)$$

The input impedance of the antenna is calculated by finding the power dissipated in the patch for a unit voltage at the feed port and is given by

$$Z_m = |V|^2 / [P + 2j\omega(W_E - W_M)] \quad (2.46)$$

where  $P = P_d + P_c + P_{SW} + P_r$ ,  $P_{SW}$  is the power carried away by surface waves,  $W_E$  is the time-averaged electric stored energy, and  $W_M$  is the time-averaged magnetic energy. The voltage  $V$  equals  $E_z d$  averaged over the feed-strip width ( $d$  is the substrate thickness). The far-zone field and radiated power are computed by replacing the equivalent magnetic-current ribbon on the patch's perimeter by a magnetic line current of magnitude  $\mathbf{K}d$  on the ground plane ( $xy$  plane). The magnetic current source is given by

$$\mathbf{K}(x, y) = \hat{\mathbf{n}} \times \hat{\mathbf{z}}E(x, y) \quad (2.47)$$

where  $\hat{\mathbf{n}}$  is a unit vector normal to the patch's perimeter and  $\hat{\mathbf{z}}E(x, y)$  is the component of the electric field perpendicular to the ground plane.

The limitations of the cavity model arise from the very approximate modeling of the fields outside the patch. The radiation field is accounted for by artificially increasing the dielectric loss inside the cavity by introducing the concept of effective loss tangent. Thus the radiated power needs to be estimated a priori before the voltage at the edges of the patch can be computed.

A cavity model for microstrip patch antennas may also be formulated by considering a planar two-dimensional resonator with an impedance boundary wall all around the edges of the patch. A direct form of network analogue (DFNA) method for the analysis of such a cavity model has been discussed by Coffey and Lehman [45]. In this version of the cavity model approach, the fringing field and the radiated power are not included inside the cavity but are localized at the edges of the cavity resonator. This procedure is conceptually more accurate, but the solution for fields in a cavity with complex admittance walls is much more difficult to evaluate. Numerical methods become necessary for implementing this version of the cavity model.

The cavity model approach (including the version with impedance walls) does not allow any external mutual coupling among microstrip patches to be modeled and accounted for.

The multiport network modeling approach mentioned below and discussed in Chapter 4 overcomes these limitations and is the most versatile of the network modeling approaches for microstrip patches.

*Multiport Network Model (MNM)* In the multiport network modeling approach, the fields underneath the patch and those outside the patch are modeled separately. In this respect, the MNM approach differs significantly from the cavity model discussed earlier. However, the characterization of fields underneath the patch is similar to that in the cavity model (except for the equivalent loss tangent concept used in the cavity model to account for radiation). Thus the MNM approach may be considered as an extension of the cavity model method.

Details of the MNM approach for microstrip patches on single-layer and two-layer substrates are discussed in Chapter 4.

**2.3.1.2 EM Simulation Based Numerical Models** An alternative to the use of network models for microstrip patch antennas is to employ general purpose electromagnetic (EM) simulation software for the evaluation of currents or field distribution associated with microstrip patch antennas. Various techniques for EM field simulation [46–48] have been developed to the level of user-friendly commercially available software during the last decade.

*Integral Equation Based Full Wave Analysis* The most commonly used method of electromagnetic simulation of microstrip patch antennas is based on the moment-method solution of the current distribution on the conducting patch and the associated feed structure. This method is discussed in Chapter 5 which covers applications of this approach to the analysis of integrated circuit–antenna modules. This approach has also been used in several electromagnetic simulation softwares (like HP’s Momentum, Sonnet Software’s Em, Ansoft’s Strata, and Zeland Software’s I3D) developed for the design of microwave integrated circuits and printed antennas.

The integral equation based full wave analysis approach, when applied to microstrip antennas, is comprised of the following basic steps: (1) formulation of an integral equation in terms of electric current distribution of the patch and the associated feed structure; (2) solution for the current distribution using the method of moments; (3) evaluation of the network parameters ( $S_{11}$ ,  $Z_{in}$ , etc.) at the input port or multipoint parameters for antennas with two (or more) ports; and (4) evaluation of the radiation characteristics from the electric current distribution on the patch and so on.

In this approach (also in other EM simulation based methods), modeling and analysis of microstrip antennas are closely integrated in a single procedure. The computer-aided design procedure shown in Fig. 2.3 gets modified as shown in Fig. 2.19. Two difficult steps in this procedure are (1) the choice of the initial design (usually transmission line modeling approach is used for this step); and (2) design parameter modifications. Optimization techniques similar to those used for microwave circuits can be used for this purpose. Because of the computer-intensive nature of EM simulation software, antenna optimization using EM simulation becomes a very slow process. Nevertheless, use of EM simulators for circuit and antenna optimization has gained some acceptance in recent years [49]. Specialized techniques like space mapping and decomposition [50] and the use of artificial neural networks [29,51] have been developed for making efficient use of EM simulation in optimization and design, and these are applicable to microstrip antenna design also.

*Finite-Difference Time Domain Simulation of Microstrip Patches* In addition to the integral equation formulation for full wave analysis of microstrip patches, finite-difference time domain (FDTD) simulation is also used for these antennas. A detailed discussion of FDTD fundamentals and implementation is contained in Chapter 6. Basic formulation of the FDTD method (as a central difference

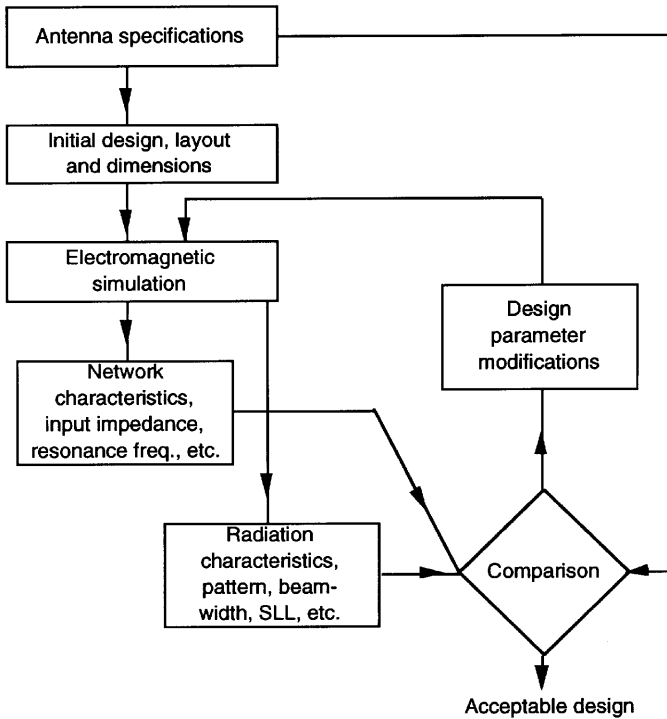
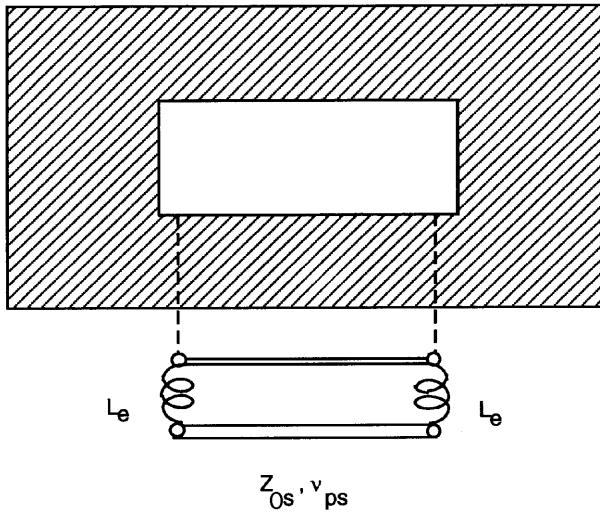


FIGURE 2.19 Microstrip antenna design using EM simulators.

discretization of Maxwell's curl equations in both time and space) is well known [46–48] and is identical for circuit and antenna problems. However, details of the implementation by various researchers differ with respect to excitation treatment, boundary conditions, and postprocessing of results to obtain parameters of interest in the frequency domain. These issues are discussed in Chapter 6.

**2.3.1.3 Modeling of Slot Antennas** Slot antennas can be considered to have evolved from slot transmission lines [12] in a manner similar to the evolution of microstrip patch antennas from microstrip transmission lines. Based on this analogy, a transmission line model can be used for rectangular slot resonators as shown in Fig. 2.20 and extended to the transmission line model for a slot antenna as shown in Fig. 2.21. The conductance  $G_r$  represents the radiation conductance of the slot. Note that  $G_r$  is connected at the midpoint of the half-wavelength resonant slot, which is the location of the maximum voltage across (and hence that of the maximum magnetic current along) the slot. This conductance  $G_r$  can be evaluated by equating the power radiated by the slot to the equivalent power dissipated in  $G_r$  when a



**FIGURE 2.20** A transmission line resonator model of a resonant slot.

voltage  $V_s$  exists across the conductance. That is,

$$G_r = \frac{2P_{rad}}{V_s^2} \tag{2.48}$$

Inductors  $L_e$  represent the inductance due to slotline short-circuited terminations at the two ends of the resonant slot. The value for  $L_e$  is obtained from the characterization of short-circuited ends of a slotline [12]. The equivalent model shown in Fig. 2.21a does not include representation of the feedline. A slotline-fed half-wave resonant slot can be modeled by the equivalent network shown in Fig. 2.21b. The discontinuity reactance contributed by the junction between the feeding slotline and the resonant slot is not shown in Fig. 2.21b and needs to be included for accurate modeling and analysis of the resonant slot antenna.

Figure 2.21c depicts the implementation of the equivalent transmission line model for a one-wavelength resonant slot fed at the midpoint by a coplanar waveguide (CPW) feed. Note that, in this case, two radiation conductances  $G_r$  are included at the two points of the maximum voltage across the slot. A network for representing the external mutual coupling between the two halves of the antenna needs to be incorporated and is not shown in Fig. 2.21c. Also, as for the model shown in Fig. 2.21b, the discontinuity reactance at the junction of the feedline and the slot is not included in Fig. 2.21c.

The basic idea of the equivalent transmission line modeling of rectangular slot antennas has been verified [52] by comparison with full wave electromagnetic simulation. Just like transmission line models for microstrip patches, this modeling

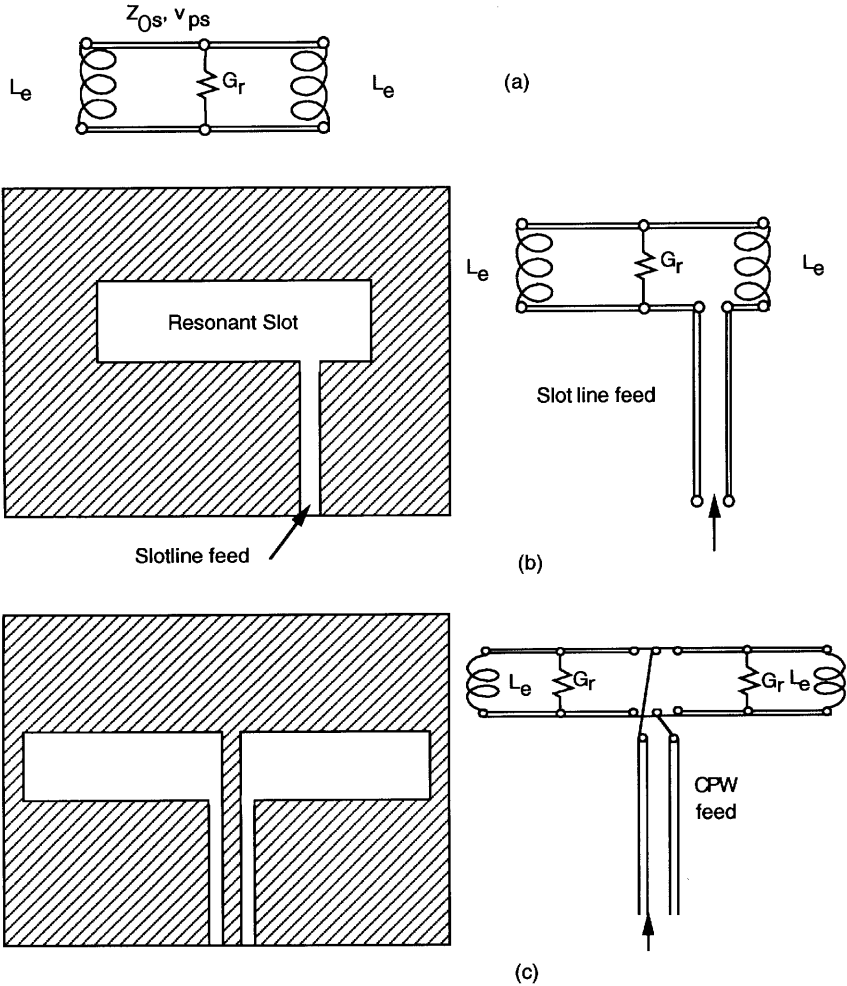


**FIGURE 2.21** (a) Transmission line model for a slot radiator (feed not included), (b) Transmission line model for a slotline fed, slot antenna, (c) Transmission line model for a CPW line fed slot antenna.

approach is expected to play a significant role in the initial first-order design of slot antennas and integrated circuit-antenna modules incorporating slot antennas.

In addition to the network modeling of slot antennas described in this section, numerical modeling based on electromagnetic simulation (discussed earlier for microstrip patches) is equally valid and employed for slot antennas also. In the integral equation formulation for slot structures, it is appropriate to solve for equivalent magnetic current distribution in the slot regions in place of electric



current distribution over the conductor areas (as commonly carried out for microstrip structures).

### 2.3.2 Analysis of Printed Patches and Slots

The computer-aided analysis of printed antennas is generally carried out in two broad steps: (1) evaluation of the aperture field in terms of equivalent electric and/or magnetic current distribution on the top surface of the substrate, and (2) evaluation of the far field from the aperture field distribution. Usually the network characteristics of the antenna (such as resonance frequency, input impedance, and bandwidth) are computed in step (1); and radiation characteristics (such as beamwidth and direction, side-lobe level, and polarization) become parts of computations in step (2).

When the network modeling approach is used for a microstrip patch antenna, network solution techniques are used for finding network parameters, namely, input impedance for single-port radiators and  $S$ -parameters for two-port (or multiport) radiators. In addition, solution of the network model yields voltage distribution along the periphery of the patches. This voltage distribution is written in terms of the equivalent magnetic current distribution, which is used for the calculation of the radiation field—step (2) in the procedure outlined above.

When integral equation based EM simulation is used for modeling and analysis of microstrip patch antennas, the first part of the computation results in electric current over the conducting patch and the associated feed structure. This electric current distribution can be used for finding the radiation field in the far zone of the antenna. The Green's function expressing the field produced by an infinitesimal electric current element on the ground dielectric substrate is already known. In fact, this Green's function (see Chapter 5) is the starting point for the integral equation formulation. An integral of this Green's function weighted by the current distribution yields the total field and when evaluated with the far-field approximation provides results for the radiation field.

When simulating slot antennas by the moment-method based integral equation approach, we solve for the equivalent magnetic current distribution in the slots (the nonconducting portion on the upper surface of the substrate). In this case, the far field is evaluated by using a Green's function for fields produced by an elementary magnetic current source.

When FDTD simulation is used, it becomes necessary to limit the computational domain by enclosing the antenna in a virtual box. The next step is the evaluation of the equivalent electric and magnetic current densities,  $\mathbf{J}_s$  and  $\mathbf{M}_s$ , which are related to the field components on the surface of the box by  $\mathbf{J}_2 = \hat{\mathbf{n}} \times \mathbf{H}$  and  $\mathbf{M}_s = -\hat{\mathbf{n}} \times \mathbf{E}$ ; with  $\hat{\mathbf{n}}$  being a normal outward unit vector on the surface of the box. Since the field components on the surface of the virtual box calculated by FDTD are in the time domain, one makes use of the discrete Fourier transform (DFT) to obtain the corresponding frequency domain phasor quantities. Chapter 6 contains the details of this procedure.

Common to all of the above methods of evaluating the aperture field in terms of electric/magnetic currents is the near-field to far-field transformation for evaluating

the antenna characteristics. This transformation is based on the surface equivalence theorem (for details, see texts like [53]). Far-field evaluation starts with the computation of two vector potentials  $\vec{A}$  and  $\vec{F}$  as:

$$\vec{A} = \mu \iint_{S'} \frac{\vec{J}_s e^{-jk r''}}{4\pi r''} dS' \quad (2.49)$$

$$\vec{F} = \varepsilon \iint_{S'} \frac{\vec{M}_s e^{-jk r''}}{4\pi r''} dS' \quad (2.50)$$

The electromagnetic fields at a far-field point,  $\mathbf{P}$ , shown in Fig. 2.22, are as follows:

$$\vec{E} = -j\omega\vec{A} - \frac{j\omega}{k^2} \nabla(\nabla \cdot \vec{A}) - \frac{1}{\varepsilon} \nabla \times \vec{F} \quad (2.51)$$

$$\vec{H} = -j\omega\vec{F} - \frac{j\omega}{k^2} \nabla(\nabla \cdot \vec{F}) - \frac{1}{\mu} \nabla \times \vec{A} \quad (2.52)$$

Since  $r' \ll r$  for the far-field point  $\mathbf{P}$ , we can assume

$$r'' = \sqrt{r^2 + r'^2 - 2rr' \cos \Psi} \cong r - r' \cos \Psi \quad (2.53)$$

and the two vector potentials in Eqs. 2.49 and 2.50 can be rewritten as

$$\vec{A} = \mu \frac{e^{-jkr}}{4\pi r} \iint_{S'} \vec{J}_s e^{jkr' \cos \Psi} dS' \quad (2.54)$$

$$\vec{F} = \varepsilon \frac{e^{-jkr}}{4\pi r} \iint_{S'} \vec{M}_s e^{jkr' \cos \Psi} dS' \quad (2.55)$$

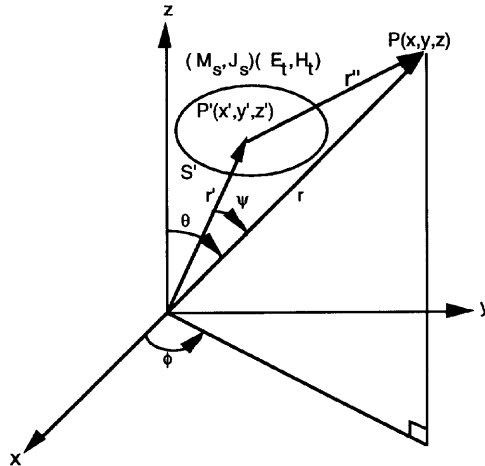


FIGURE 2.22 Coordinate system used for discussing near-field to far-field transformation.

where

$$r' \cos \Psi = r' \cdot \hat{r} = x' \sin \theta \cos \phi + y' \sin \theta \sin \phi + z' \cos \theta \quad (2.56)$$

Since the integrands in Eqs. 2.54 and 2.55 are functions of  $\vec{J}_s$ ,  $\vec{M}_s$ ,  $r'$ , and  $\Psi$  only, we can define two new radiating vectors,  $\vec{N}$  and  $\vec{L}$ , as shown below:

$$\vec{N} = \iint_{S'} \vec{J}_s e^{jkr' \cos \Psi} dS' \quad (2.57)$$

$$\vec{L} = \iint_{S'} \vec{M}_s e^{jkr' \cos \Psi} dS' \quad (2.58)$$

which are related to the vector potentials  $\vec{A}$  and  $\vec{F}$  by

$$\vec{A} = \mu \frac{e^{-jkr}}{4\pi r} \vec{N} \quad (2.59)$$

$$\vec{F} = \varepsilon \frac{e^{-jkr}}{4\pi r} \vec{L} \quad (2.60)$$

Now, if we substitute Eqs. 2.59 and 2.60 into Eqs. 2.51 and 2.52 and drop the terms that decay faster than  $1/r$ , we can obtain the radiating fields at the far-field point as follows:

$$E_\theta = \eta H_\phi = -j \frac{e^{-jkr}}{2\lambda r} (\eta N_\theta + L_\phi) \quad (2.61)$$

$$E_\phi = -\eta H_\theta = j \frac{e^{-jkr}}{2\lambda r} (-\eta N_\phi + L_\theta) \quad (2.62)$$

Consequently, we can calculate the time-averaged Poynting vector (average power density) at a far-field point ( $r$ ,  $\theta$ ,  $\phi$ ) as follows:

$$\begin{aligned} W_r &= \frac{1}{2} \text{Re} \left[ \vec{E} \times \vec{H}^* \right] = \frac{1}{2} \text{Re} [E_\theta H_\phi^* - E_\phi H_\theta^*] \\ &= \frac{\eta}{3\lambda^2 r^2} \left[ |N_\theta + \frac{L_\phi}{\eta}|^2 + |N_\phi - \frac{L_\theta}{\eta}|^2 \right] \end{aligned} \quad (2.63)$$

By simply multiplying the above power density by the square of the distance,  $r^2$ , we obtain the radiation intensity of the antenna at a certain direction ( $\theta$ ,  $\phi$ ) as follows:

$$U = \frac{\eta}{8\lambda^2} \left[ |N_\theta + \frac{L_\phi}{\eta}|^2 + |N_\phi - \frac{L_\theta}{\eta}|^2 \right] \quad (2.64)$$

Thus we note that the second broad step mentioned in the beginning of this section on computer-aided analysis is a straightforward implementation of the equivalence theorem in electromagnetics.

## 2.4 CAD CONSIDERATIONS FOR INTEGRATED CIRCUIT–ANTENNA MODULES

### 2.4.1 NonIntegrated and Partially Integrated Modules

CAD considerations for integrated circuit–antenna modules depend on the level of integration. As discussed in Section 1.5 and depicted in Table 1.4, circuit–antenna modules can be grouped into three classes: nonintegrated, partially integrated, and fully integrated. In the case of nonintegrated modules, circuit and antenna functions are designed separately with their external ports matched to a standardized impedance level (usually 50  $\Omega$ ). Software for microwave circuit and antenna CAD available separately are useful for this class of circuit–antenna modules.

For partially integrated circuit–antenna modules, circuit and antenna functions interact through the transmission structure connecting them. A common example is a microstrip patch located on the top surface of a grounded substrate with a feed-through leading to the circuit located below the ground plane. Design of this class of integrated circuit–antenna modules would typically consist of the following steps:

1. Design of the antenna for desired radiation characteristics. This may make use of any design tools or CAD software available for antenna design.
2. Characterization of the input impedance of the antenna over the frequency range of interest/concern. This frequency range could be wider than the operating frequency range of the antenna. For example, if we have a high gain amplifier feeding the antenna it may be desirable to ensure the stability of the amplifier even outside the antenna bandwidth.
3. Modeling of the feed-through connecting the antenna to the circuit over the frequency range mentioned in step (2). Normally the feed-through is either a vertical probe passing through a circular hole in the ground plane or only an aperture (circular or rectangular) in the ground plane. The latter provides EM coupling between the antenna above and the feedline below the ground plane. In any one of these cases, a model can be derived using electromagnetic simulation of the “feed-through.” ANN modeling [28] can provide an accurate model based on results obtained from the electromagnetic simulation.
4. Initial design of the circuit portion.
5. Evaluation of the circuit performance with frequency-dependent input impedance of the antenna connected through the wide-band model of the feed-through. Optimization of the circuit design is needed at this stage. Optimizers built into the commercially available microwave circuit CAD tools are appropriate for this purpose.
6. Characterization of the output of the circuit part including the output impedance and the signal level (or Thevenin’s equivalent in network terminology) over the desired bandwidth of the antenna.

7. Reevaluation of the radiation performance of the antenna accounting for output characteristics of the circuit portion. In case this performance is found to be inadequate, a redesign of the antenna and/or of the circuit portion may be needed.

### 2.4.2 Fully Integrated Circuit–Antenna Modules

In this case the circuit and antenna portions interact not only through the physical interconnects but also through the EM coupling among various parts responsible for circuit and antenna functions. Thus it is not possible to design the circuit and antenna functions separately and a concurrent design approach is needed. This concurrent design approach calls for integration of the network analysis used for the circuit design and the field analysis used for the antenna design. There are two different methodologies that have been proposed for handling this integration of two apparently different approaches: (1) network analysis based approach using network modeling of antennas, and (2) integration of network analysis in the numerical algorithms for EM simulation of fields. Some key features of these approaches are presented in this section and details are discussed in later chapters in this book.

**2.4.2.1 Total Network Modeling Approach** This approach makes use of a network model for antennas. The transmission line model, cavity model, and multiport network model mentioned earlier (and discussed later in Chapters 3 and 4) are appropriate for this purpose.

The key feature of this approach is that the antenna and electromagnetic couplings among the various parts in the antenna and circuit portions are represented in terms of equivalent network models. The resulting overall network can be analyzed, designed, and optimized using the network-theoretic methods that have been developed extensively over the past several decades. Chapters 3 and 4 discuss the details of this approach.

**2.4.2.2 Integration of Network Analysis with EM Simulation** Methods of incorporation of certain elements of network analysis in electromagnetic simulation algorithms have been developed both for frequency domain and time domain simulations. Two different strategies have been developed for this purpose. One of these directly incorporates the representation of lumped circuit elements as additional boundary conditions in electromagnetic formulation. This has been tried in both the frequency domain [54,55] and the time domain [56,57]. This approach needs each circuit element to be described using data tables or explicit formulas. The second strategy combines an EM simulator (for the passive distributed parts of the circuit–antenna module) with a network simulator for the active and/or lumped components and circuits. This approach has become more popular [58,59].

*Frequency Domain Simulation* The incorporation of lumped circuit elements in the moment-method solution of the integral equation formulation for planar circuit–

antenna modules is discussed in Chapter 5. Circuit elements are considered to be much smaller compared to wavelength and hence can be analyzed by circuit theory. Original integral equations are modified to incorporate the voltage–current relationship constraints imposed by circuit elements. For example, when a series impedance is connected across a gap in a microstrip-like structure, surface current  $J_s$  and the electric field  $E$  at that location can be related to the series impedance  $Z_s$ . This relationship is combined into the generalized impedance matrix encountered in the moment-method solution of the integral equation for surface current on the conducting portion of the circuit–antenna module. The resulting solution yields the field simulation taking the lumped element behavior into account.

A dual treatment is applicable when dealing with CPW circuits and/or slot antennas [60]. In this case the integral equation is formulated in terms of magnetic current distribution in a slot and the circuit-element characterization is incorporated in terms of an admittance matrix. This approach has been illustrated for an active CPW-fed slot antenna with a bipolar amplifier inserted in the CPW feed line [60].

A similar approach is used for incorporating circuit elements in the finite-element method (FEM) in the frequency domain [54,55]. In three-dimensional (3-D) FEM, the volume is meshed by tetrahedral elements. When edge elements are used as basis vectorial fields to approximate the electric field and Galerkin’s method is employed, the unknown edge voltages  $[e]$  are given by

$$[Y][e] = [i] \quad (2.65)$$

where  $[i]$  is the excitation current vector and  $[Y]$  is an admittance matrix that relates the interaction between edges. The matrix term  $Y_{ee}$  can be seen on the self-admittance of edge while  $Y_{ek}$  is the mutual admittance between the edge  $e$  and edge  $k$ . Any edge can be compared to a port and if a lumped element is connected to this kind of port, we have (by Kirchhoff’s laws)

$$\sum_{k=1}^M Y_{ek} e_k + y_c e_e = 0 \quad (2.66)$$

where  $M$  is the number of associated edge voltages and  $y_c$  is the admittance of the lumped element. Relation 2.66 is used to introduce, in the admittance matrix  $[Y]$  of Eq. 2.65, an additional term that corresponds to the admittance  $y_c$  of the lumped element. When a two-port lumped circuit is connected between two edges  $e$  and  $e'$ , the corresponding four terms in  $[Y]$  get modified. This inclusion of one-port and two-port lumped elements in FEM simulation is shown schematically in Figs. 2.23a and 2.23b, respectively.

A more efficient way of analysis (particularly when dealing with nonlinear lumped circuits) is not to connect the lumped circuit during the field simulation but to create additional ports as shown in Fig. 2.24a. After the multiport characterization is obtained by field simulation, the lumped circuit is connected to the additional internal ports as shown in Fig. 2.24b. The combination of Fig. 2.24b is

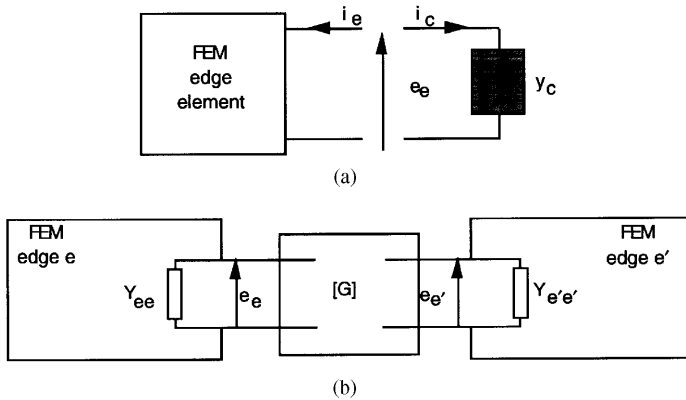


**FIGURE 2.23** (a) One-port lumped circuit element connected to an FEM edge. (b) Two-port circuit connected to two edge elements in an FEM simulation.

then analyzed by network theory. Implementation of this method is illustrated in [54,55].

This concept of introducing ports at the location of the lumped circuit, while carrying out EM field simulation, has more general applications. Analysis of an oscillator grid and array reported in Chapter 8 of this book also uses this method. The grid of oscillator–antenna or amplifier–antenna cells is uniformly periodic and is considered to be infinite in the two lateral dimensions. Field and current distributions in each cell can be expressed as a two-dimensional series of modes. By matching fields at the two interfaces, expressions are derived for the electric field coefficients on two sides in terms of the surface current coefficients. Unknown coefficients for currents are solved by the moment-method approach. As discussed in Chapter 8, this leads to the driving-point impedance across the gap where active devices are mounted. The resulting field analysis based network characterization of the passive part of the circuit–antenna modules is used for design of circuit functions like grid amplifier and grid oscillators.

*Time Domain Simulation* FDTD and TLM (transmission line matrix) methods have been modified to incorporate lumped circuits in EM field simulation. The extension of the finite-difference time domain (FDTD) method to integrated circuit–antenna modules is discussed in Chapter 6. The basic formulation for incorporating lumped linear and nonlinear circuit elements into the FDTD algorithm was proposed originally by Sui et al. [57] for two-dimensional (2-D) problems and generalized to 3-D configurations later by Picket-May et al. [56]. The key step is to include a lumped electric current density term  $\vec{J}_L$  in the conduction and displacement currents on the right-hand side of Maxwell’s equation for curl  $\vec{H}$ . This yields

$$\nabla \times \vec{H} = \epsilon \frac{\partial \vec{E}}{\partial t} + \sigma \vec{E} + \vec{J}_L$$

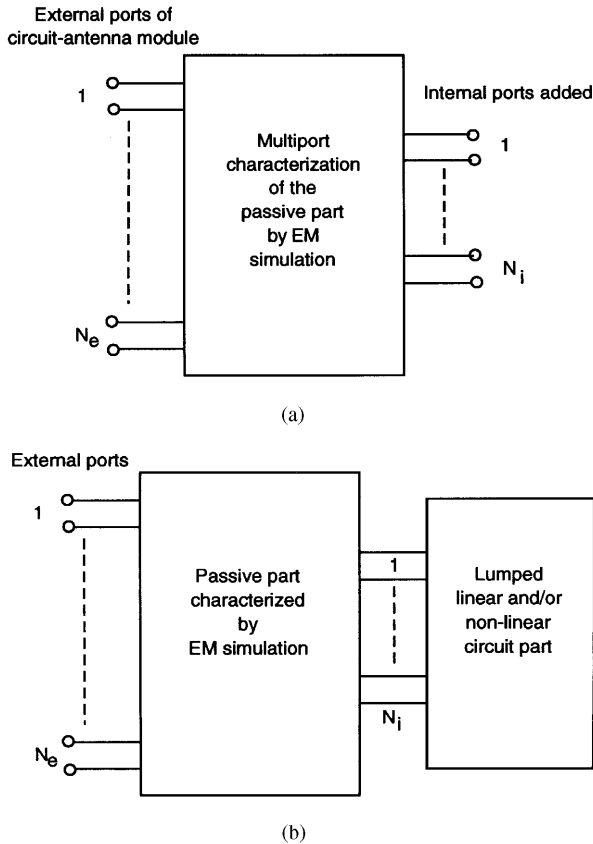


**FIGURE 2.24** (a) Additional internal ports added to the passive part of a circuit-antenna module for its characterization by EM field simulation. (b) Connection of the circuit part to multiport characterization of the passive part of a circuit-antenna module.

Properties of the lumped element relate this lumped current to the voltage developed across that particular Yee cell. The lumped current  $I_L (= J_L \Delta_y \Delta_z$  for an  $x$ -oriented element) gets updated at each time step in the FDTD simulation.

As in the case of frequency domain simulation also, the above approach of directly implementing lumped circuit elements and devices into the FDTD algorithm becomes inefficient when lumped devices have complicated equivalent circuits and when multiport lumped circuits are involved. An equivalent source approach [59] allows a direct access from FDTD algorithm to a network simulator (like SPICE) used for circuit analysis. This equivalent source approach is based on writing a Norton equivalent of the Yee cell (starting from the integral form of the Ampere law) or a Thevenin equivalent based on the integral form of Faraday's law. An example of this implementation is given in Chapter 6.



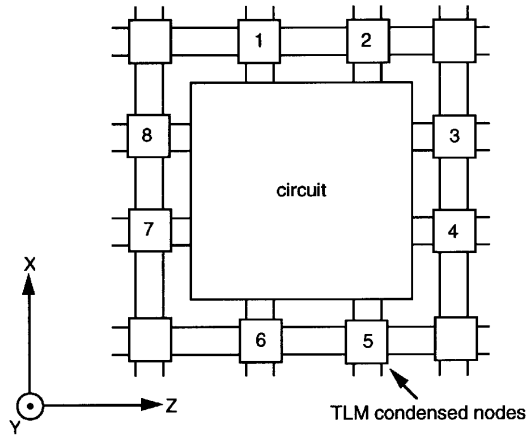


FIGURE 2.25 A lumped element circuit introduced in the TLM analysis mesh.

When the TLM method is used for integrated circuit–antenna modules, arbitrary, multiport, nonlinear devices (or lumped circuits) can be incorporated into a three-dimensional (3-D) condensed node TLM mesh [61]. Figure 2.25 illustrates a lumped circuit displacing a number of nodes in TLM simulation. In general, the nodes interfacing to the circuit are connected to the circuit via two ports at each node. These two ports are polarized parallel and perpendicular to the plane of the circuit. A typical interface of the circuit to one of the TLM nodes is shown in Fig. 2.26. The reflected and incident discretized signals from the circuit to the node “*p*” are denoted as  ${}_q V_p^r$  and  ${}_q V_p^i$ , respectively, where *q* is the counter for mesh time steps  $q \Delta t < t < (q + 1) \Delta t$ . Signals from the node to the circuit are first interpolated,

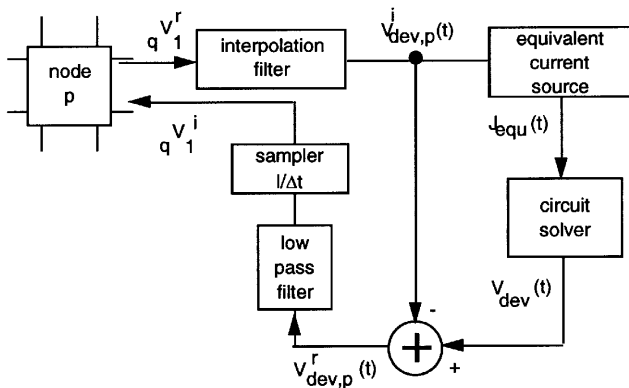


FIGURE 2.26 Typical interface between a TLM mode and one-port lumped element circuit. (From [61], copyright © 1993 by John Wiley & Sons; reproduced with permission.)

resulting in a continuous time signal incident on the circuit element. As  ${}_{q+1}V_p^r$  depends on  ${}_qV^r$  at the surrounding nodes, an explicit interpolation is possible for  $q \Delta t < t \leq (q+1) \Delta t$ . The forcing function for the device differential equation solver (or for the circuit simulator) is an equivalent current source (Norton equivalent), which is related to  $V_{\text{dev},p}^i(t)$  and the impedance of the interconnecting line in the TLM mesh. Reflected voltage from the lumped element to node  $p$  is passed through a lowpass filter to remove high-frequency components above the Nyquist rate that would otherwise cause aliasing errors in the TLM mesh. This arrangement can be extended to multiport circuits. Interpolation filters at the circuit input ports allow the update interval in the circuit solver to be smaller than the time step in the TLM mesh.

The methodology shown in Fig. 2.26 for the TLM method is also applicable to other time domain simulators (like FDTD). It allows circuit simulators like SPICE to be coupled to time domain field simulators.

## 2.5 SUMMARY

This chapter has summarized the CAD issues related to integrated circuit–antenna modules. Various features of the generalized design process have been mentioned. As in other design domains, the three design philosophies applicable to the design of integrated circuit–antenna modules are the conventional approach, the CAD approach, and the knowledge-aided approach. Various aspects of the CAD approach for microwave circuits and for printed (microstrip/slot) antennas have been reviewed. For fully integrated circuit–antenna modules, the CAD approach is necessary and the tools needed for this are being developed. The knowledge-aided design (KAD) approach may also be important to improve design capability but is as yet relatively undeveloped.

After summarizing the position on the CAD of circuits and antennas, this chapter concludes with a review of CAD methods for integrated circuit–antenna modules. Some of these methods are described in the following chapters. Final comments on the current status of CAD for integrated modules are included in the concluding chapter of this book.

## REFERENCES

1. Hopgood, A. A., "Systems for design and selection," in *Knowledge-Based Systems for Engineers and Scientists*, CRC Press, Boca Raton, FL, 1993, Chap. 8.
2. Green, M., "Conceptions and misconceptions of knowledge aided design," in *Knowledge Aided Design*, Academic Press, New York, 1992, Chap. 1.
3. Tong, C., and Sriram, D., *Artificial Intelligence in Engineering Design*, Academic Press, New York, 1992.

4. Gupta, K. C., "Emerging trends in millimeter-wave CAD," *IEEE Trans. Microwave Theory Tech.*, vol. MTT-46, June 1998, pp. 747–755.
5. Gupta, K. C., "ANN and knowledge-based approaches for microwave design," in *Directions for the Next Generation of MMIC Devices and Systems*, N. K. Das and H. L. Bertoni (eds.), Plenum, New York, 1996, pp. 389–396.
6. Watson, P. M., Gupta, K. C., and Mahajan, R. L., "Development of knowledge-based artificial neural network models for microwave components," *1998 IEEE Int. Microwave Symp. Dig.*, Baltimore MD, June 1998, pp. 9–12.
7. Chandrasekaran, B., "Generic tasks in knowledge-based reasoning—high-level building blocks for expert system design," *Expert*, vol. 1, no. 23, 1986.
8. Chandrasekaran, B., "Design problem solving: A task analysis," in *Knowledge-Aided Design*, M. Green (ed.), Academic Press, New York, 1992, Chap. 2.
9. Gupta, K. C., Garg, R., and Chadha, R., *Computer Aided Design of Microwave Circuits*, Artech House, Norwood, MA, 1981.
10. Dobrowolski, J. A., *Introduction to Computer Methods for Microwave Circuit Analysis and Design*, Artech House, Norwood, MA, 1991.
11. Dobrowolski, J. A., *Computer-Aided Analysis, Modeling and Design of Microwave Networks—The Wave Approach*, Artech House, Norwood, MA, 1996.
12. Gupta, K. C., Garg, R., Bahl, I. J., and Bhartia, P., *Microstrip Lines and Slotlines*, 2nd ed., Artech House, Norwood, MA, 1996.
13. Edwards, T. C., *Foundations for Microstrip Circuit Design*, 2nd ed., Wiley, New York, 1991.
14. Bhartia, P., and Pramanick, P., "Fin-line characteristics and circuits," *Infrared and Millimeter Waves*, vol. 17, Academic Press, New York, 1988.
15. Hoffman, R. K., *Handbook of Microwave Integrated Circuits*, Artech House, Norwood, MA, 1987.
16. Bahl, I. J., and Bhartia, P., *Microwave Solid State Circuit Design*, John Wiley, New York, 1988.
17. Hammerstad, E. O., and Bekkadal, F., "Microstrip Handbook," ELAB Report STF44 A74169, University of Trondheim, Norway, 1975.
18. Mehran, R., "Frequency dependent equivalent circuits for microstrip right angle bends, T-junctions and crossings," *Arch. Elek. Ubertragung*, vol. 30, 1976, pp. 80–82.
19. Jansen, R. H., and Koster, N. H. L., "A unified CAD basis for frequency dependent characterization of strip, slot and coplanar MIC components," *Proceedings 11th European Microwave Conference*, Amsterdam, 1981, pp. 682–687.
20. Jansen, R. H., "Hybrid mode analysis of end effects of planar microwave and millimeter-wave transmission line," *Proc. IEE*, Part H, vol. 128, 1981, pp. 77–86.
21. Koster, N. H. L., and Jansen, R. H., "The equivalent circuits of the asymmetrical series gap in microstrip and suspended substrate lines," *IEEE Trans. Microwave Theory Tech.*, vol. MTT-30, Aug. 1982, pp. 1273–1279.
22. Jansen, R. H., "The spectral domain approach for microwave integrated circuits," *IEEE Trans. Microwave Theory Tech.*, vol. MTT-33, Oct. 1985, pp. 1043–1056.
23. Koster, N. H. L., and Jansen, R. H., "The microstrip step discontinuity: A revised description," *IEEE Trans. Microwave Theory Tech.*, vol. MTT-34, Feb. 1986, pp. 213–223.

24. Katchi, P. B., and Alexopoulos, N. G., "Frequency dependent characteristics of microstrip discontinuities in millimeter-wave integrated circuits," *IEEE Trans. Microwave Theory Tech.*, vol. MTT-33, Oct. 1985, pp. 1029–1035.
25. Jackson, R. W., and Pozar, D. M., "Full-wave analysis of microstrip open-end and gap discontinuities," *IEEE Trans. Microwave Theory Tech.*, vol. MTT-33, Oct. 1985, pp. 1036–1042.
26. Mosig, J. R., and Gardiol, F. E., "Analytical and numerical techniques in the Green's function treatment of microstrip antennas and scatterers," *Proc. IEE*, Part H, vol. 130, 1983, pp. 175–182.
27. Wu, C. I., Chang, D. C., and Brim, B. L., "Accurate numerical modeling of microstrip junctions and discontinuities," *Int. J. Microwave MM-Wave Computer-Aided Eng.*, vol. 1, no. 1, 1991, pp. 48–58.
28. Watson, P. M., and Gupta, K. C., "EM-ANN models for microstrip vias and interconnects in multilayer circuits," *IEEE Trans. Microwave Theory Tech.*, vol. 44, Dec. 1996, pp. 2495–2503.
29. Watson, P. M., and Gupta, K. C., "Design and optimization of CPW circuits using EM-ANN models for CPW components," *IEEE Trans. Microwave Theory Tech.*, vol. 45, Dec. 1997, pp. 2515–2523.
30. Mahajan, R. L., and Gupta, K. C., "Physical-neural network modeling for electronic packaging applications," Proceedings Wireless Communications Conference, Boulder, CO, August 1996, pp. 157–162.
31. Rousset, J., Harkouss, Y., Collantes, J. M., and Campovecchio, M., "An accurate neural network model of FET for intermodulation and power analysis," 26th European Microwave Conference, Czech Republic, Sept. 1996.
32. Chua, L. O., *Introduction to Non-Linear Network Theory*, McGraw-Hill, New York, 1969.
33. Chua, L. O., and Lin, P. M., *Computer-Aided Analysis of Electronic Circuits*, Prentice Hall, Englewood Cliffs, NJ, 1975, Chaps. 5, 7, 10, 11.
34. Nakhla, M. S., and Vlach, J., "A piecewise harmonic balance technique for determination of periodic response of nonlinear systems," *IEEE Trans. Circuits Syst.*, vol. CAS-23, 1976, pp. 85–91.
35. James, J. R., and Hall, P. S. (eds.), *Handbook of Microstrip Antenna*, Vols. I and II, Peter Peregrinus, London, 1989.
36. Richards, W. F., "Microstrip antennas," in *Antenna Handbook—Theory, Applications and Design*, Y. L. Lo and S. W. Lee (eds.), Van Nostrand Reinhold Company, New York, 1988, pp. 10.1–10.74.
37. Gupta, K. C., and Benalla, A., *Microstrip Antenna Design*, reprint volume, Artech House, Norwood, MA, 1988.
38. James, J. R., Hall, P. S., and Wood, C., *Microstrip Antenna Theory and Design*, Peter Peregrinus, London, 1981.
39. Bahl, I. J., and Bhartia, P., *Microstrip Antennas*, Artech House, Dedham, MA, 1980.
40. Gupta, K. C., "Two-port transmission characteristics of rectangular microstrip patch radiators," *1985 IEEE AP-S Int. Antennas Propag. Symp. Dig.*, pp. 71–74.
41. Benalla, A., and Gupta, K. C., "Transmission line model for 2-port rectangular microstrip patches with ports at the non-radiating edges," *Electron. Lett.*, vol. 23, 1987, pp. 882–884.

42. Benalla, A., and Gupta, K. C., "Two-dimensional analysis of one-port and two-port microstrip antennas," *Scientific Rept. 85*, Electromagnetics Laboratory, University of Colorado, May 1986, p. 48.
43. Lo, Y. T., Solomon, D., and Richards, W. F., "Theory and experiment on microstrip antennas," *IEEE Trans. Antennas Propag.*, vol. AP-27, 1979, pp. 137–145.
44. Richards, W. F., Lo, Y. T., and Harrison, D. D., "An improved theory for microstrip antennas and applications," *IEEE Trans. Antennas Propag.*, vol. AP-29, 1981, pp. 38–46.
45. Coffey, E. L., and Lehman, T. H., "A new analysis technique for calculating the self and mutual impedance of microstrip antennas," Proceedings Workshop Printed Circuit Antenna Technology, New Mexico State University, 1979, pp. 31.1–31.21.
46. Itoh, T. (ed.), *Numerical Techniques for Microwave and Millimeter-Wave Passive Structures*, John Wiley, New York, 1989.
47. Sadiku, M. N. O., *Numerical Techniques in Electromagnetics*, CRC Press, Boca Raton, FL, 1992.
48. Taflove, A., *Computational Electrodynamics: The Finite-Difference Time-Domain Method*, Artech House, Norwood, MA, 1995.
49. Bandler, J. W. (guest ed.), "Special Issue on Automated Circuit Design Using Electromagnetic Simulators," *IEEE Trans. Microwave Theory Tech.*, vol. 45, no. 5, Part II of Two Parts, May 1997.
50. Bandler, J. W., Biernacki, R. M., Chen, S. H., and Huang, Y. F., "Design optimization of interdigital filters using aggressive space mapping and decomposition," *IEEE Trans. Microwave Theory Tech.*, vol. 45, no. 5, May 1997, pp. 761–769.
51. Veluswami, A., Nakhla, M. S., and Zhang, Q.-J., "The application of neural networks to EM-based simulation and optimization of interconnects in high-speed VLSI circuits," *IEEE Trans. Microwave Theory Tech.*, vol. 45, no. 5, May 1997, pp. 712–723.
52. Haeusler, M., and Gupta, K. C., "Equivalent transmission line modeling of rectangular slot antennas," (to be published).
53. Balanis, C. A., *Advanced Engineering Electromagnetics*, Wiley, New York, 1989.
54. Guillouard, K., Wong, M.-F., Hanna, V. F., and Citerne, J., "A new global finite element analysis of microwave circuits including lumped elements," *IEEE Trans. Microwave Theory Tech.*, vol. 44, no. 12, Dec. 1996, pp. 2587–2594.
55. Bailargeat, B., Larique, E., Verdeyme, S., Aubourg, M., Sommet, R., and Guillon, P., "Coupled localized and distributed elements analysis applying an electromagnetic software in the frequency domain," *1997 IEEE-MTTS Int. Microwave Symp. Dig.*, Denver CO, June 1997, pp. 1021–1024.
56. Piket-May, M., Taflove, A., and Baron, J., "FDTD modeling of digital signal propagation in 3D circuits with passive and active loads," *IEEE Trans. Microwave Theory Tech.*, vol. 42, no. 8, August 1994, pp. 1514–1523.
57. Sui, W., Christensen, D. A., and Durney, C. H., "Extending the two-dimensional FDTD method to hybrid electromagnetic systems with active and passive lumped elements," *IEEE Trans. Microwave Theory Tech.*, vol. 40, no. 4, April 1992, pp. 724–730.
58. Heinsen, S., Kunisch, J., and Wolff, I., "A unified framework for computer-aided noise analysis of linear and nonlinear microwave circuits," *IEEE Trans. Microwave Theory Tech.*, vol. 39, Dec. 1991, pp. 2170–2175.

59. Thomas, V. A., Jones, M. E., Picket-May, M., Taflove, A., and Harrigan, E., "The use of SPICE lumped circuits as sub-grid models for FDTD analysis," *IEEE Microwave Guided Wave Lett.*, vol. 4, no. 5, May 1994, pp. 141–143.
60. Vourch, E., Drissi, M., and Citerne, J., "A full-wave analysis of active uniplanar structures," *IEEE Antenna Propag. Soc. Int. Symp. 1995 Dig.*, Newport Beach, CA, vol. 2, June 1995, pp. 1062–1065.
61. Nielsen, J. S., and W. J. R. Hofer, "Modeling of nonlinear elements in a three-dimensional condensed node TLM mesh," *Int. J. Microwave MM-Wave CAE*, vol. 3, no. 1, 1993, pp. 61–66.

*CHAPTER THREE*

---

# Circuit Simulator Based Methods

---

**PETER S. HALL**

School of Electronic and Electrical Engineering  
The University of Birmingham  
Edgbaston, Birmingham, UK

**VINCENT F. FUSCO**

Department of Electrical and Electronic Engineering  
Queens University of Belfast  
Belfast, UK

**MARTIN J. CRYAN**

Dipartimento di Ingegneria Elettronica dell'Informazione  
Università degli Studi di Perugia  
Perugia, Italy

## 3.1 INTRODUCTION TO EQUIVALENT CIRCUIT SIMULATION

In the active integrated antenna design process, there is a need for simulation tools that give results with good accuracy but with fast execution times. These tools can then be used both at the conceptual design stage, where fast simulation allows

selection of appropriate configuration, and for design optimization, where the chosen active integrated antenna can be adjusted to meet its broad requirements. Simulators based on equivalent circuits have long been used in microwave circuit design to perform these functions. This chapter reviews recent progress in the application of these methods to active integrated antennas.

In many cases, commercial software packages intended for microwave circuit simulation have been extended to include antenna equivalent circuits. These predict the circuit performance of the active antenna, which, for single radiating element devices, is the primary indicator of successful performance; radiation is likely to be similar to that of the passive antenna. Radiation patterns can then be calculated using an equivalent current source model using excitations derived from the circuit simulator. Examples of these methods are given in this chapter.

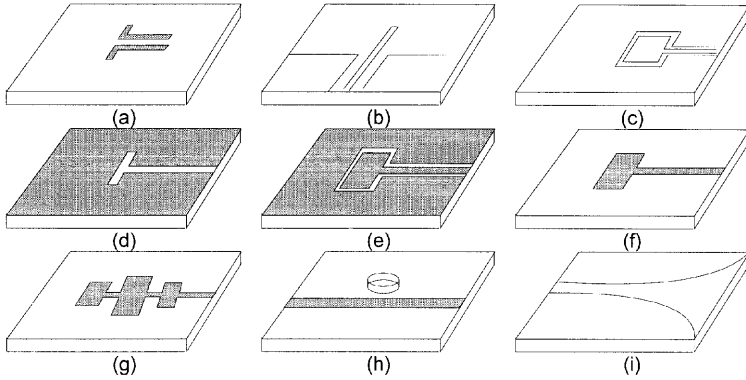
In other cases, alternative methods have been adopted. For example, for arrays of coupled oscillators time domain solution of simultaneous differential equations, based on very simple equivalent circuits, is a more appropriate way of simulating the dynamic performance. Similar methods are now yielding closed-form expressions for spectral performance of active patch oscillators. The approach to coupled oscillator arrays is noted in this chapter and covered extensively in Chapter 7. Details of spectral characteristic analysis are given here.

### 3.1.1 Antennas for Active Integrated Antennas

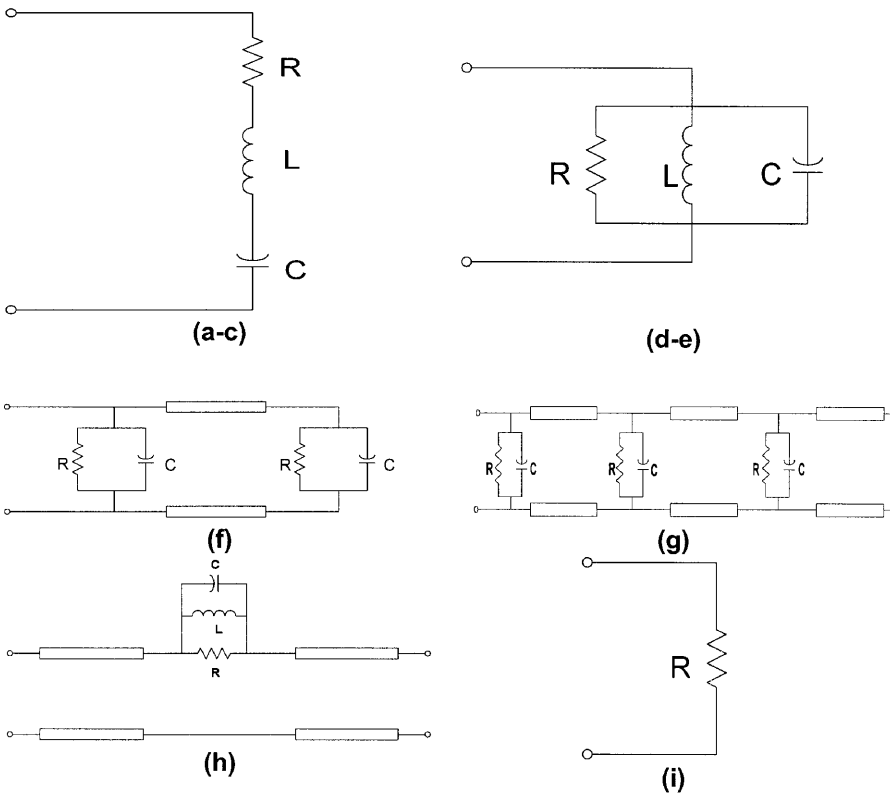
There are a wide range of antennas now used in active integrated antennas. One of the primary characteristics that allow integration is that the antenna is planar and hence amenable to construction using printed circuit, microwave integrated circuit, (MIC), or monolithic microwave integrated circuit, (MMIC) techniques.

Figure 3.1 shows a number of antenna types that have been used in integrated structures. Although the collection is not exhaustive, it illustrates those types that allow device integration. Use of some of these types is described in Chapter 1. Figure 3.2 gives the approximate equivalent circuit for the types shown in Fig. 3.1. The dipole and its variants are electric sources and can be represented close to resonance by a series resonant circuit [1]. Narrow bandwidth equivalent circuits are useful for single-frequency situations such as frequency estimation of oscillator–antenna modules and amplified transmit or receive antenna simulation. They are limited, however, when used for time domain analysis or calculation of spectral performance. The slot and its variants are magnetic sources and can be represented as a parallel equivalent circuit [2]. Again this is useful over only a narrow bandwidth and will not be useful where higher order modes are excited on the antenna. The microstrip antenna is magnetic in nature and, for a rectangular patch, consists of two parallel equivalent circuits separated by a transmission line [3]. More details of patch modeling are given in Section 3.1.2. Other types of microstrip antennas will have different equivalent circuits. For example, the series connected patch array of Fig. 3.1g [4] can be represented by a cascade of microstrip lines and parallel resonant circuits representing the patch edges. The cascade can be terminated with an open circuit to form a resonant array or with a  $50\text{-}\Omega$  load to represent a traveling wave





**FIGURE 3.1** Typical antenna types used in active integrated antennas: (a) printed dipole, (b) printed monopole, (c) printed loop, (d) slot, (e) slot loop, (f) microstrip patch, (g) microstrip array, (h) dielectric resonator, and (i) tapered slot.



**FIGURE 3.2** Approximate equivalent circuits of antennas of Fig. 3.1 (annotation relates to Fig. 3.1).

array. Dielectric resonators have been used as active antenna elements and the equivalent circuit is as shown in Fig. 3.1h [5]. The resistor represents both radiation and material loss. The tapered slot is an example of a traveling wave antenna and its terminal impedance properties can be represented over a wide frequency range by a resistor, although close to cutoff this equivalent circuit may be inappropriate.

### 3.1.2 Microstrip Patch Antenna Circuit Models

Microstrip patch antennas can be modeled with varying degrees of accuracy. Each modeling strategy gives rise to different physical insights about the problem. For an active antenna element the location of the tap-in point for intrinsic impedance match is a primary design criterion. This must be achieved in a way that is compatible with the electrical circuit synthesis approach needed for active antenna realizations, while simultaneously allowing primary antenna characteristics such as far-field copolar and cross-polar patterns to be evaluated. The simplest approach involves representing the antenna element as a very wide (low impedance) section of microstrip transmission line of length  $L$  (Fig. 3.3). Here the patch edges and ground plane represent the radiating apertures for the antenna. Thus the antenna is viewed as a section of transmission line normally about one-half wavelength long with a high impedance load comprised of a capacitance (due to edge fringe fields) and resistance (due to radiation) placed at each end of the line. Accurate models using this philosophy have been devised [6].

It should be noted that this class of model does not take into account higher order modes, which ultimately degrade cross-polar radiation levels. This is a particular problem for active antennas where cross-polar levels of better than  $-15$  dB cannot be obtained without taking special precautions. The model presented in Fig. 3.3 is valid when the patch resonator element is narrow, that is,  $w \leq \lambda$ . It includes mutual coupling between the main radiating slots, which, if not included, lead to inaccurate impedance tap-in point modeling. Here  $Y_s$  represents the slot radiating admittance and  $Y_m$  the mutual coupling between principal radiating slots. The detailed design equations for this three-port transmission line equivalent model can be found in [6].

By formulating the design equations in a modern microwave CAD package [7], lengths and widths of the antenna element are first established for a given frequency of operation, given that the substrate dielectric constant and height  $h$  are known. Then keeping the frequency of operation constant, lengths  $L_1$  and  $L_2$ , which determine the location of the antenna tap-in point, are varied until an input admittance  $Y_{in}$  can be assigned. Normally this admittance is the complex conjugate of the active device admittance. In this way an intrinsic match can normally be found for the device without the need for additional matching structures that can affect overall radiation patterns [8]. In some cases this approach will not directly yield the intrinsic matching condition. When this happens, the length of the element is allowed to vary within confined limits as part of the optimization process. Thus an intrinsic impedance match can always be found since the antenna is now operated slightly off-resonance.

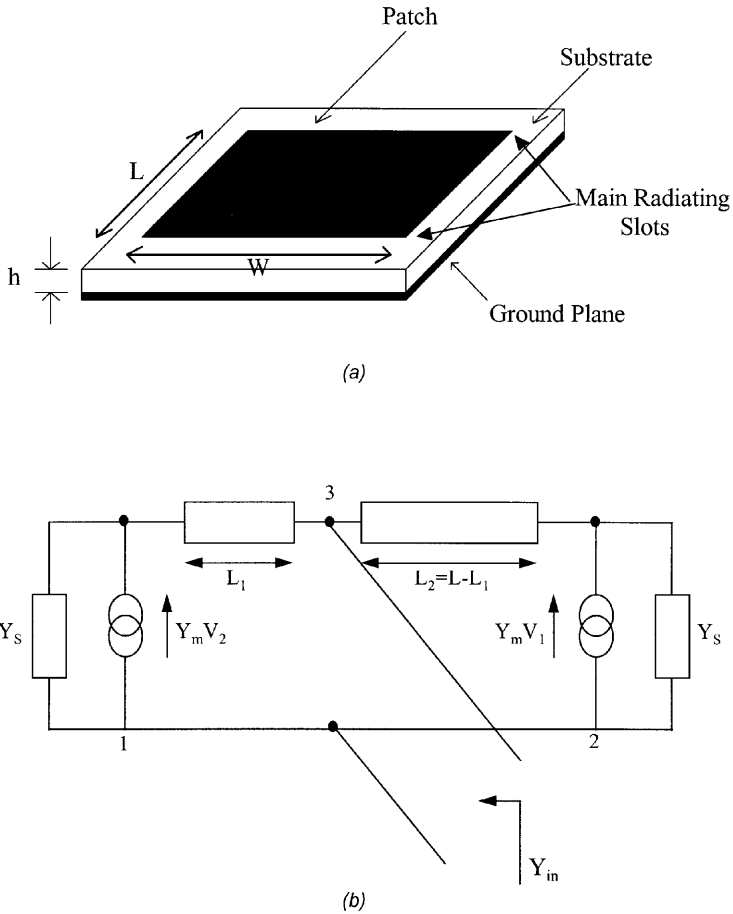
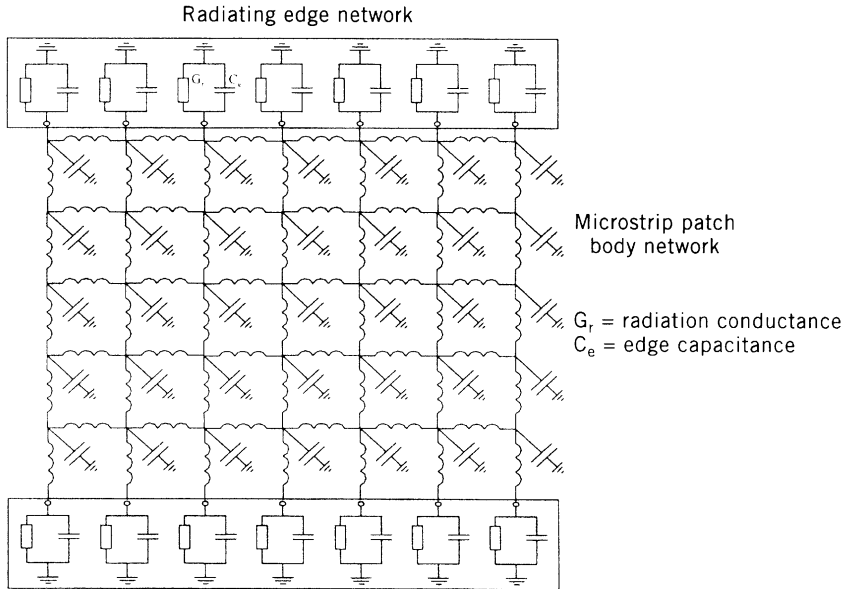


FIGURE 3.3 Microstrip patch resonator: (a) physical and (b) three-port model.

A second modeling strategy that is directly compatible with linear active antenna synthesis uses a two-dimensional equivalent circuit model. Here the radiating edges of the patch antenna together with the patch body are represented in the frequency domain by a circuit network equivalent of Maxwell's equation [9,10]. This approach facilitates the visualization of the EM fields on the antenna and other distributed circuitry associated with the active antenna in a way that is directly compatible with conventional nodal admittance circuit simulation. Figure 3.4 shows a typical two-dimensional network model for the patch antenna. With this model the  $E_\theta$  and  $E_\phi$  far-field components can easily be found by calculating the far-field radiation vector  $\mathbf{L}$  as defined in [10]. Copolarization and cross-polarization levels as well as tap-in location can also be evaluated by this procedure. The disadvantage of this approach is that it is very slow when used directly in a SPICE-type time domain circuit



**FIGURE 3.4** Two-dimensional patch antenna model.

simulation, as is necessary when active antenna transient or injection locking behavior is an issue.

A third approach that is sometimes convenient is to use a cavity model [11,12]. Modern CAD simulation tools, such as [7], have the facility that computer code can be incorporated directly for functional evaluation. With this approach, the antenna is replaced by a grounded dielectric resonant cavity with lossy dielectric. By impressing a magnetic current loop onto the grounded electric slab, the radiated power is computed and the radiation patterns for the antenna are obtained from the resulting magnetic current distribution. This approach is very useful when an impedance map over the antenna body is required and/or when the antenna does not operate in its fundamental mode. Also, the model can be used directly in order to establish simplified lumped circuit models for the antenna. These are particularly useful when time domain studies are required since all of the salient circuit features of the patch antenna are compactly represented.

### 3.1.3 Equivalent Circuits for Passive Components

There are several circuit media that have been used in integrated active antennas. The primary types are indicated in Fig. 3.5. There have been many good reviews of transmission media and their properties, such as [13,14]. Closed-form expressions are available for these media and many of the commercial software packages incorporate them.

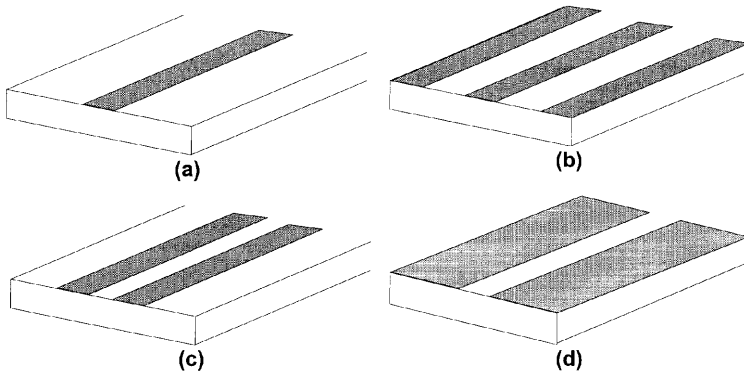


**FIGURE 3.5** Transmission media used in active integrated antennas: (a) microstrip, (b) coplanar waveguide, (c) coplanar stripline, and (d) slotline.

Discontinuities in the medium, such as changes in impedance, bends, and T junctions, need careful characterization to enable reliable equivalent circuits to be derived. Much work has been done and Hoffman [14], for instance, gives many examples, some of which are shown in Fig. 3.6.

The equivalent circuit models are limited in their applicability. Within the range of circuit parameters, often given in terms of line width as a ratio of wavelength, frequency, and substrate parameters, the accuracy may be better than a few percent. Outside these parameters, the discontinuity may behave in an anomalous way, due, for instance, to the generation of higher order modes within wide transmission lines or surface waves within thick substrates.

Choice of discontinuity model is not always clear and the full equivalent circuit model should be compared with measurements where possible. As indicated in Sections 3.1.2 and in 3.2.1, the microstrip patch can be modeled by transmission line sections with appropriate end admittances. However, the reactive effects at the line connection point have not been modeled, primarily because the available disconti-

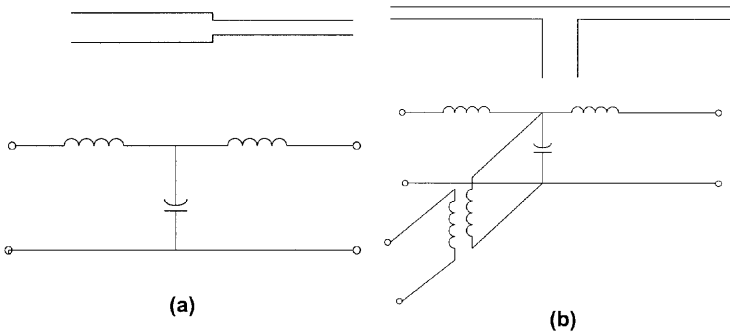


**FIGURE 3.6** Typical microstrip discontinuities and their equivalent circuits: (a) step and (b) T junction.

nuity models, the step or T junction, are not characterized for such line widths. In this case, however, the overall model was sufficient to give resonant frequency prediction within a few percent of that measured. In other configurations, however, this may not be the case and caution needs to be exercised in equivalent circuit construction.

### 3.1.4 Equivalent Circuits of Active Devices

Both two- and three-terminal active devices have been used in integrated active antennas for a variety of functions such as power generation, application, mixing, and control. Choice of device depends on both function and compatibility with the transmission medium used. Similarly, choice of transmission medium and antenna type will depend on availability of active devices. The compatibility of a solid state device with a transmission medium has been discussed in [13].

Equivalent circuit characterization of the active device is of crucial importance to active antenna simulation. Full performance prediction can only be achieved using both linear and nonlinear device characterization. In particular, for oscillator analysis, where accurate frequency and power level are required, for amplifier linearity analysis, and for mixer action, nonlinear models are required. However, first-order analysis of oscillators and amplifier antennas can be performed with linear device models.

Figure 3.7 shows typical small signal active device equivalent circuits [4]. Modern circuit simulators contain such models together with associated component values for manufacturers' devices. Some discussion of large signal models is given in

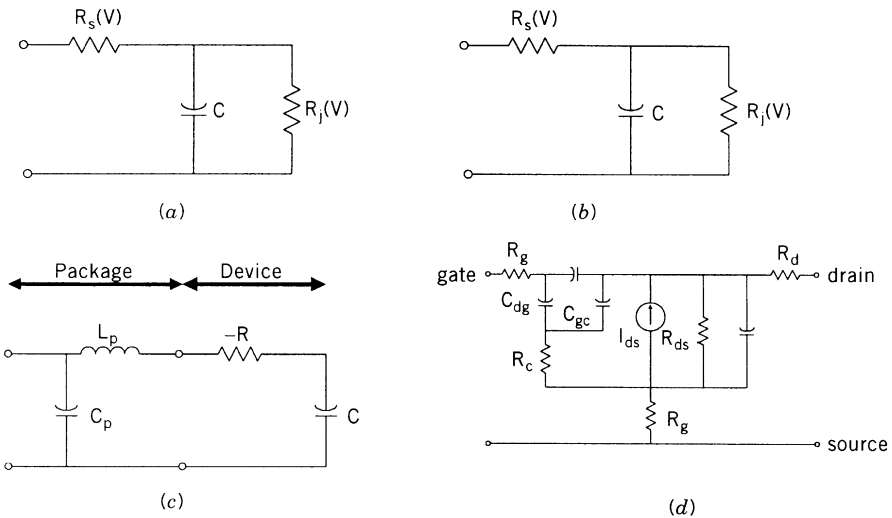


**FIGURE 3.7** Typical small signal equivalent circuits of typical active devices: (a) varactor diode (pill package), (b) beam lead Schottky-barrier mixer diode or varactor diode, (c) packaged Gunn diode, and (d) MESFET.

the next section. In most of the examples in this chapter, models contained in the simulator [7] were used in the computations.

### 3.1.5 Large Signal Equivalent Models

When active antennas are used as elements in power combining arrays, the active devices act as primary power sources for the active antenna and, for accurate design, must be well characterized. Large signal characterization is an important requisite since it is only under this operating condition that the power-producing oscillator action of the active antenna will reach a stable limit cycle. Thus any quantitative assessment of the behavior of the active antenna element depends on an intimate knowledge of the subtle interactions between device and circuit. A demanding part of the design procedure needed prior to initiating the design is a requirement for experimentally validated large signal models for the active device. The derivation of these models such that they provide a realistic estimate of the large signal performance is a subject of intense research [15–18]. For the purposes of illustration, a typical nonlinear model for a GaAs MESFET is shown in Fig. 3.8 [19]; other active devices such as IMPATT, Gunn, BJT, HBT, and HEMTs all have roles to play in active antenna circuit design.

The goal of the large signal modeling technique is to represent the device as a three-terminal network, the performance of which is designed to reproduce device performance under dc, small signal, and large signal modes of operation. Each of the nonlinear elements within the device are characterized by functional equations. The coefficients of these equations, along with the linear element values, are usually determined by numerical optimization, within physical constraints, to reproduce the

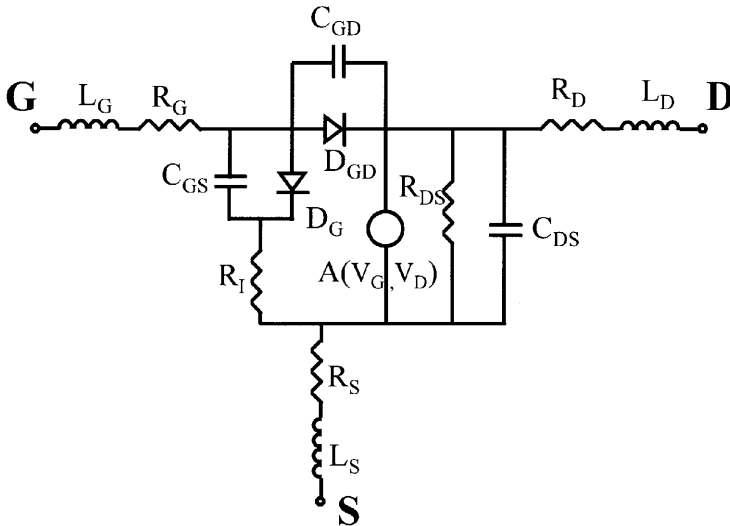


FIGURE 3.8 Typical large signal MESFET model.

actual measured terminal behavior of the device, preferably under all operational modes. Such a model should be used in the CAD algorithm for active microstrip antenna modeling for power-producing antennas.

Active GaAs three-terminal devices, such as a MESFET, are fabricated by growing an n-type epilayer onto a very pure GaAs substrate. The source and drain terminals are formed by making ohmic contacts onto the n-type epilayer, while the gate contact is achieved by the formation of a Schottky-barrier connection over the channel region. The bias voltages between the gate and the source,  $V_{GS}$ , and the drain and source,  $V_{DS}$ , are used to control the current flow through the device. The operation of the MESFET will not be detailed here as there are several established texts that provide a comprehensive analysis of the physical behavior and electrical properties of such devices [20,21].

Figure 3.8 shows the large signal MESFET model circuit.

There are a number of linear elements included in the MESFET model.  $L_S$ ,  $L_G$ , and  $L_D$  represent the inductances associated with the bond wires connecting the MESFET to the outside world. The resistances  $R_D$  and  $R_S$  account for the metallization contact resistances at the terminals and for the resistance presented by the n-type material between the drain and gate terminals and the source and gate terminals, respectively.  $R_G$  models the contact resistance of the metallization at the gate terminal. The resistance  $R_I$  accounts for the intrinsic impedance of the conducting channel between the source and gate terminals. The capacitance and resistance in the device n-type channel are modeled by the parallel combination of the elements  $R_{DS}$  and  $C_{DS}$ . The capacitive effect of the Schottky-barrier terminal between the gate and drain is characterized by  $C_{GD}$ .

There are four nonlinear elements included in the large signal MESFET model. These are diodes  $D_G$  and  $D_{GD}$ , which represent the rectification effects at the Schottky-barrier gate terminal, the capacitance  $C_{GS}$ , which models the gate to source capacitance at the Schottky barrier, and the voltage-controlled current source,  $I_D$ , which simulates the conducting action of the n-type channel under the gate terminal.

The nonlinear currents flowing in the diodes,  $I_{DG}(t)$  and  $I_{DGD}(t)$ , may be represented by Eqs. 3.1–3.3, where  $V_{GD}(t)$  is the voltage across the element  $D_{GD}$ .

$$I_{GD}(t) = I_{SAT} \left( \exp\left(\frac{V_{GD}(t)}{N \cdot V_T}\right) - 1 \right) \quad V_{GD}(t) > (-5NV_T) \quad (3.1)$$

$$I_{GD}(t) = -I_{SAT} \left( 1 + \exp\left(-\frac{V_{BR} + V_{GD}(t)}{V_T}\right) \right) \quad V_{GD}(t) < (-V_{BR} + 50V_T) \quad (3.2)$$

$$I_{GD}(t) = -I_{SAT} \quad (-5NV_T) \geq V_{GD}(t) \leq (-V_{BR} + 50V_T) \quad (3.3)$$

where  $N$  is the ideality factor of the diode,  $V_{BR}$  is the reverse breakdown voltage of the junction,  $I_{SAT}$ , the reverse bias leakage current, and  $V_T$  is 25 mV at room temperature. These three equations account for forward conduction, reverse conduction, and saturation conduction. The current  $I_{DG}(t)$  flowing in the diode  $D_G$  is found using the same model.



The most important of the nonlinear elements is the drain-to-source current model,  $I_D(t)$ . This must account for all the conductance mechanisms associated with the variable depth of the depletion region under the gate terminal. The model used here for illustration is that due to Curtice [22]. This voltage-controlled current source is characterized by the  $V$ - $I$  relationship in Eq. 3.4:

$$I_D(t) = (A_0 + A_1 V_A + A_2 V_A^2 + A_3 V_A^3) \tanh[\Gamma V_D(t)] + \frac{V_D(t) - V_{DSDC}}{R_{DSO}} \quad (3.4)$$

where

$$V_A = V_G(t)[1 + \beta(V_{DSO} - V_D(t))] \quad (3.5)$$

The parameters  $A_0$ ,  $A_1$ ,  $A_2$ , and  $A_3$  are the Curtice transconductance coefficients of the device,  $R_{DS}$  is the dc output conductance of the device,  $\beta$  is the coefficient to control the change of the pinch off current due to the drain voltage, and  $\Gamma$  defines the magnitude of drain current at which saturation occurs.  $V_{DSO}$  is the voltage at which the transconductance coefficients were evaluated.  $V_{DSDC}$  is set to the drain-to-source bias level. This  $I$ - $V$  relationship is not valid for all operating values of gate voltage. The physical  $I$ - $V$  characteristic is not symmetrical about the origin of its axes, and thus to ensure integrity of the function in Eq. 3.4 the following criteria are applied:

$$I_D(t) = 0.0 \quad \text{where} \quad I_D(t) < 0.0 \quad (3.6)$$

and

$$I_D(t) = 0.0 \quad \text{where} \quad (V_G(t) - V_{TO}) < 0.0 \quad (3.7)$$

$V_{TO}$  is the turn-on voltage of the device.

The final nonlinear element in the large signal model is the capacitance  $C_{GS}$ . The relationship used to represent this capacitance is dependent on whether  $V_G(t)$  is above or below the built-in potential of the gate contact,  $V_{BI}$ . Two capacitance-to-voltage relationships are thus required, as shown in Eqs. 3.8 and 3.9:

$$C_{GS}(t) = \frac{C_{GSO}}{\sqrt{1 - \frac{V_G(t)}{V_{BI}}}} \quad V_G(t) < V_{BI} \quad (3.8)$$

and

$$C_{GS}(t) = \frac{1}{\sqrt{(1 - F_C)}} \left( \frac{C_{GSO}}{1 + \frac{V_G(t) - (F_C V_{BI})}{2V_{BI}(1 - F_C)}} \right) \quad V_G(t) \geq V_{BI} \quad (3.9)$$

**TABLE 3.1 Large Signal MESFET Model Coefficients**

Parameter	Value
$I_{SAT}$	$1.4 \times 10^{-10}$ A
$N_{IGD}, N_{ICS}$	1.54
$V_{BR}$	17.0 V
$C_{GSO}$	0.385 pF
$V_{BI}$	0.844 V
$A_0$	0.071
$A_1$	0.066
$A_2$	0.007
$A_3$	-0.0036
$\beta$	0.01
$\Gamma$	4.0
$V_{TO}$	-2.2 V
$R_{DS}$	600 $\Omega$
$V_{DSO}$	2.0 V
$V_{DSDC}$	3.0 V
$F_C$	0.5
$R_i$	12.5 $\Omega$
$R_S, R_D$	1.5 $\Omega$
$R_G$	6.54 $\Omega$

The parameter  $F_C$  is a fitting coefficient, which is varied to obtain the best agreement between the measured and modeled values of  $C_{GS}$ .

The model described here is that developed by Tang [23]. The parameters for this model are listed in Table 3.1 and provide a good fit to the dc and measured large signal harmonic performance of an actual device.

The device topology, together with the appropriate governing equations, can be incorporated directly into the circuit simulation together with the antenna model so that the overall active antenna circuit can be simulated under dc small signal or large signal modes of operation depending on the functional requirements needed for the active antenna application, oscillator, amplifier, and so on. Fortunately, modern nonlinear CAD simulation tools have a variety of validated standard large signal models available so that one does not have to build a verified model from scratch each time.

### 3.2 LINEAR SIMULATION USING EQUIVALENT CIRCUIT MODELS

In this section examples are presented of the simulation of active integrated antennas. The examples use models based on the antenna and passive component equivalent circuits described in Section 3.1, together with linear, small signal device models.

### 3.2.1 Microstrip Patch Oscillator

An important class of integrated active antenna is the microstrip patch oscillator. This is a highly integrated transmit module that can form a building block in complex systems such as full duplex transmit–receive modules [24] or phase shifterless beam scanning applications [25]. In this section the transmission line model will be used in the small signal design of a 4-GHz patch oscillator. This is the first stage in the oscillator design and will be followed by a full nonlinear simulation in the Section 3.3.1.

Figure 3.9 shows the patch antenna. In this case, a nonradiating edge feed is used in order to obtain appropriate matching conditions, which will be discussed in the nonlinear design. The accuracy of the equivalent circuit model implemented on Hewlett Packard Microwave Design System (MDS) software is limited to approximately 1% for resonant frequency and in the region of 20–50% for input impedance. This can lead to problems when very tight specifications have to be met. However, as a first iteration design tool, some useful results can be obtained. The closed-form nature of the model allows very fast computation times, which in turn allow the important feature of optimization to be used as part of the design process.

The input reflection coefficient ( $S_{11}$ ) is shown in Fig. 3.10 compared with the equivalent circuit model. It can be seen that the resonant frequency is well predicted. However, agreement for the magnitude of  $S_{11}$  is less good. The agreement is much improved when symmetrical radiating edge feeding such as inset feeding is used, since this generates fewer orthogonal currents, which cannot be modeled by the simple equivalent circuit used here.

The patch oscillator design discussed here was first proposed by Birkeland and Itoh [26]. The drain of a GaAs metal semiconductor field effect transistor (MESFET) is connected to the patch at the feed point shown in Fig. 3.9 and short circuit transmission lines are connected to gate and source terminals. A schematic of the oscillator is shown in Fig. 3.11. The oscillator can be considered as having series feedback in the source such that a negative resistance is obtained looking into the gate terminals. The gate transmission line then presents the required reactance to

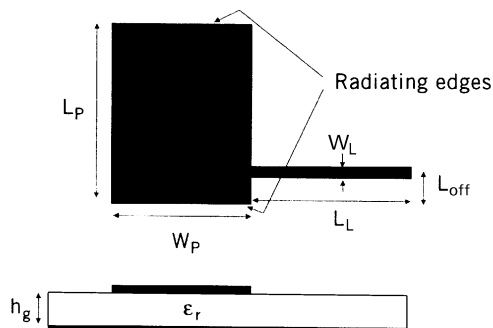


**FIGURE 3.9** Nonradiating edge-fed microstrip patch antenna.  $L_p = 24.0$  mm,  $W_p = 20.0$  mm,  $L_{off} = 5.0$  mm,  $W_L = 1.57$  mm,  $h = 0.508$  mm and  $\epsilon_r = 2.2$ .

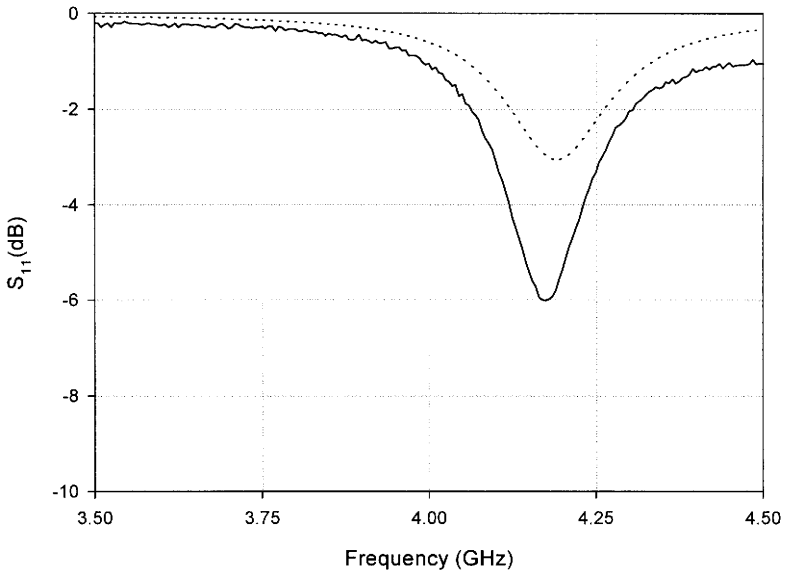


**FIGURE 3.10** Measured (—) and modeled (---) input reflection coefficient for a microstrip patch of Fig. 3.9 using the transmission line model.

obtain oscillation at a particular frequency. The details of this design approach are covered in a number of texts [21,27].

The oscillator design procedure begins with linear simulation to determine the approximate oscillation frequency. The analysis component is used to estimate the loop gain of the circuit. If the magnitude of the loop gain is greater than unity and the phase has a zero crossing, then the circuit has the potential for oscillation. For stable oscillation the Nyquist criterion must be satisfied, which states that the  $1 + j0$  point must be enclosed in a clockwise direction by the locus of the loop gain. If these

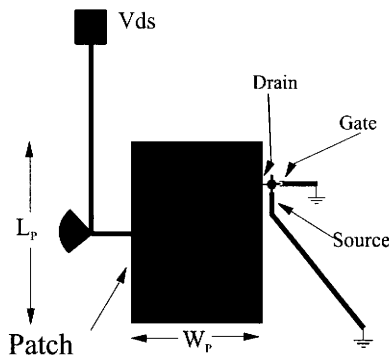


**FIGURE 3.11** Schematic layout for a microstrip patch oscillator.  $L_p = 24.0$  mm,  $W_p = 20.0$  mm.

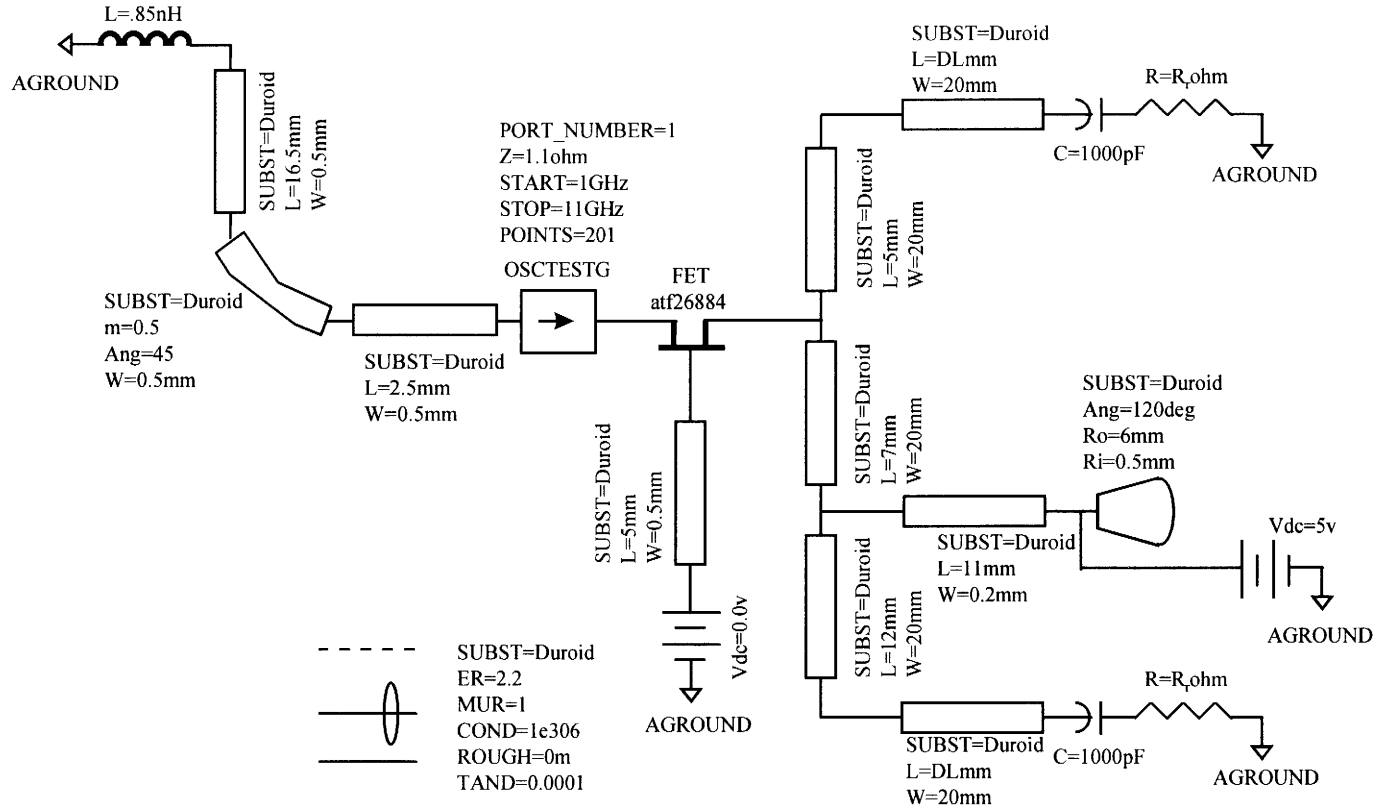
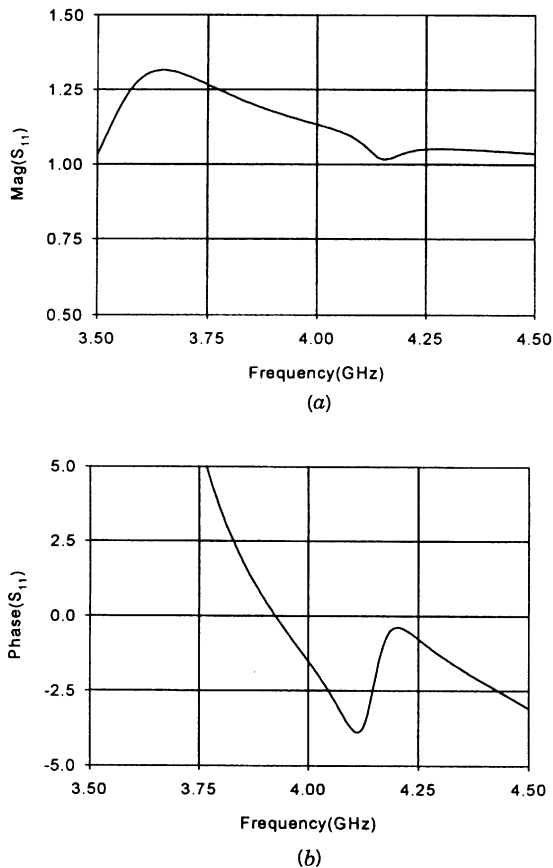


FIGURE 3.12 HP MDS circuit layout for a 4-GHz microstrip patch oscillator of Fig. 3.11.

two conditions are met, then stable oscillation in the large signal simulation is almost guaranteed. Figure 3.12 shows the circuit page layout for a 4-GHz patch oscillator including an implementation of the equivalent patch model.

The circuit shows the patch model constructed from five transmission lines, of which two of length “DL” are end extensions due to the fringing field. The radiation resistances are shown as “ $R_r$ ” and are in series with 1000-pF capacitors to dc block the drain–source bias current. The analysis port component is positioned at the source terminal. This was found to be the best position for later large signal simulations. The gate and source transmission lines are terminated by inductances to ground to simulate the wire short connections. The values have been obtained by measurement. These inductances are quite critical to the design and it is important that good estimates of their values are obtained.

Figure 3.13 shows the results of the simulation. It can be seen that the magnitude of the loop gain is greater than unity across the whole band and there is a zero crossing of phase, implying the circuit has the potential for oscillation. In addition,



**FIGURE 3.13** Simulated loop gain for circuit of Fig. 3.12: (a) magnitude and (b) phase.

the phase can be seen to cross zero only once and is passing from positive to negative, implying clockwise rotation around the  $1 + j0$ . Thus the circuit is likely to oscillate.

An estimate of the oscillation frequency can be made from Fig. 3.13. Steady-state oscillation occurs when the magnitude of the loop gain equals unity and the phase crosses zero. After the initial startup of the oscillator, as the amplitude of the oscillations begins to grow, the nonlinear nature of the active device means that the amplitude will approach a saturated level. This implies that the loop gain will decrease from its small signal value, finally reaching unity at some particular power level and frequency. Thus the best estimate obtainable from the small signal results is the zero crossing point of the loop gain phase, in this case 3.925 GHz.

The measured spectrum of the oscillator is shown in Fig. 3.14. The spectrum is measured at 30 cm from the oscillator using a broadband antenna connected to a spectrum analyzer. The measured output frequency is 3.97 GHz, 1.2% greater than the small signal prediction. This good agreement suggests that the operating frequency is primarily determined by the oscillator, where it is believed that the modeling accuracy is better than that of the patch. It is concluded that good oscillation frequency prediction can be made with a relatively coarse patch model.

### 3.2.2 Integrated Amplifier Patch Antenna

Amplifiers have been integrated with antennas to improve performance on receive by either reducing the effects of feeder losses [28], or increasing the gain [29] and

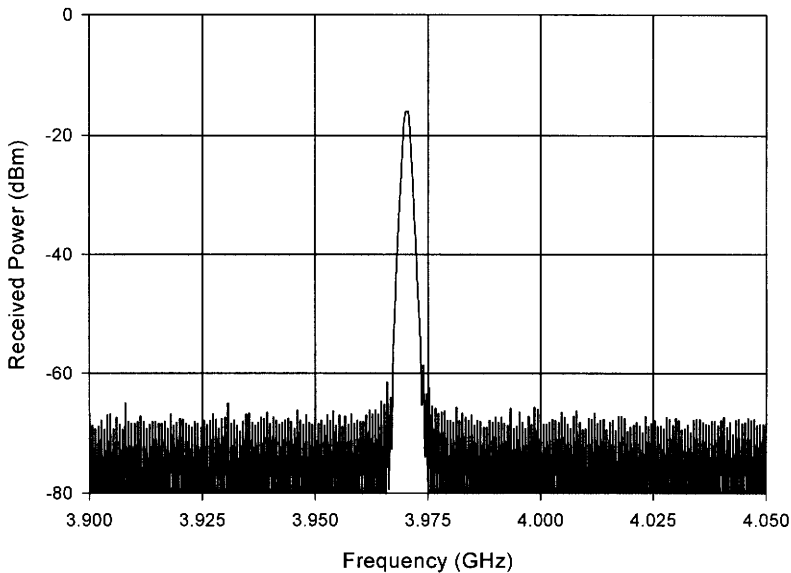


**FIGURE 3.14** Measured output spectrum of microstrip patch oscillator of Fig. 3.12 with  $V_{ds} = 5.0$  V.

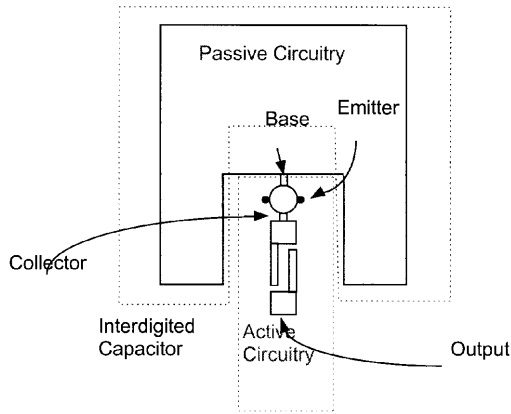


**FIGURE 3.15** Half-wavelength patch with integrated amplifier.

bandwidth [30]. Figure 3.15 shows a compact half-wavelength microstrip patch antenna with integrated amplifier [29]; a gain increase of 8 dB over a passive patch was reported.

Low noise amplification (LNA) at microwaves using GaAs FETs, HEMTs, or BJTs is a well-established technology. The procedure for the design of standalone LNA circuits involves synthesis of a lossless input matching network to transform the generator impedance, usually  $50 \Omega$ , into the complex impedance,  $Z_{opt}$ , required by the chosen transistor for optimum noise [31]. In more advanced designs, lossless series or parallel feedback may be added to allow simultaneous optimization of the noise figure and input VSWR [32].

Several authors [29,30] have described low noise receiving antennas in which the antenna output impedance is transformed directly into  $Z_{opt}$ . A more closely integrated structure has been suggested [33], in which the positioning of a transistor within a quarter wave patch antenna is used to create series and parallel feedback and impedance transformation. The structure of this circuit is illustrated in Fig. 3.16. The overall length  $L$  of the patch is chosen to give resonance at the required center frequency. The insertion distance  $L_i$  and the distance  $L_t$  from the grounded edge to the transistor both affect the impedance seen by the transistor and the degree of

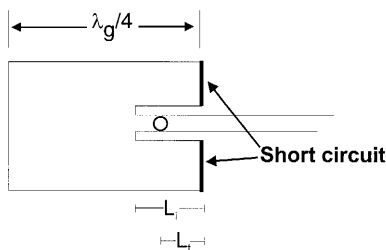


**FIGURE 3.16** Quarter wave patch low noise amplifier layout.



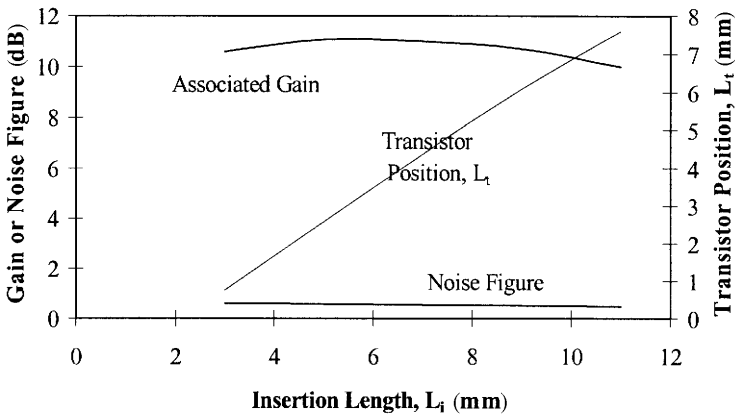


FIGURE 3.17 Optimum noise figure, gain, and transistor position for low noise active patch.

series and parallel feedback. A microstrip transmission line model can be used to demonstrate the expected effects of these design variables on the gain and noise figure. This procedure has been used to show that for given values of  $L$  and  $L_i$  there is a value of  $L_t$  that gives a minimum value of noise figure at a frequency close to the unloaded resonant frequency of the antenna. The maximum gain,  $G_{assoc}$ , associated with this combination of design variables is obtained by conjugately matching the output of the antenna.

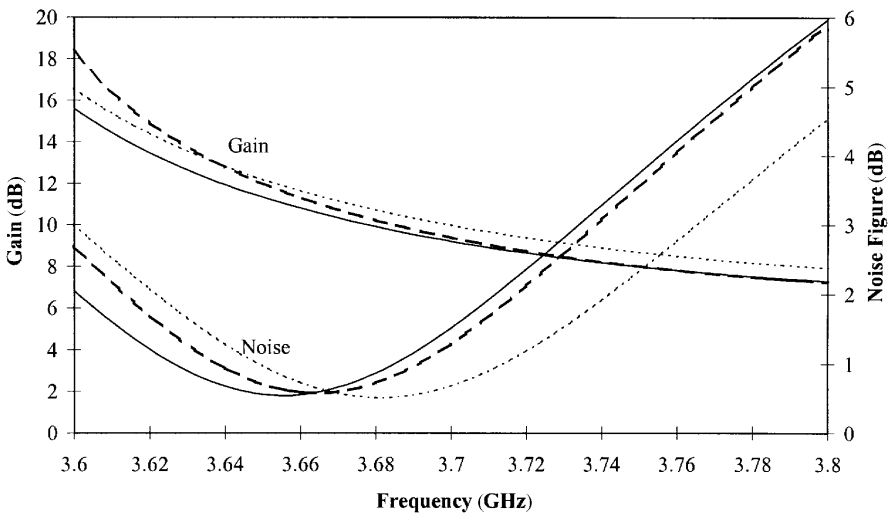


FIGURE 3.18 Gain and noise figure for three active LNA patch geometries. Insert: 9 mm ( $\cdots$ ), 7 mm (—), and 5 mm (---).

Example results are shown in Fig. 3.17, where the optimum values of  $L_i$ ,  $F$ , and  $G_{\text{assoc}}$  are plotted against  $L_i$ . The quarter wavelength patch antenna in this example, designed for a frequency of 3.7 GHz, has an overall length of 12 mm, a width of 20.0 mm, and the substrate has thickness 1.143 mm and dielectric constant 2.22. The transistor used in this simulation was an AT10136 packaged GaAs FET, with an optimum noise figure (in common source configuration) of 0.5 dB. Note that with  $L_i$  of 11 mm, the noise figure is below this optimum. This occurs because of the effects of the feedback inherent in the active antenna. A reduction in gain is also apparent in this condition. This is consistent with the fundamental restriction that the optimum noise measure is invariant with lossless embedding [34].

Figure 3.18 shows a plot of gain and noise figure against frequency for three different combinations of dimensions. The bandwidth is less than that reported for some less compact integrated antennas [35]. Broadening of the bandwidth within a closely integrated structure will require further experimentation with alternative coupling structures. The simplified analysis, based on MDS [7] models, serves to demonstrate the effects of the available design variables but ignores other effects, such as lateral current spreading at the end of the insert. A more elaborate model, such as the empirical model of Ormiston et al. [33], is needed to take such effects into account in a rigorous design.

### 3.2.3 Design and Simulation of an Active Circulator Antenna Transceiver Module

Active circulators have been of interest for many years with their inherent advantages of size and weight over conventional ferrite devices [36,37]. In this section the design and simulation of a hybrid, active circulator antenna module are discussed. It is based on a phase cancellation technique and is integrated with a microstrip antenna forming a fully duplexed transceiver module [38].

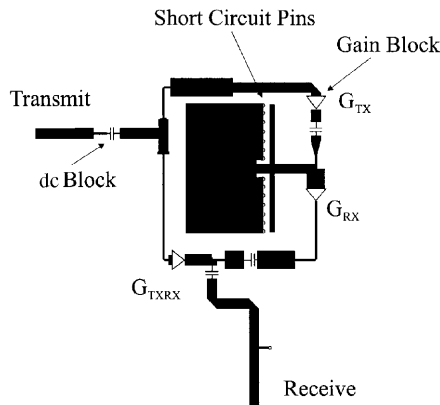


FIGURE 3.19 Schematic layout of an active circulator antenna.

Figure 3.19 shows a schematic of the circuit. The transceiver operates at a single frequency of 3.745 GHz and is linearly polarized with the same polarization for transmit and receive. Power at the transmit port is split, one portion being amplified by  $G_{TX}$  and passing to both the antenna and the receive port; the other passing directly to the receive port via  $G_{TXRX}$ . Thus there are two paths between transmit and receive. By adjusting the gains and phase lengths in the circuit, isolation between transmit and receive can be obtained. Receive power is coupled into the circulator and passes through  $G_{RX}$  to the receive port since the reverse isolation of  $G_{TX}$  and  $G_{TXRX}$  prevent power coupling back into the transmitter. A quarter wavelength short circuit, inset-matched microstrip antenna is placed in the center of the ring. The antenna measures 20 mm by 12 mm and the whole circuit occupies less than 50 mm by 40 mm when constructed on a substrate with dielectric constant of 2.2. The circuit is fully planar, with only dc bias inductors placed on the underside of the board.

The circuit was designed using a commercial circuit simulator [7]. The  $S$ -parameters of one of the gain blocks were measured at ten different gain levels and imported into the simulator. This was necessary for optimization of the amplifier gains and the widths and lengths of the transmission lines for simultaneous matching and isolation. Equations were used to ensure changes in one line length were compensated by changes elsewhere in the ring. After each optimization process, the ring geometry was checked using the auto layout facility. The antenna port was treated as an ideal 50- $\Omega$  termination. While this led to straightforward design and layout, it also led to reduced performance, which will be discussed later.

Figure 3.20 compares measured and simulated results. The measurements of transmit and receive gains show a maximum transmit gain of 17.75 dBi and a maximum receive gain of 11.64 dBi. These are  $\sim 10$  dB higher than the simulated results, which, however, do not include the antenna gain of about 4 dBi. Figure 3.20b shows the power coupled from transmit to receive ports. The best measured performance is obtained at 3.745 GHz with a value of  $-26.9$  dB. This isolation is obtained over a narrow bandwidth, which is typical for cancellation methods. The

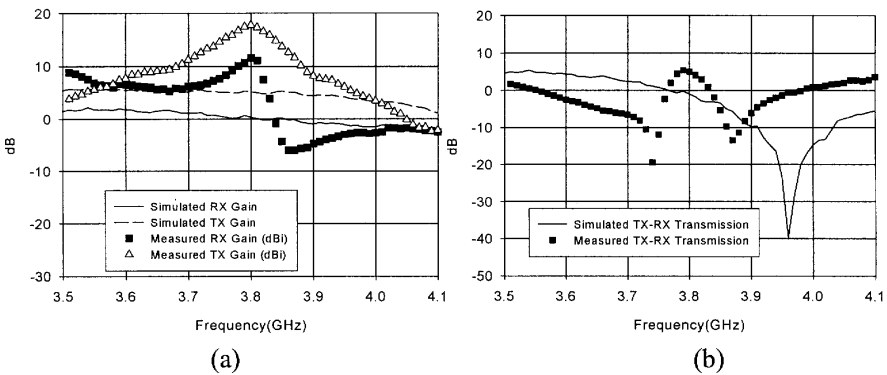


FIGURE 3.20 Measured and simulated performance of active circulator antenna: (a) transmit and receive gains and (b) TX-RX transmission.

double dip in the measured results is not well predicted, as a 50- $\Omega$  termination was used to represent the antenna. If a resonant load is used, a second dip is observed at the patch resonance frequency. The simulation showed an accuracy in prediction of operating frequency of 5.4%.

### 3.2.4 Calculation of Radiation from Antenna–Circuit Modules

All of the equivalent circuit based methods in this chapter solve the circuit problem. However, as radiation is the primary function of active integrated antennas, fast, compact radiation solutions are also desirable. In this section calculation of the radiation performance of microstrip active antennas is described. The method could, in principle, be extended to other media, such as slotline or coplanar waveguide based antennas. The method uses an equivalent radiation source current distribution in the plane of the antenna and circuit. The current excitations are determined from solution of the circuit problem and hence the method could be integrated within a commercial simulation package.

Figure 3.21 shows a three-terminal device in an infinite microstrip line, together with its  $S$ -parameter based equivalent circuit. By representing this current discontinuity by equivalent magnetic and electric current sources [39], it is possible to express the radiated fields in closed form [40]:

$$\begin{aligned}
 E_{\theta'} = & -C \left[ \frac{(\varepsilon - 1) \cos \theta' + \sqrt{\varepsilon} \sin^2 \theta'}{\sqrt{\varepsilon} - \cos \theta'} [(1 - S'_{22})I_{1f} - S'_{22}I_{2f}] \right. \\
 & - \frac{(\varepsilon - 1) \cos \theta' - \sqrt{\varepsilon} \sin^2 \theta'}{\sqrt{\varepsilon} + \cos \theta'} \\
 & \left. \times [S'_{11}I_{1f} + (S'_{12} - 1)I_{2f}] - 2\sqrt{\varepsilon} \cos \theta' \left( \frac{S_{sg}}{1 + S_{ss}} I_{1f} + \frac{S_{sd}}{1 + S_{ss}} I_{2f} \right) \right] \cos \phi'
 \end{aligned} \tag{3.10}$$

$$\begin{aligned}
 E_{\phi'} = & C \left[ \frac{\varepsilon - 1}{\sqrt{\varepsilon} - \cos \theta'} [(1 - S'_{21})I_{1f} - S'_{22}I_{2f}] - \frac{\varepsilon - 1}{\sqrt{\varepsilon} + \cos \theta'} (S'_{11}I_{2f}) \right. \\
 & \left. - 2\sqrt{\varepsilon} \left[ \left( \frac{S_{sg}}{1 + S_{ss}} I_{1f} + \frac{S_{sd}}{1 + S_{ss}} I_{2f} \right) \right] \right] \sin \phi'
 \end{aligned} \tag{3.11}$$

where

$$C = j \frac{60kh e^{-jkr}}{\sqrt{\varepsilon} r} \tag{3.12}$$

Here,  $\varepsilon$  is the effective dielectric constant of the microstrip line,  $k$  is the free-space wavenumber, and  $r$  is the distance from the origin, which is at the device location.  $\theta'$  and  $\phi'$  are defined in Fig. 3.21a. The three terms in each expression relate to

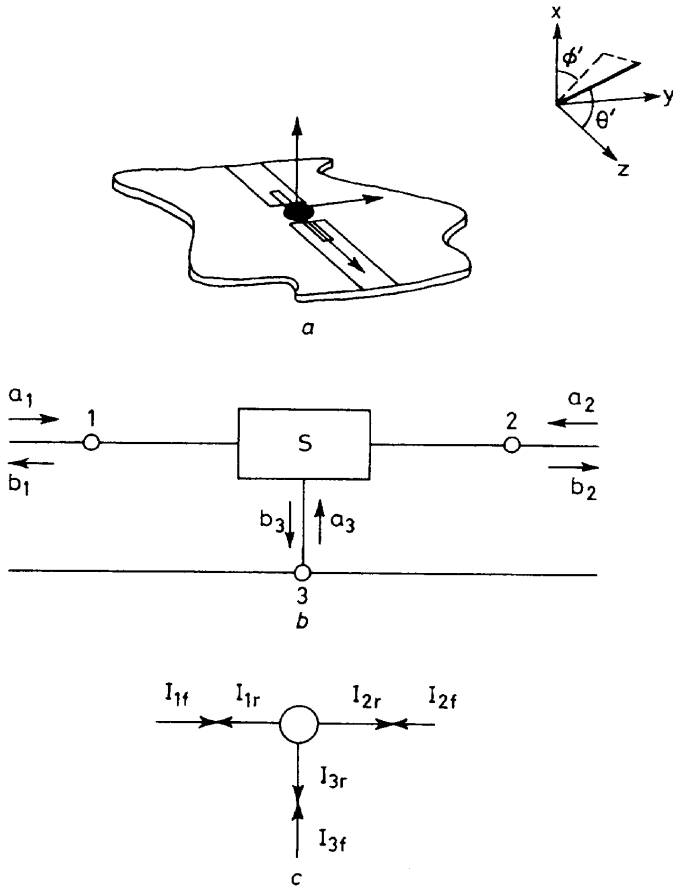


**FIGURE 3.21** Transistor in microstrip line: (a) geometry, (b) equivalent circuit, and (c) equivalent circuit used in radiation calculation. (From [40], reprinted with permission of IEE.)

radiation from the current leaving port 2, the current incident and reflected from port 1, and the current in the grounded port 3, respectively, as shown in Fig. 3.21b.  $S_{sg}$ ,  $S_{sd}$ , and  $S_{ss}$  are three port S-parameters, Fig. 3.21c.

By integrating the field expressions, the power radiated can be found. Figure 3.22 shows this power as a percentage of the incident power for a typical 10-dB gain transistor, compared to that radiated by an equivalent line with an open circuit [41], at the position of the transistor. It can be seen that the transistor gives significantly higher radiation particularly at low frequencies when the gain is high. The high frequency falloff is associated with the transistor gain saturation.

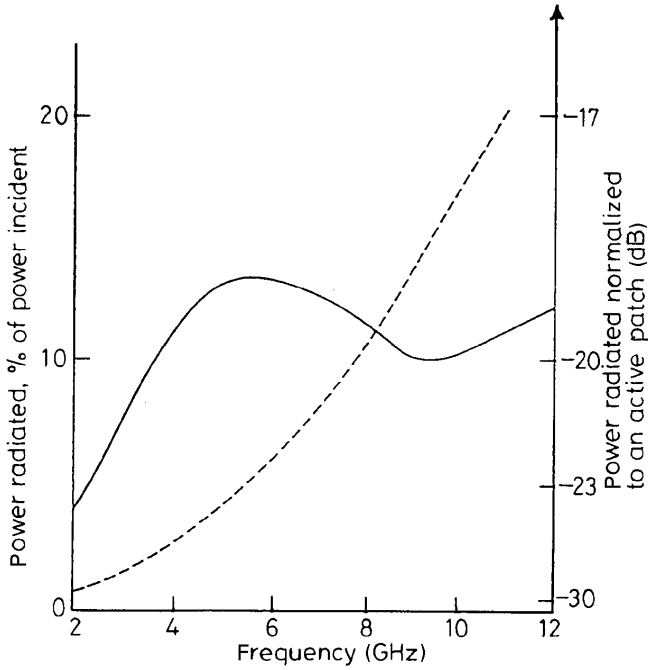


**FIGURE 3.22** Calculated total power radiated by HP Avantek ATF-26884 transistor. Power normalized to incident power and to that from an active patch incorporating a 10-dB amplifier. Bias  $V_{ds} = 5$  V,  $I_{ds} = 30$  mA, common source mode. Substrate  $\epsilon_r = 2.2$ ,  $h = 1.59$  mm, — transistor, - - - open circuit. (From [40], reprinted with permission of IEE.)

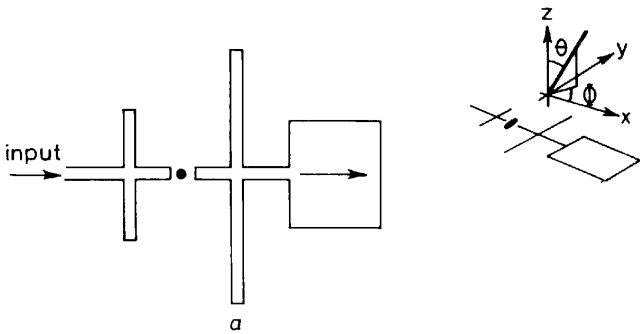


**FIGURE 3.23** Active patch configuration. (From [40], reprinted with permission of IEE.)

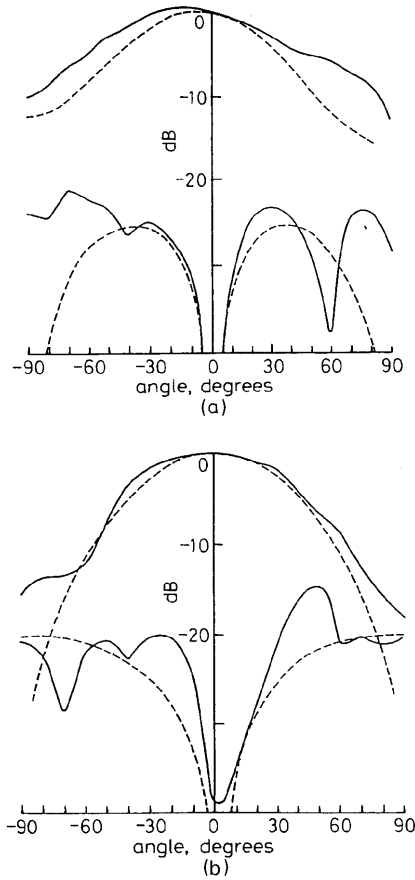


**FIGURE 3.24** Radiation pattern of active transmitting antenna of Fig. 3.23. Inset shows coordinate system. (a)  $\Phi = 0^\circ$  E plane, (b)  $\Phi = 90^\circ$  H plane, upper curves copolarization, lower cross-polarization. — Measured, - - - calculated. (From [40], reprinted with permission of IEE.)

When the transistor is part of an active antenna, as, for example, in Fig. 3.23, then the overall radiation field is given by

$$\begin{aligned}
 \mathbf{E}_{\text{rad}} = & jhK \left[ \mathbf{R} \times \int \mathbf{M} \exp(jk_0 r \cos \phi) dc \right] \\
 & + jhK \sum_q M_q \exp(jk_0 r_q \cos \phi_q) \left[ \sin(\phi - \gamma_q) \boldsymbol{\theta} - \cos \theta \cos(\phi - \gamma_q) \boldsymbol{\Phi} \right] \\
 & + (E_\theta \boldsymbol{\theta} + E_\phi \boldsymbol{\Phi})
 \end{aligned} \tag{3.13}$$

where the first term represents the patch radiation, the second the passive discontinuities, such as open circuits, bends, or T junctions, and the third the active devices, with  $E_\theta$  and  $E_\phi$  given by Eqs. 3.10 and 3.11, respectively, after applying the appropriate coordinate transform from  $\theta', \phi'$  to  $\theta, \phi$  space.  $K = \exp(-jk_0\tau)/\lambda_0\tau$ ,  $k_0 = 2\pi/\lambda_0$ ,  $\theta$  and  $\phi$  are defined in Fig. 3.23, and  $\tau_q$ ,  $\Psi_q$ , and  $\Upsilon_q$  specify the location and orientation of the  $q$ th discontinuity [42].  $M = Vw_e/h$ , where  $V$  is the source distribution voltage,  $w_e$  is the line equivalent width, and  $h$  is the substrate height.

Figure 3.24 shows the calculated radiation patterns of the transmitting amplifier–patch combination shown in Fig. 3.23, compared to measurements. Good agreement is noted. Radiation from the transistor is polarized parallel to the patch and contributes to significant copolar pattern distortion in the  $E$  plane. Radiation from the matching stubs is cross-polarized and is comparable to that due to the patch higher order modes. Similar calculations can be made for a receiving configuration.

In the transmit case, it is the transistor and amplifier output matching stubs that contribute most to unwanted radiation. The transistor gain effectively renders negligible radiation from the input matching stubs and other circuiting such as corporate feeds. Similarly, in the receive case, the transistor and input matching stubs are the most significant; the transistor gain makes unwanted reception from further circuit elements small.

The example above shows a successful application of a simple technique for calculation of radiation from integrated active antennas. It is limited in accuracy both by the accuracy of the equivalent circuit simulation and by the fact that the current source equivalents assume infinitely long interconnecting lines. It is clearly going to be less accurate for some of the highly compact oscillator and amplifier patches shown elsewhere in this chapter. Nevertheless, its simple formulation make it suitable for fast design and simulation needs.

### 3.3 NONLINEAR SIMULATION USING EQUIVALENT CIRCUIT MODELS

In order to accurately analyze and design active integrated antennas, it is essential to perform large signal, nonlinear analysis. There are several places where it can be seen to be important. In the case of antenna oscillators, nonlinear analysis will give more accurate prediction of oscillation frequency, radiated power, and spectral output. In coupled oscillator arrays, important dynamic effects can be analyzed. For integrated amplifying antennas, whether transmit or receive, it will provide information on linearity and, in particular, intermodulation effects and for mixers it is essential for modeling the mixing action.

#### 3.3.1 Harmonic Balance Synthesis

Active antenna oscillator designs represent a demanding aspect for circuit synthesis. This is due mainly to the dual use of the antenna element both as the radiating element and as the oscillator resonant load. A synthesis technique for this type of



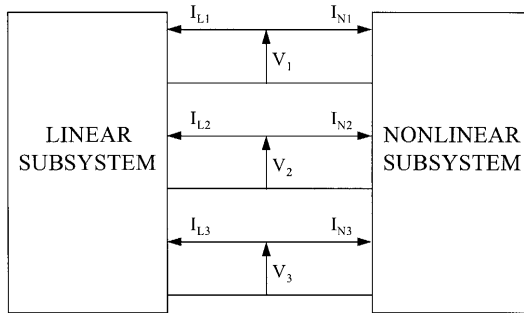


FIGURE 3.25 General form of system partitioned for harmonic balance analysis.

situation, which accounts for the full nonlinear behavior of the large signal device, is based on optimal oscillator design [43] adapted to include the microstrip patch antenna as the oscillator resonant load [44]. The synthesis process uses numerical optimization as the core for a harmonic balance procedure, which finds a set of complex terminal large signal voltages and currents at, for a MESFET, the gate and drain of the device. These terminal conditions are selected by the harmonic balance procedure such that the specified added power necessary from the device,  $P_{add}$ , at the desired frequency of oscillation for given device dc bias conditions is derived as [45]

$$P_{add}(f) = -\frac{1}{2} \text{Re}[V_{gs}(f)I_{gs}^*(f) + V_{ds}(f)I_{ds}^*(f)] \tag{3.14}$$

The use of harmonic balance techniques for high frequency circuit analysis was originally detailed by Hicks and Kahn [46] and Fillicori and Naldi [47]. Peterson and co-workers first applied this technique to the large signal analysis of MESFET devices in 1984 [48]. This simulation method is based around the ability to represent a nonlinear system as being made up from a linear subsystem and nonlinear subsystem, suitably interconnected. Figure 3.25 shows the general form of a system partitioned for harmonic balance.

Linear and nonlinear subsystems comprising the complete system may be analyzed independently. Where a high frequency electronic system is to be considered, it is generally desirable to represent the linear subsystem elements in a frequency domain form, typically  $Y$ - or  $S$ -parameters, while the nonlinear subsystem components may be represented by the appropriate time domain functional relationship. The solution of the system is achieved by balancing the terminal currents of the linear and nonlinear subsystems,  $I_L$  and  $I_N$ , at their interface. Usually this is done by fulfilling Kirchoff's current law at each of the interconnected ports in the system in the spectral domain. A Fourier transformation is used to convert time domain data to frequency domain data and vice versa. Kirchoff's current law solutions are reached by employing an iterative optimization approach to determine the currents that satisfy current and voltage balance at interconnected ports.

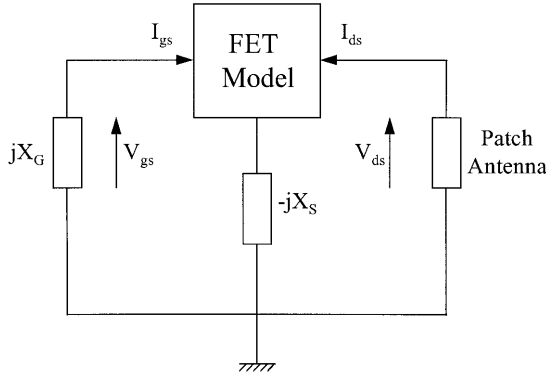


**FIGURE 3.26** Series feedback oscillator arrangement.

Once the solution is known, the external embedding circuit needed to fulfil the oscillation condition can be directly derived. For example, for the series feedback arrangement shown in Fig. 3.26, the necessary circuit elements can be obtained [50]:

$$X_G = -\frac{\operatorname{Re}[V_{gs}(I_{gs} + I_{ds})]}{\operatorname{Im}[I_{gs}(I_{gs} + I_{ds})^*]} \quad (3.15)$$

$$X_S = \operatorname{Re}[V_{gs}I_{gs}]/\operatorname{Im}[I_{gs} + I_{ds})I_{gs}^*] \quad (3.16)$$

$$X_D = -\frac{\operatorname{Im}(V_{ds}I_{ds}^*)}{|I_{ds}|^2} - X_S \frac{\operatorname{Re}[(I_{gs} + I_{ds})I_{ds}^*]}{|I_{ds}|^2} \quad (3.17)$$

$$G_D = \left[ -jX_D - \frac{V_{ds}}{I_{ds}} - jX_S \frac{(I_{gs} + I_{ds})}{I_{ds}} \right]^{-1} \quad (3.18)$$

It should be noted that the harmonic balance synthesis procedure described here does not ensure that the oscillator will start up. For this a time domain simulation must be instigated.

### 3.3.2 SPICE Time Domain Simulation

In order to fully check the active antenna's behavior, a time domain analysis is generally necessary. The procedure here is to describe the circuit equations including the large signal device as a set of state-space equations [49]. This can be done by a time domain simulator, such as SPICE, either as a full nonlinear circuit model or in a compressed form as a Van der Pol equivalent model. The first approach is useful when single active antenna elements are to be studied [50], while the latter approach is useful when multiple coupled elements are to be investigated [51]. The method allows the performance of oscillating active antenna elements to be defined under

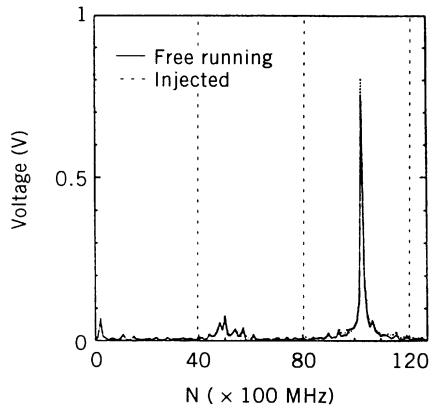
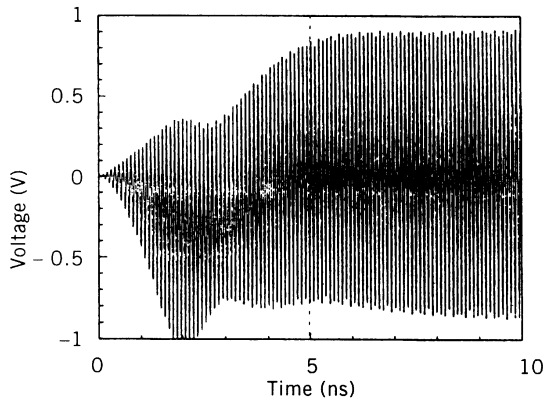
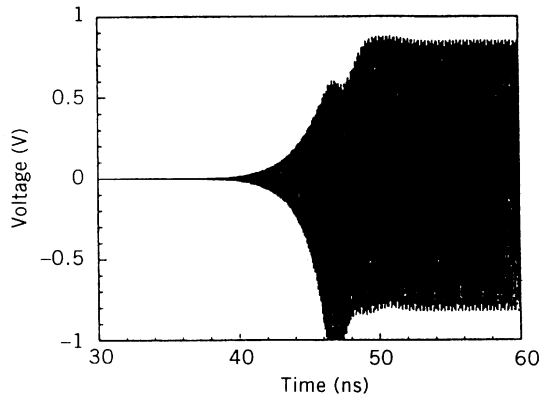
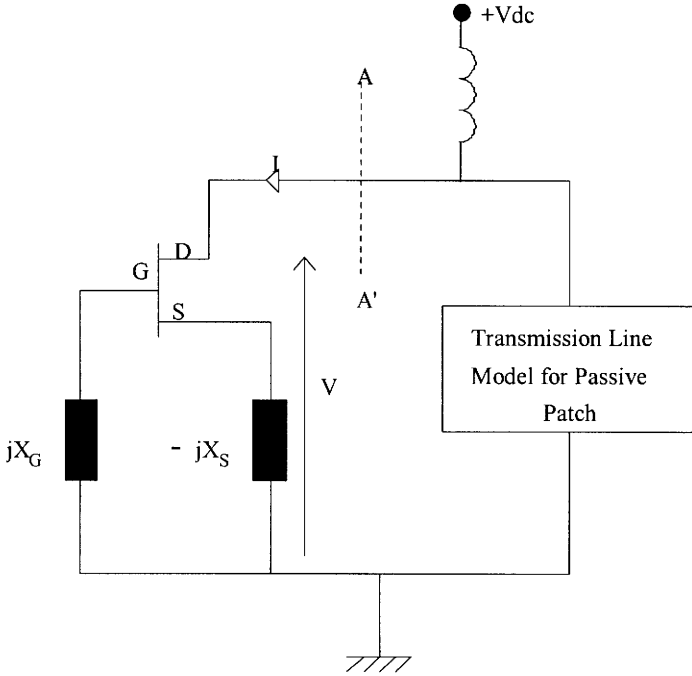


FIGURE 3.27 Startup response of active antenna: (a) free-running transient, (b) injection locked transient, and (c) steady-state Fourier response.



**FIGURE 3.28** Active antenna circuit schematic.

free-running or injection locking conditions. Figure 3.27 shows typical start-up responses of an active antenna [50].

Time domain simulation of the state-space equations for a circuit with a full time domain model is very computer intensive. Therefore this approach is not suitable where multiple active antenna oscillators are needed, for example, in a power-

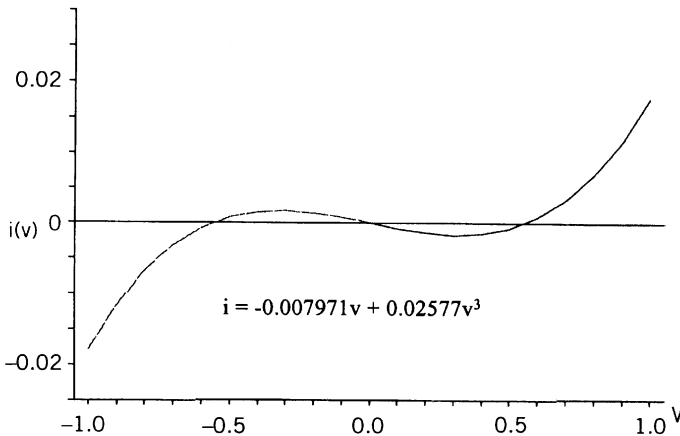


**FIGURE 3.29** Simulated nonlinear  $I$ - $V$  relationship at device plane A-A'.

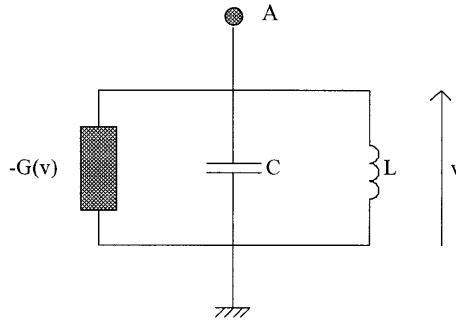


FIGURE 3.30 Van der Pol model.

combining grid arrangement. For studies such as these it is convenient to compress the full time domain model onto a simpler Van der Pol equivalent circuit [51].

In this approach, the large signal active device embedded in the oscillator feedback network is excited at port A–A' in Fig. 3.28 by a large signal sinusoidal source  $V$ , at the oscillator operating frequency  $\omega_0$ . The resulting current  $I$  flowing into the one-port is then monitored and plotted and a negative conductance is fitted according to a cubic relationship as shown in Fig. 3.29. This is the simplest functional form that will allow a limit cycle to be formed [52]. Elements  $L$  and  $C$  are found according to:

$$\omega_0 = 1/\sqrt{LC} \tag{3.19}$$

Capacitance  $C$  is directly available from the terminal voltage and current phase relationship at port A–A'.

In this way the Van der Pol equivalent model is derived, which has dynamic amplitude and frequency behavioral characteristics that are the same as the more complex full circuit model from which it was derived (Fig. 3.30).

To complete the active antenna oscillator element, terminal A in Fig. 3.30 is attached to a suitable equivalent circuit model for the radiating element. The nonlinear conductance term is generally evoked in the circuit simulator as a symbolically defined device.

### 3.3.3 Microstrip Patch Oscillator Large Signal Simulation

The first stage in a patch oscillator design is a linear simulation, as discussed in Section 3.2.1. From this an estimate of the oscillation frequency and the potential for large signal stability can be determined. A large signal analysis is then required, as shown in the schematic layout of Fig. 3.31. The circuit is identical to that shown in Section 3.2.1 except that the OSCTESTG element has been replaced by an OSCPORTG element, which will perform the harmonic balance analysis. Parameters

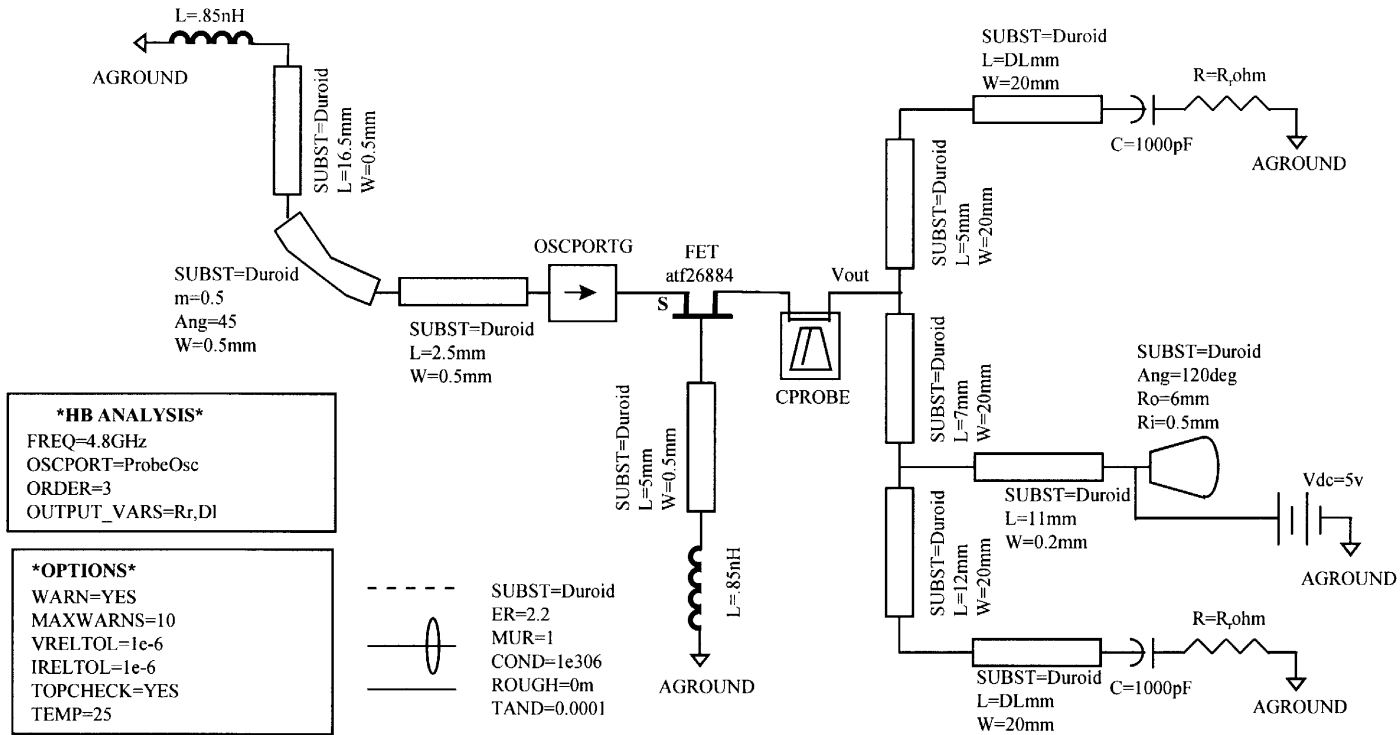


FIGURE 3.31 HP MDS circuit layout for harmonic balance simulation of a microstrip patch oscillator.

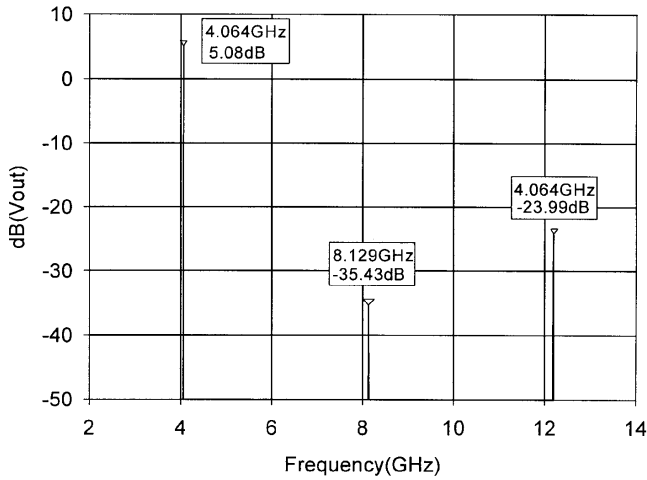


FIGURE 3.32 Harmonic balance results for  $V_{out}$  in Fig. 3.31.

are specified in an “HB analysis” box shown on the left. An estimate of the oscillation frequency and the number of harmonics to be analyzed are specified here. The HB simulation analyzes particular nodes of the circuit defined by wire labels or current probes. A wire label “ $V_{out}$ ” is shown connected to the drain of the FET.

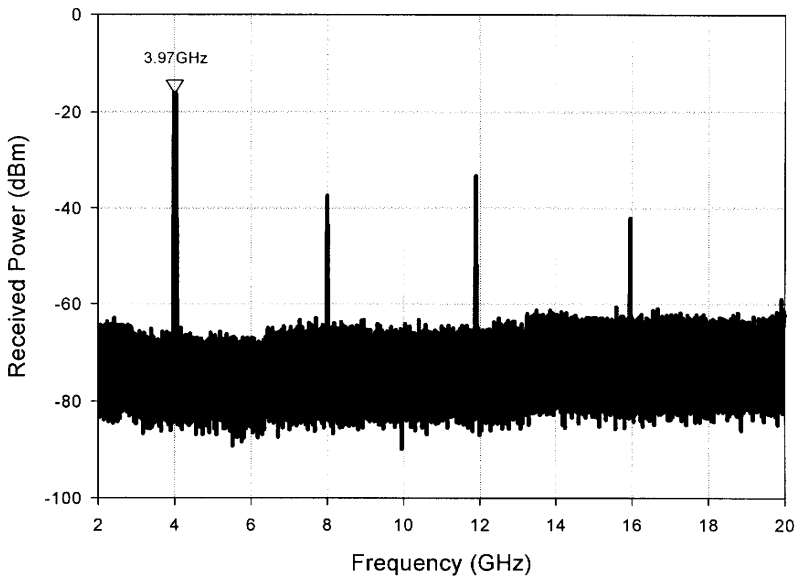


FIGURE 3.33 Measured spectrum of microstrip patch oscillator of Fig. 3.11.

The simulation results are shown in Fig. 3.32.  $V_{\text{out}}$  values are plotted in decibels (dB) against frequency. The fundamental plus two harmonics are shown, although more harmonics can be simulated at the expense of increased simulation time. The oscillation frequency of 4.064 GHz is 3.7% higher than the linear simulation estimate shown in Fig. 3.13. Figure 3.33 shows a measured spectrum for the patch oscillator of Fig. 3.11 at the same bias point of 5.0 V drain–source voltage. The oscillation frequency of 3.97 GHz is 2.4% lower than the harmonic balance estimate. This is typical of the accuracy obtainable for harmonic balance simulations. In this case the linear simulation estimate is in fact closer to the measured result, but this is not typically the case.

Manipulation of the data of Fig. 3.32 shows that reasonable agreement for output power at the fundamental has been found, with poorer agreement at the harmonic frequencies. This is due to the strong dependence of the harmonic levels on the nonlinearities of the large signal model, which are very difficult to model accurately.

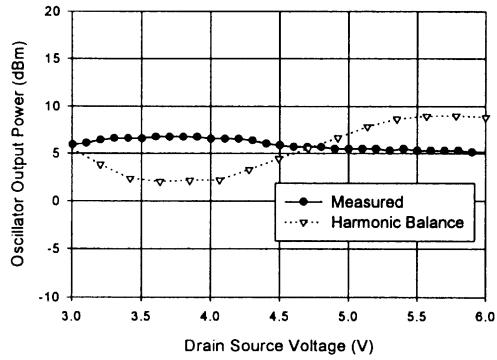
One of the main problems associated with active integrated antenna simulation is that the module has no connection at which to measure the output power. Using current commercial simulators it is very difficult to model the radiation ports associated with integrated antennas. Thus the results of Fig. 3.32 are in terms of  $V_{\text{out}}$  at the drain of the FET. However, measurements are in terms of radiated power measured at some distance from the antenna. In order to compare results,  $V_{\text{out}}$  must be converted to an average power. This can be achieved by calculating  $I_{\text{out}}$  in the harmonic balance analysis and using this to calculate the average output power. In order to convert this to radiated power, the Friis formula is used [53]:

$$P_R = P_T G_{\text{TX}} G_{\text{RX}} \left( \frac{\lambda_0}{4\pi d} \right)^2 \quad (3.20)$$

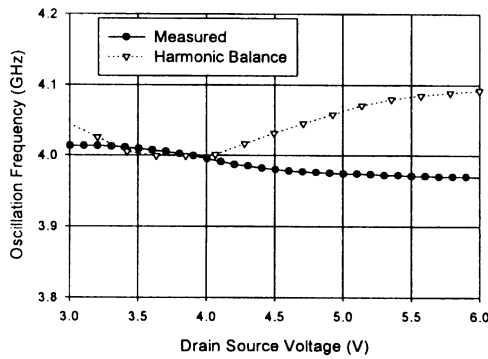
where  $P_R$  is the received power,  $P_T$  is the oscillator output power,  $G_{\text{TX}}$  is the gain of an identical passive microstrip patch,  $G_{\text{RX}}$  is the gain of the receive antenna,  $\lambda_0$  is the free-space wavelength, and  $d$  is the distance between transmitter and receiver. The results here are measured at the output of the FET. However, it is also possible to measure the power dissipated in the radiation resistances,  $R_r$ . For this particular design these two give very similar results.

Figure 3.34 shows a comparison of measured and simulated results over a range of drain–source voltage. Gate source voltage was set to zero in the model and to  $-0.8$  V in the measured case. This allows similar dc drain–source currents and voltages to be obtained, which is essential if a comparison of output powers is to be made. It can be seen that reasonable agreement has been obtained for both power and frequency. Figure 3.34a shows a typical transmitted power level of  $\sim 6$  dBm (3.98 mW). Figure 3.34b shows how the frequency can be tuned with drain–source voltage giving voltage-controlled oscillator action. This can be used in either frequency shift keying (FSK) or phase shift keying (PSK) modulation schemes [54].





(a)



(b)

**FIGURE 3.34** Large signal simulation of microstrip patch oscillator of Fig. 3.11: (a) radiated power and (b) operating frequency.

### 3.3.4 Analytic Solutions for Fundamental and Harmonic Amplitudes

Many applications, where active integrated antennas could be employed, require very low levels of harmonic and spurious radiation in order to meet electromagnetic compatibility specifications. Active integrated antennas introduce nonlinear devices directly into the antenna and thus they can exhibit high levels of harmonic radiation. Moreover, due to size constraints, it is difficult to add filters as in conventional systems. In the case of active receiving antennas it seems that by suppressing the harmonic resonances of the antenna the harmonic reception problem can be reduced [55,56]. However, with patch oscillators, due to the interdependence of the active device and the patch, the solution to the problem of harmonic radiation is more complex [57].

This section presents methods for obtaining closed-form expressions for the level of the fundamental and harmonic amplitudes in terms of circuit parameters.

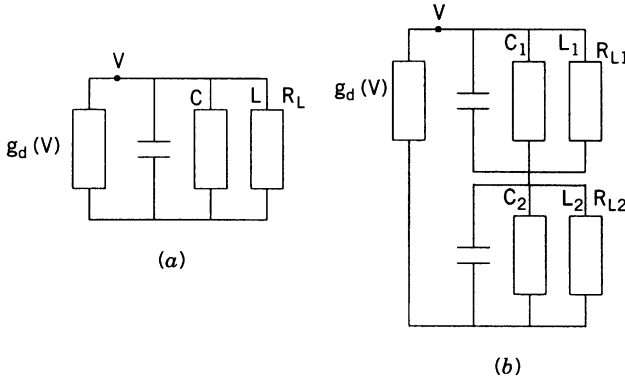


**FIGURE 3.35** Microstrip patch oscillator models: (a) single resonator and (b) dual resonator.

Although numerical methods could be used to solve this problem, greater physical insight can be obtained from closed-form expressions, which in addition will be useful for CAD.

The typical patch oscillator is shown in Fig. 3.11. A single *LCR* circuit, Fig. 3.35a, is initially used to model the fundamental resonance of a microstrip patch. This allows simple expressions for harmonic levels to be obtained. This first-order model can be extended to include higher order resonances of the patch antenna, and since these often occur at harmonic intervals they will be likely to have large effects on harmonic radiation. To model the first higher order resonance a second parallel *LCR* circuit is added in series, as shown in Fig. 3.35b.

The analysis is based on the substitution of known solutions as shown by Van der Pol [52,58]. Sinusoidal solutions are assumed and substituted into the differential equation for the oscillator. The voltage differential equation for a single *LCR* circuit is shown below:

$$\frac{d^2V}{dt^2} + \frac{dV}{dt} \frac{(g_d + G_L)}{C} + V\omega_0^2 = 0 \tag{3.21}$$

where  $g_d$  is the nonlinear conductance derived from the current–voltage relationship:

$$I = -g_0V + g_1V^2 + g_2V^3 \tag{3.22}$$

Differentiating Eq. 3.22 with respect to  $V$  we find

$$g_d = -g_0 + 2g_1V + 3g_2V^2 \tag{3.23}$$

Also,  $\omega_0 = 1/\sqrt{LC}$ ,  $G_L = 1/R_L$ , and  $G_L$  is the load conductance.

It is reasonable to assume the solution of Eq. 3.21 to be a sum of sinusoids. In order to obtain accurate solutions it has been found necessary to include the first three terms:

$$V = a_1 \sin(\omega_0 t) + a_2 \sin(2\omega_0 t) + a_3 \sin(3\omega_0 t) \quad (3.24)$$

This is substituted in Eq. 3.21 and since steady-state solutions are sought it is assumed that

$$\frac{da_i}{dt} = \frac{d^j a}{dt^j} = 0 \quad i = 1, 2 \quad j = 1, \dots, n \quad (3.25)$$

It has been found that after this substitution, terms higher than  $2\omega_0$  can be ignored while maintaining good accuracy. The result is expanded and an equation is obtained with the following form:

$$A \cos(\omega_0 t) + B \sin(\omega_0 t) + C \cos(2\omega_0 t) + D \sin(2\omega_0 t) = 0 \quad (3.26)$$

Since these four terms are orthogonal, the coefficients  $A$ ,  $B$ ,  $C$ , and  $D$  can be equated to zero, resulting in four simultaneous equations for  $a_1$  and  $a_2$ . Only two of these equations are required and in this case the correct solutions have been obtained using  $A$  and  $D$ . If it is assumed that  $a_2 \ll a_1$ , which is true for typical values of  $g_0$ ,  $g_1$ ,  $g_2$ , and  $G_L$ , then

$$a_1 = \sqrt{\frac{4(g_0 - G_L)}{3g_2}} \quad (3.27)$$

$$a_2 = \frac{a_1^2 g_1}{3\omega_0 C} \quad (3.28)$$

From Eq. 3.27 if  $a_1$  is to be real then  $|g_0| > G_L$ . This is the well-known small signal oscillation startup criterion [60] which can also be written as  $|r_0| > R_L$  for the series resonant case. Equation 3.28 shows that the level of the first harmonic is proportional to  $g_1$ , which is intuitively correct, since Eq. 3.22 shows that first harmonic terms are generated by the  $V^2$  term involving  $g_1$ . As the quality factor of a parallel LCR circuit is given by

$$Q = \omega CR \quad (3.29)$$

it can be seen that the level of the first harmonic ( $a_2$ ) is inversely proportional to the  $Q$  of the resonator. This highlights a problem when using microstrip patches as resonators since the higher the  $Q$  of the patch the narrower its bandwidth. Thus a compromise between antenna performance and harmonic level may well be required.

A harmonic balance analysis of the oscillator using a circuit simulator validates these results. The conductance coefficients of Eq. 3.23 were obtained using analysis with swept input power. Using the input admittance–voltage data and by fitting a polynomial to the real part, the conductance coefficients were obtained at a single frequency. A symbolically defined device (SDD) was then used within the simulator

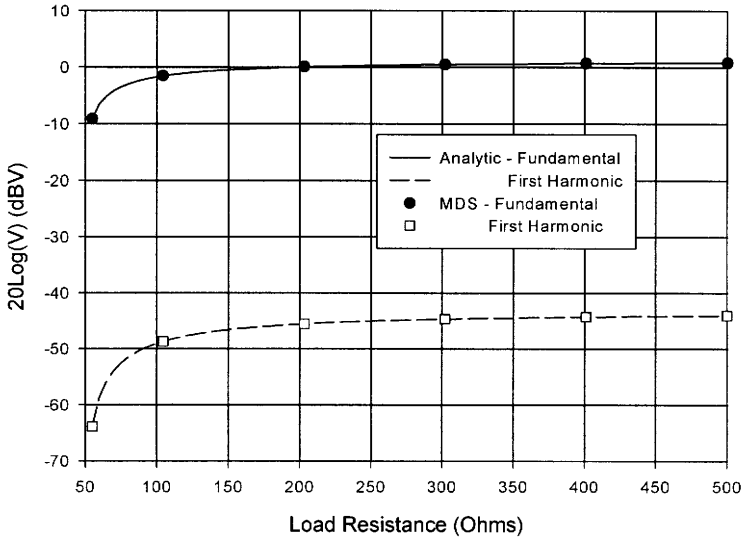


**FIGURE 3.36** Output voltages of microstrip patch oscillator using single *LCR* circuit (Fig. 3.35a).  $g_0 = 20$  mS,  $g_1 = 5$  mS,  $g_2 = 20$  mS,  $C = 20$  pF, and  $L = 0.2$  nH.

to represent the nonlinear conductance. Initial results for harmonic levels with respect to  $R_L$  are shown in Fig. 3.36. Good agreement has been obtained between the closed-form expressions and harmonic balance. It is seen that as the load resistance approaches the value of the device negative resistance, the level of first harmonic decreases, and this is consistent with the concept of a low perturbation oscillator design approach. The levels of first harmonic shown are much lower than the  $-20$  dBc typically obtained for patch oscillators. This suggests that the single *LCR* circuit does not adequately model the patch.

In order to model the first higher order resonance of a microstrip patch, another parallel *LCR* circuit can be introduced as shown in Fig. 3.35b. The voltage differential equation for this circuit is

$$\begin{aligned} \frac{d^4 V}{dt^4} + \frac{d^3 V}{dt^3} \left( \frac{g_d}{C_1} + \frac{g_d}{C_2} + \alpha_1 + \alpha_2 \right) + \frac{d^2 V}{dt^2} \left[ g_d \left( \frac{\alpha_2}{C_1} + \frac{\alpha_1}{C_2} \right) + \alpha_1 \alpha_2 + \omega_1^2 + \omega_2^2 \right] \\ + \frac{dV}{dt} \left[ g_d \left( \frac{\omega_2^2}{C_1} + \frac{\omega_1^2}{C_2} \right) + \alpha_2 \omega_1^2 + \alpha_1 \omega_2^2 \right] + V \omega_1^2 \omega_2^2 = 0 \end{aligned} \quad (3.30)$$

where  $\alpha_i = 1/R_{Li}C_i$  and  $\omega_i = \sqrt{1/L_iC_i}$ , for  $i = 1, 2$ .

Equation 3.30 shows the large increase in complexity obtained by including a second resonance in the model. However, by following the procedure detailed above, four simultaneous equations for  $a_1$  and  $a_2$  can again be obtained. The equations, however, do not have straightforward solutions as in the single *LCR* case. To obtain solutions, a similar approximation to that taken in the single *LCR* case is used. It is

assumed that the presence of the first harmonic will not greatly affect the level of the fundamental and thus a solution of the form

$$V = a_1 \sin(\omega_0 t) \tag{3.31}$$

is used. Substituting this in Eq. 3.30 gives a solution for  $a_1$ , as shown in Eq. 3.32, which is similar to that obtained earlier. This can now be used as the basis for obtaining the first harmonic amplitude. The solution given in Eq. 3.24 is substituted in Eq. 3.30, where  $a_1$  is given in Eq. 3.32. The solution for the first harmonic is given in Eq. 3.33:

$$a_1 = \sqrt{\frac{4(g_0 - 1/R_{L1})}{3g_2}} \tag{3.32}$$

$$a_2 = \frac{60C_2g_1^2R_{L2}R_t + C_1[80g_1^2R_{L2}R_t + 11g_2(-3R_{L1} + R_{L2}R_f)]}{108(4C_1 + 3C_2)g_1g_2R_{L2}R_f} + \frac{\sqrt{-144C_2^2g_1^2R_{L2}^2R_t(-25g_1^2R_t + 33g_2R_f) + C_1^2[80g_1^2R_{L2}R_t + 11g_2(-3R_{L1} + R_{L2}R_f)]^2}}{108(4C_1 + 3C_2)g_1g_2R_{L2}R_f} + \frac{\sqrt{-24C_1C_2g_1^2R_{L2}R_t(-400g_1^2R_{L2}R_t + 11g_2[15R_{L1} + 19R_{L2}R_f])}}{108(4C_1 + 3C_2)g_1g_2R_{L2}R_f} \tag{3.33}$$

where  $R_t = R_{L1} + R_{L2}$  and  $R_f = -1 + g_0R_t$ .

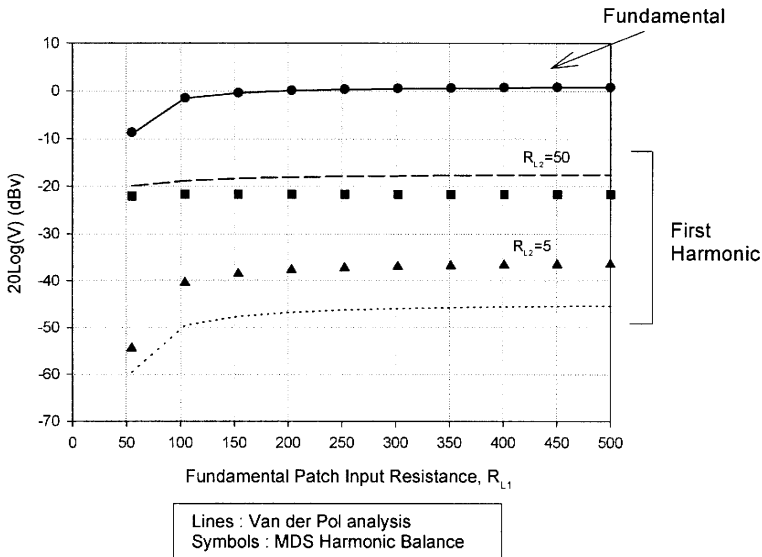
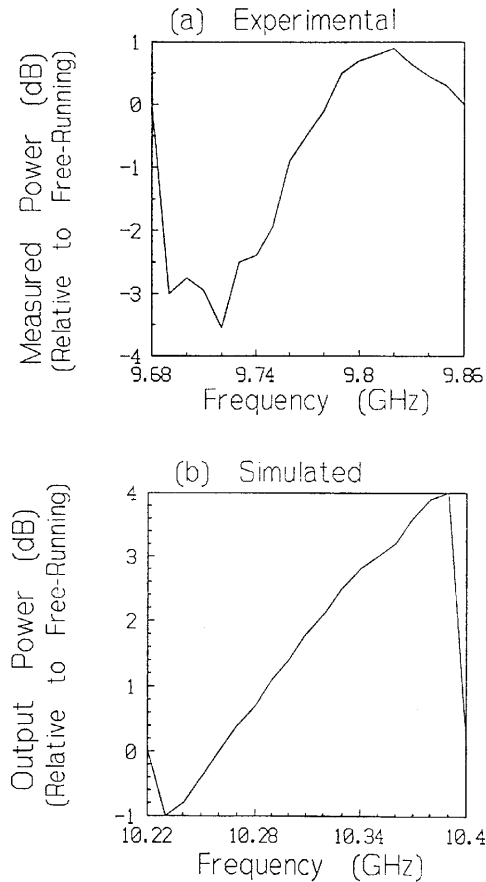
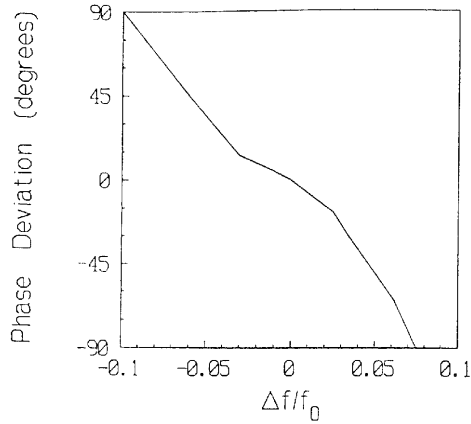


FIGURE 3.37 Output voltages of microstrip patch oscillator using dual LCR circuit (Fig. 3.35b). Values as in Fig. 3.36;  $L_1 = 0.2$  nH,  $C_2 = 20$  pF,  $L_2 = 0.05$  nH, and  $R_{Li} = 1/G_{Li}$ .

The closed-form expressions were again compared with results from a circuit simulator and are shown in Fig. 3.37. The output voltages for the fundamental and first harmonic are plotted versus fundamental input resistance and at different values of first harmonic input resistance. The level of the first harmonic is now much closer to that measured. The agreement between the analytic expressions and the numerical method for the fundamental is very good and the agreement for the first harmonic is reasonable across a wide range of input resistance values. These results seem intuitively correct since as the first harmonic resistance approaches zero the first harmonic amplitude should tend toward that seen in the single-resonator case. It is noted that the first harmonic input resistance is always less than  $50 \Omega$ ; this is to ensure that simultaneous oscillations do not occur, which cannot currently be analyzed by the above method. The results of Fig. 3.37 show that if harmonic suppression is required then low resistances are required at all harmonic frequencies.



**FIGURE 3.38** Injection locked active antenna output power. Bias tee input level =  $-2$  dBm. (From [50], reprinted with permission of John Wiley & Sons.)



**FIGURE 3.39** Active antenna locking frequency phase response. (From [50], reprinted with permission of John Wiley & Sons.)

This agrees with the results found for receive-type active antennas [55,56]. Preliminary studies have shown that patch antennas such as quarter wave short circuit patches, which short circuit the first harmonic mode, give very good harmonic suppression.

### 3.3.5 Injection Locking and Direct PSK Encoding

The presence of an injection locking signal introduced into an active antenna oscillating element can lead to some very interesting effects. It is well known that a low power signal whose frequency lies close to that of a free-running oscillator (here an active antenna element) can lead to frequency entrainment and oscillator phase noise improvement [59]. This signal known as the injection locking signal can be fed

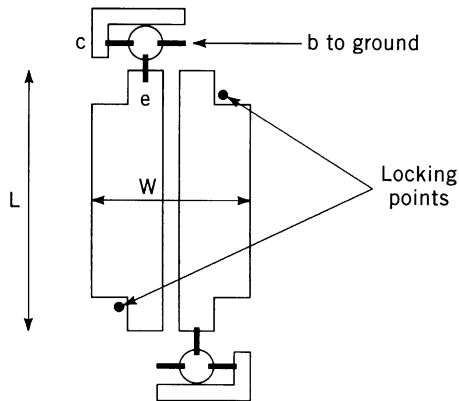


**FIGURE 3.40** Active array element for 360° phase control. (From [62], reprinted with permission of IEE.)

directly into a circuit port on the active antenna. This leads to a highly controllable situation where features such as external  $Q$ -factor of the active antenna oscillator can be accessed by classical injection locking methods. A second method, which exploits the fundamental nature of the circuit, is to introduce the injection locking signal by a spatially remote source. This technique eases circuit configuration requirements but is more difficult to characterize, particularly in equivalent circuit based computer simulation.

Injection locking has been shown to reduce transient startup time, to allow control of the active antenna output power [50] (Fig. 3.38) and output phase of the active antenna signal relative to the injection locking signal (Fig. 3.39), as the injection locking signal is varied.

With a single injection locked oscillator, a maximum of  $180^\circ$  phase shift is theoretically possible. However, by using two sequentially rotated antennas, nearly  $360^\circ$  phase shift can be obtained (Fig. 3.40) [60]. These observations indicate that the injection locked active antenna oscillator may form the basis for a beam-steered array [61,62]. If the injection locking signal is applied to the active antenna within the antenna's locking range and the frequency of the injection signal is held constant, then the frequency of oscillation of the active antenna cannot vary.

However, due to the dependence of the active antenna free-running oscillator frequency on device bias, these elements can be frequency pushed by dc bias perturbation. Thus an interesting possibility exists whereby an injection locked active antenna with its frequency fixed is then dc bias frequency pushed. Under these conditions the frequency of the whole arrangement cannot change so that the dc bias pushing must be accommodated by the phase of the output signal of the active antenna changing relative to the injection locking signal. So with no modification to the already established equivalent circuit modeling approaches already detailed in this chapter, a class of direct phase shift keying active antennas can be developed [63]. Here, the agreement between simulation using the time domain analysis

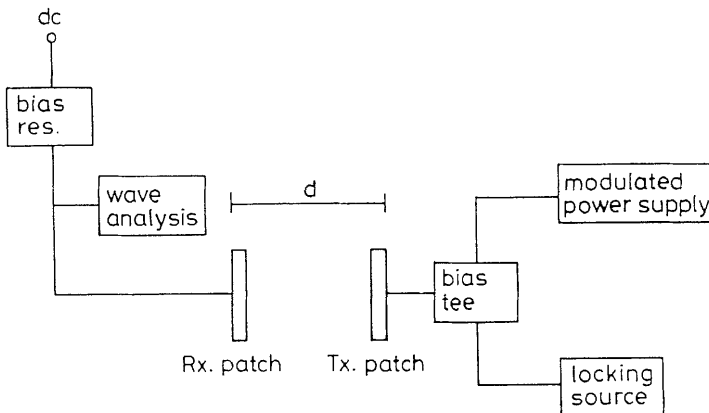


**FIGURE 3.41** Active patch communication link using phase modulation. (From [64], reprinted with permission of IEE.)



approach of this chapter is excellent, establishing that under dc bias control nearly  $180^\circ$  of phase variation can be achieved.

This type of antenna has great potential as a short haul, low cost communication link [64]. Two active antennas face each other (Fig. 3.41). One is injection locked and its output signal modulated under dc bias control, as before. The output signal from the encoder active antenna acts as a remote beacon, which injection locks the second active antenna. This second antenna operates as a self-oscillating mixer [65] and hence serves as a demodulator. With this arrangement, 6-dB improvement in detection sensitivity and direct decoding of a directly encoded microwave carrier at 9 GHz are obtained.

### 3.3.6 Active Antenna Packaging Effects

The effect that external packaging would have on the performance of an active antenna circuit is likely to be quite profound. Mainly this is so since the intrinsic high level coupling between active device and antenna has to date in the published literature necessitated sacrifice of isolation between these component parts of the active antenna. The effect that a partially reflecting dielectric cover has on frequency of operation of active antenna oscillating elements has been studied by only a few authors [66,67]. Ostensibly, the active antenna oscillator will have its frequency pulled due to the presence of reflected energy from the top cover. Following the work presented in [67], by using the cavity model [12] for the resonator element an equivalent LC representation of this element can be found. A dielectric top cover with known reflection coefficient,  $r$ , is then coupled to this model by a  $377\text{-}\Omega$  transmission line representing the free-space separation and the resulting load comprising top cover, free-space separation, and antenna presented across the active device terminals. By solving for the oscillation condition of zero net resistance and conjugate resistance at oscillation, an expression for the frequency pulling,  $\Delta f$ , induced as a result of a packaging top cap was derived in [67] as

$$\Delta f = f_0 \frac{k|\rho/k_0 d| \sin \phi}{Q_e[(1 + 2|\rho/k_0 d|) \cos \phi + |\rho/k_0 d|^2]} \quad (3.34)$$

Here  $f_0$  is the free running frequency of the active antenna oscillator,  $k_0$  the free-space wavenumber,  $d$  the separation distance between antenna and top cap,  $Q_e$  the external  $Q$ -factor of the patch resonator as defined for a parallel tuned circuit, and  $K$  a constant introduced to account for the mismatch between the transmission line free-space coupling model and the antenna radiation resistance. Figure 3.42 shows the effect of the top cap diminishing with increased separation distance between it and the active antenna element. These results show an asymmetry in the operating frequency of the active antenna as a function of separation distance. Here a steeper rising edge than falling edge in the curve presented is evident. The implication of this for active antenna design is the normal radome design rule that, for an electrically transparent cover, the distance between a passive antenna and the cover should be an integer multiple of one-half wavelength, that is, the zero

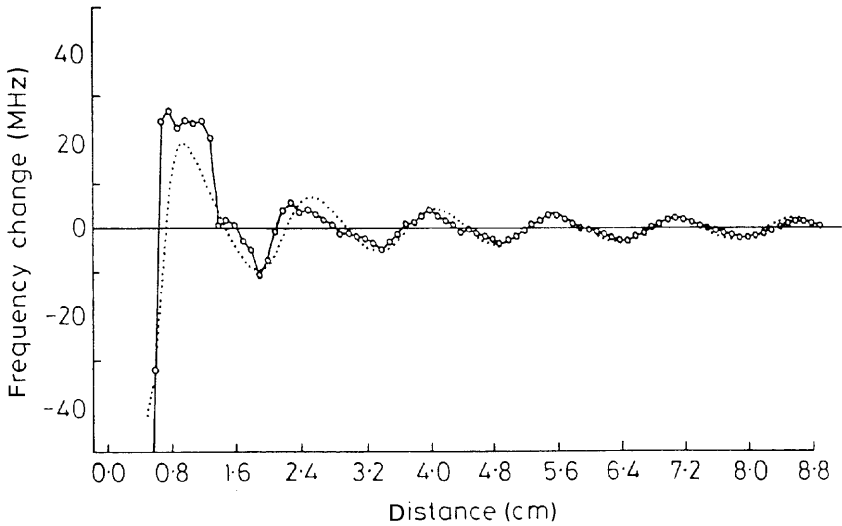


**FIGURE 3.42** Frequency pulling under lossy coupling for dielectric cover thickness  $t = 0.64$  mm,  $\rho = 0.5$ ,  $\lambda = 29.79$  mm,  $Q_e = 32.7$ ,  $K = 0.25$ . — Experiment, ... theory. (From [67], reprinted with permission of IEE.)

crossings in Fig. 3.42. After near-field effects have been removed, this result is also valid for an active antenna. However, in addition, for an active antenna, for a given small perturbation in cover position the effect on the output frequency of the active antenna will be greater at odd multiples of one-half wavelength as compared to even multiples. Thus these regions are best avoided when positioning the top cover of the active antenna package.

**3.3.7 Frequency Doubling Active Patch Transponder**

Recently, interest has been shown in the use of frequency doubling techniques for the development of active antenna transponder circuits [68,69]. Using the equivalent

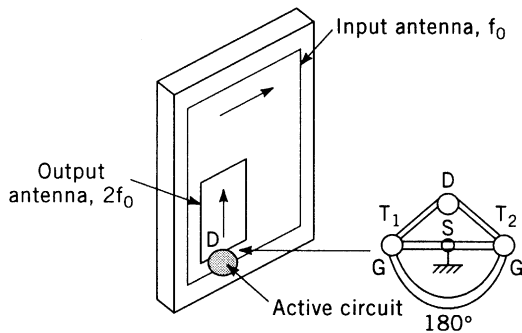


**FIGURE 3.43** Balanced doubler active patch transponder.

design and evaluation techniques previously discussed in this chapter, it is reasonably straightforward to extend the design methodology for a single-device situation to a dual-device configuration. The objective this time is to develop an active frequency doubling transponder device: that is, an active antenna that normally is dormant until it receives a signal at a known frequency, at which point it produces an output at a different frequency. In its simplest embodiment this output signal will be harmonically related to the input signal. The output signal may be encoded for identification purposes.

It is known that high order harmonics can be produced by nonlinear systems when driven hard. This is true for MESFET devices, where, for certain bias conditions, such as high negative gate bias, very nonlinear operation occurs [70].

To make the design procedure as simple as possible, two MESFETs can be operated in a balanced push–push configuration (Fig. 3.43). Here the drains of each MESFET are connected together and their sources grounded. Both devices are dc biased from the same source. In this configuration full wave rectification of the input signal can be made to occur at each device.

By introducing a  $180^\circ$  phase difference between the gate inputs of the MESFETs, all odd harmonics including the fundamental frequency will self-cancel, while even harmonics will self-reinforce. This gives potential for conversion gain. The idling filter sections normally associated with doubler design are largely unnecessary in the active antenna realization since the narrow bandwidths of the input and output microstrip patch antennas automatically provide frequency selectivity.

Conjugate impedance matched tap-in points on the input and output microstrip patch antennas are selected at the respective patch resonant frequency, thereby ensuring maximum conversion gain. Conversion gain is defined here to mean the ratio of the reradiated power at the second harmonic to the input signal power at the fundamental frequency.

In order to achieve a high degree of isolation between input and output antennas, these antennas can be mounted in cross-polarized fashion and in back-to-back fashion. For the configuration in Fig. 3.43 [68], a theoretical conversion gain of 8 dB was predicted at 4.7 GHz using large signal equivalent circuit modeling techniques. The experimentally measured conversion gain of the system was estimated to be 2 dB. It should be noted that considerable and yet unresolved difficulties exist in accurately determining the input and output power levels at the antenna radiating elements in order to get an accurate assessment of experimental conversion gain for the system. In addition to this type of harmonic transponder, nonharmonically related active antenna transponder structures have been reported by Probanz and Itoh [71].

### 3.4 CONCLUSIONS

This chapter has described the use of the equivalent circuit method for the analysis and simulation of antenna–circuit modules. Typical equivalent circuits have been shown and their uses illustrated by a number of design applications. On the whole,

the methods give fast computation and are thus suitable for optimization applications.

The description of the analyses has been divided into linear and nonlinear methods and this highlights a natural division between what are, in general, straightforward processes and those that require significant additional modeling effort. Linear simulation will give first-order estimates of, for example, oscillating antenna operating frequency and amplifying antenna gain. However, only limited simulation is possible for the interaction between the various parts of the antenna-circuit module and the radiation performance. Nonlinear analysis will give better prediction of oscillator frequency and amplifier performance in addition to providing oscillator power and spectral response, the nonlinear performance of amplifiers, and simulation of mixer behavior.

Equivalent circuit methods combine analyses, well known to specialists in both printed circuit antennas and microwave circuits, in a straightforward way that is amenable to implementation on current circuit simulators. The potential and limitations of the combination are largely those noted for either area. Equivalent circuits of antennas are limited in the way that radiation modeling information can be extracted. Equivalent circuits of active devices can be very complex and require long run times, particularly if large signal performance is required. In spite of these limitations, equivalent circuit modeling of antenna-circuit modules provides an accessible entry into simulation that will be of use to many designers. Research and development of the method will continue to bring improvements to both accuracy and computational speed.

## REFERENCES

1. King, R. W. P., *Theory of Linear Antennas*, Harvard University Press, Cambridge, MA, 1958, pp. 141ff.
2. James, J. R., Hall, P. S., and Wood, C., *Microstrip Antenna Theory and Design*, IEE/Peter Peregrinus Ltd., London, 1981.
3. James, J. R., and Hall, P. S. (eds.), *Handbook of Microstrip Antennas*, IEE/Peter Peregrinus, London, 1991.
4. Metzler, T., "Microstrip series array," *IEEE Trans.*, vol. AP-29, 1981, pp. 174–178.
5. Chang, K., *Microwave Solid State Circuits and Applications*, Wiley, New York, 1994, pp. 388ff.
6. Pues, H., and Van de Capelle, A., "Accurate transmission-line model for the rectangular microstrip antenna," *IEE Proc.*, vol. 131, pt. H, no. 6, Dec. 1984, pp. 334–339.
7. Hewlett Packard, Microwave Design System.
8. Fusco, V. F., and Burns, H. O., "Series feedback active microstrip synthesis and characterisation," *IEE Electron. Lett.*, vol. 27, no. 24, Nov. 1991, pp. 2246–2248.
9. McDowall, D. S., and Fusco, V. F., "Electromagnetic far field modeling for an active microstrip antenna module," *Microwave Opt. Technol. Lett.*, vol. 6, no. 5, April 1993, pp. 275–277.

10. Kron, G., "Equivalent circuit of field equations of Maxwell—I," *Proc. Inst. Radio Engineers*, May 1994, p. 289.
11. Lo, Y. T., and Richards, W. F., "Theory and experiment on microstrip antennas," *IEEE Trans. Antennas. Propag.*, vol. AP-27, 1979, pp. 137–145.
12. Richards, W. F., Lo, Y. T., and Harrison, D. D., "An improved theory of microstrip antennas and applications," *IEEE Trans. Antennas Propag.*, vol. AP-29, no. 1, Jan. 1981, pp. 38–46.
13. Navarro, J. A., and Chang, K., *Integrated Active Antennas and Spatial Power Combining*, Wiley, New York, 1996, pp. 7ff.
14. Hoffman, R. K., *Handbook of Microwave Integrated Circuits*, Artech House, Norwood, MA, 1987.
15. Willing, H. A., Rauscher, C., and de Santis, P., "A technique for predicting large-signal performance of a GaAs MESFET," *IEEE Trans. MTT*, vol. 40, no. 12, Dec. 1978, pp. 1017–1023.
16. Tajima, Y., Wrona, B., and Mishima, K., "GaAs FET large-signal model and its application to circuit design," *IEEE Trans. Electron. Dev.*, vol. ED-28, no. 2, Feb. 1981, pp. 171–175.
17. Sango, M., Pitzalis, O., Lerner, L., McGuire, C., Wang, P., and Childs, W., "A GaAs MESFET large-signal model for non-linear analysis," *IEE Symp. MTT*, June 1988, pp. 1053–1056.
18. Curtice, W. R., "A MESFET model for use in the design of GaAs integrated circuits," *IEEE Trans. Microwave Theory Technique*, vol. MTT-28, no. 5, May 1980, pp. 448–456.
19. Maas, S., *Non-linear Microwave Circuits*, Artech House, Norwood, MA, 1988, Chap. 2.
20. Ladbroke, P. H., *MMIC Design, GaAs FETs and HEMTs*, Artech House, Norwood, MA, 1989.
21. Soares, R., *GaAs MESFET Circuit Design*, Artech House, Norwood, MA, 1988.
22. Curtice, W. R., "A non-linear GaAs FET model for use in the design of output circuits for power-amplifiers," *IEEE Trans. MTT*, vol. 33, no. 12, Dec. 1985, pp. 1383–1393.
23. Tang, A., *Optimised Design of Frequency Multipliers*, PhD. Thesis, The Queen's University of Belfast, Sept. 1993.
24. Cryan, M. J., Hall, P. S., Tsang, K. S. H., and Sha, J., "Integrated active antenna with full duplex operation," *IEEE Trans. Microwave Theory Technique*, Oct. 1997.
25. Zarroug, A., Hall, P. S., and Cryan, M., "Active antenna phase control using subharmonic locking," *Electron. Lett.*, vol. 31, no. 11, pp. 842–843, May 1995.
26. Birkeland, J., and Itoh, T., "Quasi-optical planar FET transceiver modules," *IEEE MTT-S Dig.*, pp. 119–122, 1989.
27. Vendelin, G. D., Pavio, A. M., and Roche, U. L. *Microwave Circuit Design Using Linear and Non-linear Techniques*, Wiley, New York, 1990.
28. Meinke, H. H., "Active antennas," *Nachrichtentech. Z.*, vol. A, Dec. 1966, pp. 697–705.
29. Robert, B., Razban, T., and Papiernik, A., "Compact amplifier integration in square patch antenna," *Electron. Lett.*, vol. 25, no. 19, Sept. 1992, pp. 1808–1810.
30. An, H., Nanwelaers, B., and Van de Capelle, A. R., "Broadband active microstrip antenna design with the simplified real frequency technique," *IEEE Trans. Antennas Propag.*, vol. AP 42, no. 12, Dec. 1994, pp. 1612–1619.

31. Rothe, H., and Dahlke, W., "Theory of noisy fourpoles," *Proc. IRE*, vol. 44, June 1956, pp. 811–818, June 1956.
32. Haus, H. A., and Adler, R. B., *Circuit Theory of Linear Noisy Networks*, Wiley, New York, 1959.
33. Ormiston, T. T., Gardner, P., and Hall, P. S., "A novel highly compact low noise active antenna," IEE Colloquium on RF and Microwave Components for Communication Systems, 23 April 1997. Digest no. 1997/126.
34. Ormiston, T. D., Gardner, P., and Hall, P. S., "Microstrip short-circuit patch design equations," *Microwave Opt. Technol. Lett.*, vol. 16, no. 1, Sept. 1997, pp. 12–14.
35. Boglione, L., Pollard, R. D., and Postoyalko, V., "Optimum noise-source reflection-coefficient design with feedback amplifiers," *IEEE Trans. Microwave Theory Techniques*, vol. 45, no. 3, Mar. 1997, pp. 402–407.
36. Tanaka, S., Shimomura, N., and Ohtake, K., "Active circulators—the realisation of circulators using transistors," *Proc. IEEE*, vol. 53, no. 3, Mar. 1965, pp. 260–267.
37. Ayasli, Y., "Field effect transistor circulators," *IEEE Trans. Magnetics*, vol. 25, no. 5, Sept. 1989, pp. 3242–3247.
38. Cryan, M. J., and Hall, P. S., "An integrated active circulator antenna," *IEEE Microwave Guided Wave Lett.*, vol. 7, no. 7, July 1997, pp. 190–191.
39. Lewin, L., "Radiation from discontinuities in stripline," *IEE Proc. C*, vol. 107, 1960, pp. 163–170.
40. Hall, P. S., and Morrow, I. L., "Analysis of radiation from active microstrip antennas," *IEE Proc. Microwaves Antennas Propagation*, vol. 141, no. 5, Oct. 1994, pp. 359–366.
41. Wood, C., Hall, P. S., and James, J. R., "Radiation conductance of open circuit low dielectric constant microstrip," *Electron. Lett.*, vol. 14, 1978, pp. 121–123.
42. Hall, P. S., and Hall, C. M., "Coplanar corporate feed effects in microstrip patch array design," *IEE Proc. H*, vol. 135, no. 3, 1988, pp. 180–186.
43. Choo, E. B. L., Stewart, J. A. C., and Fusco, V. F., "CAD of non-linear optimum output power MESFET oscillators," *Microwave Opt. Technol. Lett.*, vol. 1, no. 8, 1988, pp. 277–281.
44. Fusco, V. F., "Series feedback integrated active microstrip antenna synthesis and characterisation," *IEE Electron. Lett.*, vol. 28, no. 1, Jan. 1992, pp. 89–91.
45. Fusco, V. F., Drew, S., and McDowall, D. S., "Synthesis and performance of an active microstrip antenna," *Int. J. Microwave Millimetre-wave CAE*, vol. 4, no. 1, 1994, pp. 100–110.
46. Hicks, R. G., and Kahn, P. J., "Numerical analysis of non-linear solid state device excitation in microwave circuits," *IEEE Trans.*, vol. MTT-30, Mar. 1982, pp. 251–259.
47. Filicori, F., and Naldi, C., "An algorithm for the periodic or quasi-periodic steady state analysis of non-linear circuits," *IEEE Symp. Circuits Syst.*, May 1983, pp. 366–369.
48. Peterson, D. L., Pavio, A. M., and Kim, B., "A GaAs FET model for large signal applications," *IEEE Trans.*, vol. MTT-32, no. 3, Mar. 1984, pp. 276–281.
49. Kraus, A.D., *Circuit Analysis*, West Publishing Company, 1991.
50. Fusco, V. F., Drew, S., and McDowall, D. S., "Synthesis and performance of an active microstrip antenna," *Int. J. Microwave Millimetre-wave CAE*, vol. 4, no. 1, 1994, pp. 100–110.

51. Humphrey, D. E. J., Fusco, V. F., and Drew, S., "Active antenna array behaviour," *IEEE Trans. Microwave Theory Techniques*, vol. 43, no. 8, Aug. 1995, pp. 1819–1825.
52. Van der Pol, B., "The non-linear theory of electrical oscillators," *Proc. IRE.*, vol. 22, no. 9, Sept. 1934, pp. 1051–1086.
53. Balanis, C. A., *Antenna Theory Analysis and Design*, Wiley, New York, 1982.
54. Fusco, V. F., "Active antenna phase modulator performance," 23rd European Microwave Conference, Madrid, Spain, Sept, 1993, pp. 248–251.
55. Elkhazmi, E., McEwan, N. J., and Moustafa, J., "Control of harmonic radiation from an active microstrip patch antenna," *Journ. Int. Nice Antennas*, Nov. 1996, pp. 313–316.
56. Radisic, V., Qian, Y., and Itoh, T., "Class F power amplifier integrated with circular sector microstrip antenna," *IEEE MTT-Symp. Dig.*, June 1997, pp. 687–690.
57. Cryan, M. J., and Hall, P. S., "Spectral control of integrated active antennas," ICAP 97, Edinburgh, UK, Apr. 1997, pp. 1.518–1.521.
58. Van der Pol, B., "On oscillation hysteresis in a triode generator with two degrees of freedom," *Philos. Mag.*, vol. 43, Sept. 1922, pp. 700–719.
59. Kurokawa, K., "Injection locking of microwave solid state oscillators," *Proc. IEEE*, vol. 61, no. 10, 1973, pp. 1386–1410.
60. Hall, P. S., Morrow, I. L., Haskins, P. M., and Dahele, J. S., "Phase control in injection locked microstrip active antennas," *IEEE MTT-S Symp.*, 1999, pp. 1227–1230.
61. Stephan, K. D., and Young, S. L., "Mode stability of radiation-coupled inter-injection locked oscillators for phased arrays," *IEEE Trans. MTT*, vol. 36, no. 5, May 1988, pp. 921–924.
62. Morrow, I. L., Hall, P. S., and James, J. R., "Measurement and modeling of a microwave active patch phased array for wide angle scanning," *IEEE Trans. Antennas Propag.*, vol. 45, no. 2, Feb. 1997, pp. 297–304.
63. Drew, S., and Fusco, V. F., "A phase modulated active antenna," *Electron. Lett.*, vol. 29, no. 10, May 1993, pp. 835–836.
64. Sancheti, S., and Fusco, V. F., "Self-detection performance of an FET active patch antenna under injection locking and its application for PM signal detection," *IEE Proc.—H Microwaves Antennas Propag.*, vol. 141, no. 4, Aug. 1994, pp. 253–256.
65. Fusco, V. F., "Self-detection performance of an active microstrip antenna," *IEE Electron. Lett.*, vol. 28, no. 14, July 1992, pp. 1362–1363.
66. York, R. A., and Compton, R. C., "Measurement and modelling of radiative coupling in oscillator arrays," *IEEE Trans. MTT*, vol. 4, no. 3, 1993, pp. 438–444.
67. Sancheti, S., and Fusco, V. F., "Active antenna top-cover frequency pulling effects," *IEE Proc. Microwave Antennas Propag.*, vol. 141, no. 5, Oct. 1994, pp. 374–376.
68. Linden, P. A., and Fusco, V. F., "Frequency doubling active patch antenna transponder," *Microwaves and R.F. '96*, London, pp. 344–348.
69. Singh, D., Gardner, P., and Hall, P. S., "Integrated push-push frequency doubling active microstrip transponder," *Electron. Lett.*, vol. 33, no. 6, 13 Mar. 1997, pp. 505–506.
70. Rauscher, C., "High frequency doubler operation of GaAs field effect transistors," *IEEE Trans. MTT*, vol. 31, 1983, p. 462.
71. Probanz, C. W., and Itoh, T., "Quasi-optical microwave circuits for wireless applications," *Microwave J.*, Jan. 1995, pp. 64–80.

## CHAPTER FOUR

---

# Multiport Network Method

---

### **K. C. GUPTA**

Department of Electrical and Computer Engineering  
University of Colorado  
Boulder, CO

### **RAJAN P. PARRIKAR**

Space Systems/LORAL  
Palo Alto, CA

## **4.1 INTRODUCTION: NETWORK MODELING OF ANTENNAS**

As brought out in earlier chapters, analysis and design of integrated circuit–antenna modules require development of efficient analysis and design techniques that are applicable to both circuit and antenna parts of the module. All the efficient circuit analysis and design methods (even at RF and microwave frequencies) are based on network modeling of components. It would be advisable to have similar tools for the analysis and design of integrated circuit–antenna modules. Fortunately, microstrip patch antennas (the most commonly used class of printed antennas) are amenable to network modeling. The transmission line model (TLM) for rectangular patch antennas discussed in Chapter 2 is a very simple network model and, as discussed in Chapter 3, can be used for analysis and design of integrated circuit–antenna modules. The cavity model for microstrip patch antennas discussed in Chapter 2 was developed to overcome several limitations in the transmission line model. The



multiport network model (MNM) is a further extension of the cavity model approach and provides a more refined network representation. When any one of these network models is used for microstrip patch antennas, commercially available network simulators for RF and microwave design can be used for design of integrated circuit–antenna modules also.

## 4.2    MULTIPORT NETWORK MODEL (MNM) FOR MICROSTRIP PATCHES

### 4.2.1    MNM Approach

The multiport network model of microstrip patch antennas [1,2] may be considered as an extension of the cavity model discussed in Chapter 2. In this modeling approach, the electromagnetic fields underneath the patch and outside the patch are modeled separately. The patch itself is analyzed as a two-dimensional planar network [3], with a multiple number of ports located all around the edges as shown in Fig. 4.1. Each port represents a small section (of length  $W_i$ ) of the edge of the patch.  $W_i$  is chosen small enough for the fields over this length to be assumed as uniform. Typically, for a rectangular patch, the number of ports along each radiating edge is taken to be four and along each nonradiating edge the number is taken to be eight. Thus, a  $24 \times 24$  matrix is typically adequate for the characterization of the interior fields of a rectangular patch.

For patches of regular shapes (rectangles, circles, rings, sectors of circles and of rings, and three types of triangles), this multiport planar network model can be analyzed by using two-dimensional impedance Green’s functions available for these shapes [3,4]. A multiport Z-matrix characterization representing the fields underneath the patch can be derived from Green’s function as

$$Z_{ij} = \frac{1}{W_i W_j} \int_{W_i} \int_{W_j} G(x_i, y_i | x_j, y_j) ds_i ds_j \tag{4.1}$$

where  $x_i, x_j, y_i, y_j$  denote the locations of the two ports of widths  $W_i$  and  $W_j$ , respectively. Green’s function  $G$  is usually a doubly infinite summation with terms corresponding to various modes of the planar resonator (rectangular or circular or triangular) with magnetic walls.

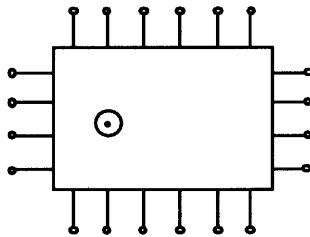
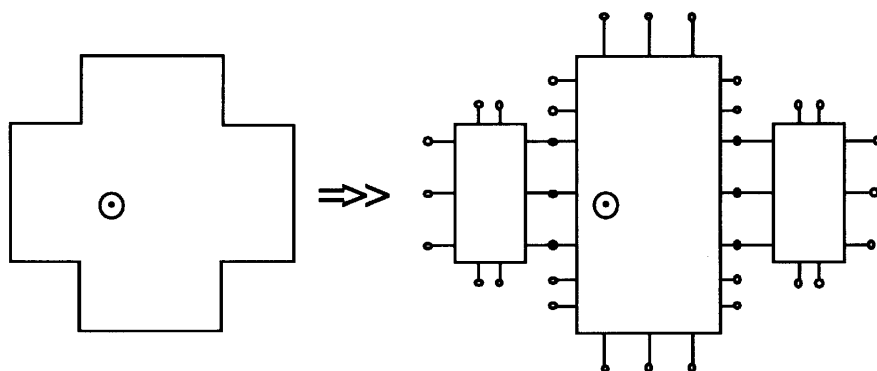


FIGURE 4.1    Multiport representation of a rectangular patch.

For patches of composite shapes (such as a “cross” shape shown in Fig. 4.2a), a multiport network model can be written by treating the composite shape as a combination of the elementary shapes for which Green’s functions are available. The cross shape of Fig. 4.2a can be considered as a combination of three rectangular segments as shown in Fig. 4.2b. Segmentation and desegmentation methods [3,4] are used for evaluating the  $Z$ -matrix of a composite shape from those of the elementary segments. If the patch or one of the segments of a composite patch is of an irregular shape for which a Green’s function is not available, a technique called the “contour integral method” [3,4] can be used to evaluate the  $Z$ -matrix.

In the multiport network modeling of radiating microstrip patches, the fields outside the patch (namely, the fringing fields at the edges, the surface-wave fields, and the radiation field) are accounted for by adding equivalent edge admittance networks (EANs) connected to the various edges of the patch. This representation is shown in Fig. 4.3 for the case of the rectangular patch shown in Fig. 4.2. EANs are multiport networks consisting of parallel combinations of the capacitances  $C$  (representing the energy stored in the fringing field) and the conductances  $G$  (representing the power carried away by radiation and surface waves) as shown in Fig. 4.4. Each capacitance–conductance pair is connected to a port of the planar equivalent circuit of the patch. Inductances connected between various ports represent the energy stored in fringing magnetic fields. Values of capacitance and conductance in the edge admittance networks may be obtained from the various analyses reported in the literature [4–7].

The flexibility of the multiport network model leads to several advantages when compared with the conventional cavity model discussed in Chapter 2 (Section 2.3.1.1). For example, the parasitic reactances at the junction between the feed line and the patch can be incorporated in the multiport network model by considering a small section of the feed line as an equivalent planar circuit connected to the patch at a finite number of (typically five) ports. Solution of this network problem (depicted



**FIGURE 4.2** (a) A cross-shaped microstrip patch; (b) multiport network model of the cross-shaped microstrip patch.

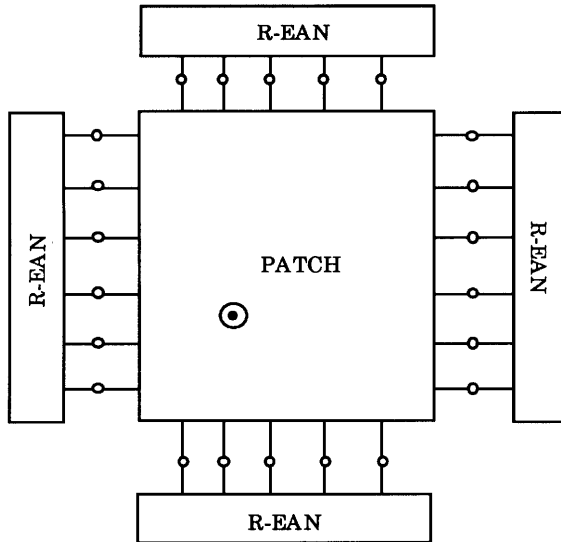


**FIGURE 4.3** Edge admittance networks (EANs) connected to the multipoint representation of a rectangular patch.

in Fig. 4.5) is equivalent to the expansion of the fields (in the feed line as well as in the patch) in a series of eigenfunctions and matching the fields at the interface.

Also, the multipoint network model outlined above can be extended to incorporate the effect of mutual coupling between the two radiating edges [8,19] by inserting a mutual coupling network (MCN) as shown in Fig. 4.6. The edge admittance terms associated with various ports at the edges constitute the diagonal terms of the admittance matrix for MCN. The nondiagonal terms of this matrix are obtained from the “reaction” between the equivalent magnetic current sources at the two corresponding sections of the edges. Similar MCNs may also be included between the

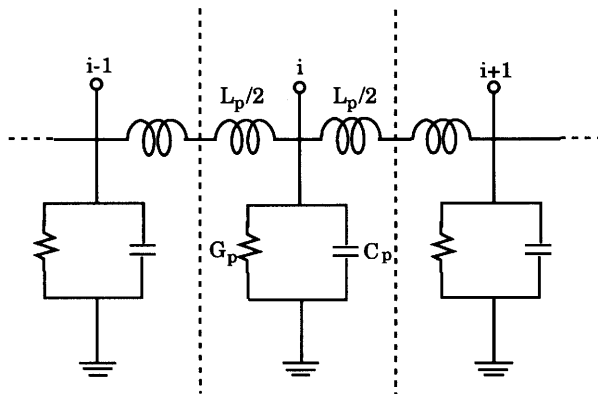


**FIGURE 4.4** Elements of an edge admittance network.

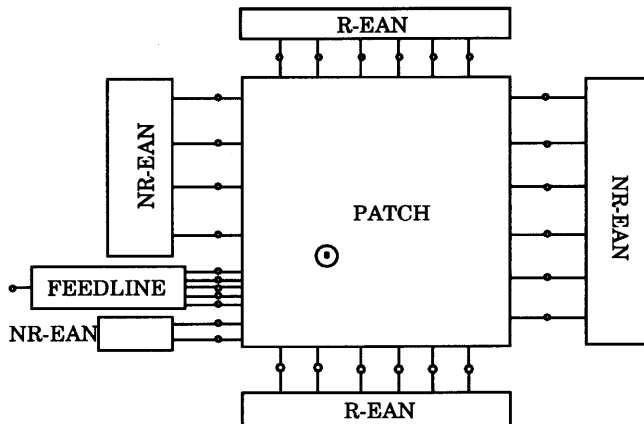


FIGURE 4.5 Incorporation of feed-junction reactance in multiport network model of a rectangular patch.

nonradiating edges, between a radiating edge and a nonradiating edge, or between two edges of different patches in an array.

It may be noted that in the multiport network model, the characterization of fields underneath the patch is conceptually similar to that used in the conventional cavity model. In both of these models, the fields under the patch are considered two-dimensional with no variations in the direction perpendicular to the substrate. For

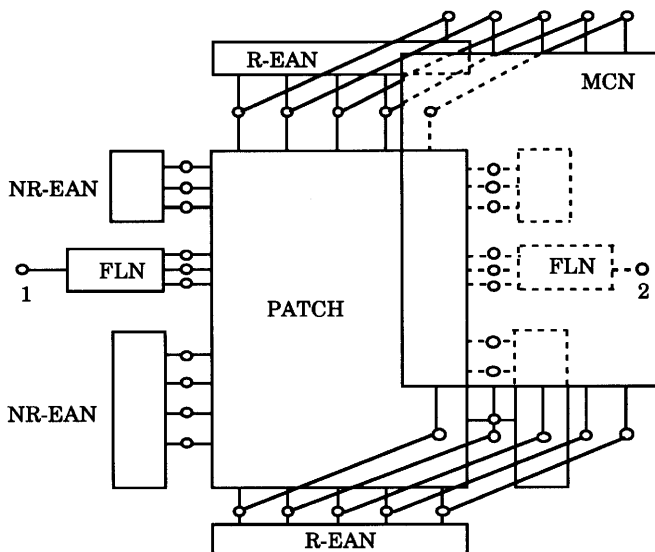


FIGURE 4.6 Incorporation of mutual coupling in multiport network model of a rectangular patch.

this reason, the limits of the applicability of the technique in terms of substrate permittivity and thickness are similar to that for the cavity model. Also, both of these methods will not be accurate when applied to narrow-width microstrip dipoles rather than to the wide microstrip patches discussed in this chapter.

Green's functions used for evaluating impedance-matrix characterization for patches of various shapes are discussed in the next subsection. Derivation of the Z-matrix is also included therein.

## 4.2.2 Z-Matrix Characterization of Planar Segments

**4.2.2.1 Green's Functions** For practical microstrip antennas, the thickness of the substrate is much smaller than the wavelength. Therefore, fields underneath the patch do not vary in the  $z$ -direction (perpendicular to the substrate). The electric field has a  $z$ -component only. Since  $\partial E_z / \partial z = 0$ , we may define a voltage  $V(x, y)$  given by

$$V(x, y) = -E_z(x, y)d \quad (4.2)$$

where  $d$  is the substrate thickness. When a magnetic-wall boundary condition is assumed at the edges of the patch,  $V(x, y)$  satisfies the boundary condition given by

$$\frac{\partial V(x, y)}{\partial p} = 0 \quad (4.3)$$

where  $p$  denotes the direction perpendicular to the edge of the patch antenna. If we consider a  $z$ -directed electric current source  $J_z(x_0, y_0)$  located at  $(x_0, y_0)$ , the voltage  $V(x, y)$  is related to the source current through a two-dimensional impedance Green's function  $G(x, y|x_0, y_0)$  defined by

$$V(x, y) = \iint_D G(x, y|x_0, y_0)J_z(x_0, y_0)dx_0 dy_0 \quad (4.4)$$

where the source current  $J_z$  is distributed over a region  $D$  in the  $xy$  plane. These Green's functions are known [3,4] for several "regular shapes" shown in Fig. 4.7.

When a microstrip antenna is excited by a probe feed perpendicular to the substrate, as shown in Fig. 4.8, the current density may be related to the axial current through the  $z$ -directed probe. For patches excited by a microstrip line feed, the current  $J_{in}$  flowing into the patch can be expressed as an equivalent  $z$ -directed electric current sheet  $J_z$  as follows. At the magnetic wall surrounding the patch (as shown in Fig. 4.9),

$$\mathbf{J}_z = \hat{\mathbf{p}} \times \mathbf{H}_t \quad (4.5)$$

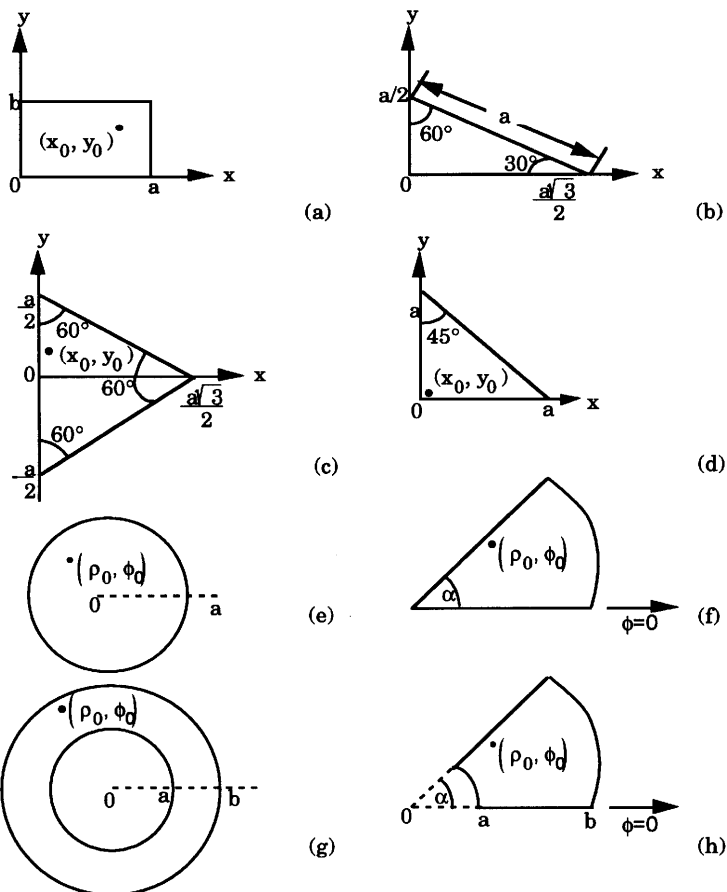


FIGURE 4.7 Various geometries of the planar segments for which Green's functions are available.

and for the planar waveguide model of the microstrip line feeding the patch

$$\mathbf{J}_{in} = \hat{\mathbf{z}} \times \mathbf{H}_t \tag{4.6}$$

Thus  $|J_z| = |J_{in}|$ . If the effective width of the microstrip line is  $W_j$  (for the  $j$ th port), the input current at the port  $j$  may be written as

$$I_j = W_j |J_z| \tag{4.7}$$

**4.2.2.2 Evaluation of Z-matrix from Green's Functions** Green's functions discussed above may be used to find the Z-matrix characterization of various planar segments of the shapes shown in Fig. 4.7 with respect to specified locations of external ports. These external ports may be either of the probe-feed type (Fig. 4.8) or

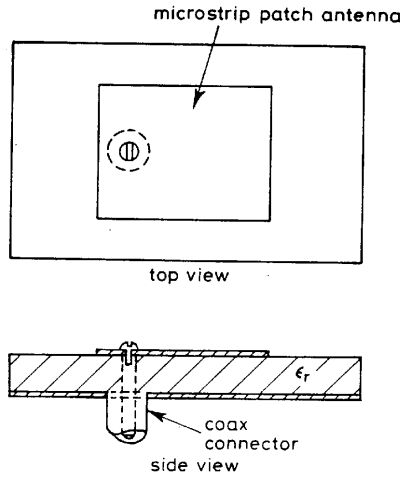


**FIGURE 4.8** Microstrip patch antenna with a probe feed perpendicular to the substrate.

the microstrip-feed type (Fig. 4.9) or a combination of these. The evaluation of the Z-matrix is based on Eq. 4.1 and involves the integration of  $G(x, y|x_0, y_0)$  over the extent of the two ports corresponding to the specific element of the Z-matrix. For a microstrip line feed with an effective width  $W_i$ , the integral is carried out over the width  $W_i$ . For a probe-feed type of external port, the integration is carried out over a circular path corresponding to the cylindrical surface of the probe. Alternatively, the

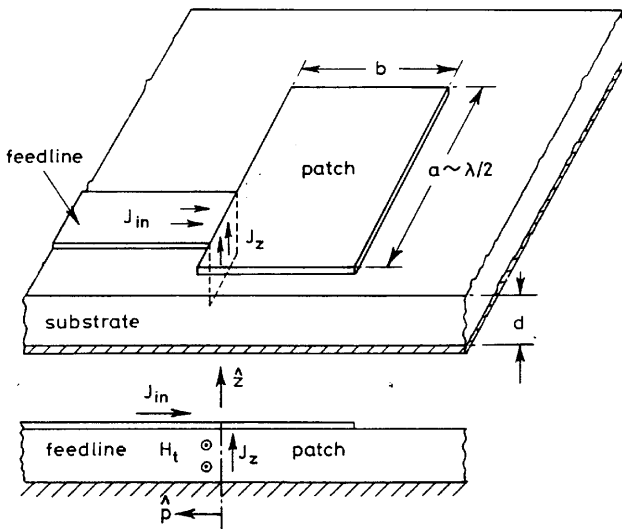


**FIGURE 4.9** Equivalence between the port current and the z-directed fictitious current density at the junction between a microstrip line feed and a patch.

circular probe may be replaced by an equivalent strip and the integration carried over this equivalent width.

**4.2.2.3 Z-Matrix for Rectangular Segments** Green's functions for various geometries, discussed in [3,4], appear as series involving double-infinite summations. In numerical computations of the Z-matrix elements, order of integration and summations can be interchanged. For rectangular segments, the integrals involved may be carried out analytically. When the sides of the rectangle are oriented along the  $x$ - and  $y$ -axes, the impedance-matrix element  $Z_{pq}$  for the two ports (say, port  $p$  and port  $q$ ) may be written in the following form [9]:

$$Z_{pq} = \frac{j\omega\mu d}{ab} \sum_{m=0}^{\infty} \sum_{n=0}^{\infty} \sigma_m \sigma_n \phi_{mn}(x_p, y_p) \phi_{mn}(x_q, y_q) / (k_x^2 + k_y^2 - k^2) \quad (4.8)$$

where, for ports oriented along the  $y$ -direction,

$$\phi_{mn}(x, y) = \cos(k_x x) \cos(k_y y) \operatorname{sinc}\left(\frac{k_y w}{2}\right) \quad (4.9)$$

and for ports oriented along the  $x$ -direction

$$\phi_{mn}(x, y) = \cos(k_x x) \cos(k_y y) \sin\left(\frac{k_x w}{2}\right) \quad (4.10)$$

The function  $\operatorname{sinc}(z)$  is defined as  $(\sin z)/z$ , and

$$\begin{aligned} k_x &= \frac{m\pi}{a}, & k_y &= \frac{n\pi}{b} \\ \sigma_m &= \begin{cases} 1, & m = 0 \\ 2, & m \neq 0 \end{cases} \\ k^2 &= \omega^2 \mu \epsilon_0 \epsilon_r (1 - j\delta) \end{aligned}$$

where  $\delta$  is the loss tangent of the dielectric.

The length of the rectangle is  $a$ , its width is  $b$ , and height of the substrate is  $d$ . The points  $(x_p, y_p)$  and  $(x_q, y_q)$  denote the locations of the  $p$  and  $q$  ports, respectively.

It has been shown [9] that the doubly infinite series in Eq. 4.8, along with Eqs. 4.9 and 4.10, can be reduced to a single infinite series by performing the inner summation. The choice of summation over  $n$  or  $m$  depends on the relative locations of the ports  $p$  and  $q$ , and also on the aspect ratio of the rectangular segment. We consider two different cases.



**Case 1:** When both the ports ( $p$  and  $q$ ) are oriented along the same direction ( $x$  or  $y$ ). We may write  $Z_{pq}$  as

$$\begin{aligned}
 Z_{pq} = & -CF \sum_{\ell=0}^L \sigma_{\ell} \cos(k_u u_p) \cos(k_u u_q) \cos(\gamma_{\ell} z_{>}) \cos(\gamma_{\ell} z_{<}) \\
 & \times \frac{\text{sinc}(k_u w_p/2) \text{sinc}(k_u w_q/2)}{\gamma_{\ell} \sin(\gamma_{\ell} F)} \\
 & - jCF \sum_{\ell=L+1}^{\infty} \cos(k_u u_q) \cos(k_u u_p) \text{sinc}\left(\frac{k_u w_p}{2}\right) \\
 & \times \text{sinc}\left(\frac{k_u w_q}{2}\right) \frac{\exp[-j\gamma_{\ell}(v_{>} - v_{<})]}{\gamma_{\ell}}
 \end{aligned} \tag{4.11}$$

where

$$(v_{>}, v_{<}) = \begin{cases} (y_{>}, y_{<}), & \ell = m \\ (x_{>}, x_{<}), & \ell = n \end{cases}$$

and

$$C = j\omega\mu d/ab$$

When the two ports are oriented in the  $y$ -direction we choose  $\ell = n$ , and when they are along the  $x$ -direction,  $\ell$  is put equal to  $m$ . Also,

$$\begin{aligned}
 F &= \begin{cases} b, & \ell = m \\ a, & \ell = n \end{cases} \\
 (u_p, u_q) &= \begin{cases} (x_p, x_q), & \ell = m \\ (y_p, y_q), & \ell = n \end{cases} \\
 \gamma_{\ell} &= \pm\sqrt{k^2 - k_u^2} \\
 k_u &= \begin{cases} m\pi/a, & \ell = m \\ n\pi/b, & \ell = n \end{cases}
 \end{aligned}$$

and

$$(z_{>}, z_{<}) = \begin{cases} (y_{>} - b, y_{<}), & \ell = m \\ (x_{>} - a, x_{<}), & \ell = n \end{cases}$$

The sign of  $\gamma_{\ell}$  is chosen so that  $\text{Im}(\gamma_{\ell})$  is negative;  $w_p$  and  $w_q$  are widths of ports  $p$  and  $q$ , respectively. Also, we use

$$y_{>} = \max(y_p, y_q) \quad y_{<} = \min(y_p, y_q)$$

and a similar notation for  $x_>$  and  $x_<$  when  $\ell = n$ . The choice of the integer  $L$  in Eq. 4.11 becomes a trade-off between fast computation and accuracy. A compromise is to select  $L$  so that  $\gamma_\ell F$  is less than or equal to 100.

**Case 2:** When the two ports ( $p$  and  $q$ ) are oriented in different directions ( $x$  and  $y$ ), various elements of the  $Z$ -matrix may be given by

$$\begin{aligned}
 Z_{pq} = & -CF \sum_{\ell=0}^L \sigma_\ell \cos(k_u u_p) \cos(k_u u_q) \cos(\gamma_\ell z_<) \\
 & \times \cos(\gamma_\ell z_>) \frac{\text{sinc}(k_u w_i/2) \text{sinc}(\gamma_\ell w_j/2)}{\gamma_\ell \sin(\gamma_\ell F)} \\
 & - CF \sum_{\ell=L+1}^{\infty} \cos(k_u u_p) \cos(k_u u_q) \\
 & \times \text{sinc}\left(\frac{k_u w_i}{2}\right) \frac{\exp[-j\gamma_\ell (v_> - v_< - w_j/2)]}{\gamma_\ell^2 w_j} \quad (4.12)
 \end{aligned}$$

The choice of  $\ell$  is made by noting that, for convergence of the last summation in the above equation, we need

$$(v_> - v_< - w_j/2) > 0 \quad (4.13)$$

We choose the index of the inner summation so that this condition is satisfied. This condition may be written more explicitly as

$$\ell = m, \quad \text{if } \{\max(y_p, y_q) - \min(y_p, y_q) - w_j/2\} > 0 \quad (4.14)$$

$$\ell = n, \quad \text{if } \{\max(y_p, y_q) - \min(y_p, y_q) - w_j/2\} > 0 \quad (4.15)$$

When both of these conditions are satisfied, any choice of  $\ell$  will ensure convergence.

If  $\ell = n$ ,  $w_i$  corresponds to the port oriented along the  $y$ -direction and  $w_j$  corresponds to the port along the  $x$ -direction. On the other hand, if  $\ell = m$ ,  $w_i$  is for the port along the  $x$ -direction and  $w_j$  for the port along the  $y$ -direction.

**4.2.2.4 Z-Matrix for Circular Segments** For circular-shaped patches, the impedance Green's function is given in [3,4]. When ports are located along the circumference of the circle (as shown in Fig. 4.10), various elements of the  $Z$ -matrix [10] may be written as follows. For any port  $i$ , the  $Z$ -matrix element  $Z_{ii}$  may be written as

$$Z_{ii} = \frac{2j\omega\mu da^2}{\pi W_i^2} \sum_{n=0}^{\infty} \sum_{m=1}^{\infty} \frac{\sigma_n \{1 - \cos[2n \sin^{-1}(W_i/2a)]\}}{n^2 (a^2 - n^2/k_{nm}^2)(k_{nm}^2 - k^2)} \quad (4.16)$$

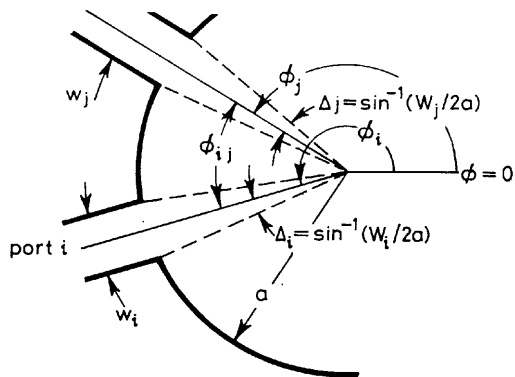


FIGURE 4.10 Various parameters for ports located at the circumference of a circular segment.

Off-diagonal terms of the impedance matrix are found to be

$$Z_{ij} = \frac{2j\omega\mu da^2}{\pi W_i W_j} \sum_{n=0}^{\infty} \sum_{m=1}^{\infty} \frac{\sigma_n}{n^2(a^2 - n^2/k_{nm}^2)(k_{nm}^2 - k^2)} \times \{\cos[n(\Delta_i - \Delta_j)] - \cos[n(\Delta_i + \Delta_j)]\} \cos(n\phi_{ij}) \tag{4.17}$$

where

$$\Delta_{ij} = \sin^{-1}(W_{ij}/2a)$$

Similar expressions for computation of the Z-matrices for planar segments of other geometries shown in Fig. 4.7 have not been reported so far.

**4.2.2.5 Z-Matrices for Segments of Arbitrary Shape** When we come across segments of arbitrary shapes for which Green’s functions do not exist, the impedance matrix can be found by a method known as the “contour integral method” [11]. The contour integral method is based on Green’s theorem in cylindrical coordinates. The RF voltage at any point  $M(s)$  inside the periphery of an arbitrarily shaped planar segment shown in Fig. 4.11a is given by

$$4jv(s) = \oint_C \left\{ H_0^{(2)}(kr) \frac{\partial v(s_0)}{\partial n} - v(s_0) \frac{\partial H_0^{(2)}(kr)}{\partial n} \right\} ds_0 \tag{4.18}$$

where  $H_0^{(2)}$  is the zero-order Hankel function of the second kind and  $r$  is the straight-line distance between the point  $M(s)$  and the source point on the periphery (given by  $L(s_0)$ ). The integral on the right-hand side of Eq. 4.18 is evaluated out over the entire

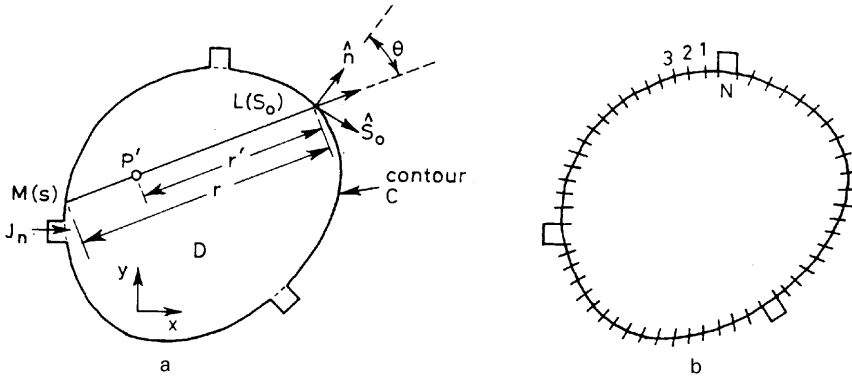


**FIGURE 4.11** (a) Configuration of a planar segment for analysis by contour integral method; (b) division of the periphery into  $n$  sections for the analysis.

periphery. The RF voltage at any point *just* inside the periphery can be derived from the above relationship. We obtain

$$2jv(s) = \oint_C \{k \cos \theta H_1^{(2)}(kr)v(s_0) + j\omega\mu d J_n(s_0)H_0^{(2)}(kr)\} ds_0 \quad (4.19)$$

where  $H_1^{(2)}$  is the first-order Hankel function of the second kind, and  $J_n$  denotes line current density flowing into the segment at  $s_0$ . The variables  $s$  and  $s_0$  denote distances along the contour  $C$  and  $r$  is the distance between the two points  $M$  and  $L$  (specified by  $s$  and  $s_0$ ) as shown in Fig. 4.11a. The angle  $\theta$  is between the straight line joining points  $M$  and  $L$  with the normal to the periphery at  $L$ . Line current density  $J_n$ , flowing into the segment at a coupling port, is given by

$$J_n = \frac{1}{j\omega\mu d} \frac{\partial v}{\partial n} \quad (4.20)$$

For the numerical calculation of the impedance matrix, we divide the periphery into  $N$  sections having arbitrary widths  $W_1, W_2, \dots, W_N$ , as shown in Fig. 4.11b. The periphery is divided in such a manner that each coupling port contains an integral number of sections. For greater accuracy, wider coupling ports may be divided into a multiple number of sections. We set  $N$  sampling points, one at the center of each section, and assume each section is a straight edge. It is further assumed that the widths of the sections are so small that the magnetic and electric fields can be considered constant over each section. With these assumptions, the line integral in Eq. 4.19 can be replaced by summation over the  $N$  sections. The resulting expression is given by

$$2jv_\ell = \sum_{m=1}^N \{kv_m G_{\ell m} + j\omega\mu d i_m F_{\ell m}\} \quad (4.21)$$

where  $v_\ell$  is the voltage over the  $\ell$ th section and  $i_m (= J_m W_m)$  is the total current flowing into the  $m$ th section. The matrix elements  $G_{\ell m}$  and  $F_{\ell m}$  are given as

$$G_{\ell m} = \begin{cases} \int_{W_m} \cos \theta H_1^{(2)}(kr) ds_0, & \text{if } \ell \neq m \\ 0, & \text{otherwise} \end{cases} \quad (4.22)$$

and

$$F_{\ell m} = \begin{cases} \frac{1}{W_m} \int_{W_m} H_0^{(2)}(kr) ds_0, & \text{if } \ell \neq m \\ 1 - \frac{2j}{\pi} \left( \ln \frac{kW_\ell}{4} - 1 + \gamma \right), & \text{otherwise} \end{cases} \quad (4.23)$$

In Eq. 4.23,  $\gamma (= 0.5772 \dots)$  denotes Euler's constant. In the above discussion we assume that the current can be fed into the planar circuit from all the  $N$  sections and  $i_m$  denotes the current fed from the  $m$ th section. This yields the impedance matrix for the  $N$ -port circuit. This matrix can be used to obtain the impedance matrix for any specified number and location of ports on the planar circuit being analyzed. Equation 4.21 is written for each section  $\ell$  on the periphery of the planar circuit. All these equations may be combined into a matrix equation of the form:

$$\mathbf{A}\mathbf{v} = \mathbf{B}\mathbf{i} \quad (4.24)$$

where  $\mathbf{v}$  and  $\mathbf{i}$  are the voltage and the current vectors at each section.  $\mathbf{A}$  and  $\mathbf{B}$  denote  $N$  by  $N$  matrices, determined by the shape of the circuit. The elements of these matrices, obtained from Eq. 4.21, are

$$\begin{aligned} a_{\ell m} &= -kG_{\ell m}, & \text{for } \ell \neq m \\ a_{\ell \ell} &= 2j \end{aligned} \quad (4.25)$$

and

$$b_{\ell m} = j\omega\mu dF_{\ell m} \quad (4.26)$$

From Eq. 4.24, the impedance matrix for the  $N$  sections, considered as ports, is obtained as

$$\mathbf{Z}_N = \mathbf{A}^{-1}\mathbf{B} \quad (4.27)$$

In practice, the coupling ports are connected to only a few of the  $N$  sections. Rows and columns corresponding to the sections that are open-circuited can be deleted from  $\mathbf{Z}_N$ . If each coupling port covers only one section, the matrix thus obtained (after deleting rows and columns corresponding to the open sections from  $\mathbf{Z}_N$ ) is the

required impedance matrix. If some coupling ports extend to more than one section, the sections in these coupling ports are like subports and the procedure detailed in [3,4] can be used to obtain the overall admittance matrix at the coupling ports (and hence impedance matrix, if desired).

### 4.2.3 Edge Admittance and Mutual Coupling Networks

In the MNM approach, the edge fields (comprised of the fringing fields at the edges, the surface-wave fields, and the radiation fields) are modeled by introducing equivalent edge admittance networks (EANs) connected to the edges of the patch (as shown in Figs. 4.3 and 4.5). When a microstrip patch has a polygon shape (rectangular and triangular geometries), the periphery of the patch is divided into edges. Each edge may have a different voltage distribution. For geometries similar to the circular patch, the total periphery is taken as a single edge. The EAN for each edge is a multiport network consisting of combinations of a capacitance  $C$ , an inductance  $L$  (representing the energy stored in the fringing electric and magnetic fields, respectively), and a conductance  $G$  (representing the power carried away by radiation and by surface waves). A portion of a typical EAN is shown in Fig. 4.4. Similar sections are connected to the other ports of the equivalent planar multiport representation of the patch. The elements of the Y-matrix characterizing the EANs are computed from the equivalent circuit shown in Fig. 4.4.

**4.2.3.1 Edge Conductance** The edge conductance  $G$  in an EAN consists of two ports: a radiation conductance  $G_r$  and a surface-wave conductance  $G_s$ . The conductances  $G_r$  and  $G_s$  associated with an edge of a microstrip patch are defined as equivalent ohmic conductances (distributed or lumped). These conductances,  $G_r$  and  $G_s$ , when connected to the edge of the patch (continuously or at discrete ports) will dissipate a power equal to that radiated ( $P_r$ ) and to that launched as a surface wave ( $P_s$ ) by the patch, respectively. When the voltage amplitude distribution along an edge is given by  $f(\ell)$ , the conductances  $G_r$  and  $G_s$  of the edge are obtained as [2]

$$G_{r,s} = \frac{2P_{r,s}}{(1/W) \int_0^W f^2(\ell) d\ell} \quad (4.28)$$

where  $\ell$  denotes the distance along the edge of the patch and  $P_{r,s}$  values are computed for a voltage distribution  $f(\ell)$ . If we select  $n$  uniformly spaced ports (each representing a section of length  $W/n$ ) along the edge, the conductance  $G_p$  connected to each of the ports is taken as  $(G_r + G_s)/n$ .

The concept of edge conductance discussed above can be implemented only when  $f(\ell)$  is known a priori. In most of the cases, microstrip antennas are operated near the resonance frequency of the patch and  $f(\ell)$  is known at least approximately. For more accurate results, iterative computations may be needed. Starting from an approximate  $f(\ell)$ , an analysis based on the MNM model is carried out to evaluate the

voltages at the  $n$  ports on the edge. This computed voltage distribution is then used as a modified  $f(\ell)$ , and the computations of  $G_r$  and  $G_s$  are repeated. A method for computing the radiated power ( $P_r$ ) from the edges of a microstrip patch (on a thin substrate without cover layer) is based on the representation of the edge field in terms of an equivalent magnetic current line source (see [4, Sec. 11.4.6]). For thin substrates without any cover layer,  $G_s$  is much smaller than  $G_r$  and hence may be neglected [12, pp. 53–59].

The procedure just described yields an equivalent conductance that is distributed uniformly over sections of the edge. The resulting edge admittance network is a diagonal matrix. The mutual conductance among all sections is incorporated in the calculation of the power radiated from the edge. This method requires a priori knowledge of the voltage distribution along the edge. A modified method [13] does not need any such information. In this method, equivalent magnetic-current element sources are placed at the location of each section at the periphery. The elements of the Y-matrix characterizing the edge conductance network are obtained by equating the power flow associated with these magnetic currents (obtained from the Poynting vector) to the power dissipated in the equivalent network. The diagonal terms of the Y-matrix are equal to the self-radiation conductances of the corresponding segments. The off-diagonal terms are equal to the real parts of the mutual coupling admittances between the two corresponding segments. It may be noted that in this modified method, the real part of mutual coupling among different sections of the edge is included in the off-diagonal terms of the conductance networks, whereas the reactive part is included (as in the earlier approach also) in the inductance and the capacitance networks.

The generalized edge conductance network, based on this modified approach, is shown schematically in Fig. 4.12. The current source shown in this figure accounts for the mutual coupling among various sections of the edge. Similar current sources are also attached to the other nodes 1 through  $n$ . These are not shown in the figure. The transfer conductance  $g_{ji}$  is the real part of the complex mutual coupling  $Y_{ji}$  between the sections  $j$  and  $i$ . The mutual admittance  $Y_{ji}$  represents the electric current induced in the  $j$ th section as a result of a unit magnetic current (or voltage) at the  $i$ th

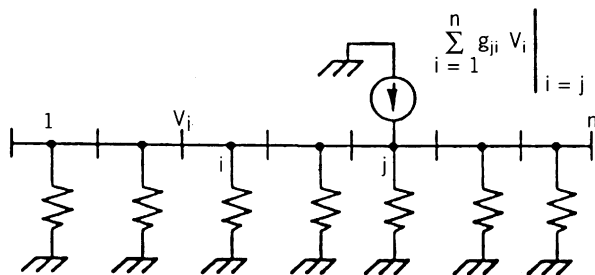


FIGURE 4.12 Generalized edge conductance network used when the field distribution along the edge is not known a priori.

section. Computation of  $Y_{ji}$  (also used for equivalent mutual coupling networks) is discussed later. The resulting edge conductance matrix has the following form:

$$[G_e] = \begin{matrix} & \begin{matrix} 1 \\ \vdots \\ n \end{matrix} \\ \begin{matrix} 1 \\ \vdots \\ n \end{matrix} & \begin{bmatrix} g_{11} & g_{12} & \cdots & g_{1n} \\ g_{21} & & & \\ \vdots & & \ddots & \vdots \\ g_{n1} & \cdots & \cdots & g_{nn} \end{bmatrix} \end{matrix} \quad (4.29)$$

Note that in the edge admittance matrix  $[Y_e]$  the contributions of fringing capacitances and inductances must be included as discussed later in this section. Also, it may be pointed out that actual values of the voltages  $V_i$  and  $V_j$  are not needed to compute  $Y_{ji}$  or  $g_{ji}$ . The diagonal terms  $g_{ii}$  are self-conductances of individual sections given by

$$g_{ii} = \frac{W_i^2}{90\lambda_0^2} \quad (4.30)$$

where  $W_i$  is the width of the  $i$ th section and  $\lambda_0$  is the free-space wavelength at the operating frequency.

Various formulas for edge conductance are summarized in [14, Chap. 9, Sec. 9.4.1].

**4.2.3.2 Edge Capacitance** The edge capacitance  $C$  accounts for the energy stored in the fringing electric field at the periphery of the patch. The fringing capacitance is defined as the excess of the total capacitance of the patch over that which would exist if the patch were considered as a two-dimensional capacitor with magnetic walls at the open edges. As in the case of the edge conductance, the edge capacitance is also distributed uniformly over the  $n$  ports ( $C_p = C/n$ ). Closed-form expressions for the edge capacitance are available for simple shapes, namely, rectangular [5,7] and circular [15] geometries. The evaluation of the edge capacitance of an arbitrarily shaped microstrip patch is described in [16].

**4.2.3.3 Edge Inductance** The edge inductance  $L$  accounts for the energy stored in the fringing magnetic field at the edge of the patch. As in the cases of  $G$  and  $C$ , the edge inductance is also distributed uniformly over the  $n$  ports ( $L_p = L/n$ ). For the nonradiating edges of a rectangular patch operating in the dominant mode, the fringing inductance per unit length  $L_e$  and the fringing capacitance per unit length  $C_e$  (for  $\epsilon_r = 1$ ) are related by  $L_e = \mu_0\epsilon_0/C_e$  ( $\epsilon_r = 1$ ).

When the voltage distribution along an edge is uniform, the voltages at two adjacent ports on the edge are equal, and hence no current flows through the edge inductance. In this case, the edge inductance need not be included and the EAN simplifies to parallel pairs of capacitance and conductance only. This situation occurs at the radiating edges of a rectangular patch operating in the dominant mode.



The common practice for evaluating the resonance frequency of two-dimensional resonators (incorporating the fringing fields) is to use effective dimensions larger than the actual physical dimensions. Calculation of these effective dimensions is carried out by finding the total electrostatic capacitance and equating it to the parallel-plate capacitance of effective dimensions. However, it may be noted here that the use of effective dimensions not only adds the fringing capacitance at the edges but also modifies the magnetic field distribution. Thus the use of effective dimensions for the analysis of microstrip patches, using the cavity model with magnetic-wall boundary, is consistent with the MNM approach that includes both inductance and capacitance. The fringing edge inductance  $L_e$  per unit length and the fringing capacitance per unit length are related as  $L_e = \mu_0 \epsilon_0 / C_e (\epsilon_r = 1)$ .

**4.2.3.4 Mutual Coupling Network** As shown in Fig. 4.6, the mutual interaction between the fringing fields associated with any two edges can be expressed in terms of a network model. The basic idea of using an admittance element to represent mutual coupling between two radiating edges was initially proposed in [17] in conjunction with the transmission line model of microstrip antennas. The multiport mutual coupling network shown in Fig. 4.6 is an extension of this concept suitable for incorporating in the multiport network model of microstrip patch antennas.

**4.2.3.5 Evaluation of Mutual Coupling Networks** For computation of external mutual coupling between various edges of a microstrip patch antenna on a thin substrate, the field at the edge may be modeled by equivalent line sources of magnetic current placed directly on the ground plane at the location of the edges. This is illustrated in Fig. 4.13. Magnetic currents  $\mathbf{M}$  are given by

$$\mathbf{M} = -\hat{\mathbf{n}} \times E\mathbf{d} \quad (4.31)$$

where  $d$  is the height of the substrate. The product  $(-E\mathbf{d})$  is the voltage  $V(x, y)$  defined in Eq. 4.2.  $\hat{\mathbf{n}}$  denotes a unit vector normal to the ground plane as shown. For the  $E$ -field in the direction indicated in this figure, both magnetic current sources  $\mathbf{M}$  are in the  $y$ -direction, that is, directed out of the plane of the paper.

The coupling between two magnetic current line sources is evaluated by dividing each of the line sources into small sections, each of length  $dl$ . The magnetic field produced by each of these sections (on the line source 1) at the locations of the various sections on the line source 2 can be written by using fields of a magnetic current dipole in free space [18]. The configuration and coordinate system is shown in Fig. 4.14. We have

$$H_\theta = j \frac{k_0 M dl \sin \theta}{4\pi\eta_0 r} \left\{ 1 + \frac{1}{jk_0 r} - \frac{1}{(k_0 r)^2} \right\} e^{-jk_0 r} \quad (4.32)$$

$$H_r = \frac{M dl \cos \theta}{2\pi\eta_0 r^2} \left\{ 1 + \frac{1}{jk_0 r} \right\} e^{-jk_0 r} \quad (4.33)$$

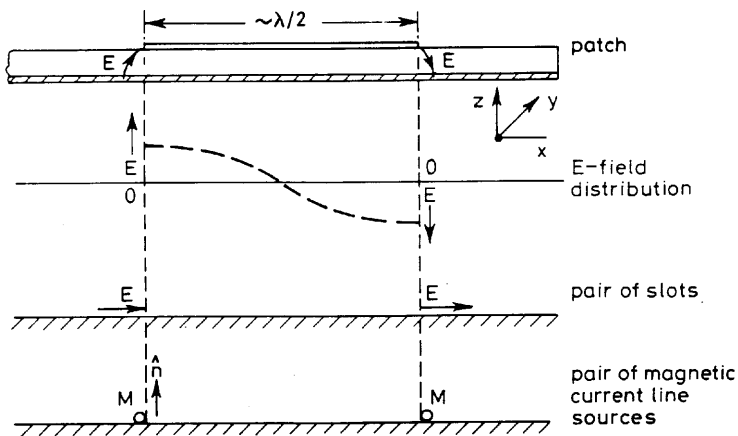


FIGURE 4.13 Modeling of the fringing field at the patch edges in terms of magnetic-current line sources.

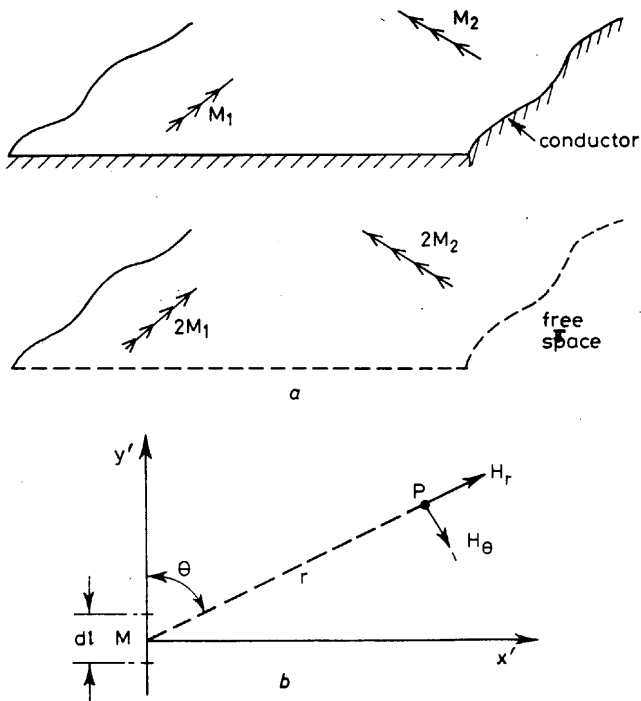


FIGURE 4.14 (a) Two arbitrarily spaced magnetic-current elements; (b) the coordinate system used for computation of fields.

Here  $k_0$  is the free-space wavenumber and  $r$  is the distance between the point  $P$  and the magnetic current element  $M dl$ . When the two edges (say,  $i$  and  $j$ ) are oriented arbitrarily, as shown in Fig. 4.15a, the magnetic field  $H$  at  $(x_j, y_j)$  produced by a source  $dl_i M$  at  $(x_i, y_i)$  may be written as

$$\mathbf{H} = \hat{\mathbf{x}}H_x + \hat{\mathbf{y}}H_y \tag{4.34}$$

with

$$H_y = H_{y'} \cos \theta_i - H_{x'} \sin \theta_i \tag{4.35}$$

$$H_x = H_{y'} \sin \theta_i + H_{x'} \cos \theta_i \tag{4.36}$$

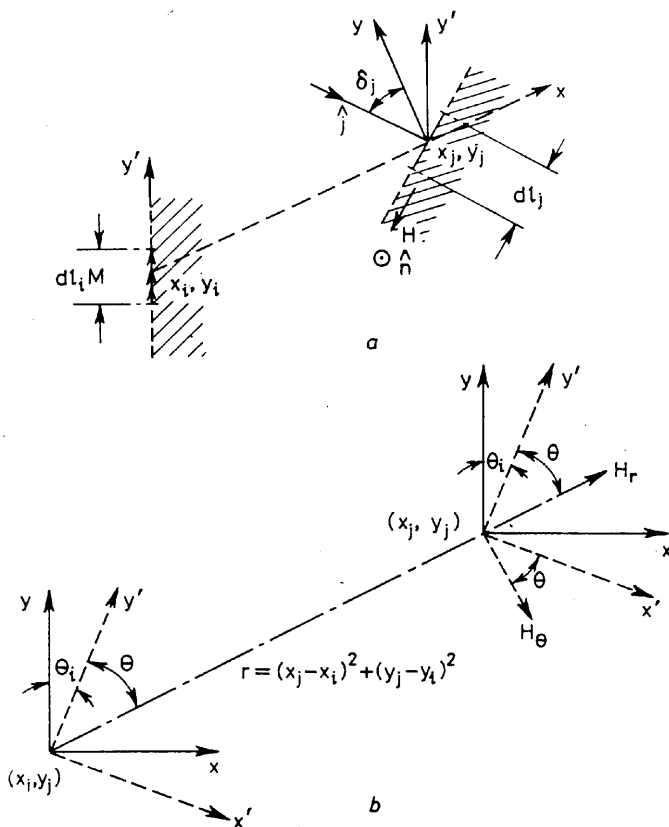


FIGURE 4.15 (a) Configuration showing sections  $i$  and  $j$  of two patch edges; (b) two different coordinate systems used for mutual coupling calculations.

where

$$H_{x'} = H_\theta \cos \theta + H_r \sin \theta \tag{4.37}$$

$$H_{y'} = -H_\theta \sin \theta + H_r \cos \theta \tag{4.38}$$

Coordinate systems  $(x, y)$  and  $(x', y')$  are illustrated in Fig. 4.15b. Mutual admittance between sections  $j$  and  $i$  may be written in terms of the electric current density  $J_j$  induced in the upper surface of the edge segment  $j$ . We have

$$\mathbf{J}_j = \hat{\mathbf{n}} \times \mathbf{H} = (-H_x \cos \delta_j - H_y \sin \delta_j) \hat{\mathbf{j}} \tag{4.39}$$

The current density induced on the surface of the edge section  $j$  underneath the patch is  $-J_j$ . The mutual admittance between sections  $i$  and  $j$  is given by the negative of the current flow into section  $j$  (underneath the patch) divided by the voltage at section  $i$ , that is

$$Y_{ji} = -(-J_j dl_j / M_i) \tag{4.40}$$

The second minus sign in Eq. 4.40 is due to the fact that the direction of current for defining the admittance matrix of a multiport network is directed into the network as shown in Fig. 4.16. The two edges shown in Fig. 4.15a may be the edges of a single radiating patch or those of the two different patches in an array environment. When the mutual coupling between two patches is being computed, several individual edges of the two patches contribute to the mutual coupling network (MCN). An MCN configuration taking the four radiating edges into account is shown in Fig. 4.17. Here, the MCN is connected to four ports along each radiating edge. In practice the number of sections considered on each edge for mutual coupling calculations is usually larger (typically 12). However, while using MCN for antenna analysis (by segmentation), a small number of ports along radiating edges (typically 4) is sufficient. Thus the original mutual admittance matrix ( $48 \times 48$  for 12 ports along each edge) is reduced to a smaller size ( $16 \times 16$  as shown) by paralleling the ports in subgroups of three each. Contributions of nonradiating edges can also be incorporated in MCN. This is not shown in the figure. Detailed computations [19] indicate that the mutual coupling contribution by nonradiating edges is usually much smaller and may be ignored in a first-order approximation.

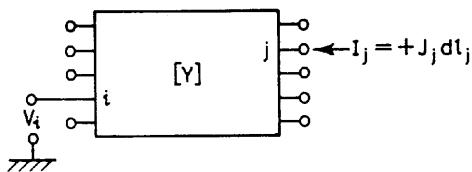
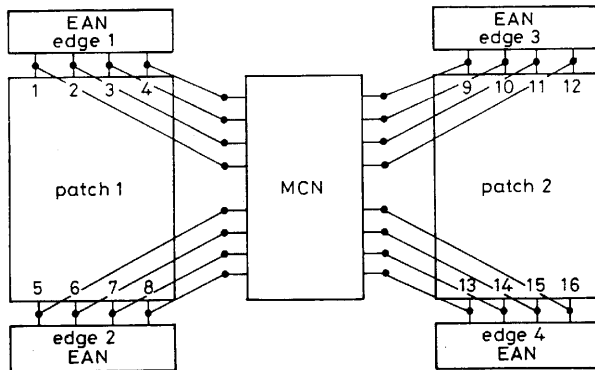


FIGURE 4.16 Representation of the mutual coupling by an admittance matrix.



**FIGURE 4.17** A mutual coupling network (MCN) representing the coupling between two adjacent patches in an array.

Mutual coupling computations based on the above formulation have been verified [19] by comparison with the available experimental results [20]. A very good agreement between the computation and experimental results has been reported.

It may be noted that the preceding method of evaluating mutual coupling (based on the equivalent magnetic current model shown in Fig. 4.13) is valid only for electrically thin substrates where the effect of surface waves along the substrate is negligible. This modeling approach has been extended to microstrip patches on thin substrates, but covered by a relatively thicker dielectric cover layer [21]. The mutual coupling in this case is dominated by the effect of surface waves in the thicker cover layer.

When the substrate thickness is increased, the equivalent magnetic current model for Fig. 4.13 becomes more and more inaccurate. In principle the multiport network modeling of mutual coupling between two patches is possible if more rigorous analytical/numerical techniques [22,23] are extended to formulate a network representation of mutual coupling.

#### 4.2.4 Analysis of Multiport Network Model

The most salient advantage of the multiport network model for microstrip patches is the fact that various analysis and optimization techniques available for multiport networks can now be used for analysis and optimization of integrated circuit–antenna modules. The most widely used techniques for such planar networks are segmentation [3,4] and desegmentation [3,4] methods. These two network analysis techniques are reviewed in this section.

**4.2.4.1 Segmentation Method** The name *segmentation* was first given to this network analysis method when it was used for planar (two-dimensional) microwave circuits by Okoshi and Takeuchi [24]. The basic idea is to divide a single large planar circuit into simpler *segments*, which have regular shapes and can therefore be

characterized relatively easily. An example of such a segmentation is shown in Fig. 4.18 where a ring-shaped geometry is broken down into four rectangular segments for which Green's functions are available. For the multiport network model of a two-port microstrip antenna shown in Fig. 4.6, each of the components (shown by rectangular boxes in the figure) can be considered as a *segment* for application of the segmentation method. Essentially, the segmentation method gives us the overall performance parameters of the multiport network, when the characterization of each of the segments is known. Originally the segmentation method was formulated [24] in terms of S-matrices of individual segments; however, it was subsequently realized [25] that a Z-matrix formulation is more efficient for microwave planar circuits (also for microstrip antennas). In this section, we will describe the procedure based on Z-matrices.

For illustrating the procedure, we consider a multiport network consisting of only two segments *A* and *B*, as shown in Fig. 4.19. Various ports of these two segments are numbered as shown. The external (unconnected) ports of segment *A* are called  $p_a$  ports (which may be more than one). Similarly, the external unconnected ports of segment *B* are called  $p_b$  ports. Connected ports of segment *A* are named  $q$  ports and the connected ports of segment *B* are designated as  $r$  ports.  $q$  and  $r$  ports are numbered such that  $q_1$  is connected to  $r_1$ ,  $q_2$  to  $r_2$ , and so on. As a result of these interconnections, we can write

$$V_q = V_r \quad \text{and} \quad i_q = -i_r \tag{4.41}$$

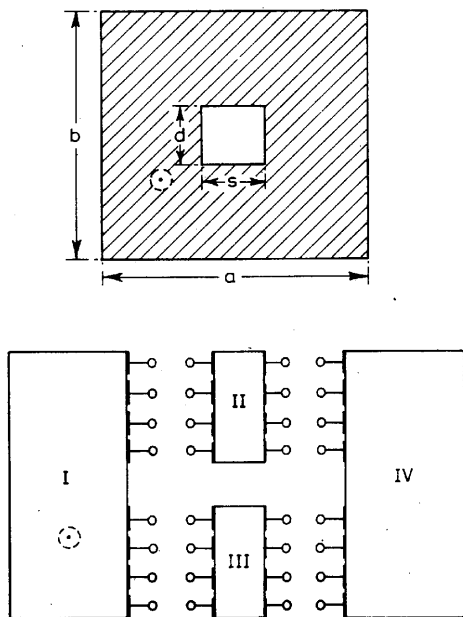


**FIGURE 4.18** Segmentation of a ring-shaped structure into four rectangular segments.

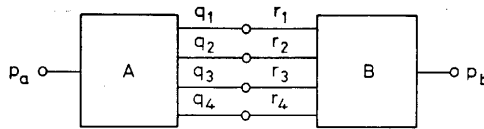


FIGURE 4.19 Two connected multiport networks *A* and *B*.

*Z*-matrices of segments *A* and *B* may be written as

$$\mathbf{Z}_A = \begin{bmatrix} Z_{p_a} & Z_{p_a q} \\ Z_{q p_a} & Z_{q q} \end{bmatrix}, \quad \mathbf{Z}_B = \begin{bmatrix} Z_{p_b} & Z_{p_b r} \\ Z_{r p_b} & Z_{r r} \end{bmatrix} \quad (4.42)$$

where  $Z_{p_a}$ ,  $Z_{p_a q}$ ,  $Z_{q p_a}$ ,  $Z_{q q}$ ,  $Z_{p_b}$ ,  $Z_{p_b r}$ ,  $Z_{r p_b}$ , and  $Z_{r r}$  are submatrices of the appropriate dimensions. As we are dealing with reciprocal components

$$Z_{p_a q} = (Z_{q p_a})^t \quad \text{and} \quad Z_{p_b r} = (Z_{r p_b})^t \quad (4.43)$$

*Z*-matrices of the segments *A* and *B* can be written together as

$$\begin{bmatrix} V_p \\ V_q \\ V_r \end{bmatrix} = \begin{bmatrix} Z_{pp} & Z_{pq} & Z_{pr} \\ Z_{qp} & Z_{qq} & 0 \\ Z_{rp} & 0 & Z_{rr} \end{bmatrix} = \begin{bmatrix} i_p \\ i_q \\ i_r \end{bmatrix} \quad (4.44)$$

where

$$\mathbf{V}_p = \begin{bmatrix} V_{p_a} \\ V_{p_b} \end{bmatrix}, \quad \mathbf{i}_p = \begin{bmatrix} i_{p_a} \\ i_{p_b} \end{bmatrix}$$

and

$$Z_p = \begin{bmatrix} Z_{p_a} & 0 \\ 0 & Z_{p_b} \end{bmatrix}, \quad Z_{pq} = \begin{bmatrix} Z_{p_a b} \\ 0 \end{bmatrix}$$

$$Z_{pr} = \begin{bmatrix} 0 \\ Z_{p_b r} \end{bmatrix}$$

and

$$Z_{qp} = (Z_{pq})^t, \quad Z_{rp} = (Z_{pr})^t$$

The superscript “*t*” indicates the transpose of a matrix; 0 denotes a null matrix of appropriate dimensions.

It may be noted that interconnection conditions 4.41 have not been used for writing Eq. 4.44, which represents a rearrangement of individual matrices  $\mathbf{Z}_A$  and  $\mathbf{Z}_B$  given in Eq. 4.42. Relations 4.41 can now be substituted in the Eqs. 4.44 to eliminate  $V_q, V_r, i_q,$  and  $i_r$ . The resulting expression may be written as  $\mathbf{V}_p = [\mathbf{Z}_{AB}]i_p$ , where

$$[\mathbf{Z}_{AB}] = \begin{bmatrix} Z_{p_a} & 0 \\ 0 & Z_{p_b} \end{bmatrix} + \begin{bmatrix} Z_{p_a q} \\ -Z_{p_b r} \end{bmatrix} [Z_{q q + Z_{r r}}]^{-1} [Z_{q p_a} + Z_{r p_b}] \quad (4.45)$$

It is seen that the size of  $\mathbf{Z}_{AB}$  is  $(p_a + p_b) \times (p_a + p_b)$ . The second term on the right-hand side is a product of three matrices of sizes  $(p_a + p_b) \times q, q \times q,$  and  $q \times (p_a + p_b)$ , respectively. From a computational point of view, the most time-consuming step is the evaluation of the inverse of a matrix of size  $q \times q$ , where  $q$  is the number of interconnected ports.

**4.2.4.2 Desegmentation Method** There are several planar configurations that cannot be analyzed by the segmentation method discussed above. For example, the configuration shown in Fig. 4.20 cannot be partitioned into regular segments for which Green's functions are known. In cases like this, an alternative method called desegmentation [3,4] is useful. The concept of desegmentation can be explained by considering the example of a rectangular patch with a circular hole. Referring to Fig. 4.20, we note that, if a circular disk called segment  $\beta$  (Fig. 4.20c) is added to the configuration of Fig. 4.20a, the resulting configuration  $\gamma$  is a rectangular segment shown in Fig. 4.20b. Green's functions are known for both the circular (Fig. 4.20c) and rectangular (Fig. 4.20b) shapes, and therefore Z-matrices for characterizing both of these components may be derived. The desegmentation method allows us to derive the Z-matrix of the configuration  $\alpha$  shown in Fig. 4.20a when the Z-matrices of the rectangular segment in Fig. 4.20b and the circular segment in Fig. 4.20c are known. For deriving a relationship among the Z-matrices of the three shapes we consider a generalized configuration (shown in Fig. 4.21). Here, region  $\beta$  is not included in the  $\alpha$  segment. Ports  $p_1, p_2,$  and so on are external ports of  $\alpha$ . Characterization of  $\alpha$  is required with respect to these ports. In general,  $p$  ports

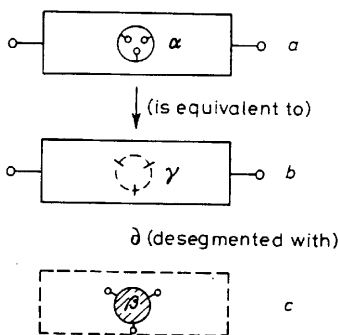


FIGURE 4.20 Concept of desegmentation.



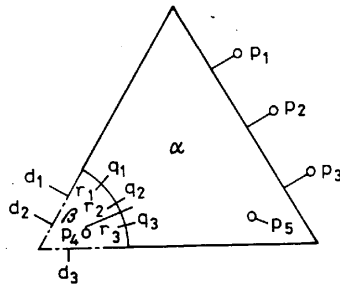


FIGURE 4.21 Port nomenclature used in desegmentation procedure.

may also be located on the part of the periphery of  $\alpha$  where the segment  $\beta$  is connected. An example of this is port  $p_4$  shown in Fig. 4.21. The Z-matrices of  $\beta$  and  $\gamma$  segments are known and may be written as

$$\mathbf{Z}_\beta = \begin{bmatrix} Z_{rr} & Z_{rd} \\ Z_{dr} & Z_{dd\beta} \end{bmatrix} \quad \text{and} \quad \mathbf{Z}_\gamma = \begin{bmatrix} Z_{pp\gamma} & Z_{pd} \\ Z_{dp} & Z_{dd\gamma} \end{bmatrix} \quad (4.46)$$

As in the case of segmentation, ports  $q$  (of  $\alpha$ ) and ports  $r$  (of  $\beta$ ) are numbered such that  $q_1$  is connected to  $r_1$ ,  $q_2$  to  $r_2$ , and so on. Ports  $d$  are unconnected (external) ports of the segment  $\beta$ . Evaluation of  $\mathbf{Z}_\alpha$  is simplified when the number of  $d$  ports is made equal to the number of  $q$  (or  $r$ ) ports. The number of  $q$  (or  $r$ ) ports depends on the nature of field variation along the  $\alpha$ - $\beta$  interface and, as in the case of segmentation, is decided by iterative computations. On the other hand, the number of  $d$  ports is arbitrary and can always be made equal to that of  $q$  (or  $r$ ) ports after that number has been finalized. Under these conditions, the impedance matrix for the  $\alpha$  segment can be expressed [26] in terms of Z-matrices of  $\beta$  and  $\gamma$  segments as

$$\mathbf{Z}_\alpha = -Z_{pp\gamma} - Z_{pd}\{Z_{dd\gamma} - Z_{dd\beta}\}^{-1}Z_{dp} \quad (4.47)$$

It may be noted that the size of  $\mathbf{Z}_\alpha$  is  $p \times p$  since all the specified ports of the  $\alpha$  segment have been numbered as  $p$  ports.

For implementation of the desegmentation method,  $d$  ports of the  $\beta$  segment need not be located on the periphery of the  $\beta$  segment. In fact, in the case of the rectangular patch with a circular hole (Fig. 4.19a), no region is available on the periphery of the circular  $\beta$  segment for locating  $d$  ports. As shown in Fig. 4.22,  $d$  ports may be located inside the circular region. In this case, three  $d$  ports— $d_1, d_2, d_3$ —are shown located inside the  $\beta$  segment. Since Green's functions are valid for any point on the segment (or on the periphery), the desegmentation procedure remains unchanged. More detailed discussion of the desegmentation method is contained in [3,4].

Segmentation and desegmentation methods are used for finding the input impedance at the feed point of the antenna (as a function of frequency). Voltages

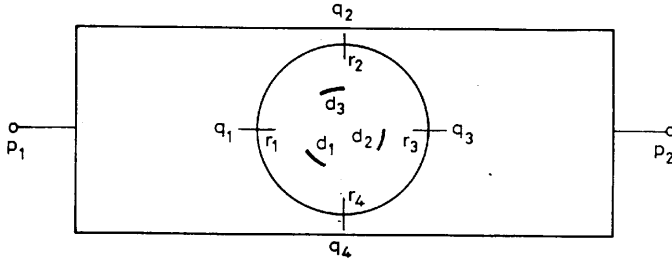


**FIGURE 4.22** A configuration where the desegmentation procedure requires location of  $d$  ports inside the  $\beta$  segment.

at the edges of the patch (where EANs are connected as shown in Figs. 4.5 and 4.6) are also calculated by extension of results discussed above. This voltage distribution is used to evaluate the radiation field of the antenna as discussed later in Section 4.3.4.

### 4.3 MNM FOR TWO-LAYER MICROSTRIP ANTENNAS

#### 4.3.1 Two-Layer Configurations for Circuit–Antenna Modules

In the two-layer configurations for integrated circuit–antenna modules, circuit elements are fabricated on the lower substrate and the radiating patches are located on the upper substrate. The excitation of the radiating patch is due to electromagnetic coupling between the patch and the feed circuitry on the lower level underneath the patch. The advantages of using two-layer configurations are (1) flexibility in design for optimizing both circuit and antenna functions, thus providing the best surface real estate usage; (2) increased patch to ground plane spacing, implying an increase in radiated power and, consequently, increased antenna bandwidth and efficiency; and (3) a decrease in the spacing between the feed circuitry and the ground plane, leading to a reduction in spurious radiation from the circuit discontinuities [27–29].

Two types of structures, suitable for monolithic and hybrid integration, respectively, have been suggested. A typical monolithic configuration is shown in Fig. 4.23. The lower substrate in this case is GaAs ( $\epsilon_r = 12.9$ ) and the upper layer is a thin passivating layer, typically silicon nitride ( $\epsilon_r = 7$ ). The height of the passivating layer is very small (typically 1–2  $\mu\text{m}$ ) compared to the GaAs substrate (100–150  $\mu\text{m}$ ). In the monolithic configuration, the dielectric constants and the heights of the two layers are constrained by the monolithic technology requirements and are thus not designable parameters for antenna design.

A two-layer configuration suitable for hybrid integration is shown in Fig. 4.24. In this case the thickness of the lower layer, used to locate circuit elements, is much smaller than that of the upper layer. The lower layer has a dielectric constant that is much higher than the upper layer and it becomes possible to design a feeder patch

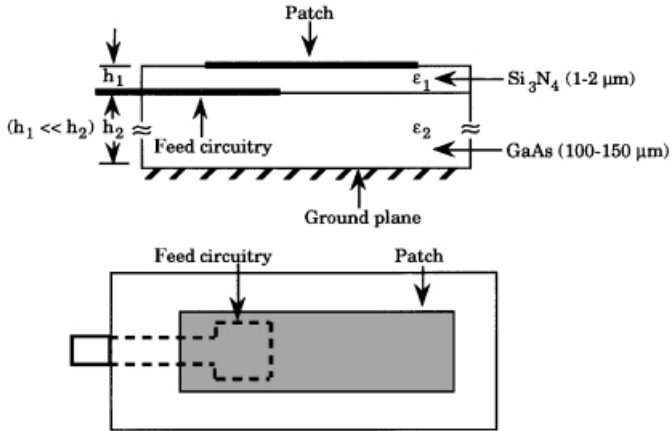


FIGURE 4.23 A monolithic two-layer configuration.

(in addition to other circuit elements) on the lower substrate such that it is resonant at approximately the same frequency as that of the radiating patch.

### 4.3.2 Two-Layer Patch Antennas

The two-layer microstrip patch antenna is the precursor of the two-layer integrated circuit–antenna modules. The early investigations into electromagnetically coupled two-layer antennas were on printed microstrip dipoles [30]. Oltman and Huebner [30] examined various configurations of printed dipoles for optimum characteristics, such as bandwidth, efficiency, and radiation, and proposed a circuit model based on transmission line analysis. A rigorous moment-method solution to the printed dipole problem has also been reported [31].

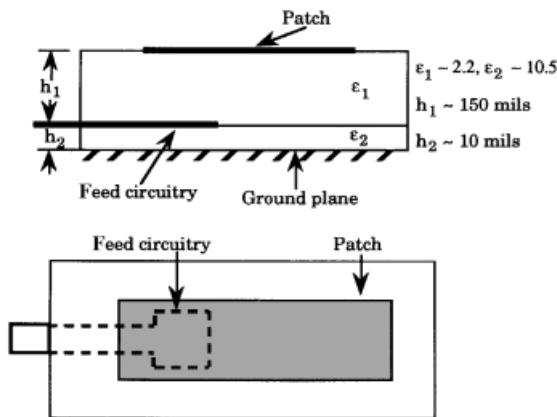


FIGURE 4.24 A hybrid two-layer configuration.

An experimental study of a proximity coupled (electromagnetically coupled) microstrip patch antenna has been presented by Pozar and Kaufman [32], demonstrating a bandwidth of 13%. The study also shows cross-polarization levels to be 20 dB below the copolarization levels. A generalized moment-method analysis of a rectangular microstrip patch antenna fed by a microstrip line has been developed [33–34]. A similar type of moment-method analysis on circular patch antenna has also been carried out [35], and the effect of the line feed and patch overlap on the VSWR has been investigated. These full wave analyses have led to the development of graphical guidelines for electromagnetically fed microstrip patch antennas for both the rectangular and circular shapes [36]. Extensive experimental investigations of electromagnetically coupled rectangular patch antennas, including a detailed parametric study, have been reported [37–39].

### 4.3.3 The MNM Approach for Two-Layer Patch Antennas

As discussed for single-layered configurations, the multiport network model (MNM) approach is an extension of the cavity model that essentially converts the electromagnetic boundary-value parameter of the radiating structure into an equivalent network problem. In this treatment, the antenna configuration is modeled by three (or more) interconnected multiport subnetworks. Each of these subnetworks represents the fields associated with the distinct physical regions of the radiating configuration. The procedure involves the characterization of each of the subnetworks by an equivalent Z-matrix and combining them to yield an overall network representation of the entire radiating configuration. The relevant antenna characteristics such as the input impedance and radiation characteristics are then evaluated from the overall network.

Consider the two-layer EMC radiating patch configuration of Fig. 4.25. The configuration shown is suitable for integration in hybrid circuits since the height of its lower substrate is much smaller than the upper substrate ( $h_2 \ll h_1$ ). To illustrate the underlying idea the MNM model will be developed for this hybrid case.

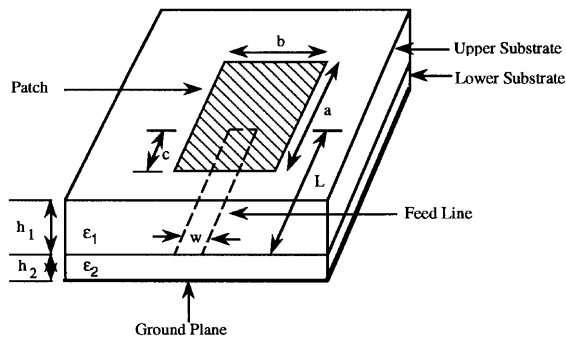


FIGURE 4.25 The two-layer EMC patch configuration.

In Fig. 4.25, the excitation of the radiating patch takes place by electromagnetic coupling between the feed circuitry on the lower layer and the radiating patch on the upper layer. This method of excitation differs in its mechanism from the conventional one-layer microstrip line feed, which is located on the same substrate as the patch and makes physical contact with it. In developing an MNM model for this two-layer configuration the issue of excitation of the patch by electromagnetic coupling has to be addressed. The fields associated with the feed structure and the radiating patch are identified and modeled separately by their respective subnetwork components. The fields responsible for the radiated power and the power loss due to surface waves are also delineated and modeled by another subnetwork component. Finally, the subnetworks are combined to construct the overall network model of the radiating configuration. In the following discussion, each of the subnetworks is discussed in detail.

**4.3.3.1 The Patch Network (PN)** The microstrip patch antenna, regardless of the method of excitation used, is essentially a resonant structure wherein the field distribution in the region underneath the patch resembles that of a resonant electromagnetic cavity. The PN accounts for the electromagnetic fields in the region underneath the radiating patch. This region is viewed as a two-layer open cavity surrounded by perfect magnetic walls (zero tangential magnetic field) on the sides and perfect electric walls (zero tangential electric field) on the top and bottom as shown in Fig. 4.26.

The electromagnetic field distribution in the cavity is expanded in terms of an infinite series of modes satisfying the boundary conditions at the cavity walls [40].

*Modeling the Excitation* The radiating configuration is excited by a feed structure (usually in the form of a metallic strip) underneath the patch at the interface of the two layers of the substrate. The fields associated with this feed structure can be considered as “source” fields for the radiating patch. From this viewpoint, the coupling from the feed structure to the radiating patch is due to the fringing fields at the periphery of the feed structure as shown in Fig. 4.27.

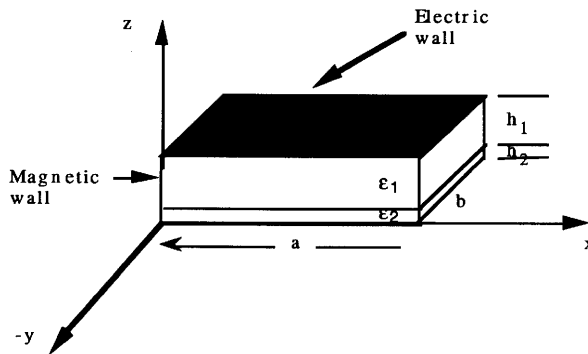
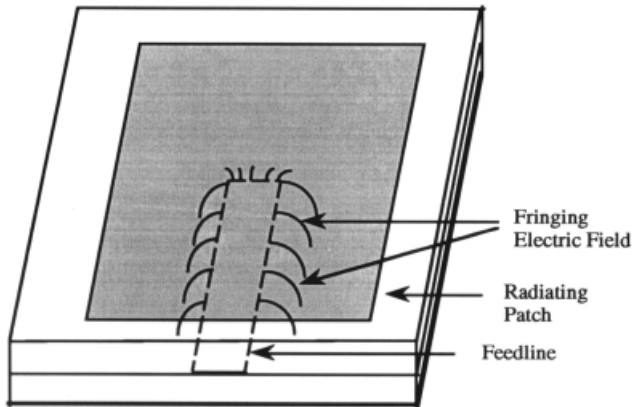


FIGURE 4.26 A two-layer open electromagnetic cavity.



**FIGURE 4.27** Fringing electric field at the feedline periphery.

The effect of these fringing fields as sources of excitation is modeled by placing equivalent magnetic current elements at the periphery of the feed structure. The justification for this procedure follows from the Schelkunoff's equivalence theorem [40,41].

*Development of the Z-Matrix for PN* The development of the Z-matrix for the PN follows from the analysis of the cavity fields. The edges of the patch are subdivided into smaller segments and ports are placed on each of these segments. The number of segments is determined on the basis of the field variation along the edges of the patch. The more rapid the field variation along a patch edge, the larger the number of ports that must be placed along it so that the variations are accounted for accurately. The patch is typically excited in the vicinity of its dominant mode ( $TM_{100}$ ) for which the field distribution along the radiating edges is invariant. Therefore, the number of ports along the radiating edges in this case is kept to a minimum to reduce the computation time, the actual number being determined iteratively to ensure numerical convergence. The contribution to the radiated power from the nonradiating edges of the patch is relatively small but is needed when the value of the cross-polarization level is required.

The edges of the feed structure are also subdivided into a number of smaller segments and ports are located on each of them. The locations of the ports in this case represent the presence of equivalent magnetic current sources.

A schematic diagram showing the placement of ports along the patch and the feedline is shown in Fig. 4.28. The fields at the "patch ports" due to a magnetic current element at a "feed port" are computed and a hybrid matrix representation is obtained. The Z-matrix is obtained by an appropriate transformation of the hybrid matrix, details of which are presented later in the section.

**4.3.3.2 The Feed Network (FN)** The FN models the fields associated with the feed structure located at the interface of the two layers. The feed structure for the EMC patch is typically a stripline or a stepped width stripline as shown in Fig. 4.29.

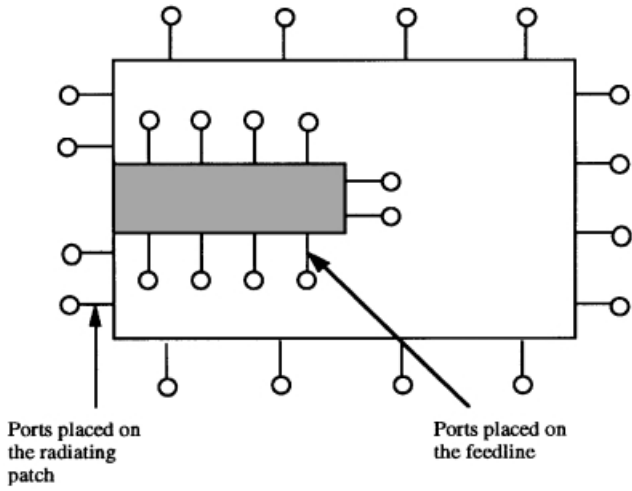
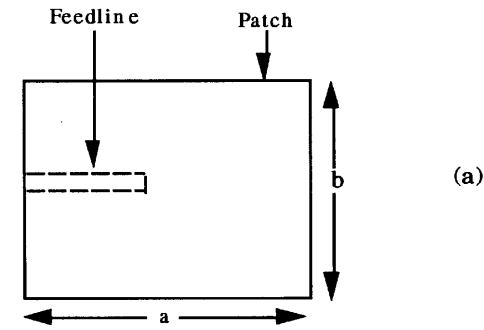
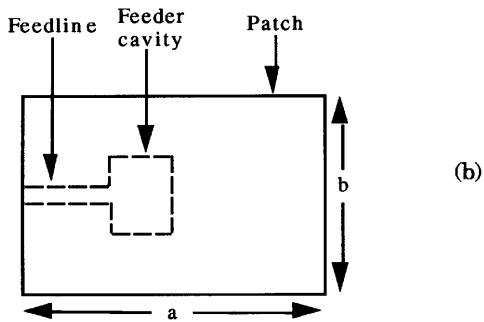


FIGURE 4.28 Ports placement on the patch and feedline.



(a)



(b)

FIGURE 4.29 Feed structures for patch excitation.

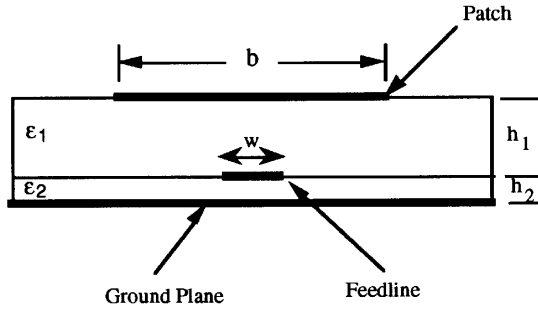


FIGURE 4.30 Cross-sectional view of patch and feedline.

Consider the configuration of Fig. 4.25, where the patch is excited by a simple feedline underneath it. A cross section of this arrangement, shown in Fig. 4.30, shows a resemblance to a two-layer asymmetric stripline configuration with the feedline and bound on the top and the bottom by the patch and the ground plane, respectively. The feedline configuration is thus treated as a transmission line structure supporting the quasi-TEM mode of propagation.

The static spectral domain technique is applied to analyze the asymmetric stripline configuration and yields its effective dielectric constant and characteristic impedance. An equivalent planar waveguide model is constructed from these parameters and two-dimensional planar analysis [42] is used to compute the Z-matrix of the feed structure. This completes the characterization of the FN.

A typical FN has one port at the input and several output ports that get connected to the input ports of the PN. The FN itself may consist of two or more subnetworks depending on the layout of the feed configuration as shown in Fig. 4.31. In this figure, segment (y) represents the planar waveguide model for the portion of the feed structure underneath the patch and the ports of this segment are connected to the

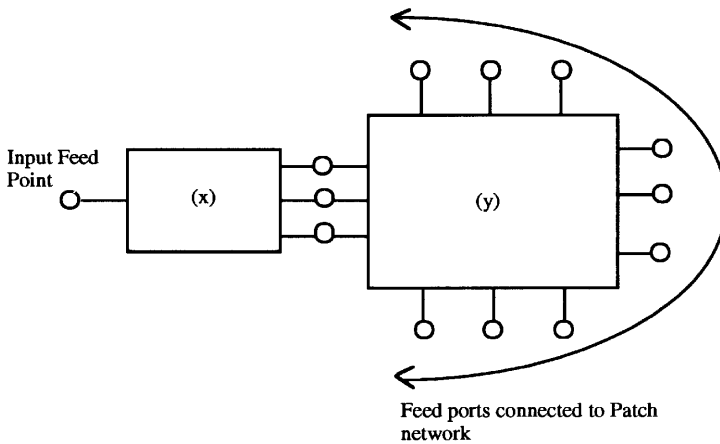


FIGURE 4.31 Block diagram of the feed network.



ports of the PN. Segment ( $x$ ) represents the short section of microstrip line outside the patch, as is usually the case for a practical configuration.

An interesting feed arrangement is possible if a feeder patch is located on the lower substrate (Fig. 4.29b) to act as a source of excitation to the radiating patch on the upper substrate. This feeder patch can be designed to have dimensions that are smaller than, and a resonance frequency close to, that of the radiating patch. These objectives can be met if the lower substrate has a higher dielectric constant than the upper one.

**4.3.3.3 The Edge Admittance Network (EAN)** As in the case of single-layer microstrip patch antennas, the edge admittance network (EAN) models the fields external to the patch, namely, the fringing fields, the radiated field, and the surface-wave field. Development of the edge admittance network is identical to that discussed for the single-layer patch in Section 4.2.3.

**4.3.3.4 The Overall Network** The overall network model of the radiating configuration is obtained by connecting the three networks (PN, FN, and EAN) together. The three Z-matrices representing the PN, FN, and EAN are combined using the segmentation method [3,4,43] discussed earlier in Section 4.2.4. The procedure results in a Z-matrix ( $1 \times 1$ ), which represents the input impedance of the antenna structure. The overall network model is as shown in Fig. 4.32.

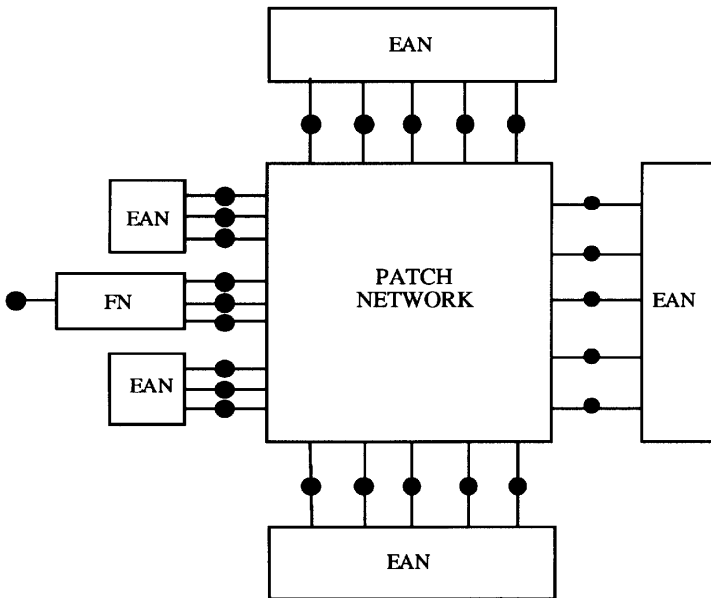


FIGURE 4.32 Overall multiport network model of the configuration.

The segmentation method also gives the voltages at the PN–EAN connected ports. The voltage distribution so obtained is expressed as an equivalent magnetic-current distribution and is used for the computation of the radiation field and the far-field patterns of the radiating configuration.

#### 4.3.4 Mathematical Formulation

In this section a brief discussion of the mathematical development of the MNM model for a two-layer circuit–antenna radiating configuration is presented.

**4.3.4.1 Voltages at the Edges of the Patch** The evaluation of the Z-matrix of the PN requires computation of the voltages induced at the radiating edges of the patch due to equivalent magnetic current elements placed at the periphery of the feed structure.

The voltage between the ground plane and a port on the edge of a patch is, by definition,

$$v = - \int_0^h \mathbf{E} \cdot d\mathbf{l} \quad (4.48)$$

where  $d\mathbf{l}$  is the incremental length vector in the direction of the contour of integration.

Using the standard procedure for evaluating the cavity fields due to a source excitation [40], the total contribution to the voltage from summing all the modes may be written as

$$v = - \sum_i B_{iE} \int_0^h \mathbf{E}_i \cdot d\mathbf{l} \quad (4.49)$$

where

$$B_{iE} = \frac{j\omega_i}{\omega^2 - \omega_i^2} \int_v M H_i^* dV \quad (4.50)$$

$M$  being the infinitesimal magnetic-current element and  $H_i$  being the source-free cavity modes;  $\omega_i$  are the corresponding resonance frequencies. The integration in Eq. 4.49 is along the  $z$ -coordinate (Fig. 4.26) and hence

$$v = - \sum_i B_{iE} \int_0^h \mathbf{E}_i \cdot \hat{\mathbf{z}} dz \quad (4.51)$$

where  $\hat{\mathbf{z}}$  is the unit vector in the  $z$ -direction.

Since the integrand in Eq. 4.51 comprises a dot product, the only contribution to the integral comes from the  $z$ -component of the electric field. Substituting the modal expression for  $E_z$  gives

$$v = - \sum_i B_{iE} \int_0^h E_{0i} \cos \alpha_1 x \cos \alpha_2 y \cos \alpha_3 z \, dz \quad (4.52)$$

where  $E_{0i}$  represents the modal magnitude coefficient of the electric field component  $E_z$ .

The integration in Eq. 4.52 is only over the  $z$ -coordinate with the result that the voltage  $v$  is equal to zero if  $\alpha_3$  is different from zero. The implication is that higher order modes varying in the  $z$ -direction do not contribute to the edge voltage. When  $\alpha_3 = 0$ , Eq. 4.52 can be reduced further to

$$v = -h \sum_i E_{0i} B_{iE} \cos \alpha_1 x \cos \alpha_2 y \quad (p = 0) \quad (4.53)$$

A detailed mathematical development is found in [44]. The formulation developed here requires a summation over an infinite number of modes to obtain the total fields in the cavity. In practice, however, computation is terminated after a finite number of modes determined by the convergence of the series.

**4.3.4.2 Equivalent Current Over a Port Width** In the process of computing the  $Z$ -matrix of the PN, an intermediate hybrid matrix is first evaluated as an intermediate step. The evaluation of a submatrix of this hybrid matrix necessitates the calculation of the equivalent electric current into (or out of) a port due to a magnetic-current element source located along the width of the port.

The calculation developed here is for the case where the magnetic-current element is oriented in the  $y$ -direction (as shown in Fig. 4.33). Extension to the case of an arbitrarily oriented port is a minor modification of the treatment given herein.

In Fig. 4.33, the magnetic-current element is centered at  $(a_0, b_0)$ . The equivalent linear current density into the width of the port is related to the tangential component of the magnetic field by  $\mathbf{J} = \hat{\mathbf{n}} \times \mathbf{H}$ , where  $\hat{\mathbf{n}}$  is the unit outward normal vector to the surface. Since the port in Fig. 4.33 is oriented in the  $y$ -direction, the desired component of the equivalent electric current into (or out of) the port is  $J_x$ .

Recognizing that any contribution to  $J_x$  comes solely from  $H_y$ , the current  $I$  is written as

$$I = \int_{b_0-w/2}^{b_0+w/2} \sum_i B_{iH} \mathbf{H}_i \cdot \hat{\mathbf{y}} \, dy \quad (4.54)$$

where  $\hat{\mathbf{y}}$  is a unit vector in the  $y$ -direction, and

$$B_{iH} = \frac{j\omega}{\omega^2 - \omega_i^2} \int_v M H_i^* \, dV \quad (4.55)$$

The integral in Eq. 4.54 is over the width of the port.

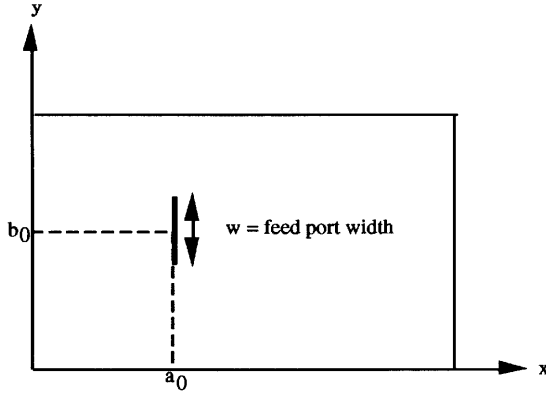


FIGURE 4.33 Current calculation at the feed port.

**4.3.4.3 Hybrid Matrix for PN** The hybrid matrix relating voltages and currents at the feed and the patch ports is defined by

$$\begin{bmatrix} \vec{V}_E \\ \vec{I}_F \end{bmatrix} = \begin{bmatrix} [H_{11}] & [H_{12}] \\ [H_{21}] & [H_{22}] \end{bmatrix} \begin{bmatrix} \vec{V}_F \\ \vec{I}_E \end{bmatrix} \tag{4.56}$$

- where  $\vec{V}_E$  = vector containing the edge ports' voltages
- $\vec{I}_E$  = vector containing the edge ports' currents
- $\vec{V}_F$  = vector containing the feed ports' voltages
- $\vec{I}_F$  = vector containing the feed ports' currents

The submatrix  $[H_{11}]$  relates the voltages at the edge ports to the impressed voltages at the feed ports. The expressions for the fields in the cavity derived earlier are used to calculate the voltages at the edge ports for a magnetic-current source excitation.

$[H_{12}]$  is the submatrix relating the edge port voltages to the edge port currents with the feed ports shorted. When the feed ports are shorted, the fields underneath the patch may be considered to have no variation in the  $z$ -direction. The configuration can therefore be treated as a two-dimensional planar structure and its  $Z$ -matrix evaluated from Green's function analysis [3,42]. The development of the  $Z$ -matrix from Green's function analysis of a planar rectangular segment has been discussed earlier in Section 4.2.2.

$[H_{21}]$  relates the currents and voltages at the feed ports with the edge ports open. Again, three-dimensional analysis is used to obtain this submatrix. The electric current is calculated from the  $H$ -field.

$[H_{22}]$  relates the currents at the feed ports due to impressed currents at the edge ports with the feed ports shorted. Two-dimensional analysis is applicable to this computation also. However, it can be shown that this submatrix is the negative transpose of  $[H_{11}]$ .

The Z-matrix for the PN is obtained by casting Eq. 4.56 in the following form:

$$\begin{bmatrix} \vec{V}_E \\ \vec{V}_F \end{bmatrix} = \begin{bmatrix} [Z_{EE}] & [Z_{EF}] \\ [Z_{FE}] & [Z_{FF}] \end{bmatrix} \begin{bmatrix} \vec{I}_E \\ \vec{I}_F \end{bmatrix} \quad (4.57)$$

where

$$[Z_{FF}] = [H_{21}]^{-1} \quad (4.58)$$

$$[Z_{FE}] = -[H_{21}]^{-1}[H_{22}] \quad (4.59)$$

$$[Z_{EF}] = [H_{11}][-H_{21}]^{-1} \quad (4.60)$$

$$[Z_{EE}] = [H_{12}] - [H_{11}][H_{21}]^{-1}[H_{22}] \quad (4.61)$$

**4.3.4.4 Segmentation and Far-Field Calculations** Once the Z-matrices of the feed network (FN), the patch network (PN), and the edge admittance network (EAN) are computed, they are combined by using the segmentation method to yield the overall  $[1 \times 1]$  impedance matrix of the radiating structure.

The FN is first combined with the PN and the resulting network is connected to the EAN to give the overall network representation of the radiating configuration. The segmentation method also yields the voltages at the edge ports so that the far-field radiation patterns of this configuration can be calculated.

The radiation vector is given by [12]

$$L = -2 \sum_n^{N_p} \hat{\mathbf{a}}_t W_n V_n e^{jk_0 \rho_n \sin \theta \cos(\phi - \phi_0)} \quad (4.62)$$

where  $W_n$  and  $V_n$  are the width and voltage, respectively, at the  $n$ th edge port and  $\hat{\mathbf{a}}_t$  is the unit tangential vector along the contour of the patch as shown in Fig. 4.34.

The  $E$ -field components of the radiation field are derived from Eqs. 4.32 and 4.33 and given by

$$E_\theta = -j \frac{\mathbf{L} \cdot \mathbf{a}_\phi}{2\lambda_0 r} e^{-jk_0 r} \quad (4.63)$$

and

$$E_\phi = j \frac{\mathbf{L} \cdot \mathbf{a}_\theta}{2\lambda_0 r} e^{-jk_0 r} \quad (4.64)$$

### 4.3.5 Examples

The MNM model developed for EMC patch antennas fed by a simple feedline has been compared with full wave analysis and experiment. The PMesh full wave analysis moment-method program developed at the University of Colorado at

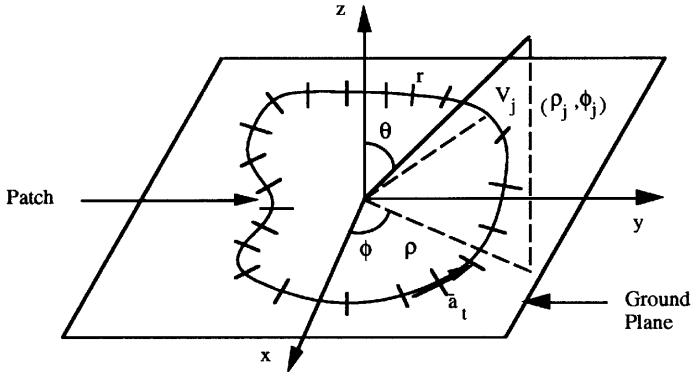


FIGURE 4.34 Patch geometry for far-field calculations.

Boulder [45] was used to investigate the configuration of Fig. 4.35. For the following parameters, the comparison with MNM is shown in Fig. 4.36:  $a = 2.5$  cm,  $b = 4$  cm,  $c = 1.25$  cm,  $w = 5$  mm,  $\epsilon_1 = \epsilon_2 = 2.2$ , and  $h_1 = h_2 = 1.58$  mm. For a more detailed discussion and for additional cases, the reader is referred to [44,46].

Additional studies of the radiating structure were also carried out to estimate the effect of the changes in parameters such as the width of the radiating patch, the dielectric constants of the substrates, and the width of the feedline.

**4.3.5.1 Effect of Patch Width on Input Impedance** For the following physical and electrical parameters, the case has been investigated experimentally [39] and also by using the MNM technique;  $a = 2.22$  cm,  $w = 2.4$  mm,  $L = 7.61$  cm,  $h_1 = 1.5874$  mm,  $h_2 = 0.794$  mm,  $\epsilon_1 = 2.2$ , and  $\epsilon_2 = 2.33$ .

Figure 4.37a shows the variation in the real part of the input impedance for a patch width  $b = 1$  cm. The experimental value of the input impedance is seen to

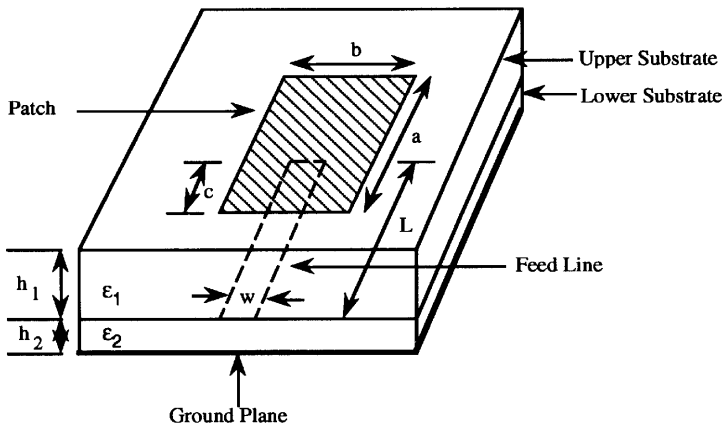
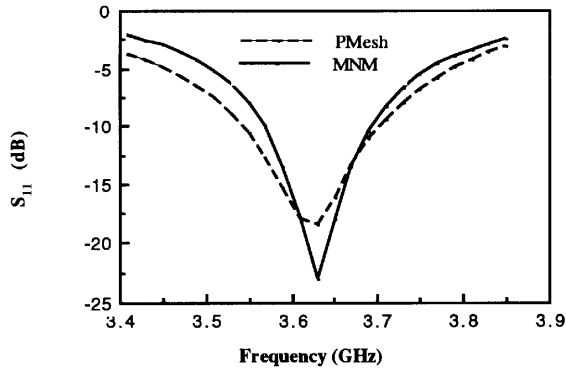


FIGURE 4.35 The two-layer configuration for an EMC patch.



**FIGURE 4.36**  $S_{11}$  versus frequency — PMesh and MNM. (From [46], copyright © 1998 by IEEE; reprinted with permission.)

peak at around  $c = 45\%$ , whereas the value obtained by the MNM reaches a maximum at  $c = 50\%$ .

Figure 4.37b shows the change in the real part of the input impedance for the case where the patch width  $b = 2$  cm.

Figure 4.37c shows the change in the real part of the input impedance for a patch width  $b = 3$  cm. Additional parametric results are found in [38,39].

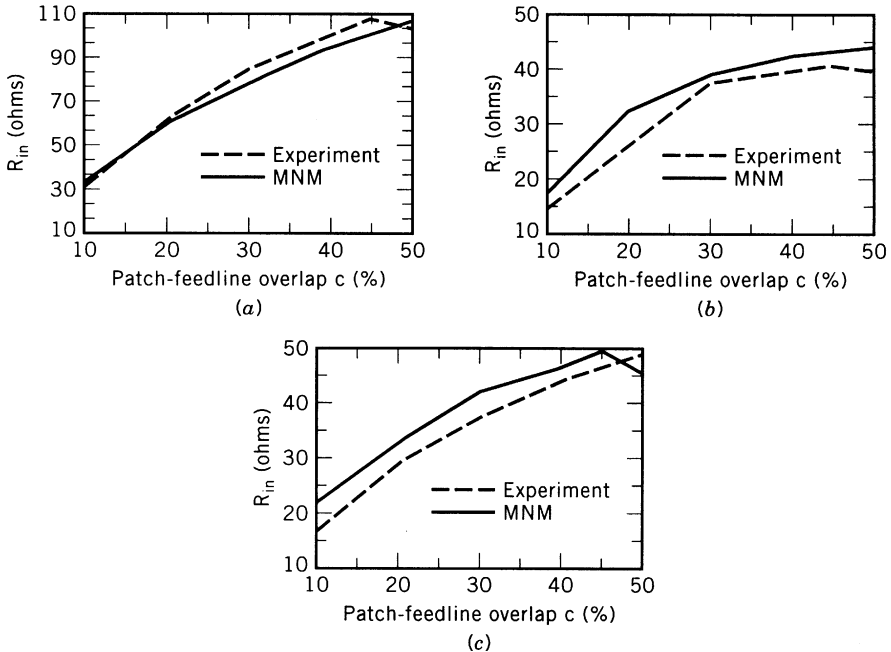


**FIGURE 4.37** Real part of input impedance with patch–feedline overlap: (a)  $b = 1$  cm; (b)  $b = 2$  cm; (c)  $b = 3$  cm. (From [46], copyright © 1998 by IEEE; reprinted with permission.)

Discussion presented in this section provides a network approach for analysis and design of two-layer integrated circuit–antenna modules with circuit elements located at the lower layer and radiating patch located at the upper layer. Although the configuration selected for discussion includes only a simple feedline at the lower layer, the method is also applicable when a more complicated circuit (including active devices) is fabricated at the lower layer.

## 4.4 MNM FOR INTEGRATED CIRCUIT–ANTENNA MODULES

### 4.4.1 Planar Circuit–Antenna Modules

As seen in other chapters of this book also, the simplest approach in integrating active devices and antennas together is to locate them on a single common substrate [47–54]. These types of circuit–antenna modules offer ease of fabrication. The design of such configurations is based on two subapproaches. In the first approach, the circuit and antenna functions are designed and tested separately and then connected together [47]. In the second approach [48–54], the antenna and circuit elements are designed concurrently, making it impractical to test them separately. Most of the examples in reported literature belong to this latter group. These include several configurations of oscillator–antennas using various types of diodes (Gunn, IMPATT, varactor) researched experimentally [55–59]. In this approach an active device is located either on the patch or on the substrate underneath the patch. Thus there is an intimate interaction between the fields associated with the device and the fields of the patch. Network analysis of some of these configurations has been presented in Chapter 3. Most of these analyses were based on the transmission line model for microstrip patches.

In this section we emphasize an analysis of single-layer microstrip patches with active devices incorporated in them based on the multiport network modeling of microstrip patches discussed in Section 4.2. Examples of varactor diode loaded and Gunn diode loaded patch antennas are presented.

### 4.4.2 Integration of Varactor Diodes with Patches

Varactor diodes may be used to tune the operating frequency of microstrip patch antennas. When a varactor diode is integrated with a radiating patch (as indicated in Fig. 4.38), it provides a variable capacitive reactance at the point of its location, thereby changing the resonance frequency of the patch. This scheme is attractive as it is simple to fabricate and the frequency tuning is easy to control.

The MNM approach for single-layer patches has been used for designing varactor loaded microstrip patch antennas. To test the validity of the MNM model, a sample configuration shown in Fig. 4.38 was investigated experimentally. The configuration was excited by a microstrip line and the measurements were done on an HP8510 network analyzer.



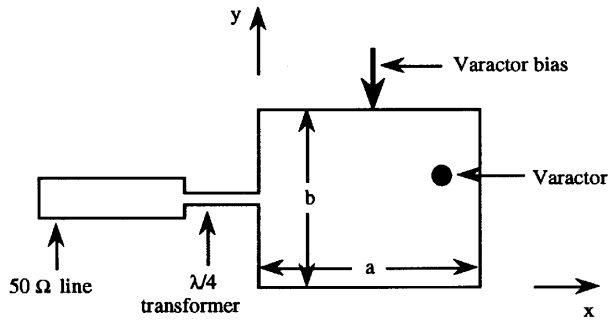


FIGURE 4.38 Gunn diode integrated with a radiating patch.

The patch was designed using MNM for an operating resonance frequency of 2.5 GHz with the following parameters:  $a = 3.914$  cm,  $b = 5$  cm, and  $h = 1.5748$  mm for  $\epsilon_r = 2.2$ . The main 50- $\Omega$  line had a length of 1.5 cm and a width of 4.866 mm. The length of the quarter-wave transformer was 2.262 cm and its width was 1.358 mm. The varactor used was MA4ST563 with a tuning capability ranging from 20 pF at 1-V bias to 2 pF at 20-V bias. The location of the varactor was at  $(x, y) = (3.5$  cm, 2.5 cm) (with origin at the lower left center). A comparison of theoretical simulation results, based on the MNM approach, with experimental results is shown in Table 4.1. The capacitance of the varactor in Table 4.1 is denoted by  $C$ , the resonance frequency of the patch by  $f$ , and the reflection coefficient by  $S_{11}$ .

From Table 4.1, it is seen that the MNM approach predicts a tuning range of 2.5 GHz to 1.15 GHz while experimental results indicate a range from 2.47 GHz to 1.06 GHz. It can also be observed that the impedance match ( $S_{11}$ ) of the patch antenna quickly deteriorates when the value of the varactor capacitance exceeds 5 pF.

Along with the experimental validation of varactor loaded patches with the MNM approach it is instructive to examine the effect of change in the varactor location on the resonance frequency of the patch. Table 4.2 shows the results of a simulation

TABLE 4.1 Varactor Loaded Patch—Comparison of MNM with Experiment

$C$ (pF)	Theory (MNM)		Experimental Results	
	$f$ (GHz)	$S_{11}$ (dB)	$f$ (GHz)	$S_{11}$ (dB)
0	2.5	-21.8	2.47	-14.3
2	2.25	-23.5	2.16	-23.3
5	1.83	-8.4	1.90	-11.2
10	1.48	-3.3	1.48	-8.1
15	1.31	-2.0	—	—
20	1.22	-1.5	—	—
25	1.15	-1.4	1.06	-12.9

**TABLE 4.2 Varactor Location Effects on Resonance Frequency Using MNM**

$c$ (pF)	$f_r$ (GHz)				
	$(x, y) = (2.2, 2.5)$	$(x, y) = (2.8, 2.5)$	$(x, y) = (3.5, 2.5)$	$(x, y) = (3.5, 3.5)$	$(x, y) = (3.5, 4.5)$
0	2.5	2.5	2.5	2.5	2.5
2	2.48	2.38	2.25	2.29	2.3
5	2.51	2.04	1.83	2.06	2.15
10	2.51	1.65	1.48	1.97	2.08
15	2.51	1.47	1.31	1.95	2.06
20	2.51	1.36	1.22	1.94	2.05
25	2.51	1.28	1.15	1.94	2.05

study carried out using MNM on the configuration shown in Fig. 4.38. The varactor is located at five different points on the patch and the change in resonance frequency for various values of capacitance is observed. The resonance frequency in the table is denoted by  $f_r$ , the capacitance by  $C$ , and the varactor location by  $x, y$  in centimeters.

The results in Table 4.2 indicate that when the varactor is located close to the center of the patch, that is, around  $(x, y) = (2.2 \text{ cm}, 2.5 \text{ cm})$ , the variation in resonance frequency, around its natural value (frequency when the varactor is not present) of 2.5 GHz, is minimal. This is to be expected as the electric field, underneath the patch and near the center of a radiating patch, is very small and hardly “sees” the presence of the varactor.

As the varactor location is varied along the resonant length of the patch and about the center of the patch width, the change in resonance frequency is seen to be pronounced when the location is close to the radiating edge of the patch. A change of resonance frequency from a value of 2.5 GHz to 1.15 GHz is seen for a location  $(x, y) = (3.5 \text{ cm}, 2.5 \text{ cm})$  within a corresponding capacitance range of 0 to 25 pF. This is accounted for by the fact that the electric field underneath the patch is close to its maximum value at this location. The variation of varactor location along the patch width is seen to diminish the range of variation of resonance frequency, as evidenced by the results of the last two columns of Table 4.2.

#### 4.4.3 Integration of Gunn Diodes with Patches

The Gunn diode is a two-terminal device that exhibits an RF negative resistance and falls in the class of devices known as “transferred electron devices” [60]. The key property of the Gunn diode that is exploited in its use in active patch antenna configurations is its ability to convert the dc bias energy to RF power output. The conversion efficiency of Gunn diodes is very small, typically less than 10%. In this section, the use of the Gunn diode as a source for the radiating patch is explored, a design procedure is proposed, and some experimental and simulation results are presented. The key step in this design is to take the known Gunn diode character-

istics and determine the most optimal location for its integration with a radiating microstrip patch.

For a Gunn diode to sustain oscillation, the external impedance presented at its terminals has to be the negative of the Gunn impedance. This impedance is determined by the mount location on the patch. Usually the location of the Gunn diode has been selected using the simple transmission line model for microstrip patches [55–57]. However, the transmission line approach does not take into account the reactive part of the Gunn impedance. The MNM technique provides information of the complete impedance at any arbitrary location underneath the patch and hence can be used to provide a more accurate design.

**4.4.3.1 The Design Procedure** The basic topology for integration of a Gunn diode with a radiating patch is shown in Fig. 4.39 and Fig. 4.40. The objective in the design process is to determine the coordinate location  $(x, y)$  of the Gunn diode that sustains oscillations and results in an optimum power output depending on the capability of the Gunn diode.

The first step involves characterization of the Gunn diode as shown in Fig. 4.41 [61]. Referring to that figure, the load impedance that the Gunn diode requires is plotted on the Smith chart with frequency and power output as the variable parameters. Thus if a Gunn diode is to be designed for integration with a radiating patch for oscillation at, say, 6 GHz, for a power output of, say, 100 mW, the Smith chart characterization in Fig. 4.41 provides the necessary impedance required for the

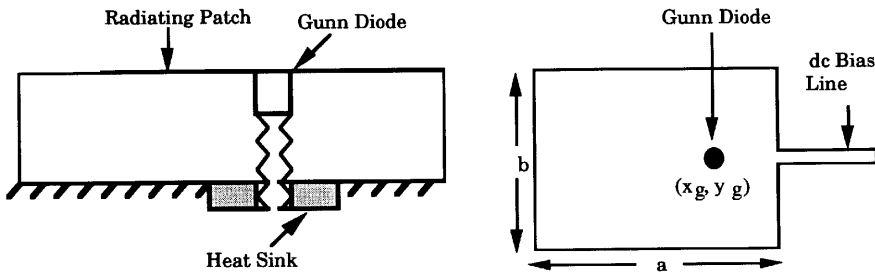


FIGURE 4.39 A varactor loaded microstrip patch antenna.

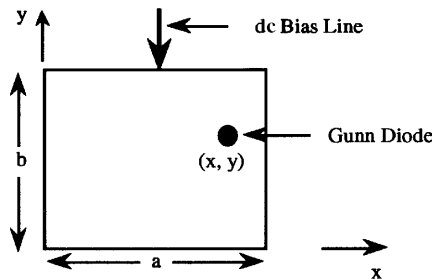


FIGURE 4.40 Topology of a Gunn diode integrated with a patch.



**FIGURE 4.41** Typical impedance characterization plot for Gunn diodes. (From MA-COM Semiconductor Products Master Catalogue, SP101, pp. 9–10, © 1988 M/A-COM; reprinted with permission.)

Gunn diode. With this value of impedance and frequency, the design problem reduces to finding the patch dimensions and the location underneath the patch that will yield the desired value of impedance. The MNM approach provides both the answers to the design problem.

Table 4.3 shows the simulation results using MNM for a radiating patch to be designed for an oscillation frequency of 6 GHz using the characterization for a MA49139 Gunn diode in Fig. 4.41 for the configuration shown in Fig. 4.40. The width  $b$  of the patch is kept constant at 2 cm; the dielectric constant  $\epsilon_r = 2.2$  and the substrate height  $h = 62$  mils.

From Table 4.3, it is seen that the location obtained from the simulation results is not centered around the patch width. Hitherto, the practice (using transmission line model) has been to center the Gunn diode along the patch width and then vary its

**TABLE 4.3 Design Example Using MNM for Gunn Diode–Patch Integration**

$P_{\text{out}}$ (mW)	$Z_{\text{in}}$ (W)	$a$ (cm)	$x$ (cm)	$y$ (cm)
100	$25 \pm j0$	2.17	0.52	1.27
600	$15 \pm j5$	1.53	0.50	1.32

location along the resonant length  $a$  to yield an empirical location for the mount. The MNM approach has the ability to specify precisely the location of the diode once the Gunn diode characteristics are known, without resorting to an empirical approach.

**4.4.3.2 Experimental Results** The Gunn diode–patch active antenna configuration of Fig. 4.40 was fabricated and tested. The dimensions of the patch were  $a = 1.3$  cm,  $b = 1.65$  cm, and  $h = 0.79375$  mm for an  $\epsilon_r = 2.2$ . The resonance frequency of a passive patch with the same physical characteristics is 7.18 GHz. Two MA49135 Gunn diodes belonging to the same batch of wafer with an operating frequency between 5 and 8 GHz and a minimum power output of 25 mW were selected. The bias voltage for diodes was maintained at 14 volts and the  $y$ -coordinate of the Gunn diode location was held fixed at 0.825 cm, that is, centered about the patch width. The antenna measurements were done with a setup consisting of a receiver horn antenna of 9-dB gain and a spectrum analyzer to record the resonance frequency and power output. The results of the investigations are recorded in Table 4.4.

From Table 4.4 it is observed that the frequency of oscillation,  $f_r$ , of the Gunn diode is a function of its location with respect to the patch. Likewise the power output ( $P$ ) of the active antenna configuration is a function of the Gunn diode location.  $Z_L$  is the value of the impedance seen at the location of the patch by the Gunn diode and the tabulated values were obtained by using the MNM model. For the two Gunn devices, it is observed that the maximum power output occurs when the real part of the impedance is in one case 13  $\Omega$  and in the other case 8  $\Omega$ . The order of magnitude of these values obtained is the same as those for the characterized Gunn diode in the Smith chart of Fig. 4.41. The respective frequencies are also seen to drop down to 6.84 GHz and 6.74 GHz, respectively. For an accurate design procedure for Gunn diode-excited microstrip patches it is essential that the Gunn diode characterization be available.

**4.4.3.3 Gunn Diode and Varactor Integrated on the Same Patch** In the preceding discussion, the radiating patch was mounted by a varactor diode alone for tuning of a resonant patch or a Gunn diode alone for excitation. If both these devices are mounted simultaneously on a resonant patch, it is possible to realize an active antenna with a tuning option. Figure 4.42 shows a schematic of such a configuration

**TABLE 4.4 Experimental Results for the Gunn Diode–Patch Configuration**

Gunn Diode Location $x$ (cm)	Gunn Diode #1			Gunn Diode #2		
	$f_r$ (GHz)	$P$ (mW)	$Z_L$ ( $\Omega$ )	$f_r$ (GHz)	$P$ (mW)	$Z_L$ ( $\Omega$ )
0.15	7.27	22.5	$95 - j66$	7.32	26.2	$64 - j63$
0.25	6.84	35.2	$13 + j54$	6.74	31.9	$8 + j45$
0.40	7.12	13.4	$51 = j33$	7.18	20.5	$57 + j7$
0.55	7.70	0.29	$0.65 + j14$	7.90	1.70	$0.42 = j16$

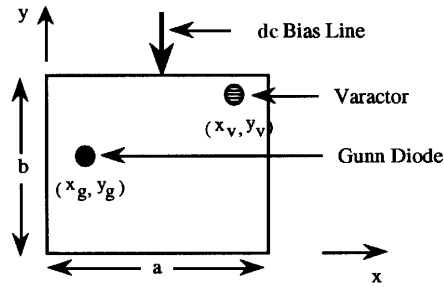


FIGURE 4.42 Gunn diode and varactor integrated with the patch.

where the varactor and the Gunn diode are located on the same patch. The details of the bias arrangement are not shown. Typically, two dc sources will be needed for biasing the two devices and a fine slot will have to be incised along the patch to isolate the two bias supplies.

The MNM method can be used to design such configurations for characterized Gunn diodes. In this example a sample design example is treated to demonstrate the iterative process used by MNM to arrive at the desired patch dimensions.

The starting point of the design procedure is the load impedance requirement of the Gunn diode at a certain design frequency. In the current example, assume this value to be a real  $8\ \Omega$  at the design frequency of 8 GHz. Furthermore, assume that the varactor capacitance ranges from 0.3 to 2 pF and that it is required that the tuning of the resonant frequency be possible either way (i.e., increase or decrease from the original value). Then, choose a value of the initial design capacitance to be, say, 1 pF. With these considerations in place for a substrate dielectric constant of 2.2, a run of the MNM procedure reveals the following design dimensions:

Length of patch,  $a = 1.94$  cm.

Width of patch,  $b = 2$  cm.

Varactor location,  $(x_v, y_v) = (1\text{ cm}, 1.5\text{ cm})$ .

Gunn diode location,  $(x_g, y_g) = (0.76\text{ cm}, 1.7\text{ cm})$ .

Impedance seen at Gunn diode location =  $7.98 + j0.03\ \Omega$ .

The number of iterations required to arrive at these values is 17. Analysis of the configuration using MNM with the dimensions arrived at yield a resonance frequency of 8.1 GHz with  $C = 0.3$  pF and 7.92 GHz with  $C = 2$  pF.

The multiport network modeling approach is well suited for other types of integrated circuit–antenna modules also.

## 4.5 SUMMARY AND REMARKS

In this chapter, a multiport network modeling (MNM) approach has been presented for analysis and design of single-layer and two-layer integrated circuit–antenna

modules. The MNM approach, which is an extension of the cavity model, was initially developed for single-layer microstrip patch antennas. Recently, the approach has been extended to two-layered electromagnetically coupled patch antennas [46].

As discussed in this chapter, the network theory based nature of this approach allows the passive circuits and active device models to be incorporated in the multiport network representation. We can look forward to more frequent applications of this method for the design of integrated circuit–antenna modules.

## REFERENCES

1. Gupta, K. C., "Multiport-network modeling approach for computer-aided design of microstrip patches and arrays," 1987 IEEE AP-S International Symposium on Antennas and Propagation, Blacksburg, VA, June 1987.
2. Benalla, A., and Gupta, K. C., "Multiport-network model and transmission characteristics of two-port rectangular microstrip antennas," *IEEE Trans. Antennas Propag.*, vol. AP-36, Oct. 1988, pp. 1337–1342.
3. Gupta, K. C., et al., *Computer-Aided Design of Microwave Circuits*, Artech House, Norwood, MA, 1981, Chaps. 8 and 11.
4. Gupta, K. C., and Abouzahra, M. D., *Analysis and Design of Planar Microwave Components*, IEEE Press, Piscataway, NJ, 1994.
5. Gogoi, A., and Gupta, K. C., "Wiener-Hopf computation of edge admittances for microstrip patch radiators," *AEU*, vol. 36, 1982, pp. 247–251.
6. Van de Capelle, A., et al., "A simple accurate formula for the radiation conductance of a rectangular microstrip antenna," *1981 IEEE AP-S Int. Symp. Antennas Propag. Dig.*, pp. 23–26.
7. Kuester, E. F., et al., "The thin-substrate approximation for reflection from the end of a slab-loaded parallel plate waveguide with application to microstrip patch antenna," *IEEE Trans. Antennas Propag.*, vol. AP-30, 1982, pp. 910–917.
8. Gupta, K. C., and Benalla, A., "Effect of mutual coupling on the input impedance and the resonant frequency of a rectangular microstrip patch antenna," *Natl. Radio Sci. Meeting (URSI) Dig.*, Jan. 1986, p. 226.
9. Benalla, A., and Gupta, K. C., "Faster computation of Z-matrices for rectangular segments in planar microstrip circuits," *IEEE Trans. Microwave Theory Tech.*, vol. MTT-34, 1986, pp. 733–736.
10. Gupta, K. C., and Abouzahra, M. D., "Analysis and design of four-port and five-port microstrip disc circuits," *IEEE Trans. Microwave Theory Tech.*, vol. MTT-33, 1985, pp. 1422–1428.
11. Okoshi, T., and Miyoshi, T., "The planar circuit—an approach to microwave integrated circuitry," *IEEE Trans. Microwave Theory Tech.*, vol. MTT-20, 1972, pp. 245–252.
12. James, J. R., Hall, P. S., and Wood, C., *Microstrip Antenna Theory and Design*, Peter Peregrinus, London, 1981.
13. Benalla, A., and Gupta, K. C., "Generalized edge-admittance network for modeling of radiation from microstrip patch antennas," *Natl. Radio Sci. Meeting (URSI) Book of Abstracts*, Jan. 1992, p. 65.

14. James, J. R., and Hall, P. S. (eds.), *Handbook of Microstrip Antennas*, Peter Peregrinus, London, 1989.
15. Chew, W. C., and Kong, J. A., "Microstrip capacitance for circular disc through matched asymptotic expansions," *SIAM J. Appl. Math.*, vol. 42, 1982, pp. 302–317.
16. Kuester, E. F., "Explicit approximation for the static capacitance of a microstrip patch of arbitrary shape," *J. Electromagnetic Waves Appl.*, vol. 2, no. 1, 1987, pp. 103–135.
17. Van Lil, E. H., and Van de Capelle, A. R., "Transmission line model for mutual coupling between microstrip antennas," *IEEE Trans. Antennas Propag.*, vol. AP-32, 1984, pp. 816–821.
18. Balanis, C. A., *Antenna Theory Analysis and Design*, Wiley, New York, 1982, p. 169.
19. Benalla, A., and Gupta, K. C., "Multiport network approach for modeling mutual coupling effects in microstrip patch antennas and arrays," *IEEE Trans. Antennas Propag.*, vol. AP-37, Feb. 1989, pp. 148–152.
20. Jedlicka, R. P., et al., "Measured mutual coupling between microstrip antennas," *IEEE Trans. Antennas Propag.*, vol. AP-29, 1981, pp. 147–149.
21. Tu, Y., and Gupta, K. C., "Mutual coupling between radiating edges of a microstrip patch antenna with a cover layer," *Electromagnetics*, vol. 9, 1989, pp. 259–271.
22. Pozar, D. M., "Input impedance and mutual coupling of rectangular microstrip antennas," *IEEE Trans. Antennas Propag.*, vol. AP-30, 1982, pp. 1191–1196.
23. Jackson, D. R., et al., "An exact mutual coupling theory for microstrip patches," *1987 IEEE AP-S Int. Symp. Antennas Propagat. Dig.*, vol. 2, 1987, pp. 790–793.
24. Okoshi, T., and Takeuchi, T., "Analysis of planar circuits by segmentation method," *Electron. Commun. Jpn.*, vol. 58-B, 1975, pp. 71–79.
25. Chadha, R., and Gupta, K. C., "Segmentation method using impedance-matrices for analysis of planar waveguide circuits," *IEEE Trans. Microwave Theory Tech.*, vol. MTT-29, 1981, pp. 71–74.
26. Sharma, P. C., and Gupta, K. C., "An alternative procedure for implementing desegmentation method," *IEEE Trans. Microwave Theory Tech.*, vol. MTT-32, 1984, pp. 1–4.
27. Lewin, L., "Radiation from discontinuities in stripline," *Proc. IEE*, vol. 107C, 1960, pp. 163–170.
28. Wood, C., Hall, P. S., and James, J., "Radiation conductance of open-circuit low dielectric constant microstrip," *Electron. Lett.*, vol. 14, Feb. 1978, pp. 121–123.
29. Abouzahra, M. D., and Lewin, L., "Radiation from microstrip discontinuities," *IEEE Trans. Microwave Theory Tech.*, vol. MTT-27, Aug. 1979, pp. 722–723.
30. Oltman, H. G., and Huebner, D. A., "Electromagnetically coupled microstrip dipole," *IEEE Trans. Antennas Propag.*, vol. AP-29, Jan. 1991, pp. 151–157.
31. Katehi, P. B., and Alexopoulos, N. G., "On the modeling of electromagnetically coupled microstrip antennas—the printed strip dipole," *IEEE Trans. Antennas Propag.*, vol. AP-32, Nov. 1984, pp. 1179–1186.
32. Pozar, D. M., and Kaufman, B., "Increasing the bandwidth of a microstrip antenna by proximity coupling," *Electron. Lett.*, vol. 23, Apr. 1987, pp. 368–369.
33. Pozar, D. M., and Voda, S. M., "A rigorous analysis of a microstrip fed patch antenna," *IEEE Trans. Antennas Propag.*, vol. AP-35, Dec. 1987, pp. 1343–1350.



34. Legay, H., et al., "Etude theorique et experimentale d'antennas plaques alimentees par couplage de proximite a une line microruban," *Ann. Telecommunications*, vol. 45, no. 3-4, 1990, pp. 192-202.
35. Davidovitz, M., and Lo, Y. T., "Rigorous analysis of a circular patch antenna excited by a microstrip transmission line," *IEEE Trans. Antennas Propag.*, vol. AP-37, Aug. 1989, pp. 949-958.
36. Splitt, G., and Davidovitz, M., "Guidelines for design of electromagnetically coupled patch antennas on two-layer substrates," *IEEE Trans. Antennas Propag.*, vol. AP-38, July 1990, pp. 1136-1140.
37. Roy, J. S., et al., "Some experimental investigations on electromagnetically coupled microstrip antennas on two-layer substrates," *Microwave Opt. Technol. Lett.*, vol. 4, May 1991, pp. 236-238.
38. Karmakar, N. C., and Bhattacharya, A., "Electromagnetically coupled patch antenna— theoretical and experimental investigations," *Microwave Opt. Technol. Lett.*, vol. 5, Mar. 1992, pp. 115-118.
39. Karmakar, N. C., and Bialkowski, M. E., "Experimental investigations into an electromagnetically coupled microstrip patch antenna," *Microwave Opt. Technol. Lett.*, vol. 5, Aug. 1992, pp. 447-453.
40. Harrington, R., *Time Harmonic Electromagnetic Fields*, McGraw-Hill, New York, 1961.
41. Balanis, C., *Advanced Engineering Electromagnetics*, Wiley, New York, 1989.
42. Okoshi, T., *Planar Circuits for Microwaves and Lightwaves*, Springer-Verlag, New York, 1985.
43. Gupta, K. C., and Sharma, P. C., "Segmentation and desegmentation techniques for analysis of two-dimensional microstrip antennas," *IEEE AP-S Symp. Dig.*, 1981, pp. 19-22.
44. Parrikar, R. P., *Network Modeling of Electromagnetically Coupled and Active Microstrip Patch Antennas*, Ph.D. Dissertation, Department of Electrical and Computer Engineering, University of Colorado, Boulder, CO, 1993.
45. Chang, D. C., and Zheng, J. X., "Electromagnetic modeling of passive circuit elements in MMIC," *IEEE Trans. Microwave Theory Tech.*, vol. MTT-40, Sept. 1992, pp. 1741-1747.
46. Parrikar, R. P., and Gupta, K. C., "Multiport network model for CAD of electromagnetically coupled microstrip patch antennas," *IEEE Trans.*, vol. AP-46, no. 4, Apr. 1998, pp. 475-483.
47. Hall, P. S., "Analysis of radiation from active microstrip antennas," *IEE Proc. Microwave Antennas Propag.*, vol. 141, no. 5, Oct. 1994, pp. 359-366.
48. Chang, K., Hummer, K. A., and Gopalakrishnan, G. K., "Active radiating element using FET source integrated with microstrip patch antenna," *Electron. Lett.*, vol. 24, no. 21, 1988, pp. 1347-1348.
49. Birkeland, J., and Itoh, T., "Two-port FET oscillators with applications to active arrays," *IEEE Microwave Guided Wave Lett.*, vol. 1, no. 5, May 1991, pp. 112-113.
50. Heinbockel, J., and Mortazawi, A., "A periodic spatial power combining MESFET oscillator," *IEEE MTT-S Int. Microwave Symp. Dig.*, 1992, pp. 545-548.
51. Birkeland, J., and Itoh, T., "FET-based planar circuits for quasi-optical sources and transceivers," *IEEE Trans. Microwave Theory Tech.*, vol. MTT-37, no. 9, Sept. 1989, pp. 1452-1459.

52. Birkeland, J., and Itoh, T., "An FET oscillator element for spatially injected locked arrays," *IEEE MTT-S Int. Microwave Symp. Dig.*, 1992, pp. 1535–1538.
53. Camilleri, N., and Bayraktaroglu, B., "Monolithic millimeter-wave impatt oscillator and active antenna," *IEEE MTT-S Int. Microwave Symp. Dig.*, 1988, pp. 955–958.
54. Fusco, V., and Burns, H., "Synthesis procedure for active integrated radiating elements," *Electron. Lett.*, vol. 26, no. 4, 1990, pp. 263–264.
55. Thomas, H., Fudgand, D., and Morris, G., "Gunn source integrated with microstrip patch," *Microwaves RF*, Feb. 1985, pp. 88–91.
56. Hummer, K., and Chang, K., "Microstrip active antennas and arrays," *IEEE MTT-S Int. Microwave Symp. Dig.*, 1988, pp. 963–966.
57. Chang, K., Hummer, K., and Klein, J., "Experiments on injection locking of active antenna elements for active phased arrays and spatial power combiners," *IEEE Trans. Microwave Theory Tech.*, vol. MTT-37, no. 7, July 1989, pp. 1078–1084.
58. York, R., and Compton, R., "Dual-device active patch antenna with improved radiation characteristics," *Electron. Lett.*, vol. 28, no. 11, May 1992, pp. 1019–1021.
59. York, R., and Compton, R., "A  $4 \times 4$  active array using Gunn diodes," *IEEE AP-S Symp. Dig.*, 1990, pp. 1146–1149.
60. Hobson, G. S., *The Gunn Effect*, Clarendon Press, Oxford, 1974.
61. *Semiconductor Products Master Catalog*, M/A-COM, 1988.

CHAPTER FIVE

---

# Full Wave Analysis in the Frequency Domain

---

**RAPHAEL GILLARD, M'HAMED DRISSI, and JACQUES CITERNE**  
LCST  
INSA Rennes  
CNRS UPRES A 6075  
Rennes, France

## 5.1 INTRODUCTION

Traditionally, components and active devices have been located far away from the antenna terminals within metallic enclosures. Recently, active solid-state devices have successfully been integrated onto planar radiating elements [1,2]. Prototype active arrays have been fabricated with microstrip antennas and associated diodes [3], MESFETs [4], or amplifiers [5] as the active elements. The obtained results have shown an improvement in performance, such as power gain and bandwidth [6]. On the other hand, power-combining techniques have been developed to overcome the output power limitation; a variety of quasi-optical configurations, which include oscillators, amplifiers, and mixers, have been investigated [7]. Unfortunately, most of these developments are still obtained using a separated approach: that is, active devices, discontinuities, and radiating elements are modeled independently from each other and connected via transmission lines. Consequently, the previous approach is limited to cases where the electromagnetic mutual coupling is supposed

to be negligible and hence the advantages, which can be obtained from the miniaturization and the optimization of the spatial location of the active device, are compromised. Furthermore, due to the direct relationship between the current distributions and the fields, this last approach allows neither the calculation of the radiating patterns for the active antenna nor their optimization. Only a global approach could overcome the problems associated with complex and highly integrated systems, in which there is no obvious distinction or boundary between the lumped and the distributed parts.

Two main strategies have been used to develop global electromagnetic approaches. The first one directly includes the representation of the lumped elements as additional boundary conditions in the electromagnetic formulation. It has been experimented with in both the time domain [8] and the frequency domain [9] using several different full wave analyses. With such a strategy, an actual global and self-sufficient tool is obtained that is independent of any particular environment. However, each new active circuit to be analyzed must be described in the electromagnetic simulator using data tables or explicit formulas. This can become a cumbersome task when the inserted circuit is a complex nonlinear one. In contrast, the second strategy benefits from the numerous libraries that are now available in commercial circuit simulators. It does, in fact, combine an electromagnetic simulator (for the passive distributed part of the studied structure) with a commercial circuit simulator (for the active localized part). The two simulators can work sequentially, as in the compression approach [10], or simultaneously, as in iterative time domain schemes [11]. The main advantage of the sequential procedure is the ability to tune the active circuit without the need of a new electromagnetic simulation. Unfortunately, unlike the simultaneous procedure, it does not directly yield the radiating patterns of the studied structure (a second electromagnetic simulation is then required).

In this chapter, we focus on a global electromagnetic approach in the frequency domain. It uses the field integral equation (FIE) solved by the method of moments (MoM). This technique has shown an excellent accuracy in the study of a wide range of passive planar circuits and antennas [12–17]. Efficient and accurate numerical implementations of the FIE are already proposed in available commercial electromagnetic simulators, such as MOMENTUM, ENSEMBLE, SONNET, and SAPHIR. Moreover, an interesting attempt to include discrete components in distributed structures has been reported. Initially proposed by Harrington as the theory of loaded scatterers [18], it was first dedicated to the analysis of wire antennas loaded with one-port elements. The formulation has been applied to active microstrip and uniplanar antennas [19,20] before being extended to nonlinear structures, either directly [21] or not [22]. All these developments are largely presented and illustrated in the following sections.

This chapter begins with the foundations of the technique of integral equations and the method of moments. The treatment of lumped elements is then discussed from both the theoretical and the numerical viewpoints. An interesting and realistic numerical characterization procedure, based on the matched load termination, is also presented. Numerous applications are considered.

## 5.2 LUMPED ELEMENTS IN THE METHOD OF MOMENTS

### 5.2.1 Integral Equations Formulation

The geometry of the general active structure to be analyzed is a multilayer planar multiport network (Fig. 5.1). The distributed part consists of metallic strips printed over dielectric layers, slots in partial ground planes located at different interfaces, and vertical strips and wires that could connect different metallic interfaces. The external discrete devices can be integrated in the planar structure. Basically, the active structure of Fig. 5.1 can be considered as a superposition of the distributed planar structure controlled by electromagnetic equations and the associated lumped devices and input/output (I/O) ports, as shown in Fig. 5.2.

An incident electromagnetic field ( $\mathbf{E}^{\text{ex}}, \mathbf{H}^{\text{ex}}$ ) induces current and charge densities over metallic surfaces, which in turn produce a diffracted electromagnetic field ( $\mathbf{E}^d, \mathbf{H}^d$ ) in such a manner that the total tangential electric field to each perfect metallic conductor vanishes:

$$\mathbf{e}_n \times [\mathbf{E}^{\text{ex}}(\mathbf{r}_i) + \mathbf{E}^d(\mathbf{r}_i)] = \mathbf{0} \quad (5.1)$$

where  $\mathbf{r}_i$  locates an observer point in the  $i$ th layer and  $\mathbf{e}_n$  is the normal vector to the considered conductor.

On the other hand, the total tangential magnetic field must be continuous across apertures; this last condition can be written as:

$$\mathbf{e}_n \times [\mathbf{H}^{\text{ex}}(\mathbf{r}_i) + \mathbf{H}^d(\mathbf{r}_i)] = \mathbf{0} \quad (5.2)$$

The electric field across apertures can be replaced by equivalent magnetic surface currents thanks to the equivalence principle [23]. Hence, the continuity of the electric field across slots is satisfied by using  $-\mathbf{M}_S$  and  $\mathbf{M}_S$  on the different sides as shown in Fig. 5.3.

The diffracted field in the various regions of the structure can be attributed to two kinds of currents: horizontal and vertical electric currents ( $\mathbf{J}_S$ ) on conductors and magnetic equivalent current  $\mathbf{M}_S$  of the covered slots:

$$\mathbf{E}^d(\mathbf{r}) = \mathbf{E}^d(\mathbf{r}_i, \mathbf{J}_S) + \mathbf{E}^d(\mathbf{r}_i, \mathbf{M}_S) \quad (5.3a)$$

$$\mathbf{H}^d(\mathbf{r}_i) = \mathbf{H}^d(\mathbf{r}_i, \mathbf{J}_S) + \mathbf{H}^d(\mathbf{r}_i, \mathbf{M}_S) \quad (5.3b)$$

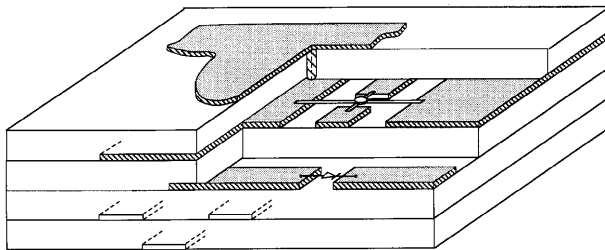
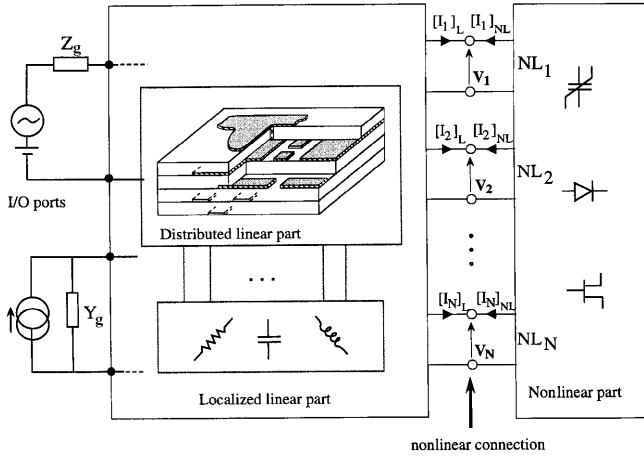


FIGURE 5.1 An active multilayer planar structure.



**FIGURE 5.2** An active multilayer planar structure partitioned into distributed and localized parts.

Using the mixed potential formulation, the total diffracted fields are derived from a vector and scalar potentials for each kind of source as

$$\mathbf{E}^d(\mathbf{r}_i) = -j\omega\mathbf{A}(\mathbf{r}_i) - \nabla V(\mathbf{r}_i) - \bar{\bar{\epsilon}}_i^{-1}\nabla \times \mathbf{F}(\mathbf{r}_i) \quad (5.4)$$

$$\mathbf{H}^d(\mathbf{r}_i) = \bar{\bar{\mu}}_i^{-1}\nabla \times \mathbf{A}(\mathbf{r}_i) - j\omega\mathbf{F}(\mathbf{r}_i) - \nabla U(\mathbf{r}_i) \quad (5.5)$$

These potentials should be expressed in terms of Green's functions of the corresponding multilayer structure; thus they can be written as follows:

$$\mathbf{A}(\mathbf{r}_i) = \iint_{S_m} \bar{\bar{G}}_A(\mathbf{r}_i, \mathbf{r}_v) \mathbf{J}_S(\mathbf{r}_v) dS \quad (5.6a)$$

$$V(\mathbf{r}_i) = \iint_{S_m} G_V(\mathbf{r}_i, \mathbf{r}_v) \rho_S(\mathbf{r}_v) dS \quad (5.6b)$$

$$\mathbf{F}(\mathbf{r}_i) = \iint_{S_a} \bar{\bar{G}}_F(\mathbf{r}_i, \mathbf{r}_v) \mathbf{M}_S(\mathbf{r}_v) dS \quad (5.7a)$$

$$U(\mathbf{r}_i) = \iint_{S_a} G_U(\mathbf{r}_i, \mathbf{r}_v) \tau_S(\mathbf{r}_v) dS \quad (5.7b)$$

where  $\mathbf{r}_v$  locates the source in the  $v$ th interface;  $S_a$  and  $S_m$  are, respectively, the surfaces of the metallization and the aperture; ( $\bar{\bar{G}}_A$ ,  $\bar{\bar{G}}_F$ ) are the dyadic dielectric Green's functions that correspond to the magnetic and the electric vector potentials created by a unit surface current in the considered structure; and ( $G_v$ ,  $G_u$ ) are the scalar dielectric Green's functions that correspond to the electric and the magnetic potentials created by a unit surface charge in the considered structure.

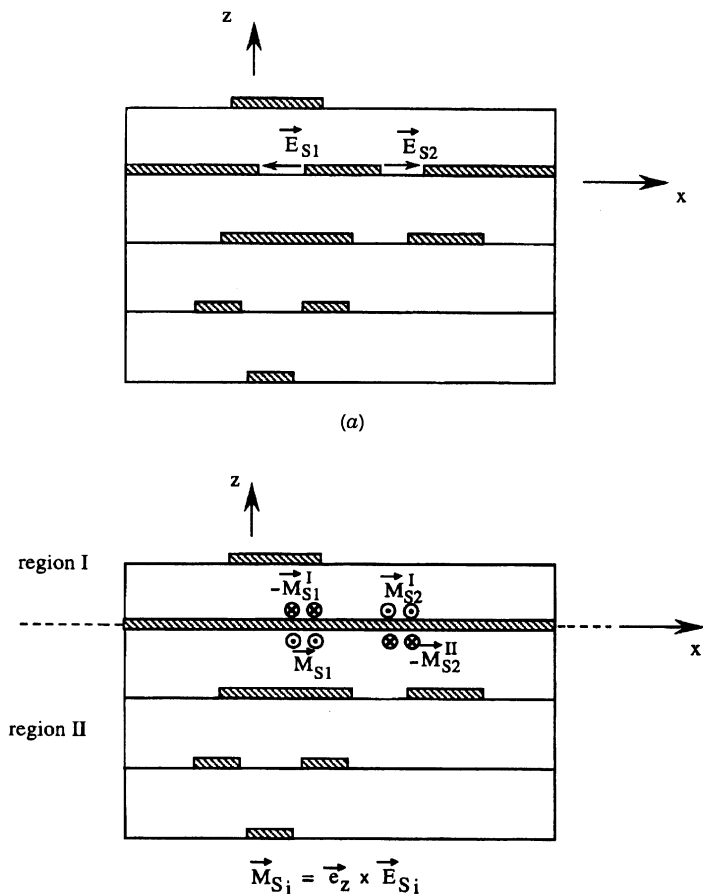


**FIGURE 5.3** (a) Cross section of a typical multilayer planar structure. (b) Equivalent problem.

Substituting from Eqs. 5.3–5.7 into Eqs. 5.1 and 5.2, the coupled integral equations for the structure can be obtained and they can be written in the following forms:

$$\begin{aligned} \mathbf{e}_n \times \mathbf{H}^{\text{ex}}(\mathbf{r}_i) = \mathbf{e}_n \times \left[ \iint_{S_a} j\omega \bar{\bar{G}}_F(\mathbf{r}_i, \mathbf{r}_v) \mathbf{M}_S(\mathbf{r}_v) \right. \\ \left. + \nabla G_U(\mathbf{r}_i, \mathbf{r}_v) \tau_s(\mathbf{r}_v) dS - \bar{\bar{\mu}}_i^{-1} \iint_{S_m} \nabla \times \bar{\bar{G}}_A(\mathbf{r}_j, \mathbf{r}_v) \mathbf{J}_S(\mathbf{r}_v) dS \right] \end{aligned} \quad (5.8)$$

$$\begin{aligned} \mathbf{e}_n \times \mathbf{E}^{\text{ex}}(\mathbf{r}_i) = \mathbf{e}_n \times \left[ \iint_{S_m} j\omega \bar{\bar{G}}_A(\mathbf{r}_i, \mathbf{r}_v) \mathbf{J}_S(\mathbf{r}_v) \right. \\ \left. + \nabla G_V(\mathbf{r}_i, \mathbf{r}_v) \rho_s(\mathbf{r}_v) dS - \bar{\bar{\epsilon}}_i^{-1} \iint_{S_a} \nabla \times \bar{\bar{G}}_F(\mathbf{r}_j, \mathbf{r}_v) \mathbf{M}_S(\mathbf{r}_v) dS \right] \end{aligned} \quad (5.9)$$

where  $\bar{\bar{\epsilon}}_i$  and  $\bar{\bar{\mu}}_i$  are the permittivity and the permeability tensors.

The magnetic Green's function components in Eq. 5.8 represent the whole potential created by magnetic current in both regions surrounding the considered slot (see Fig. 5.3). However, the magnetic Green's component appearing in Eq. 5.9 corresponds to the one created by the magnetic source placed in the same region as the considered electric source [24]. The required components are found by solving the propagation equation, with the appropriate boundary conditions, for the corresponding field. Exact expressions in terms of Sommerfeld integrals have been published and can be found for isotropic and anisotropic open structures in [12–15,24–26] and for shielded structures in [27].

### 5.2.2 Matched Terminations

Assuming that only the fundamental mode propagates on a lossless planar line away from any discontinuity, the unknown longitudinal currents distributions can be seen as the sum of an incident and a reflected wave. It can be expressed as

$$K_{sL}(u) = A \exp(j\beta u) + B \exp(-j\beta u) \quad (5.10)$$

$\beta$  is the wavenumber of the fundamental mode on the line,  $K_{sL}$  is the longitudinal component of the current density (electric current density  $J_{sL}$  for a microstrip line and magnetic current density  $M_{sL}$  for a slotline), and  $u$  the longitudinal coordinate on the line.  $A$  and  $B$  are complex coefficients representing the incident and reflected currents. As in [28], the minus sign for the reflected current wave is due to the sign convention that will be used for the calculation of scattering parameters (see Fig. 5.14)

As a consequence, a matched termination can be simulated by imposing the cancellation of the reflected wave ( $B = 0$ ). Practically, this absorbing condition is obtained by forcing the longitudinal current density at the end of the line to be equal to the longitudinal current density at an arbitrary reference plane with a phase shift equal to the electrical length between them:

$$K_{sL}(u^{\text{end}}) = K_{sL}(u^{\text{ref}}) \exp[j\beta(u^{\text{end}} - u^{\text{ref}})] \quad (5.11)$$

$u^{\text{end}}$  and  $u^{\text{ref}}$  are the longitudinal coordinates locating the end of the line and the arbitrary reference plane.

The same principle can be used to represent the excitation of a line. In that case, we replace the matched termination with an ideal source at  $u = u^{\text{end}}$ . Practically, we enforce the value of the current at that point,

$$K_{sL}(u^{\text{end}}) = K_{\text{imp}} \quad (5.12)$$

where constant  $K_{\text{imp}}$  represents an arbitrary impressed current.

Equations 5.11 and 5.12 appear as extra boundary conditions to be added to the integral equations 5.8 and 5.9.



### 5.2.3 Discrete Components

In this approach, the discrete components to be inserted in the passive distributed structure are supposed to be small compared to wavelength. As a consequence, they can be represented by lumped elements and analyzed with circuit theory (using Kirchhoff's equations). This assumption permits one to take these discrete elements into account with only a slight modification in the original integral equations 5.8 and 5.9. This approach can be illustrated by considering a one-port discrete element inserted in a metallic surface, as depicted in Fig. 5.4.

The discrete element is represented by a serial impedance  $Z_L$  inserted in an infinitesimal gap  $G_L$  (Fig. 5.5). Thanks to Ohm's law, the voltage across  $G_L$  is directly related to the current flowing through it:

$$V_L = Z_L I_L \tag{5.13}$$

Both  $V_L$  and  $I_L$  can be connected to the field and source quantities, which appear in the integral equations. First,  $I_L$  can be expressed as the flow of the electric current density  $\mathbf{J}_S$  through the gap,

$$I_L = \int_0^{W_L} \mathbf{J}_S \cdot \mathbf{e}_L dw \tag{5.14}$$

where  $W_L$  is the width of the gap and  $\mathbf{e}_L$  is a unit vector normal to the gap (the sign convention for  $V_L$  and  $\mathbf{e}_L$  is indicated in Fig. 5.4).

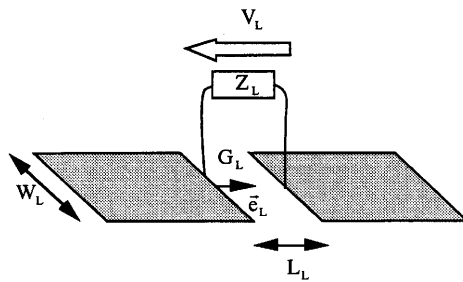


FIGURE 5.4 One-port discrete element in a metallic surface.

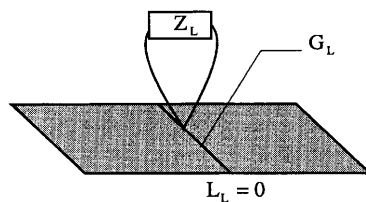


FIGURE 5.5 The infinitesimal gap.

$V_L$  is given by the curl of the total electric field along the gap

$$V_L = - \int_0^{L_L} \mathbf{E} \cdot \mathbf{e}_L dl \quad (5.15)$$

where  $L_L$  is the length of the gap. At this point, a very important assumption must be underlined: as mentioned previously, the gap  $G_L$  is supposed to be infinitesimally small. Practically, this means that  $L_L$  equals zero. Indeed, this defines the fundamental assumption of the present approach: the so-called lumped elements are basically zero-length elements.

A very important consequence is that the metallic surface in which the discrete element is inserted is supposed to be uninterrupted. At the same time, it is supposed to support a nonzero tangential electric field at the location of the infinitesimal gap. These two assumptions are paradoxical and it can be shown that this paradox could be responsible for numerical disorders if not correctly treated. However, these assumptions are essential to achieve a simple formulation of the problem. On the one hand, the fact that the metallization is uninterrupted cancels the total tangential electric field everywhere on the metallic surface (including the location of the gap). On the other hand, the nonzero voltage across the gap can be represented by a nonzero incident electric field, impressed in  $G_L$  [18]:

$$\mathbf{E}^{\text{ex}} = -V_L \delta(\mathbf{r} - \mathbf{r}_L) \mathbf{e}_L \quad (5.16)$$

with

$$\delta(\mathbf{r} - \mathbf{r}_L) \begin{cases} 1, & \text{if } \mathbf{r} \in G_L \\ 0, & \text{elsewhere} \end{cases} \quad (5.17)$$

Combining Eqs. 5.13, 5.14, and 5.16, the presence of the lumped element can be represented by a dependent incident electric field:

$$\mathbf{E}^{\text{ex}} = -Z_L \delta(\mathbf{r} - \mathbf{r}_L) \mathbf{e}_L \int_0^{W_L} \mathbf{J}_S \cdot \mathbf{e}_L dw \quad (5.18)$$

As can be seen, this incident electric field is related to the unknowns of the integral equations, that is, the electric current densities. This simple expression of the incident electric field will be used to represent the lumped element in the integral equation 5.9.

Comparing Eqs. 5.15 and 5.16, it can be noticed that the diffracted electric field is supposed to be zero at the location of the lumped element. This is consistent with the fact that a zero-length current element (the one that flows through  $G_L$ ) does not radiate. Nevertheless, this contradicts the fact that the total tangential electric field is canceled in  $G_L$  while the incident one is not. Indeed, the diffracted electric field should compensate the nonzero incident electric field in order to cancel the total one. Here again, we point out the paradox of this formulation. In fact, this simply

suggests that the current in  $G_L$  will be infinite. Mathematically, this is the only way for a zero-length current element to produce a nonzero diffracted electric field. We will see later (Section 5.3.1) that this result can also be demonstrated from a circuit analysis.

At this time, we focus on the extension of the proposed formulation to multiport lumped elements. It is straightforward. Typically, an  $N$ -port lumped element is represented by its  $N \times N$  impedance matrix

$$\begin{bmatrix} V_1 \\ \vdots \\ V_N \end{bmatrix} = \begin{bmatrix} Z_{11} & \cdots & Z_{1N} \\ \vdots & \ddots & \vdots \\ Z_{N1} & \cdots & Z_{NN} \end{bmatrix} \begin{bmatrix} I_1 \\ \vdots \\ I_N \end{bmatrix} \quad (5.19)$$

As a consequence, it is modeled as a  $N$ -pulse incident electric field, which is applied to the  $N$  infinitesimal gaps  $G_{Li}$

$$\mathbf{E}^{\text{ex}} = -\sum_{i=1}^N V_i \delta(\mathbf{r} - \mathbf{r}_{Li}) \mathbf{e}_{Li} \quad (5.20)$$

with

$$\delta(\mathbf{r} - \mathbf{r}_{Li}) \begin{cases} 1, & \text{if } \mathbf{r} \in G_{Li} \\ 0, & \text{elsewhere} \end{cases} \quad (5.21)$$

$G_{Li}$  is the  $i$ th infinitesimal gap and  $\mathbf{e}_{Li}$  is the unit vector normal to this gap.

The only new aspect of this multiport treatment consists in the relative positioning of the different loaded ports (i.e., the gaps) in the distributed structure (with the subsequent problem of the voltage reference). This difficulty will be investigated later (Section 5.3.3) for practical configurations.

The same approach is used to represent a lumped element inserted in a slot, using dual treatments.

One must keep in mind that in the present approach the incident fields are used to represent the lumped elements while the excitation of the structure is usually treated as an independent equation 5.12. Exceptionally, we will also use lumped elements (delta gap generators) to perform the numerical excitation of the studied structure. This is usually used when the value of the impressed voltage has to be controlled, as in Eq. 5.38.

#### 5.2.4 Method of Moments Resolution

Introduced to the electromagnetic community by Harrington [29], the method of moments is among the most used numerical technique to transform a functional equation into a finite matrix equation, which could then be solved by the direct or iterative matrix equation method.

The integral equations for the electric and magnetic fields in terms of the unknown surface electric and magnetic currents (Eqs. 5.8 and 5.9) can be put into an operator equation as follows:

$$\text{Lop}(\mathbf{M}_S, \mathbf{J}_S) = \mathbf{g}(\mathbf{E}^{\text{ex}}, \mathbf{H}^{\text{ex}}) \quad (5.22)$$

where  $\text{Lop}$  is a linear operator and  $\mathbf{g}$  is the source excitation (known function).

First, the unknown current densities to be determined are expanded in terms of known basis functions as follows:

$$\mathbf{J}_S = \sum_{i=1}^N I_i \mathbf{J}_i \quad (5.23)$$

$$\mathbf{M}_S = \sum_{j=1}^M V_j \mathbf{M}_j \quad (5.24)$$

where  $I_i$  and  $V_j$  are the unknown complex current amplitudes.

For a finite number  $N$  and  $M$  of basis functions, it results in a residual error defined as the difference between the exact solution and the approximated solution. The fundamental idea of the method of moments is to transform the functional equation by means of the integration of an inner product defined as a set of test functions  $U_q$ . The linear set of equations of the method of moments corresponds to the case where the functional, defined by the error, is orthogonal to the projection:

$$\sum_{i=1}^N a_i \langle U_q, \text{Lop}(\mathbf{J}_i) \rangle + \sum_{j=1}^M b_j \langle U_q, \text{Lop}(\mathbf{M}_j) \rangle - \langle U_q, \mathbf{g} \rangle = 0 \quad (5.25)$$

The more the functional is orthogonal to the test function, the better the approximation.

In the present approach, the source regions (strips and slots) of the diffracted field are subdivided into rectangular elementary domains (cells). Two adjacent cells are the support of one basis current function  $T_u$ , as shown in Fig. 5.6. The basis functions for each current component are assumed to have linear variation along the longitudinal direction and constant variation along the transverse direction (Fig. 5.6). The resulting charge basis function is a pulse, noted  $\Pi_u$ , defined along the associated current cell. When only a longitudinal current is assumed to exist (which is usually the case for I/O ports), only one transverse cell is considered and a transverse variation is introduced in the basic functions to give the correct behavior of the current density on the strip or slot port, taking into account the edge condition (Fig. 5.6). With no loss of generality, we consider the case of a single planar rectangular surface (either an aperture or a metallic patch; see Fig. 5.8). It is divided

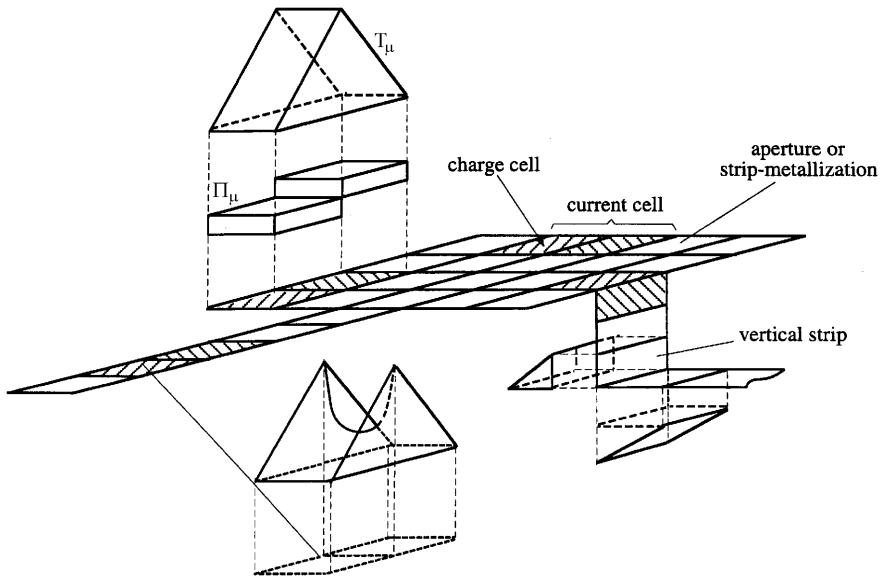


FIGURE 5.6 Current discretization and basis functions.

into  $N_x \times N_y$  charge cells in the  $x$  and  $y$ -directions, respectively. The unknown current densities are expressed in the form of a finite summation as follows:

$$\mathbf{K}_S(\mathbf{r}) = \sum_{u=x,y} \mathbf{e}_u \sum_{l=1}^{N_{x,u}} \sum_{k=1}^{N_{y,u}} K_u^{kl} T_u(\mathbf{r} - \mathbf{r}_u^{kl})$$

$$\mathbf{K}_S = \mathbf{J}_S, \mathbf{M}_S \tag{5.26}$$

$K_u^{kl}$  are the unknown complex amplitudes of the  $u$  component of the current at the center of cell  $(k, l, u)$ .  $N_{x,u}$  and  $N_{y,u}$  are the numbers of  $u$ -oriented current cells in the  $x$  and  $y$ -directions, respectively. The associated surface charge densities proceed from the continuity equation. The chosen testing functions are pulse functions defined along the segment linking the centers of the two adjacent cells. Suggested by Glisson and Wilton [30], this test procedure has been applied successfully to planar structures [16,18,24–26]. Compared to the Galerkin procedure, this choice leads to simpler expressions and consequently to less CPU time.

When vertical wires are involved, they are divided into straight wire segments and the used subdomain basic functions are also assumed to have linear variations along the wire direction. A special attachment mode is used to ensure the current density continuity at the strip–wire junction, as shown in Fig. 5.7 [25]. When vertical strips are involved, they are divided into rectangular cells and the continuity of the current is ensured by using the basic function given in [31].

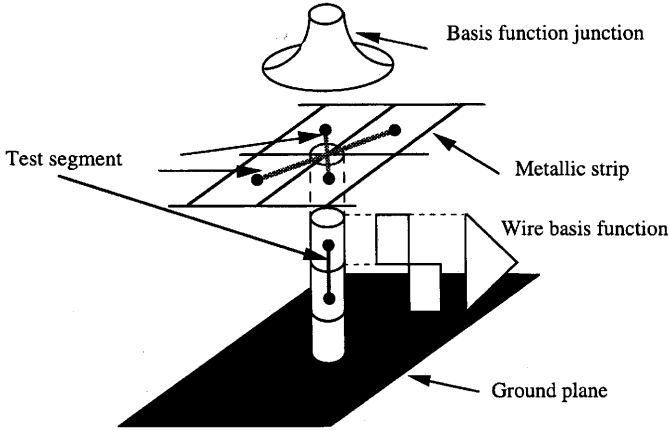


FIGURE 5.7 Strip-wire junction.

Finally, the application of the above method of moments procedure converts the integral equations into a set of linear equations and the resultant matrix describes the electromagnetic interactions between the considered subsections. The problem of the distributed part of the studied structure is thus reduced to a matrix whose general form is

$$\begin{bmatrix} \mathbf{Z} & \mathbf{T}^E \\ \mathbf{T}^H & \mathbf{Y} \end{bmatrix} \begin{bmatrix} \mathbf{I} \\ \mathbf{V} \end{bmatrix} = \begin{bmatrix} V^{\text{ex}} \\ I^{\text{ex}} \end{bmatrix} \quad (5.27)$$

where  $\mathbf{Z}$  is the generalized impedance submatrix corresponding to the discrete conductor strip/wire subsections;  $\mathbf{Y}$  is the generalized admittance submatrix corresponding to the discrete slot subsections;  $\mathbf{T}^E$  and  $\mathbf{T}^H$  are the generalized coupling submatrix between slot and strip subsections; and  $I$  and  $V$  are the subvectors of the unknown coefficients. The excitation vectors  $V^{\text{ex}}$  and  $I^{\text{ex}}$  result from the projection of the incident fields on the test segments.

Using the notations in Fig. 5.8, the impedance/admittance matrix elements can be written in general forms as

$$\begin{aligned} [Z/Y]_{m,n,v}^{k,l,u} &= P [Z/Y]_{m,n,v}^{k,l,u} + Q [Z/Y]_{m,n,v}^{k,l,u} \\ P &= A, F \quad \text{and} \quad Q = V, U \end{aligned} \quad (5.28)$$

where

$$P [Z/Y]_{m,n,v}^{k,l,u} = j\omega \int_{C_{m,n,v}} \mathbf{e}_v dl_i \iint_{S_{k,l,u}} \bar{\bar{G}}_P(\mathbf{r}_i, \mathbf{r}_v) T(r_v - \mathbf{r}_u^{k,l}) \mathbf{e}_u dS_v \quad (5.29)$$

$$\begin{aligned} Q [Z/Y]_{m,n,v}^{k,l,u} &= \frac{1}{j\omega} \iint_{S_{k,l,v}} [G_Q(\mathbf{r}_v^{m,n+}, \mathbf{r}_v) - G_Q(\mathbf{r}_v^{m,n-}, \mathbf{r}_v)] [\Pi(\mathbf{r}_v - \mathbf{r}_u^{k,l+}) \\ &\quad - \Pi(\mathbf{r}_v - \mathbf{r}_u^{k,l-})] dS_v \end{aligned} \quad (5.30)$$

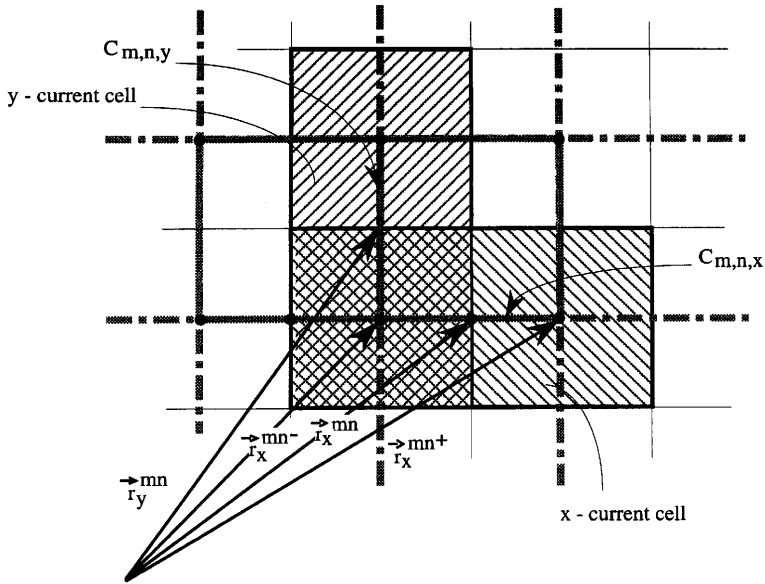


FIGURE 5.8 Network of test segments.

The contribution of vector and scalar potentials in each matrix element is expressed in terms of multiple integrals involving Hankel functions for open structures and trigonometric functions for shielded ones [25,27].

The general studied structure of Fig. 5.1 can be seen as a  $P$ -port circuit thanks to the method of moments, where  $P$  is the dimension of the generalized hybrid matrix. In order to represent the external devices connected to the planar circuit, the corresponding spatial ports are loaded by localized elements, as shown in Fig. 5.9. Basically, the active structure of Fig. 5.9 can be considered as a superposition of the distributed planar structure controlled by electromagnetic equations and the associated passive and active devices.

We now discuss how the particular loading conditions (Eqs. 5.16 and 5.20) have to be dealt with using the method of moments. As explained in Section 5.2.3, the loading condition is expressed thanks to the incident field. Consequently, it appears as a particular form of the excitation vector. For the presentation, we consider the simple case of a planar rectangular metallic surface that is loaded with a lumped impedance  $Z_L$  (Fig. 5.5). Numerically, the infinitesimal gap  $G_L$  supporting  $Z_L$  is chosen in correspondence with the meshing; that is, it lies along the border between two adjacent cells (Fig. 5.10). The corresponding test segment, say, test segment  $(m_L, n_L, v_L)$ , crosses the loaded gap and a nonzero voltage results:

$$V_{m_L, n_L, v_L}^{\text{ex}} = \int_{C_{m_L, n_L, v_L}} \mathbf{E}^{\text{ex}} \cdot \mathbf{e} \, dl = -Z_L I_{m_L, n_L, v_L} \quad (5.31)$$

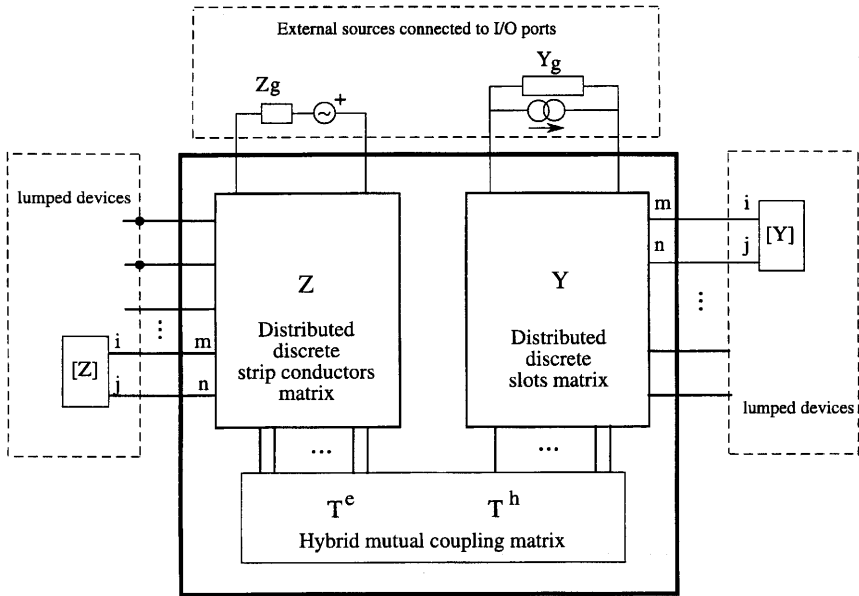


FIGURE 5.9 Equivalent network of the active distributed multilayer structure.

Due to the location of  $G_L$ , this voltage is only related to  $I_{m_L, n_L, v_L}$ , the unknown coefficient that corresponds to the value of the electric current at the middle of current cell  $(m_L, n_L, v_L)$ .

Finally, this nonzero second term of the matrix equation 5.27 can be canceled by reporting the loading condition in the matrix itself. This can be achieved simply by modifying the diagonal term of the generalized impedance matrix that accounts for the inner coupling in cell  $(m_L, n_L, v_L)$ :

$$\tilde{Z}_{m_L, n_L, v_L}^{m_L, n_L, v_L} = Z_{m_L, n_L, v_L}^{m_L, n_L, v_L} + Z_L \tag{5.32}$$

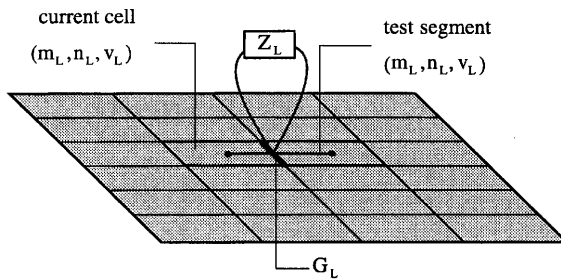


FIGURE 5.10 Numerical configuration.



When the load is inserted in a slot, the same kind of modification is performed in the generalized admittance matrix. When several cells are involved in the loading procedure (e.g., in multiport loads), all the corresponding diagonal and off-diagonal terms have to be modified [19,20].

A final point concerns the numerical form of Eqs. 5.11 and 5.12. As mentioned before, these equations, respectively, account for a matched termination and an excited termination. The discretization is straightforward. It is given for the example of a simple microstrip line, which is excited at its first extremity and matched at the other one (Fig 5.11). We assume that the line is divided into  $N$  cells. An extra half rooftop basis function is added at the extremities of the line to support the nonzero impressed currents. Let  $I_0$  and  $I_N$  be the unknown coefficients associated with these additional basis functions; Eqs. 5.12 and 5.11 yields

$$I_0 = I_{\text{imp}} \tag{5.33}$$

and

$$I_N = I_{N-1} \exp(-\beta d) \tag{5.34}$$

where  $d$  is the length of the cell.

The resultant matrix equation is

$$\begin{bmatrix} 1 & 0 & \cdots & 0 & 0 \\ Z_{1,0} & Z_{1,1} & \cdots & Z_{1,N-1} & Z_{1,N} \\ \vdots & \vdots & \ddots & \vdots & \vdots \\ Z_{N-1,0} & Z_{N-1,1} & \cdots & Z_{N-1,N-1} & Z_{N-1,N} \\ 0 & 0 & \cdots & -\exp(-\beta d) & 1 \end{bmatrix} \begin{bmatrix} I_0 \\ I_1 \\ \vdots \\ I_{N-1} \\ I_N \end{bmatrix} = \begin{bmatrix} I_{\text{imp}} \\ 0 \\ \vdots \\ 0 \\ 0 \end{bmatrix} \tag{5.35}$$

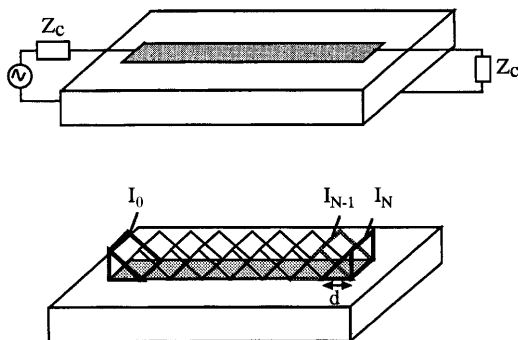


**FIGURE 5.11** Microstrip line with one excited and one matched terminations. From [28], copyright © 1994, reprinted with permission of IEEE.

In practice, Eq. 5.34 can be applied to  $N_{\text{cond}}$  successive cells in order to achieve a better matched condition. It gives

$$I_{N-j+1} = I_{N-j} \exp(-\beta d) \text{ for } 1 \leq j \leq N_{\text{cond}} - 1$$

$$I_{N-N_{\text{cond}}+1} = \frac{1}{N_{\text{ref}}} \sum_{i=1}^{N_{\text{ref}}} I_{N-N_{\text{cond}}+1-i} \exp(-\beta di) \quad (5.36)$$

In this equation,  $N_{\text{ref}}$  is an arbitrary number of reference currents. The counterpart of this improved procedure is the need for an extra length of line in order to support the  $N_{\text{cond}}$  imposed coefficients.

### 5.2.5 Virtual Network Analyzer

The resolution of the linear system of equations 5.27 yields all the current densities in the structure. All the radio electric characteristics can easily be deduced from these current densities. In this paragraph, as an illustration, we present a general procedure to perform the global characterization of an  $N$ -port planar active antenna.

The whole characterization requires  $3N$  steps. The first  $2N$  steps consist in the determination of the propagation characteristics (i.e., the characteristic impedance  $Z_c$  and the phase constant  $\beta$ ) of the  $N$  transmission lines that feed the antenna. Then, the last  $N$  steps permit the actual characterization of the  $N$ -port active antenna itself (i.e. the scattering parameters and the radiating patterns). Although they do not directly influence the characterization of the studied antenna, the first  $2N$  steps are essential for the accuracy of the final results. As a consequence, these first steps can be seen as calibration steps. Later, they will permit us to perform the whole characterization of the antenna without any external data.

We first discuss the calibration steps in which we assume the lines are not coupled. As mentioned earlier, two steps are needed for the characterization of each of the  $N$  lines. Each one involves the study of a simple structure, the so-called calibration standard. For line  $m$ , the first calibration standard (Fig. 5.12) is the open-ended line. It directly yields  $\beta_m$  as:

$$\beta_m = \frac{\pi}{d_{\text{min}}} \quad (5.37)$$

where  $d_{\text{min}}$  is the distance between two successive current minima.

The second calibration standard (Fig. 5.13) consists of a center feedline (exceptionally, we use a delta gap generator to perform this excitation) whose two ends are matched. For a microstrip line,  $z_{c_m}$  is given directly as

$$Z_{c_m} = \frac{1}{2} \left| \frac{V_{\text{imp}}}{I} \right| \quad (5.38)$$

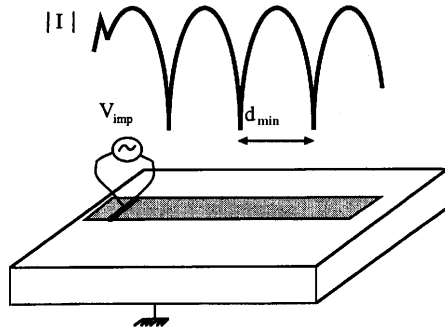


FIGURE 5.12 First calibration step. From [28], copyright © 1994, reprinted with permission of IEEE.

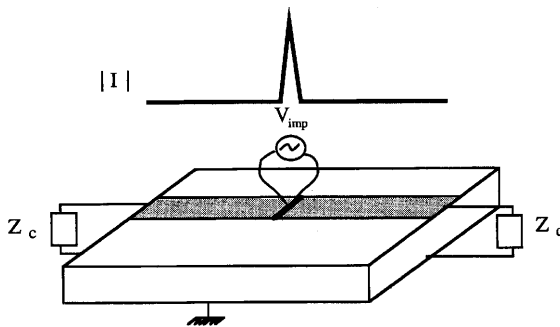


FIGURE 5.13 Second calibration step. From [28], copyright © 1994, reprinted with permission of IEEE.

$V_{imp}$  is the excitation voltage and  $I$  the electric current along the line. For slotline and CPW lines, similar expressions can be established using duality [20].

These standards are not chosen arbitrarily. The first one takes advantage of the high reflection, which imposes high precision on the location of the minima and consequently on the value of  $\beta_m$ . In the second one, the characteristic impedance is related to the input impedance seen by the voltage generator. Thanks to the matched terminations, the magnitude of the electric current remains constant along the line and it can be used in Eq. 5.38 instead of its singular value at the source point. In both cases, computation time is very short thanks to the simplicity of the standards. This procedure has been demonstrated to give very accurate results [28].

The studied  $N$ -port antenna can be seen as an  $N$ -port circuit connected to  $N$  transmission lines (Fig. 5.14) and whose  $N \times N$  scattering matrix has now to be determined:

$$b_k = \sum_{m=1}^N S_{km} a_m \tag{5.39}$$

The calculation takes advantage of the simulated matched terminations to numerically reproduce the experimental mode of operation. In the most general case it involves an  $N$ -step procedure. During step  $m$  (Fig. 5.14), line  $m$  is excited while all

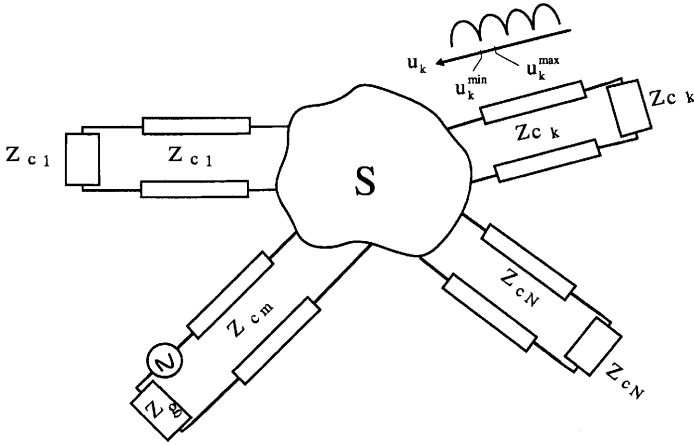


**FIGURE 5.14** Calculation of the scattering parameters (step  $m$ ). From [28], copyright © 1994, reprinted with permission of IEEE.

the other lines are matched. This leads to a particular configuration of the linear system 5.27, the resolution of which yields the corresponding currents. The  $N$  matrix elements of column  $m$  of the scattering matrix are directly related to these currents as

$$\Gamma(m_m^{\max}) = - \left[ \frac{|I(u_m^{\max})|}{|I(u_m^{\min})|} - 1 \right] / \left[ \frac{|I(u_m^{\max})|}{|I(u_m^{\min})|} + 1 \right] \tag{5.40}$$

$$S_{mm} = \Gamma(u_m^{\max}) \exp[j2\beta_m(u_m^{\text{meas}} - u_m^{\max})] \tag{5.41}$$

$$S_{km|k \neq m} = - \frac{\sqrt{Z_{c_k}}}{\sqrt{Z_{c_m}}} \frac{I_k^{\max} \exp[j\beta_k(u_k^{\text{meas}} - u_k^{\max})]}{I_m^{\max} \exp[\beta_m(u_m^{\max} - u_m^{\text{meas}})]} [1 - \Gamma(u_m^{\max})] \tag{5.42}$$

$Z_{c_m}$  is the characteristic impedance of line  $m$ .  $u_m^{\text{meas}}$ ,  $u_m^{\max}$ , and  $u_m^{\min}$  are, respectively, the longitudinal coordinates locating the plane of measurement, the plane where the current is maximum, and the plane where the current is minimum, on line  $m$ .

The computation of the radiating patterns of a passive or an active multiport antenna is largely explained in [28] and will not be discussed here as it is not essential for the following.

### 5.3 ANALYSIS OF ACTIVE LINEAR CIRCUITS AND ANTENNAS

#### 5.3.1 The Resistively Loaded Microstrip Line

##### 5.3.1.1 A First Numerical Experiment of the Lumped Element Concept

The general method presented in the previous sections is first applied to a very simple structure. It consists of a microstrip line loaded with a serial impedance  $Z_L$ , as depicted in Fig. 5.15. All results are obtained with a one-dimensional (1-D) mesh.

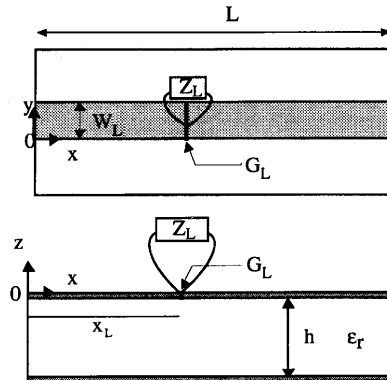


**FIGURE 5.15** Studied structure. ( $L = 50$  mm,  $x_L = 25$  mm,  $W_L = 2.47$  mm,  $h = 0.8$  mm,  $\epsilon_r = 2.17$ ,  $f = 8$  GHz). From [43], copyright © 1998, reprinted with permission of IEEE.

This canonical example will be very useful to evaluate the performances and the limitations of our modeling. In particular, it will provide a good insight into the numerical phenomena involved by the lumped element formulation.

In this section, the serial impedance is treated as a simple lumped element (i.e., a zero-length impedance in a zero-length gap). Although very attractive, this direct implementation of the method has a major drawback: the zero-length gap  $G_L$  is associated with an infinite susceptance. This can be understood very easily as it corresponds to the limit of a nonzero-length gap (with a finite susceptance) whose length tends to zero. As a consequence, the gap behaves as an infinite capacitance and the current flowing through it is supposed to be infinite. This problematic situation was already predicted using electromagnetic considerations (Section 5.2.3). Fortunately, we can now show that the actual numerical situation is better than expected. Thanks to the smoothing achieved by basis function expansion and due to their interlacing (Fig. 5.16), the current calculated at the location of the gap does not become infinite.

This means that the actual capacitance does not become infinite either. However, a remaining capacitance  $C_L$  still exists whose value is strongly dependent on the meshing (the looser the meshing, the larger the smoothing and the smaller the capacitance). It must be regarded as a numerical parasitic capacitance at least for two reasons: first, it accounts for an infinitesimally small gap with no actual physical

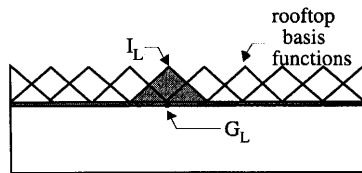


**FIGURE 5.16** Numerical representation of the lumped current. From [43], copyright © 1998, reprinted with permission of IEEE.

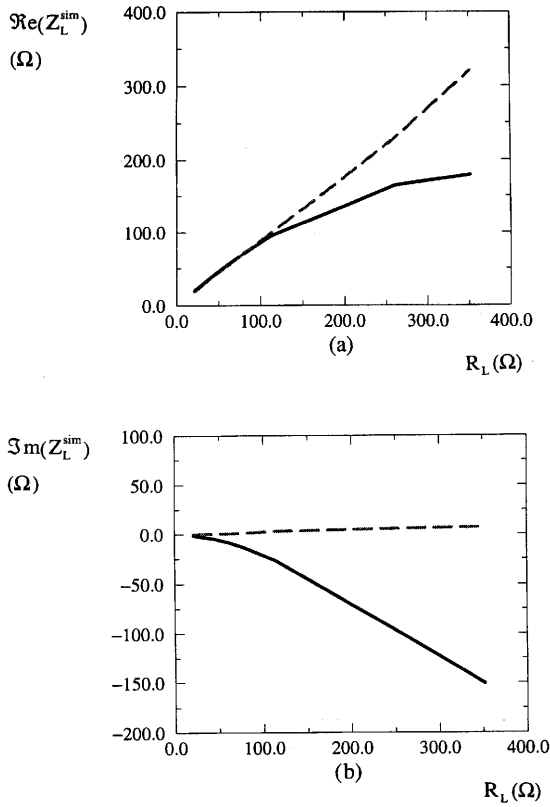


**FIGURE 5.17** Simulated impedance versus inserted impedance; —, noncorrected results; - - -, corrected results (first deembedding procedure). From [43], copyright © 1998, reprinted with permission of IEEE.

significance; second, its value does not converge with the meshing. It should be noted that the parasitic capacitance is due to the zero length of the lumped element and not to its zero transverse\* dimensions as in the FDTD technique [32]. In practice, this shunt capacitance will be present together with the inserted impedance  $Z_L$  in all the numerical simulations.

Figure 5.17 (noncorrected results) illustrates the effect of the numerical parasitic capacitance. The figure presents the simulated impedance  $Z_L^{\text{sim}}$  for different resistive values  $R_L$  of the inserted impedance  $Z_L$ .  $Z_L^{\text{sim}}$  is the resultant lumped serial impedance that actually appears at the location of the gap, calculated from (Eqs. 5.41 and 5.42).

As long as  $R_L$  remains small, the effect of the shunt capacitance is negligible and  $\tilde{Z}_L$  faithfully reproduces the value of  $R_L$ . When  $R_L$  gets larger, the shunt capacitance exerts a greater influence and  $Z_L^{\text{sim}}$  exhibits a significant capacitive behavior. An equivalent circuit for is presented in Fig. 5.18.

\* In the FDTD method, lumped elements have generally zero transverse dimensions but a nonzero length

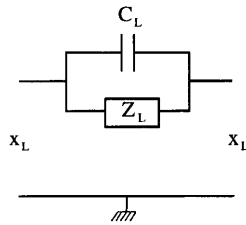


**FIGURE 5.18** Equivalent circuit for the loaded gap. From [43], copyright © 1998, reprinted with permission of IEEE.

Figure 5.19 reports the variations of the numerical parasitic capacitance  $C_L$  for different meshings and for several line configurations (the procedure used to compute  $C_L$  will be explained later).

As expected,  $C_L$  is strongly dependent on the mesh size and is less for looser meshing. It also appears that  $C_L$  is larger for wider lines, which is consistent with the fact that the coupling through a gap is larger for wider lines.

**5.3.1.2 A Deembedding Procedure** The numerical error due to the parasitic capacitance is a systematic one: when the capacitance is known, this error can be predicted and corrected. As a consequence, a numerical deembedding procedure can be used to evaluate and to compensate for this capacitance. The procedure first determines the value of the capacitance for the chosen meshing. To do so, the microstrip line is simulated with an infinite lumped impedance  $Z_L$  inserted in the gap  $G_L$ . Practically, this can be achieved by canceling the current at the location of  $G_L$  as depicted in Fig. 5.20. (Numerically, this simply suggests that the basis function associated with the lumped element has to be suppressed in the MoM resolution.)

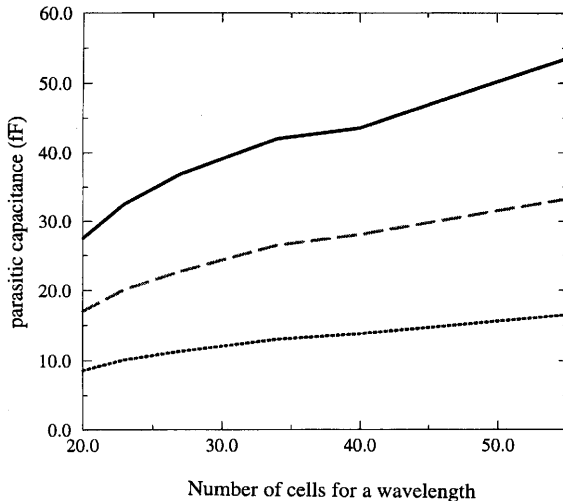


**FIGURE 5.19** Parasitic capacitance for different mesh size and linewidth: —,  $W_L = 2.47$  mm; - - -,  $W_L = 1.65$  mm; - · - ·,  $W_L = 0.82$  mm. From [43], copyright © 1998, reprinted with permission of IEEE.

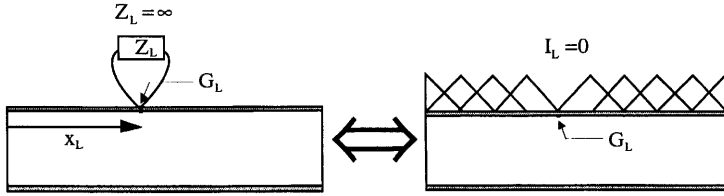


**FIGURE 5.20** Calculation of the parasitic capacitance. From [43], copyright © 1998, reprinted with permission of IEEE.

This loading configuration corresponds to that of the parasitic capacitance alone (as it lies in parallel with an infinite impedance). Its value can be derived from the resulting scattering parameters evaluated at plane  $x = x_L$ :

$$C_L = \frac{1}{j\omega Z_c} \text{Im} \left[ \frac{2S_{21}}{(1 + S_{11})^2 - S_{21}^2} \right] \tag{5.43}$$

In this equation, the scattering parameters and the characteristic impedance of the line  $Z_c$  can be computed from Eqs. 5.38, 5.41, and 5.42. Once the capacitance is known, its effect can be removed for all the following simulations. Typically, the correction simply consists of inserting a compensating impedance  $Z_L^{\text{comp}}$  when an impedance  $Z_L$  is to be simulated

$$Z_L^{\text{comp}} = \frac{Z_L}{1 - j\omega C_L Z_L} \tag{5.44}$$

With this correction, as shown in Fig. 5.17, the simulated impedance  $Z_L^{\text{sim}}$  is exactly the one to be simulated (corrected results). As a conclusion, the deembedding procedure completely suppresses the effect of the infinitesimal gap.

At that point, a fundamental problem occurs. What has been done permits robust numerical results to be obtained as the mesh dependence has been removed. However, these results do not correspond to a realistic situation. Indeed, such results would be obtained if two microstrip lines with no proximity coupling between them were connected together through a lumped impedance! In practice, the situation is much more complex. When a discrete element is inserted in a microstrip line, some proximity coupling exists between the two parts of the line. It is obvious that this coupling must be taken into account in a global electromagnetic analysis. This means it is not sufficient to suppress the parasitic coupling arising from the infinitesimal numerical gap. The analysis must also integrate the actual coupling due to the physical gap supporting the discrete element (Fig. 5.21). Of course, this coupling strongly depends on the actual size of the gap. This suggests that the length of the discrete component cannot be ignored and must be taken into account in the modeling.

**5.3.1.3 A More Realistic Modelling** A solution can be found that combines a precise modeling of the actual gap, a distribution of the lumped element, and a



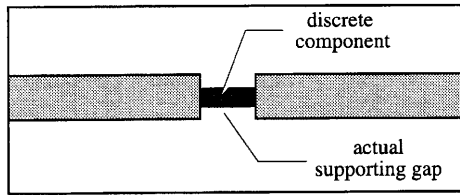


**FIGURE 5.21** Discrete element in a gap. From [43], copyright © 1998, reprinted with permission of IEEE.

revisited deembedding procedure. As shown in Fig. 5.22, the lumped element is now divided into  $N$  serial elements  $Z_L/N$  situated along a narrow metallic strip in the gap ( $N = 3$  in the figure).

In practice the width, length, and location of this strip have to be adjusted to correspond to those of the actual discrete element. This is essential when the analysis software is to be coupled with an autolayout procedure. This is also expected to directly influence the field distributions in the vicinity of the load. The first advantage of this modeling is its ability to reduce the effect of the parasitic capacitance. As demonstrated before, the capacitance gets smaller when the infinitesimal gap becomes more narrow, which is the case here. In addition, as the value of the lumped elements themselves are smaller ( $Z_L/N$  instead of  $Z_L$ ), the presence of a small shunt capacitance is not so important. The second advantage results from the realistic treatment of the physical gap. Typically, when  $Z_L$  is infinite, the current completely disappears along the narrow metallic strip (due to the shape and the interlacing of the basis functions) and the physical gap is reconstructed. The only drawback of this approach is that it uses a nonphysical narrow metallic strip to support the serial lumped elements. This is supposed to introduce a parasitic inductive effect.

Finally a deembedding procedure is still needed. It must be pointed out that such a procedure would not have been necessary anymore if the discrete element had been continuously distributed along the gap. Unfortunately, this ideal modeling is only possible using magnetic currents as proposed for the FDTD method in [35]. This solution has not been achieved yet because it requires a complete reformulation of the problem. Indeed, what we do here is slightly different. As suggested in Fig. 5.22,

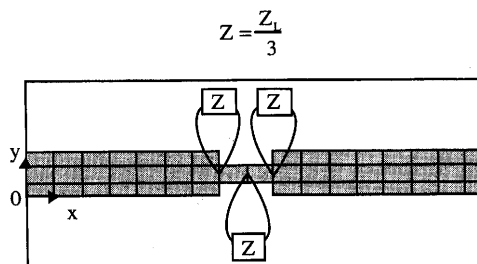


**FIGURE 5.22** Realistic numerical representation. From [43], copyright © 1998, reprinted with permission of IEEE.

the discrete component is not distributed continuously but concentrated into several serial lumped elements. As these lumped elements have zero length, they must be linked with metallic strips. In fact, these strips are needed to materialize the distance between the two edges of the gap (i.e., the length of the discrete component) and, at the same time, to achieve the electrical connection between the lumped elements. This situation has two direct consequences. First, because it still uses lumped elements, parasitic capacitances are still involved (although with less influence as already explained). Second, nonphysical artificial lines (the narrow metallic strips) are now introduced. The actual resultant load is that depicted in Fig. 5.23a. If we assume a high impedance, transmission lines can be seen as lumped inductances, and we obtain the equivalent load shown in Fig. 5.23b.

The deembedding procedure must suppress the effects of both the numerical parasitic capacitances and inductances. It must be underlined that this procedure relies on the assumption that the inserted impedance definitively represents the whole deembedded equivalent circuit of the discrete element (intrinsic parasitics included, extrinsic parasitics excluded). Numerically, this means that all the intrinsic inductive and capacitive effects of the components are represented in the lumped elements while all extrinsic effects are produced by the electromagnetic computation

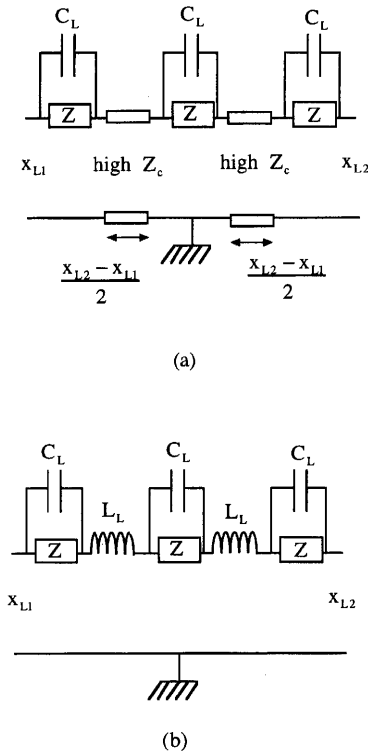


FIGURE 5.23 Equivalent circuits for the loaded gap.

itself. In other words, only the discrete element has to be inserted as its environment is already rigorously described.

We now discuss how the deembedding procedure must be achieved and in particular how the numerical parasitic elements must be calculated. As explained before, the numerical capacitance represents the parasitic coupling through the infinitesimal gap supporting the lumped elements. Theoretically, this coupling results from all the electromagnetic interactions between the two parts of the line that lie on each side of this infinitesimal gap. Nevertheless, because of the zero length of the gap, most of this coupling is achieved in the direct vicinity of the gap itself. This means that the parasitic capacitance accounts for a very local phenomenon. Practically, since it is almost perfectly localized, this phenomenon can be reproduced out of its original environment. This means that the parasitic capacitance can be computed by considering the infinitesimal gap on a simple microstrip line whose width and mesh are those of the connecting metallic strips. This structure, depicted in Fig. 5.24, can be seen as a test structure whose analysis is required as a preliminary step of the de-embedding procedure.

The same discussion can be carried out for the parasitic inductance. However, in that case, the procedure is not so rigorous because the discontinuity to be characterized is not perfectly localized. This suggests the mesh size must be sufficiently small to assume the connecting metallic strip can be regarded as a lumped inductance. Figure 5.25 presents the test structure that is used to determine this inductance.  $L_L$  is extracted from the scattering parameters of narrow metallic strips between plane  $x = x_{L1}$  and plane  $x = x_{L2}$ . Indeed, this second step simply

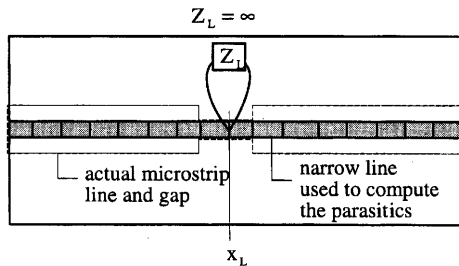


FIGURE 5.24 Calculation of the parasitic capacitance. From [43], copyright © 1998, reprinted with permission of IEEE.

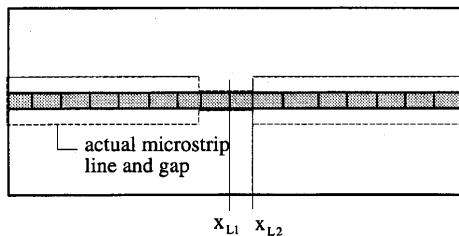


FIGURE 5.25 Calculation of the parasitic inductance. From [43], copyright © 1998, reprinted with permission of IEEE.

consists of replacing the metallic strips by ideal connecting wires (as the ones that are used in circuit simulators).

Definitively, the two parasitic elements must be calculated out of their actual environment in order not to include it in the deembedding procedure!

Once the parasitics have been determined, they must be removed from the impedance to be simulated as

$$Z_L^{\text{comp}} = \frac{(Z_L - jL_L\omega)}{1 - j\omega C_L(Z_L - jL_L\omega)} \tag{5.45}$$

Figure 5.26 illustrates the effect of this procedure. Here again, it presents the value of the simulated impedance for different inserted resistances. Three different configurations are tested: the first one is obtained by inserting the resistance in an infinitesimal gap without any correction, the second uses the first proposed modeling

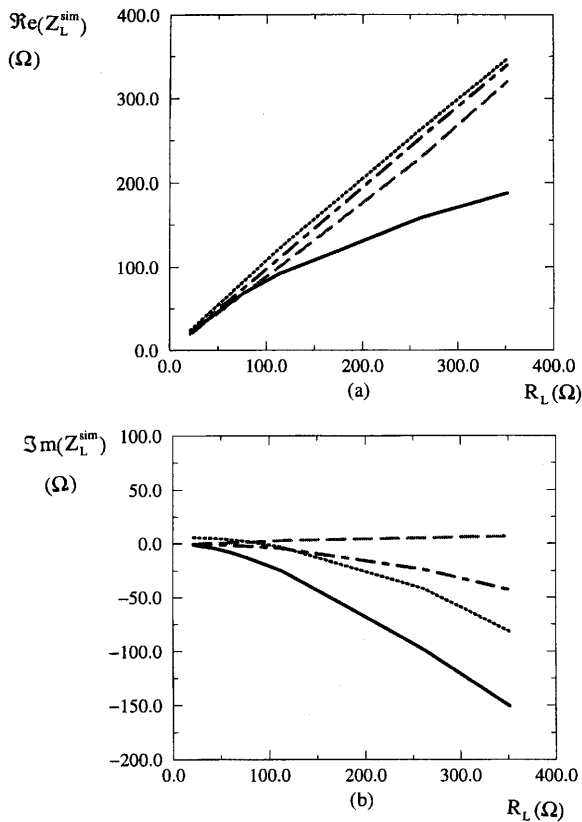


**FIGURE 5.26** Simulated impedance versus inserted impedance: —, noncorrected results; - - -, corrected results (first modeling); - · - ·, corrected results (second modeling); · · · ·, HP-EEsof results. From [43], copyright © 1998, reprinted with permission of IEEE.

(the numerical parasitic capacitance is corrected but the physical gap is not represented); and the third one uses the last proposed modeling (the physical gap is represented, and the parasitic capacitance and inductance are corrected). These three different configurations are compared with the results produced by performing the shunt connection of the resistance and of the gap, in a circuit simulator (HP-EEsof). For such a simple structure, the circuit simulator will be regarded as a benchmark.

As expected, the noncorrected configuration exhibits a significant capacitive effect, larger than the one resulting from the physical gap. Moreover, as seen previously, this effect would be largely dependent on the mesh size. The first modeling exhibits no capacitive effect at all. The second modeling is closer to the circuit simulator.

To conclude, it is essential to identify the actual theoretical capabilities and limitations of this modeling. Unlike the circuit simulator, it can be used to obtain the radiating patterns of the studied structure. This will be illustrated in the next sections. In addition, because it relies on a rigorous electromagnetic simulation, it is sensitive to the environment of the discrete element. In particular, the results will account for the precise location and dimensions of the component in the gap, which would not be the case if the equivalent circuit of the gap was simply shunt connected with the equivalent circuit of the inserted load. This can be understood more readily by stating that the two different configurations shown in Fig. 5.27 would lead to two different representations with our approach and to a unique representation with the approach using equivalent circuits.

In addition, this approach rigorously accounts for the effect of all the interconnections between the line and the discrete component as shown in [36]. Typically, bonding connections can be regarded as additional conductors (planar strips in the simplest case) and modeled in the analysis (Fig. 5.28).

Of course, in that case, the added narrow strips correspond to physical metallic conductors and must not be corrected. The main limitation of our approach probably results from the use of an equivalent circuit for the discrete element. Such a

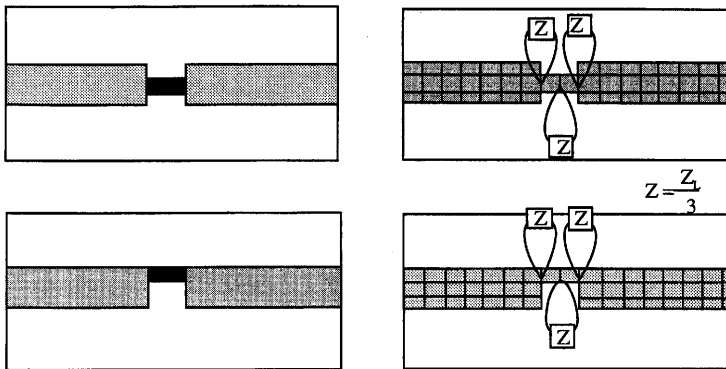


FIGURE 5.27 Two different configurations for the discrete element.

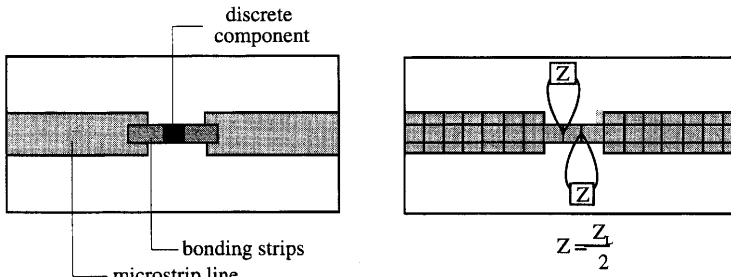


FIGURE 5.28 Discrete element with associated interconnections.

representation does not allow for investigating the effects of the electromagnetic fields on the internal behavior of this discrete element (as in [37]). Another limitation results from the surface representation of this element: only a three-dimensional (3-D) analysis would be able to account for the nonzero height of the component (for example, one expects that the coupling through the actual gap will largely be affected by a thick discrete element [38]). Finally, the required deembedding procedures do not appear as onerous additional steps because they can easily be integrated in an automatic scheme.

### 5.3.2 Analysis of Diode Controlled Planar Antennas

As a first practical example, we present the analysis of a frequency agile patch antenna [39]. The well-known principle consists of controlling the electric length of a microstrip patch antenna with two varactor diodes that are located between the radiating edges of the patch and the ground plane. As a result, the resonant frequency can be adjusted with the dc bias that is applied to the diodes. The studied structure is presented in Fig. 5.29.

The patch antenna is fed with a microstrip line that also ensures the dc biasing. This example provides a direct illustration of the one-port loading configuration. The two diodes (Macom MA4ST553-120) are represented as four serial lumped impedance elements distributed along a vertical metallic ribbon.

The equivalent circuit that is used for the diodes has been established from the designer catalogue and is also represented in Fig. 5.29. The intrinsic inductance of the vertical ribbon as well as the parasitic capacitances are removed after a preliminary deembedding procedure. Figure 5.30 presents the measured and calculated return loss for two different values of the dc bias (i.e., two different values of the capacitance in the simulation). The two results are seen to be in good agreement. The same accuracy is obtained for the radiating patterns (Fig. 5.31) at the correspondent resonant frequencies (2.25 GHz and 2.155 GHz, respectively). In fact, these patterns are not very different from those of the patch without the diodes.

In the second example, we more clearly point out the interest of such a global electromagnetic analysis. In this example (Fig. 5.32), two PIN diodes (Hewlett Packard HPND-4001) are used as switches in a crossed dipole antenna. The

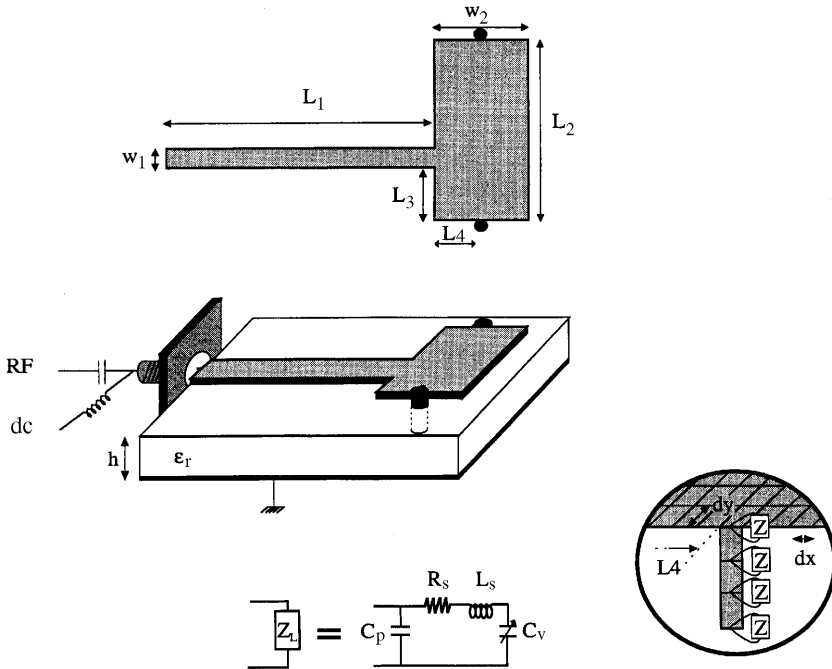


**FIGURE 5.29** The studied frequency agile antenna [39]. ( $L_1 = 75$  mm,  $W_1 = 4.61$  mm,  $L_2 = 41.5$  mm,  $W_2 = 27$  mm,  $L_3 = 13.83$  mm,  $L_4 = W_2/2$ ,  $h = 1.6$  mm,  $\epsilon_r = 2.17$ ,  $d_x = 1$  mm,  $d_y = 4.61$  mm,  $R_s = 1 \Omega$ ,  $L_s = 0.4$  nH,  $C_p = 0.13$  pF,  $C_v$  variable capacitance.)

modeling uses the same principle as previously and will not be explained again. When one diode is ON and the other is OFF, only one dipole is excited and the radiated field is linearly polarized (either vertical or horizontal). However, a very important parameter is the distance between one diode and the end of the line on which it is inserted ( $\delta_c$ ). This distance has to be as small as possible in order to obtain a compact structure. On the other hand, it must be sufficiently large to prevent direct coupling to the dipole from the part of the line that is located upstream to the diode. It is obvious that only a global electromagnetic analysis of the structure can efficiently optimize this phenomenon. As an illustration, Fig. 5.33 presents the variations of the return loss on line 1 for different positions of the diodes. When diode 1 is ON and diode 2 is OFF, the return loss exhibits two resonant frequencies. As explained in [28], the first one is due to the radiation of dipole 1 while the second one corresponds to a maximum transmission from line 1 to line 2 (via the antenna). As can be seen, the first resonance is not affected by the position of the diodes. This is due to the fact that diode 1 is ON and so it does not disturb the operating mode of dipole 1. Conversely, the second resonance is directly dependent on the position of the diodes (diode 2 in practice) because it controls the transmission between dipole 2 and line 2. Quantitatively, it appears that diode 2 is unable to reduce the coupling when it is located in the part of the line that lies beneath dipole 2 ( $\delta_c < 3$  mm).

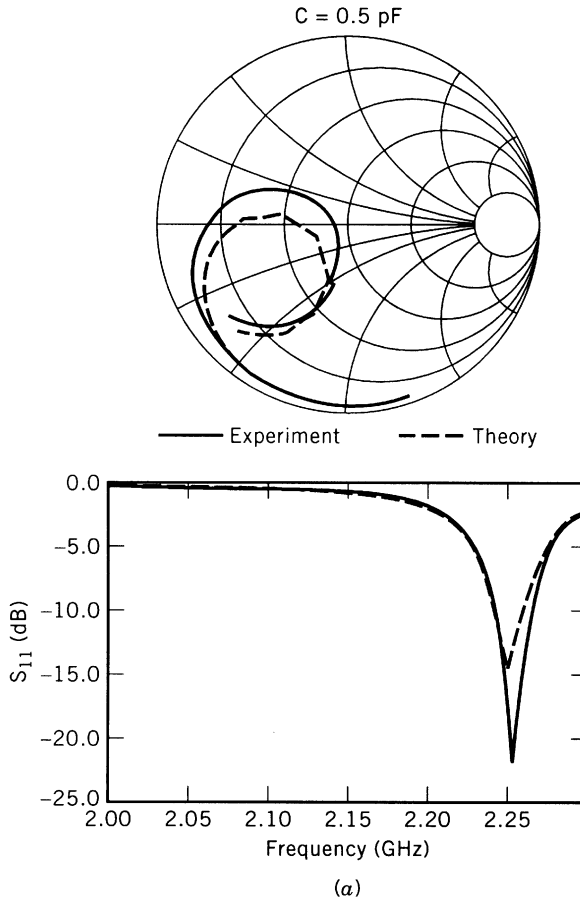


**FIGURE 5.30a** Reflection coefficient [39]:  $C = 0.5 \text{ pF}$ .

### 5.3.3 Analysis of Microstrip Active Antennas

We now focus on the representation of two-port active devices. As mentioned before (Section 5.2.3), the main new problem concerns the relative location of two ports and their voltage reference. The typical structure consists of a microstrip antenna connected to a feeding microstrip line in which an amplifier has been inserted. Such an antenna could be used as an elementary source in an active array: the amplifier would permit one to control its associated radiating element individually.

A first configuration was studied using a low noise amplifier (Avantek MSA0835) associated with an electromagnetically coupled dipole (Fig. 5.34).

From this a compact active receiving antenna was obtained [40]. In this structure, a single bias voltage was applied at the input of the line (RF output) using a biasing



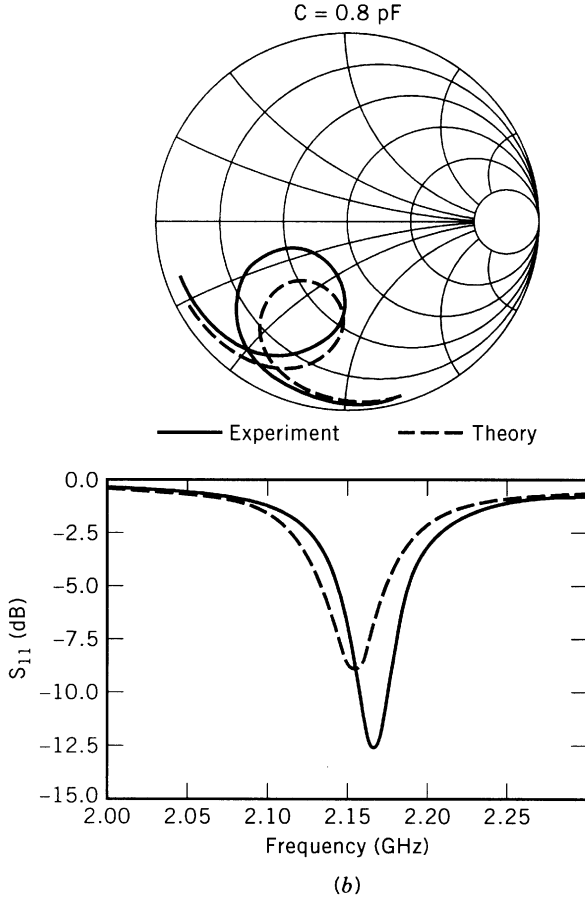


**FIGURE 5.30b** Reflection coefficient [39]:  $C = 0.8 \text{ pF}$ .

network. Figure 5.34 also presents the numerical modeling used in the global electromagnetic simulation.

The active element is represented by its impedance matrix  $Z_L$ . This matrix was directly calculated from the scattering parameters of the amplifier given in the designer catalogue ( $V_{cc} = 15 \text{ V}$ ,  $R_{bias} = 200 \Omega$ ,  $I_d = 36 \text{ mA}$ ). The two ports of the amplifier are supported by two infinitesimal gaps  $G_{L1}$  and  $G_{L2}$  with a common terminal connected to ground through a via hole. A parasitic inductance has also been computed and corrected; this corresponds to the short horizontal transmission lines between the ports and the via hole (two cells long). In this example, a virtual matched termination is added at the entrance of the microstrip line to absorb the RF power. Figure 5.35 presents the measured and computed return loss at the output of the line.

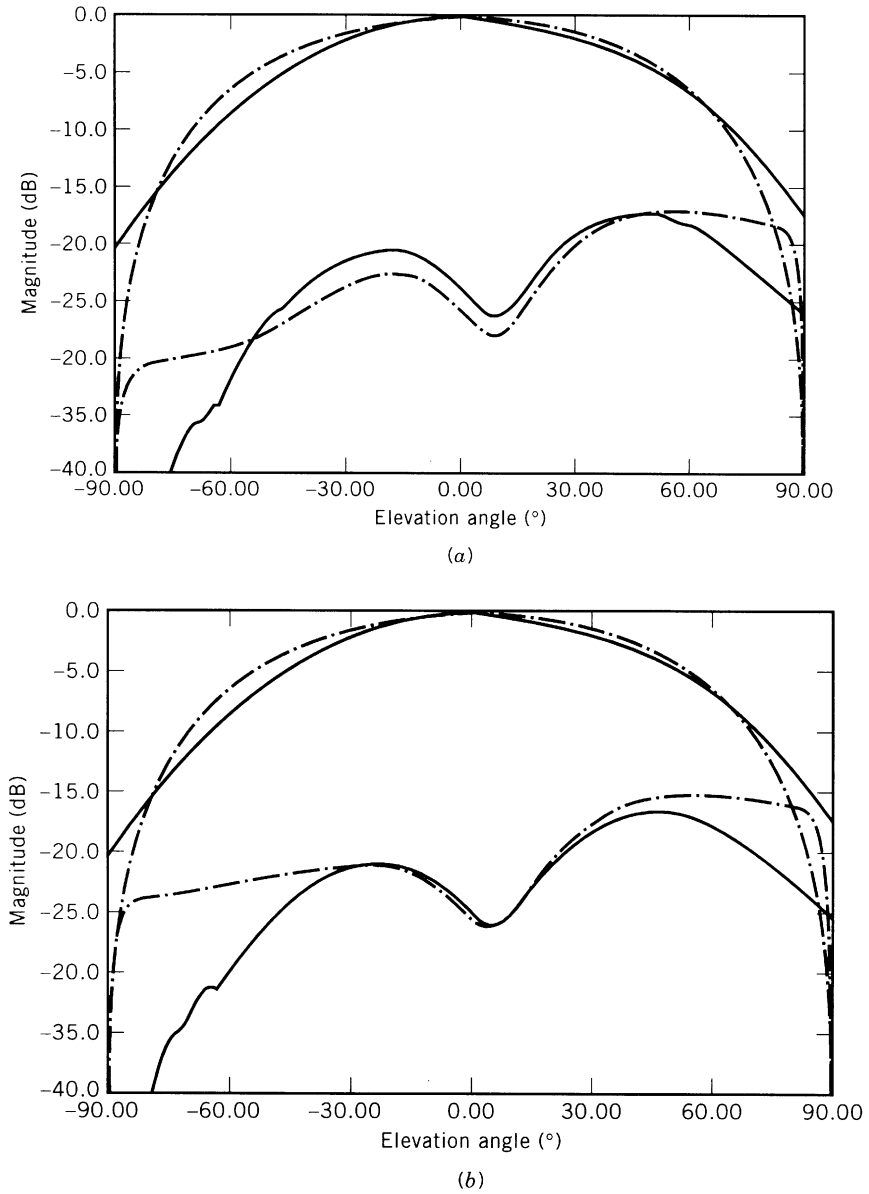


**FIGURE 5.31** Radiation patterns [39]: (a)  $C = 0.5$  pF, (b)  $C = 0.8$  pF; —, Experiment; ---, theory.

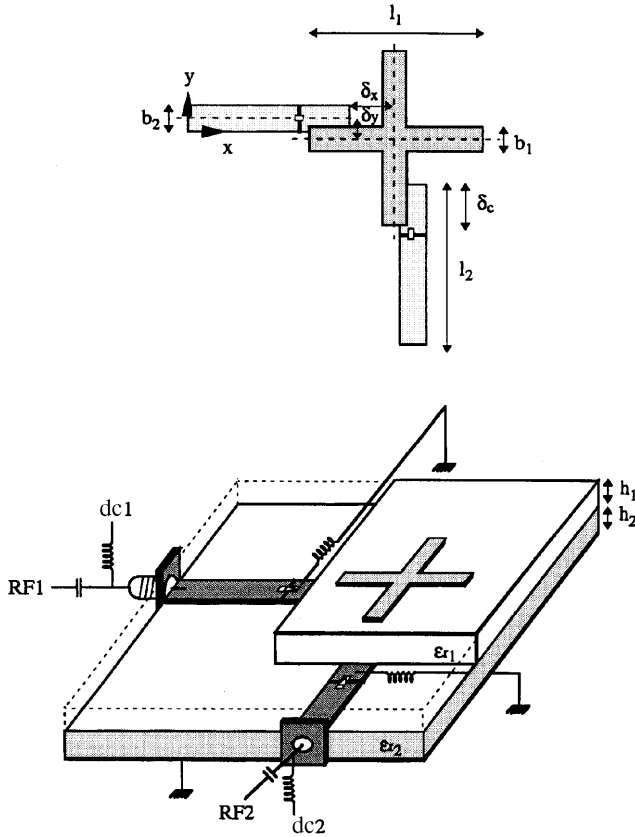


**FIGURE 5.32** The crossed dipole antenna. ( $l_1 = 11.9$  mm,  $b_1 = 1.7$  mm,  $\delta_x = 2.97$  mm,  $\delta_y = 0$  mm,  $l_2 = 38.5$  mm,  $b_2 = 2.2$  mm,  $h_1 = 1.6$  mm,  $h_2 = 0.8$  mm,  $\epsilon_{r1} = \epsilon_{r2} = 2.17$ ).

The active antenna is compared to its passive reference (i.e., the same antenna without the amplifier). Figure 5.36 presents the power received by the matched load when the dipole is excited by a copolarized wave with a normal incidence.

Both results show the accuracy that can be obtained with the present modeling. They illustrate the capabilities of the present approach to study structures in which no real separation exists between the active circuit and the radiating element. They also demonstrate that the presence of an amplifier in the direct vicinity of the antenna can significantly increase its performances in terms of bandwidth and gain simultaneously. Figure 5.37 presents the radiating patterns at 2.47 GHz. Once again, an excellent agreement is obtained. It can also be observed that the presence of the active element does not interfere with the radiating patterns.

A second configuration was recently researched. It uses an amplifier (Mini-Circuits ERA-1) associated with a microstrip-fed patch element and works as a transmitting antenna (Fig. 5.38).

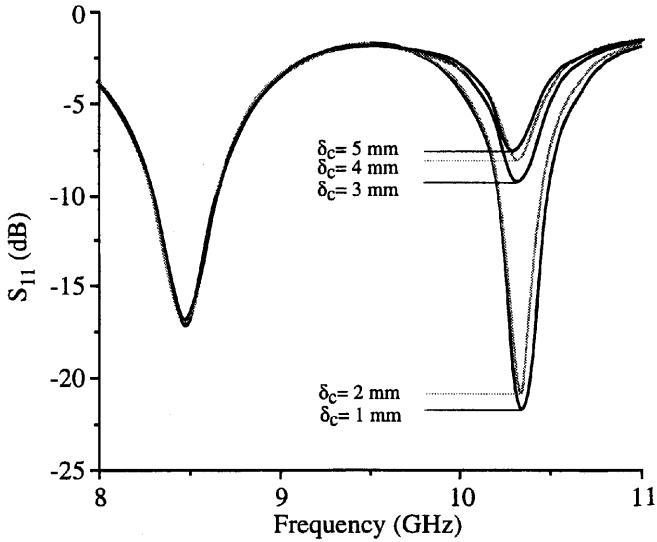


FIGURE 5.33 Return loss on port 1 (diode 1 ON, diode 2 OFF).

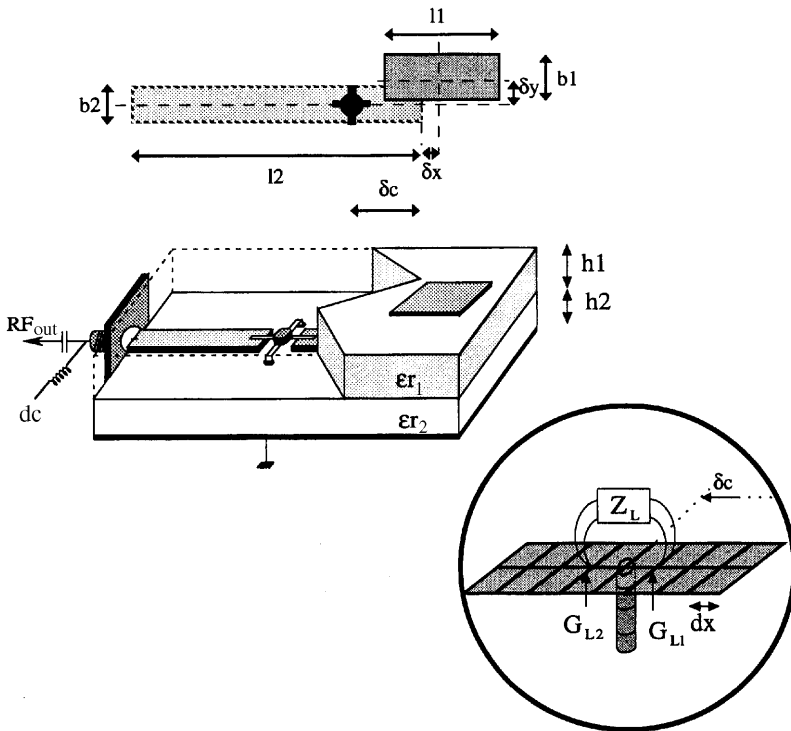


FIGURE 5.34 The receiving active antenna [40]. ( $\epsilon_{r1} = \epsilon_{r2} = 2.17$ ,  $l_1 = 43.5$  mm,  $b_1 = 2.9$  mm,  $l_2 = 68.9$  mm,  $b_2 = 2.2$  mm,  $h_1 = 1.6$  mm,  $h_2 = 0.8$  mm,  $\delta_x = 0$ ,  $\delta_y = 4.5$  mm,  $\delta_c = 18.1$  mm,  $\delta_x = 1.8125$  mm.)

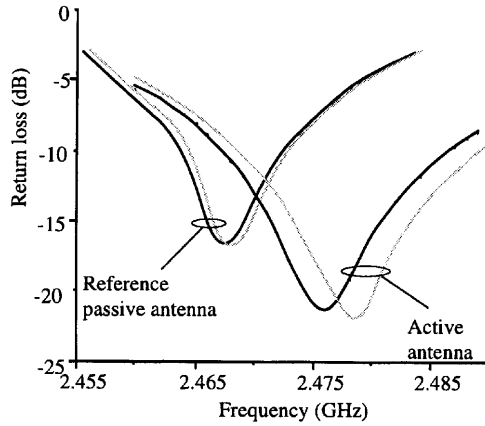


FIGURE 5.35 Output return loss: —, measurement; - - -, theory [40].

The dc bias is applied at the output of the amplifier using a  $\lambda/4$  stub. A bypass capacitance is also used at the entrance of the line to insulate the dc bias from the RF input. Figure 5.38 also presents the numerical modeling that is used in the vicinity of the amplifier.

As before, the active element is represented by its impedance matrix  $Z_L$ . This matrix is now constructed from the measured  $S$ -parameters of the amplifier ( $V_{DS} = 3.8\text{ V}$ ,  $I_d = 35\text{ mA}$ ). The main difference when compared with the previous example, appears in the modelling of the environment of the discrete component: all the horizontal and vertical metallic interconnections are now precisely described including the two ground connections, the two access lines and the associated steps

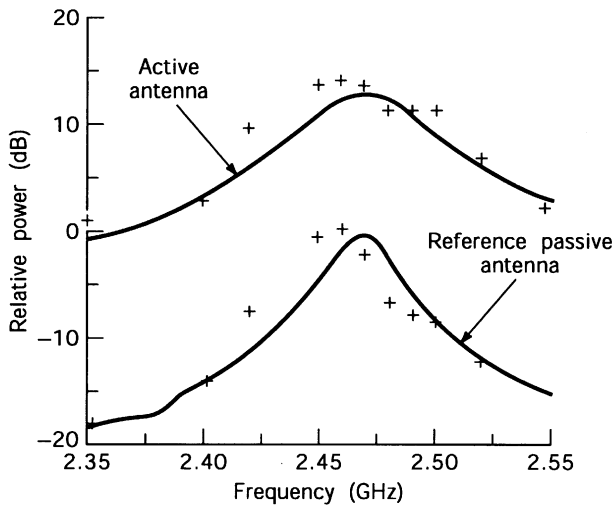


Figure 5.36 Received power: —, theory; + + +, measurement [40].

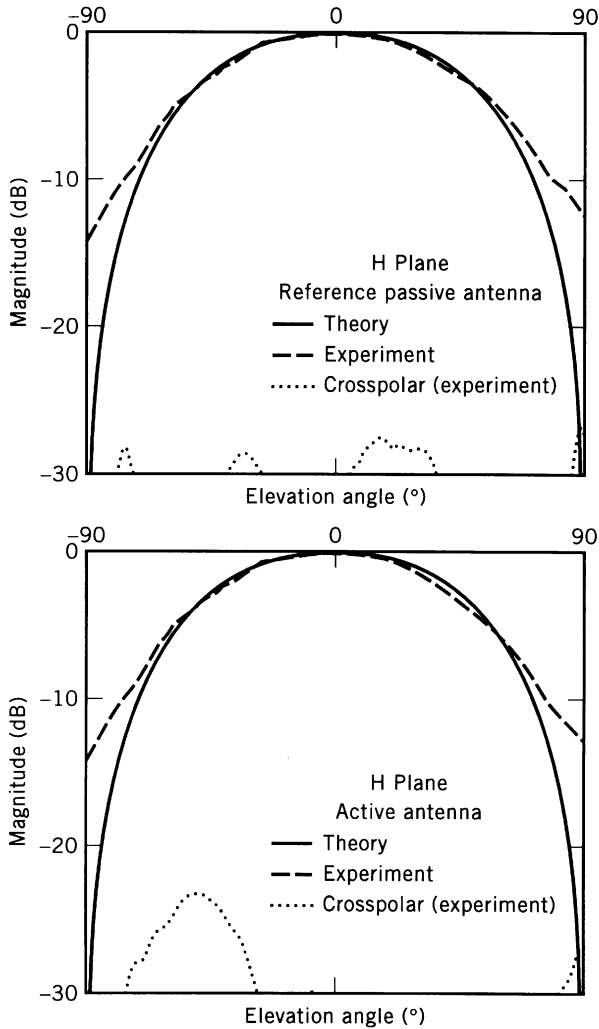
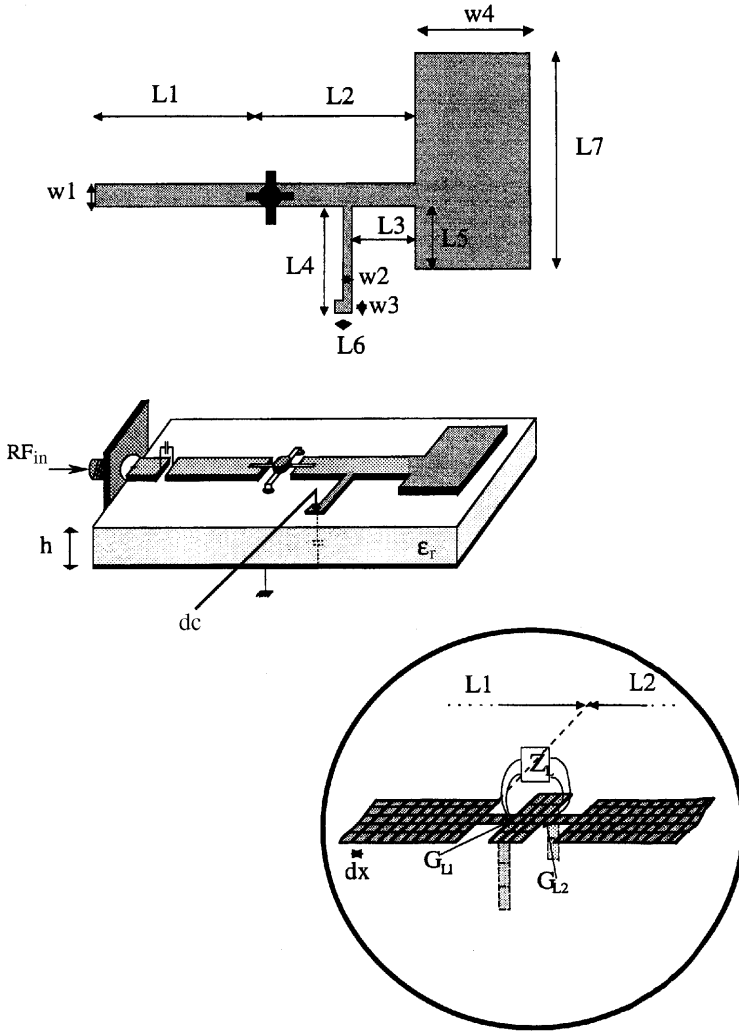


FIGURE 5.37 Radiation patterns ( $H$ -plane).

in width. Such a realistic modeling has been demonstrated to be necessary when the influence of the interconnections cannot be ignored [36]. The biasing circuitry has also been meshed (the bypass capacitors are supposed to behave as perfect short circuits at RF frequencies). Indeed, only the very active part of the discrete element is considered to be lumped. More precisely, it is treated as two coupled one-port lumped elements. The distance between these two lumped elements accounts for the length of the device. The metallic region between the two ports provides the



**FIGURE 5.38** The transmitting active antenna. ( $L_7 = 41.5$  mm,  $w_4 = 27$  mm,  $w_1 = 4.61$  mm,  $L_5 = 13.83$  mm,  $W_2 = 0.5$  mm,  $W_3 = 4.61$  mm,  $L_6 = 1$  mm,  $L_4 = 23.81$  mm,  $L_1 = 75$  mm,  $L_2 = 11$  mm,  $L_3 = 1.5$  mm,  $h = 1.6$  mm,  $\epsilon_r = 2.17$ ,  $d_x = 0.5$  mm.)

potential reference and ensures the ground connection. As previously, the numerical parasitic capacitance has been computed and is corrected in the final simulation. In the present case, no parasitic inductance is involved as no distribution is performed (as mentioned before, the way of modeling the region between the two ports is supposed to be realistic in regards to the actual ground connection).

Figure 5.39 presents the measured and calculated return loss at the entrance of the line. Here again, a good agreement is observed.

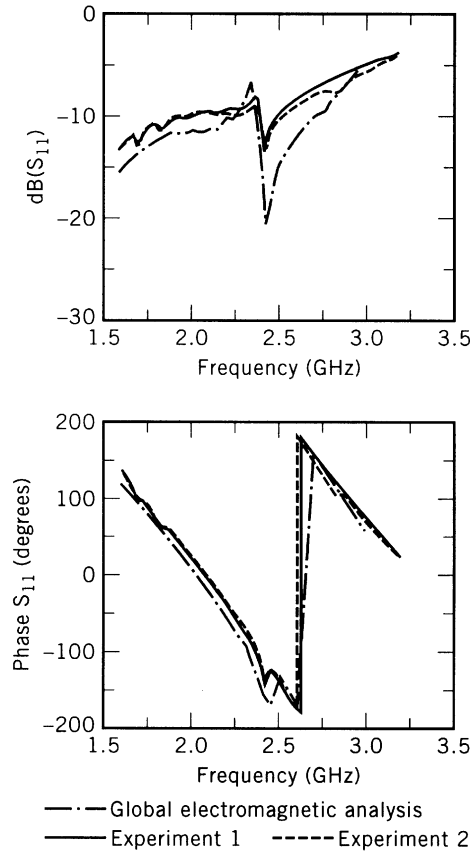


FIGURE 5.39 Input return loss.

### 5.3.4 Analysis of Active Linear Uniplanar Antennas

The developed theory is now applied to analyze a receiving active slot antenna fed by a coplanar waveguide (Fig. 5.40a). The bipolar amplifier MSA0835, used in the microstrip antenna presented in Section 5.3.3, is inserted into the strip conductor of the CPW close to the slot dipole. The dc bias is applied at the output RF line ( $V_{cc} = 15\text{ V}$ ,  $R_{bias} = 200\ \Omega$ ,  $I_d = 36\text{ mA}$ ). The amplifier is represented by its admittance matrix  $[Y]$ , which is directly calculated from the designer catalogue. The numerical configuration is given in Fig. 5.40. In order to prevent the slot mode propagation, the quadripole amplifier is symmetrically distributed in the two slots of the CPW as shown in Fig. 5.40.

The matching stub and the location of the active device are optimized using the previous approach in order to get a maximum gain at the resonant frequency of 4.9 GHz. The calculated output return loss and the gain of the active antenna (relative to the passive antenna) are compared to the measurements in Fig. 5.41. The curves show a good agreement between theoretical and experimental results. It is



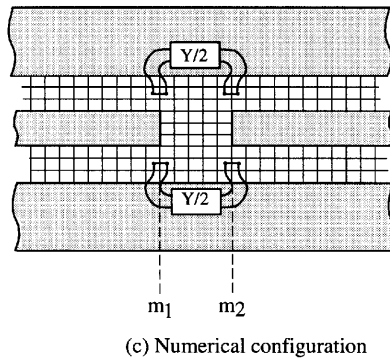
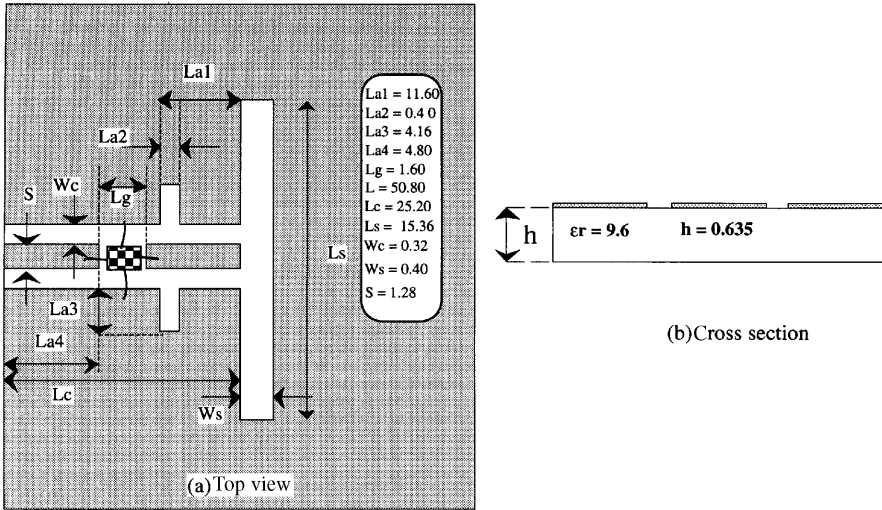


**FIGURE 5.40** Uniplanar active antenna. ( $L_{a1} = 11.60$  mm,  $L_{a2} = 0.40$  mm,  $L_{a3} = 4.16$  mm,  $L_{a4} = 4.80$  mm,  $L_g = 1.60$  mm,  $L = 50.80$  mm,  $L_c = 25.20$  mm,  $L_s = 15.36$  mm,  $W_c = 0.32$  mm,  $W_s = 0.40$  mm,  $S = 1.28$  mm,  $\epsilon_r = 9.6$ ,  $h = 0.635$  mm.)

evident that an output return loss greater than 0 dB is also predicted by the present theory. Therefore, the instability conditions can be avoided for the optimized antenna using the global approach. This confirms the accuracy between theoretical and experimental results.

The experimental radiated patterns of the active antenna have shown a small perturbation due to the stub and the gap discontinuities, which is observed in  $E$ -plane. The cross polarization of the active antenna, for both  $E$ - and  $H$ -plane, are also magnified by the gain of the amplifier [20]. In fact, only the currents'

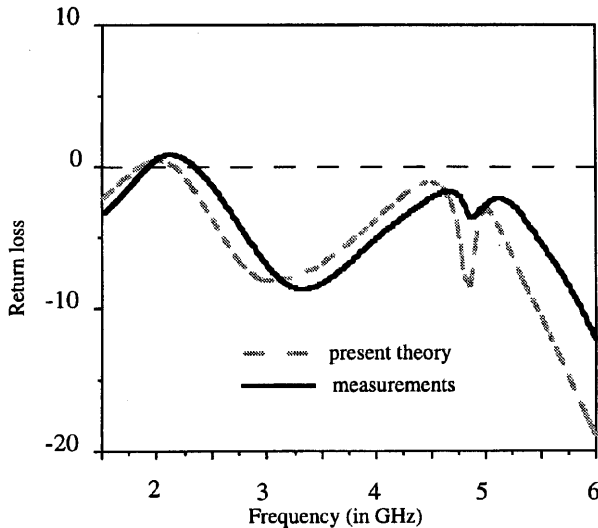


FIGURE 5.41 Output return loss.

distribution upstream to the active device is amplified. In contrast, the parasitic radiation from the RF connector, the measurements support and the feed line remains the same as for the passive structure.

## 5.4 EXTENSION OF THE APPROACH TO NONLINEAR DEVICES

### 5.4.1 Introduction

A separated approach is often used to analyze microwave circuits and antennas containing non-linear components. It consists (as was noted in the beginning of this chapter) in dividing the studied structure into several segments, which may be modeled independently from each other; the analysis and optimization of the total structure are performed with a commercial software package. The method that is widely accepted to be superior to time domain techniques for the analysis of nonlinear microwave circuits at steady-state is the harmonic balance method [33].

In this section, we present first the necessary steps to the extension of the frequency electromagnetic approach to support lumped elements operating as nonlinear ones. The formulation is based on the combination of the presented integral equation technique and the harmonic balance method. The problems related to this association and their solutions are then outlined through consideration of a simple case: a microstrip antenna loaded by a diode. Finally, a short discussion making a comparison between the global method and the compression technique is given.

### 5.4.2 Outline of the Method

The geometry of the general active structure to be analyzed is shown in Fig. 5.2. As in nonlinear problems solved by the harmonic balance (HB) technique, the structure is partitioned into two parts. One part contains the nonlinear devices and the second part corresponds to the passive multiport, which consists of linear lumped and distributed elements of the studied structure (Fig. 5.2). The multiport matrix is described in the frequency domain thanks to the MoM as presented in Section 5.2.4. The terminal behaviors of the nonlinear devices are represented in the time domain by their characteristic  $I/V$  equations. In steady state, the electrical (current and voltage) variables can be approximated by Fourier series as

$$i(t) = I_0 + 2 \sum_{n=1}^N I_{NL,n} \cos(2n\pi f_0 t + \phi_n) \quad (5.46)$$

$$v(t) = V_0 + 2 \sum_{n=1}^N V_{NL,n} \cos(2n\pi f_0 t + \phi_n) \quad (5.47)$$

$I_{NL,n}$  and  $V_{NL,n}$  are the harmonic components of the state vector,  $f_0$  is the fundamental operating frequency, and  $N$  is the number of harmonics required for the approximation of the dynamic steady-state solution.

As the linear and the nonlinear parts are interconnected and the time domain and frequency domain are related by Fourier transformation, the behavior of the active structure can be described by means of a system of nonlinear equations whose unknowns are the harmonic components of Eqs. 5.46 and 5.47 at all the connections between the two subparts. Theoretically, the problem consists of finding the state vector in such a way that the time domain voltages and currents obtained from Eqs. 5.46 and 5.47 have spectral components satisfying the MoM matrix equation at each considered harmonic.

The MoM matrix of the studied passive structure is calculated at each harmonic. The linear lumped elements are inserted following the procedure described in Section 5.2.4. However, two new additional aspects are required in the MoM matrix equation. First, the excitation of the structure cannot be as simple as Eq. 5.12. As it directly influences the nonlinear response of the loaded structure, the external generator has to be represented in a realistic way. At the fundamental frequency ( $f_0$ ), it must be represented by its internal impedance together with its emf voltage. At the higher harmonics, it will be represented by its internal impedance alone.

Second, the nonlinear discrete elements are represented by equivalent lumped voltage sources providing RF power at the all considered harmonics. Thus the excitation vector is extended to include harmonic components resulting from the Fourier series equations 5.46 and 5.47.

Practically, the internal impedance can be treated as a classical lumped impedance as in [23] or introduced through a corrective factor as in [22]. When it corresponds to the characteristic impedance of the excited line, it can also be considered as a matched termination.

All the lumped elements (one for the internal impedance of the external generators and one for each voltage generator) are connected to the passive distributed structure through infinitesimal gaps, as in the previous sections (the lumped voltages can be seen as delta-gap generators). Of course, the internal impedance can be absorbed by the passive distributed structure. Numerically, this means it can be included directly in the generalized MoM matrix as seen in Eq. 5.32. This simplification is not possible for the voltage generators because they cannot be expressed as linear functions of the current. As a consequence, they will appear explicitly in the excitation vector.

### 5.4.3 Example of Application

At this stage, we would like to consider a simple example of a nonlinear active antenna, which gives the resulting modifications in the MoM matrix equations when using the harmonic balance procedure. We consider the structure depicted in Fig.5.42. It represents a microstrip antenna loaded in its feeding line by a biased diode. For a general case, the diode's characteristic is expressed in the time domain as an exponential function:

$$i(t) = f(v(t)) = I_{\text{sat}}\{\exp[\alpha v(t)] - 1\} \quad (5.48)$$

The current  $i(t)$  is then considered as a series of current sources using Eq. 5.46. As explained in Section 5.24, the microstrip unloaded structure (i.e., the diode taken out) is represented, at each considered harmonic, by a generalized impedance matrix thanks to the MoM. With the help of the above combination procedure, the

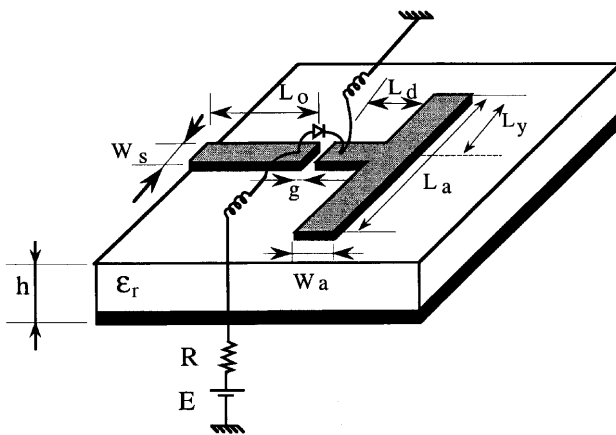


**FIGURE 5.42** Active microstrip antenna loaded with a diode. ( $W_s = 2.4$  mm,  $L_0 = 47.7$  mm,  $L_d = 2.0$  mm,  $L_y = 8.0$  mm,  $g = 0.3$  mm,  $L_a = 17.45$  mm,  $W_a = 2.2$  mm,  $h = 0.8$  mm,  $\epsilon_r = 2.17$ ,  $R = 10\Omega$ .)

excitation vector and the resulting system corresponding to the loaded antenna could be written as [21,41]

$$\begin{bmatrix} [Z_{f_0}] & [0] & & & [0] \\ [0] & [Z_{2f_0}] & & & \\ & & [\dots] & & \\ & & & [Z_{nf_0}] & [0] \\ [0] & & & [0] & [z_{Nf_0}] \end{bmatrix} \begin{bmatrix} [I_{f_0}] \\ [I_{2f_0}] \\ [\dots] \\ [I_{nf_0}] \\ [I_{Nf_0}] \end{bmatrix} = \begin{bmatrix} [V_{f_0}] \\ [V_{2f_0}] \\ [\dots] \\ [V_{nf_0}] \\ [V_{Nf_0}] \end{bmatrix} \tag{5.49}$$

where  $[Z_{nf_0}]$  is the  $n$ th harmonic generalized impedance submatrix,  $[I_{nf_0}]$  and  $[V_{nf_0}]$  are, respectively, the current and the excitation vectors at the same harmonic. Each impedance submatrix, which corresponds to interactions between discrete strip subsections, is calculated and its inverse stored.

The nonlinear dynamic steady-state analysis consists now in researching the current vector, which satisfies, by taking into account the Fourier series, both the linear frequency domain equation 5.49 and the nonlinear time domain equation 5.48. Following the previous two steps described in Section 5.4.2, we assemble two current frequency domain vectors  $[I_{NL}]$  and  $[I_L]$ . The vector  $[I_{NL}]$  corresponds to the harmonic components calculated by means of a fast Fourier transform (FFT algorithm) of the nonlinear device current (Eq. 5.48), while the vector  $[I_L]$  is obtained using the storage matrix and the voltage vector corresponding to the nonlinearity control. Under the steady state, we have

$$F([V]) = [I_{NL}] + [I_L] \tag{5.50}$$

where  $[V]$  is the voltage harmonic vector of the nonlinear device and  $F[V]$  is the harmonic balance error function, which has to be optimized for minimum discrepancy.

At this stage, the problem becomes the minimization of this last error function. For this, we use the Newton–Raphson algorithm [33,34]. It consists of solving a sequence of linearized systems of equations and iterates to a quadratic convergence near the solution.

It is well known that the main problem in the iteration process is the choice of the initial value, which leads rapidly to the final solution especially for a strong nonlinear case. For the given example, the initial best guess is derived using the assumption that the nonlinear device can be approximated by two loads in parallel. The first load is due to the initial biasing point ( $V_{0d}/I_{0d}$ ) and the second one corresponds to the dynamic load, which is defined as the derivative of the nonlinear equation at the biasing point.

### 5.4.4 Results

Figure 5.42 presents the antenna studied. The diode used is an HP 4005 beam lead. To characterize the active antenna by the present global nonlinear method, the diode

is biased with a 1.2-V source voltage. The calibrated voltage generator, which is applied at the input port of the structure, is chosen to deliver a 1-V sinusoidal signal at the frequency of 6 GHz. The nonlinear analysis is performed for the whole structure by considering five harmonics. The applied mesh rate is 28 cells per guided wavelength corresponding to the fifth harmonic. The reflection coefficient of the active antenna at the input port plane is shown relative to frequency in Fig. 5.43.

As the present example is deliberately chosen to be a simple one, the active antenna is also analyzed using a separated approach. To achieve this, the passive antenna is characterized using the integral equations technique presented in Section 5.2.1. The calculated input impedance at the diode plane ( $L = L_d$ ) is inserted as a one-port component in a circuit design software program. In this software (which is HP-MDS), the microstrip feeding line, the gap discontinuity of the diode, and the associated biasing circuit are added to complete the structure. The diode is described by the same characteristic equation as in our global approach. The obtained results are shown in the same figure. A good agreement can be observed for the return loss; the difference between both approaches remains less than 1.2 dB. The difference in magnitude may be due to the mutual coupling effects across the gap discontinuity, which were not taken into account in the circuit approach.

The nonlinear diode behavior can be increased using a 0.6-V dc bias. In Fig. 5.44, the calculated return loss and the radiation patterns are shown for the same active antenna. Radiation patterns are calculated from the current distributions at the

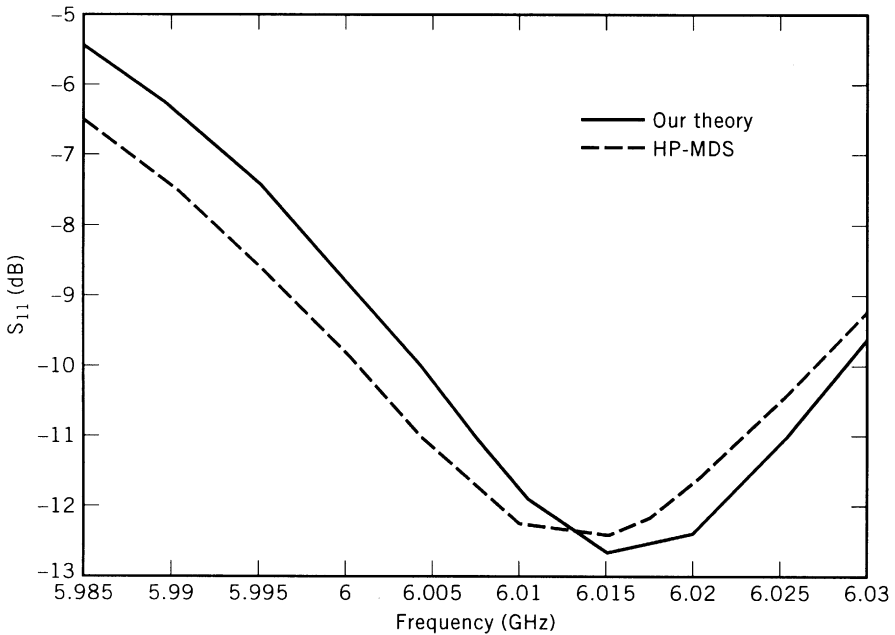


FIGURE 5.43 Comparison between global and circuit approach results.

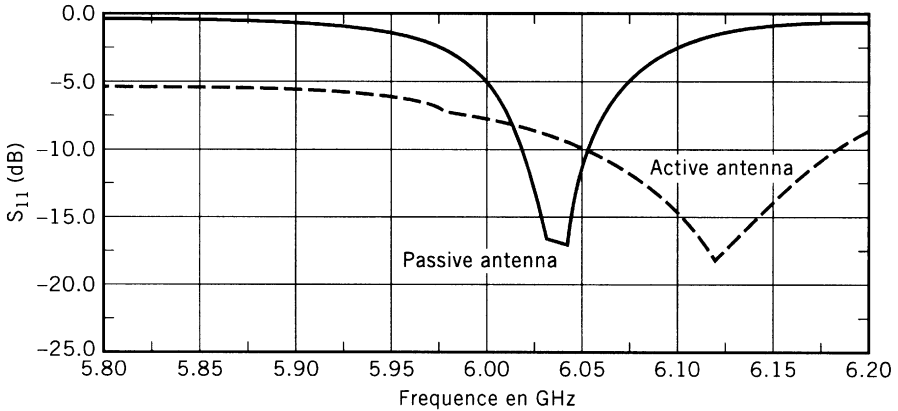


FIGURE 5.44 Input return loss.

corresponding harmonics (Fig. 5.45). The shift in resonant frequency and the important difference observed for the return loss show that nonlinearity could have an important influence on the near field antenna performance. The increased copolarization power at higher harmonics is due to conversion of energy into harmonics of the fundamental excitation frequency. Due to a mismatched condition and the conversion energy, it results in a decrease in power gain of the active antenna in the operating frequency band.

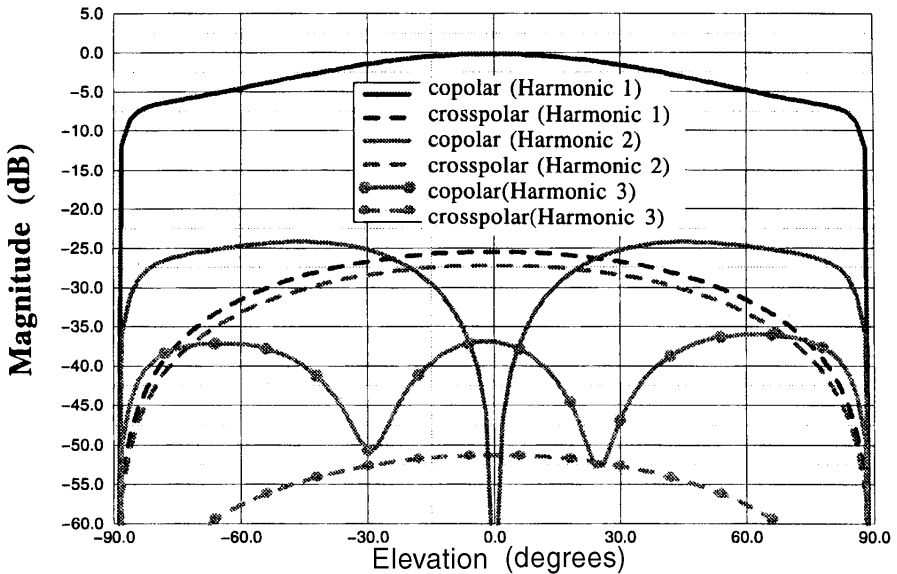


FIGURE 5.45 Radiation patterns of the nonlinear antenna.

### 5.4.5 Compression Approach

Initially proposed by Heinsen et al. [10] as a combination of a time domain method for the simulation of linear structure with the harmonic balance technique for nonlinear analysis, the compression technique is an alternative method in performing a rigorous electromagnetic analysis of active structures containing nonlinear devices. As opposed to the segmentation method, where the linear part is divided into several components, the compression technique offers a thorough analysis described by a single matrix (the compression matrix) for the entire distributed structure, including the interconnection regions where the physical nonlinear devices are inserted. The basic idea of this technique resides in the extension of the equivalent circuit model to the whole distributed part where inner ports (i.e., ports located within complex structures) are introduced to support the inclusion of lumped elements. Such ports achieve the interface between the linear distributed and the lumped devices parts. It should be appreciated that the inner port could correspond to the infinitesimal port. The compression matrix is determined in a straightforward manner by the use of electromagnetic simulations in which wave quantities are calculated from port voltages and currents [10,22,42].

Both the global and the compression formulations are general and rigorous. Moreover, the lumped devices can be placed as close as desired to the circuit discontinuities, since the electromagnetic coupling is taken into account around the lumped location.

The main advantage of the compression technique, when compared to the presented global approach (including directly lumped devices), resides, in our opinion, in carrying out the final linear and nonlinear simulations with standard circuit software. Consequently, the lumped elements can be changed without requiring further electromagnetic simulation for the distributed circuit part, albeit the space domain ports cannot be modified. However, the global approach, which operates as a unique simulator, permits optimization of either the lumped elements or their location, but at the expense of CPU time.

On the other hand, antenna application simulations are not as straightforward. The compression technique dictates that after the final circuit simulation (which gives the equivalent sources to be applied on the inner and external ports), it is necessary to return to the electromagnetic simulator in order to calculate the radiation patterns [22].

## 5.5 CONCLUSION

Because of the continued demand for low cost products, global electromagnetic approaches are becoming more and more important in the realization of high performance, low cost, and high density integrated microwave and millimeter-wave structures. Due to the complexity of the problem, many approaches have been investigated, this being aided by both the continuous increase of computing power and the maturity of a few rigorous numerical methods.



In this chapter we have presented a global electromagnetic approach for distributed structures that contain discrete devices; it is based on the association of the well-known integral equations technique solved by the method of moments and the theory of loaded scatterers. Not only does it simulate planar structures but it also performs their complete electromagnetic characterization in a numerical procedure, which is particularly realistic in regard to experimental measurements. The inclusion of multiport passive and linear active circuits has been demonstrated and illustrated by several examples involving two different technologies: microstrip and uniplanar active antennas. The global electromagnetic approach has also been extended to perform nonlinear simulations by combining the method of moment resolution with the harmonic balance technique. This extension has been presented for the case where the harmonic balance algorithm is directly integrated into the global electromagnetic simulator. For a simple active antenna a comparison with a standard analysis procedure has been made. It has been demonstrated that the new approach is capable of including nonlinear effects, which have significant influence on the radio electromagnetic performances. As an alternative solution, the compression approach involving an electromagnetic simulator (for the passive distributed part) together with a circuit simulator (for the nonlinear active part) has also been discussed.

At this time, the developed approach is still restricted to lumped representations of the discrete elements using equivalent electrical circuits. This fundamental assumption not only eliminates the effect of the electromagnetic field on the discrete elements, but it is also responsible for numerical parasitic elements that could systematically be observed in so-called global electromagnetic methods. Most of the present work has been dedicated to the investigation of these numerical parasitic elements. As a result, original deembedding procedures and distribution schemes have been proposed whose systematic use prevents numerical disorders. Finally, the developed approach appears quite general and yields accurate results. It not only provides some physical insight into the involved electromagnetic coupling mechanism but can also be used to characterize and to optimize active integrated circuits and antennas for which separated analysis results are not available or valid. It must also be pointed out that the insertion of lumped elements does not increase the computer requirements (CPU time and memory storage), which are those of conventional MoM software. As a matter of time, the main computing time is dedicated to the description of the passive distributed part of the structure.

Such CAD tools are expected to play a particularly active role in designing the next generation of integrated active antennas and microwave systems.

## Acknowledgment

The authors thank S. Dauguet, F. Goliás, and E. Vourch, whose doctoral dissertations contributed directly to this chapter, and the French research organizations—CNRS, CNET, and CNES—for their logistical and financial supports.

## REFERENCES

1. Lin, J., and Itoh, T., "Active integrated antennas," *IEEE Trans. Microwave Theory Tech.*, Dec. 1994, pp. 2186–2194.
2. Navarro, J.A., and Chang, K., *Integrated Active Antennas and Spatial Power Combining*, Wiley, New York, 1996.
3. Navarro, J.A., Hummer, K.A., and Chang, K., "Active integrated antenna elements," *Microwave J.*, Jan. 1991, pp. 115–126.
4. York, R.A., Martinez, R.D., and Compton, R.C., "Active patch antenna element for array applications," *Electron. Lett.*, vol. 26, no. 7, Mar. 1990, 494–495.
5. Johnson, H.C., Marx, R.E., Sanchez, A., and Mykiety, E. "A circularly polarized active antenna array using miniature GaAs FET amplifiers," *MTTS Dig.*, 1984, pp. 260–262.
6. An, H., Nauwelaers, B., and Van de Capelle, A., "Broadband active microstrip array elements," *Electron. Lett.* Vol. 27, no. 25, Dec. 1991, pp. 2378–2379.
7. York, R.A., and Popovic, Z.B., *Active and Quasi-optical Arrays for Solid-State Power Combining*, Wiley, New York, 1997.
8. Sui, W., Christensen, D.A., and Durney, C. H., "Extending the two-dimensional FDTD method to hybrid electromagnetic systems with active and passive lumped elements," *IEEE Trans. Microwave Theory Tech.*, vol. 40, no. 4, Apr. 1992, pp.724–730.
9. Guillouard, K., Wong, M.F., Fouad Hanna, V., and Citerne, J., "A new global finite element analysis of microwave circuits including lumped elements," *IEEE Trans. Microwave Theory Tech.*, vol. 44, no. 12, Dec. 1996, pp. 2587–2594.
10. Heinsen, S., Kunisch, J., and Wolff, I., "A unified framework for computer-aided noise analysis of linear and nonlinear microwave circuits," *IEEE Trans. Microwave Theory Tech.*, vol. 39, Dec. 1991, pp. 2170–2175.
11. Thomas, V.A., Jones, M.E., Picket-May, M., Taflove, A., and Harrigan, E., "The use of SPICE lumped circuits as sub-grid models for FDTD analysis," *IEEE Microwave Guided Lett.*, vol. 4, no. 5, May 1994, pp. 141–143.
12. Mosig, J., and Gardiol, F., "A dynamical radiation model for microstrip structures," *Adv. Electron. Electron Phys.*, vol. 59, 1982, pp. 139–237.
13. Alexopoulos, N., "Recent research advances in microstrip antennas and circuits at UCLA," *JINA*, Nice, 1988, pp. 209–211.
14. Lepeltier, Ph., Citerne, J., and Floch, J.M., "On the EMC dipole feedline parasitic radiation," *IEEE Trans. Antennas Propag.*, vol. 38, no. 6, Jun 1990, pp. 878–883.
15. Drissi, M., Fouad Hanna, V., and Citerne, J. A., "Analysis of coplanar waveguide radiating end effect using integral equations technique," *IEEE Trans. Microwave Theory Tech.*, vol. 39, no. 1, Jan. 1991, pp. 112–116
16. Dib, N., Ponchak, G., and Katehi, L., "A theoretical and experimental study of CPW shunt stubs," *IEEE Trans. Microwave Theory Tech.*, Jan. 1993, pp. 38–44.
17. Pozar, D., and Schaubert, D., *Microstrip Antennas: The Analysis and Design of Microstrip Antennas and Arrays*, IEEE Press, New York, 1995.
18. Harrington, R.F., "The theory of loaded scatterers," *Proc. IEE*, vol. 111, no. 4, Apr. 1964, pp. 617–623.
19. Gillard, R., Legay, H., Floch, J. M., and Citerne, J., "Une approche générale du concept d'antennes actives microruban à partir de la théorie des diffuseurs chargés," *Ann. Télécommun.*, vol. 46, no. 5–6, May–June 1991, pp. 251–257.

20. Vourch, E., Drissi, M., and Citerne, J. "A full-wave analysis of active uniplanar structures," AP-S Digest, New Port Beach, June 1995, pp. 1062–1065.
21. Goliás, F., Drissi, M., and Citerne, J., "A full wave analysis of active planar circuits including non-linear loads," 26th EuMC, Prague, 1996, pp. 476–479.
22. Dauguet, S., Gillard, R., Citerne, J., and Piton, G., "Extension of the compression approach to include the treatment of radiation pattern in the electromagnetic analysis of active planar antennas," AP-S Symposium, Montréal, July 1997.
23. Collin, R. E., *Field Theory of Guided Waves*, McGraw Hill, New York, 1960.
24. Drissi, M., Fouad Hanna, V., and Citerne, J. "Analysis of microstrip-slotline transition using integral equation technique," *Ann. Télécom.*, vol. 45, no. 5–6, 1990, pp. 300–305.
25. Legay, H., Gillard, R., Floch'h, J. M., and Citerne, J., "Via-hole effects on radiation characteristics of a patch microstrip antenna coaxially fed through the ground plane," *Ann. des Télécommun.*, vol. 46, no. 7–8, July–Aug. 1991, pp. 367–381.
26. Plet, J., Drissi, M., and Citerne, J. "Mixed potential integral equation technique for the characterization of microstrip antennas printed on uniaxial substrates," IEEE AP-S, Newport Beach (USA), June 1995, pp. 1266–1269.
27. Fouad Hanna, F., Achkar, J., Picon, O., Citerne, J., Drissi, M., and Amrani, C., "Analysis of some suspended stripline circuits," *Ann. Télécommun.*, vol. 47, no. 11–12, 1992, pp. 515–529.
28. Gillard, R., Corre, J. H., Drissi, M., and Citerne, J., "A general treatment of matched terminations using integral equations—modelling and applications," *IEEE Trans. Microwave Theory Tech.*, vol. 42, no. 12, Dec. 1994, pp. 2545–2553.
29. Harrington, R. F., *Field Computation by Moment Methods* Macmillan, New York, 1968.
30. Glisson, A. W., and Wilton, D. R., "Simple and efficient numerical methods for problems of electromagnetic radiation and scattering from surfaces," *IEEE Trans.*, vol. AP-29, 1980, pp. 593–603.
31. Sercu, J., Van Hese, J., Fache, N., and De Zutter, D., "Improved calculation of the inductive and capacitive interactions of vertical sheet currents in multilayered medium," EuMC, Prague 1996, pp. 533–536.
32. Pekonen, O. P., M., and Xu, J., "Rigorous analysis of circuit parameter extraction from an FDTD simulation excited with a resistive voltage generator," *Microwave Opt. Tech. Lett.* vol. 12, no. 4, July 1996, pp. 205–210.
33. Rizzoli, V., and Neri, A., "State of the art and present trends in nonlinear microwave CAD techniques," *Trans. Microwave Theory Tech.*, vol. 36, no. 2, pp. 343–365.
34. Kundert, K. S., and Sangiovanni-Vincentelli, A., "Simulation of non-linear circuit in the frequency domain," *IEEE Comput. Aided Design*, vol. CAD-5, Oct. 1986, pp. 521–535.
35. Gillard, R., Moustadir, S., Lebolzer, F., and Citerne, J., "A magnetic current formulation for the modelling of discrete elements in the FDTD method," MTT-S Symposium, Denver, CO, June 1997.
36. Dauguet, S., Loison, R., Gillard, R., Citerne, J., and Piton, G., "Rigorous global electromagnetic analysis of interconnections in MHIC applications," *Electron. Lett.*, vol. 32, no. 17, Aug. 1996, pp. 1596–1597.
37. El-Ghazaly, S., and Megahed, M. A., "Electromagnetic waves in semiconductor devices," IEEE MTT-S, 1996, Workshop: Device Field Interactions for Future Advances in Microwave and RF Circuits.

38. Lau, Y. C., Leong, M. S., and Kooi, P. S., "Modeling of chip resistors for high-frequency microwave applications with the use of the FDTD method," *Microwave Opt. Technol. Lett.*, vol. 14, no. 5, Apr. 1997, pp. 259–261.
39. Dauguet, S., Gillard, R., Citerne, and Piton, G., "Global electromagnetic analysis of microstrip agile antenna," *Electron Lett.*, vol. 33, no. 13, June 1997, pp. 1111–1112.
40. Gillard, R., Legay, H., Floch, J. M., and Citerne, J., "A rigorous analysis of a receiving active microstrip antenna," *Elec. Lett.*, vol. 27, no. 25, Dec. 1991, pp. 2357–2359
41. Goliias, F., Drissi, M. and Citerne, J., "Analyse électromagnétique globale de structures actives planaires chargées par des composants non-linéaires," JINA96, pp. 79–82
42. Linot, B., Wong, M. F., Picon, O., Fouad Hanna, V., and Drissi, M., "Nouvelle méthode d'insertion d'éléments localisés sur une ligne coplanaire avec les équations intégrales," 13th Hertzian Optics and Dielectrics Colloquium, Zaragoza, Spain, 1995, pp. 105–108.
43. Gillard, R., Dauguet, S., and Citerne, J., "Correction procedure for the numerical parasitic elements associated with lumped elements in global electromagnetic simulators," *IEEE Trans. on MTT*, vol. 46, no. 9, Sept. 1998, pp. 1298–1306.

CHAPTER SIX

---

# Full Wave Electromagnetic Analysis in the Time Domain

---

**YONGXI QIAN and TATSUO ITOH**  
Center for High Frequency Electronics  
Department of Electrical Engineering  
University of California  
Los Angeles, CA

## 6.1 INTRODUCTION

Modern numerical techniques for solving electromagnetic problems started in the mid-1960s, in close relation with the invention of a family of inhomogeneous planar transmission structures including microstrip lines and slotlines, as well as coplanar waveguides (CPW), which possessed good compatibility with the emerging integrated circuit (IC) technology during that period. Analytical techniques such as conformal mapping were widely used before that time, as powerful computers were not easily available to most researchers. By the end of the 1980s, a number of sophisticated, full wave numerical techniques for solving Maxwell's equations had been developed and established in the microwave antennas and propagation community. They include the spectral domain method, integral equation method, method of moments, method of lines, transverse resonance method, mode matching

method, finite-element method, finite-difference method in frequency or time domain, and transmission line matrix (TLM) method. A detailed treatment of these techniques can be found in *Numerical Techniques for Microwave and Millimeter-Wave Passive Structures* [1].

One of the most significant features of the above numerical techniques is that most of them provide time harmonic solutions to Maxwell's equations. The major difficulty encountered in these approaches, especially for electrically large problems and geometrically complex structures, is the inverse of matrices in relation to the solution of a set of linear simultaneous equations. Another main restriction of the frequency domain approach is that it is indirect and difficult to include lumped, nonlinear, or active circuit elements into the full wave analysis. Until recently, large signal modeling of active circuits has been done either completely in the time domain (e.g., SPICE) or by using combined techniques such as the harmonic balance method (HBM).

There are two exceptions in the above-mentioned family of numerical techniques, however, which avoid the problem of matrix inversion, and solve Maxwell's equations directly in the time and space domains. One example is the transmission line matrix (TLM) method, which exploits the analogy between field propagation in space and voltage/current propagation in a spatial transmission line network formulated as a multiple scattering process following Huygens's principle [2]. The other one is the finite-difference time-domain (FDTD) method, which has gained so much popularity that it has outgrown almost all the other approaches in the number of publications during the past few years and remains the most preferred approach for a wide range of electromagnetic problems including antenna radiation, scattering, EMC/EMI, microwave and millimeter-wave integrated circuits (MIMICs) and packaging, and almost all types of waveguiding structures from UHF up to the optical region [3].

The FDTD method, originally proposed by K. S. Yee [4], is an approach that directly solves Maxwell's equations by a proper discretization of both the time and space domains. By allocating the six electromagnetic field components on a cubic cell and applying central difference to Maxwell's partial differential equations. Yee derived a very simple "leap-frog" algorithm for updating the fields inside the problem region. Although Yee published his paper back in 1966, the method did not gain instant popularity, mainly because of the lack of an efficient and high accuracy absorbing boundary condition (ABC) to realize reflectionless truncation of open-region problems, as well as limited computer resources (CPU speed and memory capacity) available at that time. There are a number of researchers, however, who recognized the great potentials of the FDTD method and worked intensively to develop and refine the algorithm. A detailed history and comprehensive treatment of the FDTD method can be found in two recent books by Kunz and Luebbers [5] and Taflove [6].

Since both TLM and FDTD methods solve electromagnetic problems through simulation of wave interaction and propagation in the time domain, the need to solve large-scale linear simultaneous equations and related problems such as convergence,

stability, and spurious response is avoided. The most distinguished advantages of these time domain techniques, however, are their great flexibility and versatility in applying to virtually all types of electromagnetic problems, from simple one-dimensional transmission lines to the most complicated three-dimensional structures with arbitrary material properties, for both passive components and active circuits, as well as for integrated circuit–antenna modules. Such unique capabilities make these time domain approaches very promising candidates for the next-generation CAD tools, which combine electromagnetic simulation, circuit design, and optimization functionality in a completely unified fashion. In fact, these superior and unique capabilities have tempted some researchers to reformulate the finite-element method (FEM) in the time domain instead of the traditional frequency domain, in an effort to facilitate the incorporation of active devices [7].

The purpose of this chapter is twofold. We will first give a brief but complete introduction of the basic principles and implementation details of the FDTD algorithm, so that the reader should be ready to write a practically useful three-dimensional (3-D) FDTD code after reading the contents of this chapter. The second purpose is to demonstrate some examples of FDTD applications in relation to microwave integrated circuits and antennas. Finally, extension of the FDTD algorithm to incorporate lumped circuit elements and active devices and its applications in simulating practical microwave integrated circuits and antennas are introduced briefly. Although this is a research topic that is still at its infant stage, the results obtained by the extended FDTD so far have been encouraging and reveal unique EM simulation capabilities unavailable with any of the existing commercial CAD tools.

## 6.2 FDTD FUNDAMENTALS AND IMPLEMENTATION ISSUES

### 6.2.1 Maxwell's Equations and the Yee Algorithm

In a source-free, linear, isotropic and nondispersive medium, Maxwell's curl equations are

$$\nabla \times \mathbf{E} = -\mu \frac{\partial \mathbf{H}}{\partial t} - \rho^* \mathbf{H} \quad (6.1a)$$

$$\nabla \times \mathbf{H} = \varepsilon \frac{\partial \mathbf{E}}{\partial t} + \sigma \mathbf{E} \quad (6.1b)$$

where  $\varepsilon$  and  $\sigma$ ,  $\mu$  and  $\rho^*$  are, respectively, the electric permittivity (F/m) and conductivity (S/m), and magnetic permeability (H/m) and resistivity ( $\Omega/m$ ) of the medium.

In a three-dimensional rectangular coordinate system, Eqs. 6.1a and 6.1b can be expanded into the following partial differential equations:

$$\frac{\partial H_x}{\partial t} = \frac{1}{\mu} \left( \frac{\partial E_y}{\partial z} - \frac{\partial E_z}{\partial y} - \rho^* H_x \right) \tag{6.2a}$$

$$\frac{\partial H_y}{\partial t} = \frac{1}{\mu} \left( \frac{\partial E_z}{\partial x} - \frac{\partial E_x}{\partial z} - \rho^* H_y \right) \tag{6.2b}$$

$$\frac{\partial H_z}{\partial t} = \frac{1}{\mu} \left( \frac{\partial E_x}{\partial y} - \frac{\partial E_y}{\partial x} - \rho^* H_z \right) \tag{6.2c}$$

$$\frac{\partial E_x}{\partial t} = \frac{1}{\varepsilon} \left( \frac{\partial H_z}{\partial y} - \frac{\partial H_y}{\partial z} - \sigma E_x \right) \tag{6.2d}$$

$$\frac{\partial E_y}{\partial t} = \frac{1}{\varepsilon} \left( \frac{\partial H_x}{\partial z} - \frac{\partial H_z}{\partial x} - \sigma E_y \right) \tag{6.2e}$$

$$\frac{\partial E_z}{\partial t} = \frac{1}{\varepsilon} \left( \frac{\partial H_y}{\partial x} - \frac{\partial H_x}{\partial y} - \sigma E_z \right) \tag{6.2f}$$

In order to solve the above partial differential equations by using finite difference, we first need to discretize both the space and time domains, as shown in Fig. 6.1a. For an arbitrary function of space and time,  $F(x, y, z, t)$ , we can express this discretization as follows:

$$F^n(i, j, k) = F(i \Delta x, j \Delta y, k \Delta z, n \Delta t) \tag{6.3}$$

where  $\Delta x$ ,  $\Delta y$ ,  $\Delta z$ , and  $\Delta t$  are the discretization sizes along the  $x$ ,  $y$ ,  $z$ , and  $t$  axes, respectively. To calculate the value of the function  $F$ , Yee proposed a cubic cell as shown in Fig. 6.1b, which is often called the ‘‘Yee cell,’’ where the electric and magnetic field components are located at the edges and on the surfaces of the cell,

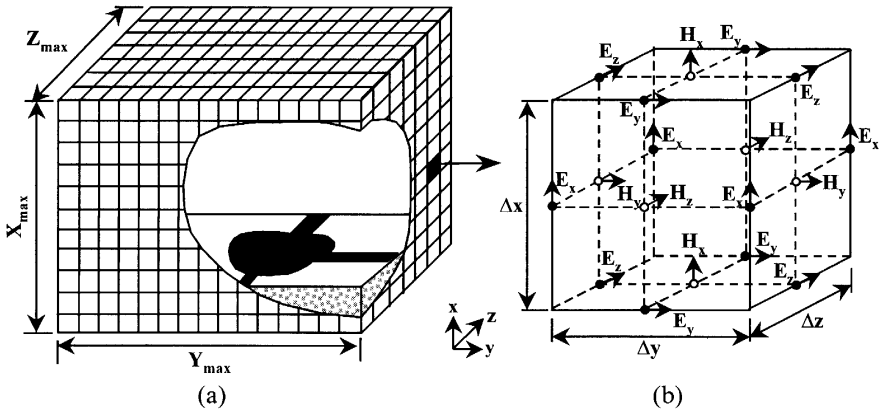


FIGURE 6.1 (a) Discretization of a computational region and (b) the Yee cell.



respectively, and are half-step offset in both space and time domains. Yee then proposed the following central difference scheme:

$$\frac{\partial F^n(i, j, k)}{\partial x} = \frac{F^n(i + \frac{1}{2}, j, k) - F^n(i - \frac{1}{2}, j, k)}{\Delta x} + O[(\Delta x)^2] \quad (6.4a)$$

$$\frac{\partial F^n(i, j, k)}{\partial t} = \frac{F^{n+1/2}(i, j, k) - F^{n-1/2}(i, j, k)}{\Delta t} \quad (6.4b)$$

which is accurate to the second order of  $\Delta x$  and  $\Delta t$ , respectively. Referring to the allocation of field components at the  $(i, j, k)$ th Yee cell as shown in Fig. 6.2, and using the above central difference expressions, we can easily derive Yee's famous "leap-frog" algorithm for updating the six electromagnetic field components with respect to a certain type of initial condition or source excitation:

$$\begin{aligned} H_x^{n+1/2}(i, j, k) &= \frac{1 - \rho^* \Delta t / 2\mu}{1 + \rho^* \Delta t / 2\mu} H_x^{n-1/2}(i, j, k) - \frac{\Delta t / \mu}{1 + \rho^* \Delta t / 2\mu} \\ &\times \left( \frac{E_z^n(i, j, k) - E_z^n(i, j - 1, k)}{\Delta y} - \frac{E_y^n(i, j, k) - E_y^n(i, j, k - 1)}{\Delta z} \right) \end{aligned} \quad (6.5a)$$

$$\begin{aligned} H_y^{n+1/2}(i, j, k) &= \frac{1 - \rho^* \Delta t / 2\mu}{1 + \rho^* \Delta t / 2\mu} H_y^{n-1/2}(i, j, k) - \frac{\Delta t / \mu}{1 + \rho^* \Delta t / 2\mu} \\ &\times \left( \frac{E_x^n(i, j, k) - E_x^n(i, j, k - 1)}{\Delta z} - \frac{E_z^n(i, j, k) - E_z^n(i - 1, j, k)}{\Delta x} \right) \end{aligned} \quad (6.5b)$$

$$\begin{aligned} H_z^{n+1/2}(i, j, k) &= \frac{1 - \rho^* \Delta t / 2\mu}{1 + \rho^* \Delta t / 2\mu} H_z^{n-1/2}(i, j, k) - \frac{\Delta t / \mu}{1 + \rho^* \Delta t / 2\mu} \\ &\times \left( \frac{E_y^n(i, j, k) - E_y^n(i - 1, j, k)}{\Delta x} - \frac{E_x^n(i, j, k) - E_x^n(i, j - 1, k)}{\Delta y} \right) \end{aligned} \quad (6.5c)$$

$$\begin{aligned} E_x^{n+1}(i, j, k) &= \frac{1 - \sigma \Delta t / 2\varepsilon}{1 + \sigma \Delta t / 2\varepsilon} E_x^n(i, j, k) + \frac{\Delta t / \varepsilon}{1 + \sigma \Delta t / 2\varepsilon} \\ &\times \left( \frac{H_z^{n+1/2}(i, j + 1, k) - H_z^{n+1/2}(i, j, k)}{\Delta y} \right. \\ &\quad \left. - \frac{H_y^{n+1/2}(i, j, k + 1) - H_y^{n+1/2}(i, j, k)}{\Delta z} \right) \end{aligned} \quad (6.5d)$$

$$\begin{aligned}
E_y^{n+1}(i, j, k) &= \frac{1 - \sigma \Delta t/2\varepsilon}{1 + \sigma \Delta t/2\varepsilon} E_y^n(i, j, k) + \frac{\Delta t/\varepsilon}{1 + \sigma \Delta t/2\varepsilon} \\
&\times \left( \frac{H_x^{n+1/2}(i, j, k+1) - H_x^{n+1/2}(i, j, k)}{\Delta z} \right. \\
&\quad \left. - \frac{H_z^{n+1/2}(i+1, j, k) - H_z^{n+1/2}(i, j, k)}{\Delta x} \right) \quad (6.5e)
\end{aligned}$$

$$\begin{aligned}
E_z^{n+1}(i, j, k) &= \frac{1 - \sigma \Delta t/2\varepsilon}{1 + \sigma \Delta t/2\varepsilon} E_z^n(i, j, k) + \frac{\Delta t/\varepsilon}{1 + \sigma \Delta t/2\varepsilon} \\
&\times \left( \frac{H_y^{n+1/2}(i+1, j, k) - H_y^{n+1/2}(i, j, k)}{\Delta x} \right. \\
&\quad \left. - \frac{H_x^{n+1/2}(i, j+1, k) - H_x^{n+1/2}(i, j, k)}{\Delta y} \right) \quad (6.5f)
\end{aligned}$$

Note that we have used semi-implicit expressions such as

$$H_x^n(i, j, k) = \frac{H_x^{n+1/2}(i, j, k) + H_x^{n-1/2}(i, j, k)}{2} \quad (6.6)$$

in obtaining the field updating equations 6.5a to 6.5f. This is necessary because when deriving Eq. 6.5a from Eq. 6.2a, for example, we need to evaluate all the field quantities on the right-hand side of Eq. 6.2a at the same time step  $n$ , including the magnetic field component  $H_x$ , which appears due to the finite magnetic resistivity  $\rho^*$ . The semi-implicit approximation of Eq. 6.6 has been found to result in numerically stable and accurate results for arbitrary values of  $\rho^*$  from zero to infinity and is straightforward to implement without the need to solve simultaneous equations for  $H_x^{n+1/2}(i, j, k)$  [6]. The same approach has been applied to the remaining five components in a similar manner.

In order to obtain sufficient spatial resolution within the computational region, the Yee cell size should be small enough so that  $\Delta x$ ,  $\Delta y$ , and  $\Delta z$  are typically 1/10 to 1/20 of the wavelength corresponding to the highest frequency of interest, although larger cells can be used in a dispersion-optimized Yee algorithm with fourth-order accurate spatial central differences [6]. Meanwhile, the time step size,  $\Delta t$ , should also be chosen properly in order to ensure the numerical stability of the above leap-frog algorithm. For a general 3-D FDTD grid, the following Curant's stability criterion should be satisfied:

$$v_{\max} \Delta t \leq \frac{1}{\sqrt{(1/\Delta x)^2 + (1/\Delta y)^2 + (1/\Delta z)^2}} \quad (6.7)$$

where  $v_{\max}$  is the highest velocity of wave propagation within the problem space and can usually be replaced by  $c = 2.997925 \times 10^8$  m/s, the speed of light in free space. For the case of passive circuits and antennas, it is usually safe to make  $\Delta t$  the largest

value allowed by the above stability condition to minimize the number of FDTD iteration steps. However, for FDTD simulations including lossy materials and nonlinear devices, it is usually necessary to choose a smaller value for  $\Delta t$  so that the FDTD iteration will not “blow up” at later time steps [6]. A more detailed discussion on this issue is given in Section 6.4.1.

**6.2.2 Treatment of PEC, PMC, and Dielectric Interfaces**

**6.2.2.1 Perfect Electric Conductor (PEC)** On the surface of a PEC, all the tangential electric field and normal magnetic field components must be zero. Referring to the allocation of field components on the Yee cell as shown in Fig. 6.2, a PEC located at the top surface of the  $(i, j, k)$ th Yee cell can be realized by simply enforcing

$$\begin{aligned}
 E_y(i, j, k - 1) = E_y(i, j, k) = E_z(i, j - 1, k) \\
 = E_z(i, j, k) = H_x(i, j, k) \equiv 0
 \end{aligned}
 \tag{6.8}$$

at any time step during the FDTD simulation. Since  $H_x(i, j, k)$  is calculated by using the four surrounding tangential electric fields, it is usually sufficient to set only the four electric field components in Eq. 6.8 to zero. Similarly, if we want to define the  $(i, j, k)$ th Yee cell as a PEC block, we can achieve this by setting all twelve electric field components and eight magnetic field components to zero values at all time steps.

**6.2.2.2 Perfect Magnetic Conductor (PMC)** To realize PMC, we need to set the tangential magnetic field and normal electric field components to zero at its

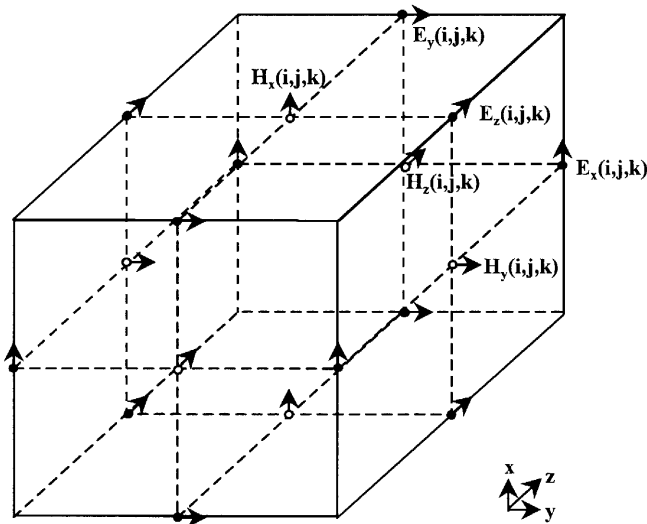


FIGURE 6.2 Allocation of field components at the  $(i, j, k)$ th Yee cell.

surface. Again referring to Fig. 6.2, we notice that it is possible to define such a PMC by using a cross section that is a half-step offset from the Yee cell's surface. For example, by enforcing

$$H_y(i, j - 1, k) = H_y(i, j, k) = H_z(i, j, k - 1) = H_z(i, j, k) \equiv 0 \quad (6.9)$$

at any time, we realize a normal-to- $x$  PMC at the midsection of the Yee cell shown in Fig. 6.2. Such a PMC can be used at the symmetric plane of some structures so that only half of the problem space need be simulated by FDTD.

**6.2.2.3 Interface Between Different Dielectric Media** At interfaces between two different dielectric materials, such as the air-dielectric interface in a microstrip line, the FDTD updating equations need to be modified properly. Usually we can discretize the problem space in such a way that the interface between different materials will be located at one of the Yee cell surfaces. For example, if there is a material interface along the  $x$ -axis, we can locate it on the top of the Yee cell, where only tangential electric field and normal magnetic field components are defined. Assuming that the electric permittivities at the two sides of this interface are  $\varepsilon_1$  and  $\varepsilon_2$ , respectively, we encounter some ambiguities in applying Eqs. 6.5e and 6.5f to update  $E_y$  and  $E_z$ . It was found that the averaged permittivity should be used to calculate correctly the tangential field components at the interface [8, 9]:

$$\left(\frac{\varepsilon_1 + \varepsilon_2}{2}\right) \frac{\partial E_y}{\partial t} = \frac{\partial H_x}{\partial z} - \frac{\partial H_z}{\partial x} - \sigma E_y \quad (6.10a)$$

$$\left(\frac{\varepsilon_1 + \varepsilon_2}{2}\right) \frac{\partial E_z}{\partial t} = \frac{\partial H_y}{\partial x} - \frac{\partial H_x}{\partial y} - \sigma E_z \quad (6.10b)$$

On the other hand, as long as the materials on both sides of the interface are non-magnetic, we have  $\mu_1 = \mu_2 = \mu_0$ . Thus the normal magnetic component will be continuous, and Eq. 6.5a can be used directly to update  $H_x$  without the need for any special treatment.

### 6.2.3 Source Excitation Techniques

In order to simulate the time domain response by using the FDTD updating equations 6.5a–6.5f, one needs to apply first either an initial condition or a certain type of source excitation to the structure. Early work used initial-condition plane wave sources [4], which can be applied successfully only for some limited applications involving one-dimensional wave scattering problems. For FDTD simulation of general three-dimensional microwave structures, it is more effective to use pulsed signal sources and excite specific field components at certain locations of the FDTD grid, so that the desired dominant mode can be launched properly. In particular, the Gaussian pulse, either baseband or modulated, has been the most

preferred source signal, mainly because it has a well-defined waveform and Fourier spectrum. A baseband Gaussian pulse can be expressed as

$$g(t) = e^{-[(t-t_0)/T]^2} \tag{6.11}$$

where  $t_0$  is the center of the pulse, and  $T$  is the pulse width at its  $1/e$  characteristic decay point. Meanwhile, a sinusoidally modulated Gaussian pulse can be defined by

$$g(t) = e^{-[(t-t_0)/T]^2} \sin 2\pi f_0(t - t_0) \tag{6.12}$$

where  $f_0$  is the modulation frequency. These two pulses have the same Fourier spectrum envelope, which also has a Gaussian profile

$$G(f) \propto e^{-(\pi T f)^2} \tag{6.13}$$

with the only difference being that the baseband Gaussian pulse has its peak of spectrum at DC, while the Fourier spectrum of the modulated Gaussian pulse is centered at  $f_0$ . Figure 6.3 shows the time domain waveform as well as the Fourier spectrum of a modulated Gaussian pulse with  $T = 100$  ps,  $t_0 = 3$  T, and  $f_0 = 15$  GHz. If we assume a useful frequency bandwidth, BW, where the amplitude of the Fourier spectrum is 10% (1% in power) that of its peak value, we find that the bandwidth corresponding to the modulated Gaussian pulse in Fig. 6.3a is approximately 10 GHz and symmetric about the modulation frequency  $f_0$ . More generally, by using Eq. 6.13, we can estimate roughly the useful frequency bandwidth for an FDTD simulation from the pulse width  $T$  with the following relations:

$$\text{BW(GHz)} \approx 1000/T(\text{ps}) \tag{6.14}$$

for the case of a modulated Gaussian pulse, and

$$f_{\text{max}}(\text{GHz}) \approx 500/T(\text{ps}) \tag{6.15}$$

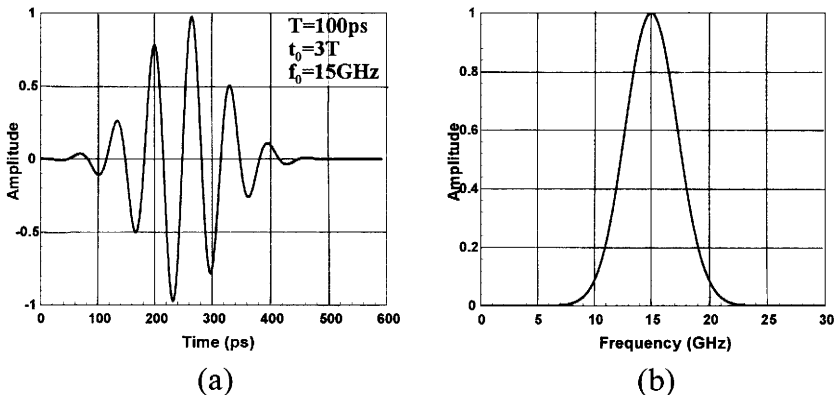
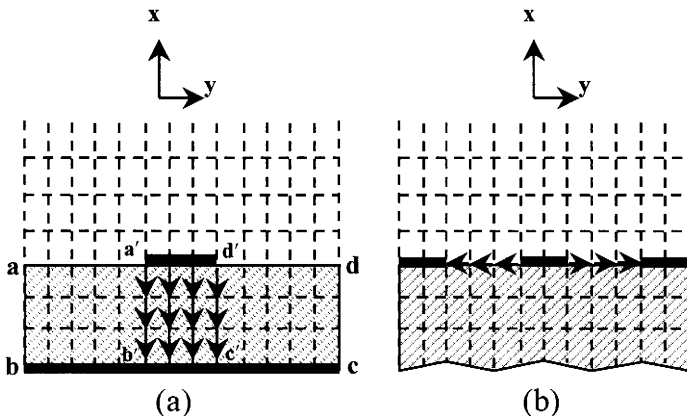


FIGURE 6.3 (a) A modulated Gaussian pulse and (b) its Fourier spectrum.

for the case of a baseband Gaussian pulse, where  $f_{\max}$  can be considered as the maximum frequency that can be calculated with reasonable accuracy by the FDTD simulation if such a Gaussian pulse is used for source excitation.

After choosing a proper type of source signal, the remaining question is how to apply it to the structure to be simulated. For the case of microwave planar circuits and antennas, which are our main interest here, the effort is to launch effectively the desired mode (mostly the dominant propagation mode) along the feedline at the input port of the circuit or antenna. Rigorously, one needs to have previous knowledge of the transverse field distribution across the feedline, either by using analytical approaches or by running a preliminary FDTD simulation for the feedline itself to obtain the correct transverse field distribution first. However, if we allow a certain “buffering” distance between the source plane and observation point, we can excite the structure in a much simpler manner and still realize a successful excitation of the actually desired propagation mode. Figures 6.4a and b show such approximate excitation schemes for the case of microstrip lines and coplanar waveguides (CPWs), respectively. In Fig. 6.4a, the vertical electric field components ( $E_x$ ) allocated on Yee cells in the source plane and between the strip conductor and ground ( $a'b'c'd'$ ) are excited uniformly. All the other field components, including  $E_x$  at the remaining part in the source plane ( $abcd$ ), are left “free-running” and updated using the normal FDTD equations 6.5a–6.5f. The reader should notice that this source excitation scheme is different from either the “electric wall” approach proposed by Zhang and Mei [8], or the alternative “magnetic wall” approach described by Sheen et al. [10]. In these two approaches, the part of the source plane excluding the excitation region ( $a'b'c'd'$ ) is enforced by either a PEC or a PMC condition during the Gaussian pulse excitation, and the whole plane ( $abcd$ ) has to be switched into an absorbing boundary after the Gaussian pulse is launched into the structure. The assumption of either PEC or PMC is artificial, however, and is not an absolute necessity in applying source excitation into the simulation structure. While in both [8] and [10] the source plane was chosen to overlap with one of the FDTD outer boundaries, we



**FIGURE 6.4** Simplified field excitation of the dominant propagation mode in (a) microstrip lines and (b) CPW structures.

found that by shifting the source plane slightly inside the FDTD grid, it becomes very easy and straightforward to apply the source excitation schemes we describe here, without the need to assume any PEC or PMC conditions. Furthermore, since the source plane is now separated from the outer boundary, which should be treated specially by using a proper absorbing boundary condition (ABC, see next subsection), we totally avoid the need for any additional “switching” of boundary conditions as required in [8] and [10]. We have employed this excitation scheme in FDTD characterization of a microwave probe head [11]. A similar approach was discussed in details by Zhao and Raisanen [12].

The last issue of concern is an effective separation of wave interactions between the source excitation and reflection from discontinuities of the simulated structure. This has been a very difficult task with the conventional “hard source” approach, where a manual “switching” from source excitation to the normal Yee updating algorithm is usually required [6]. Such a “switching” process can only be applied to finite-width pulse sources, is usually structure dependent, and requires extra lengths for the feedline in order to separate the incident and reflected waveforms completely in the time domain. To avoid these problems, we can use a novel “soft excitation” scheme as shown below. Instead of enforcing the excitation signal (e.g., a Gaussian pulse) at the source plane, we can simply superimpose it onto the Yee updating equations 6.5a–6.5f. For example, for the case of microstrip excitation as shown in Fig. 6.4a, we can introduce a Gaussian pulse excitation by modifying the updating equation for the  $E_x$  component in the area  $a'b'c'd'$  as follows:

$$\begin{aligned}
 E_x^{n+1}(i, j, k) = & e^{-(n\Delta t - t_0)^2/T^2} + \frac{1 - \sigma \Delta t/2\epsilon}{1 + \sigma \Delta t/2\epsilon} E_x^n(i, j, k) + \frac{\Delta t/\epsilon}{1 + \sigma \Delta t/2\epsilon} \\
 & \times \left( \frac{H_z^{n+1/2}(i, j+1, k) - H_z^{n+1/2}(i, j, k)}{\Delta y} \right. \\
 & \left. - \frac{H_y^{n+1/2}(i, j, k+1) - H_y^{n+1/2}(i, j, k)}{\Delta z} \right) \quad (6.16)
 \end{aligned}$$

It can easily be understood that by using this “soft excitation” scheme, any type of excitation source (both sinusoidal and pulsed) can be introduced in a very natural manner, without introducing any localized, unphysical PECs into the FDTD space as encountered in the “hard source” approach. Since the first term on the right-hand side of Eq. 6.16 will become zero after some time steps, the “switching” process mentioned above is realized automatically.

#### 6.2.4 Absorbing Boundary Condition

One of the most important issues related to FDTD is the implementation of an efficient and high accuracy absorbing boundary condition (ABC) so that the computational domain can be truncated with a finite-size FDTD grid. While it is

theoretically possible to derive exact analytical expressions for the fields at the outer boundary by using known fields inside the FDTD region, such global ABCs usually require a large amount of computer memory. As a result, most work on ABCs has been focused on local ABCs, which require only a few interior field data in the vicinity of the FDTD outer boundary.

A great variety of ABCs have been developed for FDTD over the past 30 years. The ABCs that have received major attention for effective truncation of general 3-D FDTD grids, however, can mainly be categorized into two groups. The first group is differential-based ABCs where the desired one-way wave characteristic is realized by factoring the partial differential wave equation. The most popularly used one in this category is Mur's ABC [13], which will be described in detail later in this subsection.

The second type of ABC employs the concept of absorbing materials, similar to the concept of an anechoic chamber for antenna measurements. Early work on material-based ABCs includes the conducting layer approach by Taflove and Brodwin [14] and the reflectionless absorber by Holland and Williams [15]. The perfectly matched layer (PML) proposed by Berenger [16], which represents a major breakthrough in the development of advanced ABCs for FDTD or other partial differential equation (PDE) techniques, is also based on the concept of lossy materials. It should be pointed out that the PML is still a very active research topic at the time of this writing. Interested readers are advised to refer to recent issues of *IEEE Transactions on Antennas and Propagation*, *IEEE Transactions on Microwave Theory and Techniques*, and *IEEE Microwave and Guided Wave Letters* for the latest progress in this area.

Meanwhile, there have also been efforts to improve the accuracy of existing ABCs by employing certain types of error compensation or cancellation schemes. One representative approach is the "Super ABC" proposed by Mei and Fang [17]. By finding the relationships between the electric and magnetic field errors caused by an ABC, they were able to devise an error cancellation scheme that resulted in substantial improvements for a number of existing ABCs including Engquist and Majda's first- and second-order ABCs. Another example is the geometry rearrangement technique (GRT) reported by Naishadham and Lin [18]. By superposition of two subproblems with different source or boundary locations, they realized a simple yet effective cancellation technique of the ABC-induced error for a great variety of planar transmission lines as well as discontinuity problems.

A good ABC, from the user's viewpoint, should satisfy the following criteria: (a) It should be reasonably simple to implement and does not cause too much overhead to the core computation inside the original FDTD grid. (2) It should be accurate enough to be useful in most practical engineering problems. (3) It should be as general as possible and independent of particular structures as well as their electromagnetic characteristics. (4) It should be numerically stable, with as little parameter tuning as possible. Based on these criteria, we believe that Mur's ABC is still one of the most preferred choices in implementing a general 3-D FDTD code at the current stage. Mur's first-order ABC has been used extensively in combination with Mei and Fang's "Super ABC" [19], while Mur's second-order ABC is a



completely self-contained set of formulations without requiring any additional tuning parameters. It has been found to be very stable and reasonably accurate for simulating a great variety of microwave circuits and antennas, especially planar type MICs, MMICs, and integrated antennas. On the other hand, for electromagnetic problems where an extremely large dynamic range (e.g., greater than 80 dB) is required, it becomes essential to use the most advanced PML schemes to truncate the FDTD grid. It has been demonstrated that by appropriately selecting the constitutive parameters of the PML slab, reflection errors as small as  $-100$  dB can easily be achieved over a very broad frequency range [6].

In the following, we will first present Mur's first- and second-order ABCs with some details for practical implementation, followed by a brief summary of the unsplit-field type PML, which was reported recently in the open literature. We will then compare the reflection errors of these two types of ABCs for the case of terminating a typical  $50\text{-}\Omega$  microstrip line.

**6.2.4.1 Mur's First- and Second-Order ABCs** Mur's ABC was based on the one-way wave equation, which was originally derived by Engquist and Majda [20]. Consider a general 3-D wave equation in the Cartesian coordinate system,

$$\left(\frac{\partial^2}{\partial x^2} + \frac{\partial^2}{\partial y^2} + \frac{\partial^2}{\partial z^2} - v^{-2} \frac{\partial^2}{\partial t^2}\right)E_i = 0 \quad (6.17)$$

where  $i = x, y$ , or  $z$ , and  $v$  is the wave phase velocity. For a plane wave that propagates from the  $x > 0$  region and impinges on the  $x = 0$  boundary, it is found that there will be no reflection from the boundary if the following wave equation is satisfied:

$$\left(\frac{\partial}{\partial x} - \frac{1}{v} \frac{\partial}{\partial t} [1 - (vs_y)^2 - (vs_z)^2]^{1/2}\right)E_i|_{x=0} = 0 \quad (6.18)$$

where  $i = y$  or  $z$ , and  $s_x^2 + s_y^2 + s_z^2 = v^{-2}$ . In reality, however, the incident angle of the wave reaching the boundary is unknown, and one needs to assume a certain approximation for the term  $[1 - (vs_y)^2 - (vs_z)^2]^{1/2}$  in Eq. 6.18. Using simple Taylor series expansions, Mur proposed a first-order ABC by assuming

$$[1 - (vs_y)^2 - (vs_z)^2]^{1/2} = 1 + O((vs_y)^2 + (vs_z)^2) \quad (6.19)$$

which is effective for nearly normal incident waves, and a second-order ABC by assuming

$$[1 - (vs_y)^2 - (vs_z)^2]^{1/2} = 1 - \frac{1}{2}[(vs_y)^2 + (vs_z)^2] + O((vs_y)^2 + (vs_z)^2)^2 \quad (6.20)$$

which is good for waves impinging on the  $x = 0$  boundary from incident angles even somewhat away from the normal direction. The corresponding one-way wave equations are

$$\left(\frac{\partial}{\partial x} - \frac{1}{v} \frac{\partial}{\partial t}\right) E_i|_{x=0} = 0 \tag{6.21}$$

for the first-order ABC, and

$$\left[\frac{1}{v} \frac{\partial^2}{\partial x \partial t} - \left(\frac{1}{v}\right)^2 \frac{\partial^2}{\partial t^2} + \frac{1}{2} \left(\frac{\partial^2}{\partial y^2} + \frac{\partial^2}{\partial z^2}\right)\right] E_i|_{x=0} = 0 \tag{6.22}$$

for the second-order ABC.

The remaining work is to implement the one-way wave equation into the FDTD time-stepping algorithm. Referring to the allocation of the electric field components,  $E_y$  and  $E_z$ , as shown in Fig. 6.5, the following central difference equation can be used to update these tangential field components at the  $x = 0$  boundary for the case of Mur's first-order ABC:

$$\begin{aligned} E_t^{n+1}(0, j, k) &= E_t^n(1, j, k) + \frac{v \Delta t - \Delta x}{v \Delta t + \Delta x} \\ &\times [E_t^{n+1}(1, j, k) - E_t^n(0, j, k)] \end{aligned} \tag{6.23a}$$

where  $t = y$  or  $z$ . For the top FDTD boundary at  $x = X_{\max}$ , as shown in Fig. 6.1, the field updating equations can be derived in a similar manner:

$$\begin{aligned} E_t^{n+1}(X_{\max}, j, k) &= E_t^n(X_{\max} - 1, j, k) + \frac{v \Delta t - \Delta x}{v \Delta t + \Delta x} \\ &\times [E_t^{n+1}(X_{\max} - 1, j, k) - E_t^n(X_{\max}, j, k)] \end{aligned} \tag{6.23b}$$

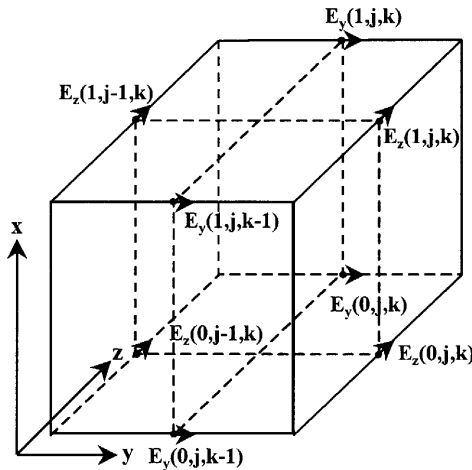


FIGURE 6.5 Tangential electric field components on Yee cell located at the  $x = 0$  boundary.

Meanwhile, the updating equations for Mur's second-order ABC are as follows:

1. At the  $x = 0$  boundary

$$\begin{aligned}
 E_t^{n+1}(0, j, k) &= -E_t^{n-1}(1, j, k) \\
 &+ \frac{v \Delta t - \Delta x}{v \Delta t + \Delta x} [E_t^{n+1}(1, j, k) + E_t^{n-1}(0, j, k)] \\
 &+ \frac{2 \Delta x}{v \Delta t + \Delta x} [E_t^n(0, j, k) + E_t^n(1, j, k)] \\
 &+ \frac{\Delta x (v \Delta t)^2}{2(\Delta y)^2 (v \Delta t + \Delta x)} \\
 &\times [E_t^n(0, j + 1, k) + 2E_t^n(0, j, k) + E_t^n(0, j - 1, k) \\
 &+ E_t^n(1, j + 1, k) - 2E_t^n(1, j, k) + E_t^n(1, j - 1, k)] \\
 &+ \frac{\Delta x (v \Delta t)^2}{2(\Delta z)^2 (v \Delta t + \Delta x)} \\
 &\times [E_t^n(0, j, k + 1) - 2E_t^n(0, j, k) + E_t^n(0, j, k - 1) \\
 &+ E_t^n(1, j, k + 1) - 2E_t^n(1, j, k) + E_t^n(1, j, k - 1)] \quad (6.24a)
 \end{aligned}$$

2. At the  $x = X_{\max}$  boundary

$$\begin{aligned}
 E_t^{n+1}(X_{\max}, j, k) &= -E_t^{n-1}(X_{\max} - 1, j, k) \\
 &+ \frac{v \Delta t - \Delta x}{v \Delta t + \Delta x} [E_t^{n+1}(X_{\max} - 1, j, k) + E_t^{n-1}(X_{\max}, j, k)] \\
 &+ \frac{2 \Delta x}{v \Delta t + \Delta x} [E_t^n(X_{\max}, j, k) + E_t^n(X_{\max} - 1, j, k)] \\
 &+ \frac{\Delta x (v \Delta t)^2}{2(\Delta y)^2 (v \Delta t + \Delta x)} \\
 &\times [E_t^n(X_{\max}, j + 1, k) + E_t^n(X_{\max}, j - 1, k) \\
 &- 2E_t^n(X_{\max}, j, k) + E_t^n(X_{\max} - 1, j + 1, k) \\
 &+ E_t^n(X_{\max} - 1, j - 1, k) - 2E_t^n(X_{\max} - 1, j, k)] \\
 &+ \frac{\Delta x (v \Delta t)^2}{2(\Delta z)^2 (v \Delta t + \Delta x)} \\
 &\times [E_t^n(X_{\max}, j, k + 1) + E_t^n(X_{\max}, j, k - 1) \\
 &- 2E_t^n(X_{\max}, j, k) + E_t^n(X_{\max} - 1, j, k + 1) \\
 &+ E_t^n(X_{\max} - 1, j, k - 1) - 2E_t^n(X_{\max} - 1, j, k)] \quad (6.24b)
 \end{aligned}$$

The update equations for the remaining four boundaries can be obtained by simple permutation of the coordinates. It should be noted that Mur's second-order ABC cannot be applied to the edges and corners of the FDTD grid, because some of the field components required in Eq. 6.24 are not available since they are located outside the FDTD outer boundaries. At these special locations, Mur's first-order ABC can be used for updating the tangential field components.

**6.2.4.2 Unsplit-Field PML Using Anisotropic Material** Berenger's original work [16] on the perfectly matched layer (PML) has stimulated a lot of research efforts to realize the "perfect" ABC for FDTD or any other PDE based numerical techniques over the past few years. For example, Fang and Wu [21] proposed a generalized perfectly matched layer (GPML) that is effective in absorbing both propagation and evanescent waves in lossless as well as lossy media. The most recent effort in PML study, however, has been focused on developing PMLs that do not require the splitting of the six electromagnetic field components in Maxwell's equations, as first suggested by Mittra and Pikel [22]. Sacks et al. [23] proposed a perfectly matched layer using anisotropic material and implemented this novel PML into an existing FEM code. Recently, this anisotropic PML has been implemented successfully into the FDTD algorithm by Gedney [24] and by Zhao and Cangellaris [25].

Assuming a lossy uniaxial medium, we can express the time-harmonic Faraday's law and Ampere's law as follows:

$$\nabla \times \mathbf{E} = -j\omega\mu_0\mu_r\bar{\bar{\mu}}\mathbf{H} \quad (6.25a)$$

$$\nabla \times \mathbf{H} = j\omega\varepsilon_0\varepsilon_r\bar{\bar{\varepsilon}}\mathbf{E} \quad (6.25b)$$

where  $\bar{\bar{\varepsilon}}$  and  $\bar{\bar{\mu}}$  are relative permittivity and permeability tensors in the following forms:

$$\bar{\bar{\varepsilon}} = \begin{pmatrix} s_x & 0 & 0 \\ 0 & s_y & 0 \\ 0 & 0 & s_z \end{pmatrix} \quad (6.26a)$$

$$\bar{\bar{\mu}} = \begin{pmatrix} s_x^* & 0 & 0 \\ 0 & s_y^* & 0 \\ 0 & 0 & s_z^* \end{pmatrix} \quad (6.26b)$$

It was shown in [24] that a perfectly matched layer (PML) that is perpendicular to the  $x$ -axis can be modeled as a uniaxial anisotropic material in which the following relationships are satisfied:

$$\frac{1}{s_x} = \frac{1}{s_x^*} = s_y = s_y^* = s_z = s_z^* \quad (6.27)$$

In this case, any plane wave incident on the uniaxial medium, regardless of its angle of incidence, polarization, and frequency, will be transmitted without any reflection into the uniaxial medium. A convenient choice for  $s_x$  that was suggested in [24] is

$$s_x = \frac{1}{1 + \frac{\sigma}{j\omega\epsilon_0}} \quad (6.28)$$

which leads to the following relative permittivity and permeability tensors:

$$\bar{\bar{\epsilon}} = \bar{\bar{\mu}} = \begin{pmatrix} \frac{1}{1 + \frac{\sigma}{j\omega\epsilon_0}} & 0 & 0 \\ 0 & 1 + \frac{\sigma}{j\omega\epsilon_0} & 0 \\ 0 & 0 & 1 + \frac{\sigma}{j\omega\epsilon_0} \end{pmatrix} \quad (6.29)$$

Substituting Eq. 6.29 into 6.25 gives Faraday's law and Ampere's law in the uniaxial medium. While the field components tangential to the PML interface ( $E_y, E_z, H_y, H_z$ ) can be discretized readily by applying the Yee algorithm as described in Section 2.1, the normal components ( $E_x$  and  $H_x$ ) need some special treatment due to the introduction of an effectively negative conductivity along the  $x$ -axis in this case, as implied by the nonphysical PML relationships in Eq. 6.27. A "two-step" update scheme, using an intermediate electric and magnetic flux density for  $E_x$  and  $H_x$ , respectively, was employed in [24] to obtain the proper update equations for these normal field components.

For a general three-dimensional problem, the FDTD lattice needs to be terminated by PML on all six sides. For PML interfaces normal to  $y$ - and  $z$ -axes, the uniaxial parameters are simply permuted and similar update expressions can be derived. However, some ambiguity occurs in the corner regions, where there is more than one normal interface boundary. In these regions a more generalized constitutive relation is necessary. The interested reader is referred to Gedney's original paper [24] for a detailed treatment on this issue.

In practical implementation of the PML scheme as described above, a spatially varying conductivity should be used in order to avoid reflections at the interface of FDTD/PML regions, as suggested originally by Berenger [16]. For a PML that starts at  $x_0$  along the  $x$ -axis, the conductivity  $\sigma$  can be chosen as follows:

$$\sigma(x) = \frac{\sigma_{\max} |x - x_0|^m}{d^m} \quad (6.30)$$

where  $d$  is the thickness of the PML, and  $m$  is the order of the polynomial variation. In practical coding the PML is usually backed by a PEC wall, and the expectant reflection error can be estimated by the following relation:

$$R_m(\theta^i) = \exp[-2\eta_0 \sqrt{\epsilon_{\text{eff}}} \sigma_{\max} d \cos \theta^i / (m + 1)] \quad (6.31)$$

where  $\eta_0$  is the wave impedance in free space, and  $\theta^i$  is the angle of incidence. It should be pointed out here that although Eq. 6.31 indicates that an arbitrarily low level of reflection could be realized by increasing  $\sigma_{\max}$ , there is always a lower bound on the achievable reflection level in practice, due to discretization errors as well as numerical rounding errors. The PML thickness,  $d$ , on the other hand, is typically chosen to be 8 to 16 cells, mainly from computer memory and CPU time considerations for a practical FDTD simulation.

**6.2.4.3 Numerical Evaluation of Mur’s ABC and PML** As a test of the numerical performance of Mur’s ABC and PML, we simulate a canonical microstrip line problem as shown in Fig. 6.6a. The microstrip line is shielded so that the

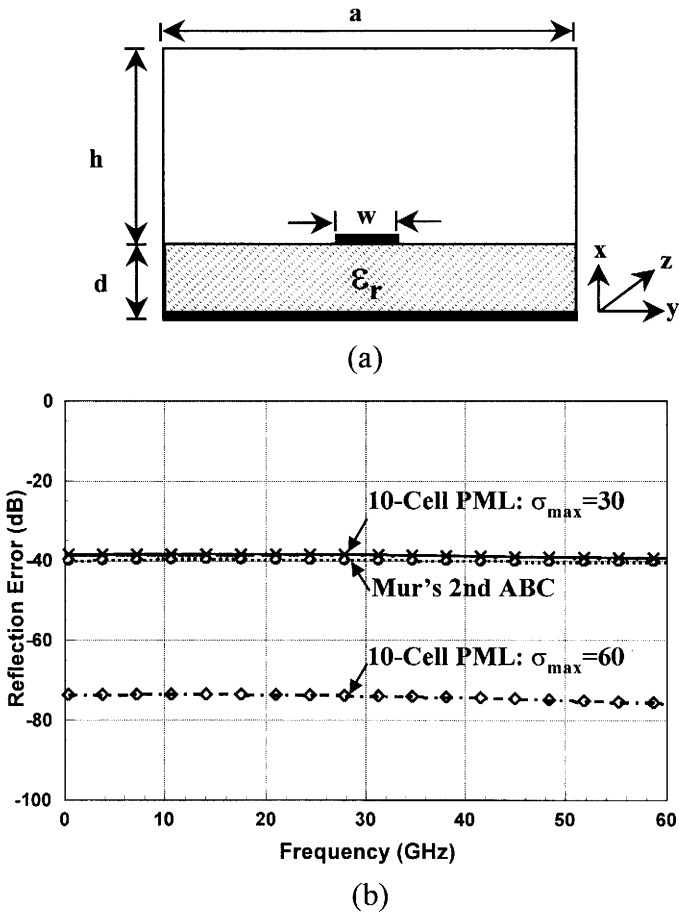


**FIGURE 6.6** (a) FDTD simulation model of a shielded microstrip line and (b) reflecton errors caused by Mur’s second-order ABC and PML with two different conductivity values.

terminating effects of the front and end ABCs only can be evaluated. The dielectric substrate is alumina with  $\epsilon_r = 9.6$  and its thickness is  $d = 0.1$  mm. The strip width of the nominal 50- $\Omega$  line is  $w = 0.1$  mm, and its length is assumed to be 4 mm in the simulation. Other dimensions are  $a = 0.7$  mm and  $h = 0.4$  mm. By choosing the Yee cell size to be  $\Delta x = \Delta y = 0.02$  mm and  $\Delta z = 0.04$  mm, we obtain an FDTD grid of  $25 \Delta x \times 35 \Delta y \times 100 \Delta z$  in total size. Next, a Gaussian pulse with  $T = 5$  ps is excited on the microstrip at a source plane that is  $10 \Delta z$  away from the front terminating ABC. By recording the time domain waveform at a certain observation point along the line, separating the small ABC induced reflection from the incident pulse, and applying a fast Fourier transform (FFT) to the ratio of the reflected and incident signals, we can obtain information on the reflection errors caused by a specific type of ABC. Both Mur's second-order ABC and the unsplit-field PML have been tested here in conjunction with an in-house, general-purpose 3-D FDTD code.

As shown in Fig. 6.6b, the reflection error caused by Mur's second-order ABC is slightly below  $-40$  dB over the frequency band of interest (DC to 60 GHz), even for the present case where the dielectric constant of the substrate is relatively high ( $\epsilon_r = 9.6$ ). The reflection becomes smaller for substrates with lower permittivity, on which most planar-type antennas are designed and fabricated. Such ABC induced reflection can be reduced further by using certain types of error compensation schemes [17,18], or by a proper gating of the time domain data before applying an FFT to obtain the frequency domain responses. Mur's ABC is very easy to implement, requires no parameter tuning, and gives reasonably accurate results for many practical engineering problems. Since it causes very little memory increase and needs no special treatment of any field components, it is among the most efficient ABCs for constructing a general purpose 3-D FDTD code.

Figure 6.6b also plots the reflection error caused by a 10-cell thick PML assuming a fourth-order polynomial in its conductivity profile ( $m = 4$ ). For the two cases with  $\sigma_{\max} = 30$  and 60, the numerically realized reflection errors are  $-38.5$  and  $-73.7$  dB, respectively, at the low frequency end. The reflection levels are quite flat over the whole frequency range from DC to 60 GHz. Meanwhile, the theoretical values of reflection as predicted by Eq. 6.31 are  $-39.3$  and  $-78.5$  dB, respectively, for these two cases. A very close agreement has been obtained, although the numerical reflection errors will eventually level off as the conductivity  $\sigma_{\max}$  keeps increasing. By appropriately choosing the constitutive parameters of the PML slab ( $\sigma_{\max}$ ,  $m$ , and  $d$ ), it is not difficult to realize reflection levels below  $-100$  dB, which is beyond the capability of Mur's ABC. The cost for such a high performance ABC, naturally, is a substantial increase in memory requirement as well as longer running time. This, however, can be alleviated by taking full advantage of the latest computer technology, which continues to offer less expensive memory and faster CPUs at a rapid pace in recent years.

### 6.3 FDTD ANALYSIS OF PASSIVE CIRCUITS AND ANTENNAS

#### 6.3.1 S-Parameters for General Microwave Circuits

Scattering parameters are very frequently used in characterizing the performance of microwave circuits. For a multiport network with  $N$  connecting ports, the  $S$ -parameters can be calculated as follows:

$$S_{mn} = \frac{\mathcal{F}[V_m(t)]}{\mathcal{F}[V_n(t)]} \sqrt{\frac{Z_{0n}}{Z_{0m}}} \tag{6.32}$$

where  $\mathcal{F}$  is the notation for Fourier transform,  $m, n = 1, 2, \dots, N$ ,  $V_m(t)$  and  $V_n(t)$  are the voltages at ports  $m$  and  $n$ , and  $Z_{0m}$  and  $Z_{0n}$  are the characteristic impedances of the transmission lines connected to ports  $m$  and  $n$ , respectively.

For a typical two-port planar circuit as shown in Fig. 6.7, the four  $S$ -parameters are

$$S_{11} = \frac{\mathcal{F}[V_{1\text{ref}}(t)]}{\mathcal{F}[V_{1\text{inc}}(t)]}, \quad S_{22} = \frac{\mathcal{F}[V_{2\text{ref}}(t)]}{\mathcal{F}[V_{2\text{inc}}(t)]} \tag{6.33a}$$

$$S_{21} = \frac{\mathcal{F}[V_{2\text{trans}}(t)]}{\mathcal{F}[V_{1\text{inc}}(t)]} \sqrt{\frac{Z_{01}}{Z_{02}}}, \quad S_{12} = \frac{\mathcal{F}[V_{1\text{trans}}(t)]}{\mathcal{F}[V_{2\text{inc}}(t)]} \sqrt{\frac{Z_{02}}{Z_{01}}} \tag{6.33b}$$

where  $V_{i\text{inc}}(t)$  and  $V_{i\text{ref}}(t)$  ( $i = 1, 2$ ) are the incident and reflected voltages at each port, and  $V_{i\text{trans}}(t)$  is the transmitted voltage at port  $i$  in response to the incident signal at another port. In general, the complex  $S$ -parameters can be expressed in the form of their magnitudes and phases. Referring to Fig. 6.7, the phase reference planes are usually defined at locations where the feeding transmission lines are

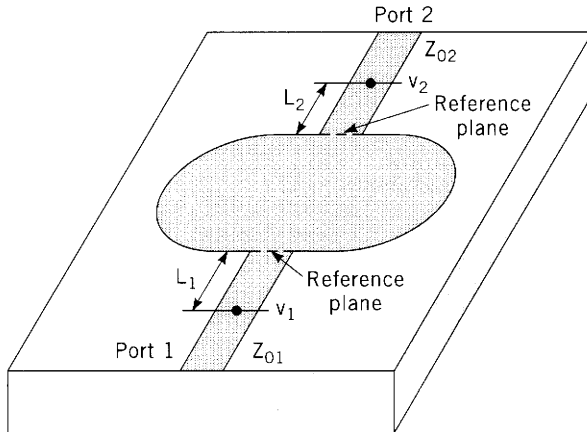


FIGURE 6.7 A general two-port microwave circuit.



connected to the circuit. However, in FDTD simulation it is a common practice to choose the observation points at some distances away from these reference planes to avoid the influence of any higher order modes at the connecting discontinuities. It is thus necessary to transform the phases of the  $S$ -parameters obtained at the observation points to the reference planes as shown in Fig. 6.7. This can easily be done by the following relations:

$$S_{11} = \frac{\mathcal{F}[V_{1 \text{ ref}}(t)]}{\mathcal{F}[V_{1 \text{ inc}}(t)]} e^{2\gamma_1 L_1}, \quad S_{22} = \frac{\mathcal{F}[V_{2 \text{ ref}}(t)]}{\mathcal{F}[V_{2 \text{ inc}}(t)]} e^{2\gamma_2 L_2} \quad (6.34a)$$

$$S_{21} = \frac{\mathcal{F}[V_{2 \text{ trans}}(t)]}{\mathcal{F}[V_{1 \text{ inc}}(t)]} \sqrt{\frac{Z_{01}}{Z_{02}}} e^{\gamma_1 L_1 + \gamma_2 L_2}, \quad S_{12} = \frac{\mathcal{F}[V_{1 \text{ trans}}(t)]}{\mathcal{F}[V_{2 \text{ inc}}(t)]} \sqrt{\frac{Z_{02}}{Z_{01}}} e^{\gamma_2 L_2 + \gamma_1 L_1} \quad (6.34b)$$

where  $\gamma_1$  and  $\gamma_2$  ( $\gamma = \alpha + j\beta$ ) are the complex propagation constants of the transmission lines connected to ports 1 and 2, respectively.

### 6.3.2 FDTD Characterization of Antennas

Antennas are of critical importance in any microwave and millimeter wave system because they serve as the “transitions” between the RF transmitting/receiving modules and the radiation and propagation of electromagnetic waves in free space. Two parameters usually come first in relation with the analysis and design of any antenna structure. The first is its radiation patterns, which essentially determine how the radiated electromagnetic fields can be controlled by the antenna. The other important parameter is the input impedance, or equivalently, the input return loss, which describes how well the antenna is matched with its feeding structure. Some other parameters to be considered include the antenna gain, efficiency, and cross-polarization, as well as mutual coupling within an antenna array environment.

It has been found that the FDTD method is a very powerful approach that can be used to calculate all the above parameters for almost all types of antenna structures. For input impedance calculation, the antenna can simply be treated as a one-port circuit terminated by ABCs at its outer boundaries. After the input return loss ( $S_{11}$ ) is obtained, the complex input impedance can be calculated easily by the following relation:

$$Z_{\text{in}} = Z_0 \frac{1 + S_{11}}{1 - S_{11}} \quad (6.35)$$

where  $Z_0$  is the characteristic impedance of the antenna feedline. The calculation of far-field radiation patterns of an antenna, on the other hand, is not a straightforward matter, because the FDTD grid is usually truncated at the near-field region in order to keep the resultant memory size from being excessively large. Fortunately, since all the near fields are available during the FDTD simulation, we can use the following near-field to far-field transformation to evaluate accurately the far-field radiation properties of the antenna.

Let us first consider the electromagnetic fields from a radiating source enclosed by a surface  $S'$ , as shown in Fig. 6.8. According to the surface equivalence theorem [26], if we have previous knowledge of the electric current density,  $\mathbf{J}_s$ , and a fictional magnetic current density,  $\mathbf{M}_s$ , on  $S'$ , we can use the following two vector potentials,

$$\mathbf{A} = \mu \iint_{S'} \frac{\mathbf{J}_s e^{-jkr''}}{4\pi r''} dS' \quad (6.36a)$$

$$\mathbf{F} = \varepsilon \iint_{S'} \frac{\mathbf{M}_s e^{-jkr''}}{4\pi r''} dS' \quad (6.36b)$$

to express the electromagnetic fields at a far-field point,  $\mathbf{P}$ , as follows:

$$\mathbf{E} = -j\omega\mathbf{A} - \frac{j\omega}{k^2} \nabla(\nabla \cdot \mathbf{A}) - \frac{1}{\varepsilon} \nabla \times \mathbf{F} \quad (6.37a)$$

$$\mathbf{H} = -j\omega\mathbf{F} - \frac{j\omega}{k^2} \nabla(\nabla \cdot \mathbf{F}) + \frac{1}{\mu} \nabla \times \mathbf{A} \quad (6.37b)$$

Since  $r' \ll r$  for the far-field  $\mathbf{P}$ , we can assume

$$r'' = \sqrt{r^2 + r'^2 - 2rr' \cos \psi} \cong r - r' \cos \psi \quad (6.38)$$

and the two vector potentials in Eqs. 6.36a and 6.36b can be rewritten as

$$\mathbf{A} = \mu \frac{e^{-jkr}}{4\pi r} \iint_{S'} \mathbf{J}_s e^{jkr' \cos \psi} dS' \quad (6.39a)$$

$$\mathbf{F} = \varepsilon \frac{e^{-jkr}}{4\pi r} \iint_{S'} \mathbf{M}_s e^{jkr' \cos \psi} dS' \quad (6.39b)$$

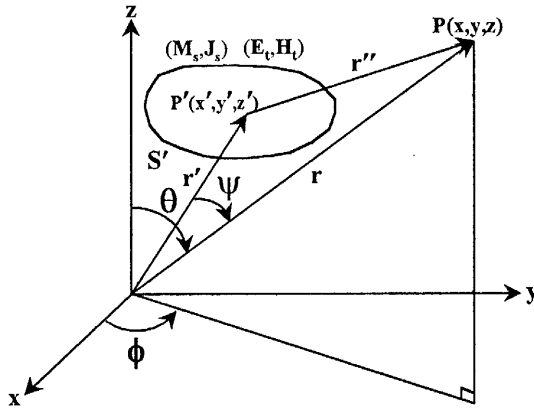


**FIGURE 6.8** Surface equivalent theorem for near-field to far-field transformation.

where

$$r' \cos \psi = \mathbf{r}' \cdot \hat{\mathbf{r}} = x' \sin \theta \cos \phi + y' \sin \theta \sin \phi + z' \cos \theta \quad (6.40)$$

Since the integrands in Eqs. 6.39a and 6.39b are functions of  $\mathbf{J}_s$ ,  $\mathbf{M}_s$ ,  $r'$ , and  $\psi$  only, we can define two new radiating vectors,  $\mathbf{N}$  and  $\mathbf{L}$ , as shown below:

$$\mathbf{N} = \iint_{S'} \mathbf{J}_s e^{jk r' \cos \psi} dS' \quad (6.41a)$$

$$\mathbf{L} = \iint_{S'} \mathbf{M}_s e^{jk r' \cos \psi} dS' \quad (6.41b)$$

which are related to the vector potentials  $\mathbf{A}$  and  $\mathbf{F}$  by

$$\mathbf{A} = \mu \frac{e^{-jkr}}{4\pi r} \mathbf{N} \quad (6.42a)$$

$$\mathbf{F} = \varepsilon \frac{e^{-jkr}}{4\pi r} \mathbf{L} \quad (6.42b)$$

Now if we substitute Eq. 6.42 into Eq. 6.37 and drop the terms that decay faster than  $1/r$ , we can obtain the radiating fields at the far-field point as shown below:

$$E_\theta = \eta H_\phi = -j \frac{e^{-jkr}}{2\lambda r} (\eta N_\theta + L_\phi) \quad (6.43a)$$

$$E_\phi = -\eta H_\theta = j \frac{e^{-jkr}}{2\lambda r} (-\eta N_\phi + L_\theta) \quad (6.43a)$$

Consequently, we can calculate the time-averaged Poynting vector (average power density) at a far-field point ( $r, \theta, \phi$ ) as follows:

$$\begin{aligned} W_r &= \frac{1}{2} \text{Re}[\mathbf{E} \times \mathbf{H}^*] = \frac{1}{2} \text{Re}[E_\theta H_\phi^* - E_\phi H_\theta^*] \\ &= \frac{\eta}{8\lambda^2 r^2} \left[ \left| N_\theta + \frac{L_\phi}{\eta} \right|^2 + \left| N_\phi - \frac{L_\theta}{\eta} \right|^2 \right] \end{aligned} \quad (6.44)$$

By simply multiplying the above power density by the square of distance,  $r^2$ , we obtain the radiation intensity of the antenna at a certain direction ( $\theta, \phi$ ) as follows:

$$U = \frac{\eta}{8\lambda^2} \left[ \left| N_\theta + \frac{L_\phi}{\eta} \right|^2 + \left| N_\phi - \frac{L_\theta}{\eta} \right|^2 \right] \quad (6.45)$$

An efficient way to implement the above near-field to far-field transformation is to define a rectangular “virtual box” as shown in Fig. 6.9, which is located a few cells

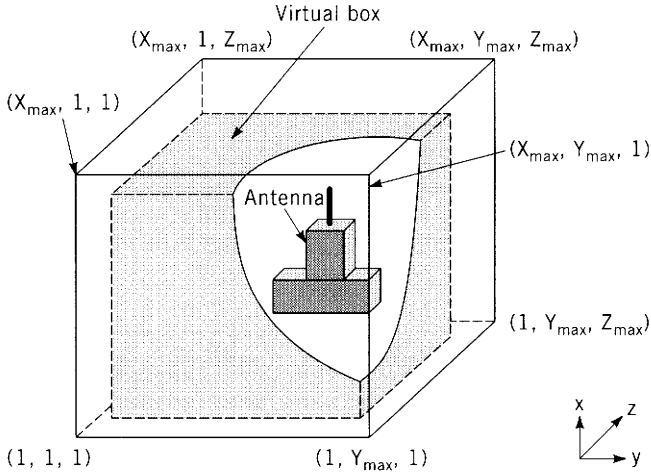


**FIGURE 6.9** The “virtual box” for near-field to far-field transformation.

inside the FDTD outer boundary. The equivalent electric and magnetic current densities,  $\mathbf{J}_s$  and  $\mathbf{M}_s$ , are related to the field components on the surface of the virtual box by

$$\mathbf{J}_s = \hat{\mathbf{n}} \times \mathbf{H}, \quad \mathbf{M}_s = -\hat{\mathbf{n}} \times \mathbf{E} \quad (6.46)$$

In a Cartesian coordinate system,  $\mathbf{J}_s$  and  $\mathbf{M}_s$  can be expanded into  $x$ ,  $y$ , and  $z$  components as

$$\mathbf{J}_s = J_x \hat{\mathbf{x}} + J_y \hat{\mathbf{y}} + J_z \hat{\mathbf{z}}, \quad \mathbf{M}_s = M_x \hat{\mathbf{x}} + M_y \hat{\mathbf{y}} + M_z \hat{\mathbf{z}} \quad (6.47)$$

and the components of the radiating vectors in Eq. 6.43 can be calculated as follows:

$$N_\theta = \iint_{S'} (J_x \cos \theta \cos \phi + J_y \cos \theta \sin \phi - J_z \sin \theta) e^{jkr' \cos \psi} dS' \quad (6.48a)$$

$$N_\phi = \iint_{S'} (-J_x \sin \phi + J_y \cos \phi) e^{jkr' \cos \psi} dS' \quad (6.48b)$$

$$L_\theta = \iint_{S'} (M_x \cos \theta \cos \phi + M_y \cos \theta \sin \phi - M_z \sin \theta) e^{jkr' \cos \psi} dS' \quad (6.48c)$$

$$L_\phi = \iint_{S'} (-M_x \sin \phi + M_y \cos \phi) e^{jkr' \cos \psi} dS' \quad (6.48d)$$

Since the field components on the surface of the virtual box calculated by FDTD are in the time domain, we can use the following discrete Fourier transform (DFT) to obtain the corresponding phasor quantities:

$$F(\omega) = \int_0^{+\infty} f(t) e^{-j\omega t} dt \quad (6.49)$$

where  $\omega = 2\pi f$ , and  $f$  is the frequency at which the far-field radiation properties are to be calculated. The advantage of using the DFT is that we can implement it directly into the FDTD iteration loop with a simple summation as follows:

$$F(\omega) = \sum_{n=0}^{NSTEP} f(n \Delta t) e^{-j\omega n \Delta t} \Delta t \quad (6.50)$$

This “running DFT” requires less computer memory than an alternative FFT scheme [27], because in the latter field components must be saved until the end of the FDTD iteration. Since we are usually interested in the antenna patterns at a single or only a few frequency points, the “running DFT” seems to be a preferred approach for this purpose.

### 6.3.3 Application Examples

**6.3.3.1 Slot Antenna Fed by Nonleaky Coplanar Waveguides** Slot antennas printed on dielectric substrates and fed by coplanar waveguides (CPWs) have widely been used in recent years, mainly due to several advantages, including their uniplanar nature and the ease of shunt connection or monolithic integration of active devices [28]. The intrinsic bidirectional radiation of the slot antenna, however, is an undesirable property in many applications. In order to realize unidirectional radiation similar to that of microstrip patch antennas, a ground plane can be added at the back side of the substrate. The introduction of the back conductor, however, will form a parallel plate and cause energy leakage due to the slow-wave nature of the parallel-plate mode. To solve this problem, a double-layered structure as shown in Fig. 6.10a has been proposed [29]. By choosing properly the dielectric constant and thickness of the two substrates, one can realize a nonleaky coplanar (NLC) structure, where the leakage due to the parallel-plate mode can be suppressed completely within the frequency range of interest.

To characterize the NLC waveguide and the NLC-fed slot antenna as shown in Fig. 6.10a, several numerical techniques such as the extended spectral domain approach (SDA) can be used [30]. We find that the FDTD is a very efficient approach for analyzing these types of structures, because the FDTD algorithm will take into account all related electromagnetic phenomena including surface-wave and parallel-plate modes as well as radiation. Another advantage is that a very broadband and high resolution frequency response can be obtained with only one FDTD simulation, if we use a Gaussian pulse for source excitation and perform an FFT at the end of the FDTD iteration.

Figure 6.10b shows the FDTD simulated complex input impedance of the NLC-fed slot antenna, as well as a comparison with results obtained by the extended spectral domain approach [30]. The parameters for the calculated structure are as follows:  $L_s = 827$  mils,  $w_s = 78$  mils,  $w = 39$  mils,  $g = 78$  mils,  $\epsilon_{r1} = 10.8$ ,  $\epsilon_{r2} = 2.2$ ,  $h_1 = 50$  mils, and  $h_2 = 125$  mils. The two results agree with each other satisfactorily and reveal a fairly broad bandwidth when the slot antenna is used near

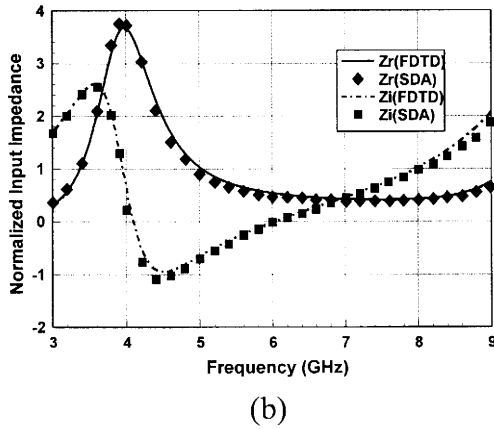
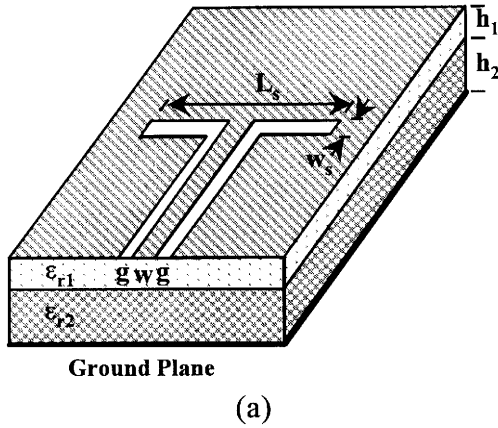


**FIGURE 6.10** (a) Configuration and (b) complex input impedance of an NLC-fed slot antenna. (From [31], copyright © 1997 by IEEE.)

its antiresonance frequency around 6 GHz. Furthermore, by introducing a novel optimized twin-slot configuration, we have shown that it is possible to reduce significantly the undesirable mutual coupling within an array environment, making this type of NLC-fed slot antenna a very promising candidate for several millimeter wave applications such as focal plane imaging arrays [31].

**6.3.3.2 Tapered Slot Antenna on Finite-Size Substrate** One of the most challenging issues in analyzing the radiation properties of planar-type antennas is to consider the influence of the finite size of the ground plane or dielectric substrate. This has been a particularly difficult task with many conventional numerical techniques such as the method of moments (MoM). The near-field to far-field transformation using the “virtual box” concept as described in the previous subsection, however, makes the FDTD method a very powerful simulation tool to

include such finite-size effects. For example, for a linearly tapered slot antenna as shown in Fig. 6.11a, it has been found that the ground plane width,  $H$ , will affect significantly the radiation patterns, and subsequently the gain of the antenna [32]. Janaswamy [32] reported both measured and MoM numerical results for a tapered slot antenna with the following parameters:  $L = 10$  cm,  $H = 3$  cm,  $w_f = 0.75$  mm, and  $\alpha = 6^\circ$ . The dielectric substrate was RT/Duroid 5870 with  $\epsilon_r = 2.33$  and  $d = 28$  mils, and its size was  $a = 8.25$  cm and  $b = 10.25$  cm. Figure 6.1b plots the  $E$ -plane ( $yz$ ) radiation pattern of the tapered slot antenna reported in [32], as well as our FDTD results. It can be seen that the FDTD simulation has successfully reproduced almost all details in the radiation pattern at all angles including the back side, and the agreement with measured results is better in general than that of the MoM analysis.

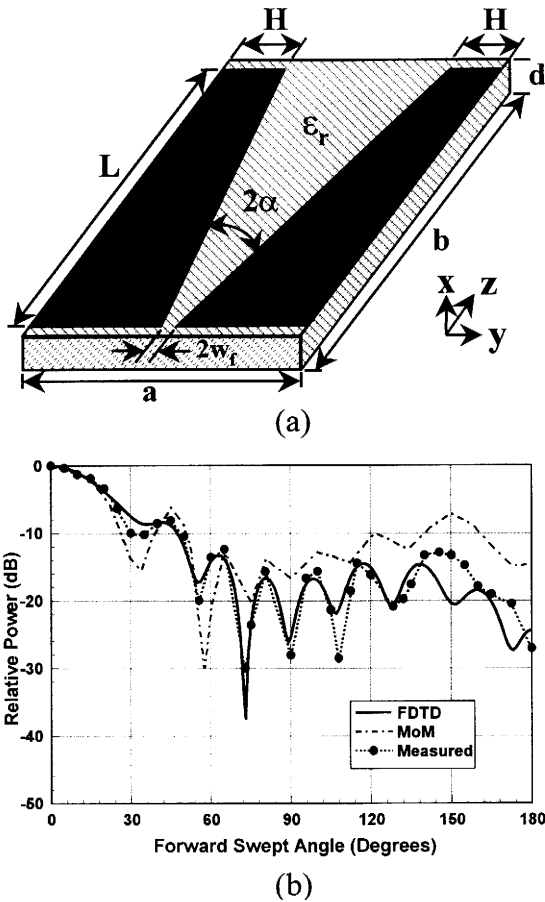


FIGURE 6.11 (a) Configuration and (b)  $E$ -plane radiation pattern of a linearly tapered slot antenna.

## 6.4 EXTENDED FDTD FOR ACTIVE CIRCUITS AND INTEGRATED ANTENNAS

### 6.4.1 Direct Implementation of Lumped Elements in FDTD Algorithm

The basic formulation for incorporating lumped linear and nonlinear circuit elements into the FDTD algorithm was proposed originally by Sui et al. [33] for 2-D problems and generalized to 3-D structures later by Piket-May et al. [34]. It was shown that lumped circuit elements can be accounted for in Maxwell's equations by adding a lumped electric current density term,  $\mathbf{J}_L$ , to the conduction and displacement currents on the right-hand side of Eq. 6.1b as follows

$$\nabla \times \mathbf{H} = \varepsilon \frac{\partial \mathbf{E}}{\partial t} + \sigma \mathbf{E} + \mathbf{J}_L \quad (6.51)$$

If we assume that the lumped element is  $x$ -oriented in the FDTD grid and placed on the edge of the  $(i, j, k)$ th Yee cell, where the electric field component  $E_x(i, j, k)$  is located, the current density can be related to the total current flowing through that Yee cell,  $I_L$ , as

$$J_L = \frac{I_L}{\Delta y \Delta z} \quad (6.52)$$

Depending on the type of lumped elements, which can be a resistor, capacitor, inductor, diode, or transistor, the element current,  $I_L$ , can be a scalar multiple, time-derivative, time-integral, or general nonlinear function of the electric potential,  $V(i, j, k) = E_x(i, j, k) \Delta x$ , developed across the  $(i, j, k)$ th Yee cell. Applying central difference to Eq. 6.51, we obtain the modified updating equation for  $E_x(i, j, k)$  to include the effect of the  $x$ -oriented lumped element as follows:

$$\begin{aligned} E_x^{n+1}(i, j, k) = & \frac{1 - \sigma \Delta t / 2\varepsilon}{1 + \sigma \Delta t / 2\varepsilon} E_x^n(i, j, k) + \frac{\Delta t / \varepsilon}{1 + \sigma \Delta t / 2\varepsilon} \\ & \times \left( \frac{H_z^{n+1/2}(i, j+1, k) - H_z^{n+1/2}(i, j, k)}{\Delta y} \right. \\ & \left. - \frac{H_y^{n+1/2}(i, j, k+1) - H_y^{n+1/2}(i, j, k)}{\Delta z} \right) \\ & - \frac{\Delta t / \varepsilon \Delta y \Delta z}{1 + \sigma \Delta t / 2\varepsilon} I_L^{n+1/2}(i, j, k) \end{aligned} \quad (6.53)$$

Since  $I_L$  is evaluated at the  $(n + \frac{1}{2})$ th time step, a semi-implicit expression similar to Eq. 6.6 should be used for the corresponding electric field component,  $E_x^{n+1/2}(i, j, k)$ , in order to ensure numerical stability of the above updating equation.



The simplest lumped element is a resistor,  $R$ , where the element current,  $I_L(i, j, k)$ , is related to the electric field,  $E_x(i, j, k)$ , by

$$I_L^{n+1/2}(i, j, k) = \frac{E_x^{n+1/2}(i, j, k) \Delta x}{R} = \frac{\Delta x}{2R} [E_x^{n+1}(i, j, k) + E_x^n(i, j, k)] \quad (6.54)$$

Substituting Eq. 6.54 into 6.53, we obtain the  $E$ -field updating equation for the resistor  $R$  as follows:

$$\begin{aligned} E_x^{n+1}(i, j, k) = & \frac{1 - \sigma \Delta t/2\varepsilon - \Delta x \Delta t/2R\varepsilon \Delta y \Delta z}{1 + \sigma \Delta t/2\varepsilon + \Delta x \Delta t/2R\varepsilon \Delta y \Delta z} E_x^n(i, j, k) \\ & + \frac{\Delta t/\varepsilon}{1 + \sigma \Delta t/2\varepsilon + \Delta x \Delta t/2R\varepsilon \Delta y \Delta z} \\ & \times \left( \frac{H_z^{n+1/2}(i, j+1, k) - H_z^{n+1/2}(i, j, k)}{\Delta y} \right. \\ & \left. - \frac{H_y^{n+1/2}(i, j, k+1) - H_y^{n+1/2}(i, j, k)}{\Delta z} \right) \end{aligned} \quad (6.55)$$

As an example, we consider a 50- $\Omega$  microstrip line terminated by a matched (50- $\Omega$ ) lumped resistor, as shown in Fig. 6.12a. The dielectric substrate is alumina with  $\varepsilon_r = 9.6$  and  $d = 0.1$  mm. The width of the microstrip is 0.1 mm as well. The lumped resistor is modeled by modifying the updating equation for the edge of the Yee cell, which is connected to the center of the microstrip terminal at one end and to a grounded via at the other end. In the FDTD simulation, a 5-ps Gaussian pulse is injected into the microstrip line, and the reflected signal from the lumped resistor is recorded and Fourier transformed to give the reflection coefficient ( $S_{11}$ ), as shown in Fig. 6.12b. While a relatively good impedance matching is realized at lower frequencies, the reflection level becomes higher as the frequency increases, mainly due to the frequency dispersion of the characteristic impedance of the microstrip line. The same trend was also observed in [35], where the performance of a chip resistor was characterized accurately up to 20 GHz by including the finite height effect into the FDTD code with lumped element models.

One of the unique features of incorporating lumped circuit elements and devices into a full wave FDTD algorithm is the capability to simulate all related electromagnetic phenomena including complicated wave-device interaction and mode competition in the case of a multimode structure. Toland et al. [36] reported FDTD simulation of mode control in a two-element active antenna, as shown in Fig. 6.13. Two microstrip patch antennas are connected with a coupling line, which can either be a simple through line or have a small chip resistor in the center. Two Gunn diodes are integrated under the microchip lines at locations shown in the figure. The diodes are modeled using an equivalent circuit, which is incorporated into the FDTD algorithm by employing the implementation approach mentioned above [37]. This two-element active antenna is expected to work at an anti-phase

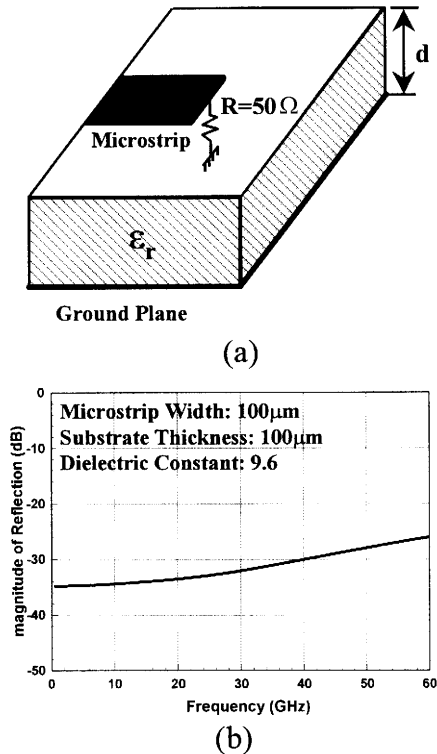


**FIGURE 6.12** (a) A microstrip line terminated with a matched lumped resistor and (b) numerical reflection due to the lumped resistor model.

mode when connected directly by a through line, but will switch to an in-phase mode if a chip resistor is placed in the center of the coupling line [38]. Figure 6.14 shows the FDTD simulated as well as measured radiation patterns for these two cases. Although there are some discrepancies between the simulated and measured oscillating frequencies, the results shown in Fig. 6.14 are very unique in that the mode competition effect within a multimode structure has been predicted successfully by the FDTD simulation, which is a capability unavailable with any existing EM or circuit simulators.

It is worth mentioning here that in order to ensure the convergence of the lumped element FDTD procedure, it is often necessary to choose the simulation time step to be smaller than the upper limit imposed by Curant's stability criterion. This is especially true when highly nonlinear devices or abrupt changes in waveforms are involved. While reducing the time step usually means longer simulation time, Ciampolini et al. [39] introduced a novel adaptive time-step algorithm, which dynamically adjusts the time step itself to ensure convergence during the simulation. Numerical examples show that the algorithm is very reliable and robust and enhances significantly the computational efficiency of the overall lumped element FDTD scheme.

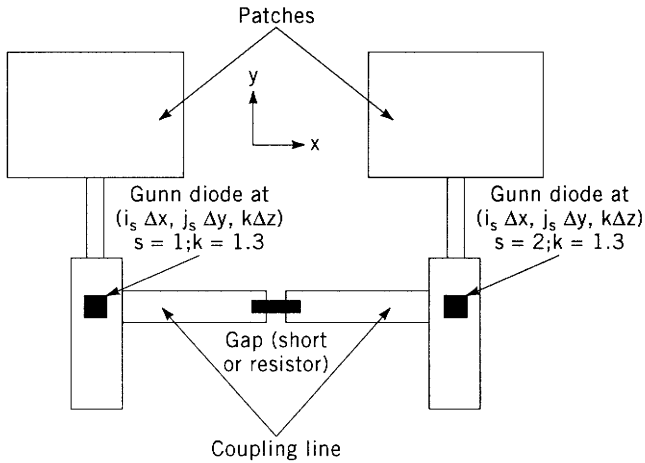


FIGURE 6.13 A two-element active antenna. (From [36], copyright © 1994 by IEEE.)

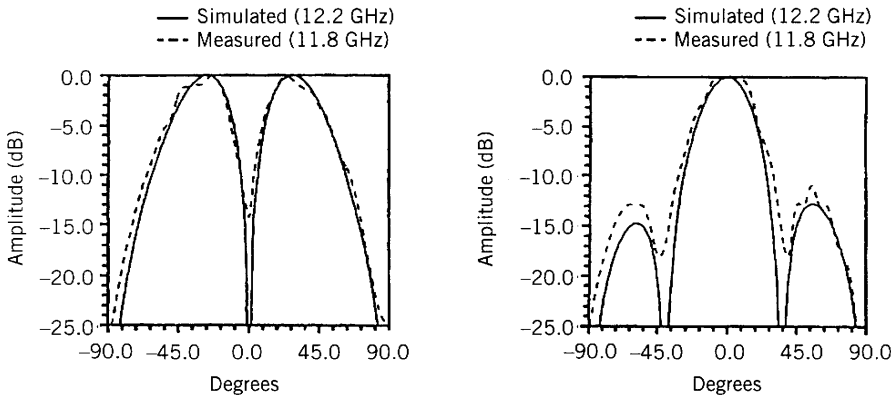


FIGURE 6.14 FDTD simulated and measured results for mode switching in the two-element active antenna shown in Fig. 6.13. (From [36], copyright © 1994 by IEEE.)

### 6.4.2 Extended FDTD Using Equivalent-Source Techniques

While the approach of directly implementing lumped elements and devices into the FDTD algorithm has been applied successfully to microwave circuits including resistors, capacitors, inductors, diodes, and bipolar junction transistors (BJTs), one disadvantage is that the derivation of the field updating equations for the lumped element subgrids will become extremely tedious when modeling lumped devices with complicated equivalent circuits. Also, this approach seems impractical when a multiport lumped circuit is involved. In an effort to alleviate these problems, Chen and Fusco [40,41] developed a dynamic interface between the active device and FDTD lattice to enable the simulation of prominent nonlinear behaviors of a large

signal FET, which is connected across multiple FDTD cells. The equivalent gate and drain currents adopted in their FET model, however, are coupled unintentionally when incorporated into the distributed-parameter FDTD algorithm. A technique for introducing an internal EM-field absorber into the FDTD three-terminal active device model was proposed and demonstrated successfully in eliminating this undesired current coupling [41].

In 1994, Thomas et al. [42] proposed a general approach that allows direct access to SPICE models by communicating the FDTD algorithm with lumped circuit simulation through an equivalent current source. A similar approach was adopted by Kuo et al. [43] for small signal simulation of a microwave MESFET amplifier. A dual approach, based on the equivalent voltage source concept, was also presented by Kuo et al. in a subsequent report [44].

To illustrate the equivalent current source approach, we can start with the integral form of Ampere's law [43]:

$$C_{\text{total}} \frac{dV_{\text{dev}}}{dt} + I_{\text{dev}} = I_{\text{total}} \quad (6.56)$$

where  $C_{\text{total}}$  is the equivalent capacitance of the FDTD cell ( $C_{\text{total}} = \epsilon A/h$ , where  $A$  and  $h$  are the area and height of the cell, respectively),  $V_{\text{dev}}$  is the terminal voltage of the active device,  $I_{\text{dev}}$  represents the current flowing through the lumped circuits, and  $I_{\text{total}}$  is the total current determined by the line integral of the magnetic fields. This equation, together with the device circuit model, leads to the equivalent circuit characterizing the device-wave interaction as shown in Fig. 6.15a. The parallel pair of current source,  $I_{\text{total}}$ , and a capacitor,  $C_{\text{total}}$ , denotes a Norton-equivalent circuit of FDTD cells as seen by the device.

Similarly, the integral form of Faraday's law leads to

$$-L_{\text{total}} \frac{dI_{\text{dev}}}{dt} - V_{\text{dev}} = V_{\text{total}} \quad (6.57)$$

where  $L_{\text{total}}$  is the total space inductance of the FDTD cell ( $L_{\text{total}} = \mu A/h$ ). The corresponding equivalent circuit as shown in Fig. 6.15b, which consists of a voltage source and a series inductor, represents the Thevenin-equivalent circuit of FDTD cells as seen from the device side.

As an application example of the above-mentioned equivalent source techniques, a microwave MESFET amplifier has been simulated by using both the equivalent current-source and voltage-source approaches [43,44]. Figure 6.16 shows the circuit layout of the microstrip-based amplifier, which consists of input/output matching networks, DC bias circuits, and a GaAs MESFET. The  $S$ -parameters of the amplifier, obtained by applying FFT to the time domain data, are shown in Fig. 6.17, together with the measurement results. The two equivalent-source approaches provide similar results that agree reasonably well with the measured data. The same technique has further been applied to FDTD simulation of packaged nonlinear active circuits [45]. By employing a large-signal-device circuit model, nonlinear properties such as

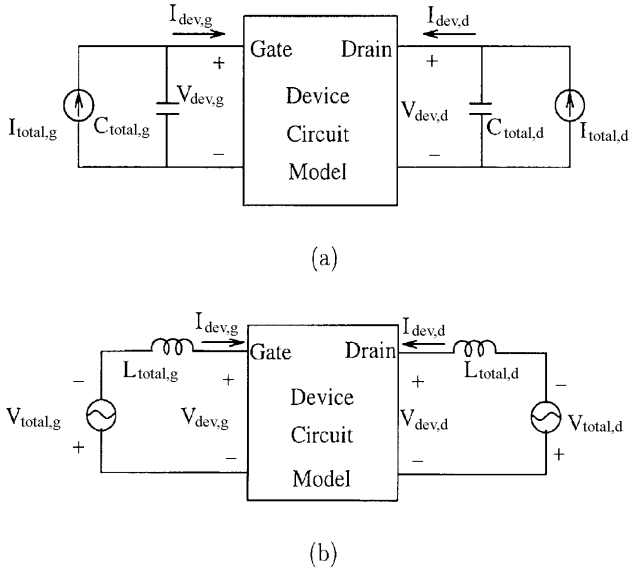


**FIGURE 6.15** (a) The Norton-equivalent circuit for simulating the device–wave interaction, and (b) the alternative Thevenin-equivalent circuit. (From [45], copyright © 1997 by IEEE.)

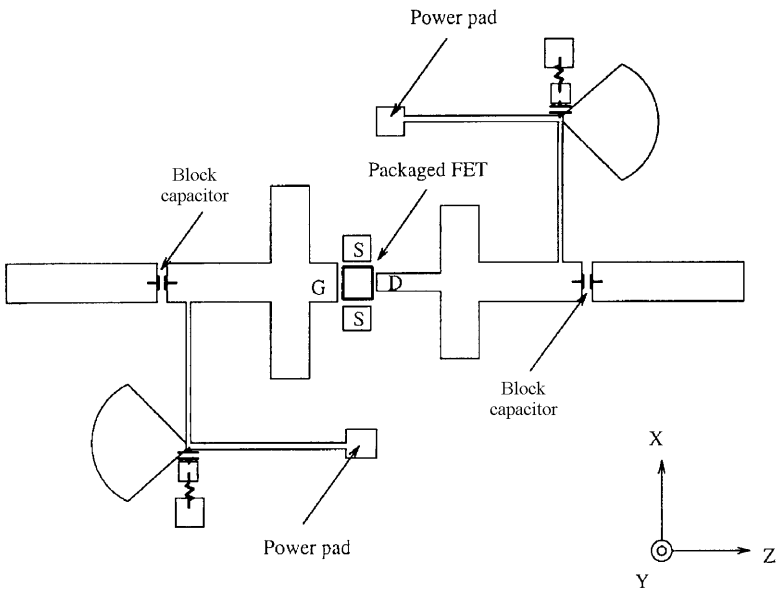


**FIGURE 6.16** The layout of a microwave amplifier simulated by the extended FDTD algorithm. (From [43], copyright © 1995 by IEEE.)

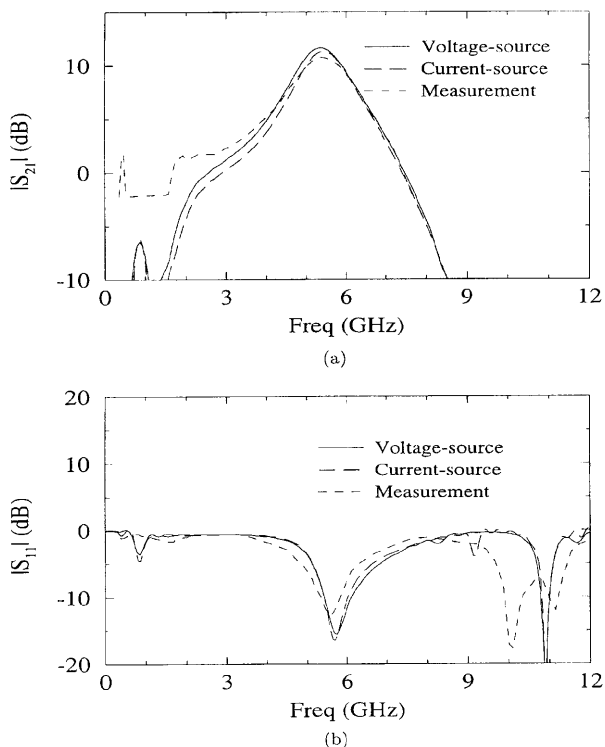


**FIGURE 6.17** Comparison of the measured and simulated  $S$ -parameters of the microwave amplifier shown in Fig. 6.16: (a)  $|S_{11}|$  and (b)  $|S_{21}|$ . (From [44], copyright © 1996 by IEEE.)

harmonic generation and intermodulation in a power amplifier can be investigated in a rigorous and straightforward manner. Moreover, the capability of including packaging effects into active circuit simulations is a unique feature unavailable with current CAD tools and should find important applications in circuit design involving complicated EMC/EMI problems.

The equivalent-source techniques mentioned above have been generalized further recently and applied successfully to the FDTD simulation of a singly balanced diode mixer [46]. These demonstrations indicate that the extended FDTD method is a very powerful simulation tool that can handle practical microwave circuits with intricate equivalent circuit models of lumped devices. The technique is particularly useful in the analysis and design of microwave active integrated antennas (AIA) [47], where electromagnetic coupling is a crucial issue for a successful design. Since in the AIA the antenna is not only used as a radiating element but also provides certain circuit functions such as diplexing and harmonic tuning, it has to be characterized with the RF circuitry as a whole entity from the very beginning. The extended FDTD should also make possible full wave analysis of novel microwave circuit configurations such as self-oscillating mixers. Such unique capabilities, which are either unavailable or

difficult to achieve with most of the currently existing EM or circuit simulators, make the extended FDTD a very promising candidate for next-generation microwave and millimeter wave CAD tools, where electromagnetic analysis and circuit simulation are integrated seamlessly and unified in an unprecedented fashion.

## ACKNOWLEDGMENT

The authors thank Dr. Chien-Nan Kuo, Dr. Min Chen, and Dr. Kuang-Ping Ma for helpful discussions and reviewing the manuscript for this chapter.

## REFERENCES

1. Itoh, T. (ed.), *Numerical Techniques for Microwave and Millimeter-Wave Passive Structures*, Wiley, New York, 1989.
2. Hofer, W. J. R., "The transmission line matrix method—theory and applications," *IEEE Trans. Microwave Theory Tech.*, vol. 33, Oct. 1985, pp. 882–893.
3. Taflove, A., "Reinventing electromagnetics: emerging applications for FD-TD computation," *IEEE Comput. Sci. Eng.*, 1995, pp. 24–34.
4. Yee, K. S., "Numerical solution of initial boundary value problems involving Maxwell's equations in isotropic media," *IEEE Trans. Antennas Propag.*, vol. 14, Aug. 1966, pp. 302–307.
5. Kunz, K. S., and Luebbers, R. J., *The Finite Difference Time Domain Method for Electromagnetics*, CRC Press, Boca Raton, FL, 1993.
6. Taflove, A., *Computational Electrodynamics: The Finite-Difference Time-Domain Method*, Artech House, Norwood, MA, 1995.
7. Guillouard, K., Wong, M., Hanna, V., and Citerne, J., "A new global time domain electromagnetic simulator of microwave circuits including lumped elements based on finite element method," *1997 IEEE MTT-S Int. Microwave Symp. Dig.*, June 1997, pp. 1239–1242.
8. Zhang, X. L., and Mei, K. K., "Time-domain finite-difference approach to the calculation of the frequency-dependent characteristics of microstrip discontinuities," *IEEE Trans. Microwave Theory Tech.*, vol. 36, Dec. 1988, pp. 1775–1787.
9. Reineix, A., and Jecko, B., "Analysis of microstrip patch antennas using finite difference time domain method," *Trans. Antennas Propag.*, vol. 37, Nov. 1989, pp. 1361–1369.
10. Sheen, D. M., Ali, S. M., Abouzahra, M. D., and Kong, J. A., "Application of the three-dimensional finite-difference time-domain method to the analysis of planar microstrip circuits," *IEEE Trans. Microwave Theory Tech.*, vol. 38, July 1990, pp. 849–857.
11. Qian, Y., Iwata, S., and Yamashita, E., "Characterization of the perturbation effect of a probe head using the FD-TD method," *IEEE Microwave Guided Wave Lett.*, vol. 4, Oct. 1994, pp. 317–319.
12. Zhao, A., and Raisanen, V., "Application of a simple and efficient source excitation technique to the FDTD analysis of waveguide and microstrip circuits," *IEEE Trans. Microwave Theory Tech.*, vol. 44, Sept. 1996, pp. 1535–1539.

13. Mur, G., "Absorbing boundary conditions for the finite-difference approximation of the time-domain electromagnetic-field equations," *IEEE Trans. EMC*, vol. 23, Nov. 1981, pp. 77–382.
14. Taflove, A., and Brodwin, M. E., "Numerical solution of steady-state electromagnetic scattering problems using the time-dependent Maxwell's equations," *IEEE Trans. Microwave Theory Tech.*, vol. 23, Aug. 1975, pp. 623–630.
15. Holland, R., and Williams, J. W., "Total-field versus scattered-field finite-difference codes: a comparative assessment," *IEEE Trans. Nuclear Sci.*, vol. 30, 1983, pp. 4583–4588.
16. Berenger, J. P., "A perfectly matched layer for the absorption of electromagnetic waves," *J. Comput. Phys.*, vol. 114, 1994, pp. 185–200.
17. Mei, K. K., and Fang, J., "Superabsorption—a method to improve absorbing boundary conditions," *IEEE Trans. Antennas Propag.*, vol. 40, Sept. 1992, pp. 1001–1010.
18. Naishadham, K., and Lin, X. P., "Minimization of reflection error caused by absorbing boundary condition in the FDTD simulation of planar transmission lines," *IEEE Trans. Microwave Theory Tech.*, vol. 44, Jan. 1996, pp. 41–46.
19. Ghouz, H., and El-Sharaway, E., "An accurate equivalent circuit model of flip chip and via interconnects," *IEEE Trans. Microwave Theory Tech.*, vol. 44, Dec. 1996, pp. 2543–2554.
20. Engquist, B., and Majda, A., "Absorbing boundary conditions for the numerical simulation of waves," *Math. Comput. Phys.*, vol. 31, 1977, pp. 629–651.
21. Fang, J., and Wu, Z., "Generalized perfectly matched layer for the absorption of propagating and evanescent waves in lossless and lossy media," *IEEE Trans. Microwave Theory Tech.*, vol. 44, Dec. 1996, pp. 2216–2222.
22. Mittra, R., and Pikel, U., "A new look at the perfectly matched layer (PML) concept for the reflectionless absorption of electromagnetic waves," *IEEE Microwave Guided Wave Lett.*, vol. 5, Mar. 1995, pp. 84–86.
23. Sacks, Z. S., Kingsland, D. M., Lee, R., and Lee, J. F., "A perfectly matched anisotropic absorber for use as an absorbing boundary condition," *IEEE Trans. Antennas Propag.*, vol. 43, Dec. 1995, pp. 1460–1463.
24. Gedney, S. D., "An anisotropic perfectly matched layer-absorbing medium for the truncation of FDTD lattices," *IEEE Trans. Antennas Propagat.*, vol. 44, Dec. 1996, pp. 1630–1639.
25. Zhao, L., and Cangellaris, A. C., "GT-PML: generalized theory of perfectly matched layers and its application to the reflectionless truncation of finite-difference time-domain grids," *IEEE Trans. Microwave Theory Tech.*, 44, Dec. 1996, pp. 2555–2563.
26. Balanis, C. A., *Advance Engineering Electromagnetics*, Wiley, New York, 1989.
27. Luebbers, R. J., Kunz, K. S., Schneider, M., and Hunsberger, F., "A finite-difference time-domain near zone to far zone transformation," *IEEE Trans. Antennas Propag.*, vol. 39, Apr. 1991, pp. 429–433.
28. Kormanyos, B., Harokopus, W., Katehi, L. P. B., and Rebeiz, G., "CPW-fed active slot antennas," *IEEE Trans. Microwave Theory Tech.*, vol. 42, Apr. 1994, pp. 541–545.
29. Liu, Y., Cha, K., and Itho, T., "Non-leaky colanar (NLC) waveguide with conductor backing," *IEEE Trans. Microwave Theory Tech.*, vol. 43, May 1995, pp. 1067–1072.
30. Lee, C. Y., Liu, Y., Cha, K., and Itoh, T., "Analysis and application of nonleaky uniplanar structures with conductor backing," *Int. J. Microwave Millimeter-Wave CAE*, vol. 6, 1996, pp. 319–327.



31. Qian, Y., and Itho, T., "Characterization and minimization of mutual coupling between NLC-fed antennas," *1997 IEEE MTT-S Int. Microwave Symp. Dig.*, June 1997, pp. 1623–1626.
32. Janaswamy, R., "An accurate moment method model for the tapered slot antenna," *IEEE Trans. Antennas Propag.*, vol. 37, Dec. 1989, pp. 1523–1528.
33. Sui, W., Christensen, D. A., and Durney, C. H., "Extending the two-dimensional FDTD method to hybrid electromagnetic systems with active and passive lumped elements," *IEEE Trans. Microwave Theory Tech.*, vol. 40, Apr. 1992, pp. 724–730.
34. Piket-May, M., Taflove, A., and Baron, J., "FD-TD modeling of digital signal propagation in 3-D circuits with passive and active loads," *IEEE Trans. Microwave Theory Tech.*, vol. 42, Aug. 1994, pp. 1514–1523.
35. Lau, Y. C., Leong, M. S., and Kooi, P. S., "Modeling of chip resistors for high-frequency microwave applications with the use of the FD-TD method," *Microwave and Opt. Technol. Lett.*, vol. 14, Apr. 1997, pp. 259–261.
36. Toland, B., Lin, J., Houshmand, B., and Itoh, T., "Electromagnetic simulation of mode control of a two element active antenna," *1994 IEEE MTTS-S Int. Microwave Symp. Dig.*, June 1994, pp. 883–886.
37. Toland, B., Lin, J., Houshmand, B., and Ithoh, T., "FDTD analysis of an active antenna," *IEEE Microwave Guided Wave Lett.*, vol. 3, Nov. 1993, pp. 423–425.
38. Nogi, S., Lin, J., and Itoh, T., "Mode analysis and stabilization of a spatial power combining array with strongly coupled oscillators," *IEEE Trans. Microwave Theory Tech.*, vol. 41, Oct. 1993, pp. 1827–1837.
39. Ciampolini, P., Mezzanotte, P., Roselli, L., and Sorrentino, R., "Accurate and efficient circuit simulation with lumped-element FDTD techniques," *IEEE Trans. Microwave Theory Tech.*, vol. 44, Dec. 1996, pp. 2207–2215.
40. Chen, Q., and Fusco, V. F., "A new algorithm for analysing lumped parameter elements using 3D FDTD method," *25th European Microwave Conf. Proc.*, Sept. 1995, pp. 410–413.
41. Chen, Q., and Fusco, V. F., "Hybrid FDTD large-signal modeling of three-terminal active devices," *IEEE Trans. Microwave Theory Tech.*, vol. 45, Aug. 1997, pp. 1267–1270.
42. Thomas, V., Jones, M., Piket-May, M., Taflove, A., and Harrigan, E., "The use of SPICE lumped circuits as sub-grid models for FDTD analysis," *IEEE Microwave Guided Wave Lett.*, vol. 4, May, 1994, pp. 141–143.
43. Kuo, C. N., Thomas, V., Chew, S. T., Houshmand, B., and Itoh, T., "Small signal analysis of active circuits using the FDTD algorith," *IEEE Microwave Guided Wave Lett.*, vol. 5, July 1995, pp. 216–218.
44. Kuo, C. N., Wu, R., Houshmand, B., and Itoh, T., "Modeling of microwave active devices using the FDTD analysis based on the voltage-source approach," *IEEE Microwave Guided Wave Lett.*, vol. 6, May 1996, pp. 199–201.
45. Kuo, C. N., Houshmand, B., and Itoh, T., "Full-wave analysis of packaged microwave circuits with active and nonlinear devices: an FDTD approach," *IEEE Trans. Microwave Theory Tech.*, vol. 45, May 1997, pp. 819–826.
46. Chen, M., Chew, S. T., and Itoh, T., "Nonlinear analysis of a microwave diode mixer using the extended FDTD," *1997 IEEE MTT-S Int. Microwave Symp. Dig.*, June 1997, pp. 67–70.
47. Lin, J., and Itoh, T., "Active integrated antennas," *IEEE Trans. Microwave Theory Tech.*, vol. 42, Dec. 1994, pp. 2186–2194.

CHAPTER SEVEN

---

# Phase-Locking Dynamics in Integrated Antenna Arrays

---

**ROBERT A. YORK**

Department of Electrical Engineering  
University of California  
Santa Barbara, CA

## 7.1 INTRODUCTION

Injection-locking (IL) and phase-locked-loop (PLL) techniques can be used to achieve synchronous operation of a number of antenna array elements. This has been exploited for power-combining and high-gain/narrowband amplification in microwave communication systems. Application of IL and PLL techniques to active integrated antennas and arrays is particularly attractive since oscillators can conveniently be designed around or within a variety of planar radiating structures, making use of the antenna as both the frequency-selective and the dissipative element (resonator and load). An additional attractive feature of IL and PLL methods in this context is the ability to manipulate the phase distribution without additional phase-shifting circuitry, suggesting a potential for low-cost beam-scanning systems.

These applications require a sound understanding of the nonlinear dynamics of individual and interacting oscillators, to ascertain regions of mutual coherence, and to establish conditions for achieving prescribed phase distributions. This chapter develops analytical methods for coupled injection- or phased-locked oscillator

arrays, suitable for predicting mode stability, transient response, and noise properties. Key results to be shown include (1) that beam control can be accomplished via control of only peripheral array elements; (2) that the oscillator equivalent circuit plays an important role in mode selection for common coupling schemes; (3) that certain coupling topologies lead to a phase noise reduction proportional to the number of oscillators; and (4) that some of the interesting array dynamics can be derived from a linear differential equation, which reduces to the Poisson equation in the steady state. The formulation for discrete array dynamics herein is also an improved and corrected version of that appearing in earlier work [1].

The analysis presented here is only one of many different approaches to the theory of nonlinear oscillations. It was first utilized by Kurokawa [2] to describe the operation and noise characteristics of microwave oscillators. The method relies on a frequency domain impedance, admittance, or scattering parameter description and is therefore particularly well suited to microwave oscillators. As we will show, Kurokawa's method is derived from a rigorous expansion of the time domain response through the inverse Fourier transform.

## 7.2 SYSTEMS OF COUPLED OSCILLATORS

The analysis of multiple-oscillator systems involves relatively minor extensions of the elementary injection-locking theory but yields significantly more complex and interesting dynamics. An oscillator array can be interconnected or externally injection-locked in a number of possible configurations; a few examples from the literature are shown in Fig. 7.1, such as a corporate fed externally locked array [3], unilateral nearest-neighbor injection-locking [4], and "inter-injection-locked" [5,6] or "mutually synchronized" [7,8] bilateral nearest-neighbor injection-locking.

A general model for analysis is shown in Fig. 7.2a. Each oscillator circuit is coupled to an  $N$ -port network, which will be described in terms of  $Y$ -parameters. The  $N$ -port includes both coupling circuits and the load. At each port we define an oscillator admittance,  $Y_{osc,i}$ , to describe the nonlinear active element and embedding circuit, which is coupled to a load admittance  $Y_{L,i}$ , the input admittance of the coupling networks at the  $i$ th port. The possibility of externally injected signals are included via the independent current sources  $I_{inj,i}$  at each port, which (if nonzero) are assumed to be coherent. From Kirchoff's current law we can write

$$\tilde{I}_{inj,i}(\omega) = \tilde{V}_i(\omega)[Y_{osc,i}(\omega, |V_i|) + Y_{L,i}(\omega)] \quad (7.1)$$

where the tilde ( $\tilde{\phantom{x}}$ ) denotes a frequency domain (phasor) quantity. From linear network theory we can write

$$Y_{L,i}(\omega) = \sum_{j=1}^N Y_{ij}(\omega) \frac{\tilde{V}_j}{\tilde{V}_i} \quad (7.2)$$

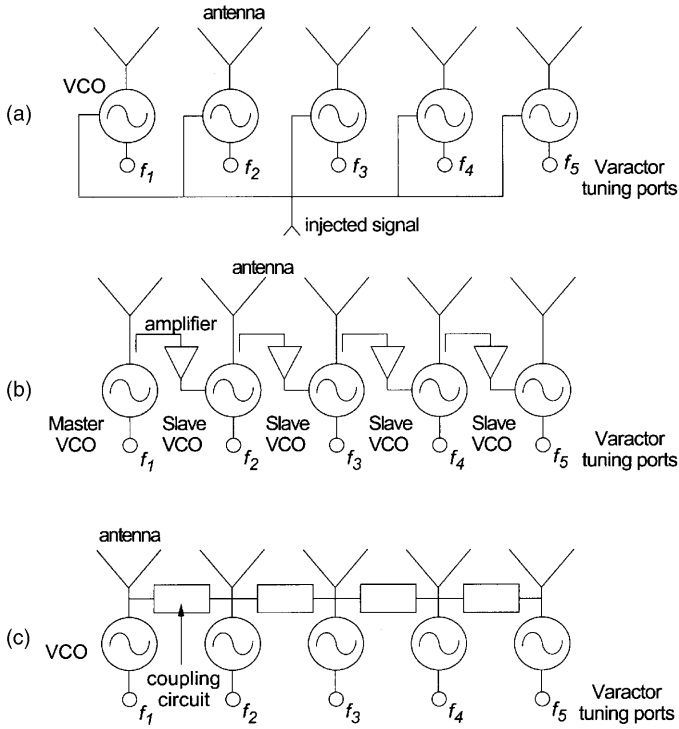


**FIGURE 7.1** A few common array topologies. (a) Each element is locked to a common reference signal, which is distributed by an RF feed network. (b) Unilateral injection-locking where each oscillator is slaved to the preceding element. (c) Bilateral nearest-neighbor coupling.

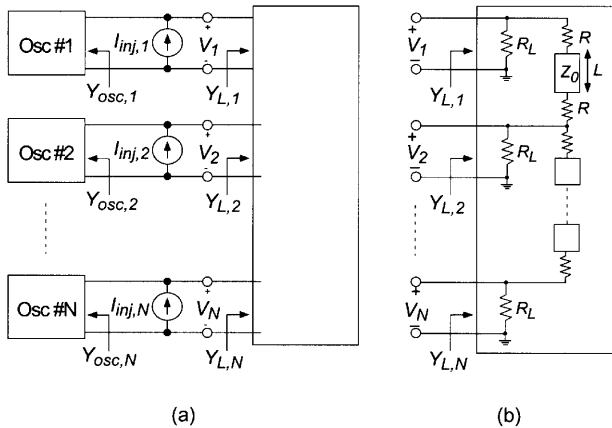


**FIGURE 7.2** (a) General model for oscillator array analysis, which includes the topologies of Fig. 7.1 as special cases. The coupling network includes the load network (usually an antenna array). (b) A simple and practical parallel-coupling network using resistively loaded transmission lines.

where  $N$  is the number of oscillators in the system. So Eq. 7.1 can be written as

$$\tilde{I}_{inj,i}(\omega) = \sum_{j=1}^N Y_{t,ij}(\omega, |V_i|) \tilde{V}_j(\omega) \tag{7.3}$$

where

$$Y_{t,ij}(\omega, |V_i|) = Y_{osc,i}(\omega, |V_i|) \delta_{ij} + Y_{ij}(\omega) \tag{7.4}$$

and  $\delta_{ij}$  is the Kronecker delta. The next critical assumption in the analysis is that each oscillator is a single-mode system, designed to produce nearly sinusoidal oscillations around a nominal center frequency  $\omega_i$ ; this is the “free-running” or unperturbed oscillation frequency of the  $i$ th oscillator. Most practical oscillators can be designed to satisfy this criterion by using an embedding circuit with a well-defined and isolated resonance at  $\omega_i$  with a sufficiently high  $Q$ -factor ( $Q > 10$ ), and terminating the device so as to provide narrowband gain around this resonance. The time-dependent output voltage can then be written (using complex notation) in the following useful forms:

$$\begin{aligned} V_i(t) &= A_i(t)e^{j[\omega_r t + \phi_i(t)]} \\ &= A_i(t)e^{j\theta_i(t)} \\ &= V'_i(t)e^{j\omega_r t} \end{aligned} \tag{7.5}$$

where  $A_i$  and  $\phi_i$  are dynamic amplitude and phase variables,  $V'_i = A_i \exp(j\phi_i)$  is the output “phasor” voltage at port  $i$ ,  $\theta_i(t) = \omega_r t + \phi_i(t)$  is the instantaneous phase, and  $\omega_r$  is a “reference” frequency that is presumably close in magnitude to the average  $\omega_i$ , but otherwise somewhat arbitrary and chosen for convenience for a particular problem. The reason for defining  $V_i(t)$  in terms of this reference frequency will become clear later but, in the meantime, can be considered as establishing a variable harmonic reference for the time variation of  $\phi$ , which proves convenient when the oscillator system is perturbed from its free-running state. The *true* time variation is obtained by taking the real part of Eq. 7.6.

Applying the inverse Fourier transform to Eq. 7.3 and exploiting the slowly varying amplitude and phase assumption, it can be shown (see Appendix) that Eq. 7.3 transforms to

$$I_{inj,i}(t) = \sum_{j=1}^N \left[ Y_{t,ij}(\omega_r, A_i) V'_j(t) + \frac{\partial Y_{t,ij}(\omega_r, A_i)}{\partial (j\omega)} \frac{dV'_j}{dt} \right] e^{j\omega_r t} \tag{7.6}$$

where we have used the notation in Eq. 7.6. As described in the Appendix, Eq. 7.6 is an approximation, valid when higher order time derivatives of amplitude and phase and higher order frequency derivatives of the total admittance are both negligible compared with the first two terms of the expansion (the two terms in the square brackets in Eq. 7.6). This is generally satisfied for oscillation around an isolated

resonance and for amplitude and phase fluctuations, which are slow compared to the carrier (an excellent assumption in practice). This result is equivalent to using a “Kurokawa substitution” for the frequency in Eq. 7.3 and can be written in the matrix notation

$$\mathbf{I}_{\text{inj}}(t) = \left[ \bar{\bar{Y}}_t \cdot \mathbf{V}' + \frac{\partial \mathbf{Y}_t}{\partial (j\omega)} \cdot \frac{d\mathbf{V}'}{dt} \right] e^{j\omega t} \quad (7.7)$$

where  $\bar{\bar{Y}}_t$  is a matrix with elements  $Y_{t,ij}$ ,  $\mathbf{I}_{\text{inj}}$  is a vector with elements  $I_{\text{inj},i}(t)$ , and  $\mathbf{V}'$  is a vector with elements  $V'_j$  (the phasor port voltages). This is a coupled set of first-order differential equations for the port voltages and can be written as

$$\frac{d\mathbf{V}'}{dt} = \left( \frac{\partial \bar{\bar{Y}}_t}{\partial (j\omega)} \right)^{-1} \cdot [\mathbf{I}_{\text{inj}} e^{-j\omega t} - \bar{\bar{Y}}_t \cdot \mathbf{V}'] \quad (7.8)$$

This in turn can be expressed as

$$\frac{dV'_i}{dt} = F_i(\mathbf{V}) V'_i, \quad i = 1, \dots, N \quad (7.9)$$

where

$$F_i(\mathbf{V}) = \sum_{j=1}^N \left( \frac{\partial \bar{\bar{Y}}_t}{\partial (j\omega)} \right)^{-1}_{ij} \left[ \frac{I_{\text{inj},j}}{V'_i} - \sum_{k=1}^N Y_{t,jk} \frac{V'_k}{V'_i} \right]$$

(Note: Equation 7.9 is a corrected and more rigorously valid version of equations that have appeared in earlier publications [1,8].) This can be solved for the amplitude and phase variations by separating real and imaginary parts to give

$$\frac{dA_i}{dt} = A_i \text{Re } F_i(\mathbf{A}, \Phi) \quad (7.10)$$

$$\frac{d\phi_i}{dt} = \text{Im } F_i(\mathbf{A}, \Phi), \quad i = 1, \dots, N \quad (7.11)$$

This is a general result for analysis of amplitude and phase dynamics in coupled oscillator systems. We can simplify the analysis further by restricting attention to “broadband” coupling networks, which satisfy

$$\frac{\partial Y_{t,ij}}{\partial (j\omega)} \approx \frac{\partial Y_{\text{osc},i}}{\partial (j\omega)} \delta_{ij} \quad (7.12)$$

in other words, coupling networks that have negligible frequency dependence near the operating frequency. This is equivalent to saying that the oscillator  $Q$ -factor is the

dominant  $Q$  of the system (see Lynch [9] for a treatment of coupling networks with a nonnegligible frequency dependence, such as resonant coupling through an external cavity). With this assumption,  $F_i$  in Eq. 7.9 is given by

$$F_i(\mathbf{V}) \simeq \left( \frac{\partial Y_{\text{osc},i}(\omega_r, A_i)}{\partial (J\omega)} \right)^{-1} \left[ \frac{I_{\text{inj},i}}{V'_i} - Y_{\text{osc},i}(\omega_r, A_i) - \sum_{j=1}^N Y_{ij}(\omega_r) \frac{V'_j}{V'_i} \right] \quad (7.13)$$

We are most interested in steady-state solutions to Eqs. 7.10 and 7.11, where all oscillators are synchronized to a common frequency,  $\omega$ , which occurs when

$$\frac{dA_i}{dt} = 0 \quad \text{and} \quad \frac{d\phi_i}{dt} = \omega - \omega_r, \quad i = 1, \dots, N \quad (7.14)$$

In this case the oscillator phases will be bounded in time if the reference frequency is chosen to be  $\omega_r = \omega$ , in which case the steady-state solutions are determined by the set of nonlinear algebraic equations

$$F_i(\mathbf{A}, \boldsymbol{\Phi}) = 0, \quad i = 1, \dots, N \quad (7.15)$$

If externally injected signals at frequency  $\omega_{\text{inj}}$  are present, the synchronized frequency (and reference frequency) can be taken as  $\omega = \omega_{\text{inj}} = \omega_r$ . However, in the absence of externally injected signals ( $I_{\text{inj},i} = 0$  for all  $i$ ), the steady-state synchronized frequency is not known a priori but must be determined from Eq. 7.15. The real and imaginary parts of  $F_i$  must equate separately to zero, so Eq. 7.15 represents a set of  $2N$  equations. Since the amplitude and phase of each oscillator are  $2N$  unknowns that must be solved for, it would appear that when  $\omega$  is also unknown there would be  $2N + 1$  unknowns, but in this case one of the phases is arbitrary and can be set to zero (only the relative phases are important physically). For externally locked arrays all of the oscillator phases are unknown, since the injected signals establish a phase reference.

Unless the oscillators are strongly coupled, the oscillation amplitudes will remain close to the free-running values. Assuming this to be the case, the amplitude and phase dynamics are uncoupled, to first order. We then can restrict attention to the phase dynamics governed by Eq. 7.11. This will simplify the analysis considerably.

To proceed further, we need to specify an oscillator model. In a well-designed oscillator, the oscillation frequency will occur in the vicinity of a reactance or susceptance null, which is assumed to be well isolated from other nulls (spectrally) to avoid mode-hopping or multifrequency operation. In a narrow range of frequencies around such a resonance, the oscillator circuit can be modeled by either a parallel or series resonant circuit, shown in Figs. 7.3a and 7.3b, respectively. For stability in the free-running case, the device in the parallel model must have a negative *conductance* that decreases with increasing oscillation amplitude. The device in the series model must have a negative *resistance* that decreases in magnitude with increasing oscillation amplitude. We assume that the array is

composed of oscillators that are stable in their free-running state. The coupling between the oscillators serves only to synchronize the frequencies via the injection-locking phenomenon and results in only a slight perturbation of the oscillators from the free-running configuration.

### 7.2.1 Parallel Oscillator Model

Using the parallel model of Fig. 7.3a, the input admittance of the  $i$ th oscillator near the resonant frequency  $\omega_i$  can be approximated as

$$Y_{\text{osc},i} \approx -G_d(A_i) + j2C_i(\omega - \omega_i) \tag{7.16}$$

where  $C_i$  is the shunt capacitance. In the free-running state, the oscillator feeds a load conductance of  $G_L$  as shown, so we can define a  $Q$ -factor for the free-running oscillator as  $Q = \omega_i R_L C_i$  and write

$$Y_{\text{osc},i} \approx -G_d(A_i) + j \frac{G_L}{\omega_{3\text{dB}}} (\omega - \omega_i) \tag{7.17}$$

where  $\omega_{3\text{dB}} = \omega_i/2Q$  is half the 3-dB bandwidth of the oscillator tank circuit. We assume that the oscillators can have slightly different free-running frequencies, but that the  $Q$ -factors and 3-dB bandwidths are all the same, to first order. From this we see that

$$\frac{\partial Y_{\text{osc},i}(\omega_r)}{\partial(j\omega)} = \frac{G_L}{\omega_{3\text{dB}}} \tag{7.18}$$

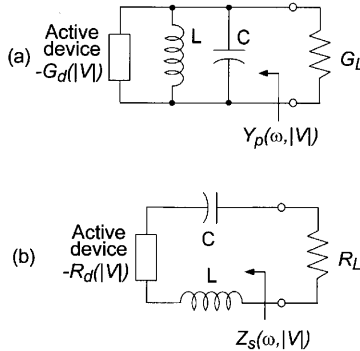


FIGURE 7.3 (a) Parallel-equivalent oscillator model; (b) series-equivalent oscillator model.



Using Eqs. 7.17, and 7.18, and 7.2, the function  $F_i$  from Eq. 7.13 is then give by

$$F_i = J(\omega_i - \omega_r) + \frac{\omega_{3\text{dB}}}{G_L} \left[ \frac{I_{\text{inj},i}}{V'_i} + G_d(A_i) - \sum_{j=1}^N Y_{ij} \frac{A_j}{A_i} e^{j(\theta_j - \theta_i)} \right] \quad (7.19)$$

### 7.2.2 Series Oscillator Model

The dynamics for a series oscillator model can be derived in similar fashion. Close to the resonant frequency ( $\omega \approx \omega_i$ ) the input impedance of the oscillator in Fig. 7.3b is given by

$$Z_{\text{osc},i} \approx -R_d(A_i) + J \frac{R_L}{\omega_{3\text{dB}}} (\omega - \omega_i) \quad (7.20)$$

Our formulation requires the input *admittance* and derivative with frequency. Assuming that the oscillators are only slightly perturbed from their free-running state, the amplitude of oscillation will remain close to the free-running value, and therefore  $-R_d(A_i) \approx R_L$ . Using this approximation, the admittance can be expressed as

$$Y_{\text{osc},i} = \frac{1}{Z_{\text{osc},i}} \approx -\frac{1}{R_d(A_i)} - J \frac{\omega - \omega_i}{\omega_{3\text{dB}} R_L} \quad (7.21)$$

and so

$$\frac{\partial Y_{\text{osc},i}(\omega_r)}{\partial (J\omega)} = -\frac{1}{\omega_{3\text{dB}} R_L} \quad (7.22)$$

Combining 7.22, 7.2, and 7.13 gives

$$F_i = J(\omega_i - \omega_r) - \frac{\omega_{3\text{dB}}}{G_L} \left[ \frac{I_{\text{inj},i}}{V'_i} + \frac{1}{R_d(A_i)} - \sum_{j=1}^N Y_{ij} \frac{A_j}{A_i} e^{j(\theta_j - \theta_i)} \right] \quad (7.23)$$

The only difference between Eqs. 7.23 and 7.19 is the sign preceding the bracketed term. Nevertheless, this has an important influence on the phase relationships, as we will see.

### 7.2.3 Phase Dynamics with Nearest-Neighbor Coupling

There are a number of ways in which oscillators can be interconnected in a broadband coupling network. Analysis for general coupling networks is discussed in [1]. We will restrict attention to a simple nearest-neighbor coupling networks that is appropriate for planar oscillator circuits, shown in Fig. 7.2b. When the coupling

resistance is chosen such that  $R = Z_0$ , this network has the following admittance parameter [8]:

$$Y_{ij} = \begin{cases} \frac{\eta_i}{2Z_0} + G_L, & i = j \\ \frac{-e^{-j\beta L}}{2Z_0}, & |i - j| = 1 \\ 0, & \text{otherwise} \end{cases} \quad \frac{\partial Y_{ij}}{\partial(j\omega)} = \begin{cases} 0, & i = j \\ \frac{\tau_g e^{-j\beta L}}{2Z_0}, & |i - j| = 1 \\ 0, & \text{otherwise} \end{cases} \quad (7.24)$$

where  $\beta L$  is the electrical length of the transmission line,  $Z_0$  is the characteristic impedance,  $\eta_i = (2 - \delta_{i1} - \delta_{iN})$ ,  $\delta_{ij}$  is the Kronecker delta function, and  $\tau_g$  is the group delay through the transmission line. For TEM or quasi-TEM lines,  $\tau_g = \beta L / \omega$ , and when  $\beta L \leq 2\pi$  then the assumptions leading to Eq. 7.13 are satisfied if  $\pi R_L / QZ_0 \ll 1$  ( $R_L = 1/G_L$ ) [8], where  $Q$  is the  $Q$ -factor of the oscillator. We will assume this constraint holds and define the following ‘‘coupling parameters’’ for future convenience:

$$\varepsilon \equiv \frac{R_L}{2Z_0} \quad \text{and} \quad \Phi \equiv \beta L \quad (7.25)$$

The independent sources representing externally injected signals are assumed to be mutually coherent at a common frequency  $\omega_{\text{inj}}$  and are written as

$$I_{\text{inj},i} = \rho_i G_L e^{j\omega_{\text{inj}}t + \psi_i(t)} \quad (7.26)$$

Substituting Eqs. 7.24 and 7.26 into Eqs. 7.19 and 7.23, and using Eq. 7.25, the phase dynamics in Eq. 7.11 are described by

$$\begin{aligned} \frac{d\phi_i}{dt} &= (\omega_i - \omega_r) \mp \varepsilon \omega_{\text{3dB}} \sum_{\substack{j=i-1 \\ j \neq i}}^{i+1} \sin(\Phi + \phi_i - \phi_j) \\ &\mp \rho_i \omega_{\text{3dB}} \sin(\phi_i - \psi_i), \quad i = 1, \dots, N \end{aligned} \quad (7.27)$$

where we have assumed uniform amplitudes  $A_i = 1$ . The upper sign is for parallel oscillators (Fig. 7.4a), while the lower sign is for series oscillators (Fig. 7.4b). This equation applies to the end elements in the array provided that any terms containing subscripts 0 or  $N + 1$  are ignored. It is also understood that  $\omega = \omega_{\text{inj}}$  when externally injected signals are present, or  $\omega$  is an unknown to be solved for otherwise.

In previous work [8], it has been demonstrated theoretically and experimentally that desired phase progressions can be established in free-running ( $\rho_i = 0$ ) nearest neighbor coupled arrays, using coupling networks like that of Fig. 7.2b, by properly detuning the oscillator free-running frequencies prior to synchronization. The coupling phase  $\Phi$  also plays an important role in determining the stable range of

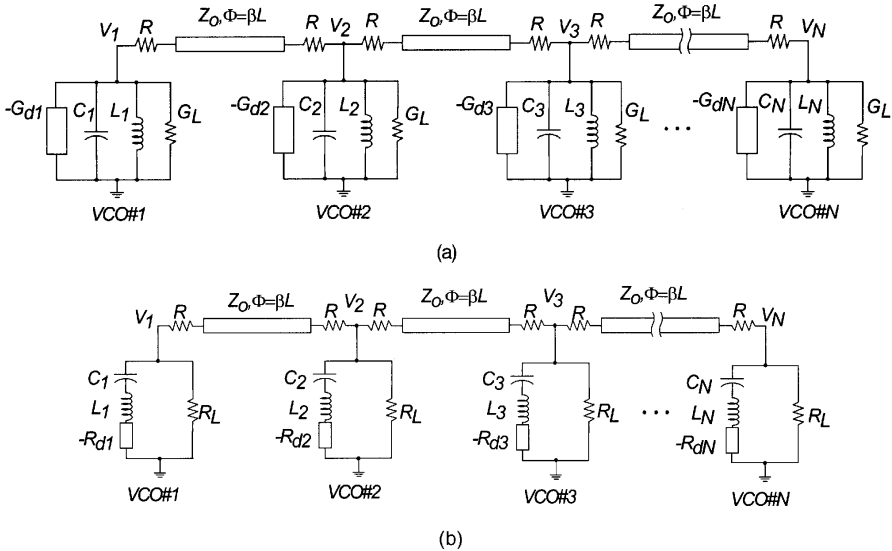


**FIGURE 7.4** Nearest-neighbor coupled-oscillator systems considered in this chapter. (a) Parallel oscillators coupled in parallel using the resistively loaded network of Fig. 7.2b; (b) Series oscillators in a similar coupling network.

phase shifts and the frequency distribution required for implementation. For example, using Eq. 7.27 for parallel oscillators we showed that beam scanning around the broadside direction can be achieved when  $\Phi = 0^\circ$  with only detuning of peripheral array elements [10], with the range of stable interelement phase shifts being  $-90^\circ < \Delta\theta < 90^\circ$ . Note that the phase dynamics Eq. 7.27 for series-type oscillators with  $\Phi = 180^\circ$  would yield exactly the same phase dynamics as the parallel type with  $\phi = 0^\circ$  (and vice versa). This means that series oscillators require a significantly different coupling circuit than parallel oscillators in order to produce the same phase distributions.

For illustrative purposes as well as practical merit, we will focus on the case where  $\Phi \approx n\pi$ , where  $n$  is an integer (the following analysis will be accurate for small deviations in coupling phase around the point  $\Phi = n\pi$ ). In this case, Eq. 7.27 becomes

$$\begin{aligned} \frac{d\phi_i}{dt} &= (\omega_i - \omega_r) \mp \epsilon\omega_{3dB} \cos \Phi \sum_{\substack{j=i-1 \\ j \neq i}}^{i+1} \sin(\phi_i - \phi_j) \\ &\mp \rho_i \omega_{3dB} \sin(\phi_i - \psi_i), \quad i = 1, \dots, N \end{aligned} \tag{7.28}$$

The phase relationships will be strongly dependent on the free-running frequencies,  $\omega_i$ . In a practical array the free-running frequency distribution can be manipulated dynamically by employing voltage-controlled oscillators (VCOs) with a varactor

tuning element. For a given coupling network we have the following analysis and synthesis problems: (1) given a set of free-running frequencies, solve for the resulting steady-state phase; or (2) given a desired phase distribution, solve for the free-running frequencies that will produce this phase relationship. The former is extremely difficult in the general case and must be carried out numerically (an alternative based on continuum modeling is discussed later). The linearity of Eq. 7.28 with respect to the free-running frequencies makes the synthesis procedure very straightforward.

For steady-state synchronous oscillation at  $\omega$ , substituting a desired phase relationship, denoted by a circumflex  $\hat{\phi}_i$ , into Eq. 7.28 gives the required free-running frequencies:

$$\omega_i = \omega \pm \varepsilon\omega_{3\text{dB}} \cos \Phi \sum_{\substack{j=i-1 \\ j \neq i}}^{i+1} \sin(\hat{\phi}_i - \hat{\phi}_j) \pm \rho_i\omega_{3\text{dB}} \sin(\hat{\phi}_i - \psi_i), \quad i = 1, \dots, N \quad (7.29)$$

This would seem to imply that we can synthesize any arbitrary phase relationship by suitably adjusting the free-running frequencies, but that is not the case; each possible solution must be checked for stability (see [1]).

Note that for a single oscillator ( $\varepsilon = 0$ ,  $N = 1$ ), both series and parallel models yield Adler's equation [11]:

$$\frac{d\phi}{dt} = (\omega_0 - \omega_{\text{inj}}) \mp \rho\omega_{3\text{dB}} \sin(\phi - \psi) \quad (7.30)$$

The difference in sign in this case is attributed to the assumed direction of the injected current (into the oscillator). That is, the sign depends on how we define the phase of the injected signal. This is also true for arrays; we can always uniformly shift the injected-signals phases by  $\pm\pi$  to change the sign of the injection terms in Eq. 7.28. This is just another way of saying that the phase reference in the injected system is arbitrary, and therefore the sign of the injection terms is not considered especially important.

#### 7.2.4 Free-Running Arrays

With no injection signals present ( $\rho_i = 0$  for all  $i$ ), Eq. 7.28 reduces to

$$\frac{d\phi_i}{dt} = (\omega_i - \omega_r) \mp \varepsilon\omega_{3\text{dB}} \cos \Phi \sum_{\substack{j=i-1 \\ j \neq i}}^{i+1} \sin(\phi_i - \phi_j), \quad i = 1, \dots, N \quad (7.31)$$

We remark in passing that, for the steady state, adding all  $N$  equations in Eq. 7.31 yields the interesting result

$$\omega = \frac{1}{N} \sum_{i=1}^N \omega_i \quad (7.32)$$

that is, the synchronized frequency is the average of the free-running frequencies.

We can cast Eq. 7.31 into a form containing only relative phases by defining

$$\begin{aligned}\Delta\phi_i &\equiv \phi_{i+1} - \phi_i, & i = 1, \dots, N-1 \\ \Delta\beta_i &\equiv \omega_{i+1} - \omega_i\end{aligned}$$

which eliminates the problem of having one arbitrary phase and also reduces the order of the system by one. It also eliminates the unknown frequency  $\omega$ , but after solving for the  $\Delta\phi_i$  we can find  $\omega$  from any one of Eqs. 7.31. The phase equations can be written in matrix form as

$$\frac{d}{dt}\mathbf{\Delta\Phi} = \mathbf{\Delta\beta} \mp \Delta\omega_m \cos\Phi \bar{\bar{\mathbf{A}}}\mathbf{s} \quad (7.33)$$

where  $\mathbf{\Delta\Phi}$  and  $\mathbf{\Delta\beta}$  are vectors with elements  $\Delta\phi_i$  and  $\Delta\beta_i$ ,  $\Delta\omega_m \equiv \varepsilon\omega_{3\text{dB}}$ , and

$$\bar{\bar{\mathbf{A}}} = \begin{bmatrix} 2 & -1 & & 0 \\ -1 & 2 & -1 & \\ & & \ddots & \\ 0 & & -1 & 2 \end{bmatrix}, \quad \mathbf{s} = \begin{bmatrix} \sin\Delta\phi_1 \\ \sin\Delta\phi_2 \\ \vdots \\ \sin\Delta\phi_{N-1} \end{bmatrix}$$

Setting the time derivative equal to zero gives an algebraic equation for the steady-state phase differences in terms of the oscillator free-running frequencies,

$$\mathbf{s} = \pm \frac{1}{\Delta\omega_m \cos\Phi} \bar{\bar{\mathbf{A}}}^{-1} \mathbf{\Delta\beta} \quad (7.34)$$

which can be solved by inverting the matrix  $\bar{\bar{\mathbf{A}}}$  and solving for the phases using the inverse sine function. The matrix  $\bar{\bar{\mathbf{A}}}$  has a simple inverse

$$A_{ij}^{-1} = \frac{j(i-N)}{N}, \quad i \geq j, \quad A_{ij}^{-1} = A_{ji}^{-1} \quad (7.35)$$

Clearly there are no possible solutions of Eq. 7.34 if any element of the column vector  $\bar{\bar{\mathbf{A}}}^{-1} \mathbf{\Delta\beta}$  has a magnitude greater than  $\Delta\omega_m |\cos\Phi|$ . When there is a valid solution for the sine vector this will correspond to  $2^{N-1}$  different solutions for the phase differences, since the inverse sine function is multivalued. The correct solution is found by stability analysis. Stability is examined by linearizing Eq. 7.33 around a steady-state solution. Denoting the perturbation to  $\mathbf{\Delta\Phi}$  as  $\mathbf{\delta}$  gives

$$\frac{d}{dt}\mathbf{\delta} = -\bar{\bar{\mathbf{M}}}\mathbf{\delta} \quad (7.36)$$

where the  $(N - 1) \times (N - 1)$  stability matrix  $\bar{\bar{M}}$  is

$$\bar{\bar{M}} = \pm \Delta \omega_m \cos \Phi \bar{\bar{A}} \bar{\bar{C}} \tag{7.37}$$

and we have defined the  $(N - 1) \times (N - 1)$  diagonal cosine matrix as

$$\bar{\bar{C}} = \begin{bmatrix} \cos \Delta \phi_1 & & & 0 \\ & \cos \Delta \phi_2 & & \\ & & \ddots & \\ 0 & & & \cos \Delta \phi_{N-1} \end{bmatrix}$$

A stable mode requires that all the eigenvalues of  $\bar{\bar{M}}$  have positive real parts. This will be true if the matrix is positive definite. The matrix  $\bar{\bar{A}}$  is always positive definite, and the matrix  $\bar{\bar{C}}$  is also positive definite when each of the phases lies in the range

$$-90^\circ < \Delta \phi_i < 90^\circ, \quad i = 1, \dots, N - 1 \tag{7.38}$$

Since the product of two positive definite matrices is also positive definite, the eigenvalues of the stability matrix are all real and positive when the phases lie in the above range, as long as  $\pm \cos \Phi > 0$ . Therefore, Eq. 7.38 represents the stable phase region for series oscillators when  $\Phi = \pi$ , and for parallel oscillators when  $\Phi = 2\pi$ .

Alternatively, the matrix  $\bar{\bar{C}}$  is negative definite when each of the phases lies in the range

$$90^\circ < \Delta \phi_i < 270^\circ, \quad i = 1, \dots, N - 1 \tag{7.39}$$

in which case the eigenvalues of the stability matrix are all real and positive when  $\mp \cos \Phi < 0$ . Therefore, Eq. 7.39 represents the stable phase region for series oscillators when  $\Phi = 2\pi$ , and for parallel oscillators when  $\Phi = \pi$ .

These results are summarized in Table 7.1 and have been verified experimentally [12]. Note that either phase range, Eq. 7.38 or 7.39, is sufficient to cause the vector  $\mathbf{s}$  in Eq. 7.34 to span all of its possible values, which proves that the stability region fills the entire existence region. Furthermore, over this range of phases the sine functions in  $\mathbf{s}$  are one-to-one. Thus for each set of tunings within the stability region

**TABLE 7.1 Ranges of Stable Phase Shifts for Different Oscillator Models and Coupling Phases**

Coupling Phase	Oscillator Model	
	Parallel	Series
$0, 2\pi$	$-90^\circ < \Delta \phi < 90^\circ$	$90^\circ < \Delta \phi < 270^\circ$
$\pi$	$90^\circ < \Delta \phi < 270^\circ$	$-90^\circ < \Delta \phi < 90^\circ$

there is a unique phase vector that implies that a unique stable synchronized state exists for a given tuning vector  $\Delta\beta$ .

### 7.3 SCANNING BY EDGE DETUNING

The analytical techniques developed above have demonstrated an ability to synthesize certain phase relationships in an oscillator array through the use of a suitable coupling scheme, and by manipulating the free-running frequencies in the array. It is natural to explore the possibility of manipulating the phase for beam control, in which case a constant phase progression is typically desired. Beam-scanning arrays using coupled oscillators have been developed for several coupling schemes. The chief advantage of this concept is the total elimination of phase shifter circuitry and, in most cases, an elimination of the RF feed network. The disadvantages of this approach are a relatively small bandwidth, limited scanning range, and difficulties in constructing oscillators with highly reproducible characteristics with high yield. However, such problems can be alleviated through advances in oscillator design, the use of phase-locked-loop techniques, and clever circuit augmentations [13].

From Eq. 7.34, we can establish the required conditions for a uniform phase progression  $\Delta\phi$  by inserting the  $(N - 1)$  element sine vector.

$$\mathbf{s} = \sin \Delta\phi(1, 1, \dots, 1)^T \tag{7.40}$$

which gives the result

$$\Delta\beta_i = \begin{cases} \pm\Delta\omega_m \cos \Phi \sin \Delta\phi, & i = 1 \\ 0, & 1 < i < N - 1 \\ \pm\Delta\omega_m \cos \Phi \sin \Delta\phi, & i = N - 1 \end{cases} \tag{7.41}$$

This implies that a uniform phase shift is induced simply by detuning the end elements of the array (relative to the central elements) by equal amounts and in opposite directions, with the amount of detuning establishing the amount of the induced phase shift [10]. Inserting the result back into Eq. 7.28 we find that the steady-state synchronized frequency is the same as the free-running frequencies of the central elements, independent of the end-element tuning since the ends are tuned in opposite directions. To summarize, the required frequency distribution is

$$\omega_i = \begin{cases} \omega \mp \Delta\omega_m \cos \Phi \sin \Delta\phi, & i = 1 \\ \omega, & 1 < i < N \\ \omega \pm \Delta\omega_m \cos \Phi \sin \Delta\phi, & i = N \end{cases} \tag{7.42}$$

The range of phase shifts that can be synthesized depends on the oscillator model and coupling network as described in Table 7.1. We see that end-fire or broadside scanning arrays are possible by proper selection of these parameters.

This simple and useful result has the disadvantage of being difficult to explain in a physically appealing manner. Recently, however, we have found that equivalent continuum models for discrete oscillator chains can provide valuable insight into the behavior of these systems. The basic idea is to pass to the limit of a continuous chain of oscillators (rather than a discrete chain), and find the partial differential equation that governs the system [1]. Applying this concept to our nearest-neighbor oscillator equations (7.28), we write

$$\phi_i - \phi_{i-1} \Rightarrow \left. \frac{\partial \phi}{\partial i} \right|_{i=1/2} \quad \text{and} \quad \phi_i - \phi_{i+1} \Rightarrow - \left. \frac{\partial \phi}{\partial i} \right|_{i+1/2}$$

Then Eq. 7.28 becomes

$$\frac{\partial \phi}{\partial t} = \omega(i) + \Delta\omega_m \frac{\partial}{\partial i} \sin\left(\frac{\partial \phi}{\partial i}\right) \quad (7.43)$$

The phase and free-running frequency variables are now continuous functions of the position  $i$ . The entire set of coupled differential equations (7.28) is therefore just a discretized version of Eq. 7.43. In the steady state synchronized state, and assuming the phase is a slowly varying function of position (small phase change between neighboring oscillators) then Eq. 7.43 is approximated by

$$\frac{\partial^2 \phi}{\partial i^2} = \frac{\omega - \omega(i)}{\Delta\omega_m} \quad (7.44)$$

This is just the one-dimensional Poisson equation. In electromagnetic terms, the phase plays the role of the electrostatic potential, while the relative oscillator tunings (which can be viewed as proportional to the dc voltage distribution for the varactor tuning elements in a VCO array) play the role of the charge distribution.

Using this result we can understand the beam-scanning method easily by analogy to electrostatics. The frequency distribution required to scan the beam is uniform except at the boundaries of the array. This would be analogous to a parallel-plate capacitor, where the charge is zero between the plates and nonzero on the plates with opposite signs on each plate. As we know, the potential varies linearly between the plates of a capacitor, with a slope proportional to the charge; therefore in the oscillator problem we expect a linear phase distribution with the phase shift proportional to the frequency tunings at the end of the array.

This beam-scanning technique has been verified experimentally. An eight-element array was constructed using the coupling topology of Fig. 7.2b and is shown in Fig. 7.5 [14]. The array was designed to operate at 8.4 GHz and featured an element separation of one-half wavelength. The maximum beam-scan range for this array was therefore  $\pm 30^\circ$  off broadside. The array was comprised of eight VCOs, each of which used an NEC 900276 packaged GaAs MESFET (two parasitic elements are shown in the figure). The oscillator was designed in a feedback



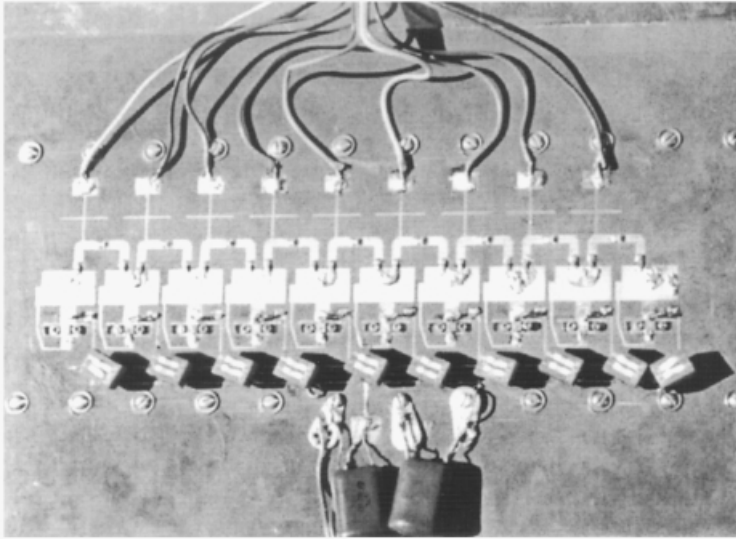


**FIGURE 7.5** Photograph of an 8.4-GHz oscillator array using feedback oscillators with a varactor-tuned patch antenna [14]. The transmission-line coupling network is based on the configuration of Fig. 7.4a. Individual varactor bias is applied via the coupling network at the top. The two end elements were inactive and served to equalize the loading along the remaining oscillators. The bias switches were used to determine the individual (free-running) oscillator tuning characteristics.

topology using a single-device amplifier with a tunable microstrip patch antenna in the feedback path. This varactor tuned patch served as a resonant load for the amplifier [15]. By adjusting the varactor bias, the free-running frequency of each oscillator was variable over a range of 150 MHz.

The effective radiated power (ERP) of the array was measured to be 8.5 W at 8.43 GHz. Figure 7.6 illustrates a typical broadside pattern, which was obtained when the free-running frequencies of the oscillators in the array were set to 8.45 GHz. Varying the end-element tunings in the manner predicted by Eq. 7.42, it was possible to scan the array from  $-15^\circ$  to  $+30^\circ$  off broadside; a representative scanned pattern is shown in Fig. 7.6b. This scanning range indicates that progressive phase shifts were achieved in the range  $-47^\circ \leq \Delta\theta \leq +90^\circ$ . A maximum phase difference of  $630^\circ$  was established between the first and last elements in the array. That the scan range is centered away from broadside is consistent with a nonzero coupling phase angle. This could be a result of a propagation delay through the chip resistors in the coupling network, which was not accounted for in this first-iteration design. Since the patterns closely resemble the theoretical patterns for a patch array, the directivity could accurately be estimated from theory, yielding a total radiated power of over 1 W for this array. This is consistent with the expected output power from the collection of devices.

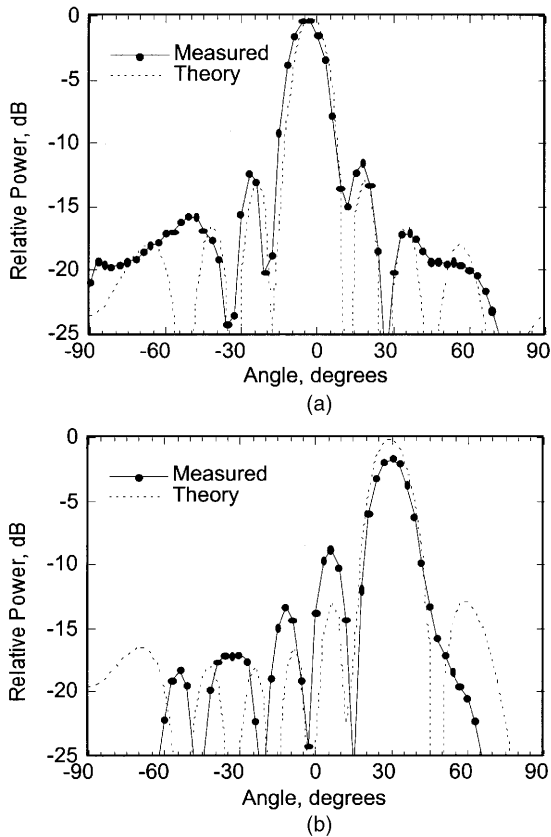


**FIGURE 7.6** Representative measured patterns for the array of Fig. 7.5 (a) A nearly broadside pattern was obtained with all the elements set to approximately the same free-running frequency. (b) A scanned pattern in the range of  $-15^\circ$  to  $+30^\circ$  off broadside was obtained by symmetrically detuning the end oscillators.

### 7.3.1 Settling Time After a Detuning Transient

A natural question to ask is: How long does it take for the oscillators to reach an equilibrium phase distribution and a common locked frequency after experiencing a detuning event? For the beam-scanning technique just described, this would relate to the maximum speed with which the beam can be moved from one angular position to another. Also of interest is the behavior of the phase distribution during this transient event. These questions will be answered qualitatively here using computer simulations of the array dynamics (Eq. 7.28).

One would anticipate that the response time of an array is intimately linked to the size of the array and the locking range; small arrays with large coupling strength would respond more rapidly. This is indeed the case. A quantitative analysis based on small perturbations has been described in [1] and yields dominant time constants

on the order of  $(L/\pi)^2/\Delta\omega_m$  for small detuning transients, where  $L$  is essentially the distance between the detuned oscillator and the farthest edge of the array. Figure 7.7 illustrates the response of an 11-element array after the center element has been detuned abruptly by  $0.5\Delta\omega_m$ . The initial state of the system is a uniform phase with all elements set at a common free-running frequency. The time scale in this figure has been normalized to the locking range according to  $\tau = \Delta\omega_m t$ . We observe a smooth variation in phase between the initial condition and steady state, with a time constant that is in close agreement with the simple theory described in [1].

Figure 7.8a shows the response of an identical array to equal and opposite step detuning of the end elements of the array, as required of the edge-scanning technique described earlier. Again, an initial zero-phase state was assumed. The phase is observed to vary gradually, leading to a variation in output beam direction as shown in Fig. 7.8b, assuming a half-wavelength spacing of array elements and a unity-gain element pattern. Again, the time constant of the system is in general agreement with the result mentioned above. Analysis of the transient dynamics using the continuum modeling technique is the subject of current research interest [16].

### 7.3.2 Enhancements

One apparent limitation of the injection-locked or coupled-oscillator topologies (for some applications) is the limited range of phase shifts that can be synthesized. This could be improved by introducing a frequency doubler circuit after each oscillator, as

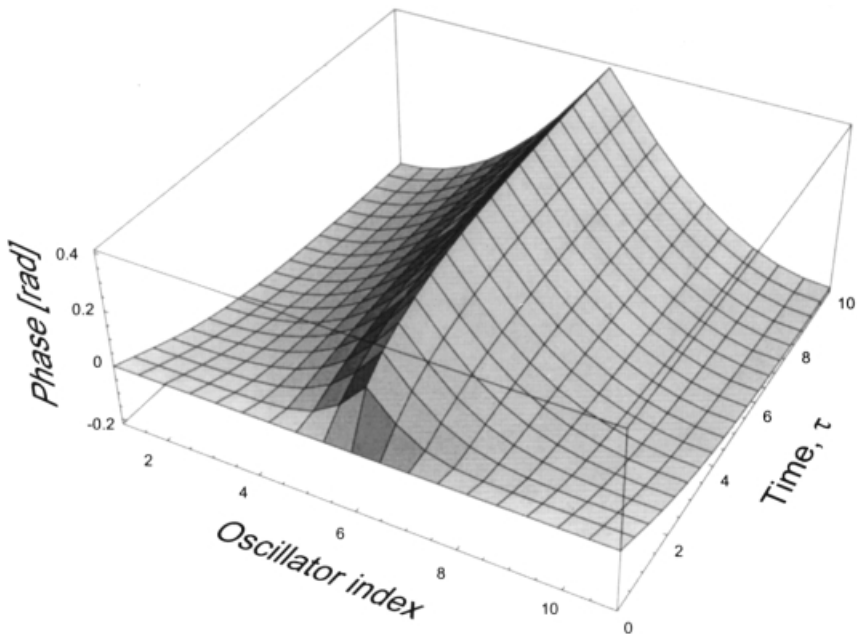
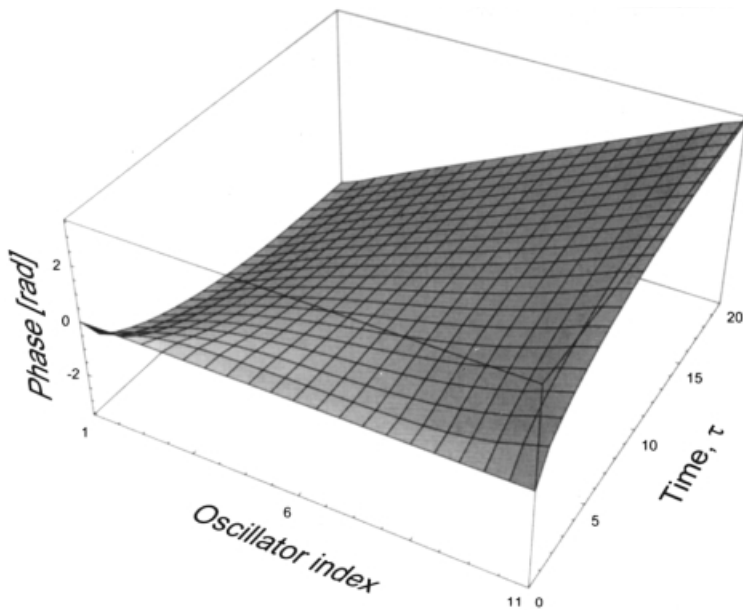
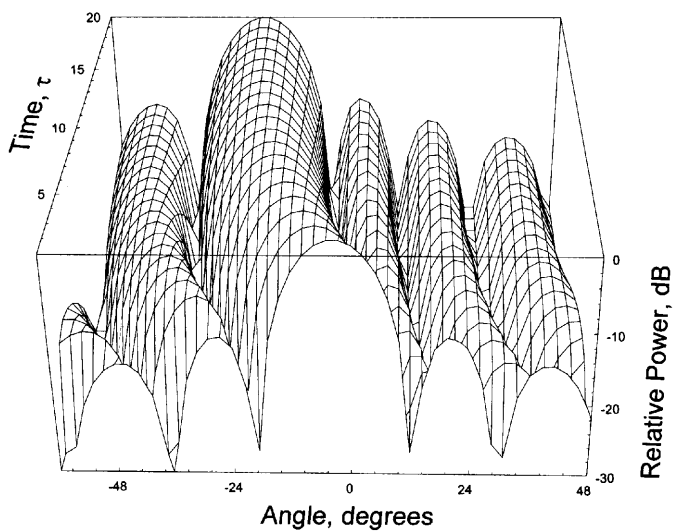


FIGURE 7.7 Evolution of phases versus normalized time ( $\tau = \Delta\omega_m t$ ) in an 11-oscillator chain after step detuning of the center element.



(a)



(b)

**FIGURE 7.8** Transient response of a scanning array using edge-detuning. (a) Evolution of phases versus normalized time ( $\tau = \Delta\omega_m t$ ) in an 11-oscillator chain after opposite detuning of end oscillators; (b) Resulting variation in array factor versus time, assuming a half-wavelength spacing of array elements.

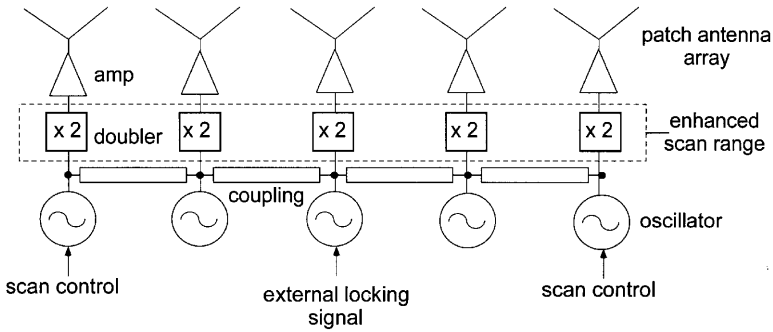


**FIGURE 7.9** The scan range of the coupled-oscillator system can be effectively doubled using a set of frequency multipliers between the oscillator outputs and the antennas.

suggested in Fig. 7.9, which effectively doubles the interelement phase shift. Despite additional circuit complexity, this technique has some additional benefits: the oscillators can be designed at a lower frequency (half the desired output frequency), which is useful because oscillators are sensitive to parasitic reactances, and also because oscillator design is simpler when the device has high gain, which is more easily achieved at lower frequencies. The range of oscillator tuning required to achieve a given scan range is also significantly reduced, which is advantageous since operation of the array near the locking band edge is undesirable due to increased phase noise, reduced modulation range, and increased sensitivity to environmental disturbances. FET-based doublers also provide a useful measure of isolation between the oscillator and load, so a stable broadband load impedance is presented to the oscillators, with the possibility of conversion gain (although this rules out quasi-optical injection-locking). A prototype array using FET doublers has been demonstrated at X-band [17], achieving a total phase variation of  $\sim 260^\circ$ .

Lowering the phase noise of the oscillator arrays will be important, particularly in a frequency-doubled array since the oscillator noise is also doubled. Low noise can be achieved by injecting a stable reference signal (which could be modulated) into a *center* element of the array, as shown in Fig. 7.9. This will be analyzed in more detail later.

Injection-locking the array to a reference source is also related to the question of modulation. The approach has inherently narrow instantaneous frequency response and hence would probably be restricted to narrowband communications. However, it is well suited to broadband FMCW radar or imaging configurations, in which case the output frequency of the array must be linearly swept over a certain bandwidth. For best resolution, wide bandwidths are required. At millimeter wavelengths it is significantly easier to achieve a certain absolute bandwidth since the carrier frequency is so much higher. In the coupled-oscillator array, this could be accomplished by linearly sweeping the tuning voltage to each array element at the same rate. The scanning technique depends only on the instantaneous difference in oscillator free-running frequencies, provided the rate is slow compared to the carrier

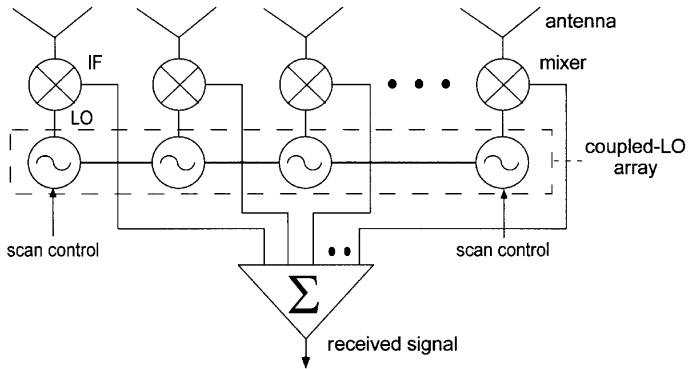


**FIGURE 7.10** The scanning technique can also be implemented in a receive mode by using the oscillator array as a set of coupled local oscillators and appropriately summing the downconverted outputs.

(which is usually the case), and hence should not be affected by an FMCW waveform, at least to first order.

The edge-detuned scanning configuration can also be employed in a receiving application [18]. This is accomplished by using the scanning oscillator array as the local oscillator for a set of mixers, as suggested in Fig. 7.10. Using early array prototypes and some commercial packaged mixers, this concept was tested by first measuring the scanning properties in transmit mode (oscillators coupled directly to antennas), followed by the receive mode. Identical scan ranges and patterns were observed in each case, as expected [18]. It may be possible to merge the transmit and receive functions, especially for FMCW imaging arrays, by making each array element a self-contained FMCW transmitter and receiver, with each array element coupled to its neighbors. This is shown schematically in Fig. 7.11. Alternatively, each array element could be a self-oscillating mixer. These concepts have not yet been tested.

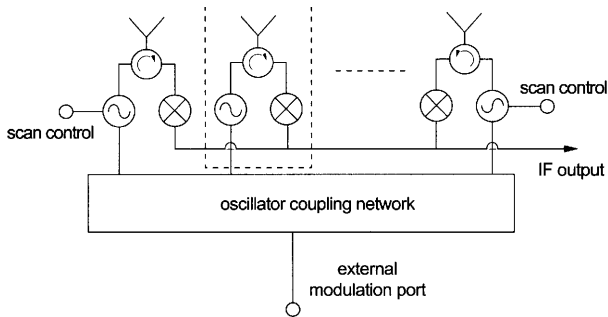


**FIGURE 7.11** A possible transmit-receive system based on coupled-oscillator technique. Each oscillator element serves as the transmitter and local oscillator (via leakage through the circulator).

## 7.4 EXTERNALLY LOCKED ARRAYS

External locking signals may be applied to one or more array elements in order to frequency- or phase-modulate the system. In a subsequent section we will also demonstrate advantages of external locking with respect to noise performance. In most applications, we would like to maintain a uniform phase progression in the presence of the externally applied locking signals. Examining Eq. 7.28 when  $\rho_i \neq 0$ , we find that the competing effects of injection-locking and mutual coupling tend to preclude uniform phase progressions unless (1) the phasing of the injected signals is identical with that arising from mutual coupling, and so tends to reinforce the desired solution; or (2) only a single array element is injection locked. These are very general observations; there may be special circumstances where careful adjustment of all the free-running frequencies and phasing of the injected signals may lead to desirable phase distributions, but these solutions are difficult to quantify analytically due to the nonlinear nature of the equations. Therefore we will consider the following two cases, which appear to have practical merit. We assume each oscillator feeds an antenna, so that injected signals can be applied quasi-optically or via local circuits, and that a parallel oscillator model is used.

**Case 1:** Global illumination of the array with  $\rho_i = \rho$  and  $\psi_i - \psi_{i-1} = \Delta\psi$ , as shown in Fig. 7.12a, with the free-running frequencies adjusted so that  $\Delta\theta = \Delta\psi$ . In this case the incident locking beam and the mutual coupling act in concert to produce an output beam emerging as if specularly reflected. The system thus resembles a quasi-optical injection-locked amplifier. The injected signal establishes a common phase reference, which we define as  $\psi_1 = 0$ . If the central array elements are adjusted so that  $\omega_i = \omega_{inj}$ , then the above assumptions are satisfied by

$$\omega_i = \begin{cases} \omega_{inj} + \Delta\omega_m \sin \Delta\psi, & i = 1 \\ \omega_{inj}, & 1 < i < N \\ \omega_{inj} - \Delta\omega_m \sin \Delta\psi, & i = N \end{cases} \quad (7.45)$$

which is independent of the locking signal strength and is the same condition required to establish a uniform phase progression in a mutually synchronized array with no locking [1]. We have also defined  $\Delta\omega_m \equiv \varepsilon\omega_{3dB}$  in Eq. 7.45. Using methods given in [1], it can be shown that this mode is stable under the conditions described in Table 7.1.

**Case 2:** A single element of the array locked to an external source, as shown in Fig. 7.12b, with the free-running frequencies adjusted to produce a uniform phase progression  $\Delta\theta$ . If the  $l$ th element is externally locked, we write  $\rho_i = \rho\delta_{li}$ , where  $\delta_{ij}$  is the Kronecker delta, and take  $\psi_l = 0$  as the phase reference for the system. Here we can distinguish between external locking of a central array element and an end element ( $i = 1$  or  $i = N$ ) of the array. In the former case, we find that a valid free-running frequency distribution is given by Eq. 7.45 with  $\Delta\psi = \Delta\theta$ . When an

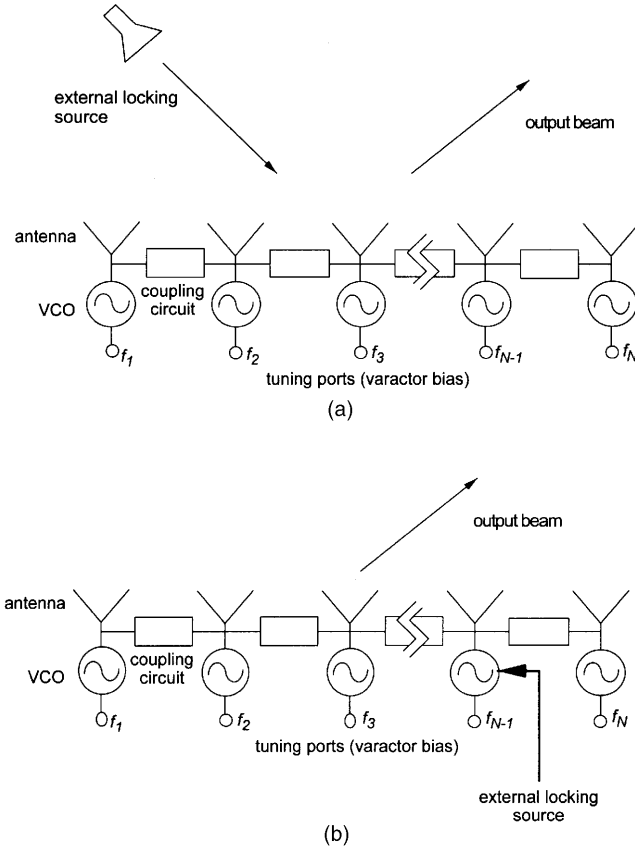


**FIGURE 7.12** Two specific cases considered in this work to illustrate external locking of arrays. (a) Globally injection-locked array (Case 1), with the locking signal applied quasi-optically; and (b) Array with single element locked to an external source (Case 2).

end element is locked, we find (for  $l = 1$ )

$$\omega_i = \begin{cases} \omega_{inj} + \omega_{3dB}(\epsilon \sin \Delta\theta - \rho \sin \hat{\phi}_1), & i = 1 \\ \omega_{inj}, & 1 < i < N \\ \omega_{inj} - \Delta\omega_m \sin \Delta\theta, & i = N \end{cases} \quad (7.46)$$

If we choose  $\rho = \epsilon$  and  $\hat{\phi}_1 = \Delta\theta$ , then the output beam is controlled only by a single frequency variable, or equivalently, a single dc voltage.

In both cases, we have tacitly assumed a phase-modulated signal. For a frequency-modulated injection signal,  $\omega_{inj}$  varies with time, and hence the phase relationships will fluctuate. This can be minimized by keeping the maximum frequency excursions to a small fraction of the locking range. This turns out to be



desirable to minimize signal distortion, as shown by Kurokawa [19] for a single oscillator.

The next step is to specify a modulation waveform and examine the time evolution of the instantaneous phase or frequency. For simplicity we consider a step change in injection frequency,  $\omega_{\text{inj}}(t) = \omega_0 + \Delta\omega u(t)$ , where  $u(t)$  is the unit step function. This is useful in establishing estimates of response time of the system for more complicated modulation signals. For the two cases elucidated above, it is assumed that the system is in equilibrium with a uniform phase of zero across the array prior to the step transient. Figures 7.13 and 7.14 show the computed evolution of the instantaneous frequency for an 11-element line array. The time scale has been normalized to the locking range using a new time variable  $\tau \equiv \varepsilon\omega_{3\text{dB}}t$ , and it is assumed that  $\rho = \varepsilon$  in each case. The response of the array under global excitation is essentially that of a single array element in the absence of mutual coupling and is observed to respond very quickly. In the case of the array with a single locked element, the response of the array is significantly slower and dictated by the number of array elements between the injected element and the array periphery, much like the response of the arrays to detuning transients as described earlier. It can also be shown from Eq. 7.28 that the modulation depth, that is, the width of the modulation spectrum, is severely limited in the case of a single locked elements to a maximum frequency step of  $\Delta\omega_m/N$ .

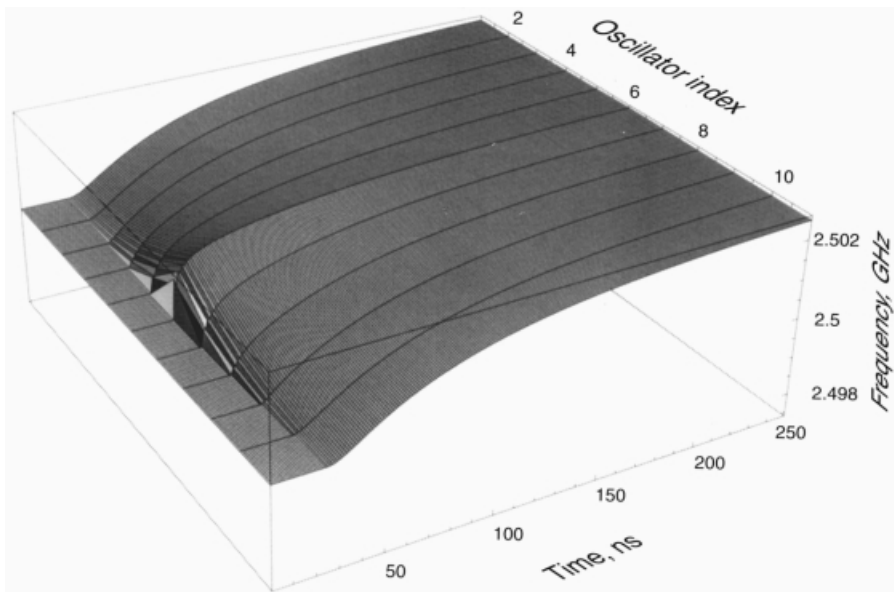


**FIGURE 7.13** Transient response of an 11-oscillator chain in response to a step change in injection-signal frequency, for a single injection point at the center of the array, showing the evolution of instantaneous frequency versus time.

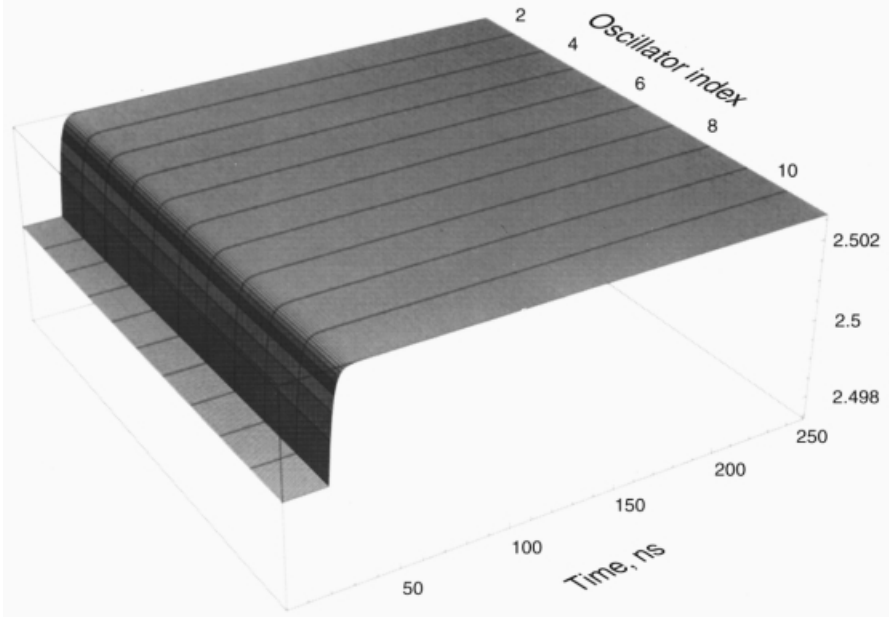


**FIGURE 7.14** Transient response of an 11-oscillator chain in response to a step change in injection-signal frequency, with the external locking signal applied globally, showing the evolution of instantaneous frequency versus time.

### 7.5 PHASE NOISE IN OSCILLATOR ARRAYS

From above we see that robust locking favors a low- $Q$  oscillator design, since this implies a large locking range. Unfortunately, low  $Q$ -factors also imply larger phase noise. External locking to a low-noise source is a possible solution. We will examine the noise characteristics of nearest-neighbor-coupled oscillator arrays in the presence of a noisy injected signal. Only phase noise is considered; amplitude noise and AM-PM noise conversion are assumed negligibly small in comparison to the PM noise in this work.

We assume parallel oscillators coupled using a network like Fig. 7.2b with  $\Phi = 2n\pi$ . Following [20,21], we model the internal phase fluctuations in the  $i$ th oscillator by a time-varying susceptance  $B_{ni}(t)$ , which modifies Eq. 7.28 as

$$\frac{d\theta_i}{dt} = \omega_i - \omega_{3dB} \left[ \varepsilon \sum_{\substack{j=i-1 \\ j \neq i}}^{i+1} \sin(\theta_i - \theta_j) + \rho_i \sin(\theta_i - \psi_i) + B_{ni}(t) \right] \quad (7.47)$$

with  $i = 1, \dots, N$ , and we have used the instantaneous phase representation. Once a steady-state solution for the phase distribution has been computed from Eq. 7.28, Eq. 7.47 is used to investigate the behavior of small fluctuations around the steady-

state solution. Making the substitutions  $\theta_i \rightarrow \hat{\phi}_i + \delta\theta_i$  and  $\psi_i \rightarrow \hat{\psi}_i + \delta\psi_{\text{inj}}$ , and assuming  $\delta\theta_i$  and  $\delta\psi_{\text{inj}}$  are small, gives

$$-\frac{1}{\omega_{3\text{dB}}} \frac{d\delta\theta_i}{dt} = \varepsilon \sum_{\substack{j=i-1 \\ j \neq i}}^{i+1} (\delta\theta_i - \delta\theta_j) \cos(\hat{\phi}_i - \hat{\phi}_j) + \rho_i (\delta\theta_i - \delta\psi_{\text{inj}}) \cos(\hat{\phi}_i - \hat{\psi}_j) + B_{ni}(t) \quad (7.48)$$

Note that all of the injected signals are assumed to be coherent (derived from the same source) and therefore all share a common time-dependent fluctuation  $\psi_{\text{inj}}$  (we assume that any relative delays in the paths of the injected signals are short compared with the coherence length of the injection source). Taking the Fourier transform and rearranging some terms gives

$$\begin{aligned} \varepsilon \sum_{\substack{j=i-1 \\ j \neq i}}^{i+1} (\tilde{\delta}\theta_j - \tilde{\delta}\theta_i) \cos(\hat{\phi}_i - \hat{\phi}_j) - J \frac{\omega}{\omega_{3\text{dB}}} \tilde{\delta}\theta_i - \rho_i \tilde{\delta}\theta_i \cos(\hat{\phi}_i - \hat{\psi}_i) \\ = \tilde{B}_i - \rho_i \tilde{\delta}\psi_{\text{inj}} \cos(\hat{\phi}_i - \hat{\psi}_i) \end{aligned} \quad (7.49)$$

where the tilde ( $\tilde{\phantom{x}}$ ) denotes a transformed or spectral variable, and  $\omega$  is the noise frequency measured relative to the carrier. This equation can be written in matrix form, using a similar notation as in [20]:

$$\bar{\bar{\mathbf{N}}} \cdot \tilde{\delta}\boldsymbol{\theta} = \tilde{\mathbf{B}}_n - \tilde{\delta}\psi_{\text{inj}} \boldsymbol{\rho}' \quad (7.50)$$

where

$$\tilde{\delta}\boldsymbol{\theta} = \begin{bmatrix} \tilde{\delta}\theta_1 \\ \tilde{\delta}\theta_2 \\ \vdots \\ \tilde{\delta}\theta_N \end{bmatrix}, \quad \tilde{\mathbf{B}}_n = \begin{bmatrix} \tilde{B}_{n1} \\ \tilde{B}_{n2} \\ \vdots \\ \tilde{B}_{nN} \end{bmatrix}, \quad \boldsymbol{\rho}' = \begin{bmatrix} \rho_1 \cos(\hat{\phi}_1 - \hat{\psi}_1) \\ \rho_2 \cos(\hat{\phi}_2 - \hat{\psi}_2) \\ \vdots \\ \rho_N \cos(\hat{\phi}_N - \hat{\psi}_N) \end{bmatrix}$$

and  $\bar{\bar{\mathbf{N}}}$  is a matrix with elements  $n_{ij}$ , which are related to the steady-state phase distribution and coupling/injection parameters. The phase fluctuations of the individual oscillator are then determined by inverting Eq. 7.50:

$$\tilde{\delta}\boldsymbol{\theta} = \bar{\bar{\mathbf{P}}} \cdot \tilde{\mathbf{B}}_n - \tilde{\delta}\psi_{\text{inj}} \mathbf{P} \cdot \boldsymbol{\rho}' \quad (7.51)$$

where  $\bar{\bar{P}} = \bar{\bar{N}}^{-1}$ , so that

$$\tilde{\delta}\theta_i = \sum_{j=1}^N p_{ij} \tilde{B}_{nj} - \tilde{\delta}\psi_{inj} \sum_{j=1}^N p_{ij} \rho'_j \quad (7.52)$$

where  $p_{ij}$  is an element of the matrix  $\bar{\bar{P}}$ .

The combined output of all the array elements is the most important quantity of interest in coupled-oscillator array applications. In previous work [20] we showed that

$$\tilde{\delta}\theta_{\text{total}} = \frac{1}{N} \sum_{j=1}^N \tilde{\delta}\theta_j \quad (7.53)$$

Using Eq. 7.52 we can write Eq. 7.53 as

$$\tilde{\delta}\theta_{\text{total}} = \frac{1}{N} \sum_{j=1}^N \sum_{i=1}^N p_{ij} \tilde{B}_{nj} - \frac{\tilde{\delta}\psi_{inj}}{N} \sum_{j=1}^N \sum_{i=1}^N p_{ij} \rho'_j \quad (7.54)$$

The power spectral density of the total phase fluctuation (i.e., the phase noise) is computed as described in [20], assuming the internal noise sources of the oscillators have the same power spectral density but are uncorrelated and also uncorrelated with the injected signal noise, which leads to a total phase noise described by

$$|\tilde{\delta}\theta_{\text{total}}|^2 = \frac{|\tilde{B}_n|^2}{N^2} \left| \sum_{j=1}^N \sum_{i=1}^N p_{ij} \right|^2 + \frac{|\tilde{\delta}\psi_{inj}|^2}{N^2} \left| \sum_{j=1}^N \sum_{i=1}^N p_{ij} \rho'_j \right|^2 \quad (7.55)$$

The first term is the contribution from all the internal noise sources, including the effects of the mutual coupling. The second term is the contribution from the noise of the external injection source. For a given coupling network and injection-locking configuration, the task of noise analysis is reduced to that of computing the matrix elements  $p_{ij}$ . As discussed in [20], in some cases these sums can be resolved analytically.

The inverse of  $\bar{\bar{N}}$  is not easily expressed for the general case, even for relatively simple coupling topologies. However, note that from the relation  $\bar{\bar{P}} \cdot \bar{\bar{N}} = \bar{\bar{N}} \cdot \bar{\bar{P}} = \bar{\bar{I}}$  we can write

$$\begin{aligned} \sum_{j=1}^N n_{ij} p_{jk} &= \delta_{ik} \\ \sum_{i=1}^N \sum_{j=1}^N n_{ij} p_{jk} &= \sum_{j=1}^N p_{jk} \left( \sum_{i=1}^N n_{ij} \right) = 1 \end{aligned} \quad (7.56)$$

The matrix elements  $n_{ij}$  are known in closed form, and it can be shown that

$$\sum_{i=1}^N n_{ij} = -\frac{J\omega}{\omega_{3\text{dB}}} - \rho_j \cos(\hat{\phi}_j - \hat{\psi}_j) \quad (7.57)$$

### 7.5.1 Globally Injected Array

Substituting the conditions for a globally illuminated array as described in the previous section (Case 1), we find

$$\sum_{i=1}^N n_{ij} = -\frac{J\omega}{\omega_{3\text{dB}}} - \rho \quad (7.58)$$

and so, from Eq. 7.56,

$$\sum_{j=1}^N p_{jk} = \frac{-1}{\rho + J\omega/\omega_{3\text{dB}}} \quad (7.59)$$

The total output noise from Eq. 7.55 is then

$$|\tilde{\delta}\theta_{\text{total}}|^2 = \frac{1}{N} |\tilde{\delta}\theta_0|^2 \frac{(\omega/\omega_{3\text{dB}})^2}{\rho^2 + (\omega/\omega_{3\text{dB}})^2} + |\tilde{\delta}\psi_{\text{inj}}|^2 \frac{\rho^2}{\rho^2 + (\omega/\omega_{3\text{dB}})^2} \quad (7.60)$$

where the term  $|\tilde{\delta}\theta_0|^2 = |\tilde{B}_n|^2/(\omega/\omega_{3\text{dB}})^2$  is recognized as the noise of a single free-running oscillator [20]. Note that in the absence of an injected signal ( $\rho = 0$ ), Eq. 7.60 reduces to

$$|\tilde{\delta}\theta_{\text{total}}|^2 = \frac{|\tilde{\delta}\theta_0|^2}{N} \quad (7.61)$$

The free-running phase noise is reduced, for all offset frequencies, by a factor of  $N$  compared with a single oscillator. This result has been shown to hold for any reciprocal coupling network [20].

Examining Eq. 7.60 near the carrier, the output noise is that of the injected signal

$$\lim_{\omega \rightarrow 0} |\tilde{\delta}\theta_{\text{total}}|^2 = |\tilde{\delta}\psi_{\text{inj}}|^2 \quad (7.62)$$

and far from the carrier the noise reduces to that of a free-running synchronized array

$$\lim_{\omega \rightarrow \infty} |\tilde{\delta}\theta_{\text{total}}|^2 = \frac{1}{N} |\tilde{\delta}\theta_0|^2 \quad (7.63)$$

The spectral characteristics of the total noise in Eq. 7.60 for intermediate frequencies are shown in Fig. 7.15a for several array sizes, assuming  $\varepsilon = 0.1$ ,  $\rho = 0.02$ , and both the internal and injected noise characteristics follow the ideal  $1/f^2$  dependence. The individual array elements were taken to have a single sideband noise of  $-60$  dBc/Hz

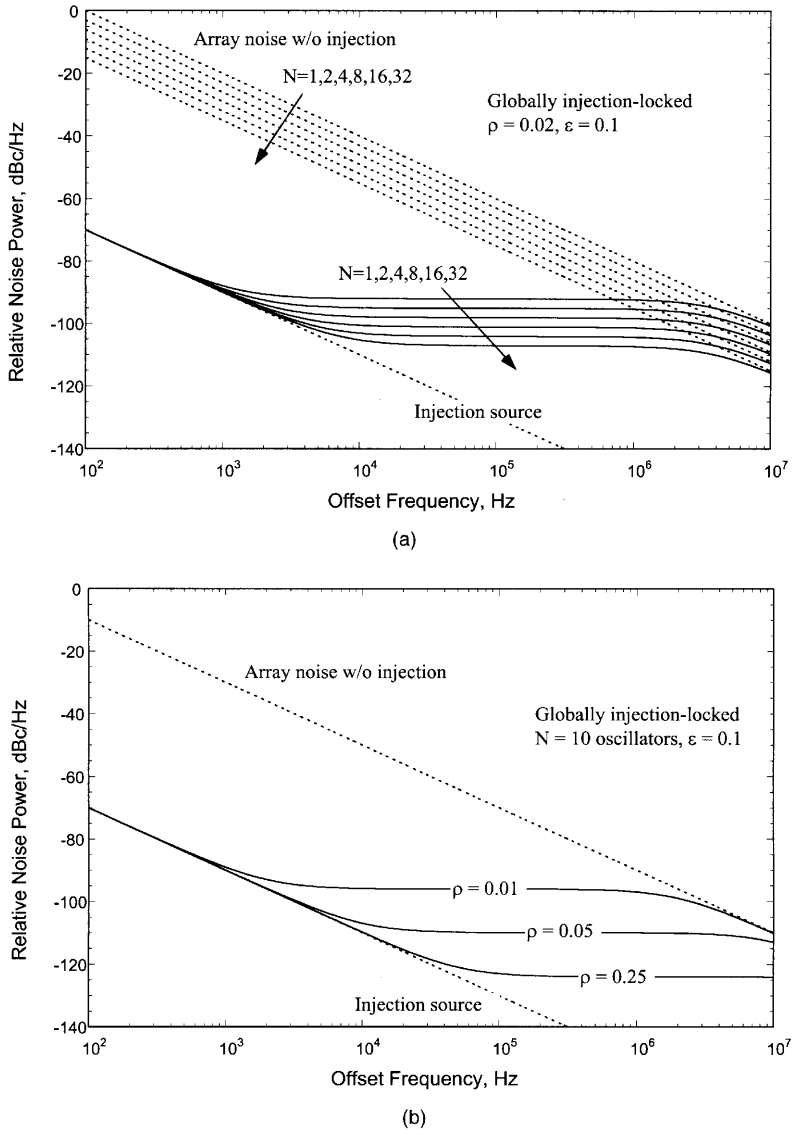


**FIGURE 7.15** Spectral characteristics of the phase noise in a globally illuminated array (Fig. 7.12) for (a) Several array sizes, both with (solid lines) and without (dotted lines) the injected signal (the noise characteristics improve slightly with increasing array size due to the mutual coupling); and (b) Several injection strengths, for the specific case of  $N = 10$ .

at 100-kHz offset, typical of a low- $Q$  microstrip MESFET oscillator, and the injection source was modeled by a similar noise source with  $-130$  dBc/Hz at 100-kHz offset. Note that the noise characteristics improve slightly with increasing array size, which is due to the  $1/N$  reduction of the contribution from the internal noise sources, arising from mutual coupling in the array. The dependence on the injected signal strength for the same parameters described above is also shown in Fig. 7.15b.

### 7.5.2 Array with One Element Externally Locked

Following a similar analysis for the case of a single array element coupled to an external locking source (Case 2), we find, for a signal applied to the  $l$ th element,

$$\sum_{i=1}^N n_{ij} = -\frac{J\omega}{\omega_{3\text{dB}}} - \rho\delta_{ij} \quad (7.64)$$

which gives, from Eq. 7.56,

$$-\frac{J\omega}{\omega_{3\text{dB}}} \sum_{j=1}^N p_{jk} - \rho p_{lk} = 1, \quad k = 1, \dots, N \quad (7.65)$$

The total noise is then given by

$$|\tilde{\delta}\theta_{\text{total}}|^2 = \frac{|\tilde{\delta}\theta_0|^2}{N^2} \sum_{j=1}^N |1 + \rho p_{lj}|^2 + \rho^2 \frac{|\tilde{\delta}\psi_{\text{inj}}|^2}{N^2} \left| \sum_{i=1}^N p_{ij} \right|^2 \quad (7.66)$$

where the property  $p_{ij} = p_{ji}$  was used. We cannot evaluate this expression analytically without first finding the elements of the  $l$ th row or column of  $\mathbf{P}$ . However, we can examine the limiting behavior near and far from the carrier. Near the carrier, Eq. 7.65 gives

$$p_{lk} \approx \frac{-1}{\rho} \quad (7.67)$$

and substituting into Eq. 7.66, gives

$$\lim_{\omega \rightarrow 0} |\tilde{\delta}\theta_{\text{total}}|^2 = |\tilde{\delta}\psi_{\text{inj}}|^2 \quad (7.68)$$

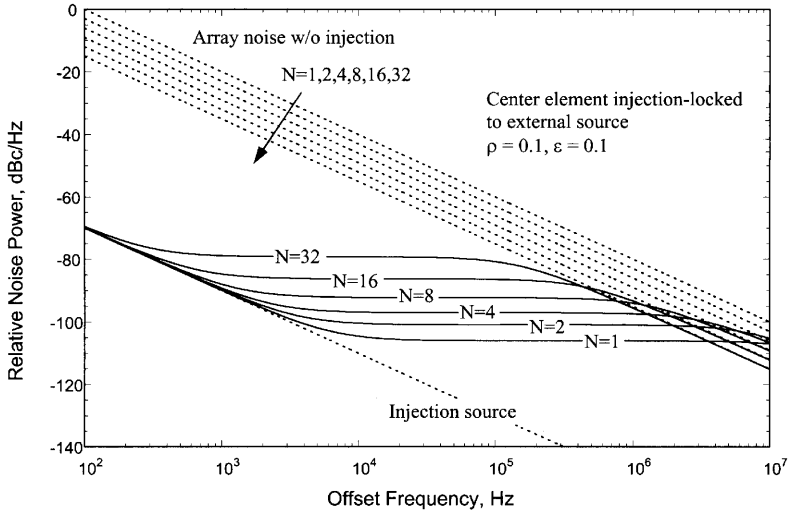
Far from the carrier we find

$$\sum_{i=1}^N p_{ij} = -\frac{J\omega}{\omega_{3\text{dB}}} \quad (7.69)$$

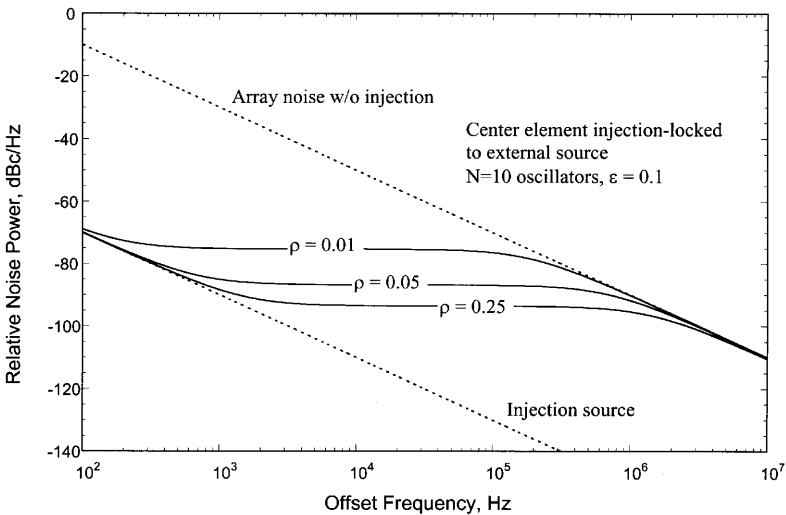
which gives

$$\lim_{\omega \rightarrow \infty} |\tilde{\delta}\theta_{\text{total}}|^2 = \frac{1}{N} |\tilde{\delta}\theta_0|^2 \quad (7.70)$$

These are the same asymptotic values as derived for the globally injected case. The behavior for intermediate frequencies is more complicated computationally but qualitatively similar with respect to frequency. Figure 7.16a illustrates the total phase noise as a function of the offset frequency for several different array sizes, with the



(a)



(b)

**FIGURE 7.16** Spectral characteristics of the phase noise in an array with the center element injection-locked (Fig. 7.13b) for (a) Several array sizes, both with (solid lines) and without (dotted lines) the injected signal (the noise characteristics degrade with increasing array size); and (b) Several injection strengths, for the specific case of  $N = 10$ .



injection signal applied to the center element. The same noise parameters were used in Fig. 7.15, but a slightly larger injected signal strength was used ( $\rho = 0.1$ ). Here we observe a significant degradation in the output phase noise with increasing array size. Figure 7.16b illustrates the dependence on the injection strength. If the injection signal is instead applied at the first array element, the noise characteristics degrade more rapidly with increasing array size (see [21]). An analysis of the individual noise fluctuations on the array confirms that the individual contributions from the array elements increase with distance from the injected signal, at a rate that depends on the coupling strength. Thus a practical system would clearly favor a large interoscillator coupling strength, a large injected signal strength, and the injected signal applied at the center of the array.

### 7.5.3 Experimental Results

A five-element linear coupled oscillator chain was used for experimental verification of the theory [21]. The array was comprised of five varactor-tuned MESFET VCOs with a nominal tuning range of 8.0–9.0 GHz, coupling as in Fig. 7.2b with coupling parameters  $\varepsilon \approx 0.5$  and  $\Phi = \beta L = 2\pi$ , and a relative injection strength of  $\rho \approx 0.25$ .

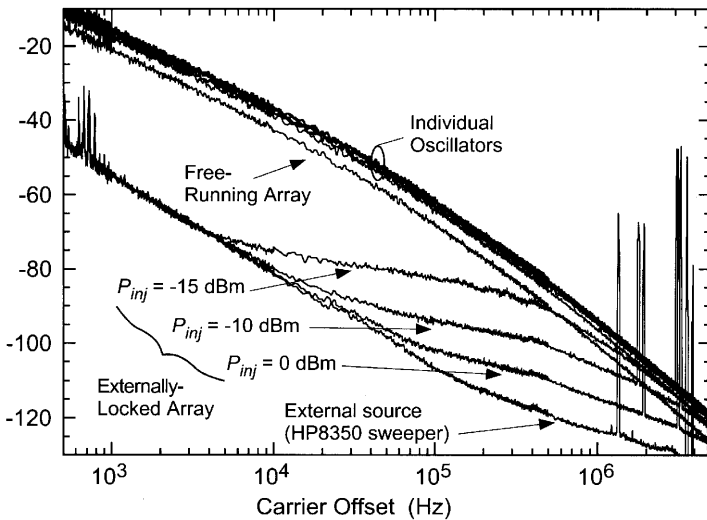


**FIGURE 7.17** Measured phase noise versus offset for a five-element X-band MESFET array, for both the free-running and externally locked cases. Noise powers of the individual (uncoupled) oscillators are also shown, illustrating the noise reduction due to mutual coupling, in general agreement with the simple models described in the text. Phase noise for the externally locked case is shown for three different locking strengths, showing good qualitative agreement with the theory (see Fig. 7.16b). Also shown is the measured noise of the injection source.

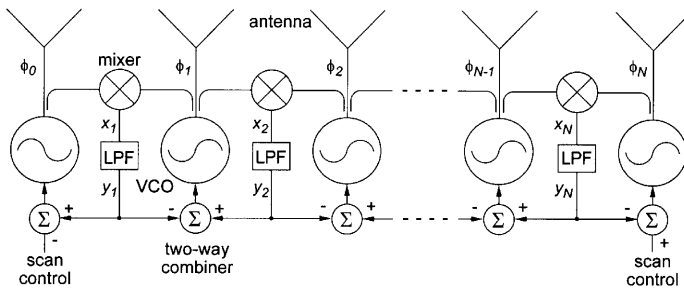
A low phase noise source signal from an HP8350B sweep oscillator was injected into the center element of the array (Case 2).

Figure 7.17 shows the measured phase noise of the individual array elements when free-running, along with the total array output under synchronized conditions (all oscillators set to a common free-running frequency), the noise of the injection source, and the array noise when locked to the injection source for three representative injection strengths. The injection frequency was tuned to the oscillators' center frequency for the measurement. The results show good qualitative agreement with Fig. 7.16. In fact, using the measured values of the injection noise and free-running array noise, the theoretical curves computed using Eq. 7.55 were virtually indistinguishable from the measurement, and thus difficult to present on the same curve for comparison. Departures from the idealized curves of Fig. 7.16 are due to the more complicated frequency dependence of the array and injected noise sources.

## 7.6 PLL TECHNIQUES

Phase dynamics in a simple zero-order PLL circuit are also governed by an equation resembling Adler's equation for injection-locking. As a result, the injection-locked systems and techniques described above can all be reproduced using phase-locked loop (PLL) techniques, at the expense of some added complexity in the circuit design. There is also a strong potential for improvement in both bandwidth and noise performance using PLLs. PLL techniques have also been employed for creating mode-locked oscillator systems for pulsed applications [23].

A coupled-PLL array system for beam scanning is shown schematically in Fig. 7.18. This is described in [9] and similar to work described in [22]. We will show that this system is directly analogous to the coupled-oscillator systems described previously and yield scanning properties by edge detuning in a similar fashion, but with a significantly larger locking/capture range. Using the notation in the figure, we



**FIGURE 7.18** A conceptual phase-locked-loop (PLL) array that mimics the behavior of the coupled-oscillator systems described in the bulk of the chapter, including scanning by edge control.

can write the following equations relating the signals in each part of the individual “loops”: for the VCO we have

$$\omega + \frac{d\phi_i}{dt} = \omega_i[1 + C_1(y_{n+1} - y_n)], \quad n = 0, \dots, N \quad (7.71)$$

where  $C_1$  is a constant describing the tuning sensitivity of the VCO, in the units of (1/volt), and  $\omega_i$  is again the free-running frequency of the VCO, in this case corresponding to the oscillation frequency in the absence of a tuning voltage. The mixer or phase detector is described by

$$x_n = C_2 \sin(\phi_n - \phi_{n-1}), \quad n = 1, \dots, N \quad (7.72)$$

where  $C_2$  is a constant describing the conversion loss (also related to the VCO output amplitude), in the units of (volt); the lowpass filter (LPF), which could represent an active amplifier, is described by

$$\frac{dy_n}{dt} = -\omega_f y_n + \omega_f x_n, \quad n = 1, \dots, N \quad (7.73)$$

where  $\omega_f$  is the filter cutoff (any gain could be included in the constant  $C_2$ ). As with the coupled-oscillator analysis, we can remove the common steady-state frequency  $\omega$  by relative phases and tunings. Letting  $\Delta\phi_n = \phi_n - \phi_{n-1}$  and  $\Delta\beta_n = \omega_n - \omega_{n-1}$ , Eqs. 7.71 and 7.73 can be approximated by

$$\frac{d\Delta\phi_n}{dt} = \Delta\beta_n + C_1\omega_0[y_{n+1} - 2y_n + y_{n-1}], \quad n = 1, \dots, N \quad (7.74)$$

$$\frac{dy_n}{dt} = -\omega_f y_n + \omega_f C_2 \sin(\Delta\phi_n) \quad (7.75)$$

where  $\omega_0$  is an average tuning. The next step is to find the steady-state points that satisfy

$$y_n = C_2 \sin(\Delta\phi_n) \quad (7.76)$$

$$\Delta\omega_n = -C_1\omega_0[y_{n+1} - 2y_n + y_{n-1}] \quad (7.77)$$

The free-running frequencies must therefore satisfy

$$\Delta\beta_n = -C_1 C_2 \omega_0 [\sin(\Delta\phi_{n+1}) - 2\sin(\Delta\phi_n) + \sin(\Delta\phi_{n-1})] \quad (7.78)$$

This is identical in form to Eq. 7.33; using the same notation we can write Eq. 7.78 as

$$\Delta\beta = -C_1 C_2 \omega_0 \bar{\mathbf{A}} \mathbf{s} \quad (7.79)$$

The similarity in form to Eq. 7.33 means that all of the same conclusions, including the ability to induce a uniform phase progression by edge detuning, apply to the coupled PLL array system. The product  $C_1 C_2$  is essentially the loop gain of the PLL, and we can see that  $C_1 C_2 \omega_0$  plays the role of the locking bandwidth. To the extent that we can increase the loop gain (by including an amplifier in place of the LPF), we

can increase the locking range enormously compared with a similar injection-locked array.

### 7.6.1 Injection-Locked Phase-Locked-Loop Circuit

To the extent that FET oscillators can be used as self-oscillating mixers, we have recently examined the possibility of making extremely simple PLL circuits by making only a slight modification to our standard VCO designs, as shown in Fig. 7.19a. The essential point is that the nonlinearity of the device will mix the oscillator output against an injected signal, so mixing products will be superimposed on the oscillator output. If these low-frequency signals are amplified and fed back to the varactor tuning element appropriately, a type of PLL is created. This is termed an

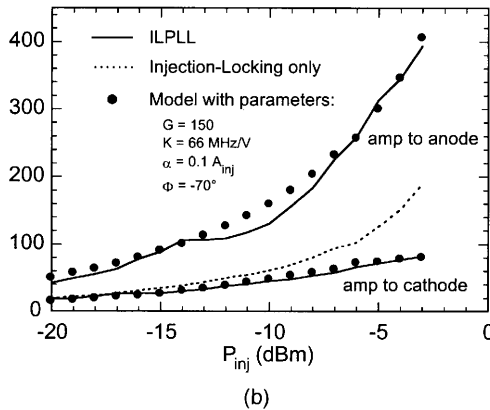
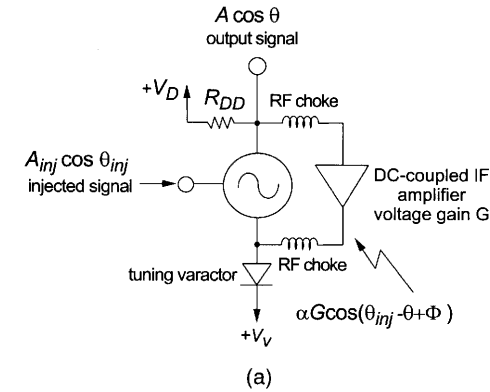


**FIGURE 7.19** (a) A simplified schematic of an injection-locked phase-locked-loop (ILPLL) system using a conventional VCO with an active lowpass feedback element. (b) Measured locking characteristics for an experimental prototype at X-band.

injection-locked phase-locked loop (ILPLL), since both IL and PLL processes are at work. We can derive an approximate dynamical equation as follows: When the oscillator is injected with an external low-level injection signal, the phase dynamics of the injection-locked oscillator are described by Adler's equation:

$$\frac{\partial \theta}{\partial t} = \omega_{\text{inj}} = \omega_0 + \Delta\omega_{\text{lock}} \sin(\theta_{\text{inj}} - \theta) \quad (7.80)$$

where  $\Delta\omega_{\text{lock}}$  is the locking range. A MESFET VCO has the  $I$ - $V$  characteristics

$$I_{ds} = I_{dss} \left( 1 - \frac{V_{gs}}{V_p} \right)^2 \quad (7.81)$$

where  $I_{dss}$  and  $V_p$  are the saturation current and pinch-off voltage of the MESFET, respectively. If the external signal is injected at the gate, then the gate voltage includes a contribution from both the oscillator and the injected signal, written as

$$V_{gs} = A' \cos \theta' + A_{\text{inj}} \cos \theta_{\text{inj}} \quad (7.82)$$

where  $A'$  and  $\theta'$  are the amplitude and phase of the free-running signal at the gate (different from the output amplitude and phase at the drain);  $A_{\text{inj}}$  and  $\theta_{\text{inj}}$  are the amplitude and phase of the injection signal. Substituting Eq. 7.82 into Eq. 7.81 gives a low-frequency mixing product that can be extracted from the drain current (or voltage) through an RF choke and expressed as a voltage:

$$\alpha \cos(\theta - \theta_{\text{inj}} + \Phi) \quad (7.83)$$

where  $\Phi$  is a possible phase shift through the device, and  $\alpha$  is related to the "mixer" conversion efficiency, on the order of

$$\alpha \approx \frac{R_{DD} I_{dss} A' A_{\text{inj}}}{V_p^2} \quad (7.84)$$

where  $R_{DD}$  is the series resistance on the drain bias circuit. This signal is then amplified and fed back to the varactor bias network, much like a phase-locked loop. The output of the dc amplifier is expressed as  $\alpha G \cos(\theta - \theta_{\text{inj}} + \Phi)$ , where  $G$  is the loop dc amplifier voltage gain, and  $\Phi$  is now the "loop" phase including any new contributions from the dc amplifier. The intrinsic VCO frequency will then respond to this time-varying bias on the varactor, so in Eq. 7.80 we should make the replacement

$$\omega_0 \Rightarrow \omega_0 \pm \alpha G K \cos(\theta - \theta_{\text{inj}} + \Phi) \quad (7.85)$$

where  $K$  is the tuning sensitivity of the VCO. The  $\pm$  sign in Eq. 7.85 refers to whether the amplifier output is connected to the cathode or anode side of the

varactor. Assuming the amplifier output is connected to the anode of the varactor, substituting Eq. 7.85 into Eq. 7.80 and making some approximations, we obtain a new phase equation

$$\frac{\partial \theta}{\partial t} = \omega_{\text{inj}} = \omega_0 + \Delta\omega'_{\text{lock}} \sin(\theta_{\text{inj}} - \theta + \Phi') \quad (7.86)$$

where

$$\Delta\omega'_{\text{lock}} = [(\alpha GK)^2 + (\Delta\omega_{\text{lock}})^2 \mp 2\alpha GK \Delta\omega_{\text{lock}} \sin \phi]^{1/2}$$

and

$$\phi' = \arctan\left(\frac{\mp \alpha GK \cos \Phi}{\Delta\omega_{\text{lock}} \mp \alpha GK \sin \Phi}\right)$$

and  $\Delta\omega'_{\text{lock}}$  is the new locking range of the system. With proper design of the circuit, the locking range of the system can be larger than that of the injection-locked VCO,  $\Delta\omega'_{\text{lock}} > \Delta\omega_{\text{lock}}$ .

This approach was verified using a simple 10-GHz prototype [24]. The VCO used an NEC32184A GaAs MESFET in a common gate configuration (for large tuning range), and a M/A-COM 46580 beam-lead hyperabrupt varactor diode. The external signal was injected at the gate using a 50- $\Omega$  microstrip transmission line. The loop dc amplifier used a two-stage BJT (NEC56708) broadband feedback amplifier with a 20-dB gain. The measured locking range is shown in Fig. 7.19b for both possible varactor configurations and also compared with the measured result for the isolated VCO. Also shown is the comparison with the model (Eq. 7.86). The figure clearly shows that the locking ranges can be improved significantly by the feedback amplifier. The locking range is more than doubled over the range of injection power examined. This is a significant improvement for the coupled oscillator applications. Note that this is not simply a loading effect whereby the amplifier decreases the  $Q$ -factor of the VCO, which is verified by the decreases in the locking range when the amplifier is connected at the cathode of the varactor diode. This is a very simple technique for increasing the locking range, which should lead to robust power-combining and scanning arrays, while simultaneously reducing amplitude fluctuations. We have recently shown that this circuit possesses exceptional near-carrier phase noise properties [25].

## 7.7 PERSPECTIVE

It is interesting to note that many of the synchronization phenomena in electrical oscillator systems have analogues in a diversity of biological and physical systems, and in fact the mathematical models are in some cases virtually identical. Examples include modeling of neural activity [26], swarms of synchronously flashing fireflies

[27], the coordinated firing of cardiac pacemaker cells [28], rhythmic spinal locomotion in vertebrates [29,30], the synchronized activity of nerve cells in response to external stimuli [27], and synchronized menstrual cycles in groups of women [31]. In the physical sciences, examples include oscillations in certain nonlinear chemical reactions [32], the collective behavior of Josephson junction arrays [33,34], laser diode arrays [35], and possibly quantum dots.

**Acknowledgments**

This work was supported in part by the U.S. Army Research Office under contract DAAH-4-93-G-0210, the Jet Propulsion Laboratory under contract JPL-960499, and an unrestricted gift from the Hughes Research Laboratories (Malibu, CA).

**APPENDIX: KUROKAWA’S SUBSTITUTION**

Consider a linear, time-invariant network described by the voltage transfer function  $H(\omega)$ ,

$$\tilde{V}_{out}(\omega) = H(\omega)\tilde{V}_{in}(\omega) \tag{A.1}$$

This equation can be expressed in the time domain using the Fourier transform pair

$$\tilde{V}(\omega) = \int_{-\infty}^{\infty} v(t)e^{-j\omega t} dt \leftrightarrow v(t) = \frac{1}{2\pi} \int_{-\infty}^{\infty} \tilde{V}(\omega)e^{j\omega t} d\omega \tag{A.2}$$

If the input signal  $V_{in}$  is a modulated sinusoid at a carrier frequency  $\omega_0$ , we can represent the time variation in the complex form

$$v_{in}(t) = A(t)e^{j[\omega_0 t + \phi(t)]} = v'_{in}(t)e^{j\omega_0 t} \tag{A.3}$$

where it is understood that the actual time variation is found by taking the real part of Eq. A.3. Note that the spectrum of the modulation alone,

$$\tilde{V}'_{in}(\omega) = \int_{-\infty}^{\infty} v'_{in}(t)e^{j\omega t} dt \tag{A.4}$$

is related to the input signal spectrum by the well-known shifting property

$$\tilde{V}'_{in}(\omega) = \tilde{V}_{in}(\omega + \omega_0) \tag{A.5}$$

Taking the inverse Fourier transform of Eq. A.1 gives

$$v_{\text{out}}(t) = \frac{1}{2\pi} \int_{-\infty}^{\infty} H(\omega) \tilde{V}_{\text{in}}(\omega) e^{j\omega t} d\omega \quad (\text{A.6})$$

$$= \frac{1}{2\pi} \int_{-\infty}^{\infty} H(\omega' + \omega_0) \tilde{V}'_{\text{in}}(\omega') e^{j(\omega' + \omega_0)t} d\omega' \quad (\text{A.7})$$

The transfer function can be expressed as a Taylor series about the carrier frequency  $\omega_0$ ,

$$H(\omega' + \omega_0) = \sum_{n=0}^{\infty} \frac{1}{n!} \frac{d^n H(\omega_0)}{d\omega^n} (\omega')^n \quad (\text{A.8})$$

Substituting Eq. A.8 into Eq. A.7 and interchanging the order of integration and summation gives

$$v_{\text{out}}(t) = \sum_{n=0}^{\infty} \frac{1}{n!} \frac{d^n H(\omega_0)}{d(\omega)^n} \left[ \frac{1}{2\pi} \int_{-\infty}^{\infty} (j\omega')^n \tilde{V}'_{\text{in}}(\omega') e^{j\omega' t} dt \right] e^{j\omega_0 t} \quad (\text{A.9})$$

The integral in square brackets is recognized as the  $n$ th derivative of the modulation, so from Eq. A.3 we can write

$$v_{\text{out}}(t) = \sum_{n=0}^{\infty} \frac{1}{n!} \frac{d^n H(\omega_0)}{d(\omega)^n} \frac{d^n (Ae^{j\phi})}{dt^n} e^{j\omega_0 t} \quad (\text{A.10})$$

The actual output is found by taking the real part of Eq. A.10. In the case of a slowly varying modulation and/or a broadband network, the higher order derivatives in Eq. A.10 diminish rapidly and the output voltage is well described by the first two terms of the expansion. Taking the first two terms and using Eq. A.3, Eq. A.10 reduces to

$$v_{\text{out}}(t) \approx v_{\text{in}}(t) \left[ H(\omega_0) + \frac{dH(\omega_0)}{d\omega} \left( \frac{d\phi}{dt} - j \frac{1}{A} \frac{dA}{dt} \right) \right] \quad (\text{A.11})$$

Kurokawa [2] appears to be the first to recognize that this result can be obtained from the state equation A.1 by substituting

$$\omega \rightarrow \omega_0 + \frac{d\phi}{dt} - j \frac{1}{A} \frac{dA}{dt} \quad (\text{A.12})$$

in the transfer function and invoking a “slowly varying amplitude and phase” assumption,

$$\frac{d\phi}{dt} \ll \omega_0, \quad \frac{1}{A} \frac{dA}{dt} \ll \omega_0 \quad (\text{A.13})$$



to expand the transfer function around the frequency  $\omega_0$ . This is referred to as the “Kurokawa substitution” in the text.

Note also that we did have to choose the carrier frequency  $\omega_0$  as the reference point for the Taylor expansion in Eq. A.8. It is a natural choice in this example, but in the case of a multiple-oscillator system there are several “natural” frequencies from which to choose. We can express the input signal (Eq. A.3) in terms of any arbitrary reference frequency by suitably redefining the phase variable to include a linearly increasing part,

$$v_{\text{in}}(t) = A(t)e^{j[\omega_r t + \phi'(t)]} \quad (\text{A.14})$$

where  $\phi'(t) = \phi(t) + (\omega_0 - \omega_r)t$ . The resulting expression for  $v_{\text{out}}(t)$  is then exactly the same as Eq. A.10 if  $\omega_r$  replaces  $\omega_0$ , and  $\phi'$  replaces  $\phi$ . One must be careful, however, when truncating the expansion under the assumption of slowly varying amplitude and phase in this case, since  $\phi'$  can vary rapidly in time compared with  $\phi$  if the new reference frequency  $\omega_r$  differs significantly from the “true” carrier frequency, which was assumed to be  $\omega_0$  in the example.

## REFERENCES

1. Lynch, J. J., Chang, H. C., and York, R. A., “Coupled-oscillator arrays and scanning techniques,” in *Active and Quasi-Optical Arrays for Solid-State Power Combining*, R. York and Z. Popović (eds.), Wiley, New York, 1997, Chap. 4.
2. Kurokawa, K., “Some basic characteristics of broadband negative resistance oscillator circuits,” *Bell Syst. Tech. J.*, Aug. 1969.
3. Birkeland, J., and Itoh, T., “A 16 element quasi-optical FET oscillator power combining array with external injection locking,” *IEEE Trans. Microwave Theory Tech.*, vol. MTT-40, Mar. 1992, pp. 475–481.
4. Lin, J., Chew, S. T., and Itoh, T., “A unilateral injection-locking type active phased array for beam scanning,” *IEEE MTT-S Int. Microwave Symp. Dig.*, June 1994, pp. 1231–1234.
5. Stephan, K. D., “Inter-injection-locked oscillators for power combining and phased arrays,” *IEEE Trans. Microwave Theory Tech.*, vol. MTT-34, Oct 1986, pp. 1017–1025.
6. Stephan, K. D., and Morgan, W. A., “Analysis of inter-injection-locked oscillators for integrated phased arrays,” *IEEE Trans. Antennas Propag.*, vol. AP-35, July 1987, pp. 771–781.
7. York, R. A., “Nonlinear analysis of phase relationships in quasi-optical oscillator arrays,” *IEEE Trans. Microwave Theory Tech.*, vol. MTT-41, Oct. 1993, pp. 1799–1809.
8. York, R. A., Liao, P., and Lynch, J. J., “Oscillator array dynamics with broadband  $N$ -port coupling networks,” *IEEE Trans. Microwave Theory Tech.*, vol. MTT-42, Nov. 1994, pp. 2040–2045.
9. Lynch, J. J., *Analysis and Design of Systems of Coupled Microwave Oscillators*, Ph.D. Dissertation, University of California at Santa Barbara, Jan. 1996.
10. Liao, P., and York, R. A., “A new phase-shifterless beam scanning technique using arrays of coupled oscillators,” *IEEE Trans. Microwave Theory Tech.*, Oct. 1993, pp. 1810–1815;

- also Liao, P., and York, R. A., "A six-element scanning oscillator array," *IEEE Microwave Guided Wave Lett.*, vol. 4, no. 1, Jan 1994, pp. 20–22.
11. Adler, R., "A study of locking phenomena in oscillators," *Proc. IRE*, vol. 34, June 1946, pp. 351–357; also reprinted in *Proc. IEEE* vol. 61, Oct. 1973, pp. 1380–1385.
  12. Chang, H.-C., Shapiro, E. S., and York, R. A., "Influence of the oscillator equivalent circuit on the stable modes of parallel-coupled oscillators," *IEEE Trans. Microwave Theory Tech.*, vol. MTT-45, Aug. 1997, pp. 1232–1239.
  13. York, R. A., "Novel beam scanning techniques for low cost commercial applications" (Invited Paper), SPIE International Conference on Millimeter Waves and Applications (San Diego), July 1995.
  14. Liao, P., and York, R. A., "A 1 watt X-band power-combining array using coupled VCOs," *IEEE MTT-S Int. Microwave Symp. Dig.* June 1994, pp. 1235–1238.
  15. Liao, P., and York, R. A., "A varactor-tuned patch oscillator for active arrays," *IEEE Microwave Guided Wave Lett.*, vol. 4, no. 10, Oct. 1994, pp. 335–337.
  16. Pogorzelski, R. J., and York, R. A., "A simplified theory of coupled oscillator array phase control," 1997 IEEE Antennas and Propagation Society Symposium, Montreal, Quebec, Canada, July 1997; Pogorzelski, R. J., and York, R. A., "Analysis of the dynamics of coupled oscillator arrays for array beamsteering," URSI National Radio Science Meeting, Boulder, CO, Jan. 1998.
  17. Alexanian, A., Chang, H. C., and York, R. A., "Enhanced scanning range in coupled oscillator arrays utilizing frequency multipliers," *1995 IEEE Antennas Propag. Soc. Symp. Dig.* pp. 1308–1310.
  18. Cao, X., and York, R. A., "Coupled oscillator scanning technique for receiver applications," *1995 IEEE Antennas Propag. Soc. Symp. Dig.*, pp. 1311–1314.
  19. Kurokawa, K., "Injection-locking of solid-state microwave oscillators," *Proc. IEEE*, vol. 61, Oct. 1973, pp. 1386–1409.
  20. Chang, H.-C., Cao, X., Mishra, U., and York, R. A., "Phase noise in coupled oscillators: theory and experiment," *IEEE Trans. Microwave Theory Tech.*, vol. MTT-45, May 1997, pp. 604–615.
  21. Chang, H.-C., Cao, X., Vaughan, M. J., Mishra, U. K., and York, R. A., "Phase noise in externally injection-locked oscillator arrays," *IEEE Trans. Microwave Theory Tech.*, vol. MTT-45, Nov. 1997, pp. 2035–2042.
  22. Martinez, R. D., and Compton, R. C., "Electronic beamsteering of active arrays with phase-locked loops," *IEEE Microwave Guided Lett.*, vol. 4, no. 6, June 1994, pp. 166–168.
  23. Lynch, J. J., and York, R. A., "Mode-locked arrays of coupled phase-locked loops," *IEEE Microwave Guided Wave Lett.*, vol. 5, no. 7, July 1995, pp. 213–215.
  24. Chang, H.-C., and York, R. A., "Enhanced MESFET VCO injection-locking bandwidth using low frequency feedback techniques," 1996 IEEE MTT-S International Microwave Symposium (San Francisco).
  25. Chang, H.-C., Cao, X., and York, R. A., "Analysis of oscillators with external feedback loop for improved locking range," *IEEE Trans. Microwave Theory Tech.*, to appear Aug. 1999.
  26. Hoppensteadt, F., *Introduction to the Mathematics of Neurons*, Cambridge University Press, 1991.
  27. Peterson, I., "Step in time: exploring the mathematics of synchronously flashing fireflies," *Sci. News*, vol. 140, Aug. 1991, pp. 136–137.

28. Matthews, P. C., and Strogatz, S. H., "Phase diagram for the collective behavior of limit-cycle oscillators," *Phys. Rev. Lett.*, vol. 65, 1990, pp. 1701–1704.
29. Cohen, A. H., Holmes, P. J., and Rand, R. H., "The nature of the coupling between segmental oscillators of the lamprey spinal generator for locomotion: a mathematical model," *J. Math. Biol.*, vol. 13, 1982, pp. 345–369.
30. Koppel, N., "Toward a theory of modelling central pattern generators," in *Neural Control of Rhythmic Movements in Vertebrates*, A. H. Cohen (ed.), Wiley, New York, 1988, Chap. 10.
31. Buck, J., *Q. Rev. Biol.*, vol. 63, 1988, p. 265; Walker, T. J., *Science*, vol. 166, 1969, p. 891; McClintock, M. K., *Nature*, vol. 229, 1971, p. 244.
32. Yamaguchi, Y., Komentani, K., and Shimizu, H., "Self-synchronization of nonlinear oscillations in the presence of fluctuations," *J. Stat. Phys.*, vol. 26, 1981, pp. 719–743.
33. Matthews, P. C., Mirollo, R. E., and Strogatz, S. H., "Dynamics of a large system of coupled nonlinear oscillators," *Physica D*, vol. 52, 1991, p. 293.
34. Tsang, K. Y., Mirollo, R. E., Strogatz, S. H., and Wisenfeld, K., "Dynamics of a globally coupled oscillator array," *Physica D*, vol. 48, 1991, pp. 102–112.
35. Wang, S. S., and Winful, H. G., "Dynamics of phase-locked semiconductor laser arrays," *Appl. Phys. Lett.*, vol. 52, 1988, pp. 1774–1776.

CHAPTER EIGHT

---

# Analysis and Design of Oscillator Grids and Arrays

---

**WAYNE A. SHIROMA**

Department of Electrical Engineering  
University of Hawaii at Manoa  
Honolulu, HI

**ERIC W. BRYERTON and ZOYA POPOVIĆ**

Department of Electrical and Computer Engineering  
University of Colorado  
Boulder, CO

## 8.1 INTRODUCTION

The emergence of millimeter-wave communication systems has created an urgent need for medium- to high-power millimeter-wave sources. Although this need has traditionally been met by vacuum devices such as klystrons and traveling-wave tubes, recent advances in semiconductor technology make it desirable to replace them with lighter and less expensive solid-state devices, which do not require high-voltage power supplies. However, due to the limited output power from millimeter-wave semiconductor devices, the outputs of many devices must be combined.

Spatial, or *quasi-optical*, power combining eliminates the need for complicated and lossy feed networks. In this approach, the output powers of a large number of

solid-state devices are coherently combined in free space. Quasi-optical power combiners can be classified as grids or arrays. Both are periodic planar arrays of devices and antennas, but their different periodicities result in a number of differences in their design and implementation. A grid consists of a periodic metal pattern loaded with active devices, where the interelement spacing is a small fraction of a wavelength and interelement coupling is strong. An array consists of an input and output antenna array with active circuits between each input and output element. The interelement spacing is a half-wavelength or larger and the interelement coupling is assumed to be weak.

Figure 8.1 shows a transmitter and receiver front end consisting of cascaded quasi-optical components. This is a new kind of architecture for microwave analog front ends that offers the following potential advantages:

- For the transmitter end, the outputs of many low-power devices are combined in air, eliminating feed lines and the associated loss and dispersion.
- The power-combining efficiency should remain constant as the number of elements increases.
- Failure of one or a few devices results in only graceful degradation, but the entire array remains operational.
- Since the noise from each device is uncorrelated, the phase noise of the oscillator array decreases as the number of elements increases. For receivers, the noise figure of the array is equal to the noise figure of a single element. This results in an increase in dynamic range of  $10 \log N$ , where  $N$  is the number of elements in the array.

The chapter begins with a full wave analysis to calculate the equivalent embedding circuit of the passive grid. Section 8.3 describes a method, easily implemented with a linear circuit simulator, to determine the oscillation frequency of a transistor connected to this embedding circuit. Optimizing this embedding circuit for maximum output power is discussed in Section 8.4. In Section 8.5, the optimum circuit is used as a benchmark for assessing a given design. Section 8.6

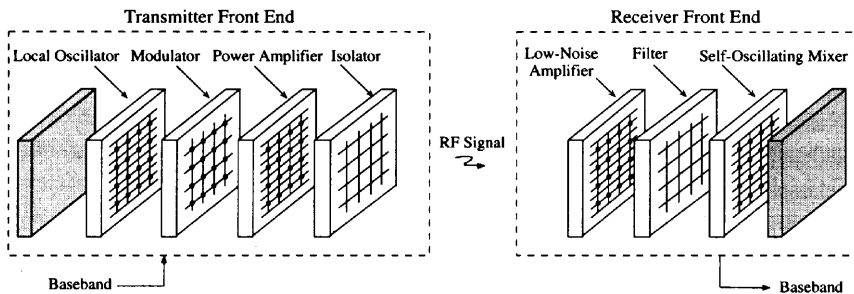


**FIGURE 8.1** Quasi-optical transmitter and receiver front ends. For simplicity, all of the components are shown as grids, although they can also be realized as active-antenna arrays.

discusses the difficult problem of transforming an optimum embedding circuit to an actual grid geometry. Finally, Section 8.7 presents the design and measurements of a high-efficiency oscillator along with its integration into an oscillator array.

Since this chapter focuses on the design and optimization of the oscillator component in this system, a brief overview of other selected quasi-optical components demonstrated to date follows. For a more complete treatment on these components and on quasi-optical power combining in general, the reader is referred to [1].

- *Quasi-optical Modulators.* Several types of X-band phase modulators have been demonstrated, including a varactor-diode-loaded grid with  $25^\circ$  of continuous phase shift, a PIN-diode-loaded grid with quadrature phase shift, and a transistor-loaded antenna array for BPSK modulation [2]. Amplitude and frequency modulation can be achieved in a grid oscillator via the dc bias [3] or by cascading varactor-diode and oscillator grids [4,5].
- *Quasi-optical Amplifiers.* A number of free-space amplifiers consisting of arrays of antennas integrated with amplifiers in microstrip or coplanar waveguides have been demonstrated [6]. Schoenberg et al. [7] devised an on-substrate lensing system utilizing delay lines for efficient input feeding, demonstrating an X-band low-noise receive lens amplifier with 1.7-dB noise figure and beam-scanning, forming, and switching capabilities [8]. In these two-dimensional power combiners, all of the dissipated power needs to be removed at the edges of the array, which could present inadequate heat sinking, especially around the center of the array. Therefore, efficiency is a prime concern and was addressed in a C-band class-E power-amplifier antenna array that delivers 2.4 W of output power with 64% power-added efficiency and 85% power-combining efficiency [9].
- *Quasi-optical Isolator.* To protect the amplifier against high-level reflections, an isolator is often used as the final stage in a transmitter. Hollung et al. [10] demonstrated an X-band quasi-optical isolator consisting of six cascaded gratings, four of which provided linear-to-circular polarization conversion. Isolation of 9 dB and 19 dB was measured for the copolarized and cross-polarized waves, respectively.
- *Quasi-optical Filters.* Filters, especially those with sharp roll-off characteristics, are essential for channelized receivers. Tunable filters offer additional system flexibility. In [11], cascaded passive gratings are shown to have useful filtering properties, especially when loaded with lumped elements; by loading the grating with varactor diodes, an electronically tunable filter was realized.
- *Self-oscillating Mixer.* For systems requiring high sensitivity, a superheterodyne system could be realized using a grid oscillator and a grid mixer [12]. The local oscillator can be eliminated by using a self-oscillating mixer, which provides its own LO. In [13], three harmonic self-oscillating grid mixers are used in an angle-diversity scheme that reduces multipath fading effects.

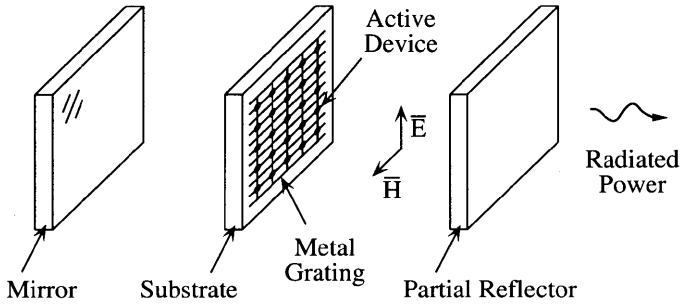


**FIGURE 8.2** A grid oscillator, consisting of an active-device array placed within a Fabry Perot cavity. From [15], copyright © 1997 by IEEE.

### 8.1.1 Grid Oscillators

A grid oscillator [14] is shown schematically in Fig. 8.2, where a metal grating is loaded with either two- or three-terminal solid-state devices. The grating is etched on a dielectric substrate and has a period much smaller than a free-space wavelength. The vertical leads of the grating serve as antennas, and the horizontal leads as dc bias lines. If properly designed, the bias lines do not affect the high-frequency performance of the active grid, as the radiated electric field is vertically polarized. A mirror is placed behind the grid to provide the positive feedback necessary for oscillation. A partially transparent reflector is sometimes placed in front of the grid; this configuration is analogous to a Fabry-Perot cavity laser, where the active grid serves as the gain medium.

When dc bias is applied, an oscillation is triggered by transients or noise, and each device oscillates at a different frequency. An incoherent wave radiates from the grid, reflects off the mirrors, and injection-locks the oscillating devices. At the onset of oscillation, different cavity modes compete, as in a laser. Since most grid oscillators use low- $Q$ , unstable Fabry-Perot resonators, the mode with the lowest diffraction loss most likely dominates [1]. After a few round trips, the higher order modes lose most of their power to diffraction, resulting in a single-frequency, self-locked, coherent oscillation.

## 8.2 FULL WAVE MODELING OF PLANAR GRIDS

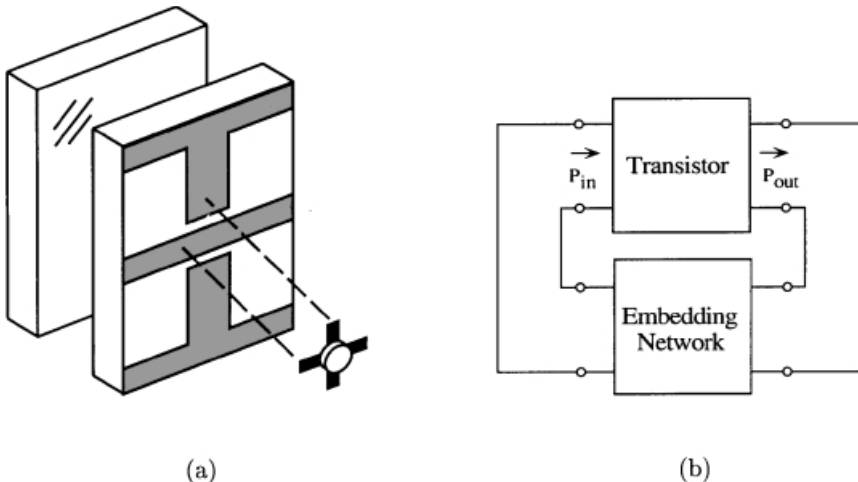
Determining the embedding impedance presented to the solid-state device is the first step in designing an active-grid array. This is a nontrivial task, due to the complicated field interactions between the devices, the metal grating, and the dielectric substrate. To make the problem tractable, edge effects are ignored by assuming that the grid is infinite in extent. In addition, each grid cell is assumed to contain an identical ac source that is phase-locked to all of the other sources in the grid. Under these conditions, planes of symmetry can be exploited to simplify the problem. Horizontal symmetry planes have electric-wall boundary conditions and

vertical symmetry planes have magnetic-wall boundary conditions. These walls extend out to infinity, forming an equivalent unit-cell waveguide.

As shown in Fig. 8.3a, the unit cell can be separated into two components: the embedding circuit (consisting of the metal grating, dielectric substrate, mirror, and free space) and the active device, which can be characterized using linear  $S$ -parameters or a nonlinear circuit model. For a transistor array, both the embedding circuit and device model can be represented as two-port networks, where the ports represent, for example, the gate-source and drain-source ports of a MESFET. A grid oscillator can then be viewed as a quasi-optical implementation of a two-port feedback oscillator (Fig. 8.3b).

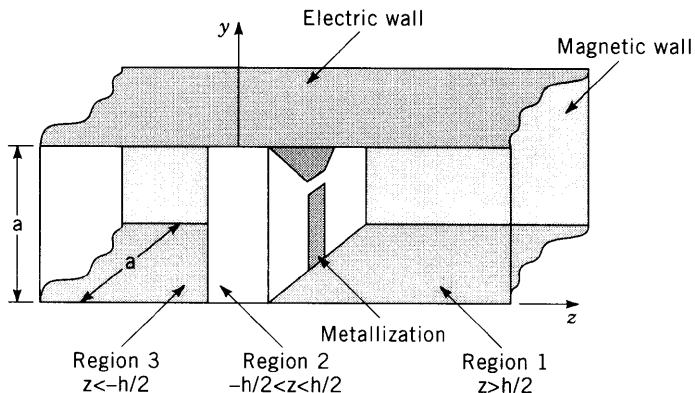
Based on the unit-cell approximation, two techniques have been developed for characterizing the embedding circuit: the induced EMF method [14] developed at the California Institute of Technology and a full wave method [16] developed at the University of Colorado. The EMF method is applicable for grid structures in which the current distribution can be reasonably approximated. The full wave technique, described in this section, does not depend on knowing the current distribution, making it possible to analyze grids with arbitrary periodic metallization.

Figure 8.4 illustrates the boundary-value problem to be solved. Regions 1 and 3 represent free space, and region 2 represents the dielectric substrate. Surface current is supported on the metallization at the interface between regions 1 and 2. Using the electric- and magnetic-wall boundary conditions of the unit-cell waveguide



**FIGURE 8.3** (a) Unit cell of a grid oscillator with the transistor and passive grid separated. (b) Feedback-oscillator model consisting of the embedding network and the transistor model.  $P_{in}$  and  $P_{out}$  represent the input and output power of the transistor, respectively. The power dissipated in the embedding network,  $P_{out} - P_{in}$ , is the actual power radiated by the grid oscillator. From [15], copyright © 1997 by IEEE.





**FIGURE 8.4** A unit-cell waveguide with an arbitrary metallization pattern printed on a dielectric substrate. The gap in the metallization represents the point where a one-port active device would be inserted.

( $\mathbf{n} \times \mathbf{E} = 0$  for an electric wall and  $\mathbf{n} \times \mathbf{H} = 0$  for a magnetic wall, where  $\mathbf{n}$  is the normal vector), the transverse electric-field components can be expressed as

$$E_x(x, y, z) = \sum_{m=1}^{\infty} \sum_{n=1}^{\infty} E_{mnx}(z) \sin\left(\frac{m\pi x}{a}\right) \sin\left(\frac{n\pi y}{b}\right) \tag{8.1a}$$

and

$$E_y(x, y, z) = \sum_{m=0}^{\infty} \sum_{n=0}^{\infty} E_{mny}(z) \cos\left(\frac{m\pi x}{a}\right) \cos\left(\frac{n\pi y}{b}\right) \tag{8.1b}$$

where  $a$  is the width and  $b$  is the height of the unit cell.

The surface current can also be expressed in a mode expansion:

$$J_x(x, y) = \sum_{m=1}^{\infty} \sum_{n=1}^{\infty} J_{mnx} \sin\left(\frac{m\pi x}{a}\right) \sin\left(\frac{n\pi y}{b}\right) \tag{8.2a}$$

and

$$J_y(x, y) = \sum_{m=0}^{\infty} \sum_{n=0}^{\infty} J_{mny} \cos\left(\frac{m\pi x}{a}\right) \cos\left(\frac{n\pi y}{b}\right) \tag{8.2b}$$

In each of the three regions, the source-free Helmholtz wave equation is solved for the electric field:

$$\nabla^2 \mathbf{E} + k^2 \mathbf{E} = 0 \tag{8.3}$$

where

$$k = \begin{cases} k_0 = \omega\sqrt{\mu_0\varepsilon_0}, & |z| > h/2 \\ k_d = \omega\sqrt{\mu_0\varepsilon_r\varepsilon_0}, & |z| < h/2 \end{cases} \quad (8.4)$$

Substituting Eq. 8.1 into Eq. 8.3 leads to the scalar ordinary differential equations

$$\left(\frac{d^2}{dz^2} + k_z^2\right)E_{mnx}(z) = 0 \quad \text{and} \quad \left(\frac{d^2}{dz^2} + k_z^2\right)E_{mny}(z) = 0 \quad (8.5)$$

where the propagation constant  $k_z$  is given by

$$k_z^2 = k^2 - \left(\frac{m\pi x}{a}\right)^2 - \left(\frac{n\pi y}{b}\right)^2 \quad (8.6)$$

The general solution of Eq. 8.5 is

$$E_{mnx}(z) = \begin{cases} c_{mnx1}e^{-jk_z z} + d_{mnx1}e^{jk_z z}, & z > h/2 \\ c_{mnx2}e^{-jk_z z} + d_{mnx2}e^{jk_z z}, & |z| < h/2 \\ c_{mnx3}e^{-jk_z z} + d_{mnx3}e^{jk_z z}, & z < -h/2 \end{cases} \quad (8.7a)$$

$$E_{mny}(z) = \begin{cases} c_{mny1}e^{-jk_z z} + d_{mny1}e^{jk_z z}, & z > h/2 \\ c_{mny2}e^{-jk_z z} + d_{mny2}e^{jk_z z}, & |z| < h/2 \\ c_{mny3}e^{-jk_z z} + d_{mny3}e^{jk_z z}, & z < -h/2 \end{cases} \quad (8.7b)$$

Expressions for the magnetic field components can be found from Eqs. 8.7 and Faraday's law,  $\nabla \times \mathbf{E} = -j\omega\mu\mathbf{H}$ . Next, the boundary conditions at the interfaces are imposed. At  $z = -h/2$ , the continuity of  $E_y$  and  $H_x$  is enforced. The continuity of  $E_y$  is also enforced at  $z = +h/2$ , but for the magnetic field,  $\mathbf{J} = \mathbf{n} \times \mathbf{H}$ , where  $\mathbf{J}$  is the surface current on the metallization.

Expressions can then be derived for the electric field coefficients  $c_{mn}$  and  $d_{mn}$  of Eqs. 8.7 in terms of the surface-current coefficients  $J_{mn}$  of Eqs. 8.2, which, in turn, can be expressed in the following way. The surface current is discretized as a sum of weighted basis functions,

$$J_x(x, y) = \sum_{m=1}^{N_x} J_{ix}R_{ix}(x, y) \quad \text{and} \quad J_y(x, y) = \sum_{m=1}^{N_y} J_{iy}R_{iy}(x, y) \quad (8.8)$$

where  $R_i$  represents the  $i$ th rooftop basis function,  $N$  is the number of basis functions, and  $J_i$  is the unknown weighting coefficient for the  $i$ th basis function. If the rooftop basis functions themselves are expressed as a Fourier series, the mode-

expansion coefficients for the current  $J_{mn}$  of Eqs. 8.2 can be expressed in terms of the unknown weights  $J_i$ :

$$J_{mnx} = \sum_{i=1}^{N_x} J_{ix} R_{imnx} \quad \text{and} \quad J_{mny} = \sum_{i=1}^{N_y} J_{iy} R_{imny} \quad (8.9)$$

where  $R_{imn}$  is the  $m$ th Fourier series coefficient for the  $i$ th rooftop basis function. The tangential electric field components are thus expressed in terms of the weighting coefficients  $J_i$  of Eqs. 8.9. By applying appropriate constraints on the electric field, the moment method is used to solve for the unknown  $J_i$ .

Once the current is found, the driving-point impedance can be calculated. A time-harmonic voltage generator is used to represent the active device, producing a constant electric field across the gap. The driving-point impedance is the ratio of the voltage across the gap to the current through the generator. The entire analysis is performed over a range of frequencies, yielding a frequency-dependent impedance. For a grid loaded with two-port active devices, there are two gaps in the metallization, one for each port. In this case, the analysis is performed twice, first with gap 1 driven by a generator while gap 2 is metallized (short-circuited), and next with gap 2 driven while gap 1 is metallized (Fig. 8.5). Since the current on the entire structure is calculated in each case, two-port  $Y$ -parameters can be determined directly and then converted to two-port  $S$ -parameters.

For a 6 mm × 6 mm unit cell with the geometry shown in Fig. 8.3a, with 112 basis functions, the analysis takes 4 seconds per frequency point on an HP 715/125 workstation.

### 8.3 GRID OSCILLATOR ANALYSIS

#### 8.3.1 Circular-Function Analysis

The generalized, steady-state oscillation condition [17] of an  $n$ -port feedback oscillator is

$$\det(\mathbf{SS}' - \mathbf{I}) = 0 \quad (8.10)$$

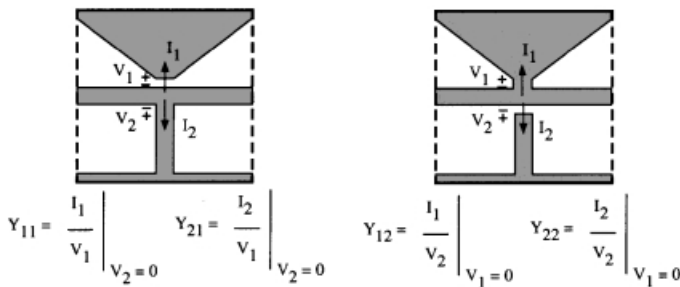


**FIGURE 8.5** For a two-port grid,  $Y$ -parameters are found first by driving gap 1 with a generator  $V_1$  while gap 2 is shorted, then driving gap 2 with generator  $V_2$  while gap 1 is shorted. From [16], copyright © 1994 by IEEE.

where  $\mathbf{S}$  and  $\mathbf{S}'$  are the  $n$ -port scattering matrices of the device and embedding networks, respectively.

For  $n = 2$ , as in Fig. 8.3b, Eq. 8.10 reduces to

$$S_{11}S'_{11} + S_{12}S'_{21} + S_{21}S'_{12} + S_{22}S'_{22} - |\mathbf{S}||\mathbf{S}'| = 1 \tag{8.11}$$

where

$$|\mathbf{S}| = S_{11}S_{22} - S_{12}S_{21}$$

and

$$|\mathbf{S}'| = S'_{11}S'_{22} - S'_{12}S'_{21}$$

A circuit simulator can be used to analyze this closed-loop circuit by breaking the loop at some point and inserting a probe (Fig. 8.6). The simulator then determines the loop gain  $b'_1/a'_1$ . If a standard circulator is used as the probe, the signal flow graph in Fig. 8.7 results. Applying Mason's rule [18] to this graph results in the following expression for the loop gain, or *circular function*, as it is referred to in [19]:

$$C = \frac{b'_1}{a'_1} = \frac{S_{11}S'_{11} + S_{21}S'_{12} - |\mathbf{S}||\mathbf{S}'|}{1 - S_{12}S'_{21} - S_{22}S'_{22}} \tag{8.12}$$

Note that when  $C = 1\angle 0^\circ$ , Eq. 8.12 is equivalent to the steady-state oscillation condition (Eq. 8.11).

If Eq. 8.12 is evaluated using the transistor's small-signal  $S$ -parameters, oscillation start-up requires that  $|C| > 1$ . To reach steady state, gain compression causes the transistor  $S$ -parameters to saturate until the condition  $C = 1\angle 0^\circ$  is satisfied at the oscillation frequency.

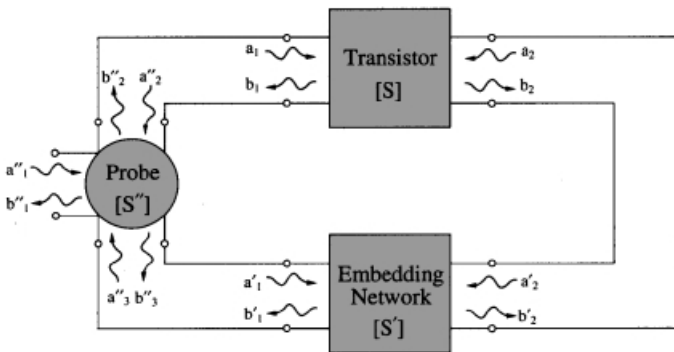


**FIGURE 8.6** Feedback oscillator with a circuit probe inserted into the feedback path. From [15], copyright © 1997 by IEEE.

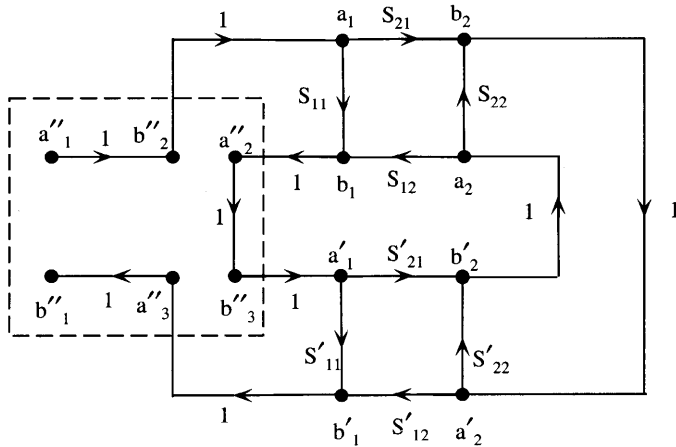


**FIGURE 8.7** Signal flow graph for the feedback oscillator with a circulator probe. The dashed box encloses the signal flow graph for the circulator. From [15], copyright © 1997 by IEEE.

Figure 8.8 illustrates the circular functions of two grid oscillators with identical unit cells, but with different substrate and mirror characteristics. Figure 8.8b shows the circular function for a transistor-loaded grid in free space, with no dielectric substrate or mirror. Since the magnitude of the circular function is less than one, no oscillation is possible. However, when the grid is backed by a 6.35-mm-thick substrate with  $\epsilon_r = 10.2$ , two modes are predicted, at 2.8 and 6.5 GHz (Fig. 8.8c). This agrees with measured oscillation modes at 2.7 and 6.4 GHz (Fig. 8.9). Which mode the oscillator preferentially locks to will be discussed shortly.

Another example is a monolithic 100-pHEMT grid oscillator that was designed by the University of Colorado, fabricated by Honeywell, and tested by TLC Precision Wafer Technology, Inc. The grid is fabricated on a 100- $\mu\text{m}$ -thick GaAs wafer and placed on a 254- $\mu\text{m}$ -thick alumina substrate metallized on one side. The unit cell is 300  $\mu\text{m}$  square with 30- $\mu\text{m}$ -wide bias lines and radiating leads. The circular function predicts an oscillation near 31.2 GHz. The measured oscillation frequency is 31.1 GHz [J. Geddes, *personal communication*]. Due to an accident during testing, the wafer was damaged, so output power and radiation pattern measurements are unavailable.

### 8.3.2 Negative-Resistance Grid Model

Since the passive embedding network for the grid is reciprocal, it can be represented as a lumped equivalent circuit as shown in Fig. 8.10a. For a typical unit cell (e.g., Fig. 8.3a), this equivalent circuit takes the form shown in Fig. 8.10b.

The capacitors  $C_1$  and  $C_2$  model the gate-source and drain-source gaps of the grid, respectively. The inductor and resistor model the lead inductance, substrate thickness, mirror position, and radiation into free space. Connecting the equivalent

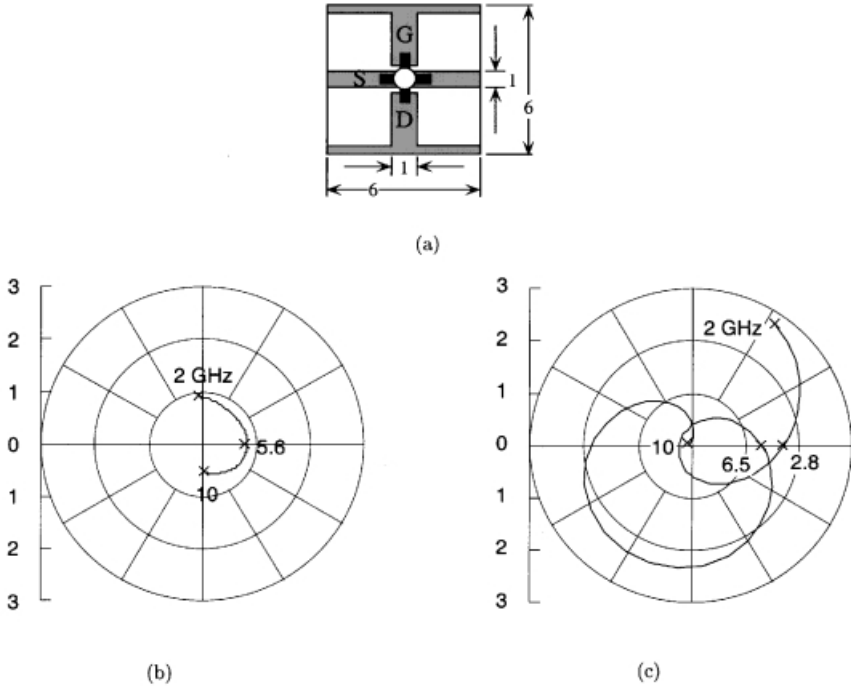


**FIGURE 8.8** Circular functions for a transistor-loaded grid (a) with identical unit cells, (b) in free space, with no substrate or mirror, and (c) backed by a thick, high-permittivity substrate and mirror. The active device is an HP-Avantek ATF-26836 General Purpose MESFET. Small-signal *S*-parameters (for  $V_{ds} = 3\text{ V}$ ,  $I_{ds} = 10\text{ mA}$ ) supplied by the manufacturer are used in the simulation. The units in (a) are millimeters. From [15], copyright © 1997 by IEEE.

circuit to the transistor results in the model shown in Fig. 8.11a. If the resistor is removed, an equivalent, one-port negative-resistance model of the grid oscillator is obtained (Fig. 8.11b). Oscillation start-up requires that the absolute value of this negative resistance be greater than the load resistance.

Figures 8.12a and 8.12b show the negative-resistance models associated with the circular functions plotted in Figs. 8.8b and 8.8c, respectively. In Fig. 8.12a, since the magnitude of the negative resistance of the embedded device is less than the load resistance, no oscillation is possible. In Fig. 8.12b, two equivalent circuits are shown, each corresponding to a different frequency. In both cases, the negative resistance is greater than the load resistance, so oscillation is possible. The mode that was most easily locked and that was most stable was the one that had the lowest load resistance. Stability analysis provides an explanation of this. For a negative-resistance oscillator, Kurokawa’s stability condition [20] states that

$$\frac{\partial R}{\partial I} \frac{\partial}{\partial \omega} (X + X') - \frac{\partial X}{\partial I} \frac{\partial R}{\partial \omega} > 0 \tag{8.13}$$

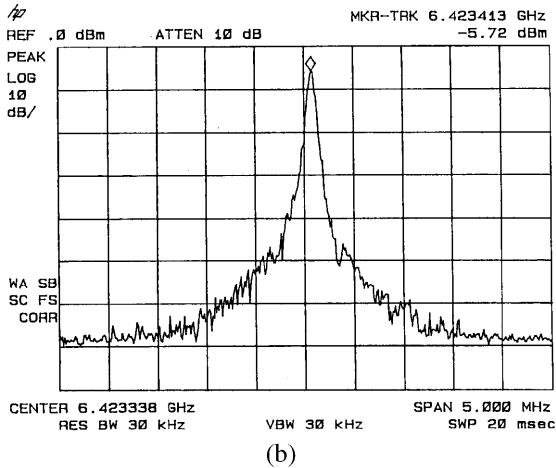
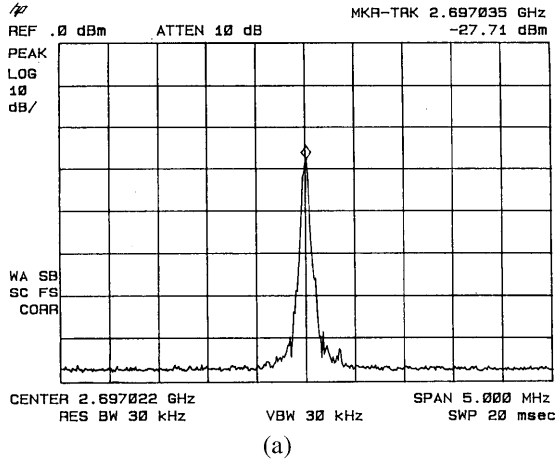


**FIGURE 8.9** Measured oscillation modes for a  $6 \times 6$  grid backed by a high-permittivity substrate and mirror: (a) 2.7 GHz and (b) 6.4 GHz. Each mode was obtained separately at different dc bias currents: 5 mA/device for (a) and 12 mA/device for (b). From [15] copyright © 1997 by IEEE.

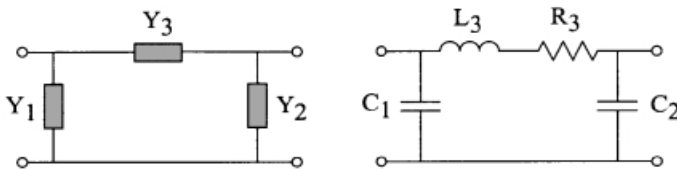


**FIGURE 8.10** (a) General lumped equivalent circuit for a two-port network, where  $Y_1 = Y_{11} + Y_{12}$ ,  $Y_2 = Y_{22} + Y_{12}$ , and  $Y_3 = -Y_{12}$ . (b) Typical form of the equivalent circuit for a grid. From [15] copyright © 1997 by IEEE.

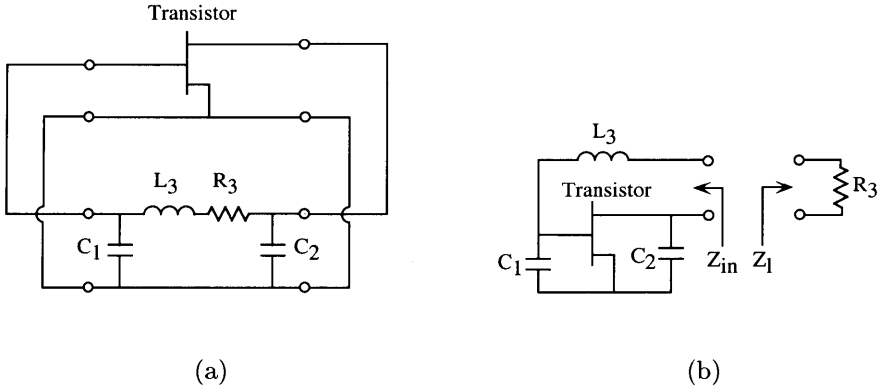


**FIGURE 8.11** (a) Transistor connected to the equivalent  $\Pi$  network. (b) Negative-resistance model of the grid oscillator. From [15] copyright © 1997 by IEEE.

where  $I$  is the current and  $\omega$  is the frequency. Gain saturation causes the device resistance to become less negative as the current increases ( $\partial R/\partial I > 0$ ), so Eq. 8.13 is satisfied if  $\partial(X + X')/\partial\omega \gg 0$ . This implies that a high- $Q$  embedding circuit results in maximum oscillator stability. Thus a multimoded grid oscillator will preferentially lock to the mode that has the lowest load resistance.

An alternative method of preferentially selecting a single mode in a multimoded oscillator is to vary the external feedback, either by using a variable-reflectance mirror [11] or by using a photonic-crystal mirror [21].

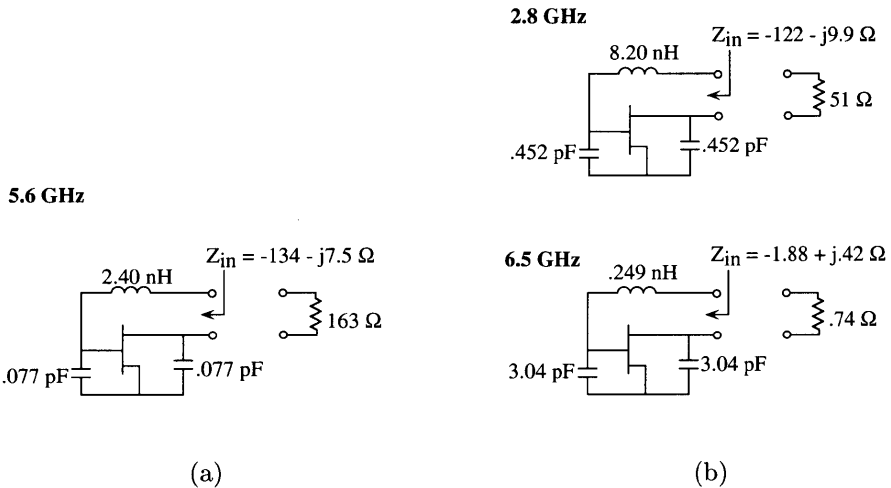


**FIGURE 8.12** Negative-resistance model for the grids associated with (a) Fig. 8.8b and (b) Fig. 8.8c. From [15] copyright © 1997 by IEEE.



### 8.4 SYNTHESIS OF THE OPTIMUM GRID EQUIVALENT CIRCUIT

The lumped equivalent circuit discussed above can be synthesized to satisfy the oscillation condition and to set the proper feedback level for maximum oscillator power. The general approach is described in [22] and is summarized here for completeness. A feedback oscillator consists of an active device connected to an embedding network (Fig. 8.13), whose “connection” conditions require

$$\begin{aligned} V_1 &= V'_1, & I_1 &= -I'_1 \\ V_2 &= V'_2, & I_2 &= -I'_2 \end{aligned} \tag{8.14}$$

Substituting the  $Y$ -parameters of the device ( $Y_{ij}$ ) and the embedding network ( $Y'_{ij}$ ) into Eq. 8.14 gives

$$\begin{aligned} Y'_{11} + AY'_{12} &= -(Y_{11} + AY_{12}) \\ Y'_{21} + AY'_{22} &= -(Y_{21} + AY_{22}) \end{aligned} \tag{8.15}$$

where  $A = V_2/V_1$ . If we assume that the embedding circuit takes the form of a  $\Pi$  network, as shown in Fig. 8.13, then

$$\begin{aligned} Y'_{11} &= Y_1 + Y_3, & Y'_{12} &= -Y_3 \\ Y'_{21} &= -Y_3, & Y'_{22} &= Y_2 + Y_3 \end{aligned} \tag{8.16}$$

Substituting Eq. 8.16 into Eq. 8.15 gives

$$\begin{aligned} G_1 + (1 - A_r)G_3 + A_iB_3 &= -g_{11} - \text{Re}(AY_{12}) \\ B_1 + (1 - A_r)B_3 - A_iG_3 &= -b_{11} - \text{Im}(AY_{12}) \\ A_rG_2 - A_iB_2 + (A_r - 1)G_3 - A_iB_3 &= -g_{21} - \text{Re}(AY_{22}) \\ A_rB_2 + A_iG_2 + (A_r - 1)B_3 + A_iG_3 &= -b_{21} - \text{Im}(AY_{22}) \end{aligned} \tag{8.17}$$

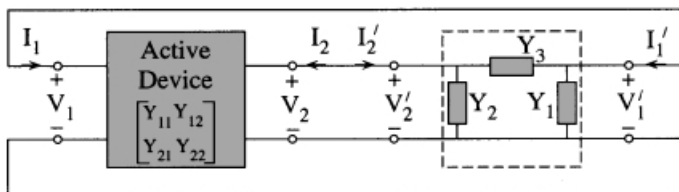


**FIGURE 8.13** A feedback oscillator consisting of an active device with known  $Y$ -parameters and an embedding network with unknown circuit elements. The embedding circuit is assumed to have a  $\Pi$  topology similar to the lumped equivalent circuit for a grid oscillator.

where

$$\begin{aligned} A_r &= \operatorname{Re}(A), & G_i &= \operatorname{Re}(Y_i), & g_{ij} &= \operatorname{Re}(Y_{ij}) \\ A_i &= \operatorname{Im}(A), & B_i &= \operatorname{Im}(Y_i), & b_{ij} &= \operatorname{Im}(Y_{ij}) \end{aligned}$$

Equations 8.17 express the unknown embedding elements  $G_i$  and  $B_i$  in terms of the voltage ratio  $A$  and the large-signal  $Y$ -parameters of the device, which are obtained either through a measurement of the associated large-signal  $S$ -parameters or through an appropriate large-signal approximation [23].

The value of  $A$  that maximizes the power delivered to the load ( $P_{\text{osc}}$ ) must now be found. This is equivalent to maximizing the added power of the device ( $P_{\text{add}}$ ), which in turn is the same as minimizing the power dissipated by the device, since

$$P_{\text{dc}} = P_{\text{add}} + P_{\text{diss}}$$

where the dissipated power is given by

$$P_{\text{diss}} = \frac{1}{2} \operatorname{Re}(V_1 I_1^* + V_2 I_2^*)$$

By setting  $\partial P_{\text{diss}}/\partial A = 0$  ( $V_1$  is assumed to be constant in [22]), we obtain the optimum voltage ratio corresponding to maximum added power,

$$A_{\text{opt}} = -\frac{Y_{21} + Y_{12}^*}{2 \operatorname{Re}(Y_{22})} \quad (8.18a)$$

Kormanyos and Rebeiz [24] refined the derivation above without assuming a constant  $V_1$  and obtained

$$A_{\text{opt}} = \frac{-2g_{11}Y_{21}}{\sqrt{N} + 2g_{11}g_{22} + j(g_{12}b_{21} + g_{21}b_{12})} \quad (8.18b)$$

where

$$N = 4g_{11}g_{22}(g_{11}g_{22} + b_{12}b_{21} - g_{12}g_{21}) - (g_{12}g_{21} + g_{21}b_{12})^2$$

Equations 8.17 express the six unknown resistive and reactive elements of the embedding network in terms of the known  $Y$ -parameters of the device and the known optimum voltage ratio  $A_{\text{opt}}$  from Eqs. 8.18. If two of these unknowns are set to zero, the other four can be determined explicitly in terms of the device's  $Y$ -parameters. Kotzebue and Parrish [25] derive expressions for six possible combinations, for both  $\Pi$ - and T-embedding networks.

From Fig. 8.10, the  $\Pi$  network for a grid oscillator is composed of purely reactive elements in the shunt legs and a resistive-reactive combination in the series arm. Therefore we set  $G_1 = G_2 = 0$  in Eqs. 8.17 and solve for the other unknowns,\*

$$B_1 = \frac{A_r}{A_i}(C_1 + C_3) + C_2 + C_4 \quad (8.19a)$$

$$B_2 = -\frac{1}{A_i}(C_1 + C_3) \quad (8.19b)$$

$$B_3 = \frac{1}{|1 - A|^2} \left\{ (A_r - 1) \left[ C_4 + \frac{A_r}{A_i}(C_1 + C_3) \right] + A_i C_1 \right\} \quad (8.19c)$$

$$G_3 = \frac{1}{|1 - A|^2} (C_1 + A_r C_3 + A_i C_4) \quad (8.19d)$$

where

$$\begin{aligned} C_1 &= -\operatorname{Re}(Y_{11} + AY_{12}), & C_3 &= -\operatorname{Re}(Y_{21} + AY_{22}), & A &= A_r + jA_i \\ C_2 &= -\operatorname{Im}(Y_{11} + AY_{12}), & C_4 &= -\operatorname{Im}(Y_{21} + AY_{22}) \end{aligned}$$

and it is implied that  $A = A_{\text{opt}}$ . The circuit element  $Y_3 = G_3 + jB_3$  is easily transformed to obtain the  $R_3 + jX_3$  of Fig. 8.10b.

The design of this network is based on the large-signal  $Y$ -parameters of the active device corresponding to the point of optimum gain compression. These parameters can be found, for example, using the approximation described by Johnson [23], who showed that the large-signal effects associated with transistor saturation can be approximated by simply reducing the device's  $|S_{21}|$  and assuming that all other  $S$ -parameters remain the same as their small-signal values.

The advantage of this synthesis approach is that a number of key elements are built-in. This approach (1) satisfies the oscillation start-up condition at small-signal levels ( $|C| > 1$ ), (2) satisfies the steady-state oscillation condition at large-signal levels ( $|C| = 1 \angle 0^\circ$ ), (3) is designed for a specified oscillation frequency, and (4) is designed for the proper level of feedback for optimum gain compression, thus maximizing oscillator power.

As an example, the optimum lumped equivalent circuit for the HP-Avantek ATF-26836 MESFET is shown in Fig. 8.14. Note that this design approach predicts that the optimum grid geometry for this device is not symmetric. Rather, the optimum grid should present a larger capacitance to the gate-source port of the transistor than to the drain-source port. A grid designed using this approach will be described later in this chapter.

\*An algebraic error for  $B_3$  and  $G_3$  in the original derivation [25] has continued to propagate in the literature [23,24,26]. The expressions here agree with those in [27].

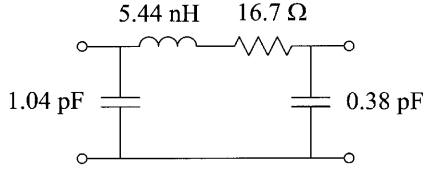


**FIGURE 8.14** Optimum lumped equivalent circuit for the HP-Avantek ATF-26836 MESFET at 3 GHz. From [15] copyright © 1997 by IEEE.

## 8.5 BENCHMARKING GRID OSCILLATOR PERFORMANCE

Once the optimum embedding network has been determined for a given transistor, the associated circular function can be computed from Eq. 8.12 and used as a benchmark for determining whether a given grid oscillator has too little or too much feedback.

It is useful to use the concept of maximum-efficient gain [28,29], defined as

$$G_{ME} = \frac{|S_{21}/S_{12}|^2 - 1}{2(K|S_{21}/S_{12}| - 1)} \quad (8.20)$$

where

$$K = \frac{1 + |S_{11}S_{22} - S_{21}S_{12}|^2 - |S_{11}|^2 - |S_{22}|^2}{2|S_{12}||S_{21}|}$$

Johnson [23] showed that the large-signal value of  $G_{ME}$  corresponding to maximum oscillator power is

$$G_{ME,opt} = \frac{G_{ME,ss} - 1}{\ln G_{ME,ss}} \quad (8.21)$$

where  $G_{ME,ss}$  is the value of Eq. 8.20 computed using the small-signal transistor  $S$ -parameters. The gain compression corresponding to the optimum operating point is then

$$GC_{opt} = G_{ME,ss} - G_{ME,opt} \quad (8.22)$$

Since the  $S$ -parameters are frequency dependent, the circular function is actually a locus of points, but the particular point of interest for this discussion is the frequency at which  $\angle C = 0^\circ$ . Two cases are shown in Fig. 8.15.

In the optimum case, the small-signal value of  $C$  should be displaced from its large-signal, steady-state value (i.e.,  $1\angle 0^\circ$ ) by an amount corresponding to  $GC_{opt}$  (Fig. 8.15a). Since this value of  $C$  corresponds to the optimum case, it is referred to as  $C_{opt}$ . There are two operating points shown in Fig. 8.15b that represent suboptimal

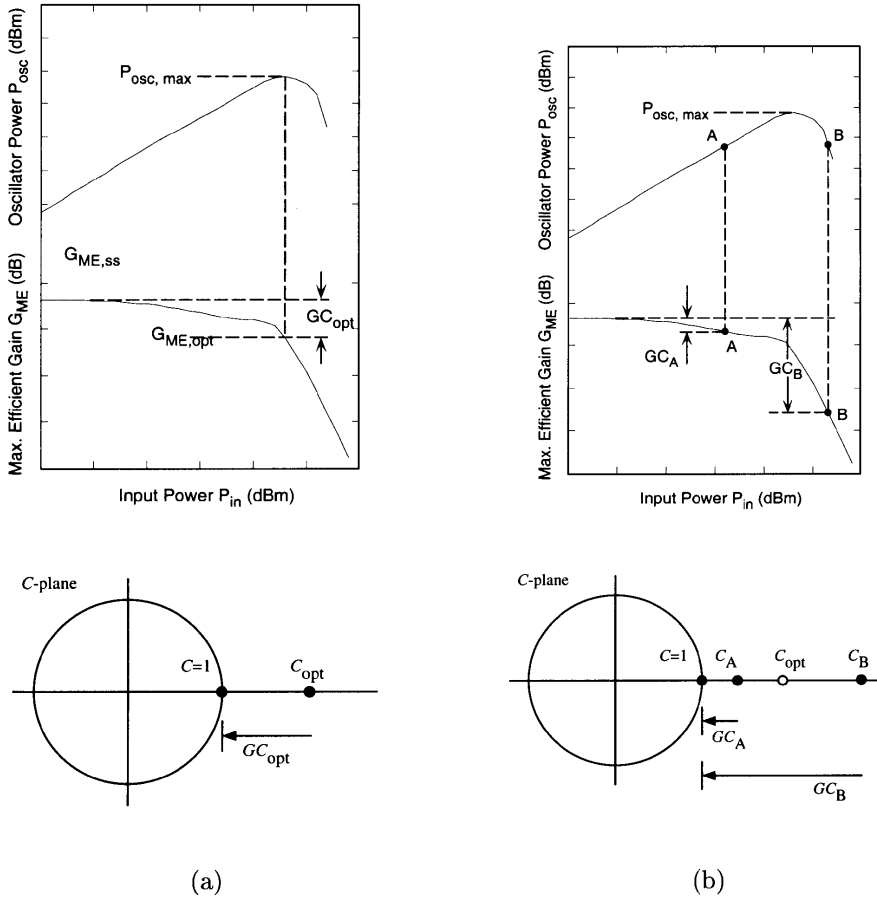


**FIGURE 8.15** Transistor saturation characteristics and circular-function plane for (a) the optimal operating point and (b) two suboptimal operating points.  $P_{in}$  is the input power to the transistor, as indicated in Fig. 8.3b, and  $P_{osc} = P_{out} - P_{in}$  is the radiated power. From [15] copyright © 1997 by IEEE.

performance. Both cases have less than the maximum available oscillator power, but for different reasons: point A suffers from gain compression that is too low ( $GC_A < GC_{opt}$ ), while point B suffers from gain compression that is too high ( $GC_A > GC_{opt}$ ). For point A, the transistor operates in the near-linear regime since the circular function requires only a small amount of gain compression to reach steady state. For point B, the transistor is heavily compressed since the feedback level is too high.

There are several disadvantages of operating at point B. In this regime, the oscillator power drops off more sharply, so it is more sensitive to design variations in the feedback network. An oscillator operating in the nonlinear regime is also more likely to have higher harmonic content. For a MESFET, point B is also associated

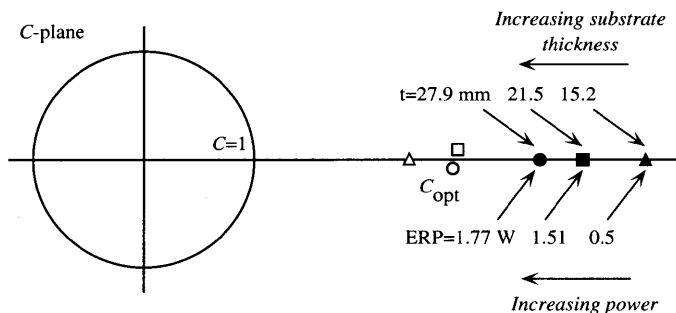


**FIGURE 8.16** Operating points corresponding to three different substrate thicknesses for a C-band pHEMT grid oscillator. The solid symbols represent the  $C$ -functions of the grids, and the open symbols represent the  $C$ -functions of the theoretical optimum networks. The measured equivalent isotropic radiated power (EIRP) is also shown. From [15] copyright © 1997 by IEEE.

with high input power at the gate, which could cause the Schottky gate diode to be driven into forward bias; this could result in a large current density in the gate metallization, which can lead to degraded device reliability.

Most grid oscillators demonstrated to date have had too much feedback [30]. The design of an optimized grid must therefore include a feedback-reduction mechanism to move the circular function toward  $C_{opt}$ .

To illustrate, consider a  $5 \times 5$  pHEMT grid oscillator with varying substrate thickness. Three  $C$ -functions, corresponding to different thicknesses of Emerson and Cuming *Eccostock HiK* ( $\epsilon_r = 10$ ), are shown in Fig. 8.16.

Since the oscillation frequency is different for each case (see Table 8.1), three different optimum embedding circuits can be derived. For the three different frequencies,  $C_{opt}$  is plotted in Fig. 8.16.

Since  $|C| > |C_{opt}|$  for all three cases, we immediately conclude that the grids have too much feedback. Moreover, the grid with the thinnest substrate is the most compressed and should have the least power. The experimental results in Table 8.1 confirm this. The existence of harmonics also supports the conclusion that these oscillators are overcompressed.

**TABLE 8.1** C-Band pHEMT Grid Oscillator

Substrate Thickness (mm)	Oscillator Frequency (GHz)			Measured EIRP (W)	Harmonics (dBc)	
	Simulated	Measured	% Error		Second	Third
15.2	6.4	6.07	5	0.50	-28	-42
21.5	4.6	4.86	5	1.51	-25	-45
27.9	5.1	5.32	4	1.77	-31	-45

Source: From [15], copyright © 1997 by IEEE.

## 8.6 OPTIMIZING GRID PERFORMANCE

The examples above demonstrate how the feedback level can be controlled by varying the substrate thickness. Another way of controlling the feedback is to alter the unit-cell geometry in some way. Hacker et al. [30] used a meandered gate lead to control the compression level in a gate-feedback grid. For a source-feedback grid, the feedback can be controlled by using an asymmetric unit cell (Fig. 8.17a), as suggested by the asymmetric optimum circuit of Fig. 8.14. The drain is connected to a short dipole radiating element, as before. However, the width of the radiating element connected to the gate is extended across the full width of the unit cell, resulting in a slot, rather than dipole radiator. By adjusting the dimensions of this slot, the amount of feedback to the gate, and hence the compression level, can be controlled to some extent.

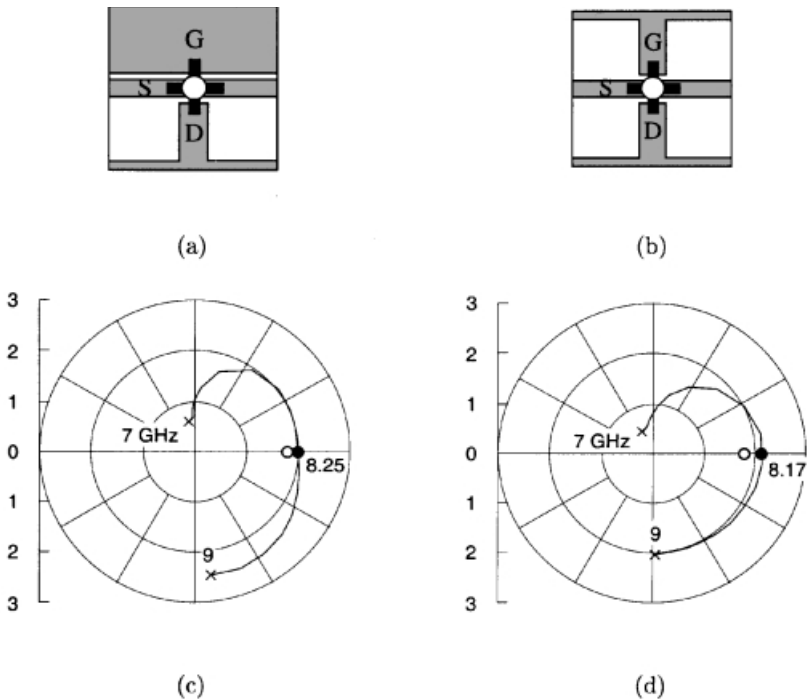


**FIGURE 8.17** Unit cell of a grid oscillator with (a) slot/dipole radiating elements and (b) dipole radiating elements. Both cells are 6 mm square and are loaded with HP-Avantek ATF-26884 MESFETs. The grids are printed on a 0.5-mm substrate (Duroid 5880,  $\epsilon_r = 2.2$ ) and placed on a second 5-mm layer (Duroid 6010.8,  $\epsilon_r = 10.8$ ), which is metallized on the back. C-functions for the (c) slot/dipole and (d) dipole grid oscillators. The solid symbols represent the C-functions of the grids, and the open symbols represent the C-functions of the theoretical optimum networks. From [15] copyright © 1997 by IEEE.

**TABLE 8.2. X-Band MESFET Grid Oscillator**

Unit-Cell Geometry	Oscillator Frequency (GHz)			Measured EIRP (W)	
	Simulated	Measured	% Error	$V_{ds} = 3\text{ V}$	$V_{ds} = 4\text{ V}$
Slot/dipole	8.3	8.57	3	0.31	0.49
Dipole	8.1	8.35	3	0.19	0.31

Source: From [15], copyright © 1997 by IEEE.

To demonstrate, two  $4 \times 4$  X-band grid oscillators were fabricated with the metallization patterns shown in Figs. 8.17a and 8.17b. Both grids have the same unit-cell dimensions, substrate, and mirror spacing. The simulated  $C$ -functions are shown in Figs. 8.17c and 8.17d. At the same dc bias level, the slot/dipole-grid oscillator demonstrated up to 58% more EIRP than the dipole-grid oscillator (Table 8.2). While both grids are slightly overcompressed, they are not as compressed as the PHEMT grids discussed earlier. No harmonics were observed for either grid.

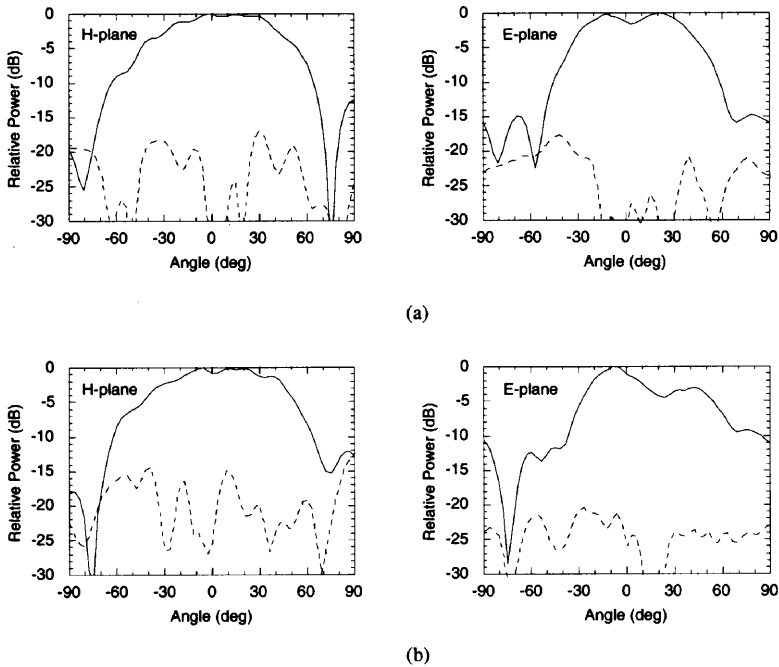


**FIGURE 8.18** Measured  $H$ - and  $E$ -plane patterns of the (a) slot/dipole and (b) dipole grid oscillators of Fig. 8.17. Solid lines represent the copolarization and dashed lines represent the cross-polarization. From [15] copyright © 1997 by IEEE.



**TABLE 8.3 Circuit Elements for  $\Pi$  Equivalent Circuit**

Case	Dielectric Thickness $t$ (mm)	Dielectric Constant $\epsilon_r$	Mirror Distance $d$ (mm)	Shunt Reactance		Series Reactance		Series Resistance $R_3$ ( $\Omega$ )
				$C_1$ (pF)	$L_1$ (nH)	$C_3$ (pF)	$L_3$ (nH)	
(a)	0	—	—	0.072			2.63	188
(b)	5.08	2.2	—	0.115			1.24	188
(c)	5.08	10.2	—	0.401		13.4		180
(d)	6.35	10.2	—	0.402		9.53		175
(e)	7.62	10.2	—	0.403		7.57		169
(f)	6.35	10.2	5	0.402		16.1		5.5

Figure 8.18 shows the measured radiation patterns. Based on an estimate of the directivity from these patterns, the highest conversion efficiency for the slot/dipole grid was 21%, while that of the dipole grid was about 10%.

Deriving the optimum lumped equivalent circuit for a given transistor is relatively simple, but it is not so straightforward to translate this equivalent circuit to an actual grid design. Some insight into how the physical parameters relate to the equivalent-circuit parameters can be obtained by looking at the  $\Pi$  circuit for a grid whose unit cell is shown in Fig. 8.19. The circuit elements take on different values depending on the dielectric and mirror properties. These effects are summarized in Table 8.3. All of these circuit elements were computed at the frequency for which  $a = \lambda_0/100$ . The particular values of dielectric constant and thickness are based on standard Duroid thicknesses.

Case (a) is for the grid in free space, without any dielectric or metal backing. All of the equivalent-circuit elements can be related to the physical grid parameters. The

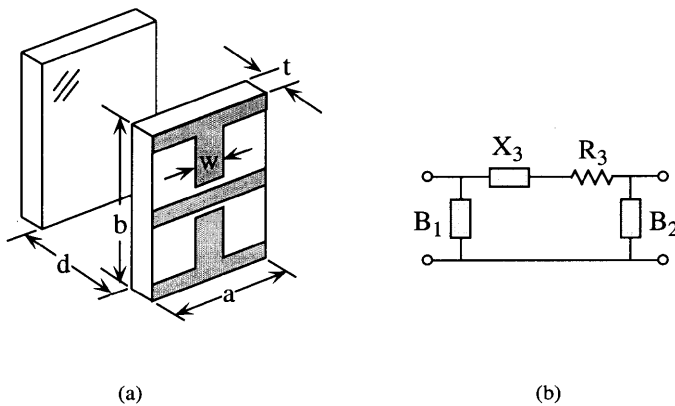


**FIGURE 8.19** (a) Unit cell for a topology commonly used for grid oscillators. The unit-cell dimensions are fixed at  $a = b = 6$  mm and  $w = 1$  mm. (b) The equivalent  $\Pi$  network. Since the unit cell is symmetric,  $B_1 = B_2$  in this case.

shunt capacitors represent the capacitance of the gaps. The series inductor represents the inductance of the leads. The resistor models the radiation into free space, which in this case is the parallel combination of the front and backside,

$$R_3 = \eta_0 \frac{b}{a} \parallel \eta_0 \frac{b}{a} = \frac{\eta_0}{2}$$

with  $b/a = 1$  for this case.

When the grid is placed on a dielectric substrate (cases (b) and (c)), the shunt capacitance increases by a factor of approximately  $(\epsilon_r + 1)/2$ . For thicker substrates (cases (d) and (e)), the dielectric also affects the series circuit elements, due to the transmission line effects.

When a mirror is added (case (f)), the shunt elements do not change, but the series resistance decreases dramatically, due to the mirror shorting out the free space. For other mirror distances, the transmission line effect of the dielectric slab can offer the opportunity for impedance matching.

## 8.7 OSCILLATOR DESIGN USING POWER AMPLIFIER TECHNIQUES

In systems, usually a low-power, low-phase-noise oscillator is amplified to achieve the desired output power. The main reason for this is that for individual oscillators, as the output power increases, the phase noise also increases. Self-locked array and grid oscillators are different in that as the number of elements increases, the output power increases, but assuming the individual noises are uncorrelated, the phase noise decreases. An example is shown in Fig. 8.20, where the spectra are shown for  $4 \times 4$ ,  $6 \times 6$ , and  $8 \times 8$  C-band grid oscillators with identical unit cells. As the number of elements increases, the spectrum narrows, indicating lower phase noise. In addition, global feedback for all the individual elements averages device performance making the system less sensitive to individual device variation. In Section 8.7.1, the design of a microstrip implementation of a feedback oscillator using a high-efficiency class-E power amplifier is described [31]. In Section 8.7.2, a four-element class-E amplifier array is converted into an oscillator array using external global free-space feedback.

### 8.7.1 Class-E Oscillator Design

A feedback oscillator configuration is used with a high-efficiency class-E amplifier as the active element. The circular-function analysis described in Section 8.3.1 is performed with a linear circuit simulator. The feedback length is adjusted for an oscillation frequency of 5.0 GHz and the amount of coupling is optimized for the correct compression point. An asymmetric microstrip branch-line coupler provides the feedback through a length of microstrip transmission line. The circuit layout is shown in Fig. 8.21.

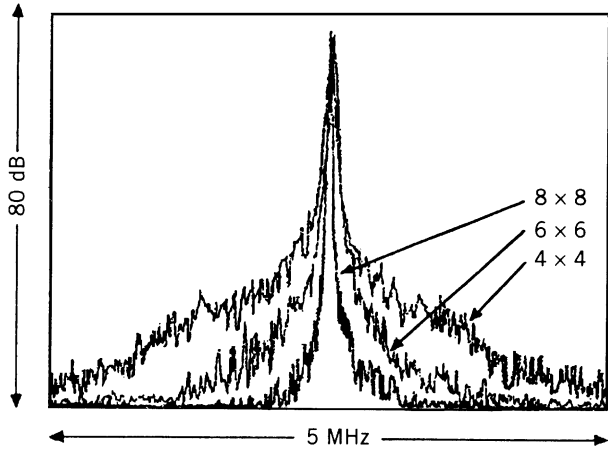


**FIGURE 8.20** Measured frequency spectra for a  $4 \times 4$ ,  $6 \times 6$ , and  $8 \times 8$  C-band grid oscillator with identical unit cells. The widest spectrum is the  $4 \times 4$  grid and the narrowest spectrum is the  $8 \times 8$  grid.

The class-E amplifier is a resonant switched-mode circuit in which a switch (transistor) turns on at zero voltage and zero derivative of voltage. Ideally, the product of the switch voltage and current is zero, resulting in 100% efficiency. In practice, the efficiency is limited by the drain-to-source saturation resistance of the transistor and other losses in the circuit. The class-E amplifier in Fig. 8.21 uses a

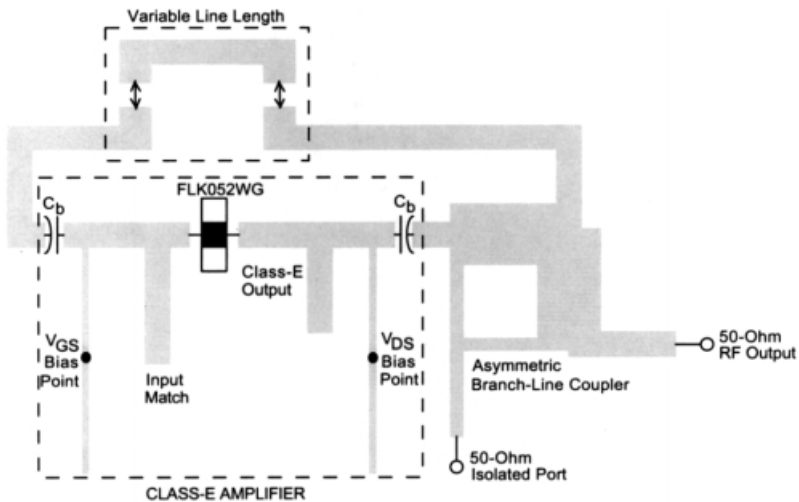


**FIGURE 8.21** Class-E oscillator layout in microstrip. The adjustable line length in the feedback loop is used to tune the oscillator to exactly 5.0 GHz. From [31] copyright © 1996 by IEEE.

Fujitsu FLK052 MESFET. The MESFET is driven as a switch and the surrounding circuitry is designed to give class-E operation. Device parasitic reactances are included in the resonant circuit design.

The input match is designed for gain by measuring  $S_{11}$  in saturation. The output circuit has a fundamental impedance for class-E operation of

$$Z_{\text{net}} = \frac{0.28015}{\omega_s C_s} e^{j49.0524^\circ} \quad (8.23)$$

where  $\omega_s/2\pi$  is the fundamental frequency, 5 GHz, and  $C_s$  is the transistor switch output capacitance, 0.4 pF [9].

Device saturation is simulated by reducing  $|S_{21}|$ . This is shown in [23] to be a reasonable approximation of the large-signal operation of a FET for small levels of saturation.

The class-E amplifier achieves maximum power-added efficiency when it is operating approximately 4 dB into compression [9]. The amount of coupling is adjusted in the simulations so that 4 dB of compression reduces  $|C|$  to unity at 5.0 GHz. The feedback length is then adjusted to make  $\angle C$  equal to zero degrees at 5.0 GHz. Since these simulations are based on small-signal  $S$ -parameters, the feedback line length is made to be tunable. After fabrication, the feedback length is experimentally tuned to produce an oscillation at exactly 5.0 GHz. The coupler was designed to couple  $-6.5$  dB of the output power to the feedback loop and  $-1.1$  dB to the load.

Figure 8.22 shows the simulated circular function for this oscillator with no saturation taken into account. Only the frequency ranges where the oscillation conditions are met are shown here. This simulation shows a low-frequency oscillation near 600 MHz, which appears to be more compressed than the desired 5-GHz oscillation. Figure 8.23 shows the two oscillation modes predicted by the circular function. Note the considerably higher harmonic content of the 600-MHz mode compared to the 5-GHz mode. This verifies the higher level of compression required for this mode as shown in Fig. 8.22. This low-frequency oscillation is suppressed in the circuit by lowering the value of  $C_b$  in Fig. 8.21. The measured oscillation frequency of the 5-GHz mode differs less than 3% from simulation.

Figure 8.24 shows the measured output power and conversion efficiency of the oscillator versus drain current for three different values of  $V_{\text{ds}}$ . The lines on the plot represent the range over which the oscillation remains stable. The maximum efficiency is 59% for  $V_{\text{ds}} = 6.5$  V and 300 mW of output power. The maximum output power is 600 mW for  $V_{\text{ds}} = 9.5$  V and 48% conversion efficiency. The oscillation frequency varies less than 1% over the entire biasing range shown here.

Table 8.4 compares the class-E amplifier and the oscillator presented here for the same bias point. Neglecting losses, the expected output power of the oscillator is the power added by the amplifier. The expected efficiency is equal to the power-added efficiency of the amplifier at this bias point. As the table shows, the efficiency is lower than the ideal level. Some of the difference is due to losses in the circuit, but most is believed to be caused by the oscillator still operating too far into

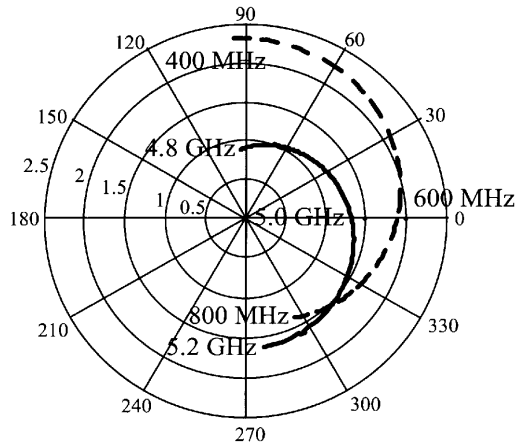


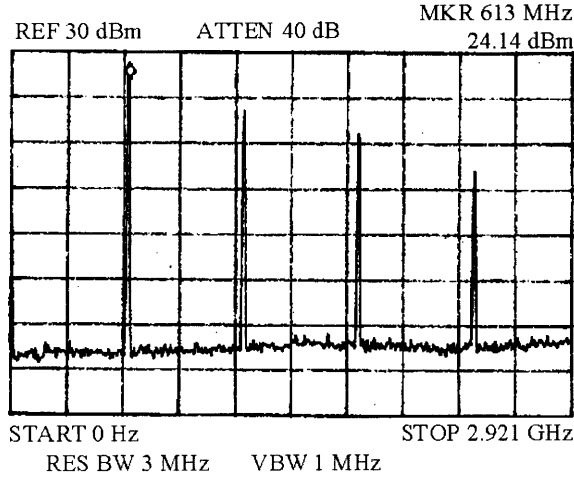
**FIGURE 8.22** Simulated circular function for unsaturated class-E oscillator. The dashed line shows an oscillation near 600 MHz and the solid line shows an oscillation near 5 GHz. From [31] copyright © 1996 by IEEE.

compression. This can be corrected in the design if the large-signal characteristics of the MESFET are known accurately. These results show the need for good nonlinear device models when designing oscillators for high efficiency and power.

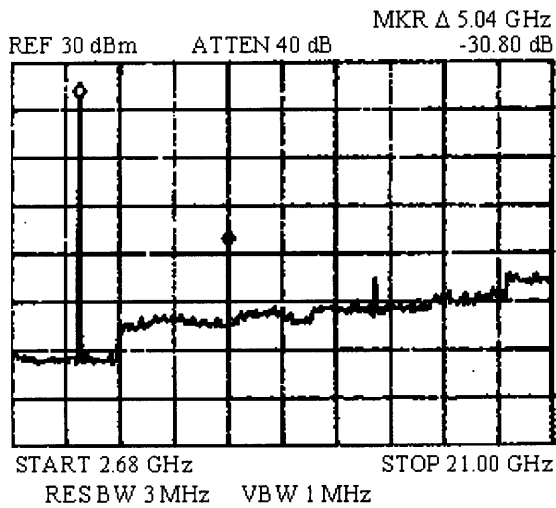
### 8.7.2 A Class-E Oscillator Array

The 5-GHz class-E amplifier used above was also successfully integrated into an active antenna array, shown in Fig. 8.25, demonstrating power combining of four elements with an 85% power-combining efficiency [9]. At 5.05 GHz, the class-E power amplifier antenna array delivers a total of 2.4 W of output power with a drain efficiency of 74% and a power-added efficiency of 64%. In this active array, a plane wave is incident on an array of antennas, each one connected to an amplifier input. The outputs of the amplifiers are each connected to an output antenna. The array of output antennas radiates an amplified plane wave [6]. The antennas are second-resonant slot antennas in the microstrip ground plane coupled to the microstrip feed lines. The input and output antennas are orthogonally polarized to provide isolation.

To convert this array into an oscillator, it is necessary to introduce positive feedback between the input and output antennas. The signal radiated by the output slot must be reflected and shifted in polarization by  $90^\circ$ . This is accomplished by placing a polarizer a quarter wavelength in front of a mirror. When the polarization is oriented  $45^\circ$  with respect to the polarization of the output wave, maximum feedback occurs. The polarizer splits the output wave into two orthogonal components. One component is reflected by the polarizer; the second component passes through the polarizer and is reflected by the mirror, but with an additional  $180^\circ$  phase shift. The net result is a reflected wave with polarization normal to the incident wave. By rotating the polarizer away from  $45^\circ$ , the amount of feedback can be reduced if



(a)



(b)

**FIGURE 8.23** Measured oscillation modes for the class-E oscillator: (a) 600 MHz and (b) 5 GHz.

needed. The same approach was used to convert a grid amplifier into a tunable oscillator in [32].

The array with external feedback is shown in Fig. 8.26. A maximum output power of 1.25 W with a corresponding conversion efficiency of approximately 40% was obtained with the polarizer at a distance of 87 mm from the amplifier array and at an angle of  $45^\circ$  with respect to the input and output antennas. This suggests that this method does not provide enough feedback.

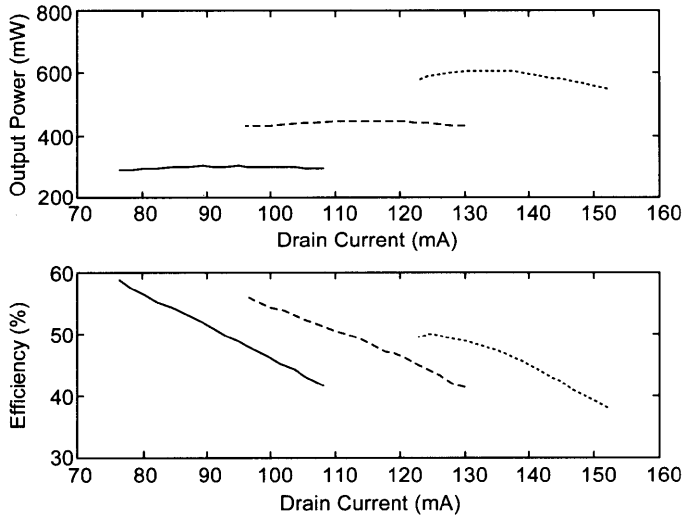


**FIGURE 8.24** Output power and conversion efficiency versus drain current,  $I_{ds}$ , for  $V_{ds} = 6.5$  V (solid line),  $V_{ds} = 8$  V (dashed line) and  $V_{ds} = 9.5$  V (dotted line). From [31] copyright © 1996 by IEEE.

### 8.8 CONCLUSION

In this chapter, we presented the work done to date on modeling and validation of grid oscillators and some related active antenna arrays. Even though there have been some attempts to analyze finite arrays of tightly coupled oscillators [M. Steer, *personal communication*], the dynamics of analyzing an entire finite array is quite complicated and has not yet been solved. However, existing theories based on infinite-array boundary conditions deal only with a unit cell and can predict the oscillation frequency and relative saturation to within 10% or better. The unit-cell approximation has been shown to be within this bound even for grids where more than 50% of the elements are edge elements. The output power is much harder to predict and requires accurate nonlinear active device models, which the authors have

**TABLE 8.4 Comparison Between Class-E Amplifier and Class-E Oscillator: Second Row Shows Oscillator Performance Based on Amplifier Measurements; Third Row Shows Measured Oscillator Data**

	$V_{ds}$	$I_{ds}$	Power	Efficiency
Amplifier	8 V	93 mA	27.8 dBm	72%
Oscillator <sub>I</sub>	8 V	93 mA	27.3 dBm	72%
Oscillator <sub>M</sub>	8 V	96 mA	26.7 dBm	56%

Source: From [31], copyright © 1996 by IEEE.

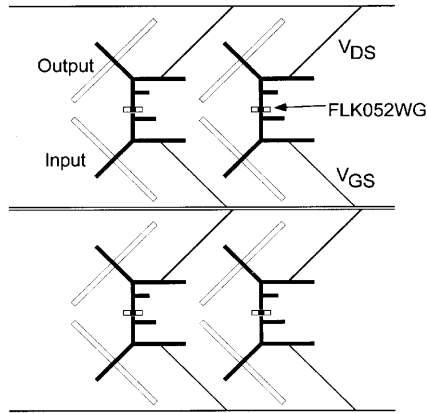


**FIGURE 8.25** The class-E power amplifier antenna array. This four-element power combiner demonstrates 2.4 W of output power at 5.05 GHz with 8.8-dB compressed gain, 74% drain efficiency, and 64% power-added efficiency.

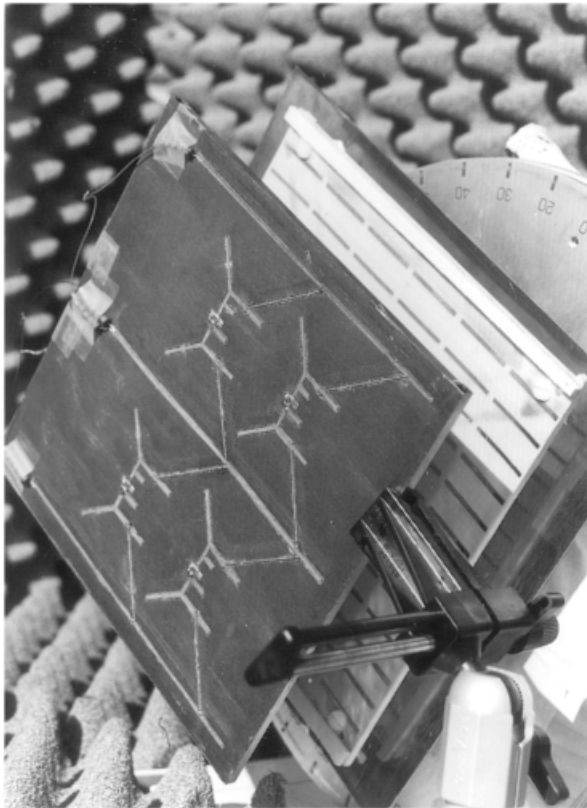


**FIGURE 8.26** The class-E external feedback oscillator array.



found hard to obtain in most cases. The inaccuracies of the device models for large-signal operation seem to be greater than potential inaccuracies resulting from an infinite-array approximation.

In terms of systems issues, the most important one seems to be that of low phase noise. We have shown that the phase noise is reduced as many oscillators lock. For lower phase noise than that obtained in free-running self-injection locked oscillator arrays, it is also possible to globally injection lock to a low-noise reference. Another systems issue is start-up time for pulsed operation. The oscillators demonstrated to date could be bias-pulsed only at low speeds, but an external switch array cascaded with an oscillator array has also been demonstrated. Passive or active frequency-selective surfaces can also be cascaded with the oscillators for feedback control as well as harmonic-level regulation.

Finally, many arguments have been made that quasi-optical technology is viable for millimeter-wave frequencies and has an advantage of being suitable for monolithic integration. This might be the case, but probably due to low yield of millimeter-wave devices across a wafer and heat management problems on GaAs, there have been very few demonstrations of monolithically integrated grid oscillators or arrays.

## REFERENCES

1. York, R. A., and Popović, Z. B. (eds), *Active and Quasi-Optical Arrays for Solid-State Power Combining*, Wiley, New York, 1997.
2. Marković, M., Hollung, S., and Popović, Z. B., "Quasi-optical phase modulators," *1996 IEEE MTT-S Int. Microwave Symp. Dig.*, June 1996, pp. 1247–1250.
3. Popović, Z. B., Weikle II, R. M., Kim, M., Potter, K. A., and Rutledge, D. B., "Bar-grid oscillators," *IEEE Trans. Microwave Theory Tech.*, vol. 38, Mar. 1990, pp. 225–230.
4. Mader, T., Bundy, S., and Popović, Z. B., "Quasi-optical VCOs," *IEEE Trans. Microwave Theory Tech.*, vol. 41, Oct. 1993, pp. 1775–1781.
5. Sun, Q., Horiuchi, J. B., Haynes, S. R., Miyashiro, K. W., and Shiroma, W. A., "Grid oscillators with selective-feedback mirrors," *IEEE Trans. Microwave Theory Tech.*, vol. 46, Dec. 1998, pp. 2324–2329.
6. Schoenberg, J., Mader, T., Shaw, B., and Popović, Z. B., "Quasi-optical antenna array amplifiers," *1995 IEEE MTT-S Int. Microwave Symp. Dig.*, May 1995, pp. 605–608.
7. Schoenberg, J. S. H., Bundy, S. C., and Popović, Z. B., "Two-level power combining using a lens amplifier," *IEEE Trans. Microwave Theory Tech.*, vol. 42, Dec. 1994, pp. 2480–2485.
8. Schoenberg, J. S. H., *Quasi-Optical Constrained Lens Amplifier*, Ph.D. thesis, University of Colorado, Boulder, 1995.
9. Mader, T. B., *Quasi-Optical Class-E Power Amplifiers*. Ph.D. thesis, University of Colorado, Boulder, 1995.
10. Hollung, S., Shiroma, W., Marković, M., and Popović, Z. B., "A quasi-optical isolator," *IEEE Microwave Guided Wave Lett.*, vol. 6, May 1996, pp. 205–206.
11. Shiroma, W. A., Bundy, S. C., Hollung, S., Bauernfeind, B. D., and Popović, Z. B.,

- “Cascaded active and passive quasi-optical grids,” *IEEE Trans. Microwave Theory Tech.*, vol. 43, Dec. 1995, pp. 2904–2909.
12. Hacker, J. B., Weikle II, R. M., Kim, M., De Lisio, M. P., and Rutledge, D. B., “A 100-element planar Schottky diode grid mixer,” *IEEE Trans. Microwave Theory Tech.*, vol. 40, Mar. 1992, 557–562.
  13. Shiroma, W. A., Bryerton, E. W., Hollung, S., and Popović, Z. B., “A quasi-optical receiver with angle diversity,” *1996 IEEE MTT-S Int. Microwave Symp. Dig.*, June 1996, pp. 1131–1134.
  14. Popović, Z. B., Weikle II, R. M., Kim, M., and Rutledge, D. B., “A 100-MESFET planar grid oscillator,” *IEEE Trans. Microwave Theory Tech.*, vol. 39, Feb. 1991, pp. 193–200.
  15. Shiroma, W. A. and Popović Z. B., “Analysis and optimization of grid oscillators,” *IEEE Trans. Microwave Theory Tech.*, vol. 45, Dec. 1997, pp. 2380–2386.
  16. Bundy, S. C., and Popović, Z. B., “A generalized analysis for grid oscillator design,” *IEEE Trans. Microwave Theory Tech.*, vol. 42, Dec. 1994, pp. 2486–2491.
  17. Khanna, A. P. S., and Obregon, J., “Microwave oscillator analysis,” *IEEE Trans. Microwave Theory Tech.*, vol. MTT-29, June 1981, pp. 606–607.
  18. Mason, S. J., “Feedback theory—further properties of signal flow graphs,” *Proc. IRE*, vol. 44, July 1956, pp. 920–926.
  19. Martinez, R. D., and Compton, R. C., “A general approach for the  $s$ -parameter design of oscillators with 1 and 2-port active devices,” *IEEE Trans. Microwave Theory Tech.*, vol. 40, Mar. 1992, pp. 569–574.
  20. Kurokawa, K., “Some basic characteristics of broadband negative resistance oscillator circuits,” *Bell Syst. Tech. J.*, vol. 48, Jul.–Aug. 1969, pp. 1937–1955.
  21. Sun, Q., Miyashiro, K. W., Horiuchi, J. B., and Shiroma, W. A., “Grid oscillators with photonic-crystal reflectors,” *1998 IEEE MTT-S Int. Microwave Symp. Dig.*, 1998, pp. 1887–1890.
  22. Vehovec, M., Houselander, L., and Spence, R., “On oscillator design for maximum power,” *IEEE Trans. Circuit Theory*, vol. CT-15, Sept. 1968, pp. 281–283.
  23. Johnson, K. M., “Large signal GaAs MESFET oscillator design,” *IEEE Trans. Microwave Theory Tech.*, vol. MTT-27, Mar. 1979, pp. 217–227.
  24. Kormanyos, B. K., and Rebeiz, G. M., “Oscillator design for maximum added power,” *IEEE Microwave Guided Wave Lett.*, vol. 4, June 1994, pp. 205–207.
  25. Kotzebue, K. L., and Parrish, W. J., “The use of large-signal S-parameters in microwave oscillator design,” *Proc. 1975 Int. Microwave Symp. Circuits Syst.*, 1975, pp. 487–490.
  26. Larson, L. E. (ed.), *RF and Microwave Circuit Design for Wireless Communications*, Artech House, Boston, 1996, p. 303.
  27. Vendelin, G. D., Pavio, A. M., and Rohde, U. L., *Microwave Circuit Design Using Linear and Nonlinear Techniques*, Wiley, London, 1990, p. 450.
  28. Kotzebue, K. L., “Maximally efficient gain: a figure of merit for linear active 2-ports,” *Electron. Lett.*, vol. 12, 16 Sept. 1976, pp. 490–491.
  29. Kotzebue, K. L., “Microwave amplifier design with potentially unstable FETs,” *IEEE Trans. Microwave Theory Tech.*, vol. MTT-27, Jan. 1979, pp. 1–3.
  30. Hacker, J. B., De Lisio, M. P., Kim, M., Liu, C.-M., Li, S.-J., Wedge, S. W., and Rutledge, D. B., “A 10-Watt X-band grid oscillator,” *1994 IEEE MTT-S Int. Microwave Symp. Dig.*, May, 1994, pp. 823–826.

31. Bryerton, E. W., Shiroma, W. A., and Popović, Z. B., "A 5-GHz high-efficiency class-E oscillator," *IEEE Microwave Guided Wave Lett.*, vol. 6, Dec. 1996, 441–443.
32. Kim, M., Sovero, E. A., Hacker, J. B., De Lisio, M. P., Rosenberg, J. J., and Rutledge, D. B., "A 6.5–11.5 GHz source using a grid amplifier with a twist reflector," *IEEE Trans. Microwave Theory Tech.*, vol. 41, Oct. 1993, pp. 1772–1774.

CHAPTER NINE

---

# Analysis and Design Considerations for Monolithic Microwave Circuit Transmit– Receive (T–R) Modules

---

LAWRENCE R. WHICKER  
LRW Associates  
Matthews, NC

## 9.1 INTRODUCTION

### 9.1.1 Active Phased Array Concepts

As indicated in Chapter 1 active phased arrays use many transmit–receive (T–R) modules that feed closely spaced individual radiating elements. The radiating elements are roughly placed at half-wavelength centers. Most present T–R modules contain T–R switches and ferrite circulators, which isolate circuit and antenna elements. This isolation allows for separate optimization of T–R module circuits and separate optimization of the radiating element. There are, however, some exceptions where GaAs substrates have contained switches, phase shifters, and radiating elements.

Active array technology is important for a number of military and commercial applications. For frequencies below about 20 GHz, radar has been the major application. Space communication at 44 GHz, 60 GHz, and 94 GHz may be important future application areas. The following paragraphs will list specific power needs for these applications. Since much of the present research on T-R module development/optimization has been funded by the military airborne radar community, this chapter will focus on these efforts.

The elements of a conventional radar will be reviewed and the power required for specific applications will be listed. These requirements will then be translated to the active array T-R module. A historical review of T-R module development will follow. The present status of T-R module circuits and packages is considered. Finally, advanced packaging concepts are described in which closer integration of the circuit-antenna elements is possible.

### 9.1.2 Conventional Radar Systems

Conventional radar systems were developed before and during World War II. They have continued to evolve with advance in key subsystem areas and in associated signal processing. The key feature in radar operation is that an RF signal is transmitted, scattered from a given target, and received back at the radar site. The received signal is amplified and processed to obtain the distance and angular position of the target.

Elements of a classical radar system consist of the following:

- Signal processor/computer.
- RF power generator.
- Pulse-shaping circuits.
- RF low noise receiver.
- Duplexer.
- Rotable antenna structure.
- RF feed structure to antenna.

The antenna needs to have a diameter of several wavelengths in order to direct the radiated energy. Features of these functions are discussed in the following paragraphs.

The RF transmitter must provide power to reach the target, be scattered, and then be received back at the system site. The received signal must be detectable by a suitable low noise receiver. The required power is determined by the radar range equation [1]. The antenna aperture size is important also as the antenna directs the radiated RF power into a concentrated beam rather than radiating energy in all directions equally. Readers are referred to [1] for a complete discussion of radar system operation. As the RF energy is transmitted and received by the same antenna, RF pulses of energy must be transmitted and received in time sequence. That is, an RF pulse of high energy is transmitted; the transmitter is turned off; a return scattered pulse is received; and the received signal is passed through a duplexer, is amplified by a low noise receiver, and is processed by the signal processor.

The mission of a radar system normally determines the frequency of operation and the required RF power level. Table 9.1 lists the frequency of operation for several types of systems.

Table 9.2 lists additional information concerning these types of radar systems.

Present/conventional radar systems are optimized to do specific system tasks. For example, antenna feed networks have been developed to provide sum and difference radiation patterns. Also, antenna radiation patterns with very low sidelobes are required for airborne applications. Computer algorithms have been developed to retrieve very small return signals from a highly cluttered background. Waveguide switching networks (such as the Butler Matrix) have been developed, which use multiple apertures and direct multiple radiated beams simultaneously. Present/conventional systems have been limited, however, by the mechanically scanned antenna.

### 9.1.3 Early Phased Array Concepts

For many radar systems it has been the desire to eliminate the rotatable antenna structure and replace it with a fixed antenna that electronically can direct energy into multiple beams simultaneously. Additionally, the antenna gimble has been a continuing reliability problem. Moreover, the speed of antenna rotation can limit the system capability.

In some antennas rows of slotted waveguides are used to make up the antenna face. The slots are placed at about a  $\lambda/2$  spacing at the operating frequency. By adjusting the operating frequency, the fractional wavelength spacing can be varied. One-dimensional scanning of the beam has been accomplished in this way. Another approach, however, has met with considerable success and has established the value of two-dimensional phased array scanning. This approach is commonly known as “passive array technology.” In this approach a conventional radar is fabricated except that the antenna structure is made up of a  $\lambda/2 \times \lambda/2$  waveguide egg crate or honeycomb, as shown in Fig. 9.1. Each cell of the structure contains a phase-shifting component that can provide a differential phase shift from  $0^\circ$  to  $360^\circ$ . In this

**TABLE 9.1 Operational Frequencies for Typical Classes of Radars**

Frequency Range	Types of Radar
200 MHz to 1 GHz based	Very long range ground
L band (1–2 GHz)	Long range surveillance
S band (2–4 GHz)	
C band (4–7 GHz)	Medium range battlefield
X band (7–11 GHz)	Airborne fire control
Ku band (12–18 GHz)	
Ka band (26–40 GHz)	Limited high resolution
60 GHz	Secure communication (space to space)
77 GHz	Possible application to auto collision avoidance
94 GHz	Short range, high resolution within fog/smoke

**TABLE 9.2 Radar Range and Power Requirements**

Frequency (GHz)	Range (miles)	RF Power (kW)	Source Type	System Type
0.2-1	> 100	100 to > 1000	Klystron/magnetron	Short pulse
1-2	> 100	100 to > 1000	Klystron/magnetron	Short pulse
2-4	50-100	50 to > 500	Klystron/CFA	Short pulse
4-7	50-100	50 to > 400	Klystron/CFA	Short pulse/pulse Doppler
7-11	25-100	1 to > 10	Klystron/TWT	Pulse Doppler
12-18	25-50	1 to > 10	Klystron/TWT	Pulse Doppler
26-40	1-10	1 to > 2	Klystron/TWT	Pulse Doppler
77	0-0.5	> 0.01	Solid state	Pulse Doppler
94	0.5-2	> 0.01	Solid state	Pulse Doppler

configuration, a network is provided that divides the RF energy so that it may pass through each phase shifter. Each phase shifter in turn feeds an individual radiating element. Configurations are shown in Fig. 9.2.

Phase-shifted elements are made up of ferrite or diode phase shifters. Although diode phase shifters were used in a few lower frequency search radar applications, the major effort and applications have used ferrite phase shifters. Diode phase shifters use a variety of circuits including switched length of transmission line or 3-dB hybrid couplers terminated in varactor diodes. For passive array applications, diode phase shifters present more insertion loss than ferrite types. In ferrite phase shifters, phase shift is obtained in increments by partially switching the magnetization of the ferrite material [2]. Ferrite phase shifters are often referred to as “latching ferrite phase shifters.” A 5-bit phase shifter would provide phase shift in increments of 0°, 22.5°, 45°, 90°, 180°, and 360°.

Most present fielded passive arrays use ferrite phase shifters. During the late 1960s and early 1970s nonreciprocal phase shifters received considerable develop-

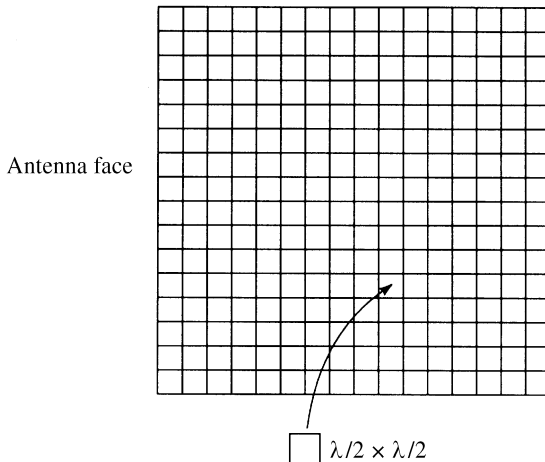


**FIGURE 9.1**  $\lambda/2 \times \lambda/2$  waveguide egg crate or honeycomb antenna structure.

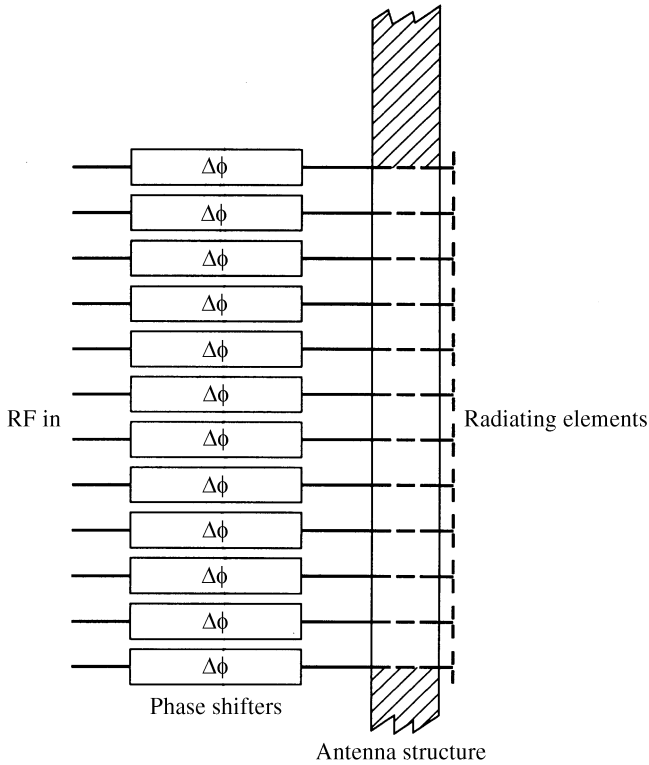


**FIGURE 9.2** Phase shifters feed individual radiators.

mental efforts [3–5]. Slightly later, emphasis changed to reciprocal phase shifters as these need not be switched between the transmit and receive operations. Today, both types are utilized in fielded systems. Nonreciprocal and reciprocal phase shifters are depicted in Fig. 9.3. A partial list of radar types that have been fielded using ferrite phase shifters are listed in Table 9.3

**9.1.4 Early Active Phased Modules**

Although passive phased arrays provided means to achieve electronic scanning, it has always been viewed as a stopgap measure. The “active phased array” goes several steps beyond the passive array. The passive grid of phase shifters is replaced

**TABLE 9.3 Radar Elements for Array and Application**

Frequency	Number of Elements per Array	Application
S-Band	4000–5000	Land/sea search
C-band	4000–5000	Ground based search
	2000–3000	Ground based
X-band	1500–2000	Airborne fire control



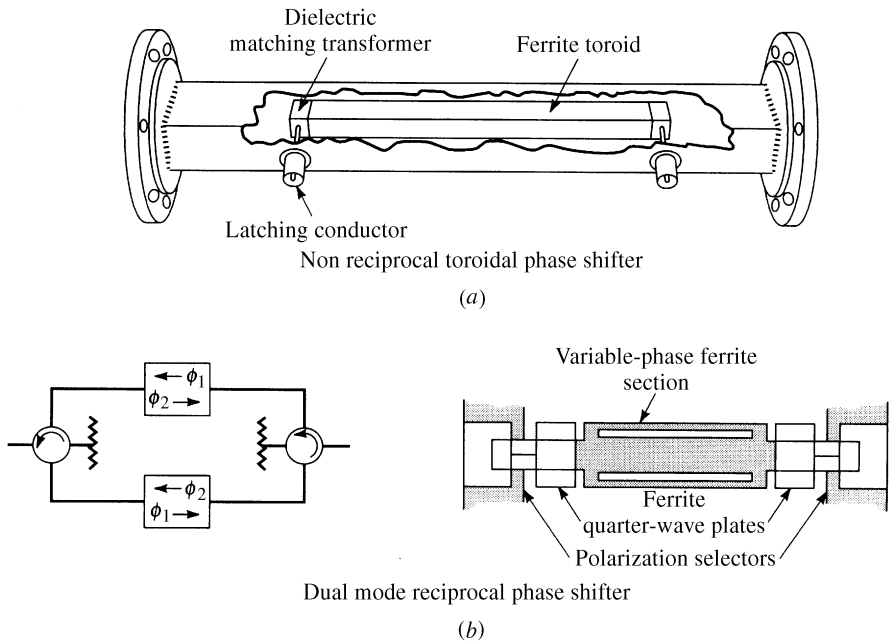


**FIGURE 9.3** (a) Nonreciprocal toroidal phase shifter and (b) dual-mode reciprocal phase shifter.

by a transmit–receive (T–R) module that includes a good portion of the radar system. The T–R module includes the RF front end fabricated in solid-state format. The module architecture may vary slightly from system to system. However, the T–R module usually includes the following:

- Solid-state transmitter
- Phase shifter
- Attenuator
- T–R switch or circulator
- Receiver protector
- Low noise amplifier
- Other required circuitry
  - Energy storage
  - Control and Switching logic
  - Bias circuitry

A simplified block diagram of a T–R module is shown in Fig. 9.4. In an active array, each module’s solid-state amplifier must provide  $1/n$  of the total radiated power. Here  $n$  is the total number of  $\lambda/2 \times \lambda/2$  elements in the array.

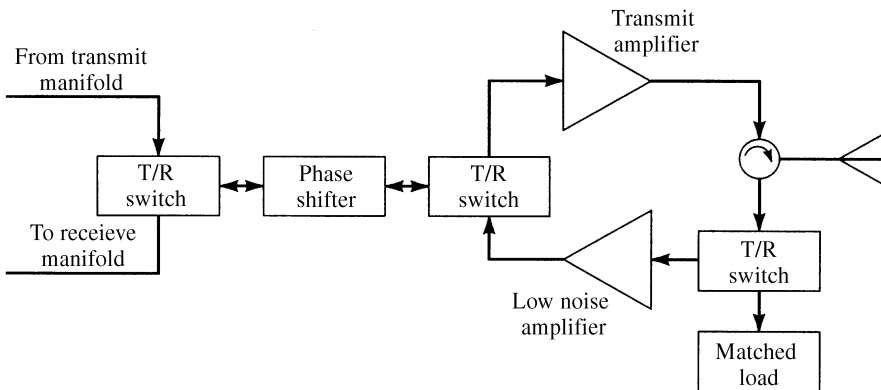


FIGURE 9.4 Block diagram of T-R module.

Work on active arrays has gone on since the late 1960s with major emphasis in the late 1980s through the mid 1990s. Thus far, the driving force has been the complex system needs of X- to Ku-band airborne radars. Here the large number of T-R modules per system and the large number of aircraft platforms per system class provide the potential quantities to justify large development programs.

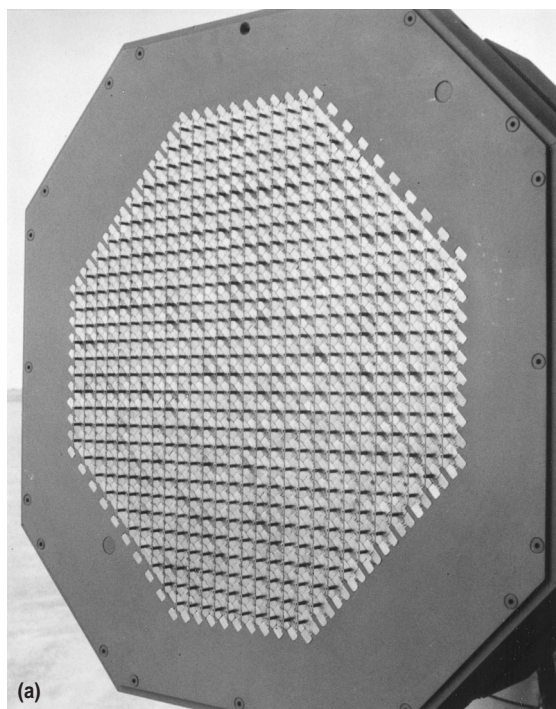
The U.S. Air Force through contractual program at Texas Instruments has provided pioneering early efforts [6–8]. These first programs were named MERA (Molecular Electronics for Radar Applications) and RASSR (Reliable Advanced Solid State Radar). A MERA module is depicted in Fig. 9.5 and a RASSR module is shown in Fig. 9.6. These modules were fabricated before X-band GaAs FETs were available. The RF transmitters in these modules utilize S-band silicon bipolar transistors and frequency multipliers to get to X-band. Such a configuration produces only a fraction of a watt with very low dc RF efficiency. Additionally, these modules contain hundreds of parts, resulting in high cost and poor reliability. However, much



FIGURE 9.5 MERA module. (Photograph courtesy of J. Wassel, Texas Instruments.)



**FIGURE 9.6** RASSR module. (Photograph courtesy of J. Wassel, Texas Instruments.)



**FIGURE 9.7a** MERA array with dipole radiating elements.



**FIGURE 9.7b** RASSR array with radiators. (Photographs courtesy of J. Wassel, Texas Instruments.)

important groundwork was performed in these programs. Figure 9.7 shows MERA and RASSR arrays.

## 9.2 PRESENT DEVELOPMENTS ON ACTIVE T-R MODULES

With continuing support from DARPA (ARPA), the three military services, and private industry, much progress has been made. Programs such as MIMIC (Microwave and Millimeter Wave Monolithic Integrated Circuits), HDMP (High Density Microwave Packaging), and MAFET (Microwave Front End Technology) have provided substantial funding. The MIMIC program has been a four-year program to support GaAs T-R module chip set optimization along with developing design and manufacturing tools to economically produce such chip sets. MAFET is a follow-on program that places emphasis on computed-aided design (CAD) and module packaging activities. These ARPA triservice programs supported major industry teams. Figure 9.8 depicts a state-of-the-art module containing nine GaAs chips [9]. Key parts of the T-R module include the following:

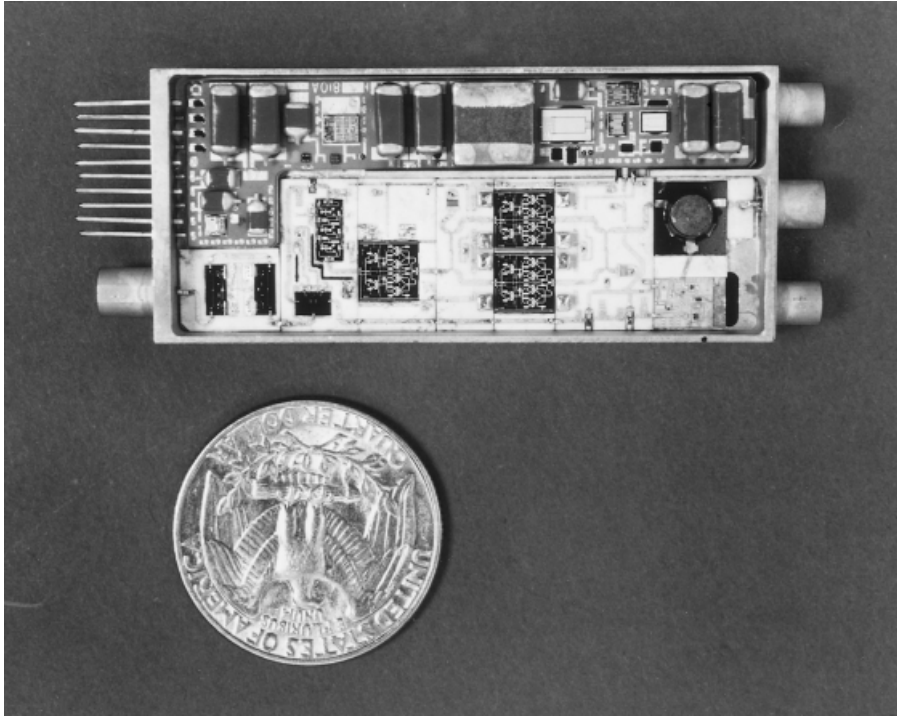


**FIGURE 9.8** State-of-the-art module that contains nine GaAs chips.

- Power amplifier (4 chips), produces 3.5 W of CW power
- Low noise receiver (2 chips), 4-dB noise figure
- Attenuator (1 chip), 0–10 dB attenuation
- Five-bit phase shifter (1 chip)
- T/R switch (1 chip)
- Three-port circulator
- Complex multiplier interconnect circuits
- Energy storage and control circuits
- Thermal network to provide heat path to external cold plate

At this time a state-of-the-art T–R module may still contain 50–100 parts. This in turn leads to small quantity costs of a few thousand dollars per unit with cost goals for quantities of 100,000 being at about the \$500–2000 range.

### 9.3 T–R MODULE DESIGN CONSIDERATIONS

In order to produce affordable T–R modules that will perform properly, complex trade-off studies are required. Some of the areas requiring studies include:

- Device types for solid-state transmitter
  - Radiated power required
  - Efficiency required
  - Cooling requirements (thermal design)
- Device types for receiver circuits
  - Noise figure required
  - Gain required
- RF chip architecture
  - Number of functions on a chip
  - Number of device types in a module
- Interconnect technology
  - Chip/wire
  - MHDI (microwave high density interconnect)
  - LTCC (low temperature cofired ceramic)
- CAD (computer-aided design)
  - How devices/circuits perform within package/module
- Packaging considerations
  - Type/cost

### 9.3.1 Design Considerations for an X-Band Module

Because much of the work in government and industry has been directed at X-Band T-R modules for airborne radar, it may be useful to focus on such designs in some detail. A good discussion of X-band module technology from a systems standpoint is given by McQuiddy et al. [10]. The material in [10] is complementary to the discussion that follows.

### 9.3.2 Power Amplifier Considerations

For a typical active array aperture, which may contain 500–2000 T-R modules, it is desirable to radiate 5–20 kW of CW power (during an RF pulse). With a 0.3 duty factor, the average power radiated would be 1.5–6 kW. In turn, this dictates that the power amplifier produce from 3 to 10 W of CW power during transmission. From a device standpoint this is a CW requirement. In an actual T-R module an additional 0.5–1 dB of power is required for losses encountered in circuitry between the amplifier and the radiating element. For an application in which it is desired to have an output power of 6 W, two 4-W amplifier power stages might be combined as indicated in Fig. 9.9. Here a final amplifier design might include 2, 3, or more chips depending on the maturity of the amplifier chips used and the degree of integration desired in the final module design.

At the present time, a variety of device technologies are available for use in power amplifiers. These include:

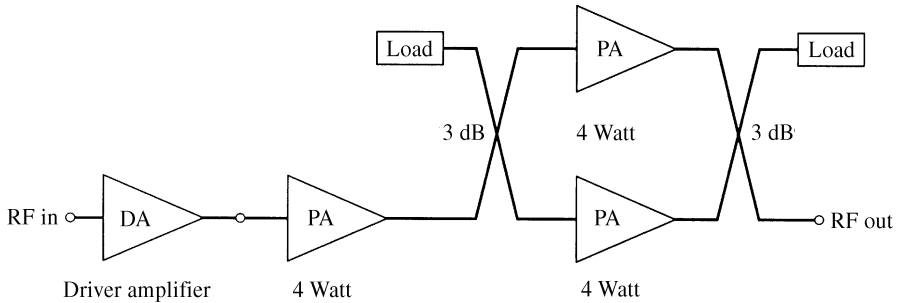


**FIGURE 9.9** Power combining of output amplifiers.

- GaAs FETs
- PHEMTs
- HFETs
- HBTs

GaAs FETS are used in most present designs although the devices with more complex doping profiles (PHEMTs, HFETs, and HBTs) may offer slightly increased efficiencies and possibly more power per unit periphery. The least mature of these device types is the power HBT (heterojunction bipolar transistor). The life of the HBT device (MTBF) has been somewhat less than the other device types. Performance of all these device types is continuing to improve.

The overall dc RF efficiency for a well-designed X-band power amplifier chain is on the order of 25–35%. Thus about three times the amplifier’s output power must be removed as heat. This is accomplished by thinning the GaAs substrate to 3–4 mils thickness. Vias are etched through the substrate material to make thermal contact with the active device region. Gold is back-filled into the vias and the resulting substrate is soldered or otherwise bonded to a thermal carrier or in some cases directly to the module housing. Strips or rows of modules are placed against a cold plate, which in turn has channels for liquid cooling. This approach is depicted in Fig. 9.10. Flip chip mounting of GaAs amplifiers has been used as an alternate approach at a few industrial organizations. This approach is depicted in Fig. 9.11. The flip chip mounting technique eliminates the need for active device vias and thinning of the GaAs substrate. However, the heat must still be removed and visual inspection of devices/circuits is difficult. For an array in which 1500 6-W modules are used, considerable cooling energy is required:

- 6.5 W generated power at amplifier
- 3.0 W estimate of other heat generated in T–R module
- 9.5 W/module × 0.3 duty factor
- 2.85 W module × 1500 T–R modules per array
- 4.5 kW/array power dissipated in heat

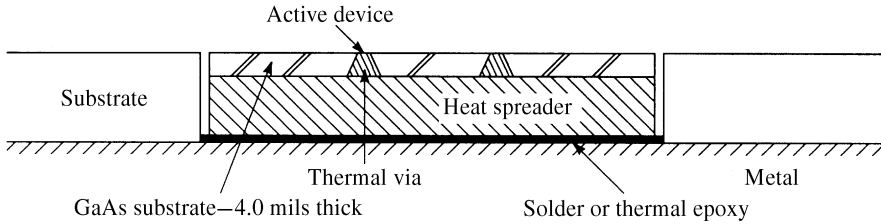


FIGURE 9.10 Removal of heat from a power amplifier.

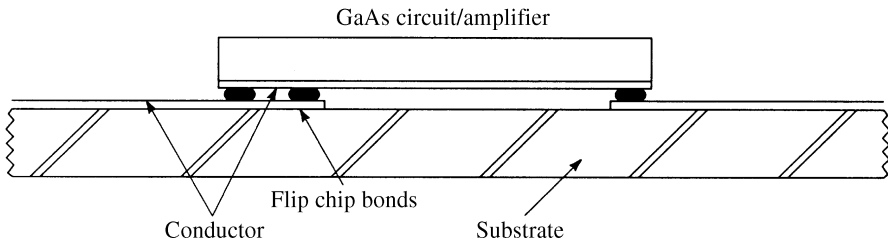


FIGURE 9.11 Flip chip mounting of power GaAs FET.

For arrays in which higher power is required, the available power from the air platform for cooling may present a major problem. Dissipated power will be discussed further under thermal considerations.

### 9.3.3 Low Noise Amplifier (LNA) Considerations

The overall T-R module receiver dynamic range requirements for a given radar design are established by the spurious-free dynamic range needed to keep spurious images of high level clutter below receiver noise level at the output of the radar signal processor. The low noise amplifier chain must overcome T-R module losses from the phase shifter, T-R switch, and attenuator, manifold losses, and the loss from the receiver protector. Typically 25–28 dB of gain is required with a corresponding noise figure of 3.0–3.5 dB. With present designs, a three-stage amplifier is usually required. T-R module LNA designs utilize both FETs and PHEMTs. At a fixed gate length, PHEMTs normally give a lower noise figure than FETs. At X-band frequencies, gate lengths of 0.4–0.5  $\mu\text{m}$  are used for both power and low noise devices. The gate length is reduced at higher frequencies. At about 35 GHz a gate length of 0.2–0.3  $\mu\text{m}$  is used. At 94 GHz, 0.15–0.1  $\mu\text{m}$  gate lengths are used. For such gate lengths, T gates are required to provide adequate conductor metal in the gate structure. Considerable discussion of higher frequency device technology is available in the literature [11,12].



### 9.3.4 Control Component Considerations

The control components included in a T-R module include:

- T-R protector
- Circulator
- Phase shifter
- Attenuator
- T-R switch

Of these, the T-R protector and circulator are usually non-GaAs individual components, while the attenuator, phase shifter, and T-R switch are fabricated on GaAs substrates. The phase shifter is the most complex of these. Five-bit phase shifters are the normal choice in T-R modules. The phase shifter designs employ switched hybrid couplers, loaded lines, and other circuit techniques to obtain small size and acceptable loss. Insertion losses as low as 5–7 dB have been obtained [10,13]. A phase shifter GaAs chip is shown in Fig. 9.12.

### 9.3.5 Chip Architecture Considerations

As indicated earlier, the overall T-R module production cost is related to the total parts count. Thus there has been a push toward fewer RF chips. Here the RF yield for an individual RF chip must be high to warrant combining multiple functions on a single chip. Figure 9.13 shows 5-, 3-, and 2-chip configurations. The chosen device technology will affect choice of the number of chips. For example, if PHEMTs are used for both power and low noise functions, then more functions may be combined. This assumes that the power and low noise doping profiles are the same. However, the use of HBTs for power devices would require a different device technology for low noise and control functions. A later section of this chapter will discuss an advance design in which single-chip T-R modules have been pursued. For present and near-term future systems 3-chip and 2-chip designs are receiving attention.

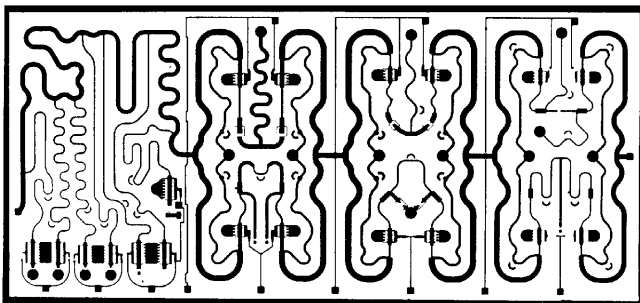
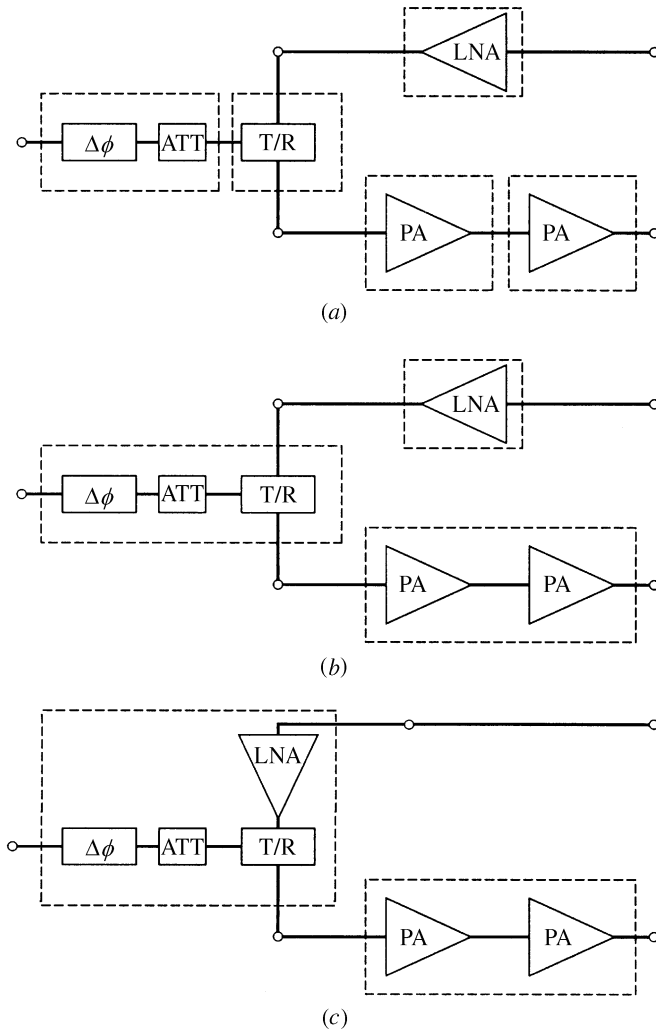


FIGURE 9.12 GaAs phase shifter chip.



**FIGURE 9.13** Candidate chip sets for T-R modules: (a) 5-chip design, (b) 3-chip design, and (c) 2-chip design.

### 9.3.6 Interconnect Technology

With many devices and circuits to be included in a single package, the interconnect technology becomes quite important. The electrical effects of the interconnects must be factored into the overall T-R module design. To date, most designs have used the chip and wire approach with many interconnects required. In some modules more than 1000 wire bonds are required. Although this approach is highly automated and used widely in the silicon industry, it is not favored by many module designers. A

batch approach is favored. Two such approaches are being considered as replacements for the conventional chip and wire approach. These are low temperature cofired ceramics (LTCCs) and microwave high density interconnects (MHDIs).

For the LTCC approach substrates within a module are replaced by a structure made up of ceramic layers that contain layers of metal interconnects. These layers are made from tapes, which are fired at somewhat lower temperatures than other ceramics. Some components such as 3-dB directional couplers, which are used for combining amplifier stages, may be fabricated directly into the LTCC layers. With this approach, some wire bonds are still required for final component assembly. The LTCC layering approach presents a three-dimensional CAD problem for circuit/device designers. At this time, good progress is being made with LTCC substrates. Tolerance on layer thickness, accuracy of metal pattern layouts, and complete three-dimensional CAD of LTCC parts are all being addressed.

The MHDi approach uses conventional ceramic substrates and makes all interconnects at one level. In this approach a layered flexible film made up of dielectric and thin metal interconnect patterns is applied as a top layer above active and passive circuits within the module. A batch processing technique is used to open windows in the dielectric film and to make connections to the circuits below. At frequencies above X-band, the electrical effects (loading) of the layer must be factored into the design. The MHDi approach is well suited for large scale production of T-R modules. As with the LTCC approach, further work is required before the full value of MHDIs can be determined.

### 9.3.7 Computer-Aided Design (CAD) Considerations

Three major ARPA/triservice programs—MIMIC, High Density Microwave Packaging (HDMP), and MAFET—have directed substantial industry and government efforts toward first-pass design and fabrication success in realizing GaAs chip sets for T-R modules. The MIMIC program has focused primarily on the RF circuits and in developing chip design libraries. The HDMP program has defined advanced three-dimensional packaging concepts and has identified needed CAD work. The MAFET program has extended the HDMP work and has considered CAD models for the entire T-R module. These programs have been partially successful. At the present time, about two design iterations are required to meet specifications for a given RF chip.

### 9.3.8 Package Considerations

T-R modules generally use a single metal housing containing input and output connectors as shown in Fig. 9.14. Two input connectors are used: one for the bias and control functions and the other for the RF input. The output is an RF connector that connects to the antenna radiating element. The T-R module is sealed usually by welding, is evacuated, and is back-filled with an inert gas. The housing material is typically made from a metal matrix composite with tailored thermal expansion characteristics. The GaAs parts are usually attached to thermal carriers, which in turn are attached to the module wall for cooling. In some designs the RF chips are

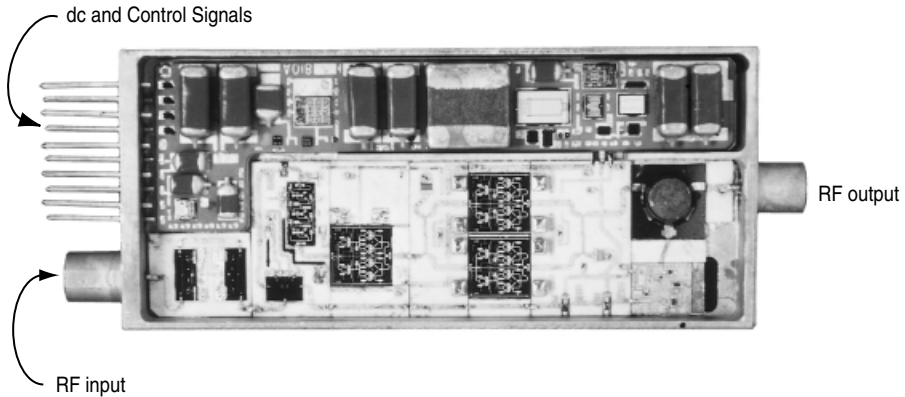


**FIGURE 9.14** Module has one port as RF input, one port for dc bias and control signals, and one port as RF output, which goes to antenna radiator.

attached directly to the module wall. Several modules are typically connected in a row to a coupling manifold. For broadband modules that might operate over the 6–18 GHz band, the output connectors need to be spaced no more than  $\lambda/2$  at the highest operating frequency. Thus placing two or four modules in a single package is desirable. Figure 9.15 shows four 4.5–18 GHz 0.5-W modules in a tray. Here the driver electronics are packaged at the input end of the tray.

### 9.3.9 Thermal Considerations

Cooling of power amplifiers has been discussed earlier. As was indicated, thermal vias through substrates that have been thinned to 3–4 mils are normally used. Thermal spreaders are applied to the module housing, which is cooled by a heat exchanger that cools the entire array face. Flip chip bonding has been the method of

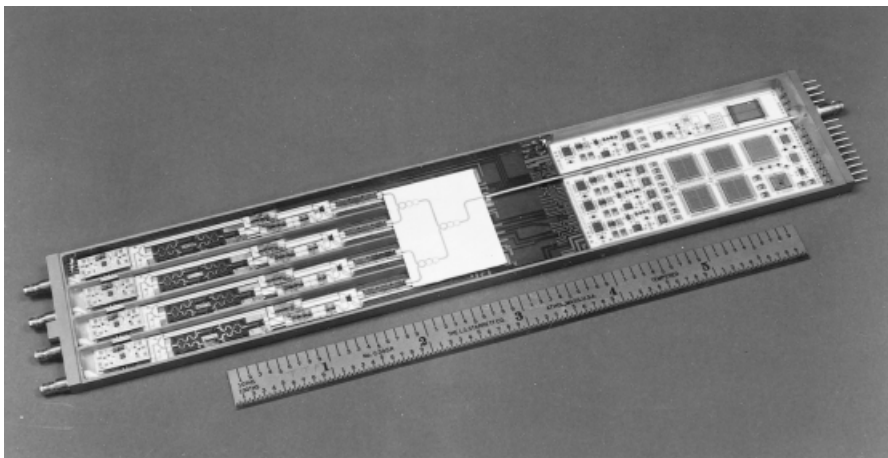


**FIGURE 9.15** Metal tray containing four broadband T-R modules.

choice at some organizations. As was indicated, heat generated in the solid-state amplifiers and other components must be channeled from the point of generation to the module housing and then on to a cooling structure. Two important factors must be considered. These include the cooling capacity of a given aircraft and the allowable temperature rise from the cooling fluid to the device junction. For a fluid temperature of 70°C an increase to 110°C should not reduce the life expectancy of the power devices.

**9.4 PRESENT TRENDS AND FUTURE DIRECTIONS**

To date, the major deterrent to active phased array systems has been the cost of fabricating and arraying large numbers of individual T-R modules into an antenna face. As indicated earlier, much hard work has gone into cost reduction studies for individual modules. The reduction of the number of circuits or other parts within a T-R cell has been important, as has automated assembly and testing. The volume production of modules for a few systems has contributed to cost reductions. ARPA/triservice programs such as MIMIC and MAFET have helped reduce the number of design cycles in module development.

Other efforts for cost savings have utilized two or four T-R modules in a common metal package. The use of LTCC substrates has been valuable in such efforts.

In present designs the cost of active arrays is further increased by the mechanical structure that holds the individual T-R modules, radiating antenna elements, RF feed structure, and cooling manifold.

An ARPA-sponsored program with Westinghouse was established in the early 1990s to explore the possibility of fabricating subarrays of modules compete with cooling and radiating elements at the same time as other structural elements. The program was named RF Wafer Scale Integration (RF-WSI). The program was completed in 1994. The RF-WSI program was followed up by three HDMP contracts to industry teams. The HDMP program was somewhat more conservative than the earlier RF-WSI program. Some key features of these programs are described below.

In the RF-WSI approach, individual T-R modules are eliminated and are replaced by a multielement coplanar subarray. A very thin RF-WSI subarray structure results, which may be flush mounted or incorporated into a vehicle's surface. The goal of the RF-WSI program was to demonstrate the realization/fabrication and testing of five 16-element subarrays. The specific performance goals for an individual T-R cell were:

Transmit:	Bandwidth	6-12 GHz
	Radiated power	0.5 W
	Phase bits	6
	Amplitude bits	5
Receive:	Bandwidth	4-12 GHz
	Noise figure	< 7 dB
	Gain	> 20 dB

In the RF–WSI program, 16 T–R cells were processed on a single 3-inch GaAs wafer. Each T–R cell was chosen to be no larger than a half-wavelength ( $\lambda/2$ ) at the highest operating frequency. The 16 T–R cells then become a layer within an overall package, which forms an active radiating subarray. The parts of the structure include:

- GaAs layer
- Cooling layer or manifold
- dc Bias circuits
- RF feed structure
- Control circuits
- Antenna radiating elements

These are depicted in Fig. 9.16. The entire subarray was less than 2 inches thick, with the circulator layer and the wideband radiating element consuming most of the thickness [13]. The block diagram of a T–R cell is given in Fig. 9.17. The completed subarray is shown in Fig. 9.18. In the RF–WSI approach, individual T–R cells are fabricated in  $\lambda/2 \times \lambda/2$  areas that are at right angles to the signal flow. Thus layers in this structure have been called “tiles” as opposed to “bricks” in the more usual architecture. In the following HDMP program these terms were widely used. The two approaches are depicted in Fig. 9.19.

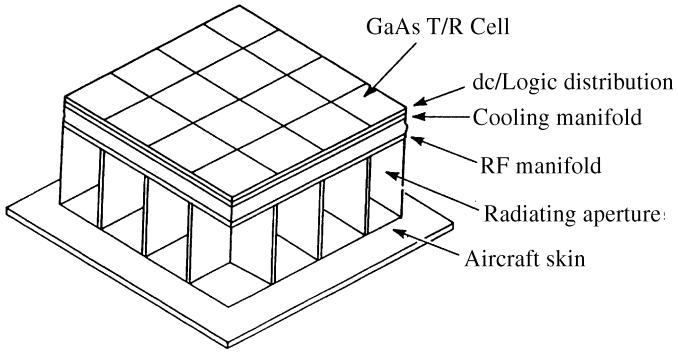
In the RF–WSI configuration, thermal, dc, and RF feed-throughs between the various layers are required. The individual layers must be thermally matched to prevent deformation or cracking as thermal cycling occurs. The realization of large area GaAs chips with high yield was accomplished by using circuit redundancy. Automatic testing and closure of mechanical switches allowed the better parts to be utilized.

The T–R cell that was developed is shown in Fig. 9.20. The redundancy in circuit elements is as follows:

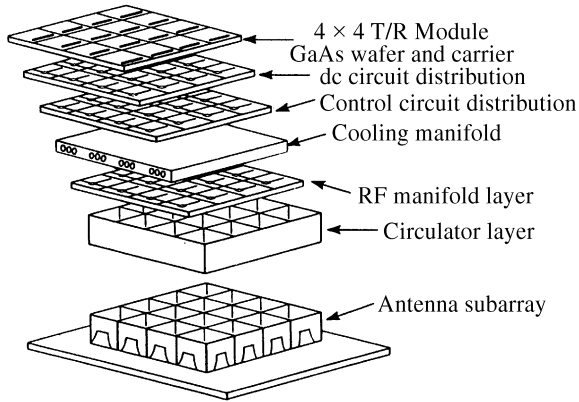
- LNA, three of five required
- T–R switch, one of three required
- Attenuator, one of three required
- 180° Analog phase shifter, one of three required
- 180° Digital phase shifter, one of two required
- Two-stage driver amplifier, two of four required
- Power amplifier, one of three required

With this degree of redundancy, about a 75% T–R cell yield was obtained.

The RF–WSI demonstration chose broadband applications with modest power requirements. The HDMP program focused on higher power radar T–R cells. This program utilized existing GaAs module chip sets. The program has been carried out by three industrial teams. The teams retained the “tile” concept and used a variety of interconnect techniques. Two teams used flip chip mounting of GaAs chips. The



(a)



(b)

FIGURE 9.16 RF-WSI subarray approach: (a) assembled view and (b) exploded view.

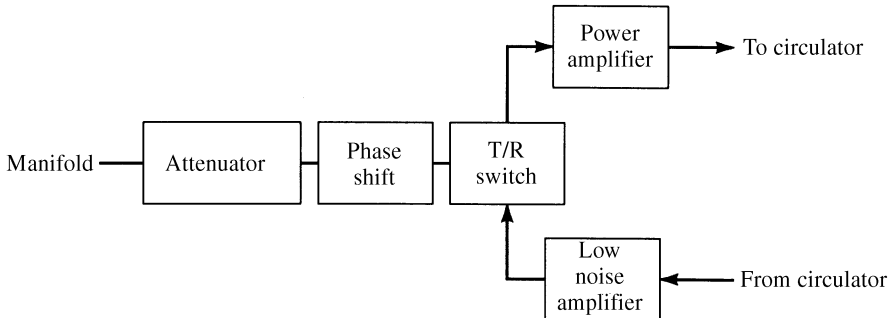
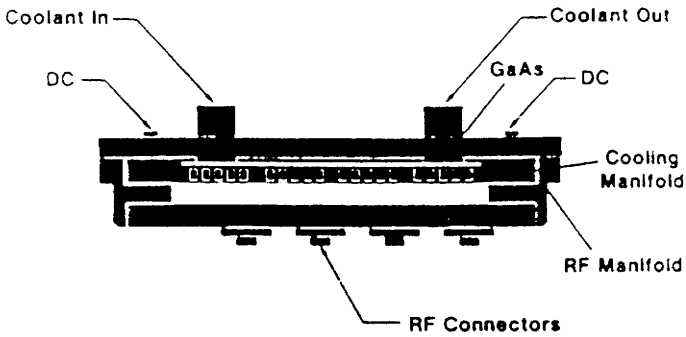
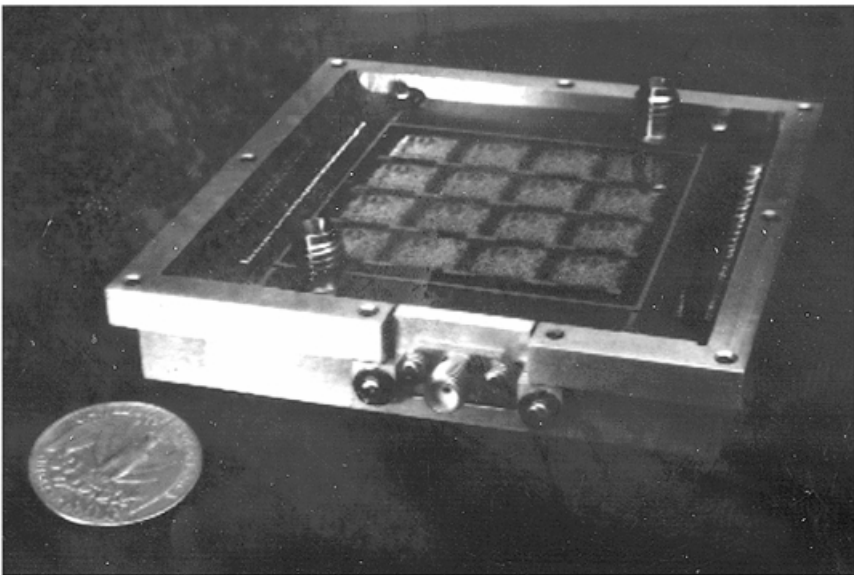


FIGURE 9.17 The block diagram of the RF-WSI cell.



(a) T/R subassembly – side view.



(b) T/R subassembly.

**FIGURE 9.18** The completed RF-WSI subarray.

HDMP program helped define CAD problems, which are still being addressed in the MAFET program. A good discussion of the Hughes team approach is found in the literature [14].

Advances gained in the RF-WSI, HDMP, and MAFET programs should lead to the next generation of active arrays. Airborne applications will continue to focus on X-band and Ku-band frequencies. New applications will be found at higher



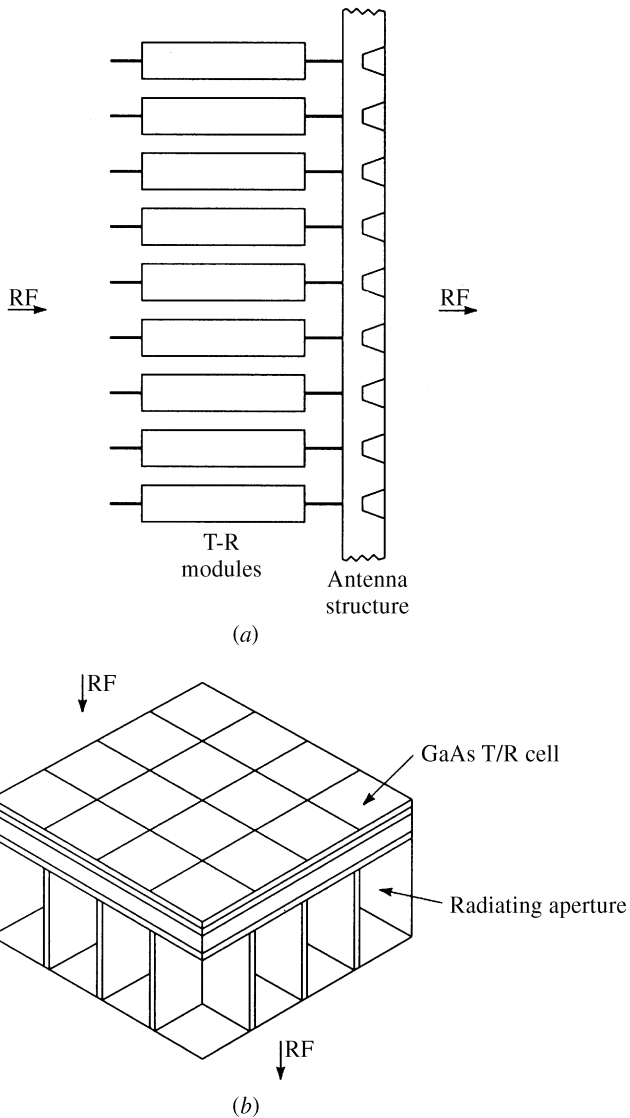


**FIGURE 9.19** The tile and brick approach to T-R module packaging: (a) brick approach and (b) tile approach.

frequencies, where element-to-element spacing is quite small. A 35-GHz T-R cell with redundancy is shown in Fig. 9.21. This cell provides 0.3 W [13] and is suitable for incorporation into an array as shown in Figs. 9.22 and 9.23. Techniques demonstrated at 35 GHz may be extended to the 60 GHz and 77–94 GHz regions. These techniques may be applied to both radar and communication arrays. At these higher frequencies, antenna radiating elements become candidates for direct integration into the module.

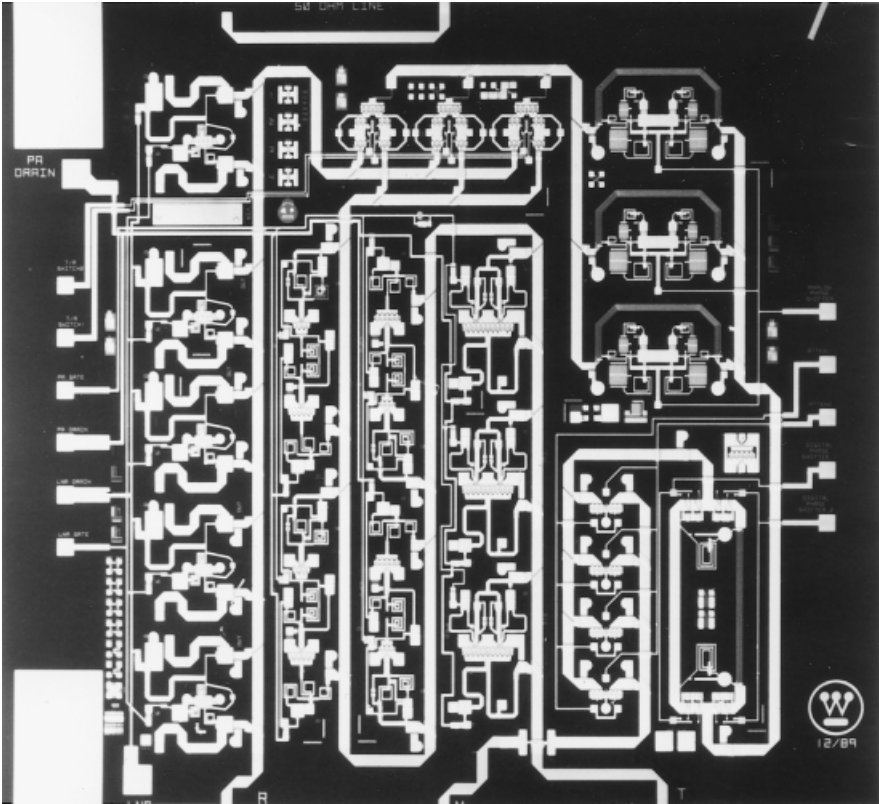


FIGURE 9.20 The RF-WSI cell with redundancy.

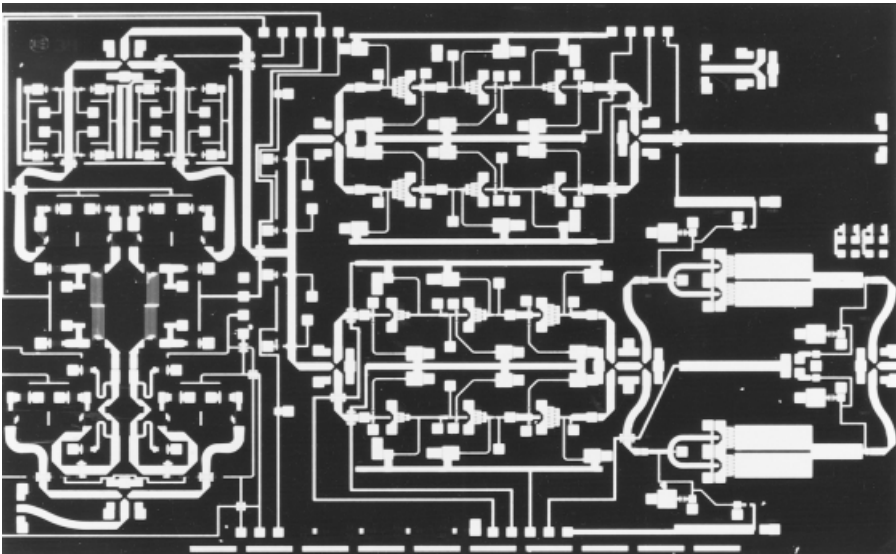


FIGURE 9.21 A 35-GHz T-R cell with built-in redundancy.

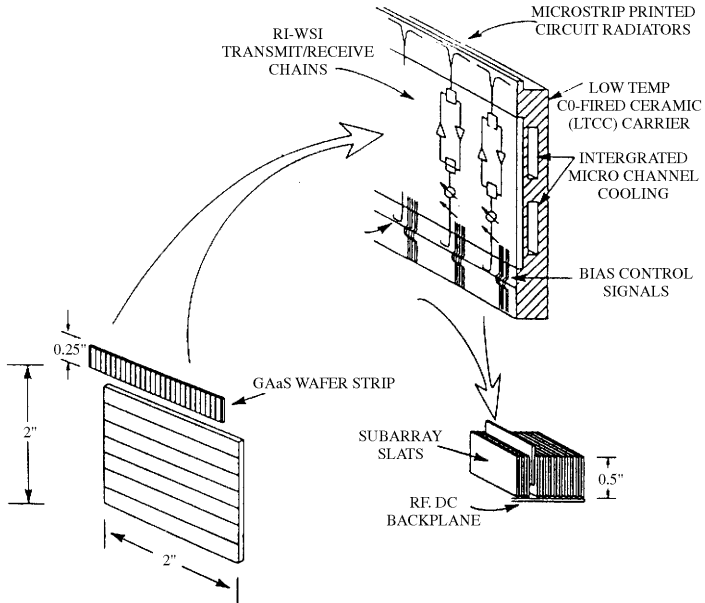


FIGURE 9.22 A 35-GHz packaging concept.

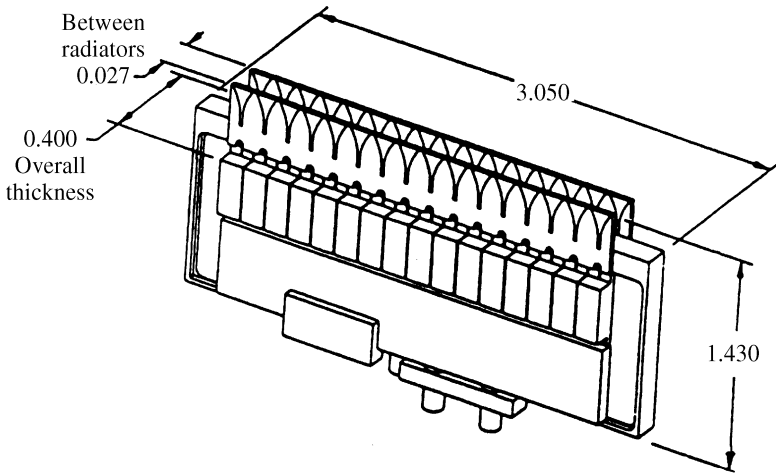


FIGURE 9.23 Double-row slat with common cooling manifold.

**Acknowledgments**

The author is grateful to Mr. John Wassel and Dr. David McQuiddy, Jr. of Texas Instruments for providing photographs of early module work. The author also is appreciative of past interactions with Mr. John Zingaro and Dr. James E. Degenford of Westinghouse (now Northrop-Grumman).

## REFERENCES

1. Skolnik, M. I. (ed.), *Radar Handbook*, McGraw-Hill, New York, 1970.
2. Whicker, L. R. (ed.), *Ferrite Control Components, Vol. 2: Ferrite Phasers and Ferrite MIC Components*, Artech House, Dedham, MA, 1974.
3. Whicker, L. R., "Recent advances in digital latching ferrite devices," *1996 IEEE Int. Convention Record*, vol. 14, part 5, 1996, pp. 49–57.
4. Boyd, C. R. Jr., "A dual-mode latching reciprocal ferrite phase shifter," *IEEE Trans. Microwave Theory Tech.*, vol. MTT-18, Dec. 1970, pp. 1119–1124.
5. Boyd, C. R. Jr., Whicker, L. R., and Jansen, R. W., "Study of insertion-phase variation in a class of ferrite phasers," *IEEE Trans. Microwave Theory Tech. Vol. MTT-18*, Dec. 1970, pp. 1084–1089.
6. Hyltin, T. M., "Modular integrated electronics radar," U.S. Patent 3454945, filed Sept. 18, 1964 and issued July 8, 1969.
7. Hyltin, T. M., and Pfeifer, L. R. Jr., "Final technical documentary report: Phase 1, Modular Electronics for radar applications," Contract Report AFAL-TR-65-318, Dec. 1965.
8. McQuiddy, D. M. Jr., Wassel, J. W., Lagrange, J. B., and Wisseman, W. R., "Monolithic microwave integrated circuits: an historic perspective," *IEEE Trans. Microwave Theory Tech.*, vol. MTT-32, no. 9, Sept. 1984.
9. Whicker, L. R., and Murphy, J. D., "RF-wafer scale integration: A new approach to active phased arrays," *1992 Proc. Int. Conf. Wafer Scale Integration*, 1992, pp. 291–299.
10. McQuiddy, D. M. Jr., Gassner, R. L., Hall, P., Mason, J. S., and Bedinger, J. M., "Transmit/receive module for X-band active array radar," *Proc. IEEE*, vol. 79, no. 3, Mar. 1991, pp. 308–341.
11. Hwang, Y., Lester, J., Schreyer, G., Zell, G., Schrirer, S., Yamauchi, D., Onak, G., Kasody, B., Kono, R., Chen, Y. C., and Lai, R., "60 GHz high-efficiency MMIC chip set development for high-power solid state power amplifier," *1997 IEEE-MTTS Int. Microwave Symp. Dig.*, 1997, pp.1179–1182.
12. Ingram, D. L., Stones, D. I., Huang, T. W., Nishimoto, M., Wang, H., Siddiqui, M., Tamura, D., Elliott, J., Lai, R., Biedenbender, M., Yen, H. C., and Allen, B., "A 6 watt Ka-band MMIC power module using MMIC power amplifiers," *1997 IEEE-MTTS Int. Microwave Symp. Dig.*, 1997, pp. 1183–1186.
13. Whicker, L. R., "Active phased array technology using coplanar packaging technology," *IEEE Trans. Antennas Propag.* vol. 43, no. 9, Sept. 1995, pp. 949–952.
14. Sturdivant, R., Ly, C., Benson, J., and Hauhe, M., "Design and performance of a high density 3D microwave module," *1997 IEEE Int. Microwave Symp. Dig.* 1997, pp. 501–504.

CHAPTER TEN

---

# Integrated Transmit–Receive Circuit–Antenna Modules for Radio on Fiber Systems

---

**HOOSHANG GHAFOURI-SHIRAZ**

School of Electronic and Electrical Engineering  
The University of Birmingham  
Edgbaston, Birmingham, UK

In this chapter we review technologies that have been provided for broadband wireless access based on millimeter-wave radio on fiber systems, and we discuss the main system requirements. A new configuration for the radio on fiber communication system that uses a dual-mode laser diode is designed and presented. Some novel transmit–receive (T–R) modules for the integration of millimeter-wave and optoelectronic devices are also presented in this chapter. These modules have solved various practical issues related to the radio on fiber interface such as size, weight, power consumption, reliability, and cost. As a first step, a diplexer is designed and integrated with a microstrip patch antenna, and then a prototype T–R module is designed and implemented. In addition, a phototransistor is integrated with a microstrip patch antenna, and the feasibility of the two-terminal phototransistor–patch oscillators has been studied.

## 10.1 SYSTEM REQUIREMENTS FOR RADIO ON FIBER

The expected increase in the demand of broadband services forced the investigation of systems that can support high data rates, large bandwidths, unrestricted connectivity, and cost effective solutions for the end-users. Communication systems incorporating both millimeter-wave radio and optical fiber elements are very attractive for transmitting broadband signals, from cost and management perspectives [1]. These systems are expected to play a significant role in telecommunication networks such as interactive multimedia services (IMSS), intelligent vehicle highway systems (IVHS), mobile broadband services (MBSs) based on picocellular architecture, and high speed millimeter-wave wireless local area networks (WLANs) [2]. Radio on fiber systems have also been proposed for the remote operation of satellite earth stations, the antenna remoting at satellite earth stations, the dropwire replacement, and the rural access by radio [1].

Millimeter-wave signals can be distributed to the remote nodes by means of optical fibers that offer huge bandwidths and very low attenuation compared to coaxial cables [3]. The use of waveguides for the distribution of the millimeter-wave signals is practically very difficult because the distances between the central site and the remote sites can be on the order of several kilometers, leading to very high material and installation costs. A significant advantage of the radio on fiber system is the concentration of all expensive equipment of the remote site at a central location, which is shared among a number of remote nodes, where control and monitoring of the system can easily be achieved. Various functions such as signal processing, up-conversion, or down-conversion can be performed centrally and therefore the system will provide maximum flexibility and reduced complexity. A simplified configuration of the radio on fiber network is shown in Fig. 10.1. The millimeter-wave signals

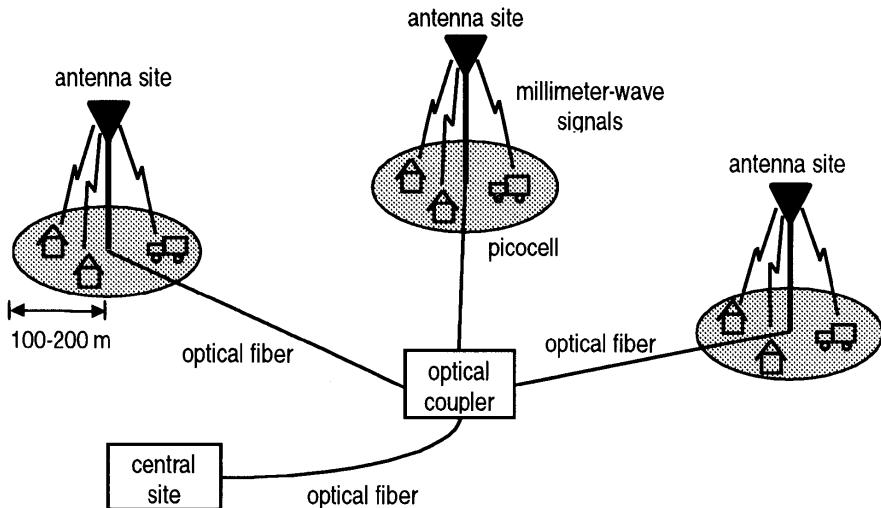


FIGURE 10.1 Simplified scenario for radio on fiber system.

are generated at the central site and placed on an optical carrier for distribution by means of optical fibers to the radio nodes or antenna sites. Each radio node or antenna site serves a cell with a diameter of a few hundred meters. The equipment required at the antenna sites can be of low cost and low complexity since the expensive equipment and circuitry are moved to the central site. Operation in the low loss silica fiber region of 1550 nm is preferred because of availability of optical amplifiers, which are required to compensate for the splitting losses encountered in passive optical networks.

The frequency bands of 62–63 GHz and 65–66 GHz have been allocated in Europe for MBSs. The move to the 60-GHz region is due to the spectral congestion at microwave frequencies. The frequencies in this region have some advantages for short-range links because the atmospheric attenuation at 60 GHz is around 14 dB/km, which means that frequency reuse in a picocellular environment leads to greater spectral efficiency [4]. Furthermore, the antennas have very small dimensions, leading to low costs when they are manufactured in volume. These features indicate the suitability of using radio on fiber systems, especially in short-range and low power links. Such a system is likely to provide the most cost-effective technology for the broadband wireless service provision.

## 10.2 OPTICAL GENERATION OF MILLIMETER-WAVE SIGNALS

Millimeter-wave modulation using commercially available optical sources and distribution of these high frequencies by means of optical fibers are not straightforward. Direct modulation of laser diodes is restricted to a maximum frequency of around 30 GHz. The modulation bandwidth can be extended to 100 GHz by using external optical modulators [5], but the use of standard fiber links with chromatic dispersion  $D = 17$  ps/(nm-km) at  $\lambda = 1550$  nm, limits the fiber link length. Due to different propagation times of the spectral components generated by the laser source, the resulting millimeter-wave power will be degraded and the signal will be distorted. According to Hofstetter et al. [6], even with ideal external modulators operating at a modulation frequency of 30 GHz, the millimeter-wave power vanishes after propagating through a 2.2-km fiber link.

Several other techniques for optical generation and distribution of millimeter-wave signals have been investigated to overcome these limitations. The main techniques are (1) the FM-IM method [7], (2) resonant enhancement of semiconductor laser response [8], (3) optical injection-locking of Fabry-Perot laser modes [9], (4) optical heterodyning [10–12], (5) the stabilized mode-locked laser diode [13], (6) master/slave injection-locked distributed feedback (DFB) laser configuration [14], and (7) a dual-mode DFB semiconductor laser [15]. The method of FM-IM uses the nonlinear properties of the dispersive fiber to convert frequency modulation of a laser to intensity modulation. The method of resonant enhancement of lasers requires a synthesizer at the millimeter-wave frequency and the devices must be able to respond to this frequency. The method of optical injection-locking of Fabry-Perot lasers requires master and slave lasers with careful optical alignment and

a high level of temperature control. Optical heterodyning involves two semiconductor lasers and requires a feedback system to control the frequency or the phase of the generated signal. The master/slave injection-locked DFB laser configuration method is similar to the method of optical injection-locking of Fabry-Perot laser modes, but in this case, the lasers are single-mode devices and each contributes a single mode to the output signal. In addition, this technique gives the benefit of allowing great flexibility in the choice of beat signal. The dual-mode laser method offers the prospect of high power levels, using one laser, which is subharmonically locked to the millimeter-wave frequency of interest. In the following sections, some of these techniques for the optical generation of millimeter-wave signals will be described in more detail.

### 10.2.1 FM-IM Method

The method of FM-IM uses the nonlinear properties of the dispersive fiber to convert frequency modulation of a laser to intensity modulation. This method of generating millimeter-wave radio signals uses a laser diode designed in such a way that its optical carrier frequency can be modulated by application of a drive signal to one of the laser terminals [7]. The optical spectrum of a frequency-modulated laser contains lines spaced by the drive frequency, and millimeter-wave signals are generated by the beating between widely spaced sidebands on a photodetector. The intensity of a pure FM signal is constant, and does not induce any photocurrent at harmonics of the drive frequency. However, if the light is propagated over a dispersive optical fiber, then the relative phases of the optical sidebands are changed, and consequently the light intensity fluctuates at harmonics of the laser drive frequency.

This technique of FM-IM has been analyzed theoretically, and modulation depth  $M_p$  of each harmonic at the output of the photodetector, which is defined as the ratio of the amplitude of the alternating photocurrent at the  $p$ th harmonic to that of dc, is given by [7]

$$M_p = |2J_p[2\beta \sin(p\phi)]| \quad (10.1)$$

where  $J_p$  is the  $p$ th order Bessel function of the first kind,  $\beta$  is the FM index of the laser, and  $\phi$  is an angle related to the fiber group velocity dispersion parameter  $D$ , as

$$\phi = \frac{1}{2}\omega^2\beta_2z = -\frac{\omega^2}{4\pi} \cdot \frac{D\lambda^2}{c}z \quad (10.2)$$

where  $\lambda$  is the free-space wavelength of the laser,  $c$  is the speed of light,  $z$  is the fiber length, and  $\omega$  is the angular frequency of the drive signal applied to the laser. The maximum modulation depth for the  $p$ th harmonic can be obtained when

$$2\beta \sin(p\phi) = j'_{p,1} \quad (10.3)$$



where  $j'_{p,1}$  is the first zero of the derivative of the  $p$ th order Bessel function. Thus to obtain the maximum modulation depth for the  $p$ th harmonic at the receiver it is necessary to adjust the FM index  $\beta$  to an optimum value. This can be achieved by choosing the fiber length such that  $p\phi = \pi/2$ .

The theoretical dependence of the modulation depth versus the FM index for different harmonics is shown in Fig. 10.2, where the value of  $\phi$  used in the calculations is 0.027 rad [7]. Fig. 10.2 indicates clearly that for the 10th harmonic an intensity modulation depth of about 60% can be achieved. The corresponding values of IM depth for the two higher harmonics are lower.

The method of FM-IM for generation of millimeter-wave signals is criticized by many researchers, as it is not appropriate for the radio on fiber system. This is because the technique of FM-IM strongly depends on the fiber length, which makes it unsuited to the provision of networked services, due to the differences in path length to the various antenna sites in the system. However, a full analysis of the FM-IM method is presented in [42].

### 10.2.2 Optical Heterodyning Method

The optical generation of millimeter-wave signals using the optical heterodyning method is based on the coherent mixing of two optical signals on a photodetector. Coherent mixing involves two optical fields of frequencies  $\nu_1$  and  $\nu_2$ , which are mixed on a photodetector. In order to show the effect of coherent mixing, the electric fields of the two optical modes are expressed (neglecting their phase terms) as

$$e_1(t) = e_{p1} \cos(2\pi\nu_1 t) \tag{10.4}$$

$$e_2(t) = e_{p2} \cos(2\pi\nu_2 t) \tag{10.5}$$

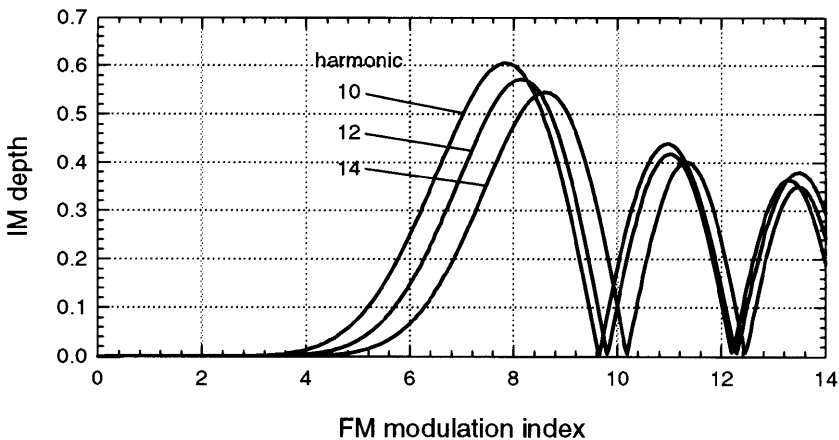


FIGURE 10.2 Modulation depth against FM index.

where  $e_{p1}$  and  $e_{p2}$  are the peak values of the electric fields. These two fields are added and mixed on the surface of a photodetector. The resulting beat photocurrent  $I_{ph}(t)$  can be expressed as

$$I_{ph}(t) \propto e_{p1}e_{p2} \cos[2\pi(v_1 - v_2)t] \quad (10.6)$$

By controlling the difference frequency  $\Delta v = v_1 - v_2$ , a millimeter-wave signal at the required frequency can be generated. When the electric field amplitude of one of the signals is modulated by the information message  $m(t)$ , then the two fields may be written as

$$e_1(t) = m(t)e_{p1} \cos(2\pi v_1 t) \quad (10.7)$$

$$e_2(t) = e_{p2} \cos(2\pi v_2 t) \quad (10.8)$$

In this case, the photocurrent generated becomes

$$I_{ph}(t) \propto e_{p1}e_{p2}m(t) \cos[2\pi(v_1 - v_2)t] \quad (10.9)$$

The resulting term in Eq. 10.9 has the required frequency and also includes the modulation information  $m(t)$ , which, if required, can be a set of subcarriers. Thus the detected photocurrent spectrum consists of a central unmodulated carrier together with two subcarriers.

One method for millimeter-wave generation is based on the Mach–Zehnder (MZ) optical modulator [16]. The MZ optical modulator has an output field described by [10,17]

$$e_{out}(t) = e_{in}(t) \cos\left(\frac{\pi V_m(t)}{2 V_\pi}\right) \quad (10.10)$$

where  $V_m(t)$  is the modulating voltage applied to the modulator,  $e_{in}(t)$  is the incident optical field, and  $V_\pi$  is the bias of the modulator. When a sinusoidal modulating signal of frequency  $\omega$  is added to the bias voltage of the modulator, the modulating signal becomes [10,17]

$$V_m(t) = V_\pi(1 + \varepsilon) + \alpha V_\pi \cos(\omega t) \quad (10.11)$$

where  $\varepsilon$  and  $\alpha$  are the bias and signal levels applied to the modulator normalized to  $V_\pi$ . Consequently, the output electric field of the modulator is given by

$$e_{out}(t) = \cos\left[\left(\frac{\pi}{2}[(1 + \varepsilon) + \alpha \cos(\omega t)]\right)\right] \cos(2\pi v_0 t) \quad (10.12)$$

where  $\nu_0$  is the optical frequency applied to the modulator. Equation (10.12) can be expanded using Bessel function expansion as

$$\begin{aligned}
 e_{\text{out}}(t) = & J_0\left(\alpha\frac{\pi}{2}\right)\cos\left(\frac{\pi}{2}(1+\varepsilon)\right)\cos(2\pi\nu_0t) \\
 & - J_1\left(\alpha\frac{\pi}{2}\right)\sin\left(\frac{\pi}{2}(1+\varepsilon)\right)\cos(2\pi\nu_0t \pm \omega t) \\
 & - J_2\left(\alpha\frac{\pi}{2}\right)\cos\left(\frac{\pi}{2}(1+\varepsilon)\right)\cos(2\pi\nu_0t \pm 2\omega t) \\
 & + J_3\left(\alpha\frac{\pi}{2}\right)\cos\left(\frac{\pi}{2}(1+\varepsilon)\right)\cos(2\pi\nu_0t \pm 3\omega t) \\
 & + \dots
 \end{aligned} \tag{10.13}$$

where  $J_i$  is the Bessel function of the first kind. It should be noted that all  $J_{2n}(\alpha\pi/2)$ ,  $n = 0, 1, \dots$ , terms will vanish when the modulator is biased at  $V_\pi(\varepsilon = 0)$ . In this case, the output spectrum of the modulator has two strong components centred at  $\nu_0$  that are separated by  $2\omega$ . It is possible to suppress the amplitude of the higher order terms to at least 15 dB below the two major components by controlling the bias point of the modulator [18].

Because both optical carriers separated by the frequency difference  $\Delta f$  are generated from one single laser with linewidth  $\Delta\nu$ , their phase noise is completely correlated. This leads to very narrow linewidth electrical signals. O'Reilly et al. [18] have shown that a fiber length of several tens of kilometers will not degrade the electrical linewidth seriously due to decorrelation of the noise processes caused by dispersion-induced differential delay. Also, there is no broadening of the electrical carrier due to the phase noise of the original laser source. However, a propagation delay between the optical carriers, caused by chromatic dispersion at the optical fiber, means that at the photodetector the phases of the two optical carriers are not completely correlated. Therefore, power degradation exists due to the broadening of the electrical linewidth of the millimeter-wave carrier. Hofstetter et al. [6] showed that for a standard single-mode fiber with chromatic dispersion of  $D = 17$  ps/(nm·km), at an operation wavelength of 1550 nm, and by use of commercially available laser with  $\Delta\nu = 20$  MHz, the fiber dispersion effect is negligibly small. For a 30-GHz millimeter-wave signal transmitted through a fiber of 100-km length, the chromatic dispersion leads to a propagation time delay of 0.41 ns, which results in a negligible power degradation of below 0.25 dB. A similar result will be obtained for a 60-GHz signal, provided that the length of the optical link  $L < 100$  km.

A block diagram of a dual-mode source arrangement is shown in Fig. 10.3. The optical source used in this technology is a conventional distributed feedback laser with an optical frequency  $\nu_0$ , which is connected to a MZ modulator. If the modulator is biased appropriately, two optical carriers will be generated. The frequencies of the two optical carriers differ by the required millimeter-wave frequency  $\Delta f$ , which is equal to twice the drive frequency  $f$  of the modulator. Therefore, if the driving frequency is 30 GHz, the two carriers are separated by 60 GHz. The two optical carriers are separated by means of a MZ filter, and by

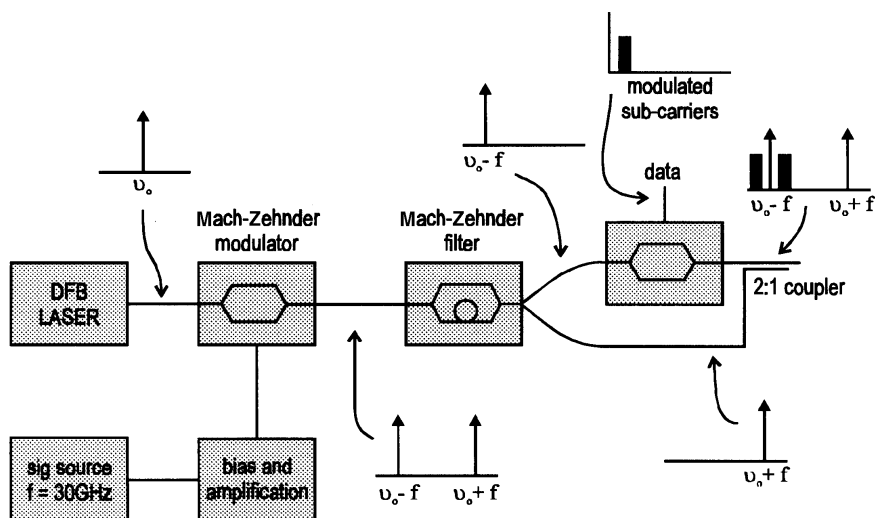


FIGURE 10.3 Dual-mode source using Mach-Zehnder frequency-doubling method.

employing another MZ modulator, one of the carriers (i.e.,  $\nu_0 - f$ ) can be modulated by the data signal. Both optical signals are sent via the optical fiber distribution network to the remote antenna sites where optical heterodyning on the photodetector takes place.

### 10.2.3 Master/Slave Injection-Locked DFB Laser Method

The technique of master/slave laser arrangement for optical generation of millimeter-wave signals was demonstrated initially by Goldberg et al. [19] and later by Schöll and Burkhard [20]. However, this technique was modified recently [14] in such a way that it generates millimeter-wave signals with high efficiency, purity, and stability. The lasers are in a series (master/slave) configuration, and very low phase noise is produced in the beat signal simply by subharmonic electrical injection of the slave laser.

The method presented by Noël et al. [14] differs from the earlier work of Goldberg et al. [19], who used a master/slave laser arrangement, in which the selection and locking of two modes from a slave Fabry-Perot laser were used to generate a beat frequency in a photodiode. In the case of Noël et al. [14], the lasers are single-mode devices and each contributes a single mode to the output. In addition, the electrical injection-locking is used to provide stability and purity to the output signal.

The arrangement of the master/slave technique is shown in Fig. 10.4. Each laser contributes a single mode, and the difference between the two optical modes is the desired millimeter-wave frequency. The output of the slave laser consists of the master laser mode and the slave laser mode. These modes will be coherently mixed on a fast photodiode to produce the desired millimeter-wave signal. However, if an

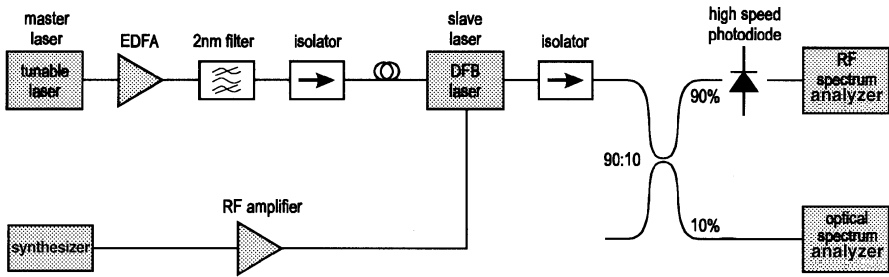


**FIGURE 10.4** Master/slave experimental arrangement for optical generation of millimeter-wave signals.#

electrical drive is used to inject the slave laser at a subharmonic of the beat frequency, a series of sidebands will be generated from the slave laser. The master laser mode, then, will lock one of the slave laser sidebands, which results in phase noise cancellation at the output signal. The resulting linewidth of the millimeter-wave signal is derived from the electrical drive source (synthesizer), which can have high purity.

In this experiment, the reported beat frequency between two optical modes (i.e., the millimeter-wave frequency) is in the range of 50 GHz. The master laser used at the output was a tunable laser, which allowed for fine detuning of the optical frequency. An erbium-doped fiber amplifier (EDFA) was used to compensate for the optical insertion loss of the slave laser. Because the EDFA produces amplified spontaneous emission, a 2-nm bandpass filter was used to remove this effect. The master laser signal was coupled to the coated facet of the DFB slave laser, and the output was taken from the uncoated facet of the slave laser.

The two optical modes were launched into a high-speed edge-coupled PIN photodiode using a 90:10 optical coupler. The output of the photodiode was observed on an RF spectrum analyzer, and the other arm of the coupler was used to monitor the optical modes on an optical spectrum analyzer. In order to show the effect of the electrical injection of the slave laser, the optical spectrum of the output is shown in Fig. 10.5.

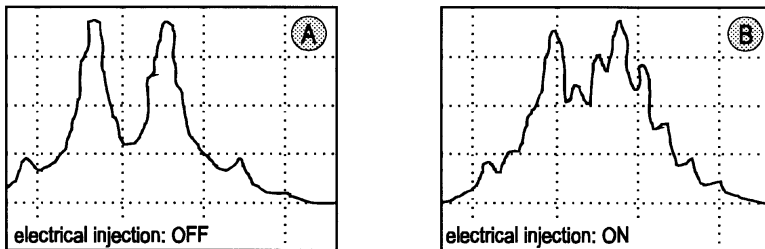


**FIGURE 10.5** Electrical injection effect on the optical spectrum of the master/slave configuration.

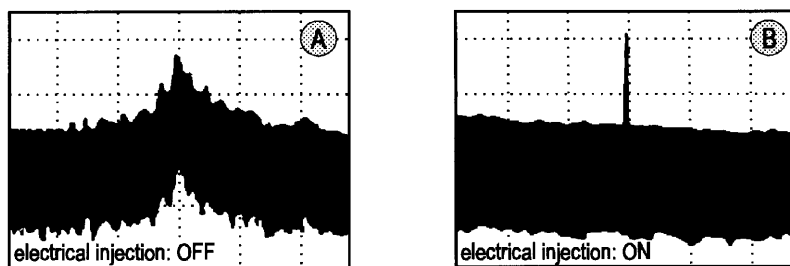


**FIGURE 10.6** Electrical injection effect on the electrical spectrum of the master/slave configuration.

When no electrical injection was applied to the slave laser, the continuous wave (CW) of the master and slave modes has a wavelength separation that corresponds approximately to the desired millimeter-wave frequency. When the electrical injection was applied, a series of sidebands were generated from the slave laser. The electrical spectrum of the photodiode output is shown in Fig. 10.6. When no electrical injection is applied, the phase noise is high. However, when the electrical injection is applied, the output signal becomes extremely pure. The signal purity is comparable to the phase noise produced by the synthesizer.

The technique of master/slave laser for optical generation of millimeter-wave signals is simple to implement and gives high purity, high power, and highly stable signals that can be tuned theoretically to any desired frequency in the range of interest. Furthermore, the chromatic dispersion should not present any problems over long transmissions, since the output optical spectrum consists of two optical modes [21].

#### 10.2.4 Dual-Mode Semiconductor Laser Method

Optical mixing is an efficient method for a millimeter-wave signal but generally requires complex feedback systems and phase control. A dual-mode laser diode developed at BT Labs is designed to provide the high power associated with optical mixing but without the need for feedback [4]. Furthermore, because the two optical modes are generated in the same cavity, it is possible to lock them in phase by applying an electrical injection signal to the device.

The laser is a specially modified multisection long-cavity DFB device in which oscillation occurs simultaneously on both sides of the Bragg frequency [22]. The difference between the frequencies of these two optical modes is the desired millimeter-wave frequency. The separation of the two optical modes can be adjusted by reducing the grating strength coefficient. The 2-nm-long DFB laser diode used in the experiment was operated in the region of 1560 nm and was divided into four sections. It was fabricated on a specially designed submount with four independent tabs to bias each section. Modulation of the device has been performed by applying the modulating signal to one of its sections.

Figure 10.7 shows the optical output spectrum of the dual-mode laser under typical operating conditions [15]. In this experiment, the optical modes were separated from each other by 0.48 nm, which corresponds to a frequency of around 57 GHz. Figure 10.7 clearly indicates that all other modes have been suppressed by more than 20 dB.

The optical output of the device is launched into a single-mode fiber and then the light coming out of the fiber is coupled into a wideband InGaAs edge-coupled PIN photodiode [23], with a dc responsivity of 0.27 A/W and a response of -10 dB relative to dc at 60 GHz. The experimental setup of the dual-mode laser and the associated circuitry for phase-locking measurements [15] is shown in Fig. 10.8.

Without electrical injection-locking of the dual-mode laser, the beat frequency signal is unstable and has a linewidth of around 100 MHz. This is because the two optical modes from the device are not phase-locked. However, when a signal with frequency of 6.3 GHz (i.e., ninth subharmonic) was injected into one of the device sections, the generated millimeter-wave signal at 57 GHz, was of high purity with a linewidth of less than 10 Hz and a locking range of about 500 MHz. The phase-locked millimeter-wave signal is shown in Fig. 10.9. As reported by Wake et al. [15], the purity of the signal did not degrade when transmitted over 25 km of optical fiber.

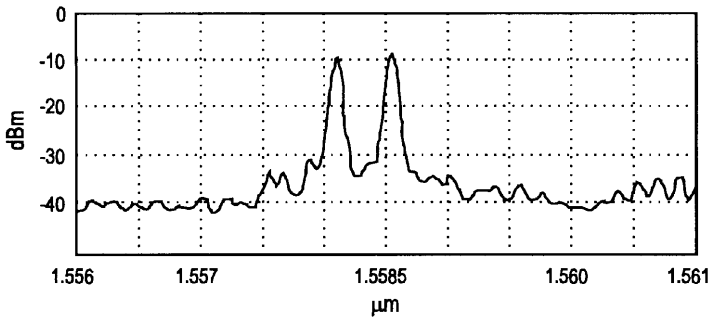


FIGURE 10.7 Optical spectrum of the dual-mode laser output.

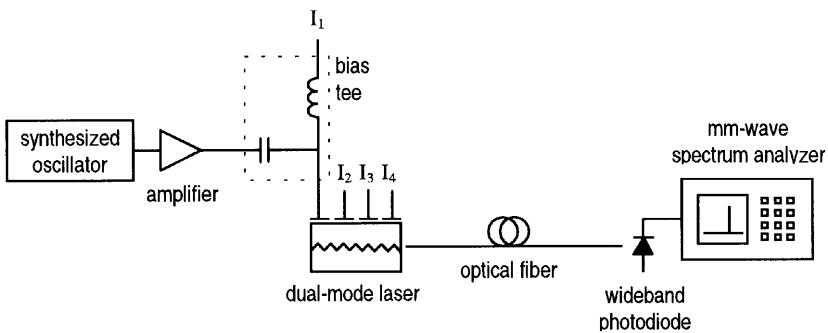


FIGURE 10.8 Experimental setup for phase-locking measurements.

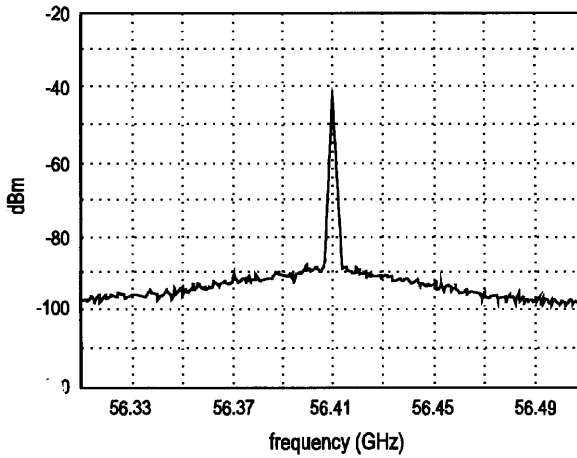


FIGURE 10.9 Electrical spectrum from phase-locked dual-mode laser.

The beat frequency can be tuned over a range of about 1 GHz by appropriate control of the individual bias current. The tuning range of the beat frequency is an important parameter, since there is a possibility for the beat frequency to be significantly different from the desired operating frequency due to the processing limitations in practice.

The modulation depth of the phase-locked signal is less than 100%, as a consequence of using subharmonic injection-locking as opposed to fundamental injection-locking. However, advantages such as simple and compact design of the device and tunability of optical output make the dual-mode laser suitable for optical generation of millimeter-wave signals.

### 10.3 OPTICAL DETECTION OF MILLIMETER-WAVE SIGNALS

Various forms of optical receiver can be considered for radio on fiber systems. The simplest is a photodiode followed by an amplifier. One approach is the use of an edge-coupled or waveguide PIN photodiode, which gives a very high bandwidth while maintaining a good responsivity [24]. Another approach is the use of optically sensitive heterojunction bipolar transistors (photoHBTs) [25–27]; electroabsorption modulators have also been suggested [28].

#### 10.3.1 Edge-Coupled PIN Photodiode Method

Edge-coupled photodiodes have been reported [23], with a bandwidth of 50 GHz and a quantum efficiency of 50%. This type of device has been used extensively in millimeter-wave radio on fiber system demonstrators. An interesting property of this device is its ability to work without an external bias. This property has been



exploited to demonstrate radio on fiber transmitters with no electrical power requirement [24].

A schematic cross-section of the photodiode is shown in Fig. 10.10. In this device, the absorber layer forms a part of the core of an optical waveguide. The core is formed using a thick nonabsorbing layer in conjunction with a thin absorber layer that allows the optical waveguide to be designed in such a way as to provide high speed operation, in addition to a large mode size for efficient coupling to optical fiber at the same time.

The frequency response of the edge-coupled PIN photodiode varies considerably depending on packaging arrangements. This specific photodiode is a fully packaged device that incorporates an internal bias network. Using a single-mode lens-ended fiber pigtail, the frequency response of the device is shown in Fig. 10.11. The bandwidth is 40 GHz but the device remains usable at 60 GHz, where its response is only 7 dB below that at dc level.

Because of the very thin absorber ( $0.13 \mu\text{m}$ ) [23], this device has the ability to work well without an external bias. The built-in junction potential can provide sufficient electric field to sweep out the photogenerated carriers. This is an interesting property, which makes this type of device efficient and suitable for detecting the millimeter-wave signals. This is because it reduces the power consumption at the remote site in a radio on fiber system.

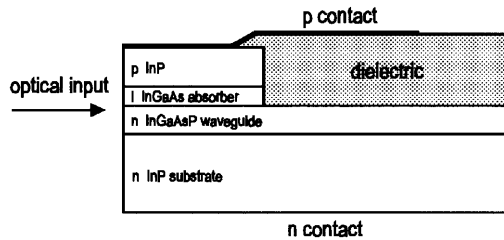


FIGURE 10.10 Schematic cross section of an edge-coupled PIN photodiode.

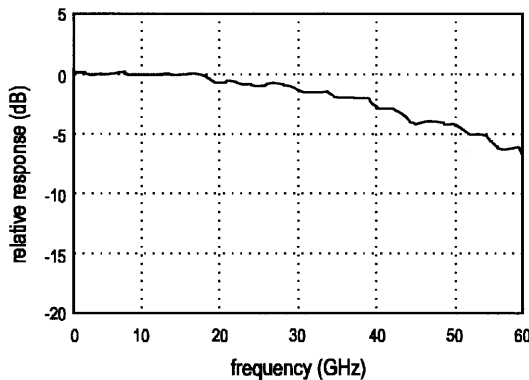


FIGURE 10.11 Frequency response of an edge-coupled PIN photodiode with internal bias network.

### 10.3.2 Heterojunction Bipolar Phototransistor Method

Optically sensitive heterojunction bipolar transistors (photoHBTs) are potentially useful devices for radio on fiber systems, where they can be used as high gain photodetectors, as optically injection-locked oscillators, and as optoelectronic mixers. A two-terminal photoHBT has been developed at BT Labs using the edge-coupled InP/InGaAs technology for efficient optical access [25–27]. A schematic cross section of the device structure is shown in Fig. 10.12.

The structure shows the edge-coupled optical input of the device, where the base bias current is supplied by the dc component of the optical input signal. It should be noted that this structure is inherently common collector.

Wake et al. [25] used an optical heterodyne technique with a matched pair of DFB lasers at a wavelength of 1550 nm, in order to generate beat frequencies up to 30 GHz. The measured frequency response of the photoHBT with emitter bias of  $-1$  V and current of 8 mA is shown in Fig. 10.13. The frequency response of the edge-coupled PIN photodiode, which is illuminated with the same optical power, is plotted on the same graph for comparison. From this figure, it is clear that the

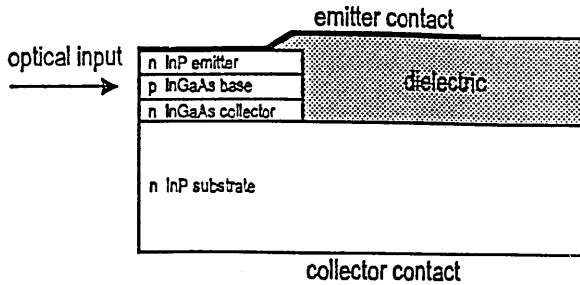


FIGURE 10.12 Schematic cross section of an edge-coupled photoHBT.

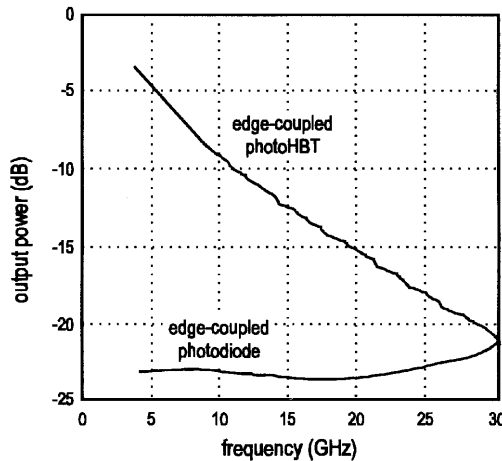


FIGURE 10.13 Frequency response of an edge-coupled photoHBT.

common-collector unity-gain frequency of the edge-coupled photoHBT is greater than 30 GHz.

The peak responsivity of the photoHBT is around 700 A/W, which was obtained with a lens-ended fiber input [25]. The current gain of the transistor was assessed by comparing its responsivity with that of an edge-coupled photodiode, and is found to be around 3000. The photoHBT is extremely simple to fabricate, since the process is based on that used for a photodiode, and combines the functionality of a millimeter-wave photodiode and power-efficient amplifier. The photoHBT is therefore of interest as a millimeter-wave photodetector with gain.

## 10.4 NEW CONFIGURATIONS FOR RADIO ON FIBER SYSTEMS

The advantages of the dual-mode laser diode [15] over other techniques for generating millimeter-wave signals, has led to the design of a new configuration of the radio on fiber system [2]. This new configuration uses the dual-mode laser at the central site of the radio on fiber network. As it is mentioned earlier, the concept of centralization is very important for this technology because it allows control and monitoring of the network from a central location. For instance, it is possible to change the millimeter-wave carrier of the network from the central site. Furthermore, the expensive equipment can be located at the central site where it can be protected from rain, wind, and sun. In addition, the equipment of the central site can be shared among all the remote sites, resulting in a great simplification. Because the dual-mode laser may provide high power levels, the remote antenna units can be operated at lower power consumption.

The integration of the remote site is also important since it allows the cost to be minimized. These requirements lead to the use of planar circuit technology. The use of microstrip antennas will make a highly integrated circuit for the radio interface module. Microstrip antennas have low profile and are light in weight. They can be conformal and are well suited to integration with microwave and millimeter-wave integrated circuits [29].

The new configuration of radio on fiber allows full-duplex operation, and it is capable of using fewer amplifiers at the remote site since it has more available power at the output of the photodetector. The return path is designed in a similar way to that of the microwave optical duplex antenna link (MODAL) demonstrator [18].

The proposed configuration of the radio on fiber system, shown in Fig. 10.14, is divided into two parts shown within dashed boxes. One part is the central site and the other one is the remote site.

The dual-mode laser diode shown in the central site generates two optical modes  $\nu_1$  and  $\nu_2$ , such that  $\nu_1 - \nu_2 = 60$  GHz, at a nominal wavelength of 1550 nm. The input of the dual-mode laser is used to intensity modulate the laser, at baseband or at a low frequency subcarrier, with the information data. The optical signal is transmitted through a standard single-mode optical fiber to the remote site, where it is coupled into a wideband PIN photodiode. The optical modes mix on the surface of the PIN photodiode. The spectrum of the photodiode output consists of a central

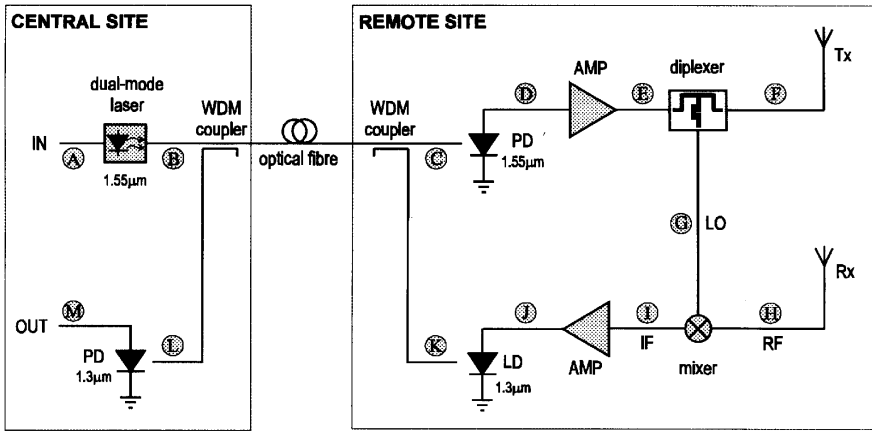


FIGURE 10.14 Block diagram of the proposed radio on fiber system configuration.

carrier at 60 GHz with two sidebands that contain the information data. The millimeter-wave signals from the photodiode are amplified and a diplexer filter selects one of the sidebands for radiation by the transmitting antenna. The diplexer also selects the unmodulated millimeter-wave carrier that is used as the local oscillator for the provision of the return path.

The return path involves a multiplier that mixes the received millimeter-wave signal with the recovered unmodulated carrier from the diplexer. The result of the mixing is a down-conversion of the received millimeter-wave signal, which is used to modulate a low-frequency laser operating at the wavelength of 1300 nm. The optical output of the laser is transmitted back to the central site through the same optical fiber by means of a wavelength division multiplexing (WDM) coupler, as shown in Fig. 10.14. At the central site the return signal is separated again by means of a WDM coupler and coupled into a low-frequency PIN photodiode.

### 10.4.1 Frequency Arrangement of the Radio on Fiber System

An example of the frequency arrangement for this configuration is given in this section. It is assumed that the dual-mode laser generates two optical signals  $\nu_1$  and  $\nu_2$ , such that  $\nu_1 - \nu_2 = 60$  GHz. In addition, a modulating subcarrier  $f_m = 2$  GHz is assumed. With reference to Fig. 10.14, the frequencies at the various positions in the diagram are shown in Table 10.1.

Since the radiating millimeter-wave signal is at 62 GHz, the receiving signal must be at different frequency and is assumed to be at 61 GHz. After mixing with the 60-GHz carrier, the resulting intermediate frequency (IF) is 1 GHz. Therefore, a low cost conventional laser is required, operating at 1300 nm, to transmit the IF signal back to the central site. This frequency arrangement is just an example. The configuration is flexible and can be adapted to the requirements of the specific application. Furthermore, the configuration is transparent to modulation format.

**TABLE 10.1 Frequency Arrangement of the Radio on Fiber System Configuration**

Position	Frequency Arrangement	Frequency
A	$f_m$	2 GHz
D	$(v_1 - v_2) + f_m, (v_1 - v_2) - f_m$	62 GHz, 58 GHz
E	$v_1 - v_2, f_m$ $(v_1 - v_2) + f_m, (v_1 - v_2) - f_m$	60 GHz, 2 GHz 62 GHz, 58 GHz
F	$v_1 - v_2, f_m$ $(v_1 - v_2) + f_m$	60 GHz, 2 GHz 62 GHz
G	$v_1 - v_2$	60 GHz
H	$(v_1 - v_2) + f_r$	61 GHz
I	$f_r$	1 GHz
J	$f_r$	1 GHz
M	$f_r$	1 GHz

**10.4.2 Noise Performance of the Radio on Fiber System**

The noise performance of the radio on fiber system is assessed by the overall noise figure of the system. However, the total noise figure of such a system has been analyzed [30–34] by taking into account the noise contributions of both central and remote sites of the system. Figure 10.15 shows a block diagram of the proposed radio on fiber system where the noise figures associated with the link are also indicated. It consists of the optical link as the first stage and the millimeter-wave link as the second stage. The optical link is defined from the input of the dual-mode laser diode up to the output of the photodetector.

Assuming that the relative intensity noise (RIN) of the dual-mode laser diode is negligible, the total noise figure of the system,  $F_T$ , can be expressed as

$$F_T = L_{opt} \cdot F_{tx} + \frac{L_{rad} \cdot F_{rx} - 1}{G_{tx}/L_{opt}} \tag{10.14}$$

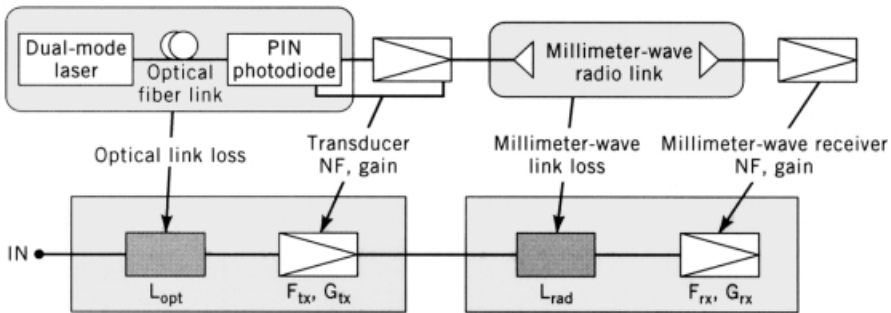


**FIGURE 10.15** Block diagram of the radio on fiber link and associated noise.

where  $L_{\text{opt}}$  is the optical link loss,  $L_{\text{rad}}$  the radio link loss,  $F_{\text{tx}}$  the transducer noise figure,  $F_{\text{rx}}$  the receiver noise figure,  $G_{\text{tx}}$  the transducer gain, and  $G_{\text{rx}}$  the receiver gain.

Some conclusions can be drawn by examining Eq. 10.14. If the transducer gain is much greater than the optical link loss, such that  $G_{\text{tx}}/L_{\text{opt}} \gg 1$ , then the total noise figure  $F_T$  depends mainly on the optical link loss  $L_{\text{opt}}$ . On the other hand, if  $G_{\text{tx}}/L_{\text{opt}} \leq 1$ , then  $F_T$  depends on all system parameters including the optical and radio link losses as well as the transducer and receiver noise figures.

## 10.5 DESIGN OF A DIPLEXER-ANTENNA UNIT

In the radio on fiber system demonstrator of the microwave optical duplex antenna link project [18], and the proposed system configuration described in Section 10.4, diplexers have been used at the remote site in order to recover the unmodulated millimeter-wave carrier, which is required for the provision of the return link. This specific design of the remote site has the advantage of allowing full-duplex operation and in addition eliminates the need of a millimeter-wave local oscillator, which would make the module more complicated in terms of size, weight, and power consumption. The use of a diplexer at the remote site is essential for the proposed system configuration and therefore it must be simple and efficient.

The selected topology for the millimeter-wave diplex filter of the MODAL project [18] was based on the use of two bandstop filters centered at the millimeter-wave carrier and the selected sideband, respectively. This network was preceded also by another bandstop filter that rejects the unwanted sideband. However, the diplexer design can be simplified further, if the narrowband nature of a patch antenna is exploited. Figure 10.16 shows the topology of a simple and efficient design of a diplexer-antenna unit, which is proposed in this research.

The idea behind this design is to use the narrowband properties of the patch antenna for the rejection of the unwanted sideband, preceded by a parallel bandstop filter for selecting the millimeter-wave carrier. The diplexer-antenna unit is based

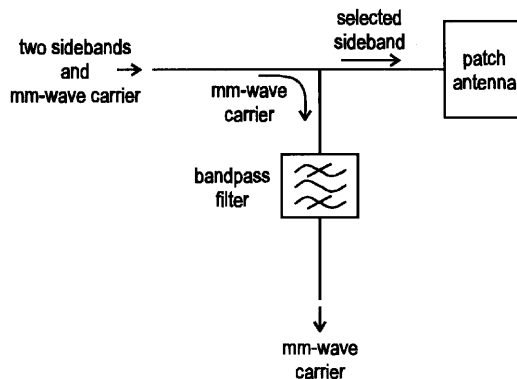


FIGURE 10.16 Diplexer-antenna unit topology.

only on passive microstrip printed circuit technology without involving any active devices or lumped elements, thus reducing the cost of the implementation.

The diplexer is designed using the Microwave Design System (MDS), which is a computer simulation package developed by Hewlett Packard, and experimental results of the integration with a patch antenna are obtained. The frequency is scaled down from 60 GHz to the microwave region of 6 GHz, since this is sufficient to prove and demonstrate the principles of the design.

### 10.5.1 Microstrip Coupled Line Filter Design

The parallel coupled transmission lines can be used to construct many types of filter. This type of filter is suitable for the purpose of the diplexer because the bandwidth that can be achieved with this type is less than 20% [35]. Fabrication of multisection bandpass coupled line filters is particularly easy in microstrip form, which provides very narrowband characteristics [36]. Therefore, the bandpass coupled line filter is chosen for the design of the diplexer.

Detailed theory on the design of coupled line bandpass filters can be found in [35] and [36]. In the following part of this section, a brief description of the design procedure is given, which is sufficient for the design of a diplexer.

Narrowband bandpass filters can be made with cascaded coupled line sections of the form shown in Fig. 10.17. A lumped-element equivalent circuit for a second order (i.e.,  $N = 2$ ) bandpass filter is shown in Fig. 10.18, where the equivalent inductor  $L$ , and capacitor,  $C$ , values are given by the following expressions [35]:

$$L = \frac{2Z_0}{\pi\omega_0} \tag{10.15}$$

$$C = \frac{1}{\omega_0^2 L} = \frac{\pi}{2Z_0\omega_0} \tag{10.16}$$

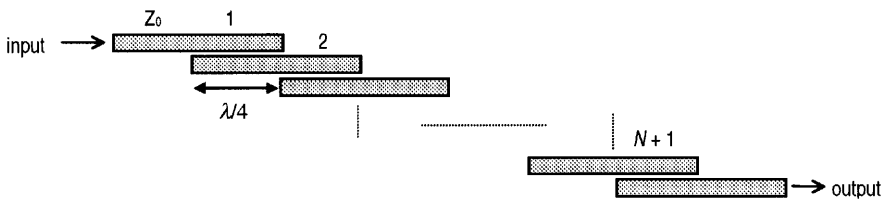


FIGURE 10.17 Layout of an  $N + 1$  section coupled line bandpass filter.

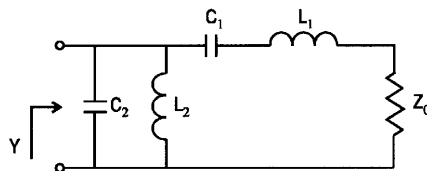


FIGURE 10.18 Lumped equivalent circuit for a bandpass filter for  $N = 2$ .

In the above equations,  $\omega_0 = 1/\sqrt{LC}$  is the center frequency of the filter, and  $Z_0$  is the characteristic impedance of the microstrip transmission line.

Each pair of coupled line sections in Fig. 10.17 leads to an equivalent shunt  $LC$  resonator. An admittance inverter occurs between two successive pairs of  $LC$  resonators. The function of admittance inverters is to transform a shunt  $LC$  resonator into a series  $LC$  resonator, which consequently leads to the equivalent circuit of Fig. 10.18.

The analysis of a single coupled line section has indicated that the length of the coupled line section must be approximately  $\lambda/4$  [35]. This means that the microstrip transmission line length between any two consecutive sections is effectively  $\lambda/2$ . The number of coupled line sections that must be used is  $N + 1$ , where  $N$  is the required order of the filter.

### 10.5.2 Bandpass Filter Design

The conventional structure of the coupled line bandpass filter is not ideal for the purpose of integration as far as the substrate space is concerned. The reason is that the cascaded form of the coupled line sections tends to occupy a substantial area of the substrate, which makes the filter implementation large. A novel idea for minimizing the substrate area occupied by the bandpass filter is to put two consecutive coupled line sections on the same line as illustrated in Fig. 10.19.

The resulting layout structure of the filter is a chopped transmission line that has coupled line sections along its length. This is a third order bandpass filter, which is equivalent to the filter of Fig. 10.17, with four coupled line sections. The length of the resulting coupled line must be approximately  $\lambda/2$ . The small gaps in the middle are necessary in order to create the coupled line structure. Although these small gaps perturb the behavior of the filter, its response can be recovered by adjusting the length and spacing of the coupled lines.

Based on the structure described above, a third order bandpass filter is designed at 6 GHz using the MDS simulation tool. Initially the length of the transmission lines was set to half of the guided wavelength  $\lambda_g$ . The guided wavelength is given by

$$\lambda_g = \frac{\lambda_0}{\sqrt{\epsilon_{\text{eff}}}} \quad (10.17)$$

where

$$\epsilon_{\text{eff}} = \frac{\epsilon_r + 1}{2} + \frac{\epsilon_r - 1}{2} \cdot \frac{1}{\sqrt{1 + 12h/W}} \quad (10.18)$$

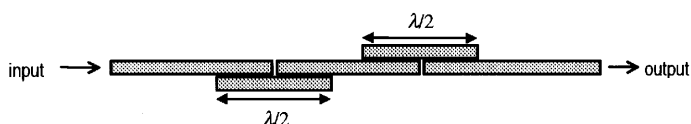


FIGURE 10.19 Layout structure of a third order bandpass filter.



In the above equations,  $\lambda_0$  is the free-space wavelength,  $\epsilon_{\text{eff}}$  is the effective dielectric constant of the substrate of thickness  $h$ ,  $\epsilon_r$  is the dielectric constant of the substrate, and  $W$  is the width of the microstrip line. The characteristic impedance  $Z_0$ , of all filter microstrip lines, is selected to be  $50 \Omega$ . For the design of the bandpass filter, MDS was used to evaluate the width of the  $50\text{-}\Omega$  line.

The optimization capabilities of the simulator are very useful since they allow for automatic adjustments of the various parameters of the circuit in order to satisfy certain conditions. The simulation circuit uses two  $S$ -parameter ports and the goal of the optimization is to maximize the transmission coefficient  $S_{21}$  at 6 GHz. The length and spacing of the coupled line sections may be varied in order to satisfy the goal. In addition, this specific design allows a narrow bandwidth for possible tolerance in the frequency of the millimeter-wave carrier. The circuit, which was used for simulation, is shown in Fig. 10.20.

The substrate used has dielectric constant  $\epsilon_r = 2.33$  and thickness  $h = 0.508$  mm. It is assumed that the frequency of the millimeter-wave carrier is 6 GHz and the frequencies of the two sidebands are 5.6 GHz and 6.4 GHz. The frequency response of the filter is shown in Fig. 10.19. The filter has a sharp roll-off in the transition-bands and almost a flat response in the pass-band. The  $-1$ -dB bandwidth of the filter is 60 MHz with 38.7-dB rejection of the 5.6-GHz component and 43.6-dB rejection of the 6.4-GHz component.

Although a third order filter is designed for the assumed specifications of the system, a second order would be sufficient for the rejection of the stopbands of the filter. However, if the two sidebands are at 5.8 GHz and 6.2 GHz, then at least a third order filter must be used. The above third order filter gives 28.4-dB rejection of the 5.8-GHz sideband and 30-dB rejection of the 6.2-GHz sideband.

### 10.5.3 Patch Antenna Matching

The diplexer-antenna unit can be matched to any impedance value depending on the design of the system. Since the bandpass filter is designed for  $50\text{-}\Omega$  impedance, the patch antenna will be matched to the same value. The easiest way to achieve the patch antenna impedance matching is to use a quarter-wavelength transformer. As is known, the imaginary part of the patch impedance is zero at the resonant frequency; therefore the patch is designed to resonate at 5.6 GHz and its impedance can be estimated either using the formulas in [37] or using the computer simulator. When the real part of the patch is determined, the characteristic impedance of the quarter-wavelength transformer  $Z_q$ , is given by

$$Z_p = \sqrt{Z_p Z_0} \quad (10.19)$$

where  $Z_p$  is the patch impedance at the resonant frequency, and  $Z_0$  is the transformed impedance, which is  $50 \Omega$  in this case. The length of the transformer line is  $\lambda_g/4$ . The matching network of a 5.6-GHz antenna is designed and simulated with a passive microwave simulator called Prelude, developed by Boulder Microwave

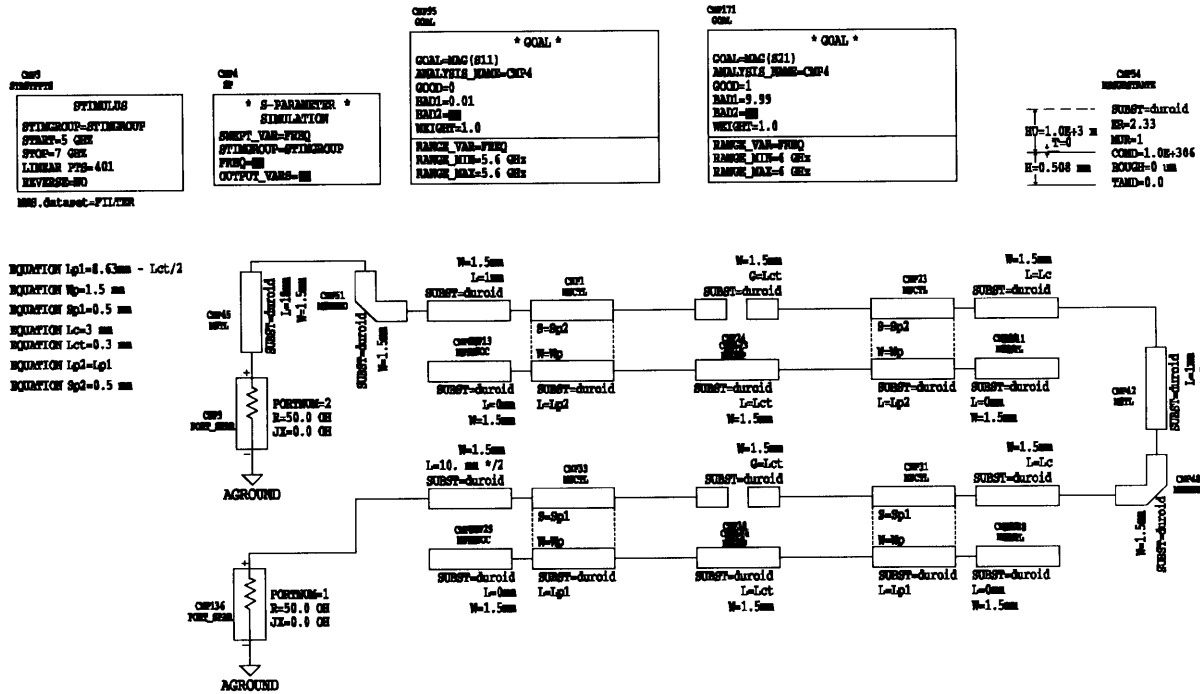


FIGURE 10.20 Simulation circuit of the 6-GHz bandpass filter.

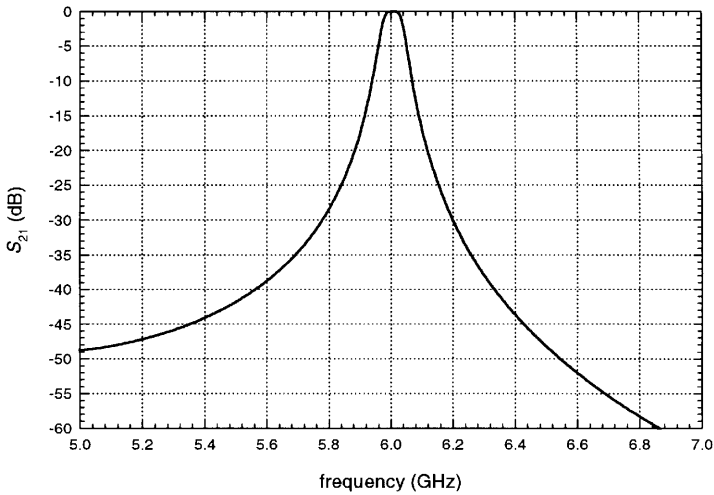


FIGURE 10.21 Frequency response of the bandpass filter.

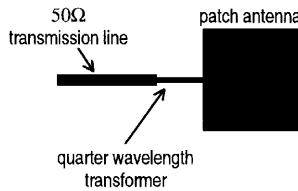


FIGURE 10.22 Simulated structure with Prelude.

Technologies. Prelude provides an easy-to-use interface for drawing and automatically meshing geometries of arbitrary shape and a powerful full-wave simulator for simulating the response of passive structures. It is based on the integral-equation and moment-method approach. The structure of the patch with its matching network is shown in Fig. 10.22.

The reflection coefficient  $S_{11}$  of the structure is measured at the input of the 50-Ω transmission line and is shown in Fig. 10.23. The reflection coefficient at 5.6 GHz is better than  $-20$  dB, which is considered a reasonable match.

If the patch antenna is not designed to resonate exactly at a specific frequency, then the impedance of the patch at the desired frequency is not purely real, and, consequently, the quarter-wavelength transformer does not transform to the required impedance. In such cases, it is possible to let the computer simulator vary the length and the characteristic impedance of the transformer line in order to achieve the 50-Ω impedance. This is often a feasible optimization.

For the design of the diplexer-antenna unit, the patch antenna was designed based on the transmission line model given in [37]. The characteristic impedance of the quarter-wavelength transformer and its length were calculated theoretically and the values were used as the initial conditions for the MDS simulator. The transmission

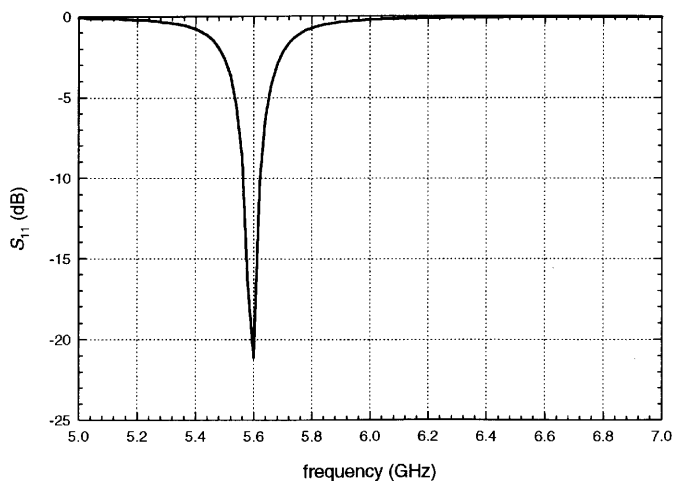


FIGURE 10.23 Reflection coefficient of a 5.6-GHz patch with matching network.

line model of the patch antenna, shown in Fig. 10.24, was used as an MDS subcircuit model for the patch oscillator circuit.

#### 10.5.4 Diplexer-Patch Integration

The integration of the diplexer and the patch antenna is based on the idea shown in Fig. 10.16. The patch antenna has a resonant frequency of 5.6 GHz. This means that if the patch is matched to a 50- $\Omega$  line at 5.6 GHz, the 6.4-GHz sideband will be reflected back since at that frequency the patch will be completely mismatched. On the other hand, the bandpass filter allows only the 6-GHz carrier to pass through and rejects the two sidebands.

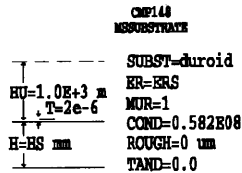
The important point of the design is the junction where the path that leads to the patch meets the input port of the bandpass filter. It is required that all the power of the 6-GHz carrier follows the direction toward the bandpass filter, and all the power of the 5.6-GHz component follows the direction toward the patch antenna for radiation. In order to achieve this goal, the point at the junction looking toward the patch antenna must be of high impedance for the 6-GHz carrier but matched to 50  $\Omega$  looking toward the bandpass filter. In addition, the point at the junction looking toward the bandpass filter must be of high impedance for the 5.6-GHz component but matched to 50  $\Omega$  looking toward the patch antenna. This impedance arrangement will force the 6-GHz carrier signal to flow in the direction of the bandpass filter and the 5.6-GHz component to flow in the direction of the patch antenna for transmission. The circuit of the diplexer-antenna unit, which is used for the simulation, is shown in Fig. 10.25.

Two  $S$ -parameter ports are used for the simulation. One is connected to the input of the circuit and the other to the output of the bandpass filter. One of the

```

EQUATION L0=300.0/FR
EQUATION KER1=(ERS-1)*((1+10*(HS/WP))^(-0.555))
EQUATION KER=0.5*(ERS+1+KER1)
EQUATION Z1=((ERS+1)/(2*pi*ERS))*(1.451+LN((WP/(2*HS))+0.94))
EQUATION Z2=(WP/(2*HS))+0.441+0.082*(ERS-1)/(ERS*ERS)+Z1
EQUATION ZP=120*pi/(2*sqrt(ERS)*Z2)
EQUATION SEE=sqrt(KER)
EQUATION VG2=LN((SEE+1)/(SEE-1))
EQUATION VG1=((KER-1)*(KER-1)/(2*KER*SEE))
EQUATION VG=((KER+1)/KER)-VG1*VG2
EQUATION RR=(ZP*ZP*L0*L0)/(60*pi*pi*HS*HS*VG)
EQUATION D1=0.412*(KER+0.3)*(WP/HS)+0.264
EQUATION DL=D1*RS/((KER-0.258)*(WP/HS)-0.8)

```



```

EQUATION HS=h
EQUATION WP=W
EQUATION LP=L
EQUATION ERS=Er

```

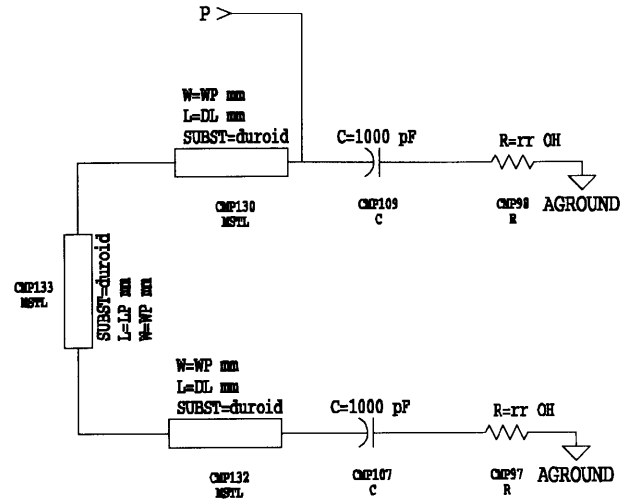


FIGURE 10.24 Transmission line model of a patch antenna for MDS.

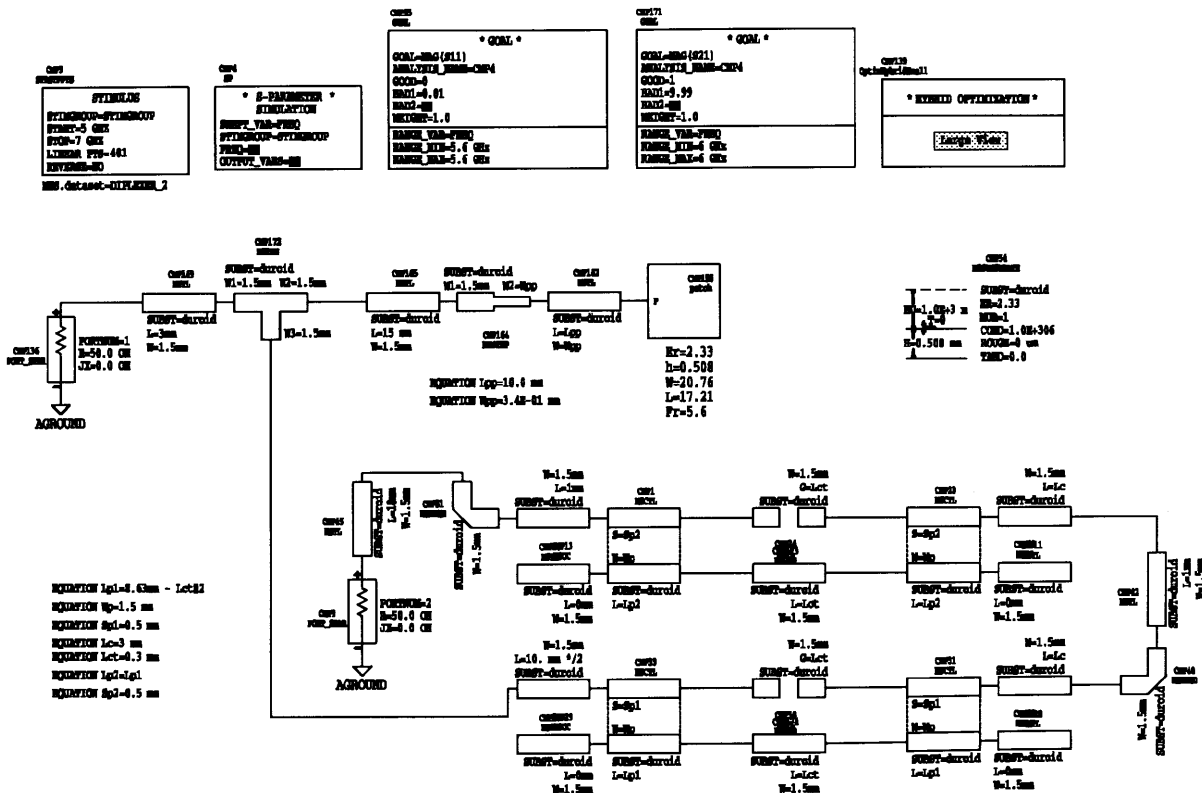


FIGURE 10.25 Diplexer-antenna simulation circuit for the MDS.

optimization goals is to minimize the reflection coefficient  $S_{11}$  of the circuit and the other is to maximize the transmission coefficient  $S_{21}$  at 6 GHz, which is the carrier passing through the bandpass filter.

The arrangement of the impedances at the junction of the circuit can be achieved using the optimization feature of the MDS. By defining the goal blocks as they are shown in Fig. 10.25, the parameters that represent the variables of the optimization are (1) the length of the microstrip line between the junction and the bandpass filter and (2) the length of the microstrip line between the junction and the matching network of the patch antenna.

The characteristic impedance of the bandpass filter at 6 GHz does not change by varying the length of the microstrip line, unlike the characteristic impedance at 5.6 GHz. Similarly, when the microstrip line length of the patch is altered, its characteristic impedance at 5.6 GHz remains unchanged but its characteristic impedance at 6 GHz is affected. This is necessary for achieving the two optimization goals.

The simulation results of the MDS are shown in Fig. 10.26. The diplexer-antenna integration seems to have very good performance. The diplexer can recover the 6-GHz carrier with an insertion loss of 0.49 dB, and has a  $-1$ -dB bandwidth of 60 MHz. The rejection of the diplexer at 5.6 GHz is 44.5 dB and the rejection at 6.4 GHz is 43.3 dB. The reflection coefficient of the circuit at 5.605 GHz is  $-33$  dB, which ensures a good matching of the patch antenna.

The actual layout of the diplexer-antenna integration is shown in Fig. 10.27, where the two arrows represent the two ports of the circuit. If necessary, the shape of the bandpass filter can be modified to fit to the dimensions of the substrate. This design is in the region of 6 GHz and the dimensions of the circuit are quite large. In the region of 60 GHz the dimensions are approximately 10 times smaller than the

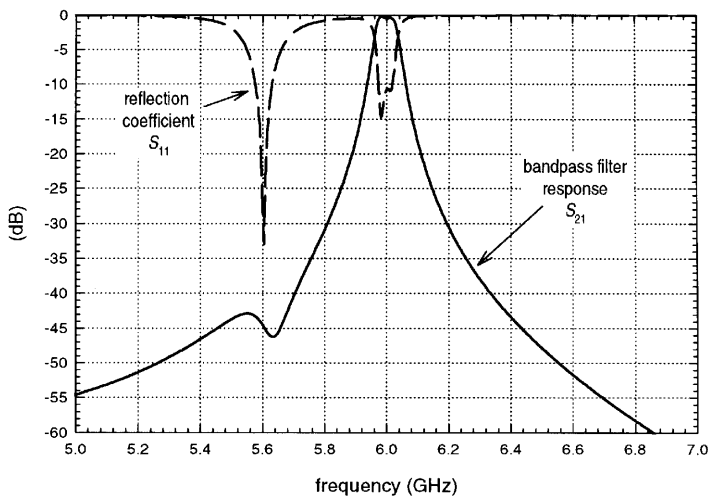
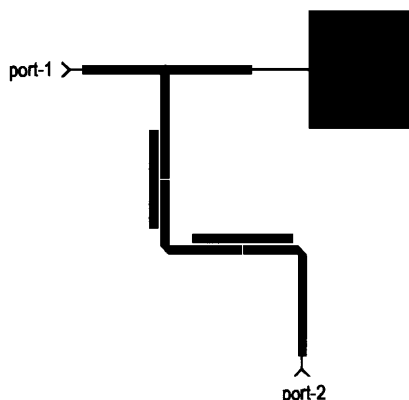


Fig. 10.26 Expected frequency response of the diplexer-antenna integration.



**FIGURE 10.27** Layout of the diplexer-antenna integration.

size of the circuit shown in Fig. 10.27, and, consequently, the result will be a compact unit for the remote site of the radio on fiber system.

From the simulation results shown in Fig. 10.26, the expected performance of the diplexer is very promising for the radio on fiber system, since it provides a simple construction based on printed circuit technology and is able to extract the unmodulated carrier with a very low insertion loss. The expected insertion loss of the diplexer, reported to the MODAL project [18], is 6 dB with the design being based on three separated filters. Therefore, the proposed design described here is better, as far as performance and simplicity are concerned.

### 10.5.5 Experimental Results

The diplexer-antenna unit was constructed as shown in Fig. 10.27 and was tested with the aid of a network analyzer. The input of the diplexer-antenna unit was connected to port-1 of the network analyzer and the output of the bandpass filter was connected to port-2. The results are shown in Fig. 10.28. As the figure indicates, the experimental and simulation results are dissimilar. The center frequency of the patch is 80 MHz lower than the predicted one, which consequently caused poor performance of the bandpass filter. This was due to the tolerance errors during the photoetching process and consequently caused mismatching at the junction point of the structure. More accurate fabrication processes must be used in order to avoid unacceptable alterations of the circuit dimensions. Furthermore, the MDS predictions were compared with a full wave simulation package called Momentum, which is based on the moments method. It was found that the results of the two simulation packages are significantly different. It should be noted that Momentum is the more accurate simulation tool. This also indicates that the simulation tool is another factor that affects the accuracy of the design.

The center frequency of the patch is 5.52 GHz with a reflection coefficient  $s_{11} = -27$  dB, and the bandpass filter has a center frequency at 5.92 GHz with an



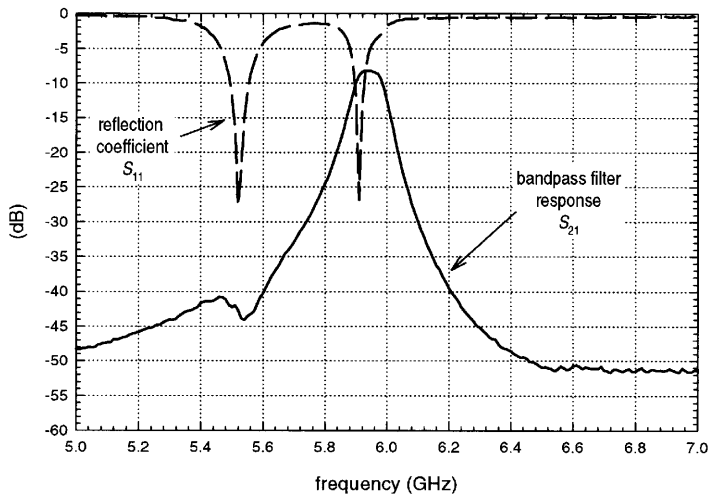


FIGURE 10.28 Experimental results of the diplexer-antenna integration.

insertion loss of 8 dB. However, as shown in Fig. 10.28, both simulation and experimental results follow the same trend.

The integration of the diplexer-antenna unit consists of two sections. One section is the bandpass filter and the other section is the patch antenna. Both sections must be matched at the junction point simultaneously and a slight mismatch of one of the two sections directly affects the other one. Therefore, the etching process must be as accurate as possible and will be more important as the frequency increases.

## 10.6 photoHBT-PATCH ANTENNA INTEGRATION

Heterojunction bipolar phototransistors (photoHBTs) are devices that provide internal gain through transistor action. With photoHBTs, it is possible to combine the functions of photodetection and amplification in one device. Performance analysis of phototransistors [38] suggests that phototransistors, if designed optimally, may have better performance than PIN-FET receivers. Furthermore, phototransistors have better noise performance than PIN-amplifier combinations at microwave frequencies.

The optically sensitive photoHBT is a potentially useful device for radio on fiber systems, where it can be used as (1) a high gain photodetector, (2) an optically injection-locked oscillator, or (3) an optoelectronic mixer. Integration of the photoHBT and patch antenna will provide a compact transmitter for the radio on fiber network

A high performance photoHBT has been developed by BT Labs [1], which combines the functionality of a millimeter-wave photodiode and a power-efficient amplifier. This photoHBT is a two-terminal device in which the base bias current is

supplied by the dc component of the optical input intensity. The peak responsivity of this device is around 700 A/W and its unity-gain frequency is greater than 30 GHz.

### 10.6.1 Microwave and Millimeter-Wave Amplifier Design

In general, a single-stage microwave or millimeter-wave transistor amplifier can be modeled by the circuit shown in Fig. 10.29, where a matching network is used on both sides of the transistor [35]. In the figure,  $\Gamma_S$  and  $\Gamma_L$  are the reflection coefficients of the input and output matching network, respectively.  $\Gamma_{in}$  and  $\Gamma_{out}$  are the reflection coefficients on the input and the output sides of the transistor, which is represented by its  $S$ -parameters, and are defined as

$$\Gamma_{in} = S_{11} + \frac{S_{12}S_{21}\Gamma_L}{1 - S_{22}\Gamma_L} \tag{10.20a}$$

$$\Gamma_{out} = S_{22} + \frac{S_{12}S_{21}\Gamma_S}{1 - S_{11}\Gamma_S} \tag{10.20b}$$

The most useful definition of power gain that can be applied to this type of circuit is the transducer power gain  $G_T$ , which is defined as the ratio of the power delivered to the load to the power available from the source, and is given by [35]

$$\begin{aligned} G_T &= \frac{1 - |\Gamma_S|^2}{|1 - \Gamma_{in}\Gamma_S|^2} |S_{21}|^2 \frac{1 - |\Gamma_L|^2}{|1 - S_{22}\Gamma_L|^2} \\ &= \frac{1 - |\Gamma_S|^2}{|1 - S_{11}\Gamma_S|^2} |S_{21}|^2 \frac{1 - |\Gamma_L|^2}{|1 - \Gamma_{out}\Gamma_L|^2} \end{aligned} \tag{10.21}$$

The overall transducer gain  $G_T$  depends on both the input and the output matching conditions and can be expressed with respect to the separate effective gain factors for the input (source) matching network  $G_S$ , the transistor  $G_0$ , and the output (load) matching network  $G_L$ , as follows:

$$G_T = G_S G_0 G_L \tag{10.22}$$

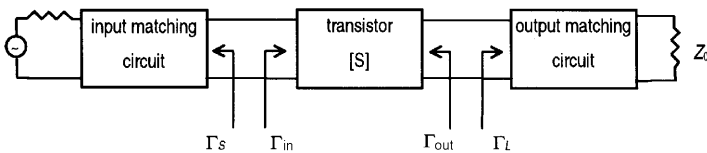


FIGURE 10.29 The general transistor amplifier circuit.

The effective gains factors are given by

$$G_S = \frac{1 - |\Gamma_S|^2}{|1 - \Gamma_{in}\Gamma_S|^2} \quad (10.23a)$$

$$G_0 = |S_{21}|^2 \quad (10.23b)$$

$$G_L = \frac{1 - |\Gamma_L|^2}{|1 - S_{22}\Gamma_L|^2} \quad (10.23c)$$

The effective gain from  $G_S$  and  $G_L$  are due to the impedance matching of the transistor.

If the transistor is unilateral, so that  $S_{12} = 0$  or negligibly small, then  $\Gamma_{in}$  reduces to  $\Gamma_{in} = S_{11}$ , and to  $\Gamma_{out}$  to  $\Gamma_{out} = S_{22}$ .

A network is unconditionally stable if  $|\Gamma_{in}| < 1$  and  $|\Gamma_{out}| < 1$ , for all passive source and load impedances (i.e.,  $|\Gamma_S| < 1$  and  $|\Gamma_L| < 1$ ), or is conditionally stable if  $|\Gamma_{in}| < 1$  and  $|\Gamma_{out}| < 1$  only for a certain range of passive source and load impedances.

Alternatively, it can be shown that an amplifier will be unconditionally stable if the following necessary and sufficient conditions are met [35]:

$$K = \frac{1 - |S_{11}|^2 - |S_{22}|^2 + |\Delta|^2}{2|S_{12}S_{21}|} > 1 \quad (10.24)$$

and

$$|\Delta| < 1 \quad (10.25)$$

where  $\Delta$  is the determinant of the scattering matrix given by

$$\Delta = S_{11}S_{22} - S_{12}S_{21} \quad (10.26)$$

Maximum gain can be realized when there is a conjugate match between the amplifier source or load impedance and the transistor. In the case of the photoHBT, the maximum gain is achieved only with the conjugate match between the transistor and the load impedance since the base of the photoHBT is fed by an optical signal. The load in this case is the patch antenna and therefore the transistor must be conjugate matched to the patch antenna.

For the integration of the photoHBT and patch antenna, the amplifier design procedure is (1) the stability test of the photoHBT, (2) the design of a 6-GHz patch antenna, and (3) the design of a matching network to match the photoHBT with the patch antenna.

### 10.6.2 The Optical Link Stability Test

Characterization of the photoHBT by its  $S$ -parameters is difficult because it is a two-terminal device. However, the amplifier can be designed if the complete optical link is considered as one device. The  $S$ -parameters of the complete optical link were measured using the experimental setup of Fig. 10.30. A single-mode laser diode of 1550 nm was used to convert the RF power from the network analyzer into a light signal, and, using a micropositioner and microscope, the fiber must be aligned so that the light hits the facet of the photoHBT. The dc bias of the laser was set to 12 mA, and the fiber was set a distance away from the the photoHBT such that the current flowing through the emitter of the transistor was 1 mA. The emitter current  $I_e$  was measured using an ammeter. With a collector-emitter voltage  $V_{ce}$  of  $-0.75$  V, a dark current of  $50 \mu\text{A}$  was observed.

The  $S$ -parameters of the optical link are shown in Fig. 10.31. The optical link is unilateral and therefore unconditionally stable because  $S_{12}$  is negligibly small, since there is no optical signal returning to the laser. However,  $S_{21}$  is also small but this is due to the  $50\text{-}\Omega$  line mismatch of the input and output port impedances.

### 10.6.3 Simulation of a 6-GHz Patch Antenna

The accurate transmission-line model for the rectangular microstrip antenna was used to design a patch antenna at 6 GHz [37]. Substrate parameters were  $\epsilon_r = 2.20$  and  $h = 0.508$  mm, and the dimensions of the patch were  $W = 16.45$  mm and  $L = 19.75$  mm. The software package that was used to simulate the patch antenna is the Prelude Design developed by Boulder Microwave Technologies. The patch antenna was characterized by its  $S$ -parameters and its reflection coefficient is shown in Fig. 10.32.

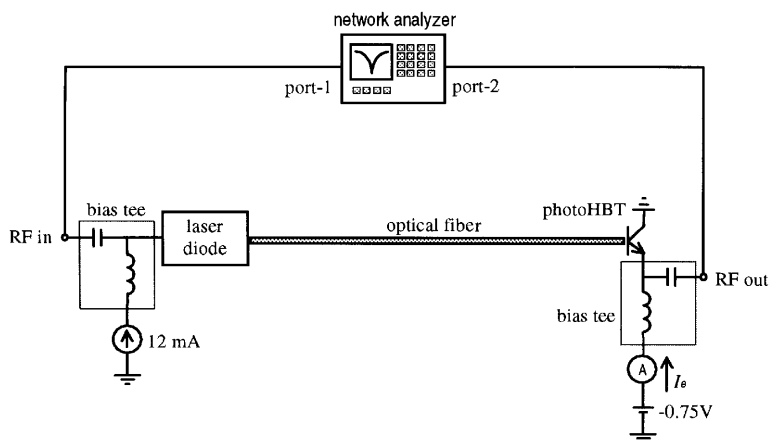


**FIGURE 10.30** Experimental setup for measuring the photoHBT output reflection coefficient.

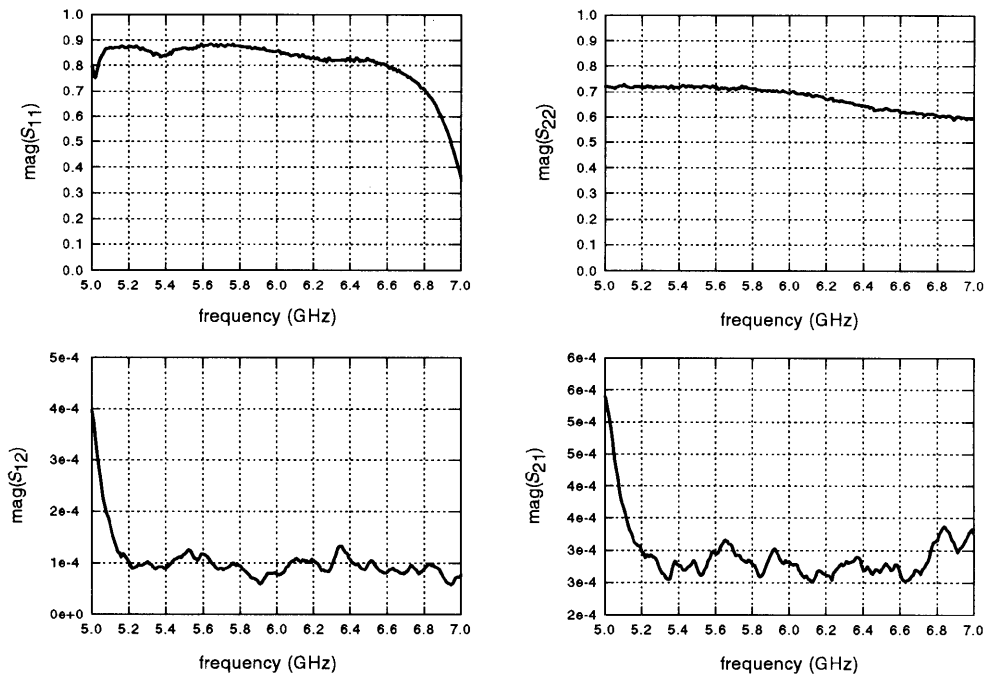


FIGURE 10.31  $S$ -parameters of the optical link.

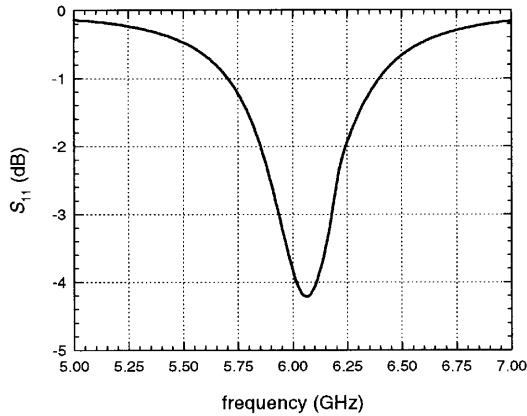


FIGURE 10.32 Reflection coefficient of the 6-GHz patch antenna.

The reflection coefficient of the patch antenna was measured with reference to  $50\ \Omega$ . Figure 10.32 shows only the magnitude of the reflection coefficient in order to see how the patch is matched to the  $50\text{-}\Omega$  impedance. However, for a complete characterization of the patch antenna, the phase component of the reflection coefficient is also required.

#### 10.6.4 Matching Network Design

Although there are various ways of matching two impedances, as a first attempt, a single section of  $50\text{-}\Omega$  microstrip transmission line was used to match the patch antenna to the photoHBT. The simulated  $S$ -parameters of the patch and the measured  $S$ -parameters of the photoHBT were imported as data blocks into the MDS simulator. The simulation circuit is shown in Fig. 10.33. In this circuit, the component CMP71 models the patch antenna, and the component CMP73 models a  $50\text{-}\Omega$  microstrip transmission line of variable length. The CMP24, which is an  $S$ -parameters port, represents the photoHBT. By running an  $S$ -parameter simulation, the signal that was reflected back to the photoHBT was observed. The length of the transmission line, which was optimized by the MDS to minimize  $S_{11}$ , was found to be 26.2 mm. The length of the line could have been shorter but an initial value of 20 mm was given to the MDS in order to allow enough space to put the photoHBT and the fiber at a suitable position on the substrate. This length could be much shorter if the photoHBT was mounted on a different base allowing more compact integration.

Currently, the available photoHBTs are mounted on Kyocera laser headers but it is difficult to put this type of mount on a substrate. If the next generation of these devices have appropriate mounts, it will be possible to use inset feed of a patch [39], so the photoHBT will be within the patch itself, making an extremely compact network.

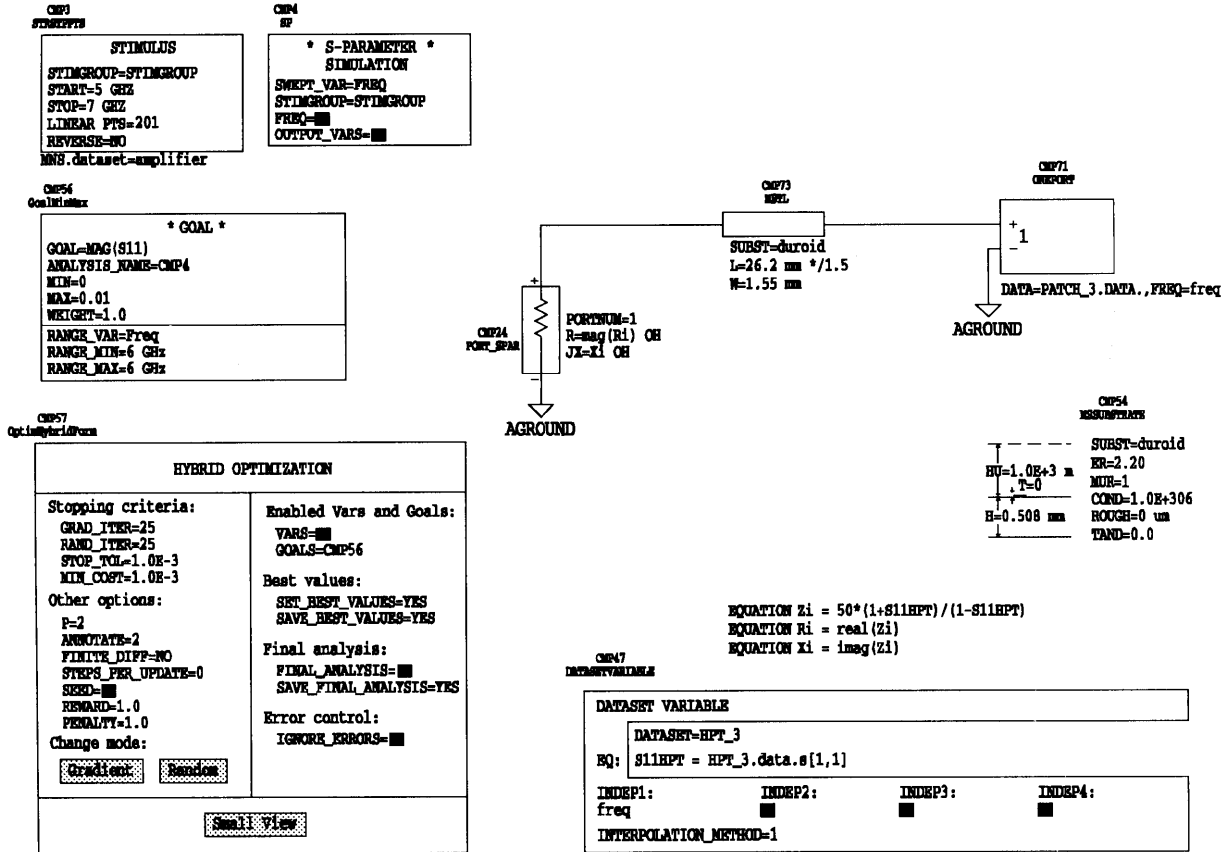


FIGURE 10.33 Simulation circuit for the photoHBT-patch antenna integration.

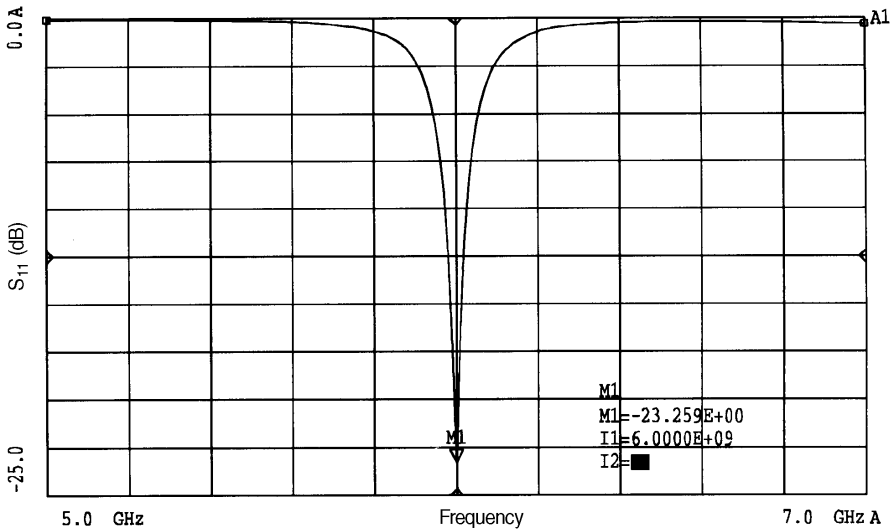


FIGURE 10.34 PhotoHBT-patch antenna matching.

The amount of signal that is reflected back to the photoHBT is shown in Fig. 10.34. The reflection coefficient at 6 GHz is  $-23.26$  dB, which is a reasonable matching for the use of a single transmission line.

### 10.6.5 Experimental Implementation

The patch antenna and the microstrip transmission line were fabricated on a Duroid substrate and the photoHBT was positioned at the edge of the substrate as shown in Fig. 10.35. A micropositioner was used to align a lens-ended fiber to the facet of the photoHBT. The patch antenna was located at a distance  $R = 1$  m from a 15-dB standard horn antenna.

By measuring the received power of the horn antenna at 6 GHz, it would be possible to compare the theoretical results with the experimental ones, using the following Friis formula [33]:

$$\frac{P_r}{P_t} = \left( \frac{\lambda}{4\pi R} \right)^2 G_t G_r \tag{10.27}$$

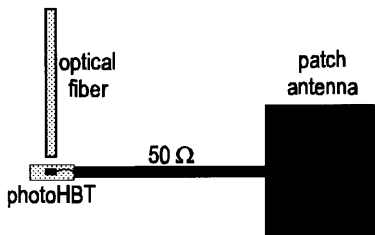


FIGURE 10.35 PhotoHBT-patch antenna integration.



where  $P_r$  is the received power from the horn antenna,  $P_t$  is the transmitted power from the patch,  $\lambda$  is the free-space wavelength, and  $G_h$  and  $G_p$  are the gain of the horn and the gain of the patch, respectively. The theoretical gain of a patch antenna can be found in [29], and the transmitted power can be estimated using Eq. 10.27. This can be compared with the output power of the photoHBT in order to assess the validity of the simulation model.

Unfortunately, it was not possible to obtain any experimental results because the transmitting power of the antenna was almost within the noise floor level. All the available photoHBTs were isolated from the circuit and tested individually. When a photoHBT was switched on for a second time, the output power decreased to a very low value on the order of  $-70$  dBm. Under these circumstances, it was very difficult to carry out the experiment. In the future, it will be possible to have more stable and reliable photoHBTs that will enable the implementation of the experiment. However, the integration of a photoHBT with a patch antenna is promising for the radio on fiber system because it provides the functions of photodetector, amplifier, and transmitter at the same time.

## 10.7 RF TRANSMIT-RECEIVE MODULE FOR THE RADIO ON FIBER SYSTEM

Rectangular patch antennas provide a good isolation between adjacent sides and they can be used for simultaneous transmit and receive functions [40]. The advantage of the integration of both functions on the same antenna element is that the size of the remote site can be reduced significantly, since the number of elements in an antenna array will be halved. A T-R module for the radio interface was designed and constructed at 6 GHz using a single patch antenna integrated with the diplexer described earlier.

The rectangular patch antenna was designed to transmit at 5.6 GHz and receive at 6.2 GHz with an isolation of about 33 dB between the transmit and receive paths. The performance of the full-duplex antenna was simulated using the MDS. Although this value of isolation is reasonable for a single element, it is not sufficient for the application of a communication system. The reason is that the power of the received signal at the antenna site can be as low as  $-60$  to  $-70$  dBm. In such a case, the power of the transmit signal that flows through the receive path is much higher than the power of the received signal. The result of this would be the saturation of the mixer at the remote site. This undesired phenomenon could be avoided if the isolation between the two antenna paths is increased well beyond the expected power of the received signal. The technique, which is used to increase the isolation of the antenna paths, is a third order bandstop filter that was connected to the 6.2-GHz side of the patch antenna. The center frequency of this filter is at 5.6 GHz and its purpose is to attenuate the power of the transmit signal that flows through the 6.2-GHz port of the antenna. Assuming that the data bandwidth is 200 MHz, then the bandwidth of the bandstop filter must also be 200 MHz.

### 10.7.1 Design of a Bandstop Filter

The design of the bandstop filter was based on the quarter-wave resonators method [35]. Quarter-wave open-circuited or short-circuited transmission line stubs look like series or parallel resonant circuits, respectively. Therefore, it is possible to use such stubs in shunt along a transmission line to implement a bandstop filter. Quarter-wavelength sections of line between the stubs act as admittance inverters to effectively convert alternate shunt resonators to series resonators. The stubs and the transmission line sections are  $\lambda/4$  long at the center frequency,  $f_0$ . For narrow bandwidths the response of such a filter using  $N$  stubs is essentially the same as that of a coupled line filter using  $N + 1$  sections, as in the case of the bandpass filter designed earlier. The internal impedance of the stub filter is  $Z_0$ , while in the case of the coupled line filter end sections are required to transform the impedance level. This makes the stub filter more compact and easier to design. A disadvantage, however, is that a filter using stub resonators often requires characteristic impedances that are difficult to realize in practice.

Fig. 10.36 shows the MDS simulation circuit of the bandstop filter used in the T-R module. The filter has three shunt quarter-wavelength stubs, a center frequency  $f_0$  at 5.6 GHz, and an internal impedance  $Z_0 = 50 \Omega$ . The substrate is a Duroid, with a dielectric constant  $\epsilon_r = 2.45$  and thickness  $h = 0.508$  mm. By allowing the characteristic impedances of the interconnecting lines and the lengths of the stubs to be variable, it is possible to fine-tune the performance of the filter according to the specifications.

The frequency response of the bandstop filter is shown in Fig. 10.37. The 5.6-GHz signal is attenuated by more than 70 dB with a stopband of 200 MHz. The response of the 200-MHz passband of the filter is not flat, and at 6.3 GHz, the attenuation is around 3 dB. However, the performance of the filter is reasonable and it will be used in the design of the T-R module.

### 10.7.2 Design of the T-R module

The structure layout of the radio module prototype circuit is shown in Fig. 10.38. The antenna receives at horizontal polarization and transmits at vertical polarization. Matching networks were added to both ports of the antenna to ensure 50- $\Omega$  impedance matching. The received signal passes through the bandstop filter, is amplified by a low noise amplifier (LNA), and then by means of a directional coupler flows to the input of a field effect transistor (FET), which acts as the mixer of the module.

At the input of the circuit, there are two signals: the 5.6-GHz signal is the selected sideband for radiation, and the 6-GHz signal is the unmodulated carrier. The 5.6-GHz signal flows in the direction of the antenna and radiates. The 6-GHz signal flows through the bandpass filter, which constitutes the diplexer of the circuit, and then by means of the directional coupler flows to the input of the FET. The result of the mixing function is a down-conversion of the received signal frequency to 0.2 GHz. Unwanted harmonics and intermodulation products can be filtered out

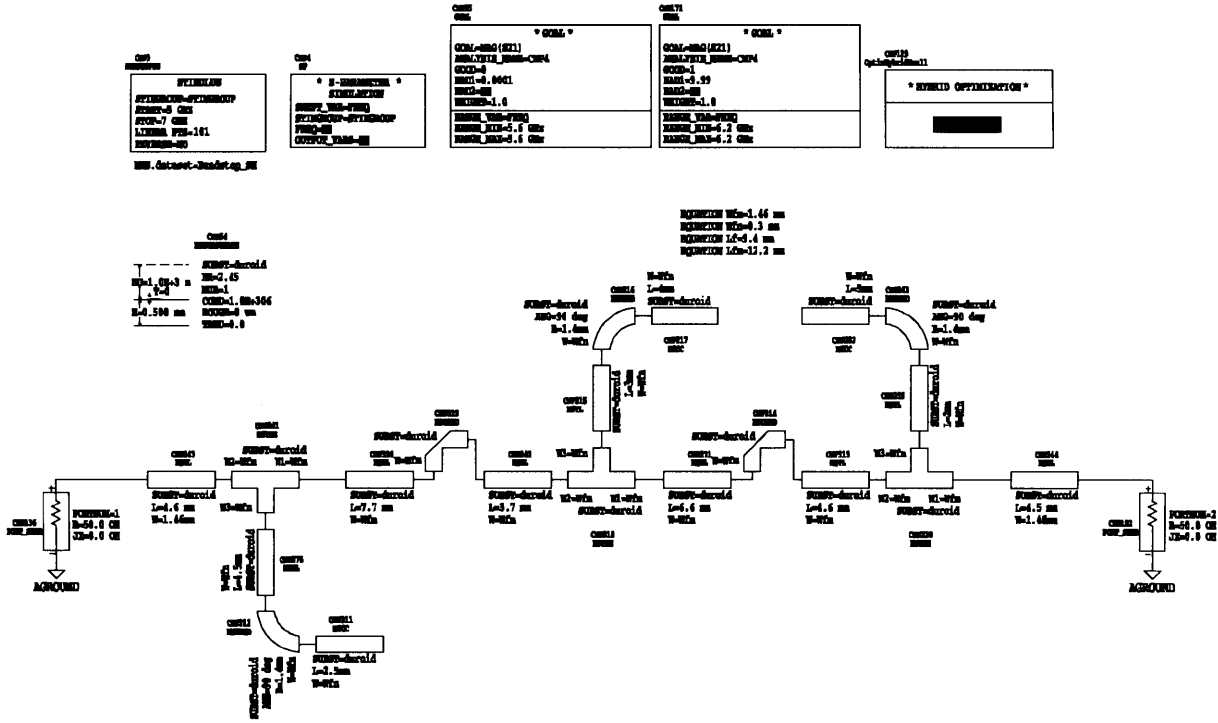


FIGURE 10.36 Simulation circuit of the bandstop filter.

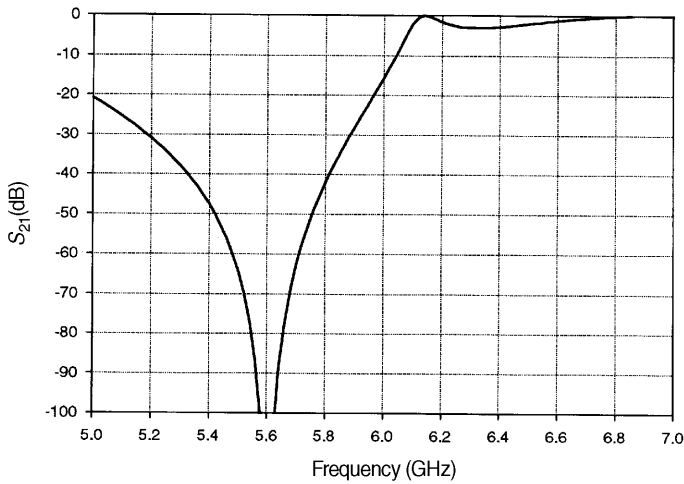


FIGURE 10.37 Frequency response of the bandstop filter.

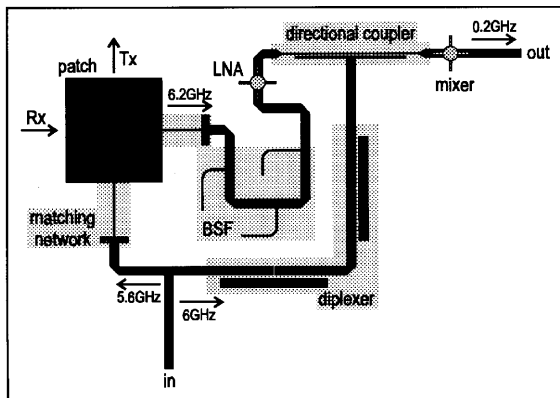


FIGURE 10.38 Structure layout of the radio T-R module prototype circuit.

using a bandpass filter if necessary. The directional coupler is designed in such a way that it has a small gap for dc blocking. The prototype circuit was designed and simulated with the aid of MDS.

Initially, the reflection coefficients of the patch antenna were measured in the planes of the matching networks. Port-1 was connected to the transmit side of the patch and port-2 was connected to the receive side of the patch. The simulated results are shown in Fig. 10.39, where the two ports of the antenna are very well matched to 50-Ω impedance with both reflection coefficients being less than -30 dB. Good matching of the antenna will ensure maximum transmit and receive signal power.

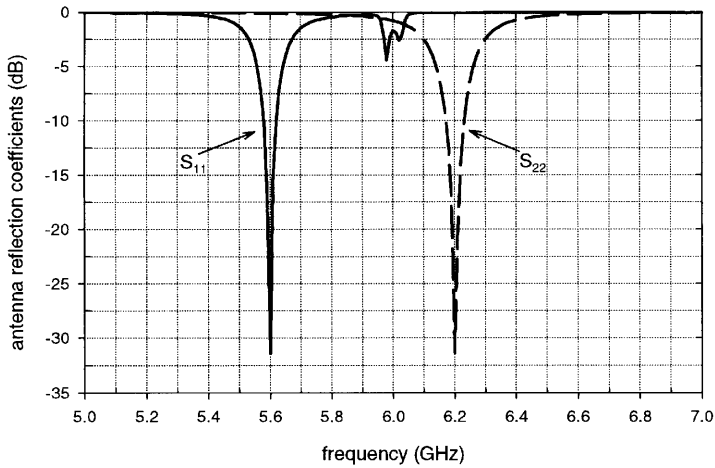


FIGURE 10.39 Reflection coefficients of the patch antenna transmit and receive ports.

The next simulation was the evaluation of the diplexer performance. Port-1 was connected to the input of the module and port-2 was connected to the input of the mixer, with the mixer removed. The frequency response of the diplexer including the directional coupler is shown in Fig. 10.40.

The insertion loss at 6 GHz is 6 dB, which is mainly due to the directional coupler. The bandwidth of the diplexer is 60 MHz. In order to test the performance of the receive path of the circuit, port-1 was used to emulate the 6.2-GHz port of the patch antenna and port-2 was connected to the input of the mixer. An amplifier of 0-dB gain was used in place of the LNA.

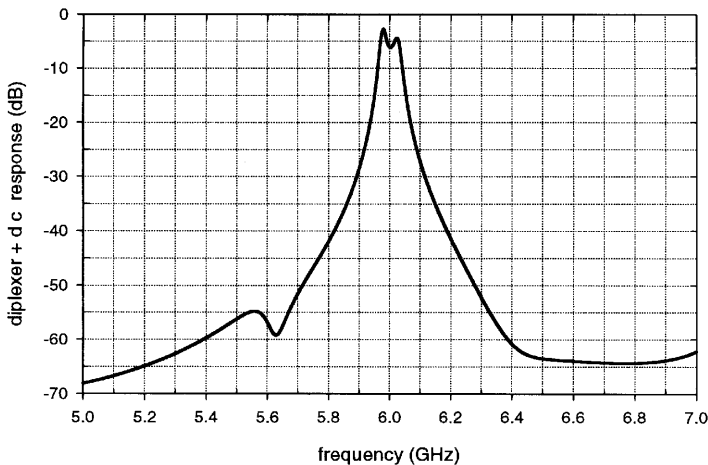
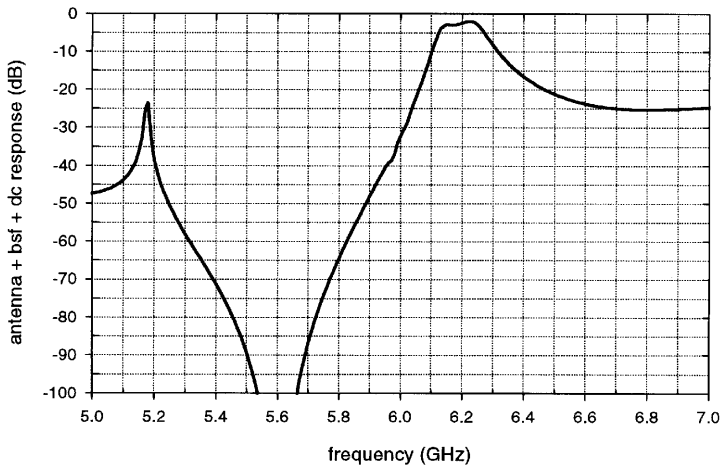


FIGURE 10.40 Transmission coefficient of the diplexer and directional coupler.



**FIGURE 10.41** Frequency response of the patch antenna, bandstop filter, and directional coupler.

Figure 10.41 shows the combined frequency response of the patch antenna, the bandstop filter, and the directional coupler, as it was measured at the input of the mixer. The bandstop filter has an attenuation of more than 70 dB at 5.6 GHz, with a stopband bandwidth of 200 MHz. This ensures that the effective isolation of the transmit and receive paths of the antenna will be in excess of 100 dB. There is also an attenuation of the received signal, which is due to the finite passband attenuation of the bandstop filter. However, the attenuation of the 6.2-GHz received signal is on the order of 3 dB and this can be rectified by amplification as long as the power of the received signal is well above the noise margin.

### 10.7.3 Experimental Results

The T-R module was constructed on a Duroid substrate of thickness  $h = 0.508$  mm and dielectric constant  $\epsilon_r = 2.45$ . The mixer was a general purpose FET (ATF26884) biased at 2 volts, and the LNA was a 1.5–8 GHz MMIC amplifier (MGA86576) biased at 5 volts. The input and output ports of the module were terminated to SMA connectors. The experimental setup is shown in Fig. 10.42.

Initially, a programmable sweep generator (WILTRON 6647B-40) was used to generate a signal that represented the LO signal and was connected to the input of the T-R module. The frequency of the LO signal was  $f_{LO} = 6$  GHz with power  $P_{LO} = 1.67$  dBm. A network analyzer (HP8720C) was connected to an 8-dB broadband antenna, which was placed 10 cm away from the module, for generating the receiving signal at frequency  $f_{RX} = 6.2$  GHz and power  $P_{RX} = 18.20$  dBm. A spectrum analyzer (HP8563E) was used to measure the IF power received from the output port of the module. The measured frequency  $f_{IF}$  of the IF signal was 200 MHz with power  $P_{IF}$  of  $-28.5$  dBm. When the amplifier of the module was switched off,

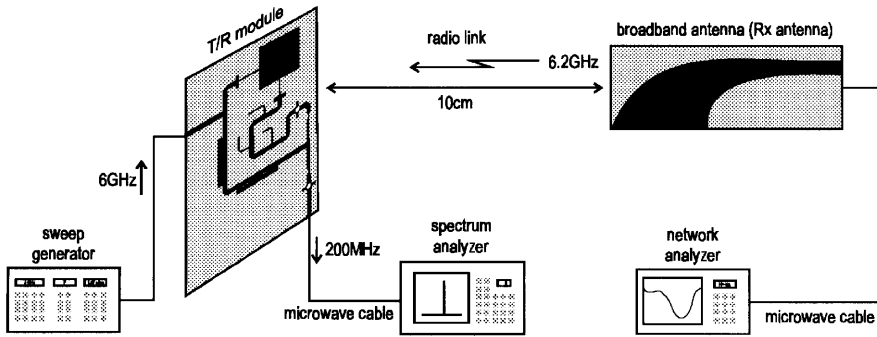


FIGURE 10.42 Experimental setup for the T-R module.

the power  $P_{IF}$  reduced to  $-35$  dBm. The received power by the module can be calculated using the Friis transmission formula and was found to be  $5.1$  dBm, assuming a patch antenna gain of  $7$  dB. Therefore, the expected output power of the mixer was in the range of  $-10$  dBm, whereas the actual output power was  $-28.5$  dBm. This attributed mainly to the fabrication tolerances, which alter the filter responses. Another reason for this low power is that the output power of the mixer is distributed over a large number of harmonics due to the intermodulation products. In addition, the mixer was a general purpose FET, whereas a good mixer design could maximize the power of the fundamental signal. The module was capable of transmitting at  $5.6$  GHz and the signal was detected by the broadband antenna and observed using the spectrum analyzer.

After the first experiment, the network analyzer was used to measure the input reflection coefficient of the module. As shown in Fig. 10.43, the matching of the LO signal is about  $20$  dB, which is very good. However, the transmit path of the patch antenna is frequency shifted and the reflection coefficient is less than  $20$  dB. Again,

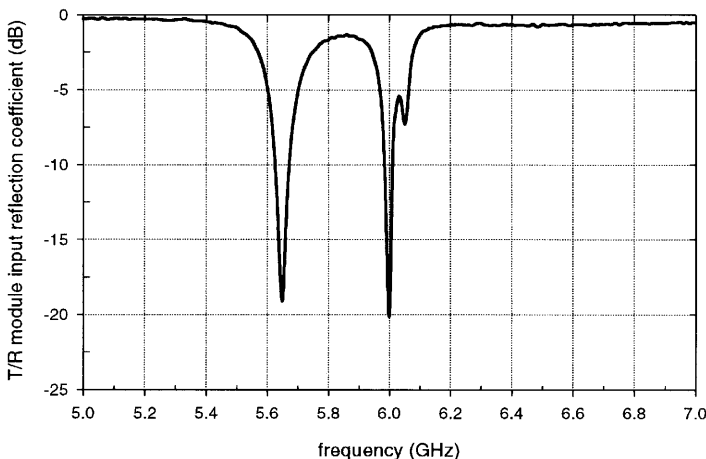


FIGURE 10.43 T-R module input reflection coefficient.

this might be due to the fabrication tolerances and because of the inaccurate predictions of the MDS.

In the next experiment, a fixed 6-GHz signal for the LO was applied to the input of the module, and by varying the RF frequency, the output of the mixer was measured on the spectrum analyzer.

From Fig. 10.44, it can be observed that the optimum center frequency IF signal is at 325 MHz with a bandwidth of around 150 MHz. This means that the patch antenna is not very well matched at 6.2 GHz but it has better performance at 6.325 GHz. However, the usable bandwidth is reasonable.

The receive radiation pattern of the module was measured at IF frequency as shown in Fig. 10.45. The pattern is shifted from the broadside radiation by 20°,

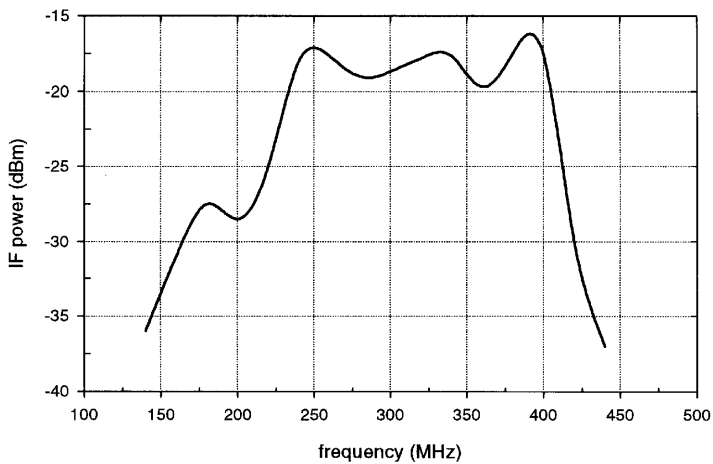


FIGURE 10.44 IF power measured at the output of the mixer.

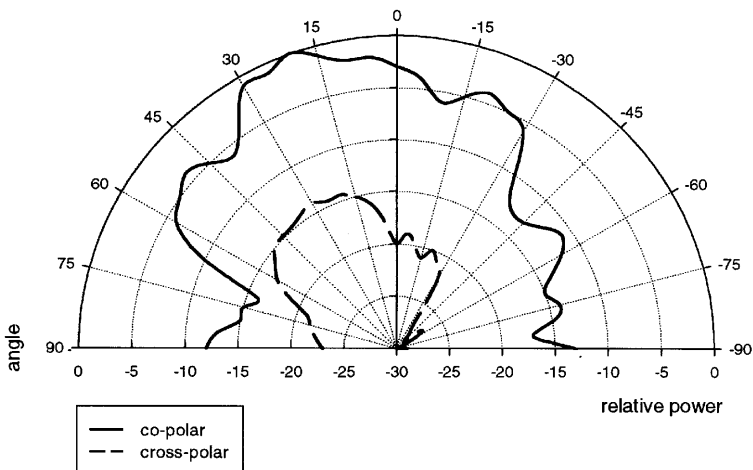


FIGURE 10.45 Radiation pattern of the T-R module measured at IF.



because of the asymmetry that exists in the geometry of the structure. The cross-polar pattern is about 15 dB lower than the copolar, which is a reasonable performance for the first experimental attempt. In general, the preliminary experimental results of the T-R module prove the feasibility of this radio interface. The planar circuit technology used for this prototype can lead to very low implementation costs. Furthermore, its compactness can satisfy the small size and integration issues associated with the radio on fiber systems.

#### 10.7.4 Fabrication and Substrate Tolerances for the T-R Module

Circuits that are based on planar technology are sometimes very sensitive to fabrication and substrate tolerances, since the dimensions of microstrip lines that constitute the passive circuit must be within a certain accuracy. In this work, possible fabrication tolerances have been taken into account, in order to investigate their effects on the performance of the bandstop filter, which is considered to be the most sensitive part of the T-R module. According to the manufacturer data sheet, the dielectric constant of the substrate was  $\epsilon_r = 2.45 \pm 0.04$ , and its thickness was  $h = 0.508 \text{ mm} \pm 0.0381 \text{ mm}$ .

Substrate dielectric constant and thickness are assumed to vary between the maximum values of the tolerance, which was  $\pm 0.04$  and  $\pm 0.0381 \text{ mm}$ , respectively. Fabrication tolerances that are taken into account were assumed to be within the range of  $\pm 0.1 \text{ mm}$ . Table 10.2 shows the tolerance effects on the performance of the bandstop filter. This table clearly shows how the width of the stubs affects the center frequency of the filter. A 0.1-mm decrement in the stubs width shifts the center frequency of the filter by 120 MHz. In the photoetching process that was used to fabricate the T-R module, very thin lines ( $< 0.3 \text{ mm}$ ) usually become thinner after exposure of the substrate to ultraviolet light. This is one of the main reasons that experimental results did not agree with simulation predictions.

The effects of fabrication tolerance of  $\pm 0.01 \text{ mm}$  on the performance of the various parts of the T-R module are also presented graphically. Figure 10.46 shows the effects of tolerances on the reflection coefficient of the full-duplex patch antenna. In both cases, small frequency shifts were observed, which can be ignored.

Fig. 10.47 shows the effects on the bandstop and bandpass filters. As was expected, the bandstop filter is more sensitive due to its very thin stubs. However, the tolerance of 0.01 mm can be considered as reasonable because the response of the bandstop filter is still within the required specifications (i.e., center frequency: 5.6 GHz, stopband BW: 200 MHz; stopband attenuation:  $> 70 \text{ dB}$ , passband attenuation:  $< 3 \text{ dB}$ ).

#### 10.7.5 Comparison of MDS and Momentum Simulations

As discussed earlier, the experimental results presented did not agree with the simulation results, at least within a degree of accuracy. Another possible lack of agreement between experimental and simulation results, is due to inaccurate predictions of the simulation packages. The MDS package was chosen for this

**TABLE 10.2 Fabrication and Substrate Tolerance Effect of the Bandstop Filter**

Fabrication and Substrate Tolerances	Stopband		Passband		Frequency Shift
	5.5 GHz (dB)	5.7 GHz (dB)	6.1 GHz (dB)	6.3 GHz (dB)	(MHz)
Original design	-64.39	-62.72	-2.13	-2.99	0
Increase stubs spacing by 0.1 mm	-64.29	-62.49	-1.17	-3.13	0
Decrease stubs spacing by 0.1 mm	-64.48	-62.94	-3.20	-2.82	0
Increase length of stubs by 0.1 mm	-84.67	-49.51	-0.027	-2.89	-60
Decrease length of stubs by 0.1 mm	-53.47	-87.57	-9.27	-2.77	+60
Increase width of stubs by 0.1 mm	-82.10	-55.15	-3.36	-2.90	-40
Decrease width of stubs by 0.1 mm	-42.39	-100.7	-9.69	-2.96	+120
Decrease all dimensions by 0.1 mm	-60.44	-67.83	-3.76	-2.97	+20
Increase all dimensions by 0.1 mm	-68.99	-58.43	-0.90	-2.99	-20
Increase dielectric constant by 0.04	-74.86	-53.62	-0.45	-2.99	-40
Decrease dielectric constant by 0.04	-57.07	-75.77	-7.50	-2.71	+40
Decrease dielectric constant by 0.01	-62.34	-65.48	-3.34	-2.96	+20
Increase substrate $h$ by 0.0381 mm	-64.26	-63.95	-3.74	-3.12	0
Decrease substrate $h$ by 0.0381 mm	-64.71	-61.20	-0.76	-2.81	0

work because it is fast and suitable for simulating passive and active circuits. However, Momentum, which is a full-wave analysis package, is more accurate but it is extremely slow (about 100 times slower than MDS) and is suitable only for simulating passive circuits.

For comparison purposes, the bandstop filter used in the T-R module was simulated with both packages. The circuit used for the MDS simulation is that of Fig. 10.36, and the circuit for the Momentum is shown in Fig. 10.48.

Figure 10.49 shows the simulated frequency response of the bandstop filter from both packages. The passband region of the filter has approximately the same performance except a small frequency shift. However, the difference in the simulated

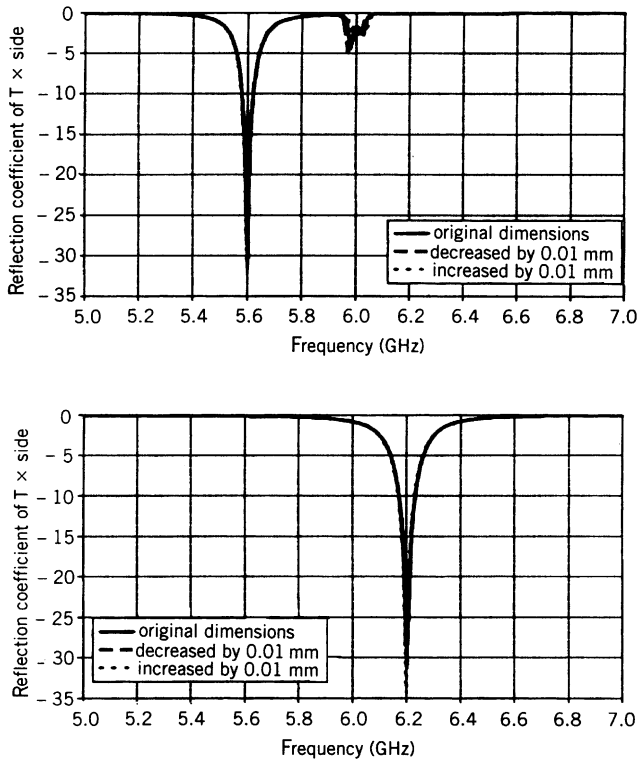


**FIGURE 10.46** Fabrication tolerances on the performance of the full-duplex patch antenna.

performance of the stopband region is very significant. The attenuation is on the order of 38 dB, which obviously does not satisfy the requirements of the design.

Momentum is experimentally verified in other circumstances and it was quite accurate as compared with the experimental measurements. The disadvantage of this package is that it requires an extremely long time to perform the simulation. For example, in this bandstop filter case, it took about 4 hours for Momentum to complete 101 simulation points. Consequently, this package is not recommended to be used for the fine-tuning of the design. On the other hand, the MDS used here is faster.

### 10.8 SUMMARY AND CONCLUDING REMARKS

The radio on fiber system was briefly outlined in this chapter, covering the main system requirements. Various techniques for the optical generation and detection of millimeter-wave signals such as FM-IM, optical heterodyning, master/slave injection-locked DFB laser, and dual-mode semiconductor lasers were described. Methods for the detection of these signals were also reported. The dual-mode

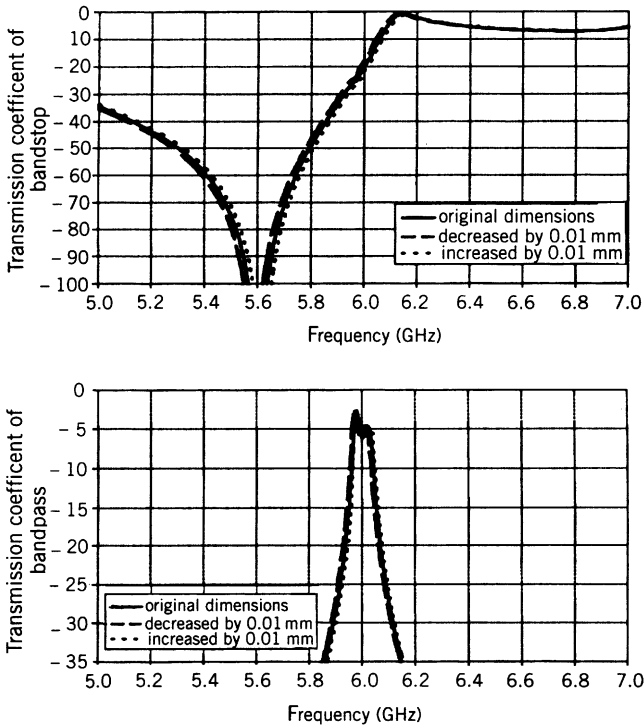


**FIGURE 10.47** Fabrication tolerances on the performance of the bandstop and bandpass filters.

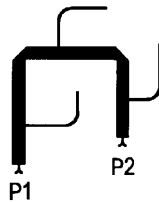


**FIGURE 10.48** Circuit used for the Momentum simulation.

laser diode was selected as the optical source for generating millimeter-wave signals at 60 GHz. The dual-mode laser is a single-chip device that offers high power levels compared to other techniques, which are more complex and expensive. The new configuration for the radio on fiber system that is proposed introduces the dual-mode laser source and simplifies the remote site by employing fewer amplifiers and a simple diplexer filter. This configuration is very promising for the radio on fiber system since it can be implemented in a compact form and offers capabilities for the integration of optoelectronic and millimeter-wave devices. The implementation of this system can be of low cost, small size, and low power consumption when optical

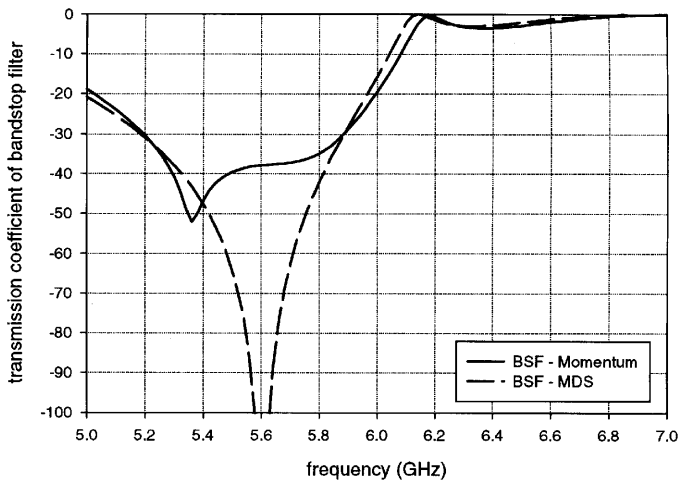


**FIGURE 10.49** MDS and Momentum simulations for the frequency response of the bandstop filter.

amplifiers are used on the optical fiber network. The power requirements of the remote site for both configurations can be minimized if injection-locked patch oscillators are used as the transmitting antennas. The use of injection-locked patch oscillators in an array form will provide extra transmitting power from each single oscillator. The individual power from each oscillator can be combined in free space, through mutual interaction of the patch oscillators, which results in a reduction of the amplification requirements.

Although the dual-mode laser is selected as the best method for generating millimeter-wave signals, a radio on fiber configuration based on electroabsorption [28] would be more attractive as far as simplicity and integration are concerned. Furthermore, the cost of the remote site would be reduced considerably, since the laser and other associated control circuitry can be eliminated. However, this study is still in its early stages and hence beyond the scope of this work. The design of a simple but efficient diplexer-antenna unit, which can be used at the remote site of the radio on fiber system for the provision of full-duplex operations has been discussed. The diplexer recovers the unmodulated carrier signal as it is detected from the optical signal transmitted from the central site of the network. This carrier signal is used for down-converting the millimeter-wave signal received from a mobile unit. The simulated and experimental results showed that both designs are promising for the radio on fiber systems. The carrier signal can be recovered with a low insertion loss from the diplexer, thus minimizing the amplification level or eliminating the amplification requirement in the best case. Furthermore, the integration of the diplexer-antenna unit, which is based on planar technology, allows low cost and compact implementation, which is desirable for the remote site of the system. The integration of a photoHBT with a patch antenna was also investigated. This integration is very useful for the remote site of the radio on fiber system where

the photoHBT replaces the high-speed photodiode and furthermore amplifies the photocurrent for extra signal power. The photoHBT can be placed within the patch antenna, using inset feed, making a very compact integration where the dimensions of the implementation will not exceed the dimensions of the patch itself.

The feasibility of an active photoHBT oscillator was also investigated but the conclusion is that the two-terminal device cannot oscillate. The reason is that the two-terminal device does not provide an electrical contact at the base, which is necessary for feedback. A possible solution is the redesign of the two-terminal photoHBT in such a way that an internal feedback is provided, which will make the device unstable. An alternative would be the use of three-terminal devices. PhotoHBT oscillators are desirable for radio on fiber systems and can be investigated when three-terminal devices become available.

A 6-GHz full-duplex prototype module was designed and implemented, for the remote site of the radio on fiber system. The T-R module uses a single patch antenna for transmit and receive functions at 5.6 GHz and 6.2 GHz, respectively. The bandstop filter preceded the LNA at the receiving path to increase the isolation between the transmit and receive paths to around 100 dB. The module integrates the diplexer for the provision of the return path and a mixer for down-conversion of the received signal, to an IF of 0.2 GHz. The prototype was an attempt to justify the use of printed circuit technology, for the application of a radio on fiber system. Radio interfaces of this type can reduce the cost and complexity of these systems.

Finally, various tolerance effects on the design of compact T-R modules and the accuracy of simulation packages were investigated. The conclusion from this investigation is that the simulation tools still have a long way to go, in order to provide accurate predictions to engineers. Fabrication process and simulation are important issues for the design of printed circuits and must be selected with care.

## REFERENCES

1. Wake, D., Westbrook, L. D., Walker, N. G., and Smith, I. C. "Microwave and millimetre-wave radio fibre," *BT Technol. J.*, vol. 1, 1993, pp. 76–88.
2. Kykkotis, C. E., Ghafouri-Shiraz, H., Hall, P. S., and Wake, D. "Optical fibre-fed radio system configurations," *Proceedings of the International Conference on Millimetre-Wave and Far-Infrared Science and Technology*, 1996, pp. 125–128.
3. Schmuck, H., Heidemann, R., and Hofstetter, R., "Distribution of 60 GHz signals to more than 1000 base stations," *Electron. Lett.*, vol. 30, 1994, pp. 59–60.
4. Lima, C. R., Wake, D., and Davies, P. A., "Compat optical millimetre-wave source using a dual mode semiconductor laser," *Electron. Lett.*, vol. 31, 1995, pp. 364–366.
5. Mitomi, O., Noguchi, K., and Miyazawa, H., "Design of ultra-broad-band LiNbO<sub>3</sub> optical modulators with ridge structure," *IEEE Trans. Microwave Theory Tech.*, vol. 43, 1995, pp. 2203–2207.
6. Hofstetter, R., Schmuck, H., and Heidemann, R., "Dispersion effects in optical millimetre-wave systems using self-heterodyne method for transport and generation," *IEEE Trans. Microwave Theory Tech.*, vol. 43, 1995, pp. 2263–2269.

7. Walker, N. G., Wake, D., and Smith, I. C., "Efficient millimetre-wave signal generation through FM-IM conversion in dispersive optical fibre links," *Electron. Lett.*, vol. 28, 1992, pp. 2027–2028.
8. Nagarajan, R., Levy, S., Mar, A., and Bowers, J. E., "Resonantly enhanced semiconductor lasers for efficient transmission of millimetre wave modulated light," *IEEE Photonics Technol. Lett.*, vol. 5, 1993, pp. 4–6.
9. Goldberg, L., Taylor, H. F., and Weller, J. F. "Microwave signal generation with injection-locked laser diodes," *Electron. Lett.*, vol. 19, 1993, pp. 491–493.
10. O'Reilly, J. J., and Lane, P. "Remote delivery of video services using mm-waves and optics," *J. Lightwave Tech.*, vol. 12, 1994, pp. 369–375.
11. Simonis, G. J., and Purchase, K. G., "Optical generation, distribution, and control of microwave using laser heterodyne," *IEEE Trans. Microwave Theory Tech.*, vol. 38, 1990, pp. 667–669.
12. Birkeland, J., and Itoh, T., "Two-port FET oscillators with applications to active arrays," *IEEE Microwave Guided Wave Lett.*, vol. 1, 1991, pp. 112–113.
13. Kitayama, K., Kuri, T., Yokoyama, H., and Okuno, M., "60 GHz millimetre-wave generation and transport using stabilized mode-locked laser diode with optical frequency DEMUX switch," *IEEE Global Telecommunications Conference*, London, 1996, pp. 2162–2169.
14. Noël, L. Marcenac, D., and Wake, D., "Optical millimetre-wave generation technique with high efficiency, purity and stability," *Electron. Lett.*, vol. 32, 1996, pp. 1997–1998.
15. Wake, D., Lima, C. R., and Davies, P. A., "Optical generation of millimetre-wave signals for fibre-radio systems using a dual-mode DFB semiconductor laser," *IEEE Trans. Microwave Theory Tech.*, vol. 43, 1995, pp. 2270–2276.
16. O'Reilly, J. J., Lane, P. M., Heidemann, R., and Hofstetter, R., "Optical generation of very narrow linewidth millimetre wave signals," *Electron. Lett.*, vol. 28, 1992, pp. 2309–2311.
17. O'Reilly, J. J., and Lane, P., "Fibre-supported optical generation and delivery of 60 GHz signals," *Electron. Lett.*, vol. 30, 1994, pp. 1329–1330.
18. O'Reilly, J. J., Lane, P. M., Capstick, M. H., Salgado, H. M., Heidemann, R., Hofstetter, R., and Schmuck, H., "RACE R2005: microwave optical duplex antenna link," *IEE Proc. J.*, vol. 140, 1993, pp. 385–391.
19. Goldbertg, L., Yurek, A. M., Taylor, H. F., and Weller, J. F. "35 GHz microwave signal generation with an injection-locked laser diode," *Electron. Lett.*, vol. 21, 1985, pp. 814–815.
20. Schöll, H., and Burkhard, H., "Ultra high repetition rate optical pulse generation by continuous light injection into a continuous wave operated distributed feedback laser," *Jpn. J. Appl. Phys.*, vol. 34, 1995, pp. 1358–1361.
21. Wake, D., Lima, C. R., and Davies, P. A. (1996), "Transmission of 60 GHz signals over 100 km of optical fibre using a dual-mode semiconductor laser source," *IEEE Photonics Technol. Lett.*, vol. 8, 1996, pp. 578–580.
22. Wake, D., "Ultrafast optoelectronic devices for fibre-radio systems," *Proceedings IEEE MTT-S Optical Microwave Interactions*, Paris, 1994, pp. 181–184.
23. Wake, D., Spooner, T. P., Perrins, S. D., and Henning, I. D., "50 GHz InGaAs edge-coupled PIN photodetector," *Electron. Lett.*, vol. 27, 1991, pp. 1073–1074.
24. Wake, D., Walker, N. G., and Smith, I. C., "Zero bias edge-coupled InGaAs photodiodes in millimetre-wave radio-fibre systems," *Electron. Lett.*, vol. 29, 1993, pp. 1879–1880.

25. Wake, D., Nelson, D. J., Harlow, M. J., and Henning, I. D. "Optically-biased edge-coupled InP/InGaAs heterojunction phototransistors," *Electron. Lett.*, vol. 29, 1993, pp. 2217–2219.
26. Wake, D., Noël, L., Moodie, D. G., Marcenac, D. D., Westbrook, L. D., and Nasset, D., "A 60 GHz 120 Mb/s QPSK fibre-radio transmission experiment incorporating an electro-absorption modulator transceiver for a full duplex optical data path," *IEEE MTT-S Int. Microwave Symp. Dig.*, 1997, pp. 591–594.
27. Frigo, N. J., Iannone, P. P., Magill, P. D., Darcie, T. E., Downs, M. M., Desai, B. N., Koren, U., Koch, T. L., Dragonne, C., Presby, H. M., and Bodeep, G. E., "A wavelength division multiplexed passive network with cost-shared components," *IEEE Photonics Tech. Lett.*, vol. 6, 1994, pp. 1365–1367.
28. Westbrook, L. D., and Moodie, D. G., "Simultaneous bi-directional analogue fibre-optic transmission using an electroabsorption modulator," *Electron. Lett.*, vol. 32, 1996, pp. 1806–1807.
29. Pozar, D. M., and Schaubert, D. H. (eds.), *Microstrip Antennas*, IEEE Press, New York, 1995.
30. Suematsu, E., and Imai, N., "A fibre optic/millimetre-wave radio transmission link using HBT as direct photodetector and an optoelectronic upconverter," *IEEE Trans. Microwave Theory Tech.*, vol. 44, 1996, pp. 133–143.
31. Cooper, G. R., and McGillem, C. D., *Modern Communications and Spread Spectrum*, McGraw-Hill, New York, 1986, pp. 252–253.
32. Couch, L. W. II, *Digital and Analogue Communication Systems*, 3rd ed., Macmillan, New York, 1990.
33. Balanis, C. A., *Antenna Theory Analysis and Design*, Wiley, New York, 1982, pp. 63–65.
34. Levine, E., Malamud, G., Shtrikman, S., and Treves, D., "A study of microstrip array antennas with feed network," *IEEE Trans. Antennas Propag.*, vol. 37, 1989, pp. 426–434.
35. Pozar, D. M., *Microwave Engineering*, Addison-Wesley, New York, 1993.
36. Cohn, S. B., "Parallel-coupled transmission-line resonator filters," *IRE Trans. Microwave Theory Tech.*, vol. 6, 1958, pp. 223–231.
37. Pues, H. and Van De Capelle, A., "Accurate transmission-line model for the rectangular microstrip antenna," *IEE Proc.*, vol. 131H, 1984, pp. 334–340.
38. Milano, R. A., Dapkus, P. D., and Stillman, G. E., "An analysis of the performance of heterojunction phototransistors for fibre optic communications," *IEEE Trans. Microwave Theory Tech.*, vol. 29, 1982, pp. 266–274.
39. Zürcher, J.-F., *Broadband Patch Antennas*, Artech House, Norwood, MA, 1995.
40. Cryan, M. J., Hall, P. S., Tsang, K. S. H., and Sha, J., "Integrated active antennas with simultaneous transmit–receive operation," *Proceedings of the 26th European Microwave Conference*, Prague, vol. 2, 1996, pp. 565–568.



## CHAPTER ELEVEN

---

# Conclusions

---

### **PETER S. HALL**

School of Electronic and Electrical Engineering  
The University of Birmingham  
Edgbaston, Birmingham, UK

### **K. C. GUPTA**

Department of Electrical and Computer Engineering  
University of Colorado  
Boulder, CO

## **11.1 INTRODUCTION**

Chapter 1 set the scene for the following chapters by giving an introduction to the topic of integrated circuit–antenna modules, with a glossary of module types and an overview of the design needs. It therefore seems appropriate to conclude the book with a final chapter that draws the many threads together by attempting to describe the current capabilities and what now needs to be done. There are obvious dangers in attempting such a description, since what we suggest is in the future may in fact be happening now and our statements of limitations of methods may be contested by their advocates. However, we feel that the benefits of this chapter will outweigh the problems and we ask the reader to take it in the spirit that it was intended.

In formulating the contents of this book, we deliberately chose analytical and simulation methods that were representative of broad classes. In this chapter we hope to broaden our coverage by referring to other techniques, however briefly, so that the reader can pursue them if required. Nevertheless, in our searches through the literature, we have found that by far the most publications concern the methods described in the earlier chapters. In this sense, the book contents accurately reflect the concentration of current activity. In the future this balance may change; we hope our comments on the future are reasonably accurate.

The topic of integrated circuit–antenna modules has long been an aspiration of engineers. It is now being realized with numerous innovative configurations being created for increasingly specific applications. Grids for power generation of millimeter wavelengths are now reaching the prototype stage at which detailed manufacturing and operational issues are being addressed. Active integrated antennas for personal devices such as smart cards and very-short-range communications are being developed.

This situation makes it very clear that improved design tools are now very much needed. The introductory chapter mentioned the need for design engineers skilled in both circuits and antennas. While this is true, they need to be supported by CAD techniques that can handle their needs and speed up the design process. It is now possible to buy commercial design software that begins to meet these needs, although much of what is described in this book is far from being available commercially. Pioneer companies developing such technology have to invest heavily in personnel and software development, often in collaboration with universities and research institutes. One of the aims of this book has therefore been to raise the profile of the topic so that commercial software providers start to accelerate the provision of tools to enable faster and more accurate design.

## 11.2 OVERVIEW OF ANALYTICAL METHODS

### 11.2.1 Introduction

The development of analytical tools for integrated circuit–antennas modules essentially concerns the integration of tools for circuits and for antennas. Such tools have been available for some time, but new developments are continually being seen. Some convergence of tools for antennas and passive circuits has been evident for some time. For example, the method of moments is now regularly used for analysis of both printed circuit antennas and circuits. The key issue is therefore the inclusion of active devices into large passive structures.

There are many parallels that can be drawn concerning modeling of active devices and passive structures:

- Numerical techniques of the type described in this book and others [1] can be applied to both. In active devices charge transport mechanisms must be appropriately modeled to extract device performance in terms of geometry,

semiconductor properties, bias, and signal level. Similarly, with passive circuits and antennas the aim is to find the performance for a given geometry and material properties.

- Equivalent circuit representations can be made of both the active and passive components. Such representations can be derived from measurements or from the numerical simulations noted above.

The differences between device and structure modeling are as follows:

- Scale is the most obvious difference. Passive circuit–antenna structures may be many wavelengths across, while active devices are usually very much smaller than a wavelength. This leads to difficulties in direct combination of numerical techniques using gridding, unless the problem is partitioned with different mesh sizes.
- Although there are a wide range of semiconductor devices available, device parameters are fixed by the supplier and the user often has no control in the device design process. On the other hand, the circuit–antenna module designer has a large degree of control in the configuration and performance of the passive part of the module. This gives rise to the situation in which the device supplier only needs a representation of the component while the module designer needs a tool to support development and optimization. Thus all of the methods described in this book use equivalent circuit device models.

### 11.2.2 Problem Scale

In comparing available methods for integrated circuit–antenna modules, it is appropriate to classify the relative scales of the problems involved. Table 11.1 shows three scales.

Radiation patterns and dynamics of arrays or grids are determined by features much smaller than a wavelength in the passive structure and, of course, in the semiconductor device. In this case the structure is too large to analyze using conventional numerical methods, such as method of moments, or finite-element or finite-difference methods and the techniques described in Chapters 7 and 8 must be used. So far, large array dynamics have only been investigated by the use of very

**TABLE 11.1 Scale of Analytical Problems**

Device	Overall Size <sup>a</sup>	Feature Size <sup>a</sup>
Antenna array or grid	Many wavelengths	Of order $\lambda/10$
Array element or grid element	Comparable to a wavelength	Of order $\lambda/10$
Semiconductor active device	10 to 100 $\mu\text{m}$	Submicron

<sup>a</sup>Sizes are approximate only and are given to indicate the order of the problem.

simplified equivalent circuit models as in Chapter 7, although for small arrays the finite-difference time-domain method has been shown to be useful (Chapter 6). The unit-cell approach, defined in Chapter 8, uses accurate element modeling combined with a Floquet mode method to represent an infinite array. In that chapter, the induced EMF method and method of moments is used. In principle, any method can be used; the use of finite-difference time-domain combined with phase walls for a passive array has recently been reported [2].

Element modeling can be performed with numerous methods and these are compared in more detail in the next section. As noted above, these are all attempts to include equivalent circuit device models into conventional methods for analyzing passive electromagnetic structures.

In most integrated circuit–antenna modules the device feature size is several orders of magnitude smaller than the passive sections. Modeling can be done in a number of ways:

- Monte Carlo method
- Drift-diffusion methods/physical modeling
- Parameter fitting methods
- Equivalent circuit methods

In Monte Carlo methods [3,4], device performance is deduced from averages of computations of the behavior of large numbers of electrons based on known scattering processes. Computation times can be large. Physical modeling methods [5] solve the electromagnetic and drift-diffusion equations in the two- or three-dimensional device interaction space. Again computation times can be great. In parameter fitting, characteristics measured across the semiconductor wafer are fitted to polynomials to allow performance to be calculated. Equivalent circuit methods [6] usually have a physical basis in that circuit components often represent well-understood mechanisms within the device. Device performance can then be calculated using circuit solvers operating in the time domain.

### 11.2.3 Comparison of methods

Table 11.2 gives a comparison of the characteristics of some of the methods used in analysis and simulation of integrated circuit–antenna modules. In the comparison, it is assumed that the methods are required for printed circuit based modules using, for example, microstrip, slotline, or coplanar waveguides.

1. *Equivalent Circuit Method.* Primarily developed for circuit design, the method has been extended to antennas, where it is appropriate for geometries that support either well-defined single-mode resonances, such as a thin microstrip patch or thin slot, or for traveling wave antennas. It will not, in principle, analyze arbitrary shaped antennas or circuit components. It is easy to incorporate active devices where these are represented by equivalent circuits.

**TABLE 11.2 Comparison of Some Analysis and Simulation Methods for Circuit–Antenna Modules**

Method	Chapter	Good Flexibility for Arbitrary Structures	High Speed	Low Complexity	Good Accuracy	Ease of Incorporating Active Device
Equivalent circuit	3	×	√√√	√√√	√	√√√
Multiport network	4	√	√√	√√	√√	√√
Integral equation	5	√	√	×	√√√	√
Finite-difference time-domain	6	√√	×	√	√√√	√
Finite element		√√√	×	×	√√√	√
Transmission line matrix		√√	×	√	√√√	√

× = poor, √ = moderate, √√ = good, √√√ = very good.

It is fast and easy to implement but, in general, has good accuracy only for well-characterized systems. Nonlinear performance can be obtained provided the device model supports it.

2. *Multiport network method (MNM)*. MNM is a network-based method that allows analysis of a wider range of antenna shapes. More computation (compared to the equivalent circuit method) is required with consequent speed reduction. It will give better accuracy in radiation pattern prediction than the equivalent circuit model.
3. *Integral Equation Methods*. These are computationally intensive methods with relatively slow speed that will handle arbitrary shaped printed antennas and dielectric layers. Finite ground planes and slabs can be dealt with only by special additions. Accuracy can be excellent, but the addition of an active device using equivalent circuit models is less straightforward, as care is needed to derive appropriate voltages and currents at device terminals.
4. *Finite-Difference Time-Domain Methods*. These are in general simpler to formulate than integral equation methods but again are computationally intensive. Finite substrate and metallization can easily be included, as can arbitrary shaped antennas and circuit components. Operation in the time domain allows nonlinear effects such as intermodulation and harmonics to be easily obtained. Care is needed with inclusion of active device equivalent circuits.
5. *Finite-Element Methods*. Little work has been done on finite-element methods for integrated circuit–antenna modules. The finite-element method in the frequency domain has recently been extended to include lumped elements [7]. Operation in the time domain gives some advantages and Guillouard et al. [8] describe the combination of the finite-element time-domain with the SPICE method. The authors are aware of no comparative studies between

this method and other methods, although as shown in Table 11.2, it is expected to have broad characteristics similar to the finite-difference time-domain method.

6. *Transmission Line Matrix (TLM) Method.* The TLM method has widely been used for a variety of electromagnetic problems, including structures with lumped elements [9] and nonlinear elements [10–13]. In principle, it can be used to model arbitrary shaped finite structures, but it is relatively complex to implement and computationally intensive and hence slow. It can be accurate and, because it is based in the time domain, can give the module's nonlinear performance. Although field components are calculated from the matrix voltage and currents, care is still required in attaching the active device model.

#### 11.2.4 Other Methods

All of the methods compared in Table 11.2 use an equivalent circuit representation of the active device. Thus the accuracy is ultimately limited by the quality of the parameter specification in the equivalent circuit. To avoid this problem, a physical model of the device can be linked to the electromagnetic structure simulator. In [14] a Si-MMIC switch at 76 GHz is analyzed by linking a  $13 \times 79 \times 64$  cell three-dimensional FD-TD simulation with a 121-point one-dimensional device simulation incorporating a charge conservation and drift-diffusion modeling. In [15] a millimeter-wave amplifier is modeled in a similar way. The device and circuit regions remain separate to allow different gridding and time stepping but computation is nevertheless quasisimultaneous. The advantage of integrated physical modeling is not only the potential for improved device simulation, but also to allow the performance of the integrated package to be included as a parameter in the semiconductor process optimization.

### 11.3 THE FUTURE

Analysis of integrated circuit–antenna modules is now a fast-moving research area where developments in analysis and simulation are leading to better understanding of the potential and limitations of the modules, together with improvements in design capabilities.

There is a continuing need to demonstrate the performance of the methods on the wide range of module configurations discussed in chapter 1. In particular, there are relatively few published studies showing accurate analysis of nonlinear performance of, for example, harmonic control in antenna oscillators and conversion loss in mixer antennas.

Such demonstrations are important to provide user confidence and understanding and to pave the way for commercial software suppliers to begin to market some of the high order methods noted in Table 11.2. Software provision must also proceed

with an awareness of the need that designers have for a variety of design tools, ranging from fast, approximate methods to those that are highly accurate and computationally intensive.

The current division between active device design and passive circuit–antenna design has been noted throughout this concluding chapter. The integration of electromagnetic solvers with physical modeling allows some optimization of the complete module, including active device processing parameters. This degree of design integration could be very important for future MMIC circuit–antennas modules. However, bearing in mind the fluctuations in device performance for a given set of processing parameters, it is not clear at this stage just how significant this development might be.

Many of the applications suggested for integrated circuit–antenna modules are in the low cost, mass market personal communications and sensor areas. In some of these applications, the effect of the local environment on the module may be significant. It may well be that the system will be set up so that it will not be vulnerable to such perturbations. Nevertheless, there may well be a future demand for analytical models that allow the effects of the local environment to be included. Environmental effects on passive antennas, such as the interaction of the head and hand on the operation of cellular telephone handsets, is now being widely investigated with, for example, the finite-difference time-domain methods. With the increasing importance of “wearable” communications devices such studies will continue. If integrated circuit–antenna modules are to have an impact on this market sector, then analyses must be capable of including such effects.

This book has described analytical techniques for the design of integrated circuit–antenna modules. Such techniques have developed in the last decade and are now of great significance for the future progress of the technology. There are challenges yet to be met and the area still remains a fertile one for analysts and engineers alike.

## REFERENCES

1. Itoh, T. (ed), *Numerical Techniques for Microwave and Millimetre Wave Passive Structures*, Wiley, New York, 1989.
2. Alexanian, A., Koliass, N. J., Compton, R. C., and York, R. A., “Three dimensional FD-TD analysis of quasi-optical arrays using Floquet boundary conditions and Berenger’s PML,” *IEEE Microwave Guided Wave Lett.*, vol. 6, no. 3, Mar. 1996, pp. 138–140.
3. Jacaboni, C., and Reggiani, L., “The Monte Carlo method for the solution of charge transport in semiconductors with applications to covalent materials,” *Rev. Mod. Phys.*, vol. 55, no. 3, 1983, p. 646.
4. Fischetti, M. V., and Laux, S. E., “Monte Carlo simulation of submicron Si MOSFETs,” in *Simulation of Semiconductor Devices and Processes*, vol. 3, G. Baccarani and M. Rudan (eds.), Pineridge Press, Swansea, UK, 1988, p. 349.
5. Hansch, W., “The drift diffusion equation and its applications to MOSFET modelling,” in *Computational Microelectronics*, Springer-Verlag, New York, 1991.

6. Ladbrooke, P. H., *MMIC design GAAs FETs and HEMTs*, Artech House, Boston, 1989.
7. Guillouard, K., Wong, F.-F., and Fouad Hanna, V., "New global finite element analysis of microwave circuits including lumped elements," *IEEE MTT-S Symp. Dig.*, 1996, pp. 355–358.
8. Guillouard, K., Wong, M.-F., Fouad Hanna, V., and Citerne, J., "New global time domain electromagnetic simulator of microwave circuits including lumped elements based on finite element method," *IEEE MTT-S Symp. Dig.*, 1997, pp. 1239–1242.
9. Russer, P., Isele, B., Sohby, M., and Hosny, E. A., "A general interface between YLM models and lumped element circuit methods," *IEEE MTT-S Symp. Dig.*, 1994, pp. 891–894.
10. Voelker, R. H., and Lomax, R. J., "A finite difference transmission line matrix method incorporating a non-linear device model," *IEEE Trans. Microwave Theory Tech.*, vol. 38, no. 3, 1990, pp. 302–312.
11. Russer, P., So, P. P. M., and Hoefler, W. J. R., "Modelling of non-linear active regions in TLM method," *IEEE Microwave Guided Wave Lett.*, vol. 1, no. 1, Jan. 1991, pp. 10–13.
12. Hoefler, W. J. R., Isele, B., and Russer, P., "Modelling of non-linear active devices in TLM," *IEE International Conference on Computation in Electromagnetics*, London, Nov. 1991, pp. 25–27.
13. Cascio, L., Tardick, G., and Hoefler, W. J. R., "Modelling of non-linear active and passive devices in three dimensional TLM networks," *IEEE MTT-S Symp. Dig.*, 1997, pp. 383–386.
14. Ciampolini, P., Roselli, L., and Stopponi, G., "Integrated FD-TD and solid state device simulation," *IEEE Microwave Guided Wave Lett.*, vol. 6, no. 11, Nov. 1996, pp. 419–421.
15. Imtiaz, S. M. S., and El-Ghazaly, S. M., "Global modeling of millimeter-wave circuits: electromagnetic simulation of amplifiers," *IEEE Trans. Microwave Theory Tech.* vol. 45, no. 12, pt. 2, Dec. 1997, pp. 2208–2216.



---

# Index

---

- Absorbing boundary condition
  - Mur's ABC, 233–237
  - PML, 233, 237–240
- Active arrays, 4, 5, 333–334
  - free-running arrays, 269–272
  - fully active, 7
  - phased array(s)
    - concepts, 333
    - egg-crate honeycomb-structure, 335
    - MERA array, 340
    - module(s) early, 337
    - radiating elements, 338
    - RASSR array, 341
    - technology, 333
  - scanning array, 12
  - semiaactive, 7
  - switching array, 12
- Active device(s), 79, 343–345
  - HBTs, 344
  - HFETs, 344
  - GaAs FETs, 339
  - PHEMTs, 344
  - silicon bipolar transistor, 339
- Active radomes and lenses, 13
- Advanced (T-R) module packaging programs, 350–356
  - HDMP, 350–351, 353
  - MAFET, 350
  - MIMIC, 350
  - RF-WSI, 350–356
- Amplifier
  - class-E, 324–325
  - integrated with patch antenna, 88
- Amplitude dynamics, 263–264
- Analysis
  - printed patches, 58
  - slots, 58
- Analytical methods
  - comparison, 413, 414
  - overview, 411
- ANN, *see* Artificial neural network
- Antenna(s), 73–75
  - active, 4, 5
  - active integrated, 4, 6
  - amplifying, 7, 10
  - arrayed radiating elements, 337
  - broadcast receive, 5
  - circulator, 91
  - conventional, 334–335
  - diplexer, 375, 381–385
  - electrically short, 7
  - equivalent circuits, 73
  - FDTD characterization, 242–246
  - frequency agile, 10
  - frequency conversion, 10
  - gimbals, 335
  - input impedance, 242
  - mixing, 10
  - optically controlled, 11
  - oscillating, 9
  - patch, 378–387
    - matching, 378–381
    - microstrip patch, 75
    - simulation, 389–391

- Antennas (*continued*)
  - phase-shifted elements, 336
  - polarization agile, 11
  - radiating elements, 333
  - radiation pattern, 96, 203, 242–246, 275, 321, 401
  - satellite communications, 5
  - self oscillating mixer, 10
  - slot, 73
    - fed by nonleaky coplanar waveguides, 246–247
    - modeling, 55–58
    - tapered slot, 74, 247–248
  - types, 73
  - vehicle
    - radio, 5
    - TV, 5
  - wideband, 7
- Arrays
  - active, *see* Active arrays
  - free-running, 269–272
  - passive, phased arrays, 335–336
  - quasi-optics, 4,6
  - receiver array, 279
  - retrodirective array, 13
- Artificial neural network (ANN), 32
- Attachment mode, 182
- Beam
  - scanning array, 12
  - switching array, 12
- Beam-steering, *see* Scanning techniques
- Bilateral nearest-neighbor injection-locking, 260–261
- Bipolar PD, *see* photoHBT
- Broadband coupling, 266
- CAD, *see* Computer-aided design
- Calibration standards, 187–189
- Cavity model, 49, 77
- Cellular handsets, 5
- Circuit-antenna integration modules
  - full, 14
  - nonintegration, 14
  - partial, 14
- Circuit-antenna modules
  - application, 5
  - types, glossary, 6–14
- Circuit model, microstrip patch antenna, 75
- Circular function, 309
- Closed form analysis for radiation, 93
- Compression technique, 211, 217–218
- Computer-aided analysis, 32
- Computer-aided design (CAD), 27–28
  - fully integrated modules, 62
  - integrated circuit-antenna modules, 61
  - microwave circuits, 29
  - nonintegrated modules, 61
  - partially integrated modules, 61
  - printed antennas, 47
- Continuum model, 273–274
- Coplanar waveguide (CPW), 213, 246
- Coupled oscillators, 260–291
- Coupling
  - delay, 267
  - networks, 261, 267–269
  - parameters, 267
  - phase, 267–268
  - resistance, 267
- Contour integral method, 123
- Deembedding procedure, 194, 196, 199
- Desegmentation method, 123, 145–147
- Design process, 14, 23
  - anatomy of, 23
  - computer-aided design (CAD), 27. *See also* Computer-aided design (CAD)
  - concept generation, 24
  - conventional procedure, 25
  - initial design, 24
  - knowledge-aided design (KAD) approach, 28
- Dielectric resonators, 74
- Digital signal processing, 2
- Diode phase shifters, 336
  - hybrid couplers terminated in varactor diodes, 336
  - switched lengths transmission line, 336
- Direct matrix equation method, *see* Matrix equation method, direct
- Discrete components, 178
- Discrete element, 194, 198
  - in a gap, 194
- Edge admittance network, 123, 135
  - edge capacitance, 137
  - edge conductance, 135
  - edge inductance, 137
  - generalized edge conductance network, 136
- Effective isotropic radiated power, 16
- Effective loss tangent, 52
- Electromagnetic (EM) simulation, 54
- Equivalence principle, 174
- Equivalent circuit models
  - active devices, 79
  - cavity model, 77
  - for nonlinear simulation, 97

- passive components, 77
  - transmission line, 75
  - two-dimensional, 76
- Fast Fourier transform (FFT) algorithm, 214
- FDTD, *see* Finite-difference time-domain
- Ferrite, 333–338
  - circulators, 333
  - latching phase shifters, 336
  - nonreciprocal phase shifters, 337, 338
  - phase shifters, 336
  - reciprocal phase shifters, 337, 338
- Fiber network local access, 5
- Filter
  - bandpass, 377
  - bandstop, 395, 399, 403
  - microstrip coupled, 376
- Finite-difference time-domain (FDTD)
  - central difference, 226
  - extended, 249–256
  - field excitation of the dominant propagation mode
    - coplanar waveguide, 231
    - microstrip, 231
  - method, 54
  - stability criterion, 227
- FM-IM, 361
- Free-running arrays, 269–272
- Frequency
  - electromagnetic approach, 211
  - conversion arrays, 13. *See also* Grid, frequency doubler
  - doubling, 115
  - shift keying (FSK), 105
- Full integration, *see* Circuit-antenna integration modules
- Galerkin procedure, 182
- Generalized impedance submatrix, 183
- Generalized admittance submatrix, 183
- Global
  - approach, 210
  - electromagnetic analysis, 199, 202
  - electromagnetic approach, 173, 218
  - formulation, 217
  - method, 211
- Green's functions, 175, 177
- Grid
  - amplifier, 8
  - directional coupler, 9
  - frequency doubler, 8
  - isolator, 9
  - modulator, 9
- oscillator(s), 8
  - analysis, 304–313
  - design, 314–319
  - optimization, 320–323
  - phase shifter, 8
  - switching array, 9
- Harmonic balance, 97
  - method, 44, 211, 212, 217–218
- Harmonics, 106
- High power transmitters, solid state, 338
- Ideal source in method of moments, *see* Method of moments, ideal source
- IL, *see* Injection-locking
- ILPLL, *see* Injection-locked phase locked loop
- Impedance/admittance matrix elements, 183
- Indoor communications, 5
- Infinitesimal gap, 178
- Injection-locked phase-locked loop (ILPLL), 293–295
- Injection locking (IL), 112, 259, 280
- Integral equations formulation, 174
- Integrated equation method, 54
- Integrated network analysis and electromagnetic simulation, 62
  - finite-difference time domain (FDTD) method, 64
  - frequency domain simulation, 62
  - time domain simulation, 64
  - transmission line matrix (TLM) method, 66
- Integration levels, 6
- Interinjection-locking, *see* Coupled oscillators
- Isotropic conversion loss, 16
- Iteration matrix equation method, *see* Matrix equation method, iteration
- KAD, *see* Knowledge-aided design
- Knowledge-aided design (KAD), 28
  - propose-critique-modify (PCM) approach for initial design, 29
- Kurokawa substitution, 296–298
- Large signal
  - equivalent models, 80–83
  - simulation, 102
- Laser
  - distributed feedback (DFB), 360, 365
  - dual-mode, 364–365
  - master/slave, 365, 366
- Linear
  - frequency domain equation, 214
  - simulation, 83–87

- Link stability, 389
- Loading condition in method of moments, *see*
  - Method of moments, loading condition
- Locking range, 267
- Low noise amplifier, 89
- Lumped elements in method of moments, *see*
  - Method of moments, lumped elements
  
- Mack-Zehnder, 363
  - frequency-doubling method, 365
  - optical modulation, 363–365
- Matching network, for photoHBT-patch antenna
  - integration, 391
- Matched termination in method of moments, *see*
  - Method of moments, matched termination
- Matrix equation method
  - direct, 180
  - integrative, 180
- Method of moments, 180
  - ideal source, 177
  - loading condition, 185
  - lumped elements, 178–179
    - concept, 189
    - N*-port, 180
  - matched termination, 177
  - mixed potential formulation, 175
  - operator equation, 181
- Microwave Design System (MDS) software, 84,
  - 91, 384, 391, 402–403
- Military radars, 5
- Millimeter-wave, 360, 369
  - band, 2
- Millimeter and submillimeter wave
  - beam scanning, 5
  - power generation, 5
  - signal processing, 5
- Mixed potential formulation in method of
  - moments, *see* Method of moments, mixed
    - potential formulation
- Mode-hopping, 264
- Modeling of circuit components, 30
- Monopole, active, 2
- Multiport network method, 121
  - analysis, 142
  - approach, 122
  - examples, 58–161
  - feed network, 151–154
  - for two-layer antennas, 147–161
  - integrated circuit-antenna modules, 161–167
    - Gunn diodes with patches, 163–167
    - varactor diodes with patches, 161–163
  - patch network, 150–151
  - mathematical formulation, 155–158
- Multiport network model (MNM), 121–158
- Mutual coupling network, 124–125, 138–142
- Mutual synchronization, *see* Coupled oscillators
  
- Nearest-neighbor coupling, 266–267
- Negative resistance, 265–266
- Newton–Raphson algorithm, 214
- Network modeling
  - antennas, 121
  - microstrip patches, 47
- Nodal admittance matrix, 33
- Noise performance, of the radio on fiber system,
  - 374
- Nonintegrated systems, *see* Circuit-antenna
  - integration modules
- Nonlinear, 97
  - circuit analysis, 43
  - dynamic steady-state analysis, 214
  - simulation, *see* Equivalent circuit models,
    - nonlinear simulation
  - time domain equation, 214
- Numerical
  - capacitance, 196
  - deembedding procedure, 192
  - parasitic capacitance, 198
  - parasitic elements, 196
  
- Operator equation for method of moments, *see*
  - Method of moments, operator equation
- Optical heterodyning, 362
- Optimization, circuit, 45
- Oscillator
  - arrays, 326–328
  - class-E, 323–326
  - grids, *see* Grid oscillators
  - model
    - parallel, 265
    - series, 266
  - modeling, 265–266
  - patch, *see* Patch oscillator
  
- Packaging effects, active antenna, 114
- Parallel oscillator model, *see* Oscillator model,
  - parallel
- Partial integration, *see* Circuit-antenna integration
  - modules
- Passive
  - grid phase shifters, 337
  - phased arrays, 335–336
- Patch
  - amplifier simulation, 88
  - array, 74
  - microstrip, 74, 84

- oscillator simulation, 84
- Perfect conductor
  - electric, 228
  - magnetic, 228
- Performance parameters, 16
- Personal communications, 2
- Personnel monitoring, 5
- Phase dynamics, 263–264, 266–272
- Phase locked loops (PLL), 259, 291–293
  - phase, noise, 283–291
  - shift keying, 105, 112
- PhotoHBT, 369, 371–372, 386
- Pin photodiode, 369–370
- PLL, *see* Phase locked loops
- Power combining
  - array, 12
  - quasi-optical, 301–302
  - spatial, 301–302
- $Q$ -factor, 262
- Quasi-optic arrays, 4, 6
- Radar systems, 334
  - classes, 335
  - conventional, 334
  - elements, 334
  - range and power, 336
  - RF-transmitter, 334–335
- Radio on fiber, 358–359, 372, 394
- Realistic modeling, active antenna analysis, 207
- Receiver array, *see* Scanning oscillator array
- Rectangular elementary domains, 181, 182
- Rectenna, 11
- Reduced mutual coupling array element, 7
- Reflection coefficient, 400
- Retrodirective array, 13
- RF-WSI program, 350–356
  - circuit redundancy, 352
  - layered architecture, 352
  - tile-approach, 354
  - (T-R) module-tile approach, 350–356
- S parameters, *see* Scattering parameters
- Satellite radar, 5. *See also* Antenna types, satellite communications
- Scanning oscillator array, 279
- Scanning techniques, 272–275
- Scattering
  - matrix analysis, 38
  - parameters, 94, 241–242
- Segmentation method, 122, 142–145, 217
- Series oscillator model, *see* Oscillator model, series
- Slowly-varying envelope approximation, 262
- Space communications, 5
- Stability analysis, 269–271
- Steady-state, 264
- Subdomain basis functions, 182
- Synchronization, *see* Coupled oscillators
- Tagging, 5
- Terrestrial communications, fiber network local access, 5
- Transceiver, single-chip, 2
- Transient analysis, 275–276
- Transmission line model
  - microstrip patch, 47
  - slot antenna, 55–58
- Transmit-receive, 279, 358, 394–402
- Transmit-receive (T-R) modules, 333–356
  - block diagram, 339
  - design considerations, 341–356
    - computer-aided design, 348
    - control components, 346
    - interconnect technology, 343, 347–378
    - low noise amplifier (LNA), 345
    - LTCC substrates, 348, 350
    - MHDI interconnects, 348
    - packaging, 343, 348–349
    - receiver circuits, 343–346
    - RF chip architecture, 343, 346–347
    - solid state transmitter, 343, 344
    - thermal considerations, 349
  - early (T-R) modules, 337–339
  - elements, 338
  - GaAs chip sets, 342
  - major parts, 342
  - MERA module, 339
  - module programs, 341
  - present trends and future directions, 350–357
    - ARPA and tri-service programs, 350–357
    - RF-WSI program, 350–357
      - 35 GHz design, 355–357
    - RASSR module, 339, 340
    - state-of-the-art, 342
- Transponder(s), 11
  - frequency doubling, 115
- Transport tolling and highway surveillance, 5
- Unilateral injection locking, 261
- Van der Pol, 110
- Wireless smart cards, 5
- X-band (T-R) module, 343–350

X-band (T-R) module, 3 (*continued*)  
  design considerations, 341–356  
  chip architecture, 346–347  
  computer-aided design, 348  
  control components, 346  
  heat removal, 345  
  interconnect technology, 347–348  
  LNA/noise figure, 345

  package design, 348  
  RF power requirements, 343–345  
  thermal design, 349

Z-matrix for patch fields, 122, 126  
  arbitrary-shaped segments, 132–135  
  circular segments, 131–132  
  rectangular segments, 129–131